HAL
open science

On the interaction of fast traveling Ocean Waves and the Atmospheric Boundary Layer : A Mechanistic Approach combining Field Measurements and High-fidelity Simulations

Liad Paskin

To cite this version:

Liad Paskin. On the interaction of fast traveling Ocean Waves and the Atmospheric Boundary Layer : A Mechanistic Approach combining Field Measurements and High-fidelity Simulations. Fluid mechanics [physics.class-ph]. École centrale de Nantes, 2022. English. NNT : 2022ECDN0012 . tel-03888161

HAL Id: tel-03888161

https://theses.hal.science/tel-03888161v1

Submitted on 7 Dec 2022

HAL is a multi-disciplinary open access archive for the deposit and dissemination of scientific research documents, whether they are published or not. The documents may come from teaching and research institutions in France or abroad, or from public or private research centers.

L'archive ouverte pluridisciplinaire **HAL**, est destinée au dépôt et à la diffusion de documents scientifiques de niveau recherche, publiés ou non, émanant des établissements d'enseignement et de recherche français ou étrangers, des laboratoires publics ou privés.

THÈSE DE DOCTORAT DE

L'ÉCOLE CENTRALE DE NANTES

ÉCOLE DOCTORALE N° 602
Sciences pour l'Ingénieur
Spécialité : *Mécanique des Milieux Fluides*

Par
Liad PASKIN

On the interaction of fast traveling Ocean Waves and the Atmospheric Boundary Layer : A Mechanistic Approach combining Field Measurements and High-fidelity Simulations

Thèse présentée et soutenue à l'Ecole Centrale de Nantes, le 15/03/2022
Unité de recherche : UMR 6598, Laboratoire de Recherche en Hydrodynamique, Energétique et Environnement Atmosphérique (LHEEA)

Rapporteurs avant soutenance :

Marie-Noëlle BOUIN	Directrice de recherche Météo France, Plouzané
Valery MASSON	Directeur de recherche Météo France, Toulouse

Composition du Jury :

Présidente :	Marie-Noëlle BOUIN	
Examinateurs :	Sukanta BASU	Associate professor Technical University of Delft, Pays-Bas
	Tihomir HRISTOV	Associate Research Scientist Johns Hopkins University, États-Unis
	Joachim REUDER	Professeur University of Bergen, Norvège
Dir. de thèse :	Sandrine AUBRUN	Professeure des universités École Centrale de Nantes
Co-dir. de thèse :	Boris CONAN	Maître de conférences École Centrale de Nantes
Co-encadrant :	Yves PERIGNON	Ingénieur de recherche École Centrale de Nantes

ÉCOLE CENTRALE NANTES

PHD THESIS IN HYDRODYNAMICS AND OCEAN

On the interaction of fast traveling Ocean Waves and the Atmospheric Boundary Layer: A Mechanistic Approach combining Field Measurements and High-fidelity Simulations.

Author
LIAD PASKIN

Director
Prof. Sandrine AUBRUN

Co-Supervisors
Dr. Boris CONAN Dr. Yves PERIGNON

July 11, 2022

DEDICATION

This Thesis is warmly dedicated to the memory of most loved and inspiring people. With greatest love and gratitude for my grandparents Ida Benbassat Paskin, and Max Paskin, that in life granted me the ethical values and educational means to pursue and achieve better goals. To the past and living memories of the scientists and professors, who either direct or indirectly shaped the content and the passion dedicated to this work.

To the unconditional love and support of my closest family. To my father Sami Paskin, who honored and advised me, teaching senses of logical and critical-thinking across uncountable challenges. To my mother Tanise Teruszkin Wiedermann, from whom kind, and love, warm me across the oceans at every moment, and during the darkest winters. To my sisters Stephanie and Caroline Teruszkin Wiedermann, who are my greatest and dearest, sense of home and hope in the future to come. To my grandfather Flavio Teruszkin, who ever inspires and supports me with his wisdom.

To my dearest friends Dan Paskin, Daniel Cozer, Eduardo Bayer, and Igor Nigri, that inspire me from my early childhood. To the dearest friends that life gifted me ever since: Breno Campitelli, Bruno Tessaro, Carlos Besso, Lucas Renzo; Maysa Paiva, Daniel Paiva, Beatriz Paiva, and Gwenael Allan. To all of you, and to the many others that grant me the major privilege of love and family. I am constantly in a state of mind we Brazilians call *'Saudade'*. In this state, missing your loved ones keeps them closer to you even in distance. My greatest deeds are achieved with you, and for you. And I long for the days when we will join together again.

Because a healthy mind cannot thrive only in *'Saudade'*, a special dedication goes to my dearest friends that supported me across the European seasons: Claire Le Gac *'De Oxum'*; Aniket Dastidar, Bernardo Kahn, Cristina Galego, Felipe Giro, Gaëtan Borba, Guillem Fox, Marcos Belchior, Maxime Chemineau, Pedro Veras Guimarães; and to all the wonderful friends surrounding and supporting us. I would not be able to overcome any winter without you by my side, and I surely got the most of our summers.

To all the friends and enlightening people that I have met and could not cite.

ACKNOWLEDGMENTS

This passionate and scientific contribution is fruit of the collaboration of numerous and dearest, persons and institutes. I've been introduced to my current career in the Federal University of Rio de Janeiro (UFRJ), still a second home to me in Brazil. For the knowledge gathered during my years of under graduation, I owe a special acknowledgment to my early professors from the Naval and Ocean Engineering courses, notably to professors Antonio Carlos Fernandes, Claudio Alexis Rodríguez, Jean-David Caprace, Sergio Hamilton Sphaier, and Theodoro Antoun Netto. While following my bachelor, I had the unique opportunity of being embraced in the LAMCE/COPPE/UFRJ laboratory, by my supervisors and friends, Prof. José Luís Drummond Alves, Dr. Carlos Eduardo da Silva, and Dr. Leandro Gazoni. Without you and the brilliant teams, colleagues and environments encountered during that period in COPPE/UFRJ, this work and the others to come would never happen.

It was fueled by their dedication in UFRJ that I've decided to expand my horizons and perspectives in another continent, language, culture, and university, at École Centrale de Nantes, France. From my courses in Hydrodynamics and Ocean, I must thanks the inspiration of Professors Antonie Ducoin, David Le Touzé, Felicien Bonnefoy, Guillaume Ducrozet, Lionel Gentaz, and Pierre Ferrant. It was driven by that inspiration that I sought for a place in the LHEEA laboratory of ECN. I was first embraced by the METHRIC team during my Master Thesis, thanks to the effort of my supervisors and friends Michel Visonneau, Emmanuel Guilmineau, Patrick Queutey, and Jeroen Wackers. Since that time until now, we have been actively supported by the information technology team of LHEEA, so I could not dissociate my career in France to the dedication of Adrien Grellier and Vincent Degat.

My experiences in LAMCE and LHEEA convinced to commit my career into research, so culminating in this Thesis. The warmest gratitude must be expressed to the EMO team of LHEEA, and to my supervisors Sandrine Aubrun, Boris Conan, and Yves Perignon. For so embracing me in LHEEA once again, investing themselves, trusting and guiding me in the pursue of the most ambitious step into my academic career, i.e., developing an original and meaningful contribution to the scientific community in the form of a PhD Thesis. You honor me with your confidence through difficult terrains and uncertain outcomes, ever listening and intervening with equal precision and commitment. The latest three years have been full of challenges, and it has been a pleasure to overcome them by your side.

During the Thesis Defense this work have been first shared and discussed in integral with the scientific community. Here, I shall recognize the invaluable contributions of the jury members to the current state-of-knowledge reported in this Thesis. Professor Tihomir Hristov, who has been a pleasure to meet after so much teaching me from his publications. Professor Sukanta Basu, whom lecture I had the chance to attend motivating me into the science of atmospheric flows. Professor Joachim Reuder, for actively collaborating to the discussion on oceanic LiDARs. Drs. Marie-Noelle Bouin and Valery Masson, for their attentive reading, and the most significant discussions that followed.

This work employs the Atmospheric, Large Eddy Simulation solver developed by Peter Sullivan, from the NCAR (National Center for Atmospheric Research) in Colorado, USA.

This work was granted access to the HPC ressources of CINES under the location A0090112000 made by GENCI (Grand Equipement National de Calcul Intensif).

ABSTRACT

In coastal areas, the wind energy industry migrates to the offshore environment, where huge spaces are still available in stronger and better behaved wind conditions. The offshore environment imposes new challenges to a well established wind energy industry. It is imperative to accurately predict and describe the offshore wind resource in order to design cost efficient solutions. The concerned flow is characterized by a turbulent Atmospheric Boundary Layer (ABL) where the ocean's dynamics significantly alter the atmospheric flow through higher heat capacity and complex wind-wave interactions important in fairly common situations.

So this Thesis reviews and extends the current knowledge regarding Wind-Wave interactions in the lower part of the Marine ABL (MABL), where they are possibly significant in the characterization of the wind resource. The MABL is investigated through physical and numerical experiments, to reveal the role of Wave Induced (WI) motions transferred from the sea into the atmosphere. Thanks to the use of complementary physical and numerical experiments, new insights on the wind-wave interaction processes are obtained.

A scanning Light Detection and Ranging (LiDAR) system is deployed to observe the propagation of WI motions approximately 18 m above the ocean. The sLiDAR registers high resolution space-time maps of the Radial Wind Speed (RWS), allowing an original two-dimensional (2D) spectral analysis rarely possible in the field. Unlike more conventional methods, the upward turbulent energy transfer from the waves to the wind is evident and well distinguishable from the atmospheric turbulence in the 2D wave-number-angular-frequency ($k-w$) spectra. This is a first to demonstrate the applicability of sLiDAR systems to measure $k-w$ dependent turbulent spectra in the Offshore Environment.

The MABL is investigated employing a Large Eddy Simulation (LES) solver. The test cases are built to investigate the WI disturbances above fast traveling waves, propagating under comparatively slow wind conditions in a situation commonly described as *old seas*. An original method is proposed to control the Wind Speed at a certain height above an arbitrary sea-state. The WI disturbances are investigated as function of varying Wave Age conditions in monochromatic wave scenarios. Non-monochromatic waves are also investigated, leading to the comparison between physical and numerical experiments in a level of detail rarely observed in the literature.

Recent developments in measuring and modelling techniques open path to a mechanistic approach, i.e., one that seeks the characterization of certain phenomena in purely physical or deterministic terms. Applied to the investigation of wind-wave interactions it consists in the direct estimation of WI velocities and pressure in the atmosphere, rather than the inference of WI disturbances in vertical wind profiles, total momentum fluxes, or TKE budget. An original methodology is proposed to characterize WI motions from the measurements in instantaneous velocities. The definition of a *Wave Related* flow is extended from *Wave Coherent* (WC) to *Wave Induced* (WI). If the waves travel with velocities sufficiently greater than the mean wind speed, that leads to WC and WI decompositions that for the first time allow their quantification in the field without any previous sea-state knowledge required.

RÉSUMÉ EN FRANÇAIS (ABSTRACT IN FRENCH)

Dans les zones côtières, l'industrie de l'énergie éolienne migre vers l'environnement marin, où de vastes espaces sont encore disponibles avec des conditions de vent plus fort et mieux contrôlé. L'environnement marin impose de nouveaux défis à une industrie éolienne pourtant bien établie. Il est impératif de prédire et de décrire avec précision la ressource éolienne en mer afin de concevoir des solutions techniques rentables. L'écoulement concerné est caractérisé par une couche limite atmosphérique (CLA), turbulente, où la dynamique de l'océan modifie considérablement l'écoulement atmosphérique par une capacité thermique plus élevée, et par des interactions vent-vagues complexes, importantes dans des situations assez courantes.

Cette thèse passe en revue et étend les connaissances actuelles concernant les interactions vent-vagues dans la partie inférieure de la CLA Marine (CLAM), où elles peuvent être importantes pour la caractérisation de la ressource éolienne. La CLAM est étudiée par des expériences physiques et numériques, afin de révéler le rôle des mouvements Induits par les Vagues (IV) transférés de la mer vers l'atmosphère. Grâce à l'utilisation d'expériences physiques et numériques complémentaires, de nouvelles perspectives sur les processus d'interaction vent-vague sont obtenues.

Un système de détection et de télémétrie par la lumière à balayage (sLiDAR) est déployé pour observer la propagation des mouvements IV à environ 18m au-dessus de l'océan. Le sLiDAR enregistre des mesures spatio-temporelles de la vitesse radiale du vent (VRV) à haute résolution, permettant une analyse spectrale bidimensionnelle (2D) originale rarement possible sur le terrain. Contrairement aux méthodes plus conventionnelles, le transfert d'énergie turbulente ascendante des vagues vers le vent est mis en évidence et est bien distinguable de la turbulence atmosphérique dans les spectres 2D en nombre d'onde-fréquence angulaire ($k-w$). C'est la première fois que l'on démontre l'applicabilité des systèmes sLIDAR pour mesurer les spectres de turbulence dépendant de $k-w$ dans l'environnement marin.

La CLAM est étudiée à l'aide d'un solveur de Simulation aux Grandes Échelles (SGE). Les cas d'essai sont construits pour étudier les perturbations IV au-dessus des vagues rapides, se propageant dans des conditions de vent relativement lent, dans une situation communément décrite par un âge des vagues élevé. Une méthode originale est proposée pour contrôler la vitesse du vent à une certaine hauteur au-dessus d'un état de mer arbitraire. Les perturbations IV sont étudiées en fonction des conditions variables de l'âge des vagues dans des scénarios de vagues monochromatiques. Les vagues non monochromatiques sont également étudiées, ce qui permet de comparer les expériences physiques et numériques à un niveau de détail rarement observé dans la littérature.

Les développements récents des techniques de mesure et de modélisation ouvrent la voie à une approche mécaniste, c'est-à-dire une approche qui cherche à caractériser certains phénomènes en termes purement physiques ou déterministes. Appliquée à l'étude des interactions vent-vagues, elle consiste en l'estimation directe des vitesses et de la pression induites par les vagues dans l'atmosphère, plutôt que les conséquences globales des perturbations IV sur les profils verticaux de vitesse du vent, les flux de quantité de mouvement totale, ou le bilan d'énergie turbulente. Une méthodologie originale est proposée

pour caractériser les mouvements IV à partir des mesures de vitesses instantanées. La définition d'un écoulement *Relatif aux Vagues* est étendue de *Coherent aux Vagues* (CV) à *Induit par les Vagues* (IV). Si les vagues se déplacent à des vitesses suffisamment supérieures à la vitesse moyenne du vent, cela conduit à des décompositions IV et CV qui, pour la première fois, permettent leur quantification sur le terrain, sans qu'aucune connaissance préalable de l'état de mer ne soit nécessaire.

Contents

Abstract iii

Résumé (In french) iv

Contents vi

List of figures xiii

List of tables xxix

Lists of Notation xxxi

0 Introduction **1**

I Theoretical, empirical and numerical frameworks **5**

I.1 **Foundation in Fluid Mechanics** 6

I.1.1 Theoretical framework 6

I.1.1.1 Incompressible Navier Stokes Equations 6

I.1.1.2 Free surface conditions 7

I.1.1.3 Reynolds Averaged Navier Stokes Equations 8

I.1.1.4 Reynolds Stress Tensor and Turbulent Kinetic Energy 8

I.1.1.5 Turbulent spectral distribution and scales 9

I.1.1.6 Large Eddy Simulation 11

I.1.2 Specific assumptions delimiting the theoretical framework 12

I.1.2.1 Water domain 12

I.1.2.2 Atmosphere 13

I.2 **Geophysical mechanisms and models** 17

I.2.1 Ocean waves 17
I.2.1.1 Sea state spectral distribution 18
I.2.1.2 Wave-driven circulation and Wave dissipation 21
I.2.2 Atmospheric Boundary Layer 22
I.2.2.1 Turbulent scales in the atmosphere 22
I.2.2.2 BL theory and the ABL at neutral conditions 24
I.2.2.3 Thermal stratification effects 26
I.2.2.4 Wind resource and harvesting prediction 29
I.3 **Wind-Wave Interaction mechanisms** 31
I.3.1 Early established theories and Wave growth 32
I.3.2 The Wave Boundary Layer and the Wave Induced flow 34
I.3.3 Boundary layer similarities in the MABL 36
I.3.3.1 Roughness length: Early to recent measuring campaigns 36
I.3.3.2 Eddy viscosity: Early to recent numerical models 37
I.3.3.3 Similarity disturbances: Measuring and modelling implications 38
I.3.4 Down to the dissipation range at laboratory scales 39
I.3.4.1 Modern measuring techniques: PIV 39
I.3.4.2 Modern modelling techniques: DNS 39
I.3.4.3 Coherent vortical structures 39
I.3.4.4 Wave breaking 41
I.3.5 Resolving the WBL at oceanic scales 43
I.3.5.1 Large Eddy Simulation 43
I.3.5.2 Deterministic coupling of resolved sea-state and air flow 44
I.3.6 Observing and quantifying the WI flow above the ocean 46
I.3.6.1 Measurements 46
I.3.6.2 Spectral evidence 47
I.3.6.3 A mechanistic approach 48
I.3.6.4 Wave coherent flow and simplified WBL equations 50

I.3.6.5 Surface following coordinates 51

II Field measurements in the Wave Boundary Layer **52**

II.1 **Experimental conditions** 54

II.1.1 Test site 54

II.1.2 sLiDAR technology and experimental setup 56

II.1.2.1 Technological challenges 56

II.1.2.2 Calibration 56

II.1.2.3 Setup 56

II.1.3 Environmental description and test-case selection 57

II.1.3.1 Meteocean conditions 58

II.1.3.2 Test cases description 60

II.1.3.3 Sea-state spectral distribution 61

II.2 **Data treatment and analyses** 62

II.2.1 Data quality and filter 62

II.2.1.1 Carrier-To-Noise Ratio 62

II.2.1.2 Spike detection and removal 63

II.2.1.3 Signal reconstruction 64

II.2.2 Energy Density Functions 65

II.2.3 Wind homogeneity and steadiness 66

II.2.3.1 Large scale non-homogeneity and unsteadiness 68

II.2.3.2 Very large scale unsteadiness 70

II.3 **Field measurements of Wave Induced Disturbances in the WBL** 71

II.3.1 Radial Wind Speed fluctuations 71

II.3.2 One-dimension turbulent spectra 73

II.3.3 Two-dimension turbulent spectra 74

II.3.3.1 Spectral gap disturbance 76

II.3.3.2 Opposing directions and the four quadrant spectra 76

II.3.4 Rising Wind and Diminishing Sea-State 79
II.3.5 Overview and discussion 81

III Numerical model description, developments, and applications 83

III.1 **Numerical problem formulation and strategy** 84
III.1.1 Problem formulation 85
III.1.1.1 Governing equations and boundary conditions 85
III.1.1.2 Discretization 87
III.1.1.3 The role of pressure 88
III.1.1.4 Turbulent Kinetic Energy budget 89
III.1.2 General numerical strategy 90
III.1.2.1 Solver setup 90
III.1.2.2 Water surface prescription 91
III.1.2.3 Post-processing 92
III.2 **Dynamically evolving pressure-gradients** 95
III.2.1 Preliminary studies and motivation 95
III.2.2 The role of large-scale pressure gradients 97
III.2.3 A large-scale dynamically evolving pressure-gradient modeler. 98
III.2.4 Flat bottom application 99
III.2.4.1 Specific numerical strategy 99
III.2.4.2 Results 100
III.2.5 Wavy bottom application 104
III.2.5.1 Specific numerical strategy 104
III.2.5.2 Results 104
III.2.6 Overview and discussion 107
III.3 **Systematic comparisons varying the wave age** 109
III.3.1 Specific numerical strategy 110
III.3.2 Results 110

III.3.2.1 Mean history profiles 110
III.3.2.2 Mean wind velocity profiles 114
III.3.2.3 Mean turbulent profiles 117
III.3.3 Discussion 123
III.4 **Different levels of Sea-State description** 125
III.4.1 Specific numerical strategy 125
III.4.2 Results 127
III.4.2.1 Mean History profiles 127
III.4.2.2 Mean wind velocity and turbulent profiles 129
III.4.3 Overview and discussion 133

IV A mechanistic approach to Physical and Numerical experiments 135
IV.1 **An enhanced perspective of the Wave Induced flow** 136
IV.1.1 Theoretical foundation 136
IV.1.1.1 Wave Coherent and Wave Induced flows 136
IV.1.1.2 Joint Space-Time modal perspective 139
IV.1.2 Monochromatic wave application 140
IV.1.2.1 Wave Induced motions 140
IV.1.2.2 Atmospheric Turbulence motions 142
IV.1.2.3 Joint Space-Time modal distribution 145
IV.1.3 Overview and discussion 146
IV.2 **Partitioning WI motions in the Turbulent Spectra above arbitrary sea-states** . 148
IV.2.1 Contour advancing segmentation of the 2D Turbulent Spectra 149
IV.2.1.1 Segmentation procedure 151
IV.2.1.2 Overview and discussion 153
IV.2.2 Numerical experiments 154
IV.2.2.1 Atmospheric turbulence and Wave induced motions 154
IV.2.2.2 Overview and discussion 158

IV.2.3 Physical experiments 160
IV.2.3.1 Atmospheric and Wave Induced 1D Spectra 161
IV.2.3.2 Wave Induced fraction 163
IV.2.3.3 Transfer Function of the Sea-State spectra into the atmosphere 164
IV.2.3.4 Overview and discussion 166
IV.3 **Towards the numerical reproduction of the sLIDAR observations** 167
IV.3.1 Sea State Reconstruction 167
IV.3.2 A numerical sLiDAR modelling the filter effect 170
IV.3.3 Numerical experiment in the flat bottom ABL 170
IV.3.3.1 Specific numerical strategy 171
IV.3.3.2 The sLiDAR filtering effect in the Atmospheric turbulence . . . 171
IV.3.3.3 Overview and discussion 173
IV.3.4 Numerical experiment in the wavy bottom ABL 174
IV.3.4.1 Specific numerical strategy 174
IV.3.4.2 The sLiDAR filtering effect in the WBL 174
IV.3.4.3 The sLiDAR filtering effect in decomposed WI motions 177
IV.3.4.4 Overview and discussion 182
IV.3.5 Comparison between physical and numerical experiments 183
IV.3.5.1 Overview and discussion 187

V Conclusion **189**

Bibliography **198**

Appendix **212**

A **Theoretical, empirical and numerical frameworks** 212
A.1 Canonical analytical solutions 212
A.1.1 Stokes wave theory 212

A.1.2 Boundary Layer theory 213
A.2 Wind-Wave interaction mechanisms 215
A.2.1 Flow description 215
A.3 Fourier Transforms 219
A.4 Numerical modelling aspects 221
A.4.1 Pressure Poisson equation 221
A.4.2 Turbulent-Viscosity models 222
A.4.3 Geometric conservation law 223
A.4.4 Time-marching scheme 223
B **Numerical model description, developments, and applications** 224
B.1 Physical scaling in the LES generated neutral MABL 224
B.1.1 Geometrical and dynamical similarities 224
B.1.2 Systematic comparisons varying the wave age 225
B.2 Review and improvement of the coupling between LES and HOS codes . 226
B.2.1 Previous Coupling procedure 227
B.2.2 Current Coupling procedure 228
B.2.3 Overview and discussion 230
C **A mechanistic approach to Physical and Numerical experiments** 230
C.1 An equivalent time scale for a space dependent filter 230
C.1.1 Mathematics 231
C.1.2 Consequence 232
C.2 On the reconstruction of velocity wave-number-frequency spectra . . . 233
C.2.1 One-dimensional base-line function 236
C.2.2 Two-dimensional approximation function 238
C.2.3 Optimization Algorithm 239
C.2.4 The reconstruction of Atm. Turbulent flow in Neutral Flat ABLs 240
C.2.5 Overview and discussion 243

LIST OF FIGURES

I.2.1 According to Edson et al. [2007] (Fig. 1), a "*few of the processes governing air-sea exchange across the coupled boundary layers*". Already much more than the ones admitted by the theoretical framework established. 17

I.2.2 An irregular sea-state composed of multiple wave components, from Pierson et al. [1955]. 19

I.2.3 Evolution of the sea-state spectra with fetch. Taken from **(alias?)** (Fig. 2.5), in turn extracted from the original in Hasselmann et al. [1973]. Fetch indicated in kilometers over the spectra. 20

I.2.4 Atmospheric motions, exemplified by the Van Der Hoven spectrum reported in der Hoven [1957]. The spectral gap splits mesoscale and microscale motions (legend, arrow and color added to the original) in the atmosphere, the latest being the focus of present studies. 23

I.2.5 Diagram depicting atmospheric scales related to different physical processes in the atmosphere, from Larsen et al. [1979]. Red dashed regions are added to the original, remarking the region of interest in current studies. 24

I.2.6 Atmospheric Boundary Layer regions and schematics, inspired in BME. . . . 25

I.2.7 Diurnal cycle of thermal stratification, from Kaimal and Finnigan [1994] (pg. 7). In this example, the convective regime follows sunrise, and the transition to the stable regime occurs just after sunset. 27

I.2.8 Representative exemplification of the mean velocity, direction and temperature profiles, in convective (a) and stable (b) conditions. From Kaimal and Finnigan [1994] (pg. 5-6). 28

I.3.1 The modern Beaufort Scale (1805-2001), taken from Journée and W.W.Massie [2001]. Even more recent images dating 2010 can be appreciated with the historical review in Centre [2010]. 31

I.3.2 Jeffrey's mechanism of wave growth [Jeffreys, 1925], relying in the flow detachment occurring at the lee-side of a sufficiently steep wave. (a) A schematic on the flow structure. (b) DNS (See section I.3.5) observations from Yang and Shen [2010]. 32

I.3.3 Miles mechanism [Miles, 1957] of wave growth/ damping, from Lighthill [1962]. Figure 1 (above): The reversed flow below the critical height, and the streamlines deformation due to the moving boundary. Figure 2 (below): A continuous vorticity distribution appears at the critical height z_c, where the mean wind $\overline{u}_1$ equals the phase velocity of the wave. 33

I.3.4 Shelter related wave growth mechanisms, from Belcher and Hunt [1993]. (a) Non-separated sheltering: streamlines are depicted above the matched height. The boundary layer thickens leeward, and shrinks windward to the crest. (b) Outer region Reynolds-stress effects: the non-separated sheltering in the inner region leads displaces the largely inviscid outer-region flow. 34

I.3.5 Coherent vortical structures in a shear layer flow. (a) From Adrian et al. [2000]: Schematics of hairpin structures (yellow) rising at the edge of roller structures (blue and violet). (b) From Adrian [2007]: longitudinal evolution of a hairpin structure, resolved with DNS. 40

I.3.6 Quadrant analysis of the PDF of longitudinal and vertical velocity fluctuation components. The elliptical iso-contours depict different DNS solutions. The hyperbolic red lines represent the threshold applied to identify sweeps and ejections in Q2 and Q4. From Jiménez [2018]. 40

I.3.7 Schematics of the coherent structures Yang and Shen [2010] observed above (a) slow and (b) fast traveling waves. From Yang and Shen [2010]. 41

I.3.8 Flow separation observed above breaking waves with PIV, from Reul et al. [1999]. 42

I.3.9 Monochromatic breaking waves in DNS resolution. The figure depicts one (left) or three (right) wave periods after the breaking event. From Yang et al. [2018]. 42

I.3.10 Large Eddy Simulation of the MABL at very different scales. In (a) the temperature fluctuation field at the first grid level (25 m height) of a planetary convective boundary layer, from Moeng et al. [2009]. In (b) Yang et al. [2014] an offshore wind farm, including the atmospheric LES resolution, a wave prescription, and wind turbine modelling through actuator disks, from Yang et al. [2014]. 43

I.3.11 Meaningful examples of air-sea interaction platforms. (a) ASIT, a fixed platform exploited during CBLAST, fig. from Edson et al. [2007]. (b) FLIP, a hybrid vessel and floating platform, fig. from Hristov et al. [2003]. (c) OCARINA, a platform buoy, fig. from Bourras et al. [2014]. 46

I.3.12 The Wave Induced signature observed in different frequency dependent turbulent spectra inside the WBL. (a) Air-pressure fluctuations and sea-state spectra, at two different periods taken from Snyder et al. [1981], and with added legends in red. (b) Longitudinal and vertical velocity fluctuation spectra, with the frequency space normalized by the wave peak frequency f_p, from [Tamura et al., 2018]. 47

I.3.13 The Wave Induced signature observed in the wave-number-angular-frequency dependent, stream-wise velocity turbulent spectra, within a LES resolved WBL. In the left (g and i) the resolved spectra is shown in the contours; the red dashed line stands for the mean wind velocity, and the red dash-dotted line for the dispersion relation. In the right (h,j), the spectra predicted by the random sweeping model of Wilczek and Narita [2012]. From Hao and Shen [2019]. 48

I.3.14 Transfer Function (TF) between the sea-state and atmospheric Wave Coherent spectra of stream-wise (a, b) and vertical (c, d) velocities. Magnitude of the TF in (a, c); phase in (b, d). Those are frequency dependent spectra, shown as function of the wave velocity c. The vertical line is the mean wind velocity at the measurement height 8.7 m. The squared refer to experimental obsrrvations, and the full line to Mile's critical layer theory prediction. From Hristov et al. [2003]. 49

I.3.15 Evidence of Mile's critical layer mechanism. In both figures, the black line indicates the critical layer height, where a wave component travels with the same velocity as the mean wind, and across that line an intense phase shift takes place as predicted in Mile's theory. (a) Phase of the vertical velocity fluctuation spectra, from Hristov et al. [2003]. (b) Phase between the vertical velocity fluctuation spectra and the sea-state free-surface elevation spectra, from Grare et al. [2013a]. 49

II.1.1 The sLiDAR on the balcony of a seafront villa at Le Croisic. Definition of: Radial (R) and vertical (z) axes; roll (ψ), pitch (elevation angle θ), and yaw (azimuth angle ϕ) angular movements. 54

II.1.2 sLiDAR position denoted by a red dot and water depth displayed by the colormap. **(a) Location of Le Croisic on the French west Atlantic coast**. The wind rose for Le Croisic has been exported from the Global Wind Atlas (GWA 3.0, `https://globalwindatlas.info`), comprehending the period 2008-2017. **(b) View of Le Croisic peninsula (France)**, with the PPI scans for wind direction determination in the black sector, and staring mode measurements lines (f-LOS) for Case01 (blue) and Case02 (red) in dashed lines. Oceanic conditions are estimated from the HOMERE hind-cast database: The grid is depicted by its nodes in yellow dots; and the probing occurs in the node depicted in magenta. 55

II.1.3 Evolution of wind and sea-state quantities around Cases 01 and 02[a-c], in subfigures (a,c,e) and (b,d,f), respectively. (a,b) PPI obtained horizontal Wind Speed (WS) and Wind Direction (WD). (b-f) Wave model (WWIII) hind-cast: In (c,d) the significant wave height (H_s) and peak period (T_p); in (e,f) the wave peak direction (α_w) and directional spreading (β_w). Horizontal lines in (a,b,e,f) for the sLiDAR fLOS-aligned direction $\phi_L - 180°$. Vertical lines for the initial, middle and final moments of the selected periods. 59

II.1.4 Free-surface variance energy density function $F(\phi, f)$ (log scale) for Case 01 (a) and Case 02a (b). The frequency dependent mean direction $\phi_0(f)$ and the peak wave direction registered closer to the sLiDAR are depicted as a black dotted line and dashed line, respectively. The mean WD and the sLidar fLOS are depicted in dot-dashed yellow and red lines, respectively. 61

II.2.1 Case 01 above; Case 02.a below. Cumulative histogram of CNR occurrences below the threshold; Mean velocity and turbulence intensity as function of the CNR threshold. 63

II.2.2 An example of the spike-removal and reconstruction procedure, selected from a time series where the spike is identified close to the established threshold. The blue full line represents a 10-min measurement of $u_R(x,t)$ with fixed position x. The orange full line represents the low frequency estimate of $u_R(x,t)$, used to identify the spike denoted by a purple dot. The yellow dotted line is the high frequency estimate of $u_R(x,t)$, used to reconstruct the spike attributing the value once in purple to the yellow dot just below. 65

II.2.3 Segmentation of the dataset of Case 01 into different grids (a,b) to address: (a) Large scale steadiness and homogeneity; (b) Very large scale steadiness. The blank spaces between $t_i + 10$ min and t_{i+1} are out of scale, for they correspond to another 10-min intervals where PPI motions are executed. . . 67

II.3.1 Staring mode 10-min records of the RWS from Case 01 at (a,b) and Case 02.a at (c,d). Mean RWS (Taylor's hypothesis) and Peak wave phase velocity (Dispersion equation) slopes as dash-dotted and dashed lines, respectively. Wave slope duplicated and spread apart by T_p (tab. II.1.3). At Case 01 the streaks appear to travel with velocities lower than the RWS, the arbitrary value of 0.5 RWS denoted in figures (a,b). 72

II.3.2 Wave-number (a,c) and frequency (b,d) 1D turbulent spectra for Case 01 (a,b) and Case 02.a (c,d). Observed 10-min spectra in light grey, and the 3-hour average in black full lines. The ESDU reference is given in black dashed lines. Vertical blue lines stand for the wave peak scales k_p and f_p, and green lines show the filter scales $k_{\gamma 0}$ and $f_{\gamma 0}$, for wave-number and frequency spectra, respectively. 73

II.3.3 Wave-number-angular-frequency 2D turbulent spectra. The mean RWS velocity is depicted in the black full line, and the wave velocity presented in dashed lines for $d = [14, 22, 30]$ m. The wave peak scale (L_p, T_p) is denoted by a star. The sLiDAR filter characteristic period and wave length are given in the green dashed, horizontal and vertical lines, respectively. 75

II.3.4 Spectral valley (dashed) and ridges (dot-dashed), observed in the 2D turbulent spectra of Case 01 at figure II.3.3. 76

II.3.5 Wave-number-angular-frequency 2D turbulent spectra for Case 02a, decomposed between opposite directions of propagation thanks to the four quadrant 2D spectra. The lines denote the characteristic scales described at figure II.3.3. 77

II.3.6 Four quadrants ($Q_{\pm\pm}$, see the appendix A.3) of the EDF of $u'_R u'_R$, referred by negative and positives wave-numbers $k_\pm$ or angular-frequencies $w_\pm$. Considering the EDF of $u'_R u'_R$ is real, $Q_{\pm\pm}$ is fold-symmetric: $Q_{++} = Q_{--}$ and $Q_{+-} = Q_{-+}$. Summing the quadrants one obtains Q_r shown in figure II.3.3. Case 01 is depicted above, with waves and wind aligned in the same sense (Ocean to sLiDAR) at quadrants Q_{++} and Q_{--}. Case 02a is depicted below, with the wind aligned to the opposite sense (sLiDAR to Ocean) at quadrants Q_{+-} and Q_{-+}. 78

II.3.7 Case 02b, to be compared to previous figures denoting Case 02a. **(a)** RWS contours as in figure II.3.1(c,d). Mean RWS (Taylor's hypothesis) and Peak wave phase velocity (Dispersion equation) slopes as dash-dotted and dashed lines, respectively. **(b)** 1D frequency spectra as in figure II.3.2d. Observed 10-min spectra in light grey, the 3-hour average in black full lines, and the ESDU reference in black dashed lines. 79

II.3.8 Wave-number-angular-frequency 2D turbulent spectra of Cases 02[b-c]. To be compared with the spectrum of Case 02a previously shown at figure II.3.3b. The mean RWS velocity is depicted in the black full line, and the wave velocity presented in dashed lines for $d = [14, 22, 30]$ m. The wave peak scale (L_p, T_p) is denoted by a star. The sLiDAR filter characteristic period and wave length are given in the green dashed, horizontal and vertical lines, respectively. 80

II.3.9 Wave-number-angular-frequency 2D turbulent spectra for Case 02c, decomposed between opposite directions of propagation thanks to the four quadrant 2D spectra. Motions traveling from the Ocean to the sLiDAR are shown. The lines denote the characteristic scales described in figure II.3.8. . 80

III.1.1 Sketch indicating the Cartesian coordinates, wind and waves aligned to x_1, the volume domain bounded below by an arbitrary single-valued wave, and above by the free-stream velocity. 85

III.1.2 Exemplification of grid 02 (Medium in table III.1.1). From the computation exploited in sections III.2 and III.3 regarding a monochromatic wave prescription. 91

III.1.3 Wind profile obtained and discussed at section III.2.4 (figure III.2.8b) for different flat bottom cases, depicted in linear-log scale revealing different regions inside the ABL. Log-law fitting by equation III.1.15 denoted by straight, transparent lines. 94

III.2.1 From Paskin et al. [2020]. Friction velocity history and velocity profiles for flat and wavy, lower BCs. The reference wind profile is described in III.1.2.3 as given by ESDU 85020. 96

III.2.2 Rejected studies of Dirichlet upper B.C.: Null Dirichlet upper B.C. (Fix Up) of $\overline{u}$ with Flat lower B.C. in blue full line; Null Newmann upper B.C. (Free Slip Up) of $\overline{u}$ with Wavy lower B.C. in orange dotted line; Null Dirichlet upper B.C. (Fix Up) of $\overline{u}$ with Wavy lower B.C. in gold dashed line. The Dirichlet upper condition combined with the Wavy lower surface induce a non-physical velocity gradient in the upper boundary. 97

III.2.3 The Mass-Spring-Damper system ruling the evolution of the longitudinal pressure gradient $\mathscr{P} = \left[\partial p/\partial x\right]_0$, according to equation III.2.3. 98

III.2.4 Mean wind velocity in the last cell layer $\overline{u}_h$. Target values $\overline{u}_{ref}$ are remarked by the horizontal lines. The non-dimensional scales are shown as computed in the solver, but the problem is expected to be self-similar with respect to the reference velocity $\overline{u}_{ref}$. Sliding statistics are taken with time averages t_{avg} varying by 10^3. 100

III.2.5 Vertically integrated non-dimensional, homogeneous, and large scale pressure gradient. Sliding statistics are taken with time averages t_{avg} varying by 10^3. 101

III.2.6 Friction velocity normalized by the target velocity. As the upper boundary velocity reaches its target, the solution becomes self-similar and the Cases converge. Sliding statistics are taken with time averages t_{avg} varying by 10^3. 101

III.2.7 Vertical mean (in ξ_1, ξ_2 and t) wind and turbulent profiles. The five cases shown with varying free-stream velocity collide with proper normalization. The normalizing friction velocity is obtained from equation III.1.6. Sliding statistics are taken with time averages $t_{avg} = 75\ T_0$. 102

III.2.8 Wind velocity profile and fitting to the outer surface layer according to equation III.1.15. The different regions exposed are discussed in section III.1.2.3, as (b) is replicated at figure III.1.3. 103

III.2.9 Different mean (in ξ_1, ξ_2 and t) history profiles for the three cases considered: Flat bottom with constant large scale $\partial p/\partial x|_0$ as the reference; Wavy bottom with constant $\partial p/\partial x|_0$; Wavy bottom with the dynamic $\partial p/\partial x|_0$ modeler here proposed. Sliding statistics are taken with time averages $t_{avg} = 75\ T_0$. 106

III.2.10 Mean (ξ_1, ξ_2 and t) wind velocity profile for the three cases considered, in different scales and normalized by different friction velocities. Sliding statistics taken with $t_{avg} = 75\ T_0$. 107

III.2.11 Different mean (ξ_1, ξ_2 and t) vertical turbulent profiles for the three cases considered. The normalizing friction velocity is obtained from equation III.1.6. Sliding statistics are taken with time averages $t_{avg} = 75\ T_0$. 108

III.3.1 Mean history profiles averaged with $t_{avg} = 75\ T_0$. (a) Wind velocity ($|\boldsymbol{u}|(z_l)$) at last vertical layer, normalized by the middle reference value u^*_{ref0}, as resolved in the computational non-dimensional domain. The horizontal lines stand for the target velocities $u_{ref} = u_h$. (b) Dynamic and slowly evolving pressure gradient controlling $|\boldsymbol{u}|(z_l)$ to match u_h. (c) Ratio between the resolved u^* and reference u^*_{ref} friction velocities, with u^*_{ref}/u^*_{ref0} given in the legend. (d) Resolved Wave Age WA(u^*). The legend shown in (c) applies to (a,b,c,d), relating the line types and colors to each case. 111

III.3.2 Same as figure III.3.1c, but averaged with $t_{avg} = 75 \cdot 10^{-3}\ T_0$. Ratio between the resolved u^* and reference u^*_{ref} friction velocities, with u^*_{ref}/u^*_{ref0} given in the legend of figure III.3.1c for each line type. 112

III.3.3 The evolution of F_p/F_τ in time, with $t_{avg} = 75\ T_0$. 113

III.3.4 Wave Age dependency of the non-dimensional form drag (F_p/F_τ). (a and c) The numerical experiments reveal F_p/F_τ denoted by the blue dots, function of the actual WA in (a), and function of the reference WA_{ref} in (c). (b and d) The negative sign of the slopes between the intervals of figures (a) and (c), respectively denoted by the blue dots in figures (b) and (d). The red dot line fits to the first 4 Cases, the yellow dotted line fits to the last four Cases, and the purple line fits for every Case. The fitted equation is III.3.1, with A and B obtained from figures (b) and (d), and C set as to match exactly the value at Case 03 where $u_{ref} = u_{ref0}$ 114

III.3.5 Mean (in ξ_1, ξ_2 and t) wind velocity profiles and fitting. In (a) the flat bottom cases presented in section III.2.4. In (b-d) the wavy bottom cases here discussed. Log fitted profiles (from equation III.1.15) are shown with transparency in (c,d). (c) Fitting to the inner region. (d) Fitting to the outer region. Sliding statistics are taken with time averages $t_{avg} = 75\ T_0$. 115

III.3.6 Mean (ξ_1, ξ_2 and t) Turbulent Kinetic Energy (TKE) vertical profiles. Decomposed, with the total TKE appearing in solid and the SGS component with transparency, or zoomed in the upper right corner. The horizontal lines depict: 5th cell layer; 10th cell layer; and non-dimensional wave-height $ka = 0.2$. Sliding statistics are taken with time averages $t_{avg} = 75\ T_0$. 117

III.3.7 Mean (ξ_1, ξ_2 and t), Turbulence Intensity profiles, for longitudinal (TI_{uu}) and vertical (TI_{ww}) velocity fluctuations. The legends correspond to the wavy cases here presented. The light gray lines represent the flat case solution of figure III.2.7c. The zoomed regions depict the intersections between the curves. Sliding statistics are taken with time averages $t_{avg} = 75\ T_0$. 118

III.3.8 Mean (ξ_1, ξ_2 and t) Turbulent kinetic energy budget profiles: Production and dissipation. In (a) the production is decomposed, with the total TKE production appearing in solid, and the resolved component with transparency. In (b) dissipation admits only SGS contributions. Sliding statistics are taken with time averages $t_{avg} = 75\ T_0$. 119

III.3.9 Mean (ξ_1, ξ_2 and t) Turbulent kinetic energy budget profiles, comprehending all the terms described at section III.1.1.4. Summing the profiles (a,b,c) one obtains the advection at (d). The legends correspond to the wavy cases here presented, and the light gray lines represent the flat case solution. Sliding statistics are taken with time averages $t_{avg} = 75\ T_0$. 121

III.3.10 (a) Mean (ξ_1, ξ_2 and t) total shear stress $\tau_{13}(z)$, and (b) its decomposition into: velocity cross-correlation ($\tau_{13}^{(r)}$, transparent in b.), and WI pressure ($\tau_{13}^{(P)}$, solid colors in b.) contributions. In (a) linear fittings appear with transparency, parameterized according to table III.3.5, and the black line represents the flat case solution. The fitting is less accurate in the near-wall region, zoomed at the upper left corner of (a). Sliding statistics are taken with time average $t_{avg} = 75\ T_0$. 122

III.3.11 Total drag F_τ as a function of WA_{ref}. Comparison between the actual value, and the one extrapolated from the linear fitting depicted in figure III.3.10a. Here a linear fitting applies to $F_\tau(\mathrm{WA}_{ref})$ and appears with dotted line in the figures; the fitting coefficients are given in table III.3.6. 123

III.4.1 Wind speed at the measurement height. For the flat case, and three different sea-states identified in the legend at (a). The horizontal line depicts the target velocity u_{ref} =4.12 m/s. Sliding statistics are taken with time different averages t_{avg} in (a) and (b). 127

III.4.2 Slowly evolving and homogeneous pressure gradient, modeled according to section III.2 to achieve the target velocity depicted at figure III.4.1. For the flat case, and three different sea-states identified in the legend at (a). Sliding statistics are taken with time different averages t_{avg} in (a) and (b). . 128

III.4.3 Resolved friction velocity (computed from equation III.1.6), and the correspondent Wave Age. For the flat case, and three different sea-states identified in the legends. Sliding statistics are taken with time average $t_{avg} = 41\ T_0$.128

III.4.4 Non-dimensional Time step and form drag. For the flat case, and three different sea-states identified in the legends. Sliding statistics are taken with time average $t_{avg} = 41\ T_0$. 129

III.4.5 Longitudinal velocity profile. The horizontal dashed line between circles depicts the measurement height h = 18.33 m= 0.14 λ. The regions discussed in section III.1.2.3 are drawn with the wind profiles at (b). Sliding statistics are taken with time average $t_{avg} = 41\ T_0$. 130

III.4.6 Longitudinal velocity profile and logarithmic fit in the outer surface layer. The horizontal line denotes the measurement height 0.14 λ. $t_{avg} = 41\ T_0$. . . 130

III.4.7 Turbulent kinetic energy profiles. The horizontal lines denote the measurement height 0.14 λ. $t_{avg} = 41\ T_0$. 131

III.4.8 Turbulent Intensity of longitudinal and vertical velocity variances. The horizontal lines denote the measurement height 0.14 λ. Sliding statistics are taken with time average $t_{avg} = 41\ T_0$. 131

III.4.9 Height dependent fictitious form drag, or WI pressure stress $\tau_{13}^{(P)}$. The horizontal line denotes the measurement height 0.14 λ. $t_{avg} = 41\ T_0$. 132

III.4.10 Turbulent kinetic energy budget analysis, considering the terms defined in section III.1.1.4. The horizontal lines denote the measurement height 0.14 λ. Sliding statistics are taken with time average $t_{avg} = 41\ T_0$. 133

IV.1.1 Numerical experiment of a monochromatic wave described in section IV.1.2. One-dimensional spectral density function $E_{u_1 u_1}(l = 2\pi/k)$. Total fluctuation spectra $E_{u_1' u_1'}$ in blue full line; Residual of the Wave Coherent filtered turbulent spectra $E^C_{\hat{u}_1 \hat{u}_1}$ in green dotted line; Wave Induced filtered Atmospheric turbulence spectra $E^I_{\hat{u}_1 \hat{u}_1}$ in red dashed line. 137

IV.1.2 One-dimensional wave-number-dependent spectral EDF of longitudinal and vertical velocities. Flat and Wavy bottom cases of section III.2.5. Wave ($\mathrm{WA}_{ref} = 60$, $ka = 0.2$) prescribed according to a fifth order solution, leading to WI disturbances at five harmonics. The spectral domain ranges between $2\pi/x_l$ and $\pi/\Delta x$, but in LES it is truncated at $(2/3)\pi/\Delta x$. 141

IV.1.3 Wave Induced fraction $\mathscr{F}_{\lambda_k}(z)$, corresponding to the squared root of the WI energy fraction according to equations IV.1.2 and IV.1.3. Obtained for longitudinal and vertical velocities. Presented and normalized (in ξ_3) separately for each harmonic ($n = 1..5$) with length $\lambda_k = \lambda/n$. 142

IV.1.4 Atmospheric turbulence spectra of longitudinal velocities presented at two different heights. Wavy and flat bottom cases with the ESDU reference. The WI filter is employed in the wave bottom case. The ESDU reference considers the variances and integral length scales obtained from each spectra, according to section III.1.2.3. 143

IV.1.5 Integral length scale of longitudinal velocities at the wave bottom case. Extracted from the turbulent spectra revealed by the different spectra in figure IV.1.1. Total fluctuations $l_0(u')$ in blue full line; residual of the Wave Coherent filtered $l_0(\hat{u}^{(C)})$ in green dotted line; WI filtered, Atm. motions $l_0(\hat{u}^{(I)})$ in red dashed line. 143

IV.1.6 Integral length scale l_0 of longitudinal and vertical velocities, at Flat and Wavy bottom cases. Obtained from the Atm. turbulence auto-spectra employing the WI filter. 144

IV.1.7 Assuming in-phase Atm. and WI motions occurring at the same scale, Atm. and WI fields are reconstructed from equations IV.1.1 and IV.1.2. **Atmospheric Turbulence** field: Iso-surfaces of Q-criterion colored by 'y' (x-z plane) vorticity; **Wave Induced** field: Middle 'y' plane, probing velocity vectors, and colored by longitudinal WI velocity. 145

IV.1.8 Wave-number-angular-frequency 2D turbulent spectra for the Wavy bottom case of a monochromatic wave ($WA_{ref} = 60$, $ka = 0.2$). The mean velocity is depicted in the black full line corresponding to Taylor's hypothesis, and the wave velocities presented in dotted lines. In (a) the wave velocities are shown for the first five harmonics. In (b) only the wave velocity is depicted. 146

IV.2.1 Schematic of the contour advancing segmentation technique, drawn from figure IV.2.3o at level $i > i_0$. Starting from i_0, the contour is segmented. The current contour C_i is defined in the wave-length-period (r, τ) domain as depicted in full black line at the figure, and is segmented into Atm. ($\hat{C}_i$) and WI ($\tilde{C}_i$) parts by the points $[p_1, p_2]_i$ depicted as red circles. Between $[p_1, p_2]_i$ a red dot-dashed line represents the reconstruction of $\hat{C}_i$. The WI region of influence is bounded by S_{WI} that stands in magenta dots and lines. Below (with smaller energy than) the $[p_1, p_2]_i$ reconstructed line, S_{WI} matches $\tilde{C}_i$. Above (with greater energy than) the $[p_1, p_2]_i$ reconstructed line, S_{WI} is defined by the previous set of points $[p_1, p_2]_j$ for $i0 < j \leq i$. 149

IV.2.2 Turbulent 2D Spectra for Cases 01 and 02.a from section II.3; and the contour based segmentation technique, advancing in i shown at $i_{0..3}$. Lines, dots, and circles are as described in figure IV.2.1. 150

IV.2.3 Turbulent 2D Spectra for Cases 01 (a-d), 02 (e-l), and 03 (m-p); and the contour based segmentation technique, advancing in i shown at $i_{0..3}$. Case 02 reveal two detached regions of WI disturbances, so the partitioning here is split in Case 02a (e-h) and 02b (i-l). Lines, dots, and circles are as described in figure IV.2.1. 151

IV.2.4 One-dimensional wave-number and angular-frequency EDF of longitudinal velocity fluctuations. Numerical experiments with different types of sea-state prescription. Atmospheric turbulence in blue full line; Total fluctuation spectra in black dotted line; Wave Induced auto-spectra in red dashed line; Wind-Wave cross-spectra in magenta dot-dashed line. The light blue vertical line denotes the wave peak period. 155

IV.2.5 Wave-number-angular-frequency 2D turbulent spectra. The lower dashed line follow the dispersion equation in the wavy cases (b-d). The upper dashed line follow the mean convection velocity u_1 and represents the Taylor hypothesis for the atmospheric turbulent part. 156

IV.2.6 Wave-number-angular-frequency 2D turbulent spectra partitioning for the wavy Cases 01 (a,b), 02 (c,d) and 03 (e,f). Atmospheric (Atm.) turbulence part in (a,c,e) and Wave Induced (WI) part in (b,d,f). The upper dashed line stands for the Taylor hypothesis and the lower dashed line for the dispersion equation. 159

IV.2.7 Atmospheric part of the resultant spectra, i.e. the Atm. auto-spectra $E_{\hat{u}_R\hat{u}_R}(k,w)$. Employing the partition described at section IV.2, The WI disturbance has been deduced from the the total fluctuation spectra, previously shown at figure II.3.3. The mean wind velocity $\overline{u}_R$ and the wave velocities c (Dispersion equation with $d = 22$ m), appear in black dashed lines. 160

IV.2.8 Decomposed atmospheric part ($E_{\hat{u}_R\hat{u}_R}$) of the 'Ocean to sLiDAR' component, of the four quadrant spectra shown in figure IV.2.7b. The black dashed lines denote wind and wave characteristic scales, as in figure IV.2.7. 161

IV.2.9 Resultant wave-number (a,c) and frequency (b,d) 1D decomposed turbulent spectra for Case 01 (a,b) and Case 02.a (c,d). The **legend** associates the five spectra depicted to: The (**Ref. ESDU**) reference; total turbulent fluctuation auto-spectra (**Total**); Atmospheric turbulence auto-spectra (**Atm.-Atm.**); Wave Induced auto-spectra (**WI-WI**); and (**Atm.-WI**) cross spectra. Vertical blue lines stand for the wave peak scales k_p and f_p, and the green lines show filter scales k_γ and $f_{\gamma 1}$. 162

IV.2.10 One-dimensional decomposed spectra ($E_{u'_R u'_R}$, $E_{\hat{u}_R\hat{u}_R}$, $E_{\tilde{u}_R\tilde{u}_R}$, and 2 $E_{\hat{u}_R\tilde{u}_R}$) for fluctuations traveling from the Ocean into the sLiDAR, at Case 02a. The legends apply as for Case 01 in figure IV.2.9, that in turn denote the resultant spectra comprehending motions in both directions, and where the explicit WI auto spectra has been omitted for Case 02a. 163

IV.2.11 Wave Induced fraction $\mathscr{F}(k)$ (Left) and $\mathscr{F}(w)$ (Right), corresponding to the squared root of the WI energy fraction according to equation IV.1.3. After integrating the 2D decomposed spectra in the 1D spectra of figure IV.2.10, $\mathscr{F}(k)$ and $\mathscr{F}(w)$ are here computed as $\mathscr{F}(k) = \sqrt{E_{\tilde{u}_R\tilde{u}_R}(k)/E_{u'_R u'_R}(k)}$ and $\mathscr{F}(f) = \sqrt{E_{\tilde{u}_R\tilde{u}_R}(f)/E_{u'_R u'_R}(f)}$. Wave peak scales denoted by vertical dotted lines, with black (Case 01) and red (Case 02a) colors corresponding to the curves of $\mathscr{F}$ shown in the legend. The filter characteristic scales (k_γ, $f_{\gamma 1}$) appear in the vertical green dotted line. 164

IV.2.12 Sea-State forcing and the atmospheric response. Sea-State forcing (F): Auto-spectra of the longitudinal orbital velocities on the free-surface (FS). Atmospheric response ($E_{\tilde{u}_R\tilde{u}_R}$): Auto-spectra of the WI flow, as previously shown at figure IV.2.9. Cases 01 and 02a superposed, with line types given in the legend. Together with the sea-state forcing, the corresponding wave peak scales are shown in vertical lines. The peak scales correspond to peaks of the FS displacement spectra, and not to the velocities spectra shown in the figures. The filter characteristic scales (k_γ, $f_{\gamma 1}$) appear in the vertical green dotted line. 165

IV.2.13 Transfer function between the Sea-State forcing and the atmospheric response shown in figure IV.2.12. Computed as TF= $\sqrt{(E_{\tilde{u}_R\tilde{u}_R})/F}$. Cases 01 and 02a superposed, with line types given in the legend. Together with the TF, the corresponding wave peak scales are given in vertical lines. The filter characteristic scales (k_γ, $f_{\gamma 1}$) appear in the vertical green dotted line. 165

IV.3.1 The PDF of the surface elevation F. $F(f,\phi)$ is obtained far from the sLiDAR, and reconstructed to match the global parameters obtained closer to the sLiDAR. (a) Integrating $F(f,\phi)$ in ϕ dimension, the reconstruction is evaluated in comparison to the 1D and 2D spectral input, obtained closer and farther to the sLiDAR, respectively. (b) The 2D spectral input $F(f,\phi)$. (c) The 2D spectral output, $F(f,\phi)$ reconstructed to match $F(f)$, ϕ and β closer to the sLiDAR. In (b) and (c) the frequency-dependent mean direction $\beta(f)$ is shown with black dotted lines as obtained from each spectra, and the value of β probed closer to the sLiDAR appears with black dashed lines. 168

IV.3.2 The interpolation of $F(f,\phi)$ into $F(k_x,k_y)$. 169

IV.3.3 Flat bottom numerical experiment evaluating the sLiDAR filter effect. Wavenumber (a) and frequency (b) 1D turbulent spectra. Cases 00 (No filter) in blue full line, Case 01 (L_γ = 25 m) in red dashed line, and Case 02 (L_γ = 50 m) in green dashed-dotted line. The filter scales $k_{\gamma 0}$ and $f_{\gamma 0}$ appear in the vertical lines associated to Case 01 and Case 02. The reference ESDU 85020 spectra is traced in black dotted lines, with parameters obtained for Case 00. The auto-correlations $\left[u'_R u'_R\right]_0$ normalizing the spectra are also obtained for Case 00. 172

IV.3.4 Wave-number-angular-frequency 2D turbulent spectra, for the flat bottom numerical experiment evaluating the sLiDAR filter effect. The mean wind velocity corresponding to the Taylor hypothesis appears in black dashed line. In Cases 01 and 02 the green dotted lines denote the characteristic filter scales L_γ and $T_{\gamma 0}$. 173

IV.3.5 Wavy bottom numerical experiment evaluating the sLiDAR filter effect. One dimensional turbulent spectra as: Case 00 (No filter) in blue full lines; Case 01 ($L_\gamma = 25$ m) in red dashed lines; Case 02 ($L_\gamma = 50$ m) in green dot-dashed lines. The filter characteristic scales k_γ and $f_{\gamma 0}$ appear in the vertical lines, with types and colors corresponding to their Case spectra. Everything normalizes by the auto-correlation $\overline{u'_R u'_R}|_0$ obtained for Case 00. The ESDU reference appears in black dashed lines with its parameters obtained for Case 00. 175

IV.3.6 Wave-number-angular-frequency 2D turbulent spectra, for the wavy bottom numerical experiment evaluating the sLiDAR filter effect. The mean wind velocity corresponding to the Taylor hypothesis appears in green full lines, and the waves velocities given by the intermediate water dispersion equation appears in red dashed lines. In Cases 01 and 02 the dotted lines denote the characteristic filter scales: L_γ in yellow, $T_{\gamma 0}$ corresponding to Taylor hypothesis in green, $T_{\gamma 1}$ corresponding to the dispersion equation in red. 176

IV.3.7 Wave-number-frequency 2D turbulent spectra for the decomposed Atmospheric Turbulence part. Wavy bottom numerical experiment evaluating the sLiDAR filter effect. The mean wind and the waves velocities appear in black dashed lines. Again, the dotted lines denote the characteristic filter scales: L_γ in yellow, $T_{\gamma 0}$ in green, $T_{\gamma 1}$ in red. 177

IV.3.8 Wave-number-frequency 2D turbulent spectra for the decomposed Wave Induced part. Wavy bottom numerical experiment evaluating the sLiDAR filter effect. Same scales as usual in (a,b,c); Scales adjusted to highlight the comparison in (d,e,f). The mean wind and the waves velocities appear in black dashed lines. Again, the dotted lines denote the characteristic filter scales: L_γ in yellow, $T_{\gamma 0}$ in green, $T_{\gamma 1}$ in red. 178

IV.3.9 Wave-number dependent 1D spectra, decomposed into Atm. turbulence and WI flow. To be compared to the ESDU reference. Wavy bottom numerical experiment evaluating the sLiDAR filter effect. The vertical dotted light blue lines stand for the wave peak wave-number, and the green for the wave-number filter scale k_γ. The ESDU reference appears in the dashed black lines. 179

IV.3.10 Frequency dependent 1D spectra, decomposed into Atm. turbulence and WI flow. To be compared to the ESDU reference. Wavy bottom numerical experiment evaluating the sLiDAR filter effect. The vertical dotted light blue lines stand for the wave peak frequency. The vertical green and red lines stand for the filter frequencies $f_{\gamma 0}$ and $f_{\gamma 1}$, respectively. 179

IV.3.11 Sea-State forcing and the atmospheric response, for the wavy bottom numerical experiments evaluating the sLiDAR filter effect. Sea-State forcing (F) in black dotted lines and circles: Auto-spectra of the longitudinal orbital velocities on the free-surface (FS). Atmospheric response ($E_{\tilde{u}_R \tilde{u}_R}$): Auto-spectra of the WI flow, as previously shown at figures IV.3.9 and IV.3.10. The vertical lines colored accordingly to each spectra denote the filter characteristic scales k_γ, $f_{\gamma 1}$. The vertical black line denote the wave peak scales k_p and f_p. 181

IV.3.12 Wave Induced fraction $\mathscr{F}(k)$ and $\mathscr{F}(f)$, for the wavy bottom numerical experiments evaluating the sLiDAR filter effect. The vertical lines colored accordingly to each spectra denote the filter characteristic scales k_γ, $f_{\gamma 1}$. The vertical black line denote the wave peak scales k_p and f_p. 182

IV.3.13 Wave-number-frequency 2D turbulent spectra for the decomposed Atmospheric Turbulence part. Comparison between physical and numerical experiments. The mean wind and the waves velocities appear in black dashed lines. The dotted lines denote the characteristic filter scales: L_γ in yellow, $T_{\gamma 0}$ in green, $T_{\gamma 1}$ in red. 183

IV.3.14 Wave-number-frequency 2D turbulent spectra for the decomposed Wave Induced part. Comparison between physical and numerical experiments. The mean wind and the waves velocities appear in black dashed lines. The dotted lines denote the characteristic filter scales: L_γ in yellow, $T_{\gamma 0}$ in green, $T_{\gamma 1}$ in red. 184

IV.3.15 Wave Induced 1D spectra. Comparison between physical and numerical experiments: Case 00.Num in blue full lines; Case 01.Num in red dashed lines; Case 01.Phys in golden dot-dashed lines. The dotted vertical black lines stand for the wave peak scales k_p and f_p, and the other vertical lines for the filter characteristic scales k_γ and $f_{\gamma 1}$. The black dotted lines and circles denote the sea-state longitudinal velocity EDF $F(k)$ or $F(f)$. Above (a,b), the spectra are normalized by the total auto-correlation obtained in Case 00, and below (c,d) the normalization occurs with respect to the WI auto-correlation obtained for each case. 185

IV.3.16 Wave Induced fraction, giving the relative intensity of WI in Total fluctuations. Comparison between physical and numerical experiments: Case 00.Num in blue full lines; Case 01.Num in red dashed lines; Case 01.Phys in golden dot-dashed lines. The vertical black lines correspond to the wave peak scales k_p and f_p, and the others to the filter characteristic scales k_γ and $f_{\gamma 1}$. 186

IV.3.17 Transfer function, giving the ratio between the WI atmospheric response to the sea-state longitudinal velocity spectra. Comparison between physical and numerical experiments: Case 00.Num in blue full lines; Case 01.Num in red dashed lines; Case 01.Phys in golden dot-dashed lines. The vertical black lines correspond to the wave peak scales k_p and f_p, and the others to the filter characteristic scales k_γ and $f_{\gamma 1}$. 187

A.1 Asymptotic Old-Sea: Monochromatic wave (Swell) of length λ and phase velocity c propagating under static wind and neutral atmospheric condition. The Stokes orbitals (represented by the spirals) and drift are extended to the atmosphere. In crests and troughs the longitudinal velocities (horizontal arrows with opposite senses) are discontinuous. The discontinuity reveals a viscous boundary layer across the free-surface. The wave is damped by the pressure distribution perfectly out of phase with the wave slope, represented by the fictitious resultant force F_p. 217

A.2 Asymptotic Young-Sea: Waves with lengths on the order of the ABL roughness length may occur in the free-surface. Turbulence generates and feeds energy to the ripples by means of fluctuating pressure forces F_p [Phillips, 1957]. In the inner region, turbulence is mostly isotropic and blocked by the free-surface. In the outer region turbulence is highly anisotropic and dependent on the other boundary conditions. The shear is positive, and the $u'w'$ correlations predominantly negative (Clock-wise turning eddies). . 217

A.3 A monochromatic wave with phase velocity c drags an initially undisturbed ABL flow. The problem is usually described in the wave following frame of reference, and a reversed flow appears below z_c where $\overline{u}_1(z_c) = c$, inducing the vorticity distribution attributed to the solution of Miles' BVP, in Miles [1957]. 218

A.4 Miles mechanism of wave growth/ damping, relying in the existence of a critical height z_c where the mean wind $\overline{u}_1$ equals the phase velocity of the wave. A discontinuity in the BVP posed by Miles [1957] appears through a continuous vorticity distribution (Orange spirals) in the critical height, which is responsible for the wave growth/ damping (F_p). 219

A.5 Sheltering related mechanisms of wave grow or damping (F_p). The (separated) sheltering theory of Jeffreys [1925] relies in the flow detachment denoted by the orange spiral. The detachment can only occur in large wave slopes, but a non-separated sheltering effect invariably occurs as described in Belcher and Hunt [1993]. In the inner region there is an asymmetric disturbance of the streamlines and stresses. In the outer region the disturbance is mostly symmetric, but displaced by the non-separated sheltering of the inner region. The (partially) out-of-phase pressure distributions leads to the resultant pressure forces F_p. 219

B.1 Previous coupling procedure developed in Cathelain [2017]. 228

B.2 Current coupling procedure, here developed. 229

C.1 Two-dimensional spectral mapping of T_f. The mean wind velocity corresponding to the Taylor hypothesis appears in black full line, and the waves velocities given by the dispersion equation appears in red full line. The filter characteristic length is L_f denoted by the green vertical line. Probing T_f along the Taylor hypothesis gives the characteristic $T_f = L_f/U$ for atmospheric motions, denoted by a black dotted line. Probing T_f along the dispersion relation gives the characteristic $T_f = L_f/c(k)$ for WI motions, denoted by a red dash-dotted line. 232

C.2 Wave-number-frequency 2D turbulent spectra for Case 00 (No filter) exploited in section IV.3.3. The dashed line corresponds to the characteristic convective velocity given by the Taylor hypothesis. In (b) an elliptical model denoted by the magenta dashed line, fits to the contour given in blue full line and dots. 235

C.3 The base-line function of the proposed model, defined in equation C.9; Multiple deviations from $[A,\ w_0,\ w_1,\ w_2, \lambda,\ \alpha,\ \beta] \leftrightarrow [A = 1,\ w_0 = 1,\ w_{10} = 0.2,\ w_{20} = 0.2,\ A_p = 10,\ \alpha_0 = 1,\ \beta_0 = 1]$. 237

C.4 The base-line function of the proposed model. Defined in equation C.9 with $[A_0 = 1,\ w_0 = 1,\ w_{10} = 0.2,\ w_{20} = 0.2,\ \alpha_0 = 1,\ \beta_0 = 1]$, and varied A_p. Fitted Gaussian $A\ \exp[-0.5\ (x - x0)^2/k^2]$ and Power law $A\ [(x - x0)^2]^{-k}$ for comparison with Narita [2017]. 238

C.5 Wave-number spectrum E_k and the peak value $A_p = E(k, w_0(k))$. 241

C.6 2d spectra $E(k, w)$ and four fitting functions $g(k, w)$ defined in table C.1. . . 242

C.7 Fitting error distribution (log[$g(k, w)$]-log[$E(k, w)$]) for the functions $g(k, w)$ defined in table C.1. 243

LIST OF TABLES

I.2.1 Approximated roughness length z_0 associated to different terrain types, from Troen and Lundtang Petersen [1989]. 26

II.1.1 Description of scans for case 01 (f-LOS 01), case 02 (f-LOS 02) and mean horizontal Wind Speed/ Direction determination (PPI). 57

II.1.2 Summary of the wind parameters. 60

II.1.3 Summary of the sea-state parameters. 60

II.2.1 Steadiness and homogeneity evaluation at the large scale motions of grid (a) in figure II.2.3, through the criteria $\mathcal{V}^{(0x,0t)}$ ($\mathcal{V}^{(1x,1t)}$ in parenthesis) established in equation II.2.3. Rate of change (%) per $\tau = 2$ min (In $\mathcal{V}^{(t)}$), and $r_b = 200$ m (In $\mathcal{V}^{(x)}$). 70

II.2.2 Steadiness evaluation at the very large scale motions of grid (b) in figure II.2.3, through the criteria $\mathcal{V}^{(0t)}$ ($\mathcal{V}^{(1t)}$ in parenthesis) established in equation II.2.3. Rate of change (%) per $\tau = 10$ min. 70

III.1.1 Description of the structured grids employed. The domain is discretized with $n_{\text{total}} = n_x\, n_y\, n_z$ cells. The aspect ratio at the first grid is kept constant $z_{w1}/\Delta x = 1/3$. 90

III.2.1 Log-Fit of eq. III.1.15: Optimal $[\alpha]$ for $RMS_{diff} < 3{\cdot}10^{-3}$ in $z_{mid} + \left[-\frac{z_{len}}{2}, +\frac{z_{len}}{2}\right]$.103

III.2.2 Log-Fit of eq. III.1.15: Optimal $[C_d/\kappa, \alpha]$ for $RMS_{diff} < 3 \cdot 10^{-3}$ in $z_{mid} + \left[-\frac{z_{len}}{2}, +\frac{z_{len}}{2}\right]$. 103

III.3.1 The parameters of figure III.3.1 probed at the final time-step, and the correspondent reference values. 112

III.3.2 The form drag dependency on the WA is here represented by equation III.3.1, fitted with parameters given below. The resultant fitting is drawn in purple at figure III.3.4c. 113

III.3.3 Log-Fit of eq. III.1.15 to the inner surface layer (1st two cells): Optimal $[\alpha]$ with $C_d = 1$. 116

III.3.4 Log-Fit of eq. III.1.15 to the outer surface layer: Optimal $[C_d, \alpha]$ for $RMS_{diff} < 3 \cdot 10^{-3}$ in $z_{mid} + \left[-\frac{z_{len}}{2}, +\frac{z_{len}}{2}\right]$. 116

III.3.5 Linear fitting to the total shear stresses revealed in figure III.3.10a. At the upper boundary $\tau_{13}(z = z_l) = 0$, so the table gives the values of $\tau_{13}(z = 0)$, sufficient to specify the linear approximation. 122

III.3.6 The total drag F_τ as a function of the WA_{ref}, is approximated in figure III.3.11 by a linear fitting with equation $F_\tau / u^{*2} = A \cdot \mathrm{WA}_{ref} + B$; and the coefficients are given hereby. 123

III.4.1 Mean history quantities, probed at the last time-step of figures III.4.1, III.4.2, and III.4.3. Sliding statistics are taken with time average $t_{avg} = 41\ T_0$. 129

III.4.2 Logarithmic fit of equation III.1.15 to the wind profile in the outer surface layer. Optimal α ($C_d = 1$) for $RMS_{diff} < 3 \cdot 10^{-3}$, in $z_{mid} + \left[-\frac{z_{len}}{2}, +\frac{z_{len}}{2}\right]$. . 130

IV.3.1 Fraction of energy lost below or above the filter characteristic scales; Ratio between the integrated EDF for Cases 01 and 02, and the integrated EDF of Case 00. 172

IV.3.2 Energy distribution and filtering deficit per Case. In Case 00 the total energy (Giving TI = 6.7% with U = 4.0 m/s) is distributed into Atm. turbulence ($E_{\hat{u}_1\hat{u}_1}$), WI motions ($E_{\tilde{u}_1\tilde{u}_1}$), and Atm-WI cross-correlations ($2E_{\tilde{u}_1\hat{u}_1}$). For Cases 01 and 02 it is shown the energy deficit with respect to Case 00, for each spectral contribution. 180

C.1 Optimized values for the parameters determining the approximated functions with four different sets (Cases) of different degrees of freedom. Fitting error log-RMS_e for each test case given in the last row. 240

Lists of Notation

Abbreviations

ABL	Atmospheric Boundary Layer
Atm.	Atmospheric, usually designating atmospheric turbulence
DNS	Direct Numerical Simulation
CFL	Courant–Friedrichs–Lewy number
Ec	Eckert number
Fr	Froude number
LES	Large Eddy Simulation
LiDAR	Light Detection And Ranging System
Ma	Mach number
MABL	Marine Atmospheric Boundary Layer
MOST	Monin Obukhov similarity theory
PIV	Particle Image Velocimetry
Pr	Prandtl number
Re	Reynolds number
sLiDAR	scanning LiDAR
TI	Turbulence Intensity
TKE	Turbulent kinetic energy
Ri	Richardson number
RWS	Radial Wind Speed
WA	Wave Age
WBL	Wave Boundary Layer
WC	Wave Coherent
WI	Wave Induced

Mathematical operators

$\lvert\cdot\rvert$	Absolute value
$\lVert\cdot\rVert$	Euclidean Norm of a vector ($\lVert\cdot\rVert_{[x]}$ in x direction)
$\cdot'$	Fluctuations
D/Dt ..	Material derivative
∇	Nabla operator
$\tilde{\cdot}$	Wave related (Coherent $\tilde{\cdot}^C$ or Wave Induced $\tilde{\cdot}^I$) fluctuation
$\hat{\cdot}$	Wave unrelated (Not Coherent $\hat{\cdot}^C$ or Atmospheric turbulence $\hat{\cdot}^I$) fluctuation
$\overset{\circ}{\cdot}$	In-quadrature counterpart of $\cdot$
$\bar{\cdot}$	Generic average ($\bar{\cdot}^{[x]}$ in x direction)
$\breve{\cdot}$	LES filtered field
$\breve{\cdot}$	LES residual field
tr	Trace of a tensor
∂	Partial derivative

GREEK SYMBOLS

β_θ ...	.....	Coefficient of thermal expansion
γ_1, ...	γ_2, γ_3 ..	3rd order Runge Kutta coefficients
$\Delta\Theta$ ..	.....	Characteristic temperature difference
Δt ...	.....	Time step
$\Delta u_{[\xi_1,\xi_2]}$,	$\Delta u_{[\xi_3]}$ ..	Transversal and vertical, velocity difference boundary conditions
Δx ...	$\Delta y, \Delta z$ ..	LES cell sizes in x, y and z directions
$\boldsymbol{\delta}$ ...	(δ_{ij}) ...	Kronecker delta Tensor
δ ...	.....	Boundary Layer height
δE ...	.....	Internal energy change
δQ ..	.....	Heat Transfer
δW ..	.....	Work Transfer
$\delta_k(\cdot)$ ..	.....	Dirac function operator.
ϵ, ...	$\boldsymbol{\epsilon}$	Dissipation, and rate-of-dissipation tensor
ϵ_0 ...	.....	Pseudo-dissipation
ϵ_{ijk} ..	.....	Permutation Symbol
ζ_1, ...	ζ_2	3rd order Runge Kutta coefficients
η ...	.....	Free-surface position
$\dot{\eta}$ ...	.....	Free-surface lagrangian vertical velocity
η_0 ...	.....	Kolmogorov scale
θ ...	.....	Temperature
θ_{FS} ..	.....	Temperature at the free-surface
θ_p ...	.....	Potential temperature
θ_v ...	.....	Virtual temperature
κ ...	.....	Von Karman constant
λ ...	.....	Wave-Length
μ, ...	(μ_w, μ_a)	Dynamic molecular viscosity (μ_w in water, μ_a in air)
μ_θ ...	.....	Thermal conductivity
ν ...	.....	kinematic molecular viscosity
ν_e ...	.....	Turbulent dummy viscosity
ν_t ...	.....	Turbulent kinematic viscosity
$\boldsymbol{\xi}$ ...	(ξ_1, ξ_2, ξ_3)	Computational coordinates
ρ ...	(ρ_w, ρ_a)	Specific mass (ρ_w in water, ρ_a in air)
ρ_∞ ..	.....	Reference specific mass
$\boldsymbol{\sigma}$ ...	.....	Cauchy Stress tensor
$\boldsymbol{\tau}^{LES}$ ..	.....	LES Sub-Grid Stress tensor
$\boldsymbol{\tau}^{(\mu)}$ ..	.....	Dynamic Viscous Shear Stress tensor
$\boldsymbol{\tau}^{(\nu)}$ ..	.....	Kinetic Viscous Shear Stress tensor
$\boldsymbol{\tau}^{(r)}$ ..	.....	Reynolds Stress tensor
$\boldsymbol{\tau}^{(W)}$ ..	.....	Wave related (Coherent or Induced) velocities Stress tensor
$\boldsymbol{\tau}^{(P)}$ ..	.....	WI pressure stress
$\boldsymbol{\tau}^{(P0)}$ ..	.....	Form drag tensor

τ ...	.....	Period
τ_0 ...	.....	Turbulent characteristic period
τ_w ..	.....	Wall Friction
ϕ ...	.....	Azimuth angle
$\phi_{\boldsymbol{u}}$ ..	.....	Velocity potential
χ ...	.....	Generic variable
ω_0 ..	.....	Characteristic angular frequency

LATIN SYMBOLS

$\boldsymbol{A}$ ...	.....	Generic matrix.
$\boldsymbol{a}$	a_{mn} ..	Wave modal amplitudes
a ...	.....	Wave amplitude
B ...	B_δ ...	Integration constants
$\boldsymbol{b}$ ...	.....	Generic vector.
$\boldsymbol{c}$ ...	.....	Generic vector.
c ...	.....	Wave phase velocity.
c_g ...	.....	Wave group velocity
c_p ...	.....	Specific heat capacity at constant pressure
c_s ...	.....	Speed of Sound
$E_{\chi_i\chi_j}$, .	$\boldsymbol{E}_{\chi_i\chi_j}$ ..	EDF of the correlation, and tensor, of generic variables χ_i and χ_j
E_k, ..	E_w, E_{kw}	wave-number k, angular frequency w, or joint $k-w$ dependent EDF
e ...	.....	Turbulent or Residual Kinetic Energy
$\mathscr{F}$ ...	.....	Wave Induced fraction
F ...	.....	Power density function of the free-surface (FS) elevation: FS spectra
F_p ...	$\tau_{13}^{(P0)}$ ..	Form drag
F_τ ...	.....	Total drag
$\boldsymbol{f}$	$(0,0,f_3)$	Coriolis vector parameter
f ...	.....	Frequency
f_0 ...	.....	Characteristic flow frequency
G ...	.....	LES filter.
$\boldsymbol{g}$	$(0,0,-g)$	Gravity vector parameter
H ...	.....	Wave height
h ...	.....	LES vertical grid position
$\dot{h}$ ...	.....	LES vertical grid speed
$\boldsymbol{I}$ ...	.....	Identity tensor
i	.....	Imaginary unit
J ...	.....	Jacobian
$\hat{\boldsymbol{j}}$	(j_1, j_2, j_3)	Unit vector
$\boldsymbol{k}$	(k_1, k_2, k_3)	Wave-number space
k ...	.....	One-dimensional wave-number

L_0	Characteristic flow length
l_0	Turbulent characteristic length
l_{DI}	Lower limit of the universal equilibrium range of Kolmogorov turbulent cascade
l_{EI}	Upper limit of the universal equilibrium range of Kolmogorov turbulent cascade
l_L	Integral length scale $\sim l_{EI}$
l_λ	Taylor micro-scale $\sim l_{DI}$
L_O	Obukhov length
L_z	Characteristic scale height
n_x, n_y, n_z .	LES number of nodes in x, y and z directions.
$P \ldots, \boldsymbol{P}$	Turbulent production term, and tensor
p	Pressure (p_w in water, p_a in air)
p_{FS}	Pressure acting in the free-surface
p_∞	Reference pressure
$Q \ldots, \boldsymbol{Q}$	Pressure-rate-of-Strain, and tensor
q	Kinematic heat flux $\overline{w'\theta_v'}$
q_h	Humidity
r	Distance
$\mathscr{R}^{[E]}$ ...	Generic right-hand-side of the equation identified by the superscript $[E]$
$R_{\chi_i\chi_j}, \boldsymbol{R}_{\chi_i\chi_j}$	Correlation function, and tensor, of generic variables χ_i and χ_j
RMS_{diff} .	Round-Mean-Squared difference
$\boldsymbol{S}$	Symmetric part of the velocity gradient $\nabla\boldsymbol{u}$ ($\boldsymbol{S}_W$ in water, $\boldsymbol{S}_a$ in air)
$S_{x\pm}$	Inlet (S_{x-}) and Outlet (S_{x+}) boundaries in the longitudinal direction
$S_{y\pm}$	Right (S_{y-}) and Left (S_{y+}) boundaries in the transversal direction
$S_{z\pm}$	Lower (S_{z-}) and Upper (S_{z+}) boundaries in the vertical direction
t	Time
t_{avg} ...	Average period
T	Wave period
T_0	Characteristic flow time
T_p	Wave peak period
T_s	Swell period
$T_{\gamma 0}$	sLiDAR filter period assuming Taylor hypothesis
$T_{\gamma 1}$	sLiDAR filter period assuming the waves dispersion relation
$T_{\mathscr{P}}$	Natural period for the dynamic pressure gradient algorithm
$T^{(r)}, \boldsymbol{T}^{(r)}$	Turbulent transport term, and tensor
$\hat{\boldsymbol{U}}$	Contravariant velocity
U	Characteristic longitudinal velocity
U_0	Characteristic flow velocity
u^*	Friction velocity
$u^*_{[\xi_1,\xi_2]}$ ..	Friction velocity for log-law boundary condition
u_{FIT} ...	Fitted average wind speed profile
$\boldsymbol{u}$	(u_1, u_2, u_3) | (u, v, w) | Velocity vector
u_0	Turbulent characteristic velocity
U_∞	Free-Stream velocity
V	Characteristic vertical velocity
$\vec{v_m}$	Lagrangian velocity of a particle.

w	Angular frequency
$\boldsymbol{x}$	(x_1, x_2, x_3) | (x, y, z) | Physical coordinates
x_l, y_l, z_l .	LES domain extension in x, y, and z directions
z^+	Non-dimensional vertical coordinate $= zu^*/\nu$
z_∞	Reference height
z_0	Roughness length
z_c	Critical height
z_i	Inversion Layer height
z_{w1} ...	First grid size in z direction

INTRODUCTION

This Thesis concerns fluid mechanics' studies of fundamental phenomena in earth sciences, in which deeper understanding is required for engineering purposes. On the offshore environment takes place different engineering activities, often encountering great technological challenges due to the physical complexities and environmental concerns. Particularly, overcoming these challenges gives access to multiple energy sources. Nowadays one could first think of currents, waves, wind and solar, but the most mature offshore energy industry is still oil and gas. It turns out that it is imperative for humanity to rapidly change its energy supply bases to clean sources, being large amount of research devoted into developing its competitiveness against the pollutant, non-renewable, and well established alternatives. Challenging as it might be, the exploitation of Offshore Renewable Energy sources offers the potential to supply a considerable amount of the global energy demand in the near future.

Wind energy harvesting is an example of well established clean energy industry, on which many nations, such as France, rely to review its energy bases in compliance with the international pact at the Paris climate conference (COP21). In coastal areas, wind turbines deployment migrate to the offshore environment, where huge spaces are available in stronger and better behaved wind conditions. The offshore environment imposes new challenges to a well established wind energy industry. Increasing the distance to the coast and water depths leads to significant rise in operational costs, that are sustained through increasing production, and more efficient engineering. It is imperative to accurately predict and describe the offshore wind resource in order to propose cost efficient solutions, as one can then act in site planning, design and operational phases to maximize production and reduce costs.

Much of the challenges encountered by the offshore wind energy industry relate to an insufficient understanding of the environment behavior, a natural subject for fluid mechanics. The concerned flow is characterized by a turbulent Atmospheric Boundary Layer (ABL), where the ocean's dynamics significantly alters the atmospheric flow through higher heat capacity, and complex wind-wave interactions that are significant in fairly common situations. Though wind-wave interactions are clearly important determining for example, the waves growth and ocean circulation processes, their impact to the wind resource is largely unknown, recently becoming a major field of interest for the scientific community. The Hydrodynamics, Energetics and Atmospheric Environment Laboratory (LHEEA) from Ecole Centrale de Nantes, France, is particularly active in studies concerning, for example: Offshore Renewable Energy sources; Ocean and Atmospheric dynamics in coastal areas; and more recently Wind-Wave interactions.

So this Thesis reviews and extends the current knowledge regarding Wind-Wave interactions in the lower part of the Marine ABL (MABL), where they are possibly significant in the characterization of the wind resource. The MABL is investigated through physical and numerical experiments, to reveal the role of Wave Induced (WI) motions transferred from the sea into the atmosphere. Given the current state-of-the-art knowledge, this general objective translates into addressing, along the Thesis, some fundamental ***scientific questions*** regarding **wind-wave interactions**.

SCIENTIFIC QUESTIONS

According to theory and observations, WI disturbances extend into limited regions above the water free surface, generally referred as the **Wave Boundary Layer** (WBL). Though coupled to this inner layer through modified turbulent scales, the outer flow behaves similarly to static bottom atmosphere flows. The WBL is usually defined as the height below which WI disturbances are significant. Though, there is no universally accepted definition of the WBL. One of the reasons is that the criteria and techniques employed in the literature, often lack sensitivity to other significant WI disturbances. After all, the WI disturbances significance strongly depends on the variable of interest. ***Is it reasonable to expect a single definition to the WBL height?***

Inside the WBL, the waves' influence directly alters the flow dynamics with the appearance of the WI flow, and notably a **Wave Induced Stress** perturbation responsible for the vertical transfer of momentum between waves and wind. The WI Stress has drawn considerable attention of the scientific community over the last decades, and is often recognized as playing a most important role in wind-wave interactions. Notably, if the waves travel sufficiently fast with respect to the mean wind speed, the momentum transfer occurs upwards, and the wind speeds up due to the waves' incidence. Naturally, a wave-driven speed-up of the mean wind profile is of major importance to characterize the wind energy resource. ***When, and up to which extend does the WI stress and the wind speed-up become significant in the MABL?***

The **Wave Induced flow** refers to wave related dynamics (Velocities and Pressure) that advect through the atmosphere, yet maintaining some of its original aspects. The WI flow is supposedly significant in the WBL, and is the origin of other disturbances that propagate even higher on the MABL. Through the experimental literature, one often observes the consequence of WI motions distorting turbulent statistics in the WBL, but one rarely encounters a direct characterization of the WI field. ***Is it possible to extract the WI flow from the instantaneous wind speed measurements?***

WI motions are an extension (transfer) of the wave's orbital at the free-surface, into the atmosphere. Hence, there exists a **Transfer Function** (TF) linking the Sea-State forcing to the atmospheric response, i.e., to the WI field. The determination of such TF shall precede any parametric description of the WI field in the MABL, but it has not yet been reported in the literature as actual measurements in the offshore environment. The reason being that the WI flow itself is hardly reconstructed from the measurements. ***Can one establish a link between multi-scale waves and wave induced motions in the atmosphere?***

To afford multiple scenarios and real time applications, prediction tools for design and operational purposes rely on semi-empirical and low-fidelity numerical solutions. **State-of-the-art wind models** consider a mean wind log-law profile based on the Monin-Obukhov Similarity Theory (MOST), superposed to randomly generated turbulent components with statistics given, e.g, by the Mann spectra. It is observed though, that the mean wind profiles and its turbulent statistics considerably deviate from MOST and Mann's predictions on the vicinity of ocean waves. The investigation of the WBL at local scales is thus desired to improve low-fidelity MABL models. ***How to improve state-of-the-art wind models' accuracy in the offshore environment?***

Overview and Methodology

Engineering sciences are based on analytic, experimental and computational approaches. The complex phenomena characteristic of most engineering problems cannot be fully accessed by analytical studies, and imposes great difficulties for the alternatives. The rise on computational resources availability, recently allowed numerical approaches to complement or even substitute experiments: Saving costs and accessing scales and phenomena which cannot be fully accessed by current experimental technologies. Computational modeling is now commonly employed as **numerical experiments**, complementing or even substituting the reciprocal **physical experiments** of field-based measuring campaigns.

The proposed methodology follows previous analytical, experimental and computational approaches presented in Part I. A brief review of some analytical foundations in fluid mechanics is described at section I.1, introducing the governing equations that describe ocean and atmospheric flows. The development departs from the conservation equations of mass, momentum and energy in a continuum, written in an Eulerian frame of reference and applied to a Newtonian fluid, i.e., the Navier Stokes equations. The physical concepts of Ocean waves, Atmospheric Boundary Layer and Wind-Wave interactions are described in the literature review of section I.2. Compared to the foundations section, these physical descriptions rely a lot more into physical and numerical experiments to complement the theory. Special attention is given to the Wind-Wave interactions subject, closing the literature review of Part I, and further developing the questions stated above at section I.3.

The field experiment conducted during the Thesis' experimental campaign is presented at part II. The wave influence in the MABL is investigated within the WBL through field measurements taken above the Ocean by a scanning Light Detection and Ranging (sLiDAR) system, deployed in Le Croisic, France. Measurements from Plan Position Indicator (PPI) scans are used to assess Wind Direction and Wind Speed providing guidance to the case selection, while time-space descriptions of the Radial Wind Speed (RWS) are explored through staring Mode scans at the selected periods. The sLiDAR operates as described along section II.1, also introducing the selected test cases. General and often original post-processing techniques are exposed along section II.2. Results of the Radial Wind Speed (RWS) captured by the staring mode operating sLiDAR follow at sections II.3. Conventional methods are employed evaluating the RWS contours, and the one-dimensional (1D) wave-number or frequency spectra. More significant to the upcoming discussions, the sLiDAR operating in the proposed configuration allows an original two-dimensional (2D) wave-number-angular-frequency spectral analysis, yet not encountered in the literature at similar scales in the offshore environment.

The numerical model exploited during the Thesis is presented at part III. The MABL is investigated employing the Large Eddy Simulation (LES) solver developed by Peter Sullivan, from the National Center for Atmospheric Research (NCAR) of the United States of America, as described in section III.1. The test cases presented are built to investigate the WI disturbances above fast traveling waves, propagating under comparatively slow wind conditions in a situation commonly described as *old seas*. While first describing the WI disturbances observed in the LES generated MABL above monochromatic waves, section III.2 also introduces an original method to control the Wind Speed at a certain height above an arbitrary sea-state. The WI disturbances are investigated as function of varying Wave Age conditions

in section III.3. Non-monochromatic waves are presented in section III.4, with the comparison between regular, 1D irregular, and 2D irregular sea-states. In the comparison of section III.4, the 2D irregular sea-state corresponds to the conditions estimated during the experimental campaign, and the mean velocity at the measurement height also matches the one observed during the campaign.

Numerical and Physical experiments are both exploited in part IV, counting in an original analysis to quantify and qualify WI motions above arbitrary sea-states. The author introduces it as an enhanced perspective of the WI flow in section IV.1, because it characterizes the WI flow in an increasing level of detail if compared to the existing alternatives. The methodology proposed extends current definitions of the Wave Coherent flow, so that in the two-dimensional wave-number-angular-frequency spectra, the total energy splits into WI and Atmospheric contributions.

At section IV.1 the WI flow is evaluated for the monochromatic case, still counting only in the 1D spectral description. In physical and numerical experiments with irregular sea-states, it is unfeasible to effectively employ the methodology proposed, or the existing alternatives, counting only in the information available from the 1D spectra. In section IV.2 the partitioning of the 2D spectra leads to the decomposition of atmospheric turbulence and WI motions for each of the physical and numerical test cases presented.

The comparison of physical and numerical experiments closes part IV in section IV.3. It is then detailed the estimation of sea-state conditions encountered during the physical experiments, to be taken as boundary conditions in the numerical experiments. It is also described the modelling of the sLiDAR filtering effect incorporated in the numerical experiments. The sLiDAR filtering effect is so evaluated in flat and wave bottom numerical experiments. Finally gathering all the developments previously presented, it is here available the comparison between physical and numerical experiments, in a level of detail rarely available in the literature.

Part I

THEORETICAL, EMPIRICAL AND NUMERICAL FRAMEWORKS

Leonardo da Vinci (1452-1519). Sketch of winds encountering vertical cliffs, and supporting bird flight. From Richardson [2019].

I.1 Foundation in Fluid Mechanics

I.1.1 Theoretical framework

I.1.1.1 Incompressible Navier Stokes Equations

Applied to an incompressible medium $(D\rho/Dt) = 0$, under the continuum hypothesis and on an Eulerian frame of reference, the mass and momentum conservation principles are locally enforced by equations I.1.1 and I.1.2, respectively [Batchelor, 2000]:

$$\nabla \cdot \boldsymbol{u} = 0, \tag{I.1.1}$$

and

$$\rho \left[\frac{\partial \boldsymbol{u}}{\partial t} + (\boldsymbol{u} \cdot \nabla)\, \boldsymbol{u} + \boldsymbol{f} \times \boldsymbol{u} \right] = \nabla \cdot \boldsymbol{\sigma} + \rho \boldsymbol{g}, \tag{I.1.2}$$

being $\boldsymbol{u}(\boldsymbol{x}, t) = u_i$ the instantaneous velocity field; $\rho(\boldsymbol{x}, t)$ the specific mass, such that its material derivative $D\rho/Dt = \partial\rho/\partial t + (\boldsymbol{u} \cdot \nabla)\,\rho$ is null; $\boldsymbol{f} = f_i \delta_{i3}$ and $\boldsymbol{g} = -g\delta_{i3}$ the Coriolis and gravity vector parameters, respectively, and with δ_{ij} the Kronecker delta.

For a Newtonian fluid, the Cauchy stress tensor $\boldsymbol{\sigma}(\boldsymbol{x}, t)$ relates to the pressure $p(\boldsymbol{x}, t)$ and the symmetric part of the velocity gradient $\boldsymbol{S}$ through the dynamic molecular viscosity $\mu(\boldsymbol{x}, t)$ with $D\mu/Dt = 0$. The kinematic molecular viscosity is $\nu = \mu/\rho$, and equation I.1.3 so introduces the shear-stress tensor $\boldsymbol{\tau}^{(\mu)} (= \rho \boldsymbol{\tau}^{(\nu)})$:

$$\begin{gathered} \boldsymbol{\sigma} = -p\boldsymbol{I} + \boldsymbol{\tau}^{(\mu)}, \qquad \text{where} \\ \boldsymbol{\tau}^{(\mu)} = 2\mu \boldsymbol{S}, \qquad \text{and} \qquad \boldsymbol{S} = \frac{\left[\nabla \boldsymbol{u} + (\nabla \boldsymbol{u})^{(T)}\right]}{2}. \end{gathered} \tag{I.1.3}$$

Expressing the first law of thermodynamics, that balances internal energy (δE) with heat (δQ) and work (δW) transfers, the energy equation is written for the unknown temperature θ. Considering previous conservation equations for a Newtonian fluid, introducing the conductivity μ_θ, specific heat capacity at constant pressure (c_p), and the coefficient of thermal expansion (β_θ), the energy balance equation is written as:

$$\begin{gathered} \rho c_p \frac{D\theta}{Dt} - \beta_\theta \theta \frac{Dp}{Dt} = 2\mu\,(\boldsymbol{S} : \boldsymbol{S}) + \nabla\left(\mu_\theta \nabla \theta\right), \qquad \text{where} \\ c_p = \left(\frac{\delta Q}{\delta \theta}\right)_{\delta p = 0}, \qquad \text{and} \qquad \beta_\theta = \frac{1}{\rho}\left(\frac{\partial \rho}{\partial \theta}\right)_p. \end{gathered} \tag{I.1.4}$$

Equations I.1.1, I.1.2 (With I.1.3), and I.1.4 are known as the incompressible Navier Stokes (NS) equations.

The incompressibility constraint (eq. I.1.1) has several implications on the flow physical and numerical behavior. For stating incompressibility, one assumes that pressure waves travels much faster than the momentum convection effect, so that both phenomena can be uncoupled. Ultimately, this assumption may be translated into a low Mach number (Ma= U_0^2/c_s^2) requirement, on which the characteristic flow velocity U_0 is much smaller than the speed of sound c_s. Additionally (Batchelor [2000]), for oscillatory flows occurring in frequency f_0 and characteristic length L_0, the quantity to be minimized is $f_0^2 L_0^2/c_s^2$, as concerning gravity body forces gL_0/c_s^2 are to be small. The first and latest conditions might become important, e.g., in acoustics and meteorology studies, respectively. The incompressibility assumptions is equivalent to stating that pressure propagate instantaneously, and the thermodynamic equation I.1.4 is uncoupled from the equation of motion I.1.2. Nevertheless the simplification comes with a price, as the limit of incompressibility introduces the saddle point problem to the Navier Stokes equations (Le Quéré et al. [2010]), which has to be handled by very specific numerical approaches, such as the one presented in Sullivan et al. [2014] and further discussed in the appendix A.4.1.

The convection term $(\boldsymbol{u}\cdot\nabla)\,\boldsymbol{u}$ is highly non-linear, and in the often encountered cases where it becomes important, the solution of the NS equations will become increasingly complex and chaotic in what's referred as a turbulent flow regime (Jiménez [2004]): The flow becomes highly unsteady as the velocity, pressure and temperature fields rapidly vary in time and space; the flow streamlines are constantly distorted, broken and rebuild, merging and collapsing with each other; and the slightest change in boundary and initial conditions will lead to a drastically different solution of the NS equations. A ratio between inertial and viscous effects, with characteristic length L_0 and velocity U_0, the Reynolds number Re= $\rho U L_0/\mu$ usually characterizes the turbulence regime.

I.1.1.2 Free surface conditions

Considering air and water domains of generalized properties α_a and α_w respectively, continuity is then imposed on velocities and stresses passing through the interface $\eta(x,y,z,t)$. The kinematic condition infers that a particle on the interface keeps attached to it so that $D\eta/Dt = 0$ leads to equation I.1.5, while the dynamic condition is simply stated by the stresses continuity in equation I.1.6 (c.f. Batchelor [2000]).

$$\frac{\partial \eta}{\partial t} + \boldsymbol{u}\cdot\nabla\eta = 0, \qquad \text{at} \qquad \eta(x,y,z,t). \tag{I.1.5}$$

$$\begin{aligned} p_a &= p_w, \quad \text{and} \\ 2\mu_a \boldsymbol{S_a} &= 2\mu_w \boldsymbol{S_w}, \qquad \text{at} \quad \eta(x,y,z,t). \end{aligned} \tag{I.1.6}$$

I.1.1.3 Reynolds Averaged Navier Stokes Equations

For turbulence chaotic nature, and because in engineering applications one is often satisfied in accessing statistical quantities such as the mean and standard deviations of the flow fields, turbulent flows are usually described by stochastic approaches. The Reynolds decomposition is stated so that for any quantity χ, the turbulent flow may be described by mean ($\overline{\chi}$) and fluctuation (χ') values such that $\chi = \overline{\chi} + \chi'$. Inserting Reynolds decomposition into the velocity and pressure fields of the incompressible Navier Stokes equations I.1.1.1, and considering averaging properties known in this context as the Reynolds axioms, give rise to the Reynolds Averaged Navier Stokes (RANS) equations. When the RANS equations are applied to an unsteady problem one refers to the Unsteady RANS (URANS) equations:

$$\frac{\partial \overline{u_i}}{\partial t} + \overline{u}_j \frac{\partial \overline{u}_i}{\partial x_j} + f_j \overline{u}_k \, \epsilon_{ijk} = -\frac{1}{\rho}\frac{\partial \overline{p}}{\partial x_i} + \frac{\partial}{\partial x_j}\left[\tau_{ij}^{(v)} - \tau_{ij}^{(r)}\right] - g\delta_{i3}, \qquad \text{where}$$
$$\tau_{ij}^{(v)} = 2\nu \overline{S}_{ij}, \qquad \text{and} \qquad \tau_{ij}^{(r)} = \overline{u_i' u_j'}. \tag{I.1.7}$$

The continuity equation I.1.1 holds on the mean and instantaneous velocity fields:

$$\nabla \cdot \overline{\boldsymbol{u}} = 0, \qquad \text{and} \qquad \nabla \cdot \boldsymbol{u}' = 0. \tag{I.1.8}$$

The term $-\tau_{ij}^{(r)}$ in equation I.1.7 has its origin on the non linear term of the Navier Stokes equations, and designate components of the Reynolds Stress Tensor $-\rho\boldsymbol{\tau}^{(r)}$ that couple mean and fluctuation fields. In a probabilistic point of view, $\boldsymbol{\tau}^{(r)}$ are the correlation functions evaluated at the origin: $R_{ij}(r=0)$ further discussed in section I.1.1.5. The turbulent kinetic energy (TKE, e) is defined in terms of $\mathrm{tr}[\boldsymbol{\tau}^{(r)}]$ so that $e = \overline{u_i' u_i'}/2$.

The URANS equations solving the mean velocities will be later generalized to the LES equations solving the filtered velocities in section I.1.1.6, and e will be then called residual turbulent kinetic energy.

I.1.1.4 Reynolds Stress Tensor and Turbulent Kinetic Energy

Subtracting equation I.1.7 from the Navier Stokes momentum equations (I.1.2 and I.1.3) one obtains the equations for the instantaneous velocity field. With additional algebra demonstrated in Pope [2000] (pg. 315), one obtains the advection equation for the Reynolds Stress tensor $\boldsymbol{\tau}^{(r)}$, which is exposed containing the Coriolis effects, e.g., in Stenberg [2016]. The Turbulent Kinetic Energy (TKE) $e = \overline{u_i' u_i'}/2$ conservation equation derives from combining the equations for the diagonals of the Reynolds Stress Tensor (e=$\mathrm{tr}[\boldsymbol{\tau}^{(r)}]/2$) that gives:

$$\frac{\partial e}{\partial t} + \overline{u_j}\frac{\partial e}{\partial x_j} = -\frac{\partial}{\partial x_j} T^{(r)} + P - \epsilon_e - g\overline{\rho' u_3'} \tag{I.1.9}$$

where the TKE production P, the pseudo-dissipation ϵ_e and fluxes $T^{(r)}$ are given by:

$$P = -\tau_{ij}^{(r)} \frac{\partial \overline{u_i}}{\partial x_j} = -\tau_{ij}^{(r)} \overline{S}_{ij}, \qquad \epsilon_e = \nu \overline{\frac{\partial u_i'}{\partial x_j} \frac{\partial u_i'}{\partial x_j}},$$
$$T^{(r)} = \frac{\overline{u_j' u_i' u_i'}}{2} + \frac{\overline{p' u_j'}}{\rho} + T^{(\nu)}, \qquad \& \qquad T^{(\nu)} = -2\,\nu \frac{\partial e}{\partial x_j}. \tag{I.1.10}$$

Alternatively, equation I.1.9 can be written in terms of the actual dissipation $\epsilon = 2\nu \overline{S_{ij}' S_{ij}'}$ and a modified viscous diffusion term $T^{(\nu)}$, but the dissipation and pseudo-dissipation have usually similar values so that many authors refer to both simply as the dissipation (Pope [2000], pg. 132). The term $\overline{\rho' u_3'}$ consider turbulence generation or dissipation by buoyancy forces, and when the state equation is given in section I.1.2.2 relating ρ' to the temperature θ' that will reveal the cross-correlation term $\overline{\theta' u_3'}$ of major importance in atmospheric flows.

The convection and production terms in equations I.1.9 and I.1.10 are in closed form, involving only linear expressions of the resolved quantities, but the fluxes and dissipation terms must be empirically modeled. The energy flux term is usually modeled according to a gradient-diffusion hypothesis that with the introduction of a general turbulent viscosity ν_e translate into:

$$T = -\nu_e \frac{\partial e}{\partial x_j}. \tag{I.1.11}$$

Production is usually positive, acting as a source on equation I.1.9, while appearing with opposite sign, i.e, a sink, on the mean flow energy equation. The turbulent kinetic energy production usually transfers energy from the mean to the fluctuation fields, but the opposite may locally occur when its value gets negative (c.f. Gayen and Sarkar [2011] and Cimarelli et al. [2019]), through the inversion of the turbulent energy cascade described in section I.1.1.5. Only the symmetric part of the velocity gradient and the anisotropic part of $\boldsymbol{\tau}^{(r)}$ affect the production.

The dissipation ϵ is strictly positive transforming e into internal energy, and generally results into negligible amounts of changes on the fluid temperature. Although on eq. I.1.10, ϵ is directly proportional to ν, at sufficiently high Reynolds numbers it is found that ϵ is independent from the molecular viscosity ν, with a rise on the Reynolds number leading to smaller turbulent scales and consequently higher turbulent velocity gradients $\boldsymbol{S}'$. At such cases, ϵ is determined by the TKE production, being sufficient to stabilize the energy flux through the turbulent cascade (Pope [2000], pg. 188) discussed in section I.1.1.5.

I.1.1.5 Turbulent spectral distribution and scales

Turbulent spectra is the term commonly used, referring to the spectral density functions of pressure or velocities fluctuations, where the energy spectral distribution may be appreciated in the wave-number k and/or frequency f domains. A great deal of the theoretical development in turbulent flow dynamics is achieved in view of the turbulent cascade that Kolmogorov developed for the wave-number dependent turbulent spectra $E_k(k)$.

Taking the distance $\boldsymbol{r} = r\hat{\boldsymbol{j}}$ between two locations on the direction $\hat{\boldsymbol{j}}$, and given the wave number $k = 2\pi/r$, the one dimensional correlation function of χ_i and χ_j is defined as $R_r = R_{\chi_i'\chi_j'}(r) = \overline{\chi_i'(x)\chi_j'(x+r)}$ and the one-dimensional spectral density function $E_{\chi_i'\chi_j'}(k)$ as twice its Fourier transform (Pope [2000], pg. 225):

$$\begin{aligned} E_{\chi_i'\chi_j'}(k) &= \frac{1}{\pi}\int_{-\infty}^{\infty}\left[R_{\chi_i'\chi_j'}\ e^{-ikr}\right]\ dr \quad \text{with} \\ R_{\chi_i'\chi_j'}(r) &= \frac{1}{2}\int_{-\infty}^{\infty}\left[E_{\chi_i'\chi_j'}\ e^{-ikr}\right]\ dk. \end{aligned} \tag{I.1.12}$$

Kolmogorv turbulent cascade The turbulent energy is transferred from larger to smaller scales in a process known as the energy cascade (Kolmogorov [1991], from the original of**?**). At larger scales, the flow pattern is highly anisotropic, being fed by the mean flow energy and sensitive to boundary conditions. A scale l_{EI} exists, from which below the statistic turbulent properties become insensitive to larger scales anisotropies and the energy density spectra $E_k(k)$ depends only on the wave number k, the dissipation rate ϵ and the kinematic viscosity $\nu = \mu/\rho$. The scale l_{EI} represents the border between the larger energy-containing range and the universal equilibrium range. Another scale l_{DI} exists above which the viscous forces are negligible compared to inertial forces, so that E does not depend on ν. On high Reynolds flow, the inertial zone exists where $l_{DI} < r < l_{EI}$ and the energy density spectra is $E = f(\epsilon, k) = C\ \epsilon^{2/3}\ k^{-5/3}$. When the inertial zone exists, l_{DI} splits the universal range into inertial and dissipation zones.

The large scale turbulent motions occurs in characteristic scales comparable to the mean flow: Given the characteristic length l_0 and velocity u_0 of the mean flow; the turbulent timescale is $\tau_0 \sim l_0/u_0$ so that the rate of energy transferred from those large scales downstream along the energy spectrum is scaled as u_0^3/l_0. The dissipation ϵ is determined by the energy transfer at large scales so that $\epsilon \sim u_0^3/l_0$.

The Kolmogorov scale η_0 is defined as the lowest scale on which turbulence can manifest. With characteristic velocity u_η, at the Kolmogorov scale the local Reynolds number $\mathrm{Re}_\eta = \eta_0\ u_\eta/\nu$ equals to one, and viscosity prevents inertial terms to generate further fluctuations. Spectral energy equilibrium at the universal equilibrium range implies the unique scale definition $\eta_0 = f(\epsilon, \nu) = (\nu^3/\epsilon)^{1/4}$. Finally with the scaling $\epsilon \sim u_0^3/l_0$ and $\mathrm{Re}_\eta = 1$:

$$\frac{\eta_0}{l_0} \sim \mathrm{Re}^{-3/4}. \tag{I.1.13}$$

The integral length scale l_L and The Taylor micro-scale l_λ are commonly referred to indicate l_{EI} and l_{DI}, respectively. According to Pope [2000] (Pages 200 and 226), l_L is related to the energy spectra with equation I.1.14 (pg. 226), and l_λ can be approximated with equation I.1.15 (pg. 200).

$$l_L = \frac{\pi E_k(k=0)}{2R_r(r=0)}. \tag{I.1.14}$$

$$l_\lambda \approx \sqrt{10}\, l_\eta^{2/3}\, l_0^{1/3}. \tag{I.1.15}$$

Spectral tensor of the velocity fluctuations Simply defined as the spectral tensor in Mann [1998] and as the velocity-spectrum tensor in Pope [2000] (pg. 220), such tensor holds the full three dimensional space correlations of the velocity fluctuations. It is defined as function of the wave-number vector $\boldsymbol{k} = 2\pi/\boldsymbol{r}$ as:

$$E_{u_i' u_j'}(\boldsymbol{k}) = \int\int\int_{-\infty}^{-\infty} \left[R_{u_i' u_j'}(\boldsymbol{r})\, e^{-i\boldsymbol{k}\cdot\boldsymbol{r}} \right] d\boldsymbol{r}. \tag{I.1.16}$$

Wave-Number-Frequency turbulent spectra The space-time correlation function of χ_i and χ_j is $R_{r\tau} = R_{\chi_i'\chi_j'}(r,\tau) = \overline{\chi_i'(x,t)\chi_j'(x+r,t+\tau)}$, and the correspondent spectral energy density function $E_{kw} = E_{\chi_i'\chi_j'}(k,w)$ twice its Fourier transform, which is consistent with the definition of $E_k = \int E_{kw} \mathrm{d}w$ according to equation I.1.12. So with $k = 2\pi/r$ and $w = 2\pi/\tau = 2\pi f$:

$$\begin{aligned} E_{\chi_i'\chi_j'}(k,w) &= \frac{1}{\pi^2}\int_{-\infty}^{\infty}\int_{-\infty}^{\infty} \left[R_{\chi_i'\chi_j'}(r,\tau)\, e^{-ikr}\, e^{-iw\tau} \right] dr\, d\tau, \qquad \text{with} \\ R_{\chi_i'\chi_j'}(r,\tau) &= \frac{1}{2^2}\int_{-\infty}^{\infty}\int_{-\infty}^{\infty} \left[E_{\chi_i'\chi_j'}(k,w)\, e^{-ikr}\, e^{-iw\tau} \right] dk\, dw. \end{aligned} \tag{I.1.17}$$

Taylor hypothesis The Taylor hypothesis is the first (Taylor [1938]) and most applied model describing the joint $(k-w)$ wave-number and angular-frequency spectral distributions of the fluctuations. Taylor pictures a frozen turbulence scenario, where the turbulent eddies evolve so slowly compared to the mean velocity u_0, that their evolution can be neglected. Turbulence is then simply advected by the mean flow, and E_{kw} is uniquely defined from E_k or E_w as:

$$\begin{aligned} E_{kw}(k,w) &= E_k(k) \quad \delta_d(w - u_0\, k) \\ &= E_w(w) \quad \delta_d(w - u_0\, k); \end{aligned} \tag{I.1.18}$$

where E_k and E_w are the one-dimensional wave-number and angular-frequency turbulent spectra; and $\delta_d(\cdot)$ the dirac function operator.

I.1.1.6 Large Eddy Simulation

The method here employed for granting the numerical solution of the atmospheric turbulent flow in chapters III and IV, classifies as a Large Eddy Simulation (LES), which consists into sufficiently refining the domain, resolving the most energetic (and larger) scales of turbulence. The velocity field is decomposed into filtered $\breve{\boldsymbol{u}}$ and residual $\check{\boldsymbol{u}}$ components. The

filtered Navier Stokes equation are solved for $\breve{\boldsymbol{u}}$. Coupling between filtered and residual scales is modeled in a much more reliable way than in RANS equations, due to the universal shape of the energy spectrum at lower quasi-isotropic scales. Ideally, a LES approach must capture all the energy-containing scales above l_{EI} (See section I.1.1.5).

The filter $G(\boldsymbol{r},\boldsymbol{x})$ is defined such that

$$\breve{\boldsymbol{u}}(\boldsymbol{x},t) = \int G(\boldsymbol{r},\boldsymbol{x})\boldsymbol{u}(\boldsymbol{x}-\boldsymbol{r},t)d\boldsymbol{r} \tag{I.1.19}$$

and

$$\int G(\boldsymbol{r},\boldsymbol{x})d\boldsymbol{r} = 1. \tag{I.1.20}$$

Contrary to URANS models, the filtered residual $\breve{\check{\boldsymbol{u}}} = \overline{\boldsymbol{u}-\breve{\boldsymbol{u}}}$ is generally non zero. Filtering the Navier Stokes equations I.1.2 and I.1.3 leads to an analogous of URANS equations I.1.7 where the Reynolds-stress tensor $\boldsymbol{\tau}^{(r)}$ gives place to the residual-stress tensor $\boldsymbol{\tau}^{LES}$:

$$\begin{gathered}\frac{\partial \breve{u}_i}{\partial t} + \frac{\partial(\breve{u}_j\breve{u}_i)}{\partial x_j} + f_j\breve{u}_k\epsilon_{ijk} = -\frac{1}{\rho}\frac{\partial \breve{p}}{\partial x_i} + \frac{\partial}{\partial x_j}\left[\tau_{ij}^{(v)} - \tau_{ij}^{LES}\right], \qquad \text{where} \\ \tau_{ij}^{(v)} = 2\nu\breve{S}_{ij}, \qquad \text{and} \qquad \tau_{ij}^{LES} \equiv \overline{\check{u}_i\check{u}_j} - \breve{\check{u}}_i\breve{\check{u}}_j.\end{gathered} \tag{I.1.21}$$

Still, the residual-stress tensor includes sub-grid information and thus has to be modeled. Different approaches are proposed to close the filtered Navier Stokes equations I.1.21, such as the Deardorff single equation presented in section III.1.1.1. The continuity equation I.1.1 holds on the filtered and residual velocity fields so that $\nabla\cdot\breve{\boldsymbol{u}} = \nabla\cdot\check{\boldsymbol{u}} = 0$.

I.1.2 Specific assumptions delimiting the theoretical framework

I.1.2.1 Water domain

Ocean waves' propagation are usually uncoupled from the Coriolis forces, since the wave's frequency is much higher than the earth rotation's frequency (P. Janseen [2004], pg. 9), and so body forces derive exclusively from a potential field: Gravity. Moreover, viscous phenomena can often be neglected due to the predominant inertial forces characteristic of the wave's motion, and sufficiently high distances from solid boundaries. If so, an initially non-rotational fluid keeps this particular property during its evolution (Batchelor [2000]). Introducing the velocity potential $\phi_{\boldsymbol{u}}$, the definition $\boldsymbol{u} = \nabla\phi_{\boldsymbol{u}}$ is sufficient to ensure the non-rotational velocity field where $\nabla\times\boldsymbol{u} = 0$. One then refers to a potential flow where the continuity equation I.1.1 reduces to Laplace's equation I.1.22.

$$\nabla^2 \phi_{\boldsymbol{u}} = 0, \qquad \forall \qquad z \leq \eta(x, y, t) \tag{I.1.22}$$

Disregarding wave breaking and white capping, the interface is identified by the unknown single-valued function $z = \eta(x, y, t)$ (Instead of $\eta(x, y, z, t)$ at section I.1.1.2). The kinematic condition now infers that the particle is kept in the interface defined by $\eta - z = 0$, so that $D(\eta - z)/Dt = 0$ (With $D(z)/Dt = u_3$ and $\partial\eta/\partial z = 0$) leads to equation I.1.23 written in terms of the velocity potential.

$$\frac{\partial \eta}{\partial t} + \nabla \phi_{\boldsymbol{u}} \cdot \nabla \eta = \frac{\partial \phi_{\boldsymbol{u}}}{\partial z}, \qquad \text{at} \qquad z = \eta(x, y, t). \tag{I.1.23}$$

The momentum equation I.1.2, if applied to a Newtonian fluid and non-rotational flow, results in the Bernoulli equation relating the velocity potential and pressure fields:

$$\frac{\partial \phi_{\boldsymbol{u}}}{\partial t} + \frac{1}{2}(\nabla \phi_{\boldsymbol{u}})^2 + g\eta = -p, \qquad \forall \qquad z \leq \eta(x, y, t). \tag{I.1.24}$$

Since viscosity is neglected, the continuity in tangential velocities and stresses may not be satisfied on the free surface. The dynamic boundary condition (Eq. I.1.6) is so limited to normal stresses, i.e., the pressure $p = p_{FS}$ acting in the Bernoulli equation I.1.24 at the free-surface $z = \eta$.

I.1.2.2 Atmosphere

Boussinesq approximation for incompressibility The incompressibility constraint discussed in section I.1.1.1, strictly prevents any buoyancy, and notably thermal effects acting in the momentum equations I.1.2. Nevertheless such forces are a key aspect of the atmospheric flow, effectively driving the wind and imposing the free convection or stable stratification regimes discussed in section I.2.2.3. Luckily, adopting the Boussinesq approximation for incompressibility, one may consider a slowly varying density field acting only in the buoyancy terms of equation I.1.2, consistently accounting for the thermal effects as wind driving sources in the atmosphere.

Such an approach relies on the dimensional considerations carefully discussed by Spiegel and Veronis [1960]. Consider that a state variable $\chi(\boldsymbol{x}, t)$ (ρ, p, or θ) decomposes into mean $\overline{\chi}(t)$, motionless (static and horizontally homogeneous) $\chi_0(x_3, t)$, and fluctuating (dynamic and resulting from motion) $\chi(\boldsymbol{x}, t)$ components. The characteristic scale height of motionless χ_0 variation is defined as:

$$H_\chi = \left| \frac{1}{\overline{\chi}} \frac{\partial \chi_0}{\partial z} \right|^{-1}. \tag{I.1.25}$$

and the crucial requirement stated in Spiegel and Veronis [1960] is that: (i) Any vertical extension of flow changes, e.g., the boundary layer height δ, is negligible compared to any scale height H_ρ, H_p, or H_θ. Particularly, integrated over the height δ_0 of maximum density variation $\Delta\rho_0$, that implies $\Delta\rho_0/\overline{\rho} << 1$. In non-linear applications such as the one here employed, it also necessary to ensure that: (ii) Motion induced fluctuations in density and pressure do not exceed the order of magnitude of its static variations, i.e., $|\Delta\chi'/\Delta\chi_0| \leq O(1)$.

Buoyancy forces & Thermodynamic State function Under these conditions, the incompressible equation of motion (eq. I.1.2) for a Newtonian fluid (eq. I.1.3) may partially incorporate slight density variations ρ' as:

$$\rho_\infty \left[\frac{\partial \boldsymbol{u}}{\partial t} + (\boldsymbol{u}\cdot\nabla)\,\boldsymbol{u} + \boldsymbol{f}\times\boldsymbol{u} \right] = -\nabla p' + \mu\nabla^2\boldsymbol{u} + \rho'\boldsymbol{g}, \tag{I.1.26}$$

while equations I.1.1 and I.1.4 still hold.

Considering changes in density due to temperature only, and consistent to the previous assumption of small changes in temperature, the state equation introduces the coefficient of thermal expansion β_θ:

$$\rho' = -\rho_\infty\beta_\theta(\theta-\theta_\infty), \tag{I.1.27}$$

and the modified pressure is given by:

$$p' = p - p_\infty + \overline{\rho}g(z-z_\infty), \tag{I.1.28}$$

Dimensional analysis of the governing equations The behavior of equations I.1.26 and I.1.4 can be studied from their non-dimensional form. Given the characteristic length L, velocity U, temperature difference $\Delta\Theta$, density $\rho_0 = \rho_\infty$, non-dimensional variables are expressed as: $\boldsymbol{u}^* = \boldsymbol{u}/U$, $\boldsymbol{x}^* = \boldsymbol{x}/L$, $t^* = t\,U/L$, $\nabla^* = L\,\nabla$, $(\theta^*-\theta^*_\infty) = (\theta-\theta_\infty)/\Delta\Theta$, $p^* = p'/(\rho_\infty U^2)$, $\boldsymbol{f}^* = \boldsymbol{f}/|\boldsymbol{f}|$. The resultant equations are:

$$\frac{Du_i^*}{Dt} = -\frac{\partial p^*}{\partial x_i} + \boldsymbol{Re}^{-1}\cdot\nabla^{*2}u_i^* + \boldsymbol{Fr}^{-1}\delta_{3,i} + \boldsymbol{Ri}\left(\theta^*-\theta^*_\infty\right)\delta_{3,i} - \boldsymbol{Ro}^{-1}f_j^*\,\overline{u}_k^*\,\epsilon_{ijk}, \tag{I.1.29}$$

$$\frac{D\theta^*}{Dt} = \boldsymbol{Ec}\cdot\beta_\theta^*\theta^*\frac{Dp^*}{Dt} + 2\boldsymbol{Ec}\cdot\boldsymbol{Re}^{-1}\cdot S_{i,j}^{*\;2} + (\boldsymbol{Pr}\cdot\boldsymbol{Re})^{-1}\cdot\nabla^2\theta^*, \tag{I.1.30}$$

revealing the non-dimensional quantities:

$$Re = \frac{\rho_0 U L}{\mu}, \qquad Fr = U^2/gL, \qquad Ri = \frac{\beta_\theta g \Delta\Theta L}{U^2},$$
$$Ro = \frac{U}{|\boldsymbol{f}|L} \qquad Ec = \frac{U^2}{c_p \Delta\Theta}, \qquad Pr = \frac{\mu c_p}{k}. \tag{I.1.31}$$

Fully turbulent flow Turbulence is caused by excessive inertial forces, which overcomes the damping effect of the fluid's molecular viscosity, increasing non-linear contributions to the Navier Stokes equations. The onset of turbulence can be determined by the Reynold's Number ***Re*** that balance those terms in the momentum conservation equation. A fully turbulent flow where ***Re***$\rightarrow \infty$ is assumed in the numerical resolution employed at chapters III and IV.

Gravity waves Froude's number ***Fr*** compares inertial and body forces (here, gravity). It is particularly important in gravity dominated phenomena including, clearly, gravity waves. In section B.1.1, ***Fr*** is shown equivalent to the Wave Age **WA**, characterizing the Wind-Wave interactions here discussed in section I.3.

Thermal Stratification Buoyancy becomes important when the absolute Richardson number ***Ri*** rises, being it a direct measure of momentum generation (or damping) capability by buoyancy, compared to inertia. This number is particularly important in atmospheric flows, where it reveals the stability of the atmospheric boundary layers [Kaimal and Finnigan, 1994], and shall be revisited in other forms in section I.2.2.3.

Coriolis forces An inertial force accounting for the earth rotation with angular frequency $\Omega = 7.3\ 10^{-5}$ rad/s, Coriolis forces are known to introduce large scale spinning motion to the atmospheric flow, and are characterized by the Rossby number ***Ro***. In sufficiently small scales, ***Ro***$>> 1$, and the Coriolis effects are negligible face to the dominant advection forces.

In the latitude ψ, the Coriolis magnitude parameter is given by $|\boldsymbol{f}| = 2\Omega\sin(\psi)$. In the physical experiment of part II (Cases 01 and 02a), e.g., $|\boldsymbol{f}| = 10^{-4}$ rad/s, and across the $L = 1$ km measuring distance, with mean velocity $U \sim 5$ m/s, ***Ro***$(U, L) \sim 50$. In the same experiment, considering the wave instead of the wind velocity would give a Rossby number $\sim 150\%$ higher. In small scale atmospheric flows such as this, the Coriolis forces are usually negligible close to the surface, where the characteristic length is instead given by the surface distance, so both the turbulent characteristic velocity and length diminish, and the turbulent time scale is kept significantly lower than the Coriolis.

The situation is more complex in wavy conditions, where the friction velocity shall evolve in the wave length scale rather than the wall distance. In the numerical experiments of section III.4) for example, one can take the characteristic friction velocity $u^* \sim 0.147$ m/s, with the wave-length $\lambda \sim 128$ m, to find ***Ro***$(u^*, \lambda) \sim 11$: Noting that within the long wave lengths considered, and face to the slow velocity differences encountered, Coriolis forces might get

increasingly important close to the surface. All of the cases here discussed in the numerical experiments of parts III ensure $\boldsymbol{Ro}(U, L) > 50$ and $\boldsymbol{Ro}(u^*, \lambda) > 10$, and Coriolis forces are neglected in the governing equations presented at section III.1.1.1.

Reversibility The Eckert number $\boldsymbol{Ec}$ measures kinetic energy against enthalpy change in the flow. If the enthalpy change becomes important on the energy balance equations, dissipation can occur. From the discussion in Spiegel and Veronis [1960], one sees that the Boussinesq hypothesis is consistent to imposing $\boldsymbol{Ec} \rightarrow 0$ so that equation I.1.30 becomes:

$$\frac{D\theta^*}{Dt} = (\boldsymbol{Pr} \cdot \boldsymbol{Re})^{-1} \cdot \nabla^2 \theta^*, \tag{I.1.32}$$

Heat advection Prandtl's constant $\boldsymbol{Pr}$ compares thermal and molecular diffusion. The Peclet number $\boldsymbol{Pe} = \boldsymbol{Pr} \cdot \boldsymbol{Re}$ gives the relative importance of heat diffusion and convection in the energy balance equation.

I.2 GEOPHYSICAL MECHANISMS AND MODELS

The offshore environment is characterized by multiple physical processes occurring simultaneously, exchanging momentum, heat, and mass through different layers of the fully coupled ocean and atmospheric boundary layers. Some of this processes are summarized in figure I.2.1, presented in Edson et al. [2007] to justify the slow progress achieved towards modelling the fully coupled Marine Atmospheric Boundary Layer, particularly regarding weather forecast applications. From their observations and in agreement to other wind-wave interaction studies reviewed in section I.3, Edson et al. [2007] indicate that wave related processes play a significant role in micro and mesoscale variabilities above the Ocean.

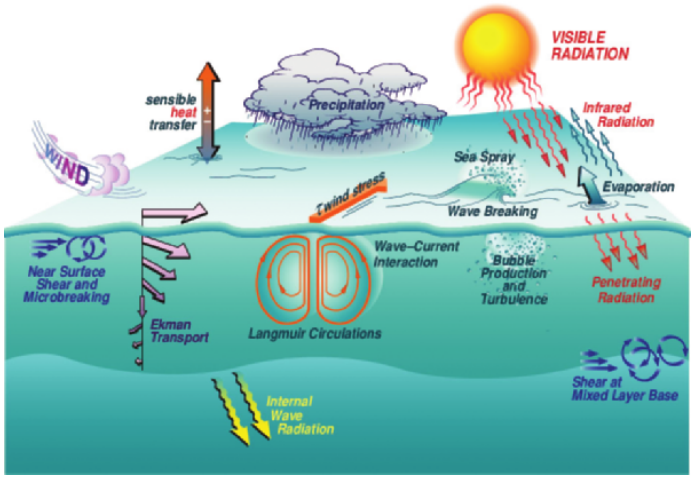

Figure I.2.1: According to Edson et al. [2007] (Fig. 1), a "*few of the processes governing air-sea exchange across the coupled boundary layers*". Already much more than the ones admitted by the theoretical framework established.

With that picture in mind, next sections present a broad, rather than exhaustive review on the coupled ocean and atmospheric systems. Naturally, focus is given to the aspects most exploited during the Thesis, that must be described within the theoretical framework established in section I.1. In section I.2.1, oceanic processes are discussed with focus given to the statistical description of ocean waves, but with mention to ocean circulation and dissipation processes. The observations presented in the Thesis regard physical measurements in the atmosphere, and the numerical reproduction of the Atmospheric Boundary Layer (ABL). So the description of the ABL receives special attention in section I.2.2, without any popper consideration of wind-wave interactions. The goal is to establish a consistent overview of a few oceanic and atmospheric processes, so the discussion can meet the specific objectives of the Thesis in section I.3, particularly considering Wind-Wave interactions.

I.2.1 OCEAN WAVES

Employing the framework of section I.1.2.1, analytical solutions of monochromatic waves are given in the appendix, describing the linear solution known as Airy wave theory (1841), and the non-linear development of Stokes' theory (1847). There are some aspects, highlighted in the next sections, that describe ocean waves better than these simplistic analytical solutions. In section I.2.1.1, the statistical nature of ocean waves is discussed, where the sea-state energy is distributed along an energy cascade in analogy to turbulence (see section I.1.1.5), but yet within potential flow and linearity assumptions. Section I.2.1.2 highlights important physical aspects of wave-driven circulation and wave dissipation the Oceanic

Mixed Layer, that cannot be described within the potential flow theory, thus not being properly exploited during the Thesis but yet, essential to understand some of the Wind-Wave interaction mechanisms discussed in section I.3.

I.2.1.1 Sea state spectral distribution

Instead of the canonical regular wave scenario, the sea-state is better described as a continuous spectral distribution of an infinite number of regular waves, as exemplified in figure I.2.2, taken from Pierson et al. [1955]. The mathematical description of the sea-state statistical variability by means of its Spectral Energy Density distribution is first developed in Pierson and Marks [1952], and is now a standard practice in the Ocean engineering industry.

Considering a directional sea-state where linear waves propagate in x and y directions, the power density function of the free-surface (FS) elevations $F(\boldsymbol{k}) = F(k_x, k_y)$ (FS spectrum) is function for example of the wave-number space (k_x, k_y), so that counting on a Fourier decomposition of the free-surface elevation $\eta(x, y)$, discretized into the wave-number space with spacing $(\Delta k_x, \Delta k_y)$ and modal amplitudes $a_{ij}(k_{xi}, k_{yj})$, then:

$$F(k_{xi}, k_{yj}) = \lim_{\Delta k_x \to 0} \lim_{\Delta k_y \to 0} \frac{1}{\Delta k_x \Delta k_y} \overline{\left[\frac{1}{2} a_{ij}^2\right]}. \tag{I.2.1}$$

The FS spectrum is also commonly given as $F(f, \phi)$, function of frequency f and direction ϕ. With the group velocity definition $c_g = \partial w / \partial k$, F scales between (k_x, k_y) and (f, ϕ):

$$F(k_x, k_y) = F(f, \phi) \frac{c_g}{2\pi (k_x^2 + k_y^2)^{0.5}}, \tag{I.2.2}$$

and the one-dimensional angular-frequency $(w = 2\pi f)$ spectra is given as:

$$F(w) = \frac{1}{2\pi} \int_0^{2\pi} F(f, \phi) d\phi. \tag{I.2.3}$$

The linearity assumption is crucial for determining that each infinitesimal segment of F, corresponds to an oceanic, dispersive, gravity wave. In that case one can generate a statistical sample of the irregular sea state by a combination of regular components, as suggested in figure I.2.2. Each wave component have their amplitudes a_{ij} determined by the discretization of the spectrum into intervals of size $\Delta\phi$ and Δn:

$$a_{ij} = \sqrt{2F(f_i, \phi_j) \Delta f \Delta \phi} \tag{I.2.4}$$

The phase information is not contained in the spectrum and is usually randomly generated for each wave component, to give a deterministic sample from this statistical description.

Thanks to the dispersion equation relating the wave-number with its angular-frequency, as in equation A.1, the spectrum F is equivalently defined either in the wave-number (k) or frequency (f) spaces. Hence, such description is particularly valuable in the present context, for it provides a convenient basis for the evaluation of many of the Wind-Wave interaction studies (c.f. Donelan et al. [1996]), further discussed in section I.3.

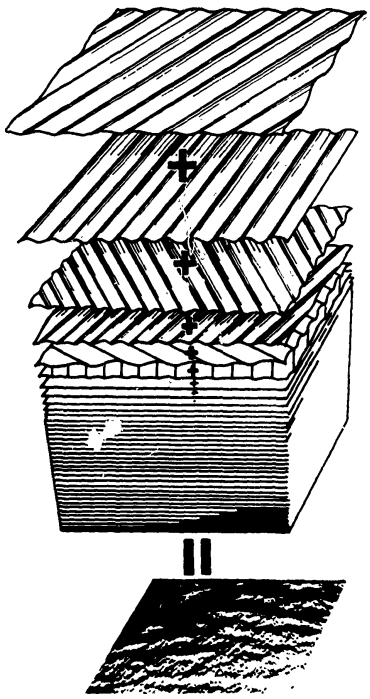

Figure I.2.2: An irregular sea-state composed of multiple wave components, from Pierson et al. [1955].

Universal Spectral Similarity A universal scaling of the sea-state spectra is imperative for describing a sea-state in terms of simple parameters, e.g., the Wave Age extensively explored in Wind-Wave interaction studies I.3. Naturally the parallel to Kolmogorov turbulence theory established in 1941 (Section I.1.1.5), suggest the existence of universal laws ruling the sea-state spectral behavior. One of the earliest accounts where the analogous behavior of sea-state and turbulent spectra is invoked explicitly, is found in Zakharov and Filonenko [1967]. While addressing what they refer as weak turbulence of capillarity waves, in the transparency region analogous to the inertial range of the turbulent cascade, Zakharov and Filonenko [1967] predict in dimensional grounds that the spectral decay in the directional wave-number space shall scale with $\boldsymbol{k}^{-7/2}$. That's quite an early prediction with strong assumptions (c.f. P. Janseen [2004], pg. 186-187), but remarkable implications as discussed below.

At large fetches and at the smallest wave scales, a universal spectral similarity is first demonstrated in Pierson Jr. and Moskowitz [1964], where the spectra are determined by wave-breaking processes in the so-called saturation zone, as previously suggested in Phillips [1958]. From their observations on North Atlantic measurements Pierson Jr. and Moskowitz [1964] proposed the Pierson-Moskowitz as a universal wave spectrum, with the high frequency part exhibiting the w^{-5} law dependency proposed in Phillips [1958]. According to that, the saturation level is determined exclusively by frequency and gravity, the spectra scales with $F(w) \sim \alpha_p g^2 w^{-5}$, and the Pierson-Moskowitz spectrum is given by:

$$F_{PM}(w, w_p, \alpha_p) = \alpha_p g^2 w^{-5} \exp\left[-\frac{5}{4}\left(\frac{w_p}{w}\right)^4\right], \tag{I.2.5}$$

in terms of the spectral peak angular-frequency w_p, and the model's constant α_p.

Within shorter fetch situations, the sea-state spectrum present considerably sharper peaks than the Pierson–Moskowitz model, which is accounted for in the JONSWAP spectrum developed in Hasselmann et al. [1973]. The JONSWAP spectra are exemplified in figure I.2.3 (Originally from Hasselmann et al. [1973]) for varying fetch distances, denoted in kilometers over the spectra. With the increasing fetch the JONSWAP spectra converges towards the Pierson-Moskowitz spectra, as non-linear wave-wave interactions displace the spectral peak towards lower frequencies. In very high frequencies, the spectra collapse saturated by wave

breaking processes, exhibiting the w^{-5} dependence of Phillips [1958]. For smaller fetches the spectra rapidly deviates from the w^{-5} law at lower frequencies, and there is a considerable overshoot captured in the JONSWAP spectra compared to Pierson Jr. and Moskowitz [1964]. The JONSWAP spectrum is defined as:

$$F_{JS}(w) = F_{PM}(w, w_p, \alpha_p) \cdot \gamma^{\exp\left[-\frac{(w-w_p)^2}{2\sigma^2\, w_p^2}\right]}, \quad \text{where} \quad \sigma = \begin{cases} \sigma_1, & \text{if } w < w_p \\ \sigma_2, & \text{if } w \geq w_p \end{cases} . \tag{I.2.6}$$

While the Pierson–Moskowitz spectrum presented a single constant α_p scaling the sea-state spectra, the JONSWAP spectra considers additional three constants (γ, σ_1, σ_2), and more importantly, the fetch dependency of α_p and w_p parameterized by the Wave Age (WA). Up to this point the $\mathrm{WA}_{10} = c_p/U_{10}$ was usually taken from the measured wind velocity at the arbitrarily chosen 10 m height, and probably from this point it has become clear that the Wind-Wave interactions, discussed in section I.3 play a major role into determining a universal shape of the sea-state spectra.

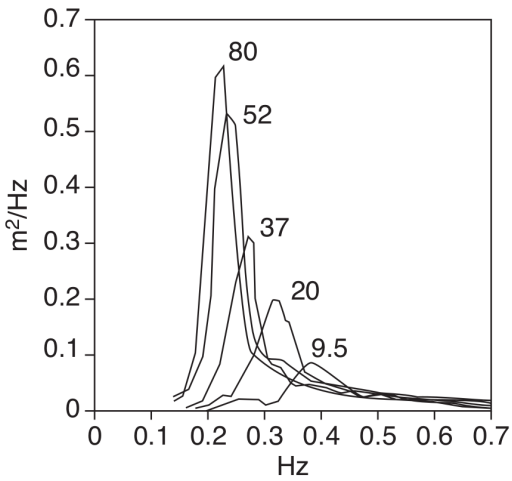

Figure I.2.3: Evolution of the sea-state spectra with fetch. Taken from P. Janseen [2004] (Fig. 2.5), in turn extracted from the original in Hasselmann et al. [1973]. Fetch indicated in kilometers over the spectra.

An alternative to Pierson Jr. and Moskowitz [1964] universal spectral similarity $F(w) \sim \alpha_p g^2 w^{-5}$ is given in Toba [1973], almost simultaneously to Hasselmann et al. [1973]. From laboratory experiments Toba [1973] identified a $-3/2$ power law in the wave significant height H_s, so similarity reasoning led to the saturated spectral region characterized by the functional $F(w) \sim u^*\ \alpha_T g\ w^{-4}$. An important contribution of such reasoning is that the friction velocity appears as the significant wind parameter, in place of the arbitrarily chosen 10 m height parametrization of the JONSWAP spectrum. Besides, the JONSWAP data has been revisited in Battjes et al. [1987], and a better agreement was found by employing a modified JONSWAP spectrum, with the scaling proposed in Toba [1973], i.e., $F_{PM} \to F_T$ in equation I.2.6, and:

$$F_T(w, w_p, \alpha_T) = u^*\ \alpha_T g\ w^{-4} \exp\left[-\left(\frac{w_p}{w}\right)^4\right]. \tag{I.2.7}$$

According to P. Janseen [2004] (pg. 48), there is extensive observational support to a constant α_T parameter, leading to accurate fittings of the modified JONSWAP spectrum with equation I.2.7 at the largest scales of the sea-state spectrum. So the functional $F(w) \sim u^*\ \alpha_T g\ w^{-4}$ is better suited to represent a universal sea-state spectrum in the lowest fre-

quencies of the saturated region, as long as $w < 3w_p$. Moreover in the directional wave-number domain that finally recovers the $\boldsymbol{k}^{-7/2}$ slope predicted in Zakharov and Filonenko [1967] (P. Janseen [2004] pg. 187).

The analogy to Kolmogorov turbulent cascade is brought back in Kitaigorodskii [1983], now employing an approximation of non-linear wave-wave interactions yet neglected in Zakharov and Filonenko [1967]. It is demonstrated in Kitaigorodskii [1983], that the non-linear interactions between different waves in the sea-state spectra sustain a spectral cascade such as Kolmogorv's, where at the larger scales ($w < 3w_p$, P. Janseen [2004] pg. 189) the inertial range scales with $F(w) \sim u^* \ \alpha_T g \ w^{-4}$, as predicted in Toba [1973]. It is also postulated in Kitaigorodskii [1983] that beneath the inertial range, the sea-state spectra is said fully saturated in the dissipation region, where the wave-breaking processes of Phillips [1958] become predominant. As consequence the sea-state spectra shall adapt from a w^{-4} slope in the inertial range, to a w^{-5} slope in the dissipation range.

Though there might be considerable evidence of a w^{-4} to w^{-5} transition, there is also a good amount of discrepancy between the exact spectral distribution obtained in different experiments above the Ocean (c.f. Kahma and Calkoen [1992]). The introduction of other Wind-Wave interaction processes, such as the ones discussed in section I.3, for determining the transition between the w^{-4} and the w^{-5} spectra is remarked e.g., in Hara and Belcher [2002].

I.2.1.2 Wave-driven circulation and Wave dissipation

First note that at sufficiently large scales, a boundary layer system is also developed beneath the water, where the ocean currents are generally subject to the same similarity theories usually employed in the atmosphere, including the log-law (Craig and Banner [1994]) and the Monin Obukhov similarity theory [P. Janseen, 2012], here presented in section I.2.2.3. Though, the boundary layer flow develops considerable differences in the upper ocean layer if compared to the atmospheric flow depicted in section I.2.2.

Wave-driven circulation Non-linear solutions of gravity waves reveal the stokes drift, phenomenon responsible for mass transport, i.e., wave-driven ocean circulation. With a major role in oceanic circulation processes, the stokes drift sums to the ocean current giving the total circulation, and induces the so called Stokes-Coriolis forcing of the ocean [Hasselmann, 1971]. In global circulation models (c.f. Janssen et al. [2013]) the Stokes-Coriolis forces are to be decoupled from the Current-Coriolis forces, and the wind-ocean momentum exchanges distributed between wave and current systems. Acting against the mean flow shear, the Stokes-Coriolis force may generate Langmuir cells and WI turbulence [Grant and Belcher, 2009] which have a penetration depth on the order of half the characteristic wavelength of the wave field (Hundreds of meters for a typical swell). Note that, probably with lesser intensity, the Stokes drift shall also propagate into the atmosphere according to the discussion in section I.3.2, where it is also subject to the Coriolis effects, but the implications of the Stokes-Coriolis forces into the atmospheric flow is unnoticed in the literature review of section I.3.

Wave damping and dissipation A possible mechanism of wave damping, mostly known for inducing the wave growth, is the Wind-Wave interactions later discussed in section I.3. Other mechanisms are to be considered in order to account for the effective total wave dissipation. Viscous forces act both on the bottom and the free surface. The viscosity acting on the bottom is important in shallow water conditions. The viscous stresses in the free surface effectively damp capilarity gravity waves (P. Janseen [2004], pg. 199), and might slowly damp longer wave trains (c.f. Perignon et al. [2014]). Wave-current interactions generate both structured and turbulent motions capable of exerting wave damping.

Most important, quasi-continuous and fully intermittent processes of white capping and wave breaking coexist, and are probably the most complex phenomena encountered in wave mechanics (c.f. Drazen et al. [2008]), leading to strong and localized wave dissipation events. The ocean current profile strongly deviates from the log-law profiles close to the free-surface, as wave breaking events generate huge amount of turbulence on depths comparable to the waves' height (c.f. Craig and Banner [1994]). Except for the pressure-related wave growth and damping mechanisms, the other aforementioned dissipation phenomena depend on the ocean's convection and viscosity, and so cannot be resolved by the proposed assumption of potential flow, presented in section I.1.2.1.

I.2.2 Atmospheric Boundary Layer

Existing between the earth's surface and the geostrophic layer, the atmospheric boundary layer (ABL) is the portion of the atmospheric flow submitted to the surface direct influence. In the geostrophic layer, which may be regarded as a the boundary condition prevailing above the ABL, the flow is in near-geostrophic balance (c.f. Lee [2018]), being insensitive to the surface conditions. The Boussinesq equations I.1.29 (with I.1.1, and I.1.30) describe the flow in the ABL, as framed in section I.1.2.2. Turbulence is generated by the shear stresses, sustained in the surface by viscous forces, and may be damped or produced by buoyant forces depending on the stability regime.

To properly describe the ABL, it is important to identify and define scales of interest in the atmosphere, which is argued and established in section I.2.2.1. Within the microscales studied, an adiabatic ABL is described in section I.2.2.2, following from Prandtl's Boundary Layer theory described in the appendix A.1.2, and sustained by empirical observations in neutral conditions. Though, atmospheric neutral conditions are rare and often just a transition between different thermal-driven regimes described in section I.2.2.3. Relying in the aforementioned aspects, wind resource low-fidelity prediction models are introduced in section I.2.2.4, so to base further arguments regarding the improvement of those models for harvesting applications in the offshore environment.

I.2.2.1 Turbulent scales in the atmosphere

A wide range of physical phenomena and flow scales coexist in the atmosphere. Luckily, as one cannot afford the multi-scale solution of the whole atmospheric system depicted in figure I.2.1, the different scales can be often identified with minor, or at least predictable, influence between each other. One of the first demonstrations of such scale dependency is

given in der Hoven [1957], reporting the horizontal wind speed variance spectra depicted in figure I.2.4. Of major implications into the atmospheric flow, and naturally to the wind energy harvesting industry (c.f. Escalante Soberanis and Mérida [2015]), the Van Der Hoven spectrum reveal a spectral gap splitting mesoscale and microscale motions in the atmosphere. Here, the main interest is towards the microscale. The spectral gap favors statistical convergence of the velocity variances, when the averages are performed within such scales. So, one of the most practical consequences of this demonstration is the establishment of 10 min average window, adopted as a standard in microsale studies (Escalante Soberanis and Mérida [2015]).

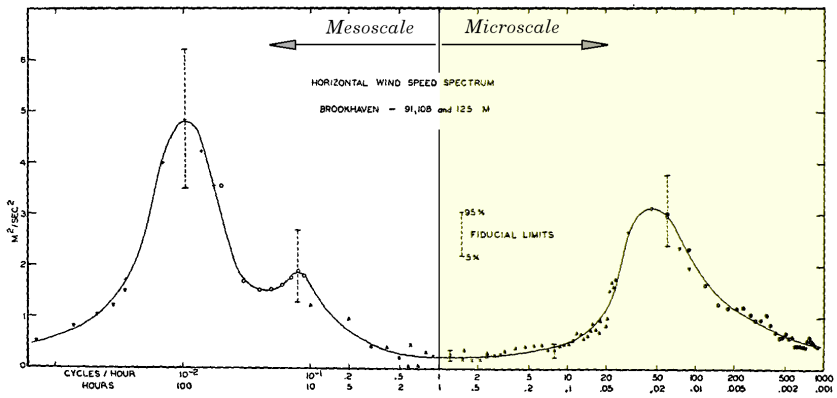

Figure I.2.4: Atmospheric motions, exemplified by the Van Der Hoven spectrum reported in der Hoven [1957]. The spectral gap splits mesoscale and microscale motions (legend, arrow and color added to the original) in the atmosphere, the latest being the focus of present studies.

Different physical processes characterize different scales in the atmosphere, such as indicated in the diagram of figure I.2.5, presented in Larsen et al. [1979]. The region of interest in this Thesis appear red and hashed in the diagram, corresponding to the microscales of figure I.2.4, and excluding the Kolmogorov dissipation range. The diagram and discussion in Larsen et al. [1979] highlight a zone of intersection between different scales and processes. So the hashed zones in the diagram designate both resolved and modeled motions in the numerical methodology described at section III.1, i.e.: The effects of the dissipation sub-range are introduced in the inertial sub-range through the LES sub-grid model; and the simplified large scale forcing mimics the influence of the Planetary Boundary Layer in the shear production subrange.

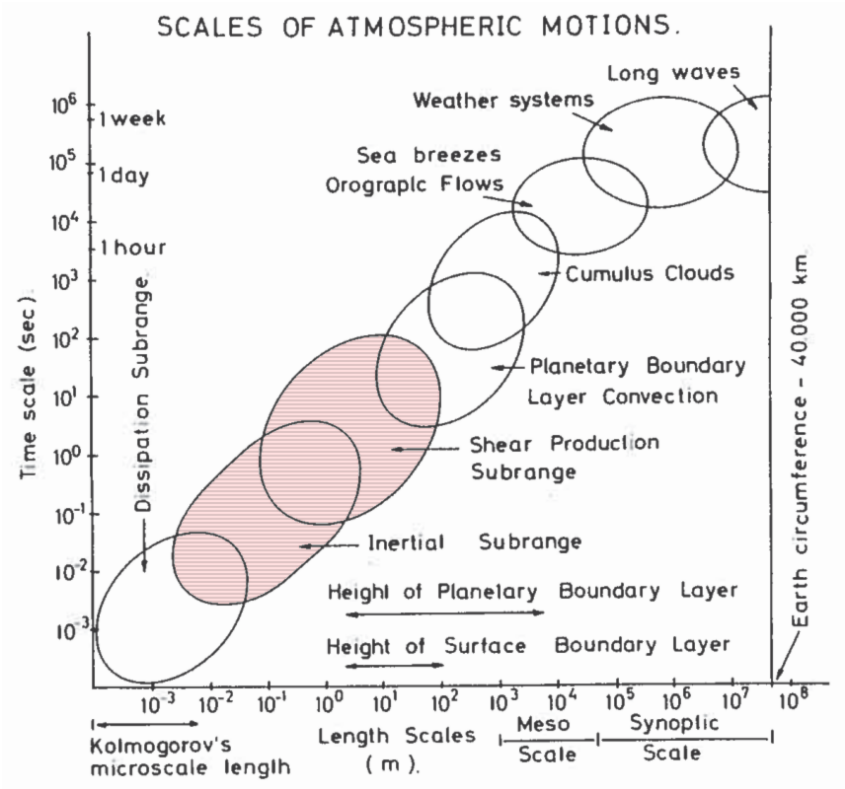

Figure I.2.5: Diagram depicting atmospheric scales related to different physical processes in the atmosphere, from Larsen et al. [1979]. Red dashed regions are added to the original, remarking the region of interest in current studies.

I.2.2.2 BL THEORY AND THE ABL AT NEUTRAL CONDITIONS

The amazing importance of Prandtl's Boundary Layer theory described in the appendix A.1.2, is that it has been shown a fundamental tool for describing numerous and different physical aspects of fluid mechanics (c.f. Aziz et al. [2013]). Notably in the ABL, one encounter at least two applications of Prandtl's theory, occurring in very different scales. Sufficiently close to the wall, the flow is invariant to the other boundary conditions, and Prandtl's Boundary Layer theory leads to universal log-law wall models, that are usually invoked as lower boundary conditions in numerical approaches, such as the one here employed and described in section III.1. Most important at this point, at large enough scales, where viscosity is usually neglected through a fully turbulent flow assumption, Prandtl's theory explain many of the flow features observed through a large portion of the Atmospheric Boundary layer. Recall from equation A.9, that Prandtl's theory leads to the log-law mean velocity profile:

$$\overline{u}_1 = \frac{u^*}{\kappa} \ln\left(\frac{z}{z_o}\right), \tag{I.2.8}$$

and to the velocity defect law given in equation A.10.

When the difference in temperature balances with the gravity effects in equation I.1.29

($\partial\theta/\partial z \approx -1^o$C/100 m), one refers to neutrally stable boundary layers, where buoyancy forces are negligible and disappear from eq. I.1.26. Despite the strong assumptions of wind steadiness and homogeneity (c.f. Larsen et al. [1979]), turns out that sufficiently apart from the surface the log-law velocity profile encounter extensive observational support at neutral buoyancy conditions. In the significant cases where buoyancy forces become important, the log-law theory is also the basis of more elaborated, state-of-the-art theories (c.f. Tong and Ding [2020]), soon described in section I.2.2.3.

Consider for example, the Atmospheric Boundary Layer depicted in figure I.2.6, bounded below by different arbitrary terrains, and above by the the free-stream velocity, with very small turbulence intensities defining the free-atmosphere. Far enough from the surface, the arbitrary terrain will appear like roughness elements to the mean flow, that can be accounted for in the roughness length z_o defining equation I.2.9. For most of the ABL extension, i.e., the surface layer in figure I.2.6, the velocity profile shall be indeed logarithmic and Prandtl's theory shall hold, as long as buoyancy forces are being negligible. The Outer Layer is the upper portion of the ABL where Coriolis forces become important. In the figure, d_0 is a statistical quantity describing the geometry of the roughness elements, and shall obviously be related to z_0, but such relation is strongly dependent on the micro-climate solution at the roughness sub layer. So rather than a purely geometrical parameter, z_0 is defined as the height where the mean wind log-law velocity profile values zero.

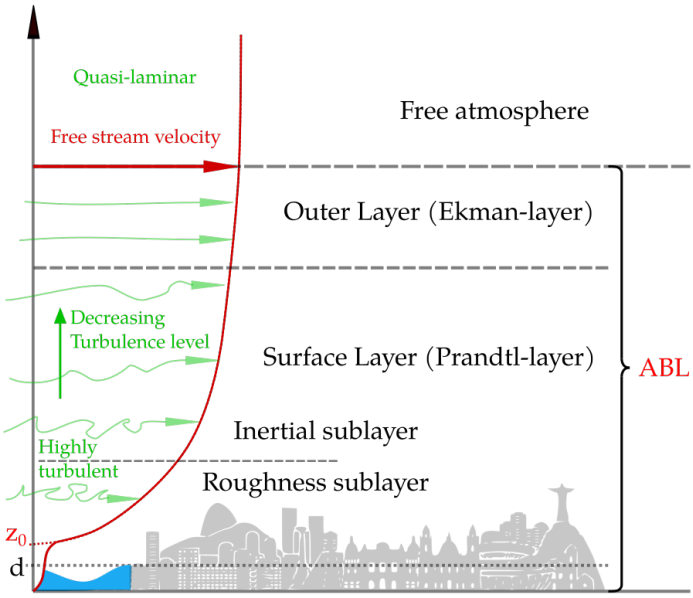

Figure I.2.6: Atmospheric Boundary Layer regions and schematics, inspired in BME.

Perfectly neutral conditions are rarely strictly encountered in the atmosphere, but are still representative of high speed winds, where inertia largely prevails over buoyancy. A notable review and notorious contribution into the subject is so presented in Counihan [1975], exploring the implications and establishing the coherence of multiple field data available from the period 1880-1972. According to Counihan [1975] there is an extensive observational support not only for the log-law velocity profile describing the mean wind across the ABL, but also for the power-law profile Sverdrup [1936] (at another publication in 1934, see Counihan [1975]) defined as:

$$\frac{\overline{u}_1}{\overline{u}_2} = \left(\frac{z_1}{z_2}\right)^{1/\alpha}, \tag{I.2.9}$$

The data in Counihan [1975] is classified in four types of terrains, according to their

roughness z_0. That is now a common practice in meteorological studies, leading e.g., to table I.2.1 summarizing a full page image given in the European Wind Atlas [Troen and Lundtang Petersen, 1989]. The original figure in Troen and Lundtang Petersen [1989] also note that typical uncertainties of z_0 values reported in table I.2.1 are on the order of $\times\div 2$ factor.

Table I.2.1: Approximated roughness length z_0 associated to different terrain types, from Troen and Lundtang Petersen [1989].

z_0	**Description**
$1{\cdot}10^{0}$	City, forest
$5{\cdot}10^{-1}$	Suburbs
$3{\cdot}10^{-1}$	Shelter belts
$2{\cdot}10^{-1}$	Many trees and/or bushes
$1{\cdot}10^{-1}$	Farmland with closed appearance
$5{\cdot}10^{-2}$	Farmland with open appearance
$3{\cdot}10^{-2}$	Farmland with very few buildings, trees etc. Airport areas with buildings and trees
$1{\cdot}10^{-2}$	Airport runway areas. Mown grass
$5{\cdot}10^{-3}$	Bare soil (smooth)
$1{\cdot}10^{-3}$	Snow surfaces (smooth)
$3{\cdot}10^{-4}$	Sand surfaces (smooth)
$1{\cdot}10^{-4}$	Water areas (lakes, fjords, open sea)

I.2.2.3 Thermal stratification effects

The idealized neutral condition is often just a local transition between (usually daylight) convectively mixed, and (usually nighttime) stable boundary layers. Basically the two regimes determine the buoyancy role in the momentum equations I.1.29: A negative (virtual) temperature gradient characterizes the unstable or convective regime, where thermal forces sustain turbulent motions at very high altitudes in the atmosphere; the positive temperature gradient characterizes stable or stratified regime, with thermal forces actually damping the turbulent motions and confining them to shorter distances from the surface.

Potential virtual temperature and humidity The definitions below follow from Kaimal and Finnigan [1994] (pg. 6-7). The potential temperature θ_p measures the deviance from the actual temperature profile to its neutrally stable (adiabatic) state, so that being c_p the specific heat at constant pressure, and g/c_p the adiabatic rate:

$$\frac{\partial \theta_p}{\partial z} = \frac{\partial \theta}{\partial z} + \frac{g}{c_p}, \tag{I.2.10}$$

that integrated in first order, at a height Δz from the surface where $\theta_p = \theta$, gives $\theta_p = \theta + \Delta z\, g/c_p$.

Over water surfaces or forests, significant moisture may be encountered and the potential virtual temperature θ_v introduced for a specific humidity q_h:

$$\theta_v = \theta_p \frac{\theta_v}{\theta}, \text{ with}$$
$$\theta_v = \theta(1 + 0.61 q_h). \tag{I.2.11}$$

Stratification regimes The solar radiation imposes the diurnal cycle of thermal forces in the atmosphere, leading to the 24 hrs diagram of figure I.2.7, taken from Kaimal and Finnigan [1994] (pg. 7). Most of the radiation kept in the surface, the convective regime usually follows sunrise, and from this moment the boundary layer height (z_i in the figure) increases until reaching a maximum, around midday when the radiation is strongest. The convective regime shall be sustained through most of the day, with the ABL bounded by the capping inversion layer, where the temperature gradient become again positive. But when radiation ceases the surface is also the fastest cooling medium in the system, so the stable regime follows around sunset. As the stable regime approaches, one or multiple shallow inversion layers rise from the cooling surface, slowly converging to a statistically steady regime with $z_i \sim [100, 200]$ m (Kaimal and Finnigan [1994]).

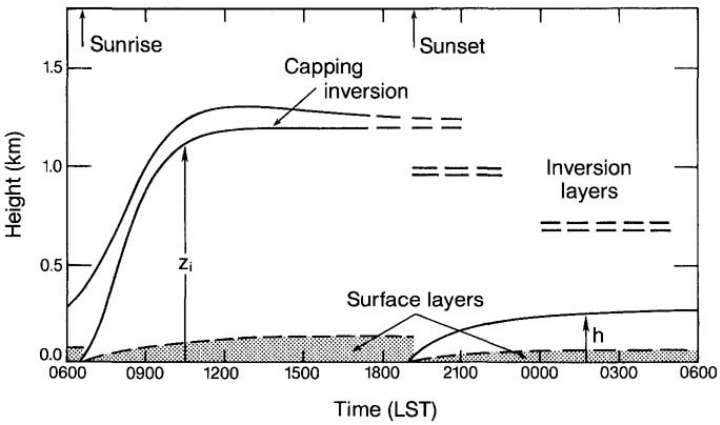

Figure I.2.7: Diurnal cycle of thermal stratification, from Kaimal and Finnigan [1994] (pg. 7). In this example, the convective regime follows sunrise, and the transition to the stable regime occurs just after sunset.

The diurnal cycle depicted is not as precise as it seems, and the radiation reaching the surface is also submitted to climate and meteorological conditions (c.f. Zhang and Klein [2010] and Kalthoff et al. [2018]). Notably a water body presents much larger heat capacity than the land, so generally above the Ocean the convective regime will appear later during the day, and the stable regime later during the night. A diurnal variability of the surface temperature is surely present, but not necessarily it will leads to positive or negative temperature gradients as pictured, and besides the system is also submitted, e.g. to seasonal cycles and ocean currents.

Associated to the induction of thermals in the atmosphere, strong buoyant forces characterize the convectively mixed regime, with mean vertical profiles exemplified in figure I.2.8a. The vertical profiles vary strongly in the surface layer, until $\sim 10\%$ z_i from the surface, and are almost constant otherwise. The convective regime is characterized by high turbulence levels, and an extended ABL boundary layer size. An inversion layer limit the ABL size at about $z_i \sim [1, 2]$ km (Kaimal and Finnigan [1994]), where $\partial\theta_p/\partial z$ becomes predominantly positive.

In stable conditions such as depicted in the mean profiles of figure I.2.8b, the hot air tends to be kept stable in the upper locations, so turbulence is damped by thermal effects.

The profiles vary gradually with height, and the size of the ABL may not be so easily defined: According to Kaimal and Finnigan [1994], it shall be defined by small enough values of turbulence (~ 5% from surface values) but it is often measured by sodars as the minimum between the velocity maximum or the inversion layer height. The mean quantities evolve slowly during the night, and statistical equilibrium is less often encountered in stable regimes.

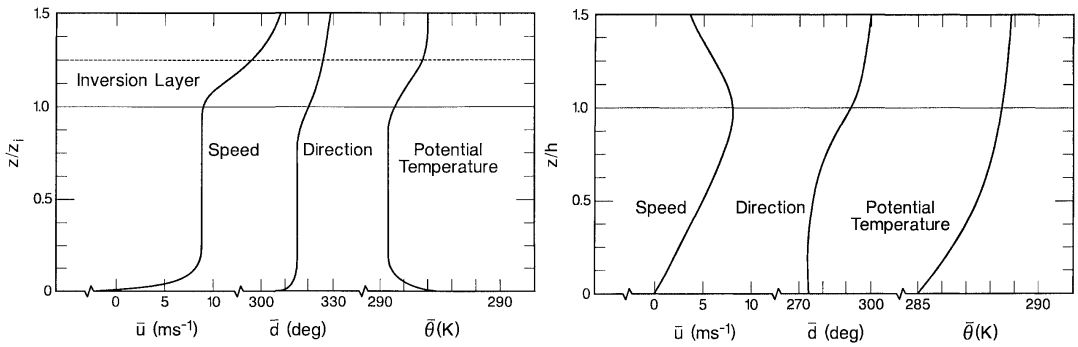

(a) Convective regime (b) Stable regime

Figure I.2.8: Representative exemplification of the mean velocity, direction and temperature profiles, in convective (a) and stable (b) conditions. From Kaimal and Finnigan [1994] (pg. 5-6).

Non-dimensional scale of buoyancy The Richardson number, first introduced in eq. I.1.31 as $Ri = \beta_\theta g \Delta\Theta L/U^2$, measures the momentum generation capability by buoyancy, compared to inertia. An alternative, local expression for the Richardson number is:

$$Ri = \frac{(g/\overline{\theta_v})(\partial\overline{\theta_v}/\partial z)}{(\partial\overline{u}/\partial z)^2}, \tag{I.2.12}$$

which better resembles the form introduced by Richarson itself in Richardson and Shaw [1920], while others are given, e.g., in Kaimal and Finnigan [1994] (pg. 14 and 15). Defined like this, Ri is negative for unstable, positive for stable, and null for neutral regimes. Beyond a certain value ($Ri_c \sim 0.25$ in Kaimal and Finnigan [1994] pg. 14), turbulence is effectively damped and the flow turns laminar.

Monin-Obukhov Similarity Theory (MOST) The latest breakthrough in characterizing the non-neutral ABL is achieved in 1946 by Obukhov (Reprint in Obukhov [1971]), extending Pradtl's boundary layer theory for situations of significant buoyancy forces, characterized by the Richardson number defined in equation I.2.12. In 1946 Obukhov set the theory basis and its relevant parameters, and in 1954 (Reprint in Monin and Obukhov [2009]) Monin and Obukhov defined the most significant non-dimensional height:

$$\frac{z}{L_{MO}} = \frac{\left(\frac{g}{\overline{\theta}_v}\right)\left(\frac{q}{c_p\rho}\right)}{\left(\frac{u^{*3}}{\kappa z}\right)}, \tag{I.2.13}$$

introducing the Monin-Obukhov length L_{MO}, i.e., the length dimensioned quantity formed by the characteristic relevant parameters: $(g/\overline{\theta}_v)$; u^*; $q/(c_p\rho)$. Here $\overline{\theta}_v$ is the surface mean potential virtual temperature, and q the kinematic heat flux $\overline{w'\theta'_v}$. The successful Monin Obukhov similarity theory (Obukhov [1971]), recently reviewed by Foken [2006b] on its 50th anniversary, argue that z/L_{MO} is sufficient to evaluate the deviance from Prandtl's log-law due to thermal instability effects. The momentum and heat fluxes across the ABL are then given by universal, empirically obtained, functions of z/L_{MO}. From that point until today, a great part of the atmospheric scientific community (c.f. Foken [2006b]) dedicates into determining these universal functions, as one should note the functional presented in Businger et al. [1971], together with the Dyer-Businger equation (see Businger [1988], dedicated to Arch Dyer) establishing the relation between momentum and heat functions.

Besides the strong assumptions of homogeneity and steadiness in the ABL, MOST also assumes constant fluxes occurring across the ABL. In the so-called Surface Boundary Layer, which covers about 10% of the ABL, a constant flux region is indeed sustained where MOST performs quite well. However, the theory shall fail when the gradients change rapidly across the boundary layer height, which is a problem often encountered in stable conditions, characterized by the presence of multiple inversion layers close above the surface [Optis et al., 2014].

I.2.2.4 Wind resource and harvesting prediction

To operate wind turbines closest to their maximum efficiency point and reduce the mechanical loadings, the wind energy industry disposes of active control mechanisms to adjust the rotor's torque and each blade's pitch angle [Salic Tom, 2019]. At this point the control algorithm relies on the wind field description to absorb power from fluctuations that can be significant if compared to the mean available power [Emejeamara et al., 2015]. It is also a clear trend that wind turbines are getting bigger and thus structural loads increasingly impact construction and maintenance costs. One of the main structural concern relates to fatigue, which may be reduced through careful design and intelligent active controls [Rezaeiha et al., 2017], both relying in fine turbulent flow descriptions.

To afford multiple scenarios and real time applications, prediction tools for design and operational purposes rely on semi-empirical and low-fidelity numerical solutions. State-of-the-art wind models adopted in solvers like HAWC2 [Rezaeiha et al., 2017] consider a mean wind log-law profile based on the MOST (see Foken [2006a], and section I.2.2.3) superposed to randomly generated turbulent components with statistics given, e.g, by the Mann spectra (Mann [1998]).

Artificial turbulence and the Mann spectra To avoid phase resolving turbulent motions, and yet account for their statistical effect in engineering structures, the methodology usually adopted relies in the prescription of second order turbulent statistics, such as the turbulent velocities auto and cross-spectra, and the spectral tensor of equation I.1.17, naturally related to the 1D (space) or 2D (space-time) spectra introduced in section I.1.1.5 (c.f. Pope [2000], pg. 220).

The idea that turbulence can be reproduced from the turbulent spectra can be traced back to Taylor [1938], by introducing a deterministic initial field with random phases, analogous to Pierson et al. [1955] ideas exemplified in figure I.2.2, but that Taylor presented in analogy to optical applications. The approach introduced by Taylor [1938] is widely exploited up-to-date, counting on a dispersion relation for turbulent motions given by the Taylor's hypothesis discussed in section I.1.1.5.

In isotropic turbulence and due to the incompressibility constraint, the relationship between two of the one-dimensional auto-correlation functions of longitudinal velocities ($E_{u_1'u_1'}(k_1)$ and $E_{u_1'u_1'}(k_2)$ for example), or the total energy density spectrum $E_{u_1'u_1'}(k)$ (where $k = |\boldsymbol{k}|$), are sufficient to determine all the double correlations of the velocity field, and hence the spectral tensor of each of the velocity components. So von Kármán [1948] develops the von Karman spectrum for $E_{u_1'u_1'}(k)$, still often employed to this days describing isotropic turbulence, and function of two parameters, i.e., the dissipation ϵ (in the term $\alpha\epsilon^{2/3}$ where α is Kolmogorov's constant), and a length scale L_k.

In the presence of shear, Mann [1994] linearize the Navier-Stokes equations with boundary layer assumptions, and employing Rapid Distortion theory arrives to simple equations governing the time evolution of the spectral tensor. He considered these equations acting in initial conditions given by the Von Karman spectra for isotropic turbulence, thus qualitatively [Mann, 1994] accounting for the reorientation and stretching of individual turbulent eddies. To close the problem avoiding the unconstrained deformation of turbulent eddies, the vortex lifetime has to be prescribed, as close as possible reproducing the physical break-up events, which introduces the parameter Ω to Mann's spectra, in addition to those of Von Karman (ϵ and L_k). In Mann [1998], the Mann spectra is compared to other models in the literature, establishing the values of Ω, ϵ, and L_k corresponding to each of these models.

The state-of-the-art method of artificial turbulence generation is probably the one presented in Mann [1998]. Besides very efficient in establishing the relationship between the velocity field and the spectral tensor, it consider and argues in favor of Gaussian distributed velocity fluctuations, contrasting to the random phases approach yet adopted in many applications.

Introduction to the Marine Atmospheric Boundary Layer (MABL) In the MABL, the ocean (thermo)dynamics' significantly alter the atmospheric flow through higher heat capacity and complex wind-wave interactions that become important in fairly common situations. The impact of the marine environment to the wind energy exploitation inside the MABL is carefully review, e.g., in Kalvig et al. [2014], where one observes the importance of poorly understood (compared to in-land applications) wind-wave interactions. These wind-wave interactions are the main subject of present Thesis, to be further discussed along its specific literature review along section I.3.

I.3 Wind-Wave Interaction mechanisms

The relation between wind and wave motions has long been evident to keen eyes observing the fluid dynamics in the offshore environment. The Beaufort scale was devised by the Irish hydrographer, and royal Navy officer, Francis Beaufort in 1805. It is a highly empirical method to measure wind speeds above the ocean from visual estimations of the sea-state behavior, based on the empirical knowledge acquainted by decades of naval expeditions along the 17th century [Centre, 2010]. The scale devised by Beaufort, reviewed along the years and exemplified in the modern pictures of figure I.3.1, survived to the trial of time until very recently, when most of the vessels are equipped with anemometers. According to Kent and Taylor [1997], still in 1990, 60% of the wind observations from the north Atlantic were visual estimates based on the Beaufort scale, motivating their systematic comparison between the Beaufort scale and modern anemometer-based techniques.

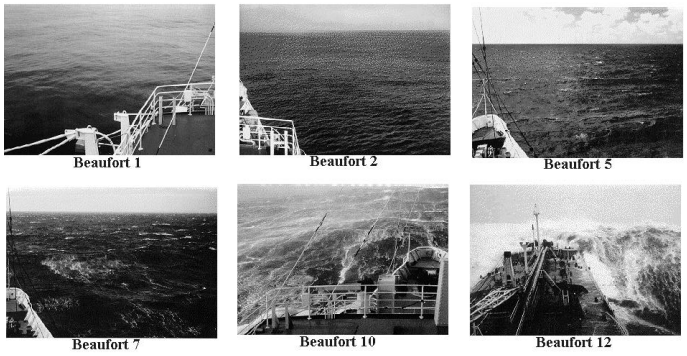

Figure I.3.1: The modern Beaufort Scale (1805-2001), taken from Journée and W.W.Massie [2001]. Even more recent images dating 2010 can be appreciated with the historical review in Centre [2010].

An implicit assumption of equilibrium between wind and waves is assumed by employing the Beaufort scale, for it implies that the wind uniquely defines the sea-state, and vice-versa, which shall occur in infinite fetch, statistically steady and homogeneous conditions. Away from the idealized equilibrium condition, one distinguish the young and old sea regimes. Young sea conditions occur when rapid winds force the free-surface, transferring its momentum to comparatively slow traveling waves. Old seas occur when fast traveling waves (notably a swell) encounter comparatively slow wind conditions in the lower part of the MABL. The non-dimensional quantity usually employed in the literature to characterize the wind-wave interaction regime is the Wave Age WA= c/U, defined as the ratio between the wave phase velocity c, and a characteristic velocity scale in the atmosphere U.

The scientific knowledge about ocean waves and turbulent dynamics has enormously evolved in the years following the Beaufort scale in 1805, for instance: The Stokes wave theory revised in section A.1.1, is introduced by Sir George Stokes in 1847; Prandtl's boundary layer theory revised in section A.1.2, is presented by Ludwig Prandtl in 1904; the Kolmogorov turbulent cascade seen in section I.1.1.5, is proposed by Andrei Kolmogorov in 1941; and the sea-state spectral decomposition seen in section I.2.1.1 is proposed by Willard J. Pierson in 1952. Simultaneously to this major achievements in fluid dynamics, the specific application of Wind-Wave interactions received increased attention from the scientific community, with some principal concepts introduced through the analytical developments of Thomson [1871], Jeffreys [1925], Miles [1957], Phillips [1957], and Belcher and Hunt [1993], covering the years of 1871-1993 described in section I.3.1. Joining the theoretical concepts aforementioned motivated the author to present the flow description in the appendix A.2.1.

Section I.3.2 presents some of the empirical observations necessary to establish the most important concepts of Wave Boundary Layer and Wave Induced flow, highlighting the aspects that receive particular attention during the thesis. In section I.3.3 the Marine Atmospheric Boundary Layer is investigated in comparison to the ABL similarity theories previously introduced at section I.2.2, with some emphasis on the chronological progress observed between early and modern, physical and numerical experiments. Very modern measuring and modelling techniques allow the flow description into the very small scales discussed in section I.3.4. The latest two sections go deeper into the numerical and empirical methodologies that most specifically resemble the ones here adopted. High fidelity and oceanic scale numerical reproductions of the MABL are achievable as discussed along section I.3.5, by employing Large Eddy Simulations, and possibly a High Order Spectral method describing the free-surface. Direct evaluations of the Wave Induced flow are reviewed in section I.3.6, that also depicts some of the technical solutions nowadays available for the offshore experimental campaigns, and particularly describe the Wave Coherent flow as an approximation to the Wave Induced flow, leading to the simplified WBL equations discussed in the section.

I.3.1 Early established theories and Wave growth

Probably the earliest attempt to develop an analytical solution of coupled wind and wave motions, is the one Lord Kelvin presents in Thomson [1871], employing a potential (non-rotational) flow assumption (see section I.1.2.1) to both water and air domains. Remarking the disagreement between Lord Kelvin's predictions and the empirical observations at the time, Jeffreys [1925] first consider the importance of strong convection forces, i.e., apparent discontinuities and turbulence, to be accounted for in the following wind-wave interactions studies. The sheltering theory, as proposed in Jeffreys [1925] and exemplified in figure I.3.2, pictures an interaction with negligible viscosity, where the air motion gives rise to boundary layer detachments starting on the wave's crest; pressure rises windward, and drops leeward on the detachment zone, feeding an existing wave system in phase with its slope. The pressure distribution is given through physical reasoning and the introduction of a sheltering coefficient.

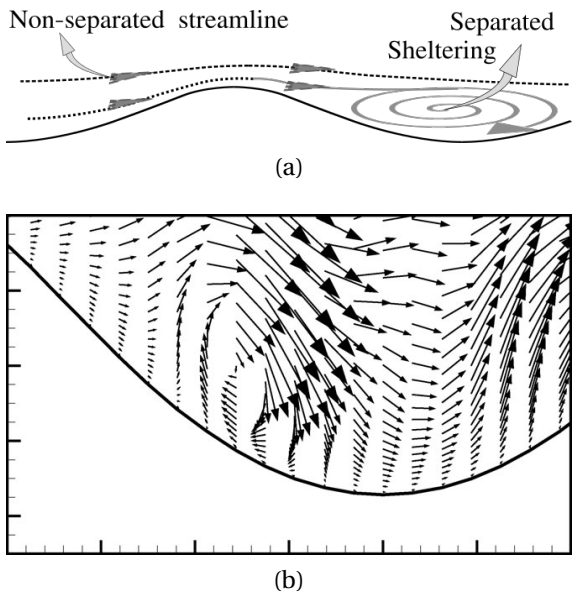

Figure I.3.2: Jeffrey's mechanism of wave growth [Jeffreys, 1925], relying in the flow detachment occurring at the lee-side of a sufficiently steep wave. (a) A schematic on the flow structure. (b) DNS (See section I.3.5) observations from Yang and Shen [2010].

From Jeffreys [1925], the next theoretical leaps were achieved simultaneously, differently but complementary, by Miles [1957] and Phillips [1957]. Miles' proposes a boundary value

problem (BVP) exemplified in figure I.3.3, coupling the linear inviscid and laminar perturbations on an initial mean velocity wind profile, and a linear irrotational gravity wave with non-deformable shape. The resultant flow includes a singularity at $z = z_c$ where $\overline{u}_1(z) = c$ introducing a continuous distribution of vorticity depicted in the figure. The vorticity distribution is responsible for the wave growth, and corresponds to a conceptual advancement on Lord Kelvin's theory of point-wise vorticities. Elegant as it is, Miles' mathematical reasoning can be less than intuitive, so that a more physically motivated discussion on this mechanism can be appreciated in Lighthill [1962].

In Miles' model, turbulence role is restricted into determining the mean wind profile, an assumption already recognized by Miles as an intrinsic, major simplification. At the proof stage, Miles [1957] acknowledges the complementary mechanism presented by Phillips [1957], who associates the wave growth to a resonance mechanism between turbulent motions and the free surface characteristic modes, leading to the exchange of momentum between the systems. Philips' turbulent mechanism of wave generation is the first to explain how wind-induced waves appear in an initially undisturbed surface. Both theories were afterwards improved and combined as first described and evaluated on Miles [1959] as the so called Miles-Philips mechanism of wave generation. Philips mechanism is predominant on the initial phases of waves generation, as the wind induces a broad-band wave spectrum energy transfer with amplitudes evolving linearly in time. At later stages of wave development, miles' mechanism takes place and waves shall grow exponentially.

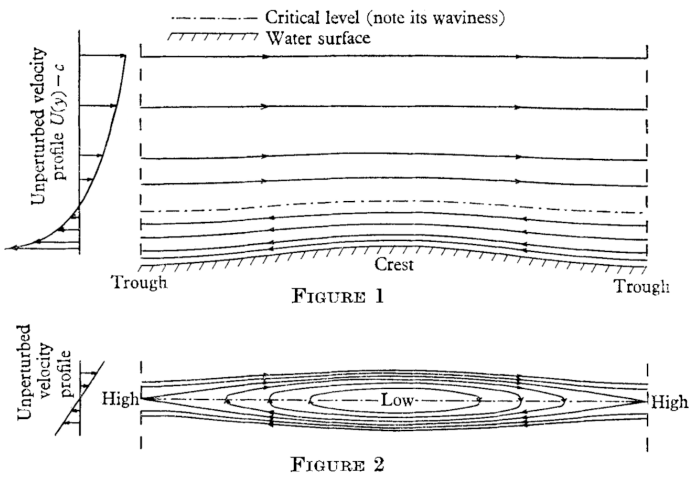

Figure I.3.3: Miles mechanism [Miles, 1957] of wave growth/ damping, from Lighthill [1962]. Figure 1 (above): The reversed flow below the critical height, and the streamlines deformation due to the moving boundary. Figure 2 (below): A continuous vorticity distribution appears at the critical height z_c, where the mean wind $\overline{u}_1$ equals the phase velocity of the wave.

Even though initially pictured for high steep wave profiles where detachment can occur, a non-separated sheltering effect ([Belcher and Hunt, 1993] and figure I.3.4) still holds for lower steep waves, where a thickening of the boundary layer invariably occurs leeward to the crest leading to asymmetrical disturbances of the Reynolds stresses. In a young wave context where the reversed region below z_c is confined to the very vicinity of the free-surface, employing a mixing length model in the inner region and rapid distortion theory in the outer region, Belcher and Hunt [1993] demonstrate that the non-separated sheltering induces the non-symmetrical, and symmetrical but longitudinally displaced, disturbances of inner and outer regions, respectively. In both regions, the difference in phases between the flow streamlines and the free-surface allow the (partially) out-of-phase slope-pressure correlations that contribute to the wave growth or damping.

An extensive review and evaluation of the wave growth mechanisms is presented in Belcher and Hunt [1993], including those already mentioned above, and: Higher order effects with respect to the wave linearity; the waves orbitals' velocity acting in the atmosphere; and variable roughness effects.

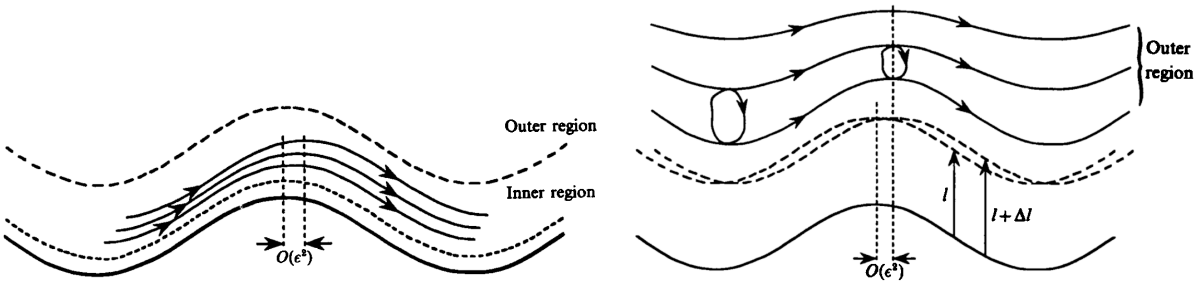

(a) (b)

Figure I.3.4: Shelter related wave growth mechanisms, from Belcher and Hunt [1993]. (a) Non-separated sheltering: streamlines are depicted above the matched height. The boundary layer thickens leeward, and shrinks windward to the crest. (b) Outer region Reynolds-stress effects: the non-separated sheltering in the inner region leads displaces the largely inviscid outer-region flow.

I.3.2 The Wave Boundary Layer and the Wave Induced flow

Rather than an exhaustive description, this section is intended to be an introduction to these subjects, that for its importance in the present context will be constantly revisited in the next sections. The text in bold highlights the aspects that most relate to the discussions presented along the manuscript, raising the scientific questions stated in the introduction at section 0.

According to theory (c.f. Miles [1957], Belcher and Hunt [1993], from section I.3.1) and observation (c.f. Tamura et al. [2018] and Hristov [2018]), the **Wave Induced disturbances** extend into limited regions above the free surface. Though coupled to this inner layer through modified turbulent scales, the outer flow behaves similarly to static bottom atmosphere flows such as usually described by the Monin-Obukhov Similarity Theory (MOST) described in section I.2.2.3. Definitions of the inner layer's height are not unique, as one could take, e.g., Mile's [Miles, 1957] critical height or the Non-separated sheltering region of Belcher and Hunt [1993] as rough approximations with possibly drastically different outcomes.

The commonly adopted strategy [Cifuentes-Lorenzen et al., 2018] is to define the **Wave Boundary Layer** as the region in which the wind or turbulent profiles strongly deviate from widely accepted In-land similarity theories, such as MOST. The problem is that Wind-Wave interactions are in fact multiple physical mechanisms acting in different manners on the wind field: Those mechanisms are very sensitive to the sea-state definition, wind and thermal stratification behavior; and each mechanism shall propagate up to different heights and disturb different quantities of the wind field. Moreover, MOST is often observed to fail due to the lack of homogeneity and steadiness in the atmosphere [Hristov and Ruiz-Plancarte, 2014], and together with measurement induced bias significant uncertainty is introduced with such definition. With that complexity in mind, Hristov and Ruiz-Plancarte [2014] note

that a simple and robust parametrization of the surface drag is unlikely to exist, which is probably valid for the WBL height parametrization, apparently equally unlikely to be found for generic sea-state and atmospheric conditions.

That said, the Wave Boundary Layer (WBL) exists in the vicinity of the free-surface, where the waves' influence directly alters the flow dynamics with the appearance of the **WI flow**, and notably a **WI Stress** perturbation ([Belcher and Hunt, 1993, Sullivan et al., 2008]) responsible for the vertical transfer of momentum between waves and wind. When the waves travel sufficiently fast in **old seas** (high WA) conditions, the upwards transfer is such that the wave signature might emerge explicitly as low-level jets ([Harris, 1966, Hanley and Belcher, 2008]), characterized by a maxima of the wind velocity profiles occurring inside the WBL.

In section I.2.1.2 the reader is introduced to Wave driven circulation, Stokes-Coriolis forces and Wave-Current interactions acting in the upper Ocean, in the ocean mixed layer. The author notices that in different intensities each of this mechanisms shall transfer into the atmosphere. Such similarities are inferred to a coupled air-sea WBL discussed in Edson et al. [2007], particularly noting the parallel between wave-current or wave-induced-wind interactions in the WBL. Their LES numerical simulations reveal atmospheric coherent structures resembling Langmuir circulations, usually associated to motions in the ocean [Grant and Belcher, 2009].

The definition of the WBL relates to the existence of the Wave Induced flow, i.e., wave related dynamics (Velocities and Pressure) that advect through the atmosphere, yet maintaining some of its original aspects described in section I.2.1. The WI flow is supposedly significant in the WBL, and is the origin of other disturbances that propagate even higher on the MABL. Such flow is sustained by the ocean waves, commonly described within an irrotational framework, as described in section I.1.2.1 and assumed in the earliest studies of Thomson [1871], that in the absence of wind could well be valid in the atmosphere. However in the turbulent shear flow of the MABL, the WI flow is submitted to other interactions theoretically framed between Jeffreys [1925] and Belcher and Hunt [1993]. Through the experimental literature, one often observes the consequence of WI motions, qualitatively confirming many aspects of the theoretical framework established, such as the exponential decay of WI disturbances [Semedo et al., 2009] with height, the existence of a critical layer mechanism [Grare et al., 2013a], and with significant scatter (c.f. the comparison in Cathelain [2017]) the wave growth rate (Montalvo et al. [2013]) prediction. A more precise **definition of the WBL and the WI flow** remains elusive though, as the WI disturbances significance is often dependent in the variables of interest, as suggested in Hristov [2018].

The theoretical developments were up to a certain point the main tools for addressing Wind-Wave interactions in the WBL, but they are obviously limited to canonical conditions. Nowadays, the ever increasing computational power and improving measuring techniques allow the evaluation of Wind-Wave interactions in complex oceanic conditions, which is the focus in this Thesis. With that in mind, the next sections extend the physical description and bibliographic review with focus in **numerical and experimental, observational approaches**. Particularly, sections I.3.6 and I.3.5 discuss the literature review that better relate, respectively, to the numerical and physical experiments conducted during the Thesis.

For the reader seeking an overall perspective of Wind-Wave interaction studies, better balanced between the trinity theory-experiment-numerics, the PhD Thesis of Ayet [2020]

focuses in the theoretical studies that might often complement the numerical and experimental studies here presented. Noting that previous theoretical models described in section I.3.1 are limited to a single monochromatic wave, instead Ayet [2020] employs a spectral framework, yet exploited only in flat bottom scenario [Katul et al., 2011], in order to study multi-scale aspects of wind-wave interactions. The consequent discussion highlights some important remarks concerning wind-waves interactions, including the importance of the stokes drift determining the spectral behavior of the smallest wind-waves, and the necessity of more detailed experimental data concerning, e.g., **space-time joint distribution Energy Density Functions (EDF)**. The theory developed establishes a promising first step towards a well desired analytical spectral model, **linking multi-scale waves and wind motions** in the atmosphere.

I.3.3 Boundary layer similarities in the MABL

I.3.3.1 Roughness length: Early to recent measuring campaigns

Historically wind measurement campaigns rely on cup anemometers, or more recently (In the 70's) sonic anemometers capable of measuring the three components of the velocity field with very high acquisition frequency, but limited to a single position per probe, and a few probes per experiment. Naturally, and often critical in field experiments, meteorological masts are involved and special attention has to be taken so that it does not interfere with the incoming wind, nor introduce significant displacements in the measuring probes. The latest is particularly hard to achieve with floating platforms in the offshore environment, where the rigid body motions have to be carefully measured and subtracted from the wind measurements. With cup anemometers attached into fixed bottom structures, the first field experiments on the wind-wave interactions consider the ABL over fetch-limited reservoirs, and that leads to the pioneer work of Charnock [1955] opening this section.

Measuring the wind profile 8 meters above a 16-m-deep reservoir with ~1 km fetch, Charnock [1955] rightfully theorizes through dimensional reasoning that the roughness length z_0 above a water surface shall scale with Charnock's constant α, in $z_0 = \alpha u^{2*}/g$, as a function of the friction velocity u^* and gravity g. Over the next decades the techniques to obtain the friction velocity evolved considerably (c.f. the HEXOS experimental campaign Smith et al. [1991]), and Charnock's theory observed to hold even in the offshore environment, while the question remains up to this date on how exactly does α scale in this case, and rather than a constant it is obviously dependent on the sea-state parameters characterizing its energy spectral distribution.

Following Charnock, much of the experimental effort in the Wind-Wave interactions is dedicated into determining the roughness length parametrization. On the reconciliation of wave growth measurements during JONSWAP and Lake Ontario, Kahma and Calkoen [1992] attributes a great deal of the previously observed discrepancies to thermal stability effects. In Donelan et al. [1993] such effort combines the measuring over Lake Ontario, North Sea and Atlantic Ocean, remarking the intrinsic difference between field and laboratory scale experiments to study the WI drag, or z_0. In wind-wave conditions and the absence of a predominant swell, Donelan et al. [1993] concludes z_0 can either scale with u^{*2}/g, or with a characteristic wave height representative of the locally generated wave field, and that α

shall definitely scale with the WA, though presenting opposite trends in laboratory or field experiments. From this moment, at least, it is generally accepted that above the ocean and for young waves, the roughness length increases with decreasing Wave Age.

Still, multiple questions remain, e.g., regarding the swell influence, the coexistence of multiple wave systems, and wind-wave (mis)alignment. Since then, multiple other experiments have been conducted in the MABL, and exploited to improve and extend previous definitions of α, describing the roughness length as function of the sea-state parameters, as one could cite e.g., Edson et al. [2013] (CBLAST campaign), Patton et al. [2019] (FINO1 campaign) and Porchetta et al. [2019] (FINO1, CBLAST).

I.3.3.2 Eddy viscosity: Early to recent numerical models

As soon as non-linearity comes into play in the theoretical framework presented in Miles [1959], some sort of numerical approximations shall be employed to obtain the solution, so for clarification the discussion is here limited to models including a minimum level of fidelity, i.e., considered to include at least some level of resolved turbulence. That definition shall include numerical models ranging from URANS with one equation closures to DNS resolution, but first one shall note the mixing length theory: The simplest first order closure to the URANS equations that imposes the linear scaling of the eddy viscosity with height, employed since Jacobs [1987] and Van Duin and Janssen [1992] to address wind-wave interactions in the asymptotic case of slow traveling waves. The mixing length theory is usually invoked by higher fidelity models to characterize the flow very close to the surface, and that's the case for example in two-layer models (c.f. [Belcher and Hunt, 1993]), when describing the flow in the inner layer, and in present LES formulation for prescribing the lower boundary condition. Above the inner layer, Belcher and Hunt [1993] employs the rapid distortion theory to describe the turbulence straining effects.

The eddy viscosity hypothesis is the predominant approach adopted in RANS with one or two equation closures, and is extensively applied to CFD simulations of ABL flows at local scales (O'Sullivan et al. [2011], Blocken [2014]). The pioneer numerical studies regarding wind-wave interactions indeed relied a lot in such schemes, but employing a six equations 2nd order turbulent closure for the Reynolds Stress Tensor (RST), Mastenbroek [1996] demonstrate that for waves traveling with velocities comparable to the wind speed, the turbulent viscosity hypothesis shall fail due to a lack of equilibrium between production and dissipation of TKE in the outer layer of Belcher and Hunt [1993]. Significantly more complex than first or second order schemes, and not subject to the eddy viscosity assumptions, there is still a significant amount of modeling in RST schemes such as the Launder-Reece-Rodi (LRR) employed in Mastenbroek [1996], and his comparison between one, two, or six equations closures reveals a strong dependency of key flow features, such as the wave growth, to the turbulent scheme employed. Nevertheless, with its assumption comprehending fast and slow waves traveling with or against the wind, Mastenbroek [1996] confirms the existence and scaling of the inner region, previously limited to slow traveling waves in Belcher and Hunt [1993]. Revisited in Cohen and Belcher [1999], the WBL model coupling mixing length and rapid distortion theory is extended to the case of fast traveling waves, and confirms the agreement to the second order closures of Mastenbroek [1996].

I.3.3.3 Similarity disturbances: Measuring and modelling implications

The physical experiments yet discussed seek the parametric description of a logarithmic wind profile, supposedly occurring above the Wave Boundary Layer. On the other side the numerical approaches described before Mastenbroek [1996] employ considerable level of modelling, dependent on the same boundary layer similarities of the logarithmic wind profile, for example: Mixing length theory; two-layer assumptions; log-law boundary conditions; and notably the eddy viscosity hypothesis.

But the definition of a WBL is as seen, not unique, and in reality even the logarithmic wind profile shall be carefully reviewed in the MABL (c.f. Cathelain [2017] and Hristov [2018]). It is so imperative to examine the Wave Induced flow and disturbances very close to the free-surface, and specially in the so-called WBL. Unfortunately, direct measurements inside the WBL can be extremely difficult to perform above the ocean, due to its proximity to the deforming surface that induces flooding risks and motions to the probing equipment.

In the ocean environment, the momentum flux (friction velocity) estimation above the ocean is a challenge by itself, reviewed e.g. in Edson and Fairall [1998] and Sjöblom and Smedman [2002]. Invariably the measurement is limited to a certain height above the free-surface, and have to be extrapolated downwards to obtain surface quantities such as the friction velocity or the form drag, and Cifuentes-Lorenzen et al. [2018] note that in the field such approach truncates the most important contribution of short waves to the growth rate, as they are probably undetected at the available measurement heights. In the early stages of Wind-Wave interaction studies, these difficulties apparently resulted in years of experimental studies with contradictory conclusions, e.g., discrediting for the lack of observational insight (c.f. Longuet-Higgins [1962] and Simpson [1969]) Miles' and Philips' theories, nowadays assumed true for its extensive observational support.

By that time, most of the experimental measurements between Charnock [1955] and Edson and Fairall [1998] were unable to detect WI disturbances to the Monin-Obukhov similarity theory, with the common explanation that the measurements occur above the WBL (Hristov and Ruiz-Plancarte [2014]). While addressing the challenge of momentum flux estimation with measurements performed at the semi-enclosed Baltic Sea (that they note might strongly differ to the open ocean), Sjöblom and Smedman [2002] offer the first field-based TKE budget dependency to different sea-state conditions. One of the main conclusions in Sjöblom and Smedman [2002] confirms the numerical suggestions of Mastenbroek [1996], regarding the lack of balance between production and dissipation inside the WBL. During swells, dissipation largely prevails, and the usually neglected turbulent transport terms become significant (notably the pressure term contribution): In these conditions that ultimately condemns traditional "inertial dissipation" methods for estimating the momentum flux [Sjöblom and Smedman, 2002], but also traditional URANS numerical approaches relying in the eddy viscosity hypothesis [Mastenbroek, 1996].

At laboratory scales those difficulties are more easily surpassed: For example in Grare et al. [2013b] one will find the momentum fluxes being evaluated inside the linear viscous sublayer, by employing modern floating masts equipped with hot-wire anemometers. Next section presents laboratory scale physical and numerical experiments, but the focus is given to the unique, small scale physical aspects that it reveals.

I.3.4 Down to the dissipation range at laboratory scales

I.3.4.1 Modern measuring techniques: PIV

Particle Image Velocimetry (PIV) is a measuring technique capable of reconstructing the flow kinematics, revealing highly detailed velocity fields rarely available with other kind of physical experiments. Requiring highly controlled experimental conditions, PIV techniques are often restricted to laboratory scale experiments, which is the case regarding its application for wind-wave interaction studies, since the studies of Reul et al. [1999] regarding two dimensional wave-breaking separation events, and up to Yousefi and Veron [2020] revealing the very detailed description of turbulent kinetic energy budgets in the WBL.

I.3.4.2 Modern modelling techniques: DNS

Recently, fully resolved turbulence is affordable in Direct Numerical Simulation (DNS) computations, though limited to very small Reynolds numbers. Apparently the first DNS model applied over a propagating wave is presented in Sullivan et al. [2000], later developed into to the LES formulation discussed in section I.3.5. Since then numerous studies such as Yang and Shen [2010] consider the detailed resolution of turbulent structures in laboratory scale WBLs.

I.3.4.3 Coherent vortical structures

In section I.1.1.3 turbulence is described as chaos, justifying the use of statistical approaches describing turbulent flows. Truth is that turbulence presents in fact a dual character of chaotic and coherent motions, since it is also a dynamic system emerging as a deterministic solution of the Navier Stokes equations I.1.1, I.1.2 and I.1.4. Measuring and resolving turbulence through PIV and DNS techniques reveals a lot of the coherent, structured nature of turbulence. An extensive review of coherent structures in (flat) wall-bounded turbulence is presented in Jiménez [2018], tracing back to Voltaire in 1764 the argument that "*randomness is an admission of ignorance that should be avoided whenever possible*".

Two kind of coherent structures have to be brought to discussion and are exemplified in figure I.3.5a (From Adrian et al. [2000]), where one encounters: Roller structures ranging from blue in the wall, to purple on the outside, elongated in the stream-wise direction and in some cases, attached to the surface; and the Hairpin vortices in yellow, appearing as packets turning around the rollers. Based in PIV measurements, exposed in figure I.3.5b, Adrian [2007] focus in Hairpin vortices existing in wall-bounded flows, and describes its generation from the roller structures attached to the wall, as sketched in figure I.3.5a. It is noted in Jiménez [2018] that hairpin structures are characteristic to low Reynolds flows, or equivalently to a small confined region on the wall vicinity; they rapidly degenerate into other coherent structures, and so are hardly observable at high Reynolds conditions. Note that even though the techniques applied to identify these structures shall go beneath the dissipation range, coherent structures are required to be long-lived, and for such be sufficiently larger than the kolmogorov scale.

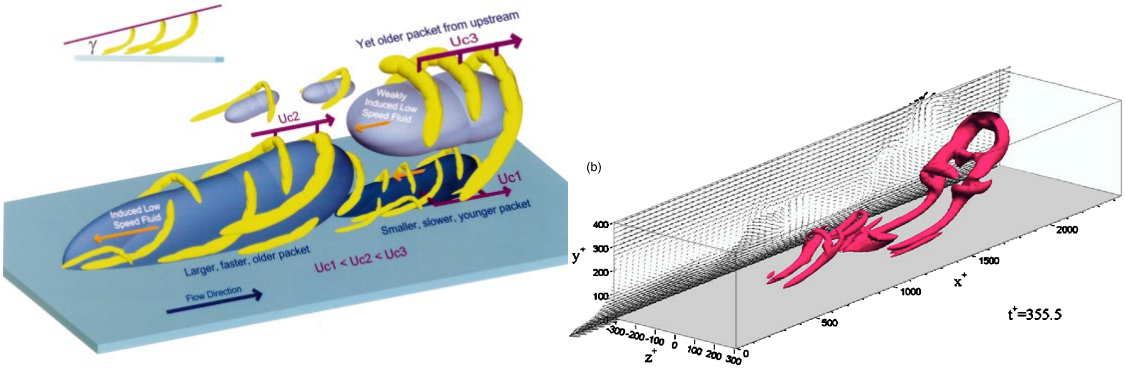

(a) (b)

Figure I.3.5: Coherent vortical structures in a shear layer flow. (a) From Adrian et al. [2000]: Schematics of hairpin structures (yellow) rising at the edge of roller structures (blue and violet). (b) From Adrian [2007]: longitudinal evolution of a hairpin structure, resolved with DNS.

Another element brought to discussion is the quadrant analysis, depicted in figure I.3.6. The figure depicts different DNS experiments gathered in Jiménez [2018], presented as elliptical isocontours of the joint Probability Density Function PDF of longitudinal and vertical velocity fluctuation components. In wall bounded turbulence, most of the energy lies in the quadrants Q2 and Q4, that characterize respectively, ejection and sweeps events ruling the lifecycle of these coherent structures. The hyperbolic red lines in figure I.3.6 indicate constant cross-correlation values, used as a threshold to identify strong sweeps and ejection events, that according to Jiménez [2018] carry approximately 60 % of the total vertical momentum flux, though representing only about 7% of the PDF volume fraction, i.e., fraction of the area of the PDF in figure I.3.6.

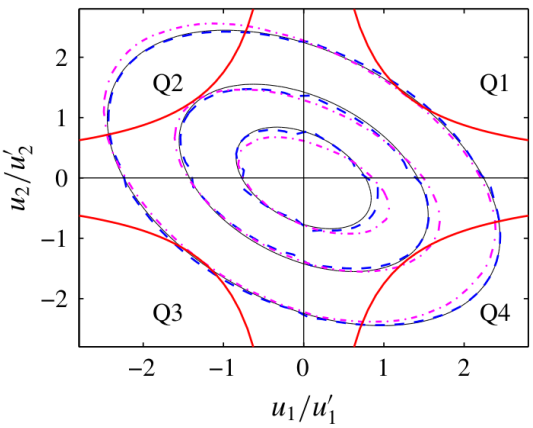

Figure I.3.6: Quadrant analysis of the PDF of longitudinal and vertical velocity fluctuation components. The elliptical iso-contours depict different DNS solutions. The hyperbolic red lines represent the threshold applied to identify sweeps and ejections in Q2 and Q4. From Jiménez [2018].

Bringing these analysis to wind-wave interactions, based in DNS computations Yang and Shen [2009] observed a quite peculiar scenario occurring above slow and fast waves as exemplified by their schematic in figure I.3.7, from Yang and Shen [2010]. It is noted the regular wave introduces a highly structured pattern to the turbulent flow, that Yang and Shen [2009] and Yang and Shen [2010] associate to the mean flow statistics (Reynolds stresses, scalar mixing, form and fiction drag) within four different phases of the wave, i.e., the crest, though, and two nodes. They identify two kinds of vortical structures: Horse shoes vortices, resembling the hairpin structures described by Adrian [2007]; and quasi-streamlined vortices corresponding to the rollers that prevail in the discussions of Jiménez [2018].

At slow waves (a) in figure I.3.7, horseshoe vortices appear close to the waves though, and quasistreamwise vortices appear on the wind-ward faces close to the wave crest. Those structures are sequentially evolving into one another along the wave length as described in Yang and Shen [2009]. They conclude these vortices stretching and turning due to the wave induced flow play an essential role determining the vortex life-cycle. For intermediate and fast waves (b) in figure I.3.7, the predominant kind of vortices are elongated quasi-stream-wise structures, bending submitted to the orbitals velocities, depicted downward below the though in the figure. It is remarkable that the horseshoe vortices identified in Yang and Shen [2010] and associated to sweeping events in the WBL, have their head wind-ward and legs lee-ward, contrary to the Hairpin structures of Adrian [2007].

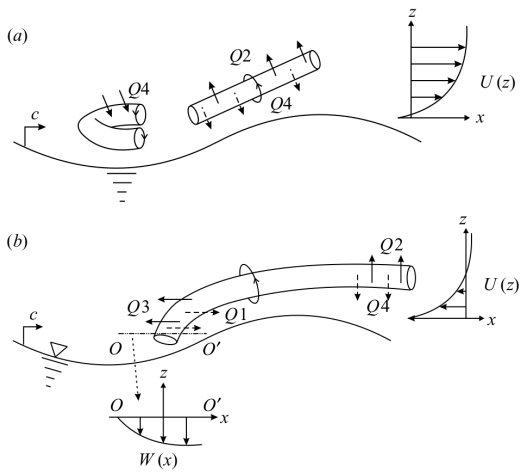

Figure I.3.7: Schematics of the coherent structures Yang and Shen [2010] observed above (a) slow and (b) fast traveling waves. From Yang and Shen [2010].

Regarding the quadrant analysis, Sullivan et al. [2000] demonstrate a considerable disturbance in old wave ages where the PDF spreads more uniformly around the four quadrants, instead of focusing in Q2 and Q4. In Yang and Shen [2010] such disturbance is observable from its contribution at different wave phases. Moreover according to the demonstration in Yang and Shen [2010], contrary to the standard view of flat bottom boundary layers, Q2 and Q4 do not necessarily indicate sweeping events in the WBL. Another hot topic exploited in Yang and Shen [2010] is the effect of the wave non-linearity in turbulent statistics and coherent structures in the WBL, noting they are responsible for intensifying these elements around the wave crests, so attenuating their strength in the waves' though.

I.3.4.4 Wave breaking

Noted during section I.2.1.2, wave-breaking events are essential processes determining, e.g., the dissipation rate, and thus the overall spectral behavior of a sea-state. Regarding wind-wave interactions, wave-breaking events also determine the momentum exchange and turbulent structures behavior in the atmosphere [Buckley et al., 2020]. For their intense, intermittent, localized behavior, occurring in the very vicinity of the free-surface, these kind of events pose tremendous difficulties to physical and numerical techniques, only recently being surpassed by DNS and PIV techniques. In that sense, Reul et al. [1999] (more deeply discussed in Reul et al. [2008]) presents a pioneer PIV study from measurements taken in the IRPHE-Luminy small wind-wave tank facility, where they describe the geometry of a separated region occurring on the leeside of a breaking wave, at figure I.3.8. The airflow separation observed in Reul et al. [1999] ressembles jeffreys' sheltering mechanism of wave growth [Jeffreys, 1925], and according to the discussion in Reul et al. [2008] they are in many aspects coherent to each other, but naturally the complexity of the physical experiment greatly exceeds the theoretical framework proposed by Jeffreys.

The observations and discussion in Reul et al. [2008] reveal a strong dependency of the separated region to the breaking waves geometry, which shall of course depend of the wave with respect to wind regime. Noting that the mechanical generated waves in the PIV experiments of Reul et al. [1999] better represent wave forcing wind conditions, Veron et al. [2007] instead employs the PIV in wind generated waves, better approaching the equilibrium condition at a larger wind-wave-current tank, from the University of Delaware. They are also capable of measuring the velocity field inside the viscous boundary layer, so besides confirming the observations of a separated region for wind-generated waves, and evaluating its consequence on the viscous stresses, Veron et al. [2007] also indicate a unique, linear relation between non-dimensional surface tangential stress and velocity.

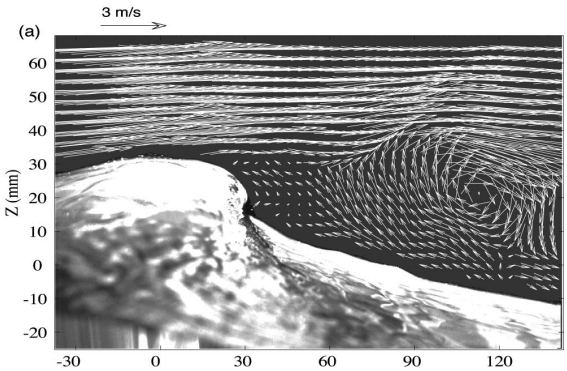

Figure I.3.8: Flow separation observed above breaking waves with PIV, from Reul et al. [1999].

For the numerical community wave-breaking events might be an even harder challenge, but very recently DNS computations start becoming available even at arbitrary geometries. Basically the cost of resolving both turbulence and free-surface dynamics grow tremendously, so there is a considerable lag between the development and application of the numerical methods employed in the recent, yet pioneer study of Yang et al. [2018]. Fully resolved turbulence and interface dynamics are coupled in Yang et al. [2018], considering a DNS method applying to both water and air domains, separated by the free-surface with dynamics tracked by a mixed level set and volume of fluid method. One will find a most relevant flow description from the discussion in Yang et al. [2018], regarding the effect of wave-breaking events over turbulence, here exemplified at figure I.3.9.

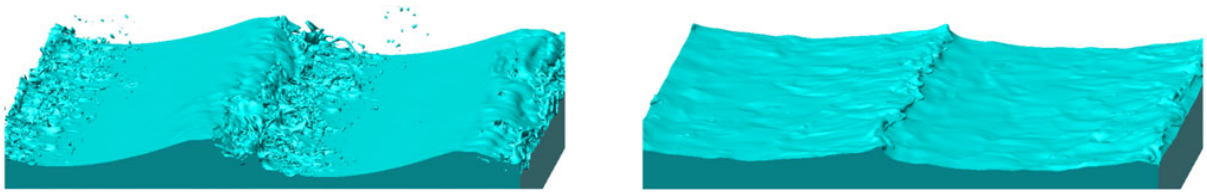

Figure I.3.9: Monochromatic breaking waves in DNS resolution. The figure depicts one (left) or three (right) wave periods after the breaking event. From Yang et al. [2018].

I.3.5 Resolving the WBL at oceanic scales

I.3.5.1 Large Eddy Simulation

To address realistic offshore conditions, Sullivan et al. [2008] and Sullivan et al. [2014] extend their DNS code into the LES formulation employed in this Thesis. The LES approach introduces limited level of modeling into the isotropic, smallest turbulent scales, theoretically resolving most of the turbulent energy and specially the anisotropic motions determined by the problem's boundary conditions: It is a methodology now responsible for modeling numerous atmospheric studies, regarding different phenomena and discretization scales (dx) ranging, e.g., from climate ($dx \sim O[\,km]$) to local wind farming ($dx \sim O[\,m]$) scales (Moeng et al. [2009], Yang et al. [2014]). Over the last two decades, LES have been widely employed evaluating the wind resource available for harvesting applications (Mehta et al. [2014]), but its use for accessing WI dynamics in the MABL is significantly more recent, and comparatively unexploited. Examining the swell effect in the wind energy source available in the MABL at moderate wind speed situations, Yang et al. [2014] note a significant increase in the fluctuations and average available power, both due to the WI motions and drag discussed in Sullivan et al. [2014] in a more phenomenological approach.

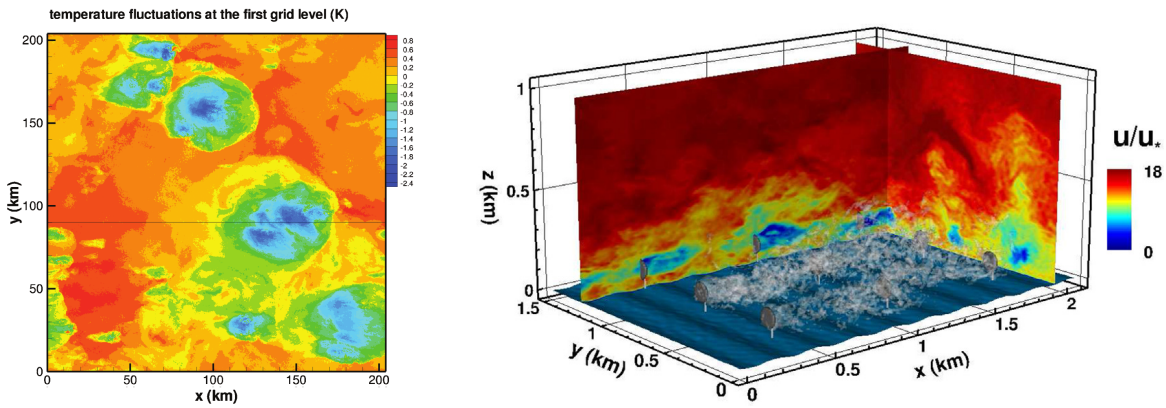

(a) (b)

Figure I.3.10: Large Eddy Simulation of the MABL at very different scales. In (a) the temperature fluctuation field at the first grid level (25 m height) of a planetary convective boundary layer, from Moeng et al. [2009]. In (b) Yang et al. [2014] an offshore wind farm, including the atmospheric LES resolution, a wave prescription, and wind turbine modelling through actuator disks, from Yang et al. [2014].

Large Eddy Simulations finally allow the reproduction of the MABL at oceanic scales, above realistic sea-states where the waves energy is also distributed into multiple scales, and where the buoyancy and turbulence effects might be resolved with limited level of modeling (c.f. Sullivan et al. [2014]). Nevertheless the LES solution is already expensive by itself if compared to URANS formulations; for considering wavy motions the situations gets significantly more complex, requiring a moving grid or remesh algorithm; and the WI flow is particularly challenging for the discretization scheme and SGS model [Hristov, 2018], built to describe small scale turbulent motions that behave substantially different from the WI flow, e.g., in terms of anisotropy, regeneration cycle and space-time correlations. Due to such

challenges, there is yet a significant amount of research required, before numerous and systematic varying studies based in LES can finally provide, accurate and consistent low order closures to the WBL reconstruction. In a feedback methodology that would ultimately feed the less costly predictive tools, still required e.g., in regional or global atmospheric forecast systems (c.f. Janssen et al. [2013] and Will et al. [2017]), and in **wind turbines design and operational wind prescription** solvers (See section I.2.2.3).

I.3.5.2 Deterministic coupling of resolved sea-state and air flow

Very recently the fully deterministic and coupled modeling of Ocean Waves and atmospheric turbulence is achievable, and available in the literature employing, e.g., the High Order Spectral (HOS, see Ducrozet et al. [2016]) method at the ocean; with a DNS or LES formulation at the atmosphere. This approach is introduced in Yang and Shen [2011] with a DNS-HOS formulation. As discussed in section I.3.4, the DNS approach is limited to laboratory scale experiments, but it is still a powerful tool for extending the phenomenological knowledge about WI and turbulent motions interactions, and particularly the DNS-HOS formulation is yet giving it some first significant outcomes. In Wang et al. [2020] for example, one encounters an original analysis leading to the spectral discretization of the turbulent kinetic energy budget.

The scale limitation may be overcome by LES-HOS formulations, as already suggested in Yang and Shen [2011] and recently presented in Cathelain [2017]: Assembling the LES developed as in Sullivan et al. [2014], with the HOS described in Ducrozet et al. [2016], coupled through the algorithm described in the appendix B.2.1. The work of Cathelain [2017] leads to the numerical tool inherited for this Thesis, and while most of the previous studies consider a 1-way coupling (Sea to Atmosphere), the fully 2-way coupled scenario is briefly addressed in Cathelain [2017], revealing some crucial aspects challenging this coupled framework that remain unresolved up to date.

In this multi-scale LES-HOS coupled scenario, wind is continuously providing energy to small scale waves, which grow rapidly in steepness. In the ocean, the waves steepness is limited by wave-breaking and white capping events triggering effective wave dissipation mechanisms, but in HOS the free-surface is a single valued function and the flow is non-rotational, so these events cannot be resolved and have to be modeled. In fact, the lack of dissipation is a well known problem with arbitrarily non-linear HOS formulations, which is extensively discussed in Ducrozet et al. [2017]. Without a dissipation mechanism, non-linear processes bring the sea-state energy down the spectrum, and the energy accumulates at small scales. Eventually non-physical wave steepness events lead to numerical instabilities, and the code crashes. To prevent those instabilities the wave-number solution space can be truncated below the physical space resolution, but the threshold is flow and non-linearity dependent. Moreover, the resolved wave steepness is a statistical quantity, that in critical events might considerably deviate from the standard deviation, becoming critical at certain instants and locations over the long periods and distances here considered: Meaning that without proper dissipation these critical events, and the HOS stability itself (the fact that it crashes or not) become a statistical quantity.

The physical inspired modeling of wave breaking and white capping dissipation in the HOS formulation is a challenge on its own, and an ongoing subject of study at the LHEEA

lab (c.f. Perignon et al. [2010], Seiffert et al. [2017] and Seiffert and Ducrozet [2018]). Employing a numerical (rather than physical) inspired low-pass filter to the HOS solution, and justifying it shall weakly affect the broad-band sea-state spectra over larger scales, Hao and Shen [2019] first exploit the LES-HOS coupling capabilities during very long (~3000 wave peak) periods, observing e.g., the importance of non-linear wave-wave interactions in the WI disturbances at the Wave Boundary Layer.

I.3.6 Observing and quantifying the WI flow above the ocean

I.3.6.1 Measurements

The measuring techniques have been rapidly evolving, and recently flow measurements are being held closer to the surface, with ever increasing accuracy and level of detail. Such measurements rely in two aspects responsible for these developments: The wind anemometer, and the structure carrying it. The sonic anemometers invented on the 70's represented a corner-stone for enabling turbulence measurements held above the ocean, specially because other state-of-the-art alternatives such as hot-wire anemometers, are on the contrary extremely delicate (c.f. Nfaoui [2012]).

Regarding the structure, multiple alternatives exist and are more appropriate to different circumstances, as extensively reviewed in Bourras et al. [2014]. Here, figure I.3.11 exemplifies three solutions: In I.3.11a ASIT, a fixed platform exploited during CBLAST in Edson et al. [2007]; in I.3.11b FLIP, a hybrid vessel and floating platform, equipped for the air-sea interaction studies of Hristov et al. [2003]; in figure I.3.11c OCARINA, a platform buoy described in Bourras et al. [2014]. Fixed platforms usually gain in reliability, and maintenance/ operational costs; as drawback they are limited to shallow waters, and the large structures often disturbs the wind as shadow effects become significant in certain wind directions. Floating platforms and vessels are extremely autonomous and versatile, as they can cruise the open oceans and operate for months uninterruptedly, though, the operational costs are enormous, and the platform may also shadow the measurements. Buoy platforms are a very interesting solution, for they can measure very low heights inside the WBL and their small structures mitigate the shadow effect, but they also rely in costly operations, and are more sensitive to long-term deterioration.

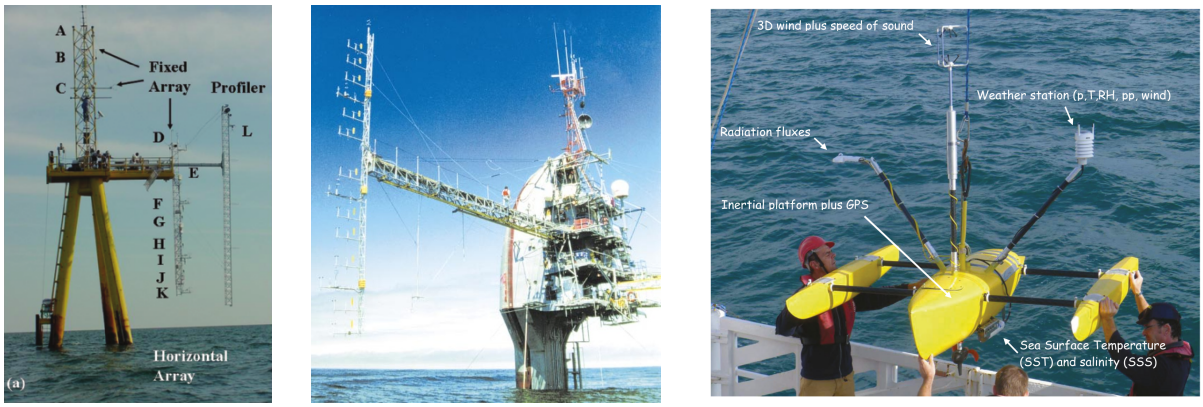

(a) (b) (c)

Figure I.3.11: Meaningful examples of air-sea interaction platforms. (a) ASIT, a fixed platform exploited during CBLAST, fig. from Edson et al. [2007]. (b) FLIP, a hybrid vessel and floating platform, fig. from Hristov et al. [2003]. (c) OCARINA, a platform buoy, fig. from Bourras et al. [2014].

I.3.6.2 SPECTRAL EVIDENCE

Regarding the direct assessment of the WI flow, a pronounced augmentation of the turbulent spectral energy distribution is often observed to occur in the waves' predominant scales. At [Snyder et al., 1981], replicated at figure I.3.12a, air-pressure sensors measure the turbulent spectra depicted in the upper part of the figure, and water-pressure sensors measure the sea state spectra at the lower part of that same figure. In more recent campaigns sonic anemometers detect the WI disturbances in the velocity fluctuations and its derived quantities, as [Tamura et al., 2018] shows replicated in figure I.3.12b, that at strong wave ages the horizontal and vertical velocities (above and below the figure, respectively) fluctuations spectra present a clear peak disturbance at the peak frequency f_p. Nevertheless, the number of failed attempts to detect WI disturbances in frequency-domain turbulent spectra is quite disturbing, as portrayed in Hristov [2018].

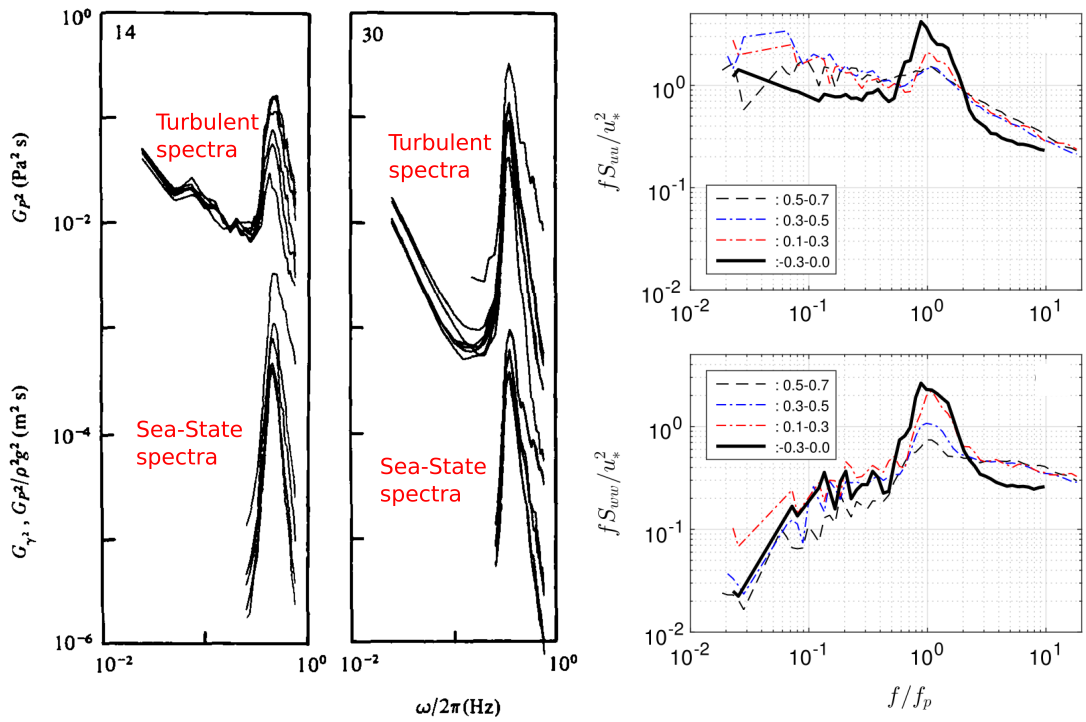

(a) (b)

Figure I.3.12: The Wave Induced signature observed in different frequency dependent turbulent spectra inside the WBL. (a) Air-pressure fluctuations and sea-state spectra, at two different periods taken from Snyder et al. [1981], and with added legends in red. (b) Longitudinal and vertical velocity fluctuation spectra, with the frequency space normalized by the wave peak frequency f_p, from [Tamura et al., 2018].

Alternatively, the turbulent sources can be distinguishable in the space-time domain looking for their characteristic velocities in the two-dimensional (2D) turbulent spectra $E(k, w)$: Turbulent motions are generally convected by mean local velocities U and shall somehow follow the Taylor's hypothesis $w = k\,U$ [Taylor, 1938, Wilczek and Narita, 2012]; while ocean waves with phase velocity $c = w/k$ follow their characteristic dispersion equation $w^2 = k\,g\,\tanh(k\,d)$, with g the gravity and d the depth in a linear wave theory framework. Unfor-

tunately the study of $k-w$ turbulent spectra (2D) has not been addressed in the literature as extensively as the wave-number or frequency 1D spectra, but the $k-w$ characterization of WI motions in the atmosphere has been previously noted within a numerical framework in Hao and Shen [2019], as exemplified in figure I.3.13.

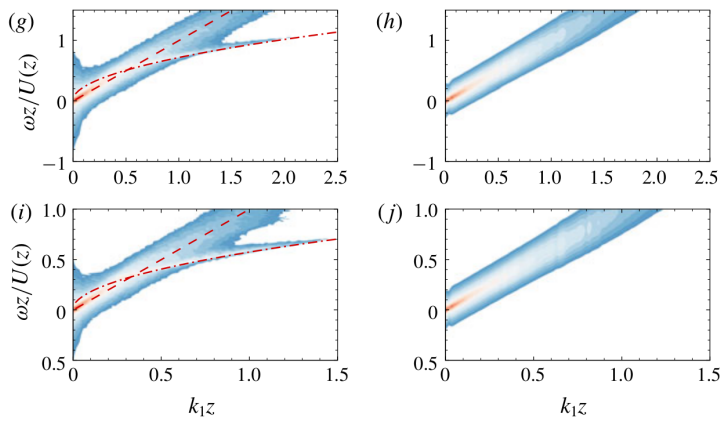

Figure I.3.13: The Wave Induced signature observed in the wave-number-angular-frequency dependent, stream-wise velocity turbulent spectra, within a LES resolved WBL. In the left (g and i) the resolved spectra is shown in the contours; the red dashed line stands for the mean wind velocity, and the red dash-dotted line for the dispersion relation. In the right (h,j), the spectra predicted by the random sweeping model of Wilczek and Narita [2012]. From Hao and Shen [2019].

I.3.6.3 A MECHANISTIC APPROACH

The recent developments in measuring techniques open the path to what Hristov and Ruiz-Plancarte [2014] describe as the mechanistic approach for obtaining wind-wave interaction observational insight: It consists in the direct estimation of WI velocities and pressure in the atmosphere, rather than the inference of WI disturbances in vertical wind profiles, total momentum fluxes, or TKE budget, and that path is widely pursued through this thesis.

One shall often encounter an ambiguity between Wave Induced and Wave Coherent flows in the literature. Because present thesis shall attempt a specific definition of the Wave Induced flow in section IV.1, it is important to note that instead of directly defining the WI field from given measurements, past studies rather consider the definition of a Wave Coherent flow, i.e., wind fluctuations occurring at the waves' scales, soon to be defined more precisely by the end of this section.

If the Wave Coherent flow approximates the Wave Induced flow, then a transfer function exists linking the sea-state and WC velocities spectra in the atmosphere. That is the transfer function exploited in Hristov et al. [2003] at 8.7 m above the surface, within Wave Age ranging in $16 < c/u^* < 40$, and here replicated at figure I.3.14: Showing the magnitudes (a, c) and phases (b, d) of the transfer function, for horizontal (a, b) and vertical (c, d) velocities. At the figure, one observes a high quality agreement between the prediction from the Critical layer theory of Miles [1957], given by the solution of the Rayleigh equations and depicted in full lines, and the measured wave coherent flow presented in Hristov et al. [2003], and shown in the squared markers.

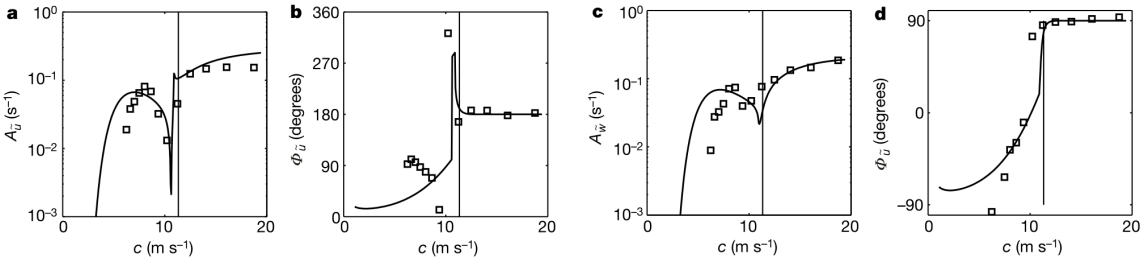

Figure I.3.14: Transfer Function (TF) between the sea-state and atmospheric Wave Coherent spectra of stream-wise (a, b) and vertical (c, d) velocities. Magnitude of the TF in (a, c); phase in (b, d). Those are frequency dependent spectra, shown as function of the wave velocity c. The vertical line is the mean wind velocity at the measurement height 8.7 m. The squared refer to experimental obsrrvations, and the full line to Mile's critical layer theory prediction. From Hristov et al. [2003].

Showing the phase of the Wave Coherent vertical velocity, as in figure I.3.15a, Hristov et al. [2003] show unmistakable evidence of Mile's critical layer mechanism, with a sharp phase shift occurring precisely at the critical layer height. Another approach to quantify the Wave Induced flow is to consider the cross-spectra of wind velocity and sea-state motions, as exploited in Grare et al. [2013a] (with FLIP), that leads in figure I.3.15b (vertical wind velocity) to the same kind of phase-shift occurring at the critical height, again attesting the validity of Mile's critical layer mechanism. In Grare et al. [2013a], one also observes a very pertinent and detailed description of WI motions and stresses. Notably, Grare et al. [2013a] observes that at 10 m height, fast waves ($c/u^* > 40$) induce an upward momentum flux that can represent about 20% of the turbulent, downward momentum flux. For intermediate Wave Ages ($20 < c/u^* < 40$), they observe that more than 90% of the momentum flux is supported by waves smaller than ~15 m. As an evidence contradicting Mile's theory, they observe Wave Coherent momentum transfer occurring above the critical layer height.

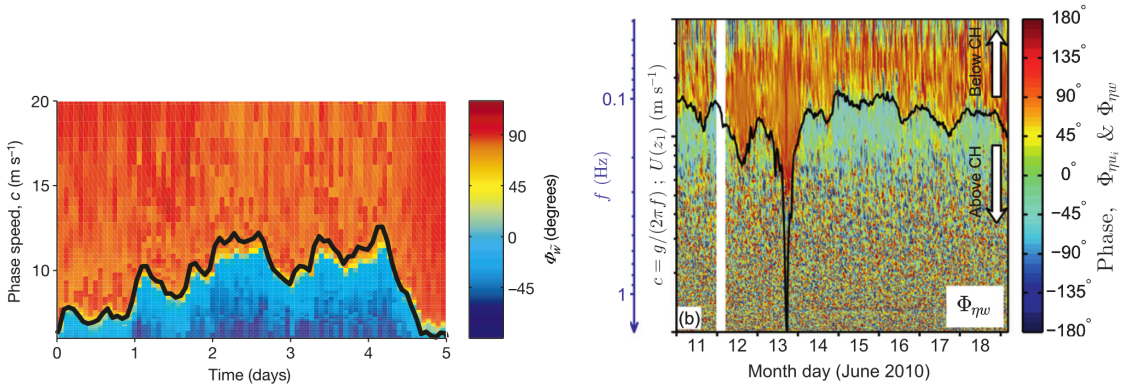

(a) (b)

Figure I.3.15: Evidence of Mile's critical layer mechanism. In both figures, the black line indicates the critical layer height, where a wave component travels with the same velocity as the mean wind, and across that line an intense phase shift takes place as predicted in Mile's theory. (a) Phase of the vertical velocity fluctuation spectra, from Hristov et al. [2003]. (b) Phase between the vertical velocity fluctuation spectra and the sea-state free-surface elevation spectra, from Grare et al. [2013a].

As first introduced in Hristov et al. [1998], the quantification of the WI response relies in the triple decomposition of a measured wind field, usually measured in time as the signal $\chi(t)$. The approach adopted so far, e.g. in Hristov and Ruiz-Plancarte [2014], and Cifuentes-Lorenzen et al. [2018], assumes uncorrelated *Atmospheric turbulence* (Atm.) and *Wave Coherent* (WC) motions, but more generally a triple decomposition applies so that $\chi = \overline{\chi} + \hat{\chi} + \tilde{\chi}$, being $\hat{\chi}$ and $\tilde{\chi}$ the Atm. and *Wave Related* fields. Imposing a filter to retain the WC flow ($\chi = \overline{\chi} + \tilde{\chi}^{C} + \hat{\chi}^{C}$), Hristov and Ruiz-Plancarte [2014] present the dynamic equations for the decomposed and uncorrelated fields, uncoupled between Wave Coherent ($\tilde{\chi}^{C}$) and turbulence ($\hat{\chi}^{C}$) balance equations.

The WC filter is so defined by projecting χ into the vector space of all wave coherent signals, i.e., those occurring at the same frequencies as the wave profile $\eta(t)$. Like-wise, the present study employs the WC filter (Eq. I.3.1) in space, so counting in the Hilbert transform discretizing η in the spectral domain, let $\overset{\circ}{\eta}_k(x)$ ($\overset{\circ}{\eta}_w(t)$) be the in-quadrature counterpart of the kth (w^{th}) wave number (angular frequency), one-dimensional free surface elevation $\eta_k(x)$ ($\eta_k(t)$), then:

$$\tilde{\chi}_k^{C}(x) = \frac{\overline{\chi(x)\eta_k(x)}^{[x]}}{||\eta_k||^2_{[x]}}\eta_k(x) + \frac{\overline{\chi(x)\overset{\circ}{\eta}_k(x)}^{[x]}}{||\overset{\circ}{\eta}_k||^2_{[x]}}\overset{\circ}{\eta}_k(x)$$

$$\tilde{\chi}^{C}(x) = \sum_k \tilde{\chi}_k^{C}(x), \qquad \text{and} \qquad \hat{\chi}^{C}(x) = \chi(x) - \tilde{\chi}^{C}(x). \tag{I.3.1}$$

The filter defined in equation I.3.1 effectively filters flow features occurring with length scale $2\pi/k$, where $\overline{\cdot}^{[x]}$ and $||\cdot||_{[x]}$ indicate, respectively, the average and norm in x direction. Such filter inherits the properties: $\tilde{\tilde{\chi}} = \tilde{\chi}$; $\tilde{\hat{\chi}} = 0$; and notably the absence of averaged correlation $\overline{\tilde{\chi}\hat{\chi}} = 0$. With these properties, the Reynolds decomposition of the Navier Stokes equations (Section I.1.1.3 and equation I.1.7) reveal the role of WC momentum fluxes $\boldsymbol{\tau}^{(W)}$:

$$\frac{\partial \overline{u_i}}{\partial t} + \frac{\partial(\overline{u}_j\overline{u}_i)}{\partial x_j} = -\frac{1}{\rho}\frac{\partial \overline{p}}{\partial x_i} + \frac{\partial}{\partial x_j}\left[\tau_{ij}^{(v)} - \tau_{ij}^{(r)} - \tau_{ij}^{(W)}\right] - \overline{\rho} g \delta_{i3}, \qquad \text{where}$$

$$\tau_{ij}^{(v)} = 2\nu\overline{S}_{ij}, \qquad \tau_{ij}^{(r)} = \overline{\hat{u}_i\hat{u}_j}, \qquad \text{and} \qquad \tau_{ij}^{(W)} = \overline{\tilde{u}_i\tilde{u}_j}. \tag{I.3.2}$$

Also thanks to $\overline{\tilde{\chi}\hat{\chi}} = 0$, the continuity equation I.1.1, the Reynolds Stress Tensor equations (omitted, but see Pope [2000], pg. 315), and the turbulent kinetic energy equations I.1.9, all apply separately to turbulent and Wave Coherent fields. For example, considering the turbulent part previously described by equation I.1.9, the Wave Coherent TKE balance equations are similarly:

$$\frac{\partial \tilde{e}}{\partial t} + \overline{\tilde{u}_j}\frac{\partial \tilde{e}}{\partial x_j} = -\frac{\partial}{\partial x_j}\tilde{T}^{(r)} + \tilde{P} - \tilde{\epsilon} - g\overline{\tilde{\rho}\tilde{u}_3}, \tag{I.3.3}$$

where the WC TKE ($\tilde{e}$) production $\tilde{P}$, the pseudo-dissipation $\tilde{\epsilon}$ and fluxes $\tilde{T}^{(r)}$ are given by:

$$\begin{aligned} \tilde{P} &= -\tau_{ij}^{(W)}\frac{\partial \overline{u_i}}{\partial x_j} = -\tau_{ij}^{(W)}\overline{S}_{ij}, \qquad & \tilde{\epsilon} &= \nu\overline{\frac{\partial \tilde{u}_i}{\partial x_j}\frac{\partial \tilde{u}_i}{\partial x_j}}, \\ \tilde{T}^{(r)} &= \frac{\overline{\tilde{u}_i\tilde{u}_j\tilde{u}_j}}{2} + \frac{\overline{\tilde{p}\tilde{u}_i}}{\rho} + \tilde{T}^{(\nu)}, \qquad \& \qquad & \tilde{T}^{(\nu)} &= -2\,\nu\frac{\partial \tilde{e}}{\partial x_j}. \end{aligned} \tag{I.3.4}$$

To arrive to the governing equations presented in Hristov and Ruiz-Plancarte [2014], one adopts the usual Boundary Layer assumptions described in the appendix A.1.2; considers that $\tilde{\rho}(\tilde{\theta})$ and $\tilde{u}_3$ are always in quadrature so the WC TKE and fluxes do not couple with temperature; that viscous dissipation is negligible in the Wave Coherent flow; and neglects third-order effects. Then with the sole assumption of infinitesimally small wave amplitudes in the sea (Linear theory), Hristov and Ruiz-Plancarte [2014] present a quasi-linear theory for the Wave Coherent flow that results in the Taylor-Goldstein equation: An advance to Miles [1957] theory (Rayleigh equation) that considers an additional buoyancy term acting on the velocity mean profiles, so highlighting the fact that Miles' theoretical framework is not conceptually limited to a logarithmic wind profile.

I.3.6.5 Surface following coordinates

A conceptually similar alternative to the WC filter relies in the phase average of a given signal to perform the decomposition, which is extensively described in Yousefi and Veron [2020], notably presenting the very detailed development of the Boundary Layer equations at orthogonal and curvilinear coordinates.

The wavy bottom surface invariably requires the problem to be formulated in surface following coordinates, and that leads to the pressure acting as a momentum flux mechanism in the NS equations [Yousefi and Veron, 2020]. Any coordinate system so defined shall match the free-surface elevation at the bottom [Ayet, 2020], where $h = \eta(x, y, t)$ and one observes the contribution of the form drag (or thrust) $\tau_{ij}^{(P0)}$, with the friction velocity definition:

$$\begin{aligned} u^{*2} &= \left[\tau_{ij}^{(\nu)} - \tau_{ij}^{(r)} - \tau_{ij}^{(W)} + \tau_{ij}^{(P0)}\right], \qquad \text{with} \\ \tau_{ij}^{(P0)} &= \frac{1}{\rho}\overline{p\frac{\partial \eta}{\partial x_i}}. \end{aligned} \tag{I.3.5}$$

Part II

FIELD MEASUREMENTS IN THE WAVE BOUNDARY LAYER

High seas (1874), of Ivan Aivazovsky. From www.wikiart.org.

A scanning LiDAR (sLiDAR) is deployed to observe Wave Induced (WI) disturbances propagating into the lower part of the Marine Atmospheric Boundary Layer (MABL), or more precisely into the Wave Boundary Layer (WBL) where they are significant. Based in original measurements performed above the ocean, this work contributes to the description of a primary mechanism taking place in the WBL: The propagation of Free-Surface dynamics into the atmosphere, the so-called Wave Induced flow.

Driven by the recent growth in wind energy exploitation, sLiDAR technologies and post-processing techniques have been experiencing a rapid growth in the last 20 years. In [Peña and Mann, 2019] (Dual sLiDAR configuration) one finds the reference to a wide range of applications, including weather and climate monitoring and forecast, fundamental studies in the ABL and turbulent flows, and multiple studies concerning the wind energy industry. As the industry moves to the offshore environment, one shall also encounter multiple LiDAR applications being performed offshore (c.f. Désert et al. [2021] for a floating LiDAR configuration).

One of the reasons for the sLiDAR success at so many different fields, is the capability of largely adapting its scanning movements to attain specifics objectives with a given configuration. It is unknown to the author, other sLiDAR measurements aiming to characterize the WI flow inside the WBL. To attain that goal, the sLiDAR here operates as described along section II.1: Fixed on the shore, facing the ocean at the location described in section II.1.1, employed according to the Calibration and Setup discussed in section II.1.2, presented with a reminder of some crucial challenges concerning the sLiDAR operating at these conditions. Wind and ocean monitoring strategies are presented at section II.1.3, also introducing the experimental cases to be exploited in the results sections.

General post-processing techniques are exposed along section II.2. Section II.2.1 present the techniques employed to evaluate data quality, treating bad quality data when necessary. The most significant results and discussions are based in the spectral analyses reviewed and described at section II.2.2. The wind steadiness and homogeneity are evaluated at section II.2.3.

Results of the Radial Wind Speed (RWS) captured by the staring mode operating sLiDAR follow at sections II.3. Through the observations here described, the WI motions are revealed by different analyses based on the RWS, i.e.: Space-Time maps of the RWS in section II.3.1; one dimension (1D), wave-number (k) and frequency (f) dependent spectra in section II.3.2; two dimensions (2D), wave-number-angular-frequency ($k-w$) dependent spectra in section II.3.3. Cases with vanishing wave signature are presented for comparison in section II.3.4.

II.1 Experimental conditions

II.1.1 Test site

From October 2020 to January 2021, the scanning LiDAR (sLiDAR), Leosphere WindCube® Scan 100S pictured at figure II.1.1, from the research laboratory in Hydrodynamics, Energetics and Atmospheric Environment (LHEEA) has been deployed in the peninsula of Le Croisic (France, see fig. II.1.2a), mostly a sub-urban area constituted of low-rised buildings and parks with a south-western rocky coastline, aligned with an 110°-290° axis for nearly 10 km (fig. II.1.2b). The prevailing wind directions at Le Croisic are South-West and North-East as shown in Fig. II.1.2a. The sLiDAR was installed on the balcony of a seafront villa, 100 m away from the coastline at a height of 18.33 m above the mean sea level (MSL) with a clear view to the North Atlantic ocean from 135° to 260°. Directly to the North-East of the sLiDAR's position (47°17'8.6"N, -2°31'1.5"E), the Penn-Avel park is a densely forested area with tall vegetation (10 m). The local ground is around 8 m above the MSL with a mean slope of 8% down to the water in the South-West direction. The installation was chosen to explore the micro-scale wind/wave interaction close to the water surface using horizontal scans.

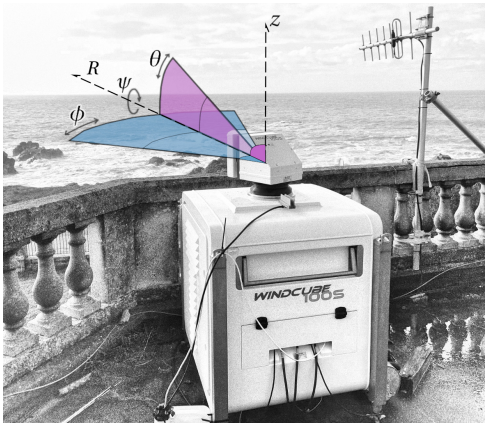

Figure II.1.1: The sLiDAR on the balcony of a seafront villa at Le Croisic. Definition of: Radial (R) and vertical (z) axes; roll (ψ), pitch (elevation angle θ), and yaw (azimuth angle ϕ) angular movements.

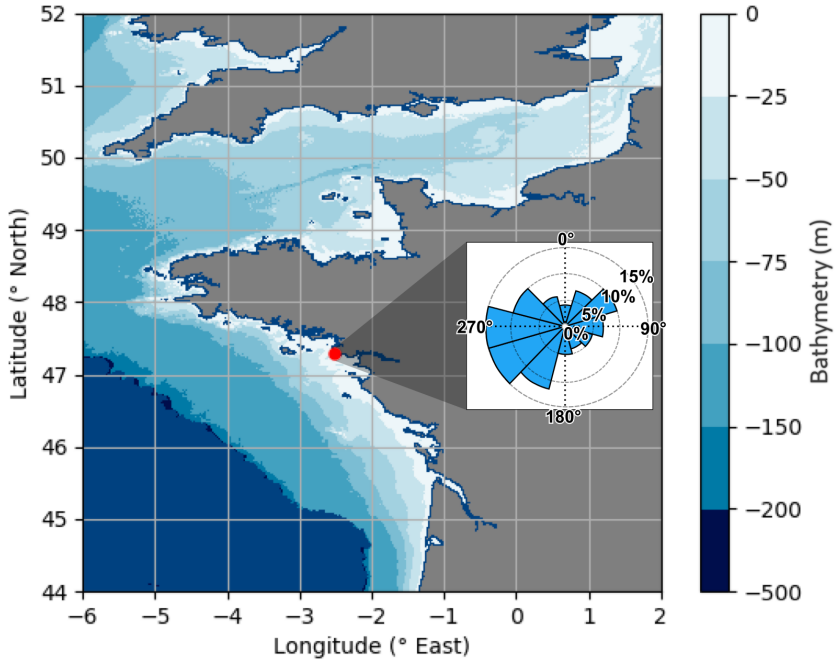

(a) Location of Le Croisic on the French west Atlantic coast.

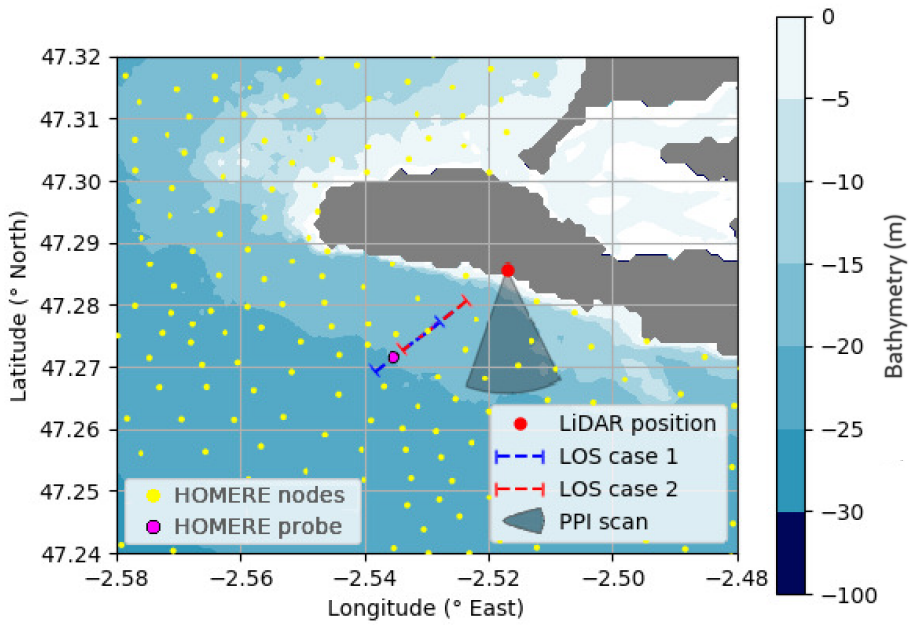

(b) View of Le Croisic peninsula (France).

Figure II.1.2: sLiDAR position denoted by a red dot and water depth displayed by the colormap. **(a) Location of Le Croisic on the French west Atlantic coast**. The wind rose for Le Croisic has been exported from the Global Wind Atlas (GWA 3.0, https://globalwindatlas.info), comprehending the period 2008-2017. **(b) View of Le Croisic peninsula (France)**, with the PPI scans for wind direction determination in the black sector, and staring mode measurements lines (f-LOS) for Case01 (blue) and Case02 (red) in dashed lines. Oceanic conditions are estimated from the HOMERE hind-cast database: The grid is depicted by its nodes in yellow dots; and the probing occurs in the node depicted in magenta.

II.1.2 sLiDAR TECHNOLOGY AND EXPERIMENTAL SETUP

II.1.2.1 TECHNOLOGICAL CHALLENGES

Current experimental setup introduces two challenges particularly important to the upcoming analysis, i.e., mitigating the bias induced by the misalignment between Wind Direction (WD) and the sLiDAR's Line-Of-Sight (LOS), and evaluating the laser volume filtering effect [Peña and Mann, 2019]. Due to misalignment, the turbulent spectrum measured along the LOS is contaminated with different components of the spectral tensor, that latest holding the full directional information of the Energy Density Function (EDF). Thus the effort of selecting sLiDAR-aligned wind conditions through this study, approaching the observations to longitudinal correlations/ spectra.

The filtering effect is observed through the mitigation of turbulent motions at small scales and is generally flow/ turbulence dependent. The light ray pulses for a few nano seconds, but in light speed that translates into a few meters, leading to the space filtering of measured velocity fluctuations. Depending on the flow, the space filtered fluctuations induce a time filter according to the characteristic velocities (U and c) advecting the turbulent structures. sLiDAR measurements are often compared to measurements performed with other instruments, such as a sonic anemometer to evaluate or correct [Bastine et al., 2015] its BIAS. Current setup does not dispose of such an instrumentation, and to the authors' knowledge no other physical experiment has been performed to assess space-time velocity correlations in similar scales above the ocean. So a $k-w$ (2D) dependent BIAS is expected in the turbulent spectra (EDF), but its implications to the joint space-time correlation functions are yet unknown to the literature. Such BIAS is further discussed during the results section, and numerically evaluated later at sections IV.3.3 and IV.3.4.

II.1.2.2 CALIBRATION

The azimuth calibration of the sLiDAR was performed using the classical hard target procedure [Shimada et al., 2020], leading to an uncertainty smaller than 0.5°. Pitch (θ) and Roll (ψ) angles (see figure II.1.1 for definitions) were adjusted to a value below 0.1° using the sLiDAR internal inclinometers. For an azimuth of 221.77° with zero elevation, configuration used in this paper, this misalignment leads to an angle of elevation offset of 0.065° pointing down to the water surface, corresponding to an altitude offset of -1.1 m per kilometer distance between the measurement and the sLiDAR's height.

II.1.2.3 SETUP

In order to assess the time and space spectral content of the turbulent atmosphere above the sea, the sLiDAR was set-up in staring mode with an elevation angle $\theta = 0°$ to measure the radial wind speed (RWS, u_R) along a horizontal fixed line of sight (f-LOS) above the water surface. The RWS is negative when the wind blows towards the sLidar in the f-LOS. During the measurement campaign, the acquisition frequency was ranging from 1 Hz to 4 Hz and the acquisition time set to 600 s for each f-LOS scan. Gates were defined at each 10 m along

a 1 km LOS, starting at least 0.5 km away from the position of the sLiDAR. Considering that the gate length was set to the smallest available on this device, L_γ = 25 m, that gives a 60% of gate overlapping. The comparison between time and space data being easier to interpret when the wind speed is aligned to the f-LOS, an azimuth angle ϕ_L = 221,77° was chosen in agreement with the prevailing wind sectors at Le Croisic (See figure II.1.2a) and with the prevailing wave direction.

To monitor the wind direction close to the area of measurement, horizontal plane position indicator (PPI) scans with 45° opening (Fig. II.1.2b) were programmed between the 10 min f-LOS scans. During 96 s (between the f-LOS scans), multiple PPI scans (6 different elevation angles θ) are registered, and the one here exploited corresponds to a 16 s long PPI Scan where θ = 0°. The RWSs measured from the PPI scan were processed along the gates following the velocity volume processing method described by Shimada et al. [2020] to obtain gate-wise horizontal Wind Speed (WS) and Wind Direction (WD). This method uses a cosinus fitting function and assumes that the wind field is homogeneous in time and space during each PPI scan, which seems particularly appropriate in offshore conditions as Shimada et al. [2020] reported an accuracy of the order of 1% for the mean wind speed and 1° for the wind direction during gate-wise 10 min averages. Current study instead, employs a 16 s (1 PPI scan) time average combined with a 1.2 km (51 gates) space average to obtain the results shown in section II.1.3.

Details on the configuration used for each scan is given in Table II.1.1 and the locations of the scans are reported in Fig. II.1.2b.

Table II.1.1: Description of scans for case 01 (f-LOS 01), case 02 (f-LOS 02) and mean horizontal Wind Speed/ Direction determination (PPI).

Scan	θ (°)	ϕ_L (°)	**Rot. speed** (°/s)	L_γ (m)	**Gate spacing** (m)	**First Gate** (km)	**Last Gate** (km)	**Acc. time** (s)	**Duration** (s)
f-LOS 01	0	221.77	0	25	10	1.00	2.00	1.00	600
f-LOS 02	0	221.77	0	25	10	0.75	1.75	0.25	600
PPI	0	[154 - 199]	3	25	25	0.50	1.7	1.00	16

II.1.3 Environmental description and test-case selection

It is here presented the monitoring of meteocean conditions performed during the experimental campaign. Atmospheric quantities are measured in the field, while Oceanic data are extracted from well established numerical hind-cast databases described further in the text. Two dates (10:12-Nov and 04:05-Nov) are exposed from which four cases (01, 02.[a-c]) are selected for further evaluation. The dates exposed indicate, through high peak period values, the presence of a swell, i.e., long energetic wave trains generated far in the ocean and usually characterizing old-seas conditions. The important difference to notice between these dates is the wind direction, which comes from the Ocean on 10:12-Nov (Case 01), and from the land on 04:05-Nov (Cases 02.[a-c]).

II.1.3.1 METEOCEAN CONDITIONS

The wind direction and the horizontal wind speed were monitored using the sLiDAR PPI scans described in section II.1.2.3. The turbulence intensity is averaged between the f-LOS scans and computed as

$$TI = \sqrt{\left\langle \frac{\overline{u'_R u'_R}}{\overline{u_R}^2} \right\rangle}, \tag{II.1.1}$$

where $u'_R = u_R - \overline{u}_R$ is the RWS fluctuation, with $\bar{\cdot}$ the space-time average operator, and $\langle\cdot\rangle$ the ensemble average (Between 10 min scans) operator. The total average RWS is so $U_R = < \overline{u}_R >$.

The atmospheric thermal stability was estimated on a three hours basis using the Richardson number introduced in equation I.1.31, here stated as:

$$Ri = \frac{\beta_\theta g \Delta T z}{U_R^2} \tag{II.1.2}$$

where $\beta_\theta = 3.4 \cdot 10^{-3}$ (1/°C) is the coefficient of thermal expansion, $z = 18.33\ m$ is the measurement height, and $\Delta T = T_{air} - SST$ is the air-sea temperature difference. The air temperature T_{air} is recorded by a PTH probe at the balcony near the sLiDAR, and the sea surface temperature (SST) comes from the MARC's database using the MARS3D model [Lazure and Dumas, 2008].

The global sea-state parameters, i.e., the significant height H_s, wave length L_p, peak period T_p, mean wave direction α_w, and wave directional spread β_w, are extracted hourly at the closest node to the sLiDAR LOS final gate, from the HOMERE hind-cast database [Accensi et al., 2017]: a WAVEWATCH III (WWIII) model using the NORGAS-UG grid ([Ardhuin, 2012], and scatter in figure II.1.2b). The water depths are also registered from HOMERE, excluding tidal variations: $d \sim 22m$ closest to the f-LOS last gate, and $d \sim 14m$ closest to the f-LOS first gate. It is so assumed that $d = 22 \pm 8$, as further discussed in section II.3.3.

At the site, the dominant semi-diurnal tide may induce significant variation of the water level, modifying the depth and the relative height between the water surface and the sLiDAR measurement. Though, tidal variations of water surface elevation occur in such large time-space scales that its effect shall not interfere with our spectral analyses, and the highest water level variation here observed is approximately ±2 m, on the order of our uncertainties for the water depth.

The wave age is here defined as $\mathrm{WA}_c = -c_p / < \overline{u}_R >$, a function of the estimated peak wave velocity $c_p = L_p / T_p$ and the measured RWS. Note that according to present convention $\overline{u}_R$ is negative when the wind comes from the ocean, and so, when the wind and wave directions are aligned $\mathrm{WA}_c > 0$. A negative WA_c value highlights the intrinsic difference of wave-opposed wind situations where $\overline{u}_R > 0$.

The monitoring of the most important meteocean variables for each date is presented in figure II.1.3.

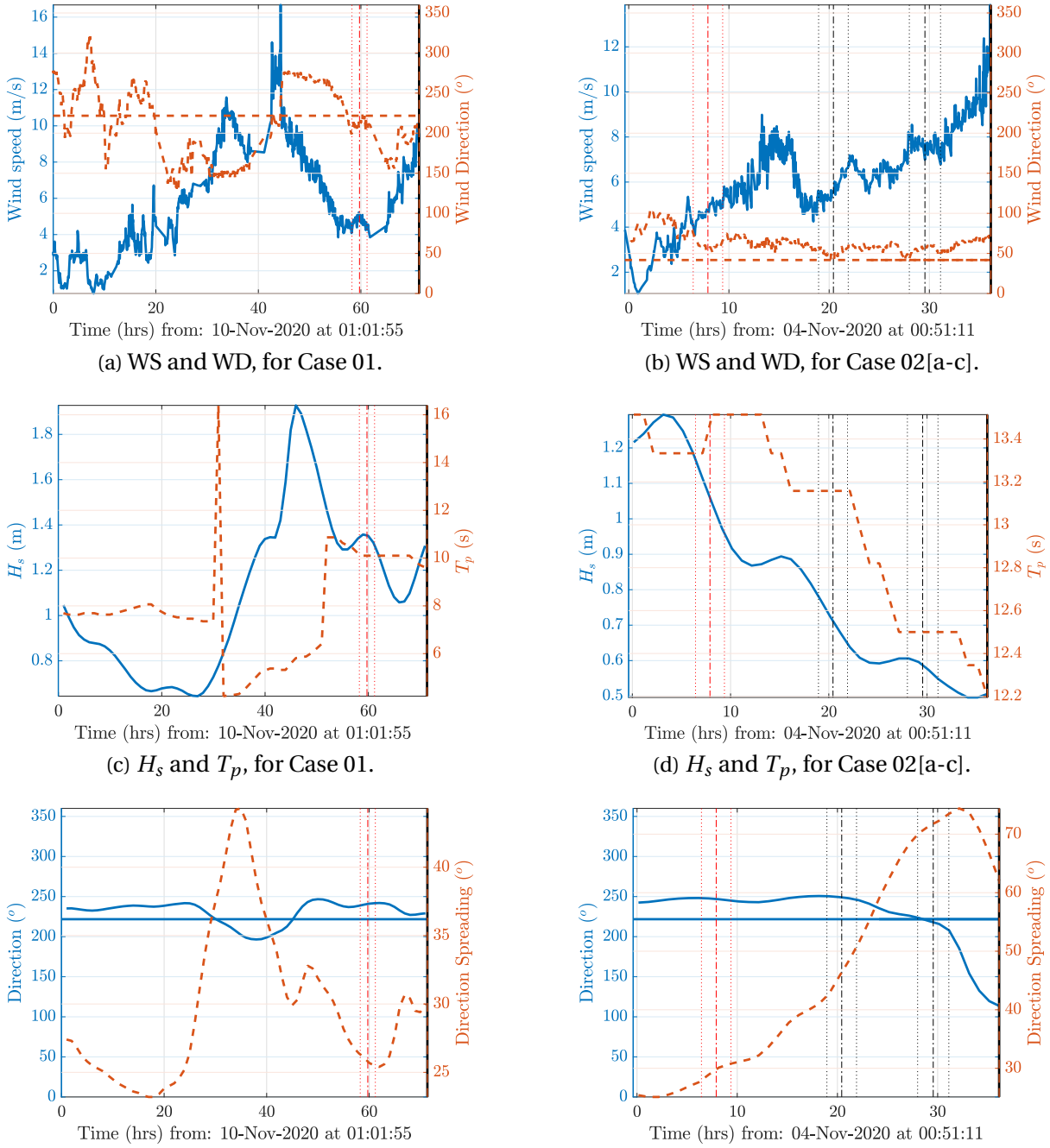

(a) WS and WD, for Case 01.

(b) WS and WD, for Case 02[a-c].

(c) H_s and T_p, for Case 01.

(d) H_s and T_p, for Case 02[a-c].

(e) α_w and β_w, for Case 01.

(f) α_w and β_w, for Case 02[a-c].

Figure II.1.3: Evolution of wind and sea-state quantities around Cases 01 and 02[a-c], in sub-figures (a,c,e) and (b,d,f), respectively. (a,b) PPI obtained horizontal Wind Speed (WS) and Wind Direction (WD). (b-f) Wave model (WWIII) hind-cast: In (c,d) the significant wave height (H_s) and peak period (T_p); in (e,f) the wave peak direction (α_w) and directional spreading (β_w). Horizontal lines in (a,b,e,f) for the sLiDAR fLOS-aligned direction $\phi_L - 180°$. Vertical lines for the initial, middle and final moments of the selected periods.

II.1.3.2 TEST CASES DESCRIPTION

In figure II.1.3, the 3-hour periods selected for further exploitation stand between vertical (Red for Case 01 and 02.a; Black for Cases 02.[b-c]) dashed lines, and the dot-dashed lines correspond to the middle time.

The Case selection seeks the best alignment of the f-LOS direction ([221.77°,41.77°]) with the mean wind and wave directions: Case 01 is one of the few possibilities in 10-12-November, but a wide range of possibilities emerges from a mostly constant WD registered in 04-05-November, leading to Cases 02.[a-c]. Case 01 and 02.a are characterized by similar Wave Age magnitude $|\mathrm{WA}_c|$, which drops significantly in Cases 02.b and 02.c through a diminishing swell and increasing WS scenario.

Main wind and sea-state statistics of the cases are summarized in tables II.1.2 and II.1.3. In average, the misalignment of the wind direction to the sLiDAR LOS is nearly 10° for Case 01 and 18° for Case 02.a, leading to a RWS by WS ratio of 99% and 95%, respectively.

Table II.1.2: Summary of the wind parameters.

Case ID	**Day**	**Start time** (UTC)	U_R (m/s)	WD (°)	**TI** (%)	ΔT (°C)	Ri_b, which sign gives (Stability)
01	12/11/2020	11:10:32	4.12	212	8.6	1.4	0.038 (Stable)
02.a	4 /11/2020	07:10:24	4.29	60	10.0	-6.2	-0.170 (Unstable)
02.b	4 /11/2020	19:41:19	5.31	51	13.7	-4.6	-0.086 (Unstable)
02.c	5 /11/2020	04:44:30	6.93	56	12.1	-7.2	-0.075 (Unstable)

Table II.1.3: Summary of the sea-state parameters.

Case ID	WA_c	H_s (m)	T_p (m)	L_p (m)	α_w (°)	β_w (°)
01	3.05	1.34	10.10	126.9	241	25.8
02.a	-3.14	1.04	13.45	181.4	247	29.9
02.b	-2.53	0.73	13.16	176.8	249	45.6
02.c	-1.92	0.59	12.50	166.2	219	71.3

Cases 01 and 02[a-c] are intrinsically different because of the 180° shift in wind direction, and the different stability regimes. Case 01 considers wave-following wind scenario, with virtually infinite fetch from the open ocean, where a near-equilibrium behavior is expected in the wind-wave interaction. In contrast, Case 02[a-c] considers a wave-opposing wind scenario with the wind coming from the land, and only ~1 km of ocean fetch. Impacted by in-land non-homogeneity and unstable stability regimes, Case 02(a-c) are therefore characterized by stronger turbulence intensities. Case 01 and Case 02a have comparable WA_c, but Case 01 presents higher (129% ratio) significant height H_s, with lower (75% ratio) peak period T_p, meaning that the sea-state energy flux (or power, in deep waters proportional to

$\sim H_s^2\ T_p$) is expected to be approximately 25% higher in Case 01 when compared to Case 02.a.

II.1.3.3 SEA-STATE SPECTRAL DISTRIBUTION

The sea-state statistical description is complemented by the spectral energy density function of free-surface displacements: $F(\phi, f)$ function of the direction ϕ and frequency f, and solution of the WWIII model equations. The sea-state full spectral content is registered in HOMERE only at a few points of the NORGAS-UG, the closest one located approximately 9 km south and 2 km east (At 47°12'N,-2°30'E) of the sLiDAR, for which $F(\phi, f)$ is shown in figure II.1.4. The figure shows $F(\phi, f)$ together with the frequency-dependent mean direction $\phi_0(f)$ traced in full line, and the wave peak direction (ϕ_p = 241° or 247°) traced in dashed line. $\phi_0(f)$ is obtained from the integration of $F(\phi, f)$ 1st momentum in ϕ, and ϕ_p is available at a grid point closer to the sLiDAR according to table II.1.3.

The difference between the directions is consistent with the expected effect of wave refraction, occurring for a sea state propagating over a variable bathymetry (See figure II.1.2b), as the sea-state evolves considerably between the $F(\phi, f)$ (Or ϕ_0) and ϕ_p probes. It is important to note that, as for turbulence, the sea-state description is statistically distributed in various scales and the sea-state spectrum is generally a combination of different swell and wind-generated wave systems, the swell and wind prevailing in low and high frequencies respectively, clearly distinguishable from one another in the wind-wave opposite direction Case 02.a.

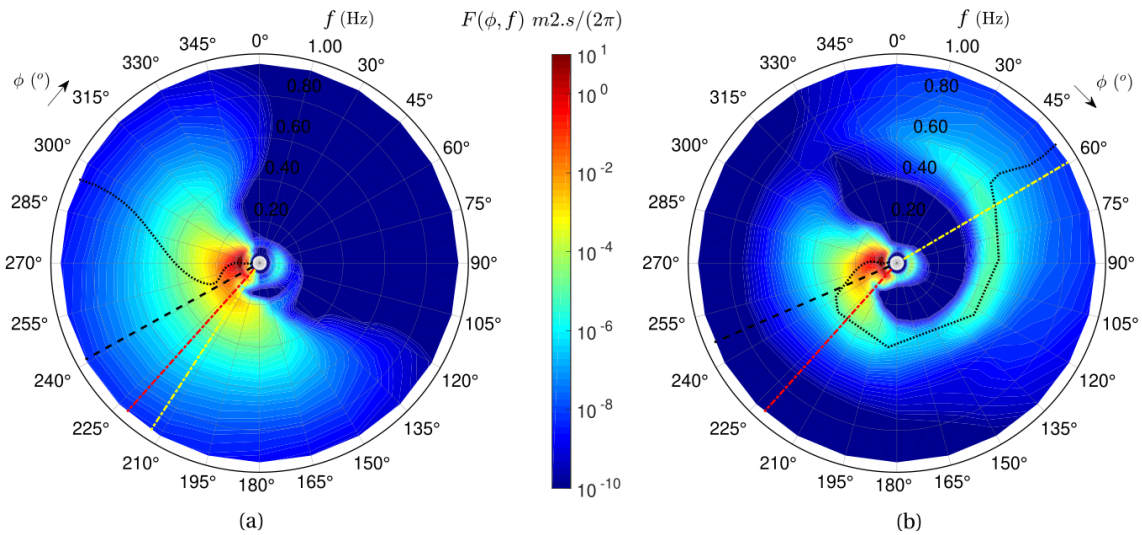

Figure II.1.4: Free-surface variance energy density function $F(\phi, f)$ (log scale) for Case 01 (a) and Case 02a (b). The frequency dependent mean direction $\phi_0(f)$ and the peak wave direction registered closer to the sLiDAR are depicted as a black dotted line and dashed line, respectively. The mean WD and the sLidar fLOS are depicted in dot-dashed yellow and red lines, respectively.

II.2 DATA ANALYSES

The following section describes the post-processing techniques developed to evaluate the staring mode dataset of the Radial Wind Speed (RWS). The dataset corresponds to measurements done during the 3 hr periods described in section II.1.3, and is segmented in 9 samples of 10 min records, spaced by another 10 min where PPI takes place. For each case, the initial dataset spans 1.5 km through 150 gates, and is further exploited in the first 1 km (101 gates) for the reasons discussed below. With different accumulation times, a 10-min series contains 600 and 2400 time-steps for Cases 01 and 02, respectively. The methodology built is tuned and exemplified for Cases 01 and 02.a., but also considered in the exploitation of cases 02.[b,c] in section II.3.4.

II.2.1 DATA QUALITY AND FILTER

The sLiDAR's measurements might be sensitive to varying atmospheric conditions that control the particle's density in the ABL, and become improper for example through an insufficient concentration of particles, or due to the ray collision with hard targets. Two methods are here discussed to identify bad quality data: (i) Fixed CNR threshold (Section II.2.1.1); (ii) RWS spike detection (Sec. II.2.1.2). Bad quality data are first removed from the dataset, and then reconstructed according to section II.2.1.3, such that the RWS can be assessed in a uniform space-time grid as required for the spectral analyses in section II.2.2.

II.2.1.1 CARRIER-TO-NOISE RATIO

The Carrier-to-Noise-Ratio evaluates the back-scattering intensity with respect to noise, such that higher its value, better the data quality (Gryning et al. [2016]). A fixed CNR value threshold, below which data is discarded to ensure high quality datasets, is usually employed in the literature with values ranging between -22 db and -29 db. However, this is shown to induce CNR-dependent statistical properties [Gryning and Floors, 2019], and becomes a hard limit in specific environmental conditions [Beck and Kühn, 2017] where the CNR naturally tends to lower values. The CNR behavior and its impact in present results have been studied prior to the definition of a CNR criteria (CNR>-29 db), and the exploited spatial range is limited to ensure higher overall CNR values of the dataset.

The fraction of data filtered as a function of the threshold is shown as cumulative histograms in Figure II.2.1(a,d), for Cases 01 (II.2.1a) and 02.a (II.2.1d). The CNR is indeed dependent on the environmental conditions, as for example its cumulative distribution shifts towards lower values in Case 02.a. As expected (Gryning and Floors [2019]), at the same time lower CNR values occur more often in more distant measurements. A higher data quality is hereby achieved limiting the total sLiDAR's LOS ranges (Blue bars in figure II.2.1), to be exploited in the first 1km distance closest to the sLiDAR (Yellow bars).

The graphs in figure II.2.1 also reveal CNR-dependent statistics for the mean RWS (figs. II.2.1b and II.2.1e) and turbulence intensity (TI, figs. II.2.1c and II.2.1f). The threshold for which the statistics become CNR dependent is proportional to the overall CNR quality: Gen-

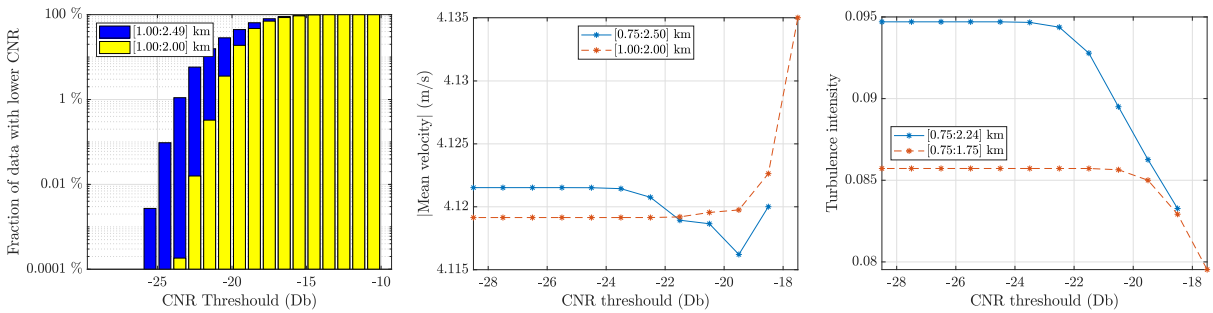

(a) Case 01: Fraction of data below the CNR threshold.

(b) Case 01: Mean velocity of data above the CNR threshold.

(c) Case 01: Mean TI of data above the CNR threshold.

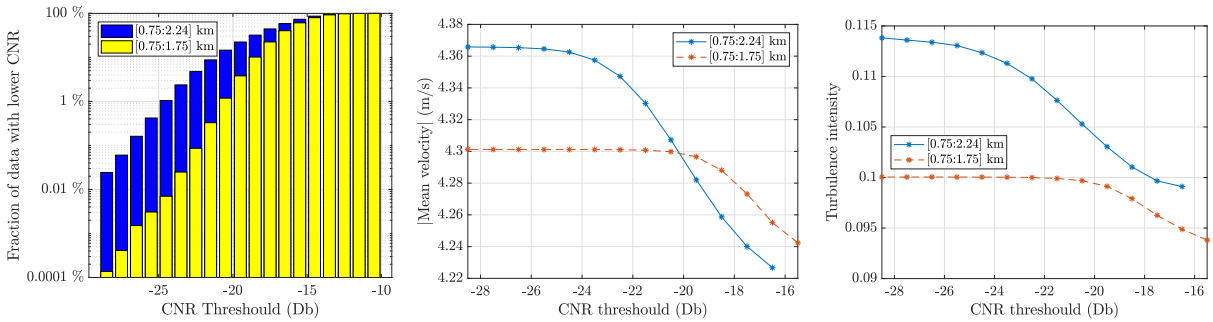

(d) Case 02.a: Fraction of data below the CNR threshold.

(e) Case 02.a: Mean RWS of data above the CNR threshold.

(f) Case 02.a: Mean TI of data above the CNR threshold.

Figure II.2.1: Case 01 above; Case 02.a below. Cumulative histogram of CNR occurrences below the threshold; Mean velocity and turbulence intensity as function of the CNR threshold.

erally higher for Case 01 and in shorter distances from the coast where the sLiDAR signal is stronger. With the limited 1 km LOS extent, independence is observed for Cases 01 and 02.a with thresholds as big as -22 db. However, independence in the mean quantities of variables such as the RWS and the TI, does not imply independence of other statistical and more sensitive quantities, such as the turbulent spectra. Referring to the cumulative histograms, a -22 db threshold discards 0.02% of the data in Case 01 and 0.08% in Case 02.a: Too much for current objectives counting in highly detailed FFT-based spectral analyses.

To perform a Fast Fourier Transform (FFT) the dataset must be uniformly distributed in space and time domains, such that data removal implies data reconstruction (Described below), which is hardly more trustworthy than the actual measurement. Indeed the spectra quality completely deteriorates with the removal of ~0.1% of the dataset: A CNR threshold of -27 db if the full LOS range were considered in Case 02.a (Blue cumulative histogram in figure II.2.1d). To avoid CNR dependent biases in future results, the lower threshold of -29 db is here adopted, together with the dataset reduction to 1 km span, discarding no data in Case 01 and a single point in Case 02.a.

II.2.1.2 Spike detection and removal

A spike is defined as data for which the difference between the measurements and its estimate exceeds a certain threshold, big enough to be considered non-turbulence related. Spike detection methods cover the mathematical description of the estimate and the def-

inition of a criterion, and vary through the literature being their performance intrinsically flow-dependent (Suomi et al. [2017]). Here the estimate is given by the low-pass filtered signal, and the threshold is imposed with respect to the difference between the measurement and its estimate. The filter standard deviation and the criterion thresholds are tuned through graphical inspection of Cases 01 and 02.a to filter non-physical outliers.

The spikes are identified in the time domain, as the short acquisition sampling period enables to capture turbulent scales smaller than the comparatively larger gate spacing. At each gate, there are $n = 1..N = [600 \text{ or } 2400]$ time steps t_n in a 10-min time series. The low pass time filter $u_\alpha(x,t)$ represents the large scale motions of the space-time dependent measurements $u(x,t)$, and are evaluated at a given position x, being the space dependency omitted below. A single parameter gaussian filter (Eq. II.2.1) is applied, where the standard deviation σ_α is tuned to 10 s by graphical inspection of Cases 01 and 02a.

$$u_\alpha(t) = \frac{\sum_{n=1}^{N} [u(t_n) \cdot W_\alpha(t_n - t)]}{\sum_{n=1}^{N} [W_\alpha(t_n - t)]}, \quad \text{with} \quad W_\alpha(t_n - t) = \frac{1}{\sqrt{2\pi}\sigma_\alpha} \exp\left[-\frac{(t_n - t)^2}{2\sigma_\alpha^2}\right]. \tag{II.2.1}$$

This method is an alternative to more simplistic approaches where $|u - \overline{u}| < m_\sigma \cdot \sigma_u$ (in which case $\overline{u}$ is the estimate), being σ_u the standard deviation of $u(t)$ and m a constant. In increased complexity, an advantage of the proposed procedure is that the estimate includes low frequency motions, such that spikes remain defined in high frequency scales: The wind might strongly deviate from its average value (Due to unsteadiness for example), yet it is only a spike if the deviation occurs during short periods.

The criterion depends on the time-wise difference $d_n = u_n - u_\alpha$ between the time-dependent signal $u_n(t)$ and its estimate $u_\alpha(t)$, in comparison to the Round Mean Square difference $\text{RMS}_{diff} = [\sum(d_n^2)/N]^{0.5}$, and to its neighbors: (i) $|d_n|/\text{RMS}_{diff} > m_{\sigma 1}$; and (ii) d_n/d_{n-1} & $d_n/d_{n+1} > m_{\sigma 2}$, tuned to $m_{\sigma 1} = 5$ and $m_{\sigma 2} = 2$ by graphical inspection of Cases 01 and 02a. This procedure identify 5 points ($\sim 0.001\%$ of all) and 305 points ($\sim 0.01\%$ of all) as spikes, for Cases 01 and 02.a, respectively.

An example is given in figure II.2.2, where the original signal appears in blue and its low-pass filter (with $\sigma_\alpha = 10s$) in red; the spike identified is shown as a purple dot, being its quality close below the threshold; the yellow lines and dot refer to the signal reconstruction described below.

II.2.1.3 Signal reconstruction

For the subsequent analyses relying on FFT algorithms, it is necessary to reconstruct the data previously discarded as described in sections II.2.1.1 and II.2.1.2. The data is substituted by its low-pass filtered (Eq. II.2.1 with $\alpha \to \beta$) signal, with high pass-bands where the (small) filter duration ($\sigma_\beta/3$) initially doubles the acquisition period, i.e., $\sigma_\beta = 6 \cdot [1, 0.25]$ s for Cases 01 and 02.[a-c], respectively. Bad quality data do not contribute to the summation in equation II.2.1.

As a last prevention against badly conditioned data, if required, an adaption of the reconstruction takes place in an iterative procedure: The filter standard deviation σ_β doubles as long as the weighting function spreads too wide in the removed data; more precisely when the gaussian weight ($\sum W_\alpha$) in equation II.2.1 is ten time larger if integrated with bad quality data, than with good quality data. This threshold is not often assessed.

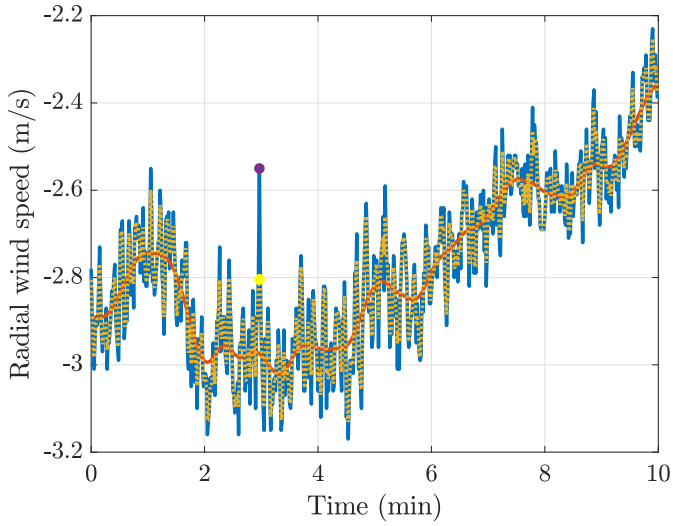

Figure II.2.2: An example of the spike-removal and reconstruction procedure, selected from a time series where the spike is identified close to the established threshold. The blue full line represents a 10-min measurement of $u_R(x,t)$ with fixed position x. The orange full line represents the low frequency estimate of $u_R(x,t)$, used to identify the spike denoted by a purple dot. The yellow dotted line is the high frequency estimate of $u_R(x,t)$, used to reconstruct the spike attributing the value once in purple to the yellow dot just below.

II.2.2 Energy Density Functions

Aiming the sLiDAR f-LOS as close as possible to the wind direction in a quasi-steady wind condition, it is here expected to approximate the RWS (u_R) to the streamwise component of the wind velocity u_1, with velocity fluctuations $u_1' = u_1 - \overline{u}_1$. The distance r is measured along the f-LOS, approximating the streamwise distance. The spectra exposed are so approximations of the longitudinal spectra $E_{u_1'u_1'} \sim E_{u_R'u_R'}$. Any deviation between wind and f-LOS directions contaminate the spectra with the full spectral tensor information (Peña and Mann [2019]).

The space-time correlation function of longitudinal velocity fluctuations is $R_{u_1'u_1'}(r,\tau)$, and the corresponding spectral energy density function $E_{u_1'u_1'}(k,w)$ twice its Fourier transform (c.f. Pope [2000]), as defined in equation I.1.17. Most described in the literature it is also here discussed the one-dimensional space and time correlations/spectra of the RWS, i.e., $E(k)$ and $E(w)$, that form Fourier pairs with the one-dimensional correlation functions $R_{u_1'u_1'}(r)$ and $R_{u_1'u_1'}(\tau)$, respectively and according to equation I.1.12.

The 1D spectra $E_{u'_R u'_R}$ are computed from the 1D correlation functions $R_{u'_R u'_R}$ for each 10-min series. Inside a 10-min series $R_{u'_R u'_R}(r)$ and $R_{u'_R u'_R}(\tau)$ are averaged in space and time, and then the ensemble average of $E_{u'_R u'_R}$ is considered between the 9 samples of 10-min series.

Because the 2D wave-number-frequency spectra can be considerably more noisy than the 1D spectra, and because turbulent eddies convected by the mean wind velocity cross the LOS 1 km span in much less than 10 min (3.33 min if $< \overline{u_R} >\sim 5$ m/s), the 2D spectra rely in the further segmentation of the data set. To obtain the 2D spectra, each of the nine 10-min series is segmented in three: $R_{u'_R u'_R}(r,\tau)$ is averaged inside a 3.33-min space-time series; and the ensemble average of $E_{u'_R u'_R}(k,w)$ is performed over 9·3 segments of 3.33-min.

II.2.3 Wind homogeneity and steadiness

Homogeneity and Steadiness are assumed, e.g., to take space and time averages that represent the statistical ensemble of a case. These conditions are hardly ever strictly achieved in nature, but an effort is made to quantify them based on the observed RWS, characterizing the quality of the dataset that leads to further results, and the main findings starting from section II.3. In the open ocean, the absence of solid obstacles favors homogeneity, but strong variability in time is often observed in the offshore environment (Baker and Gibson [1987]). Regarding the joint space-time distribution of the velocity fluctuations exploited in section II.3, it shall be here noted (c.f. the introduction in Nappo et al. [2010]) that Homogeneity and Steadiness are in fact coupled through the turbulent eddies' convection velocity. Thus, both Homogeneity and Steadiness are here considered as lack of intermittency, in space and time domains, respectively.

Different methods are disposed in the literature to evaluate the intermittency of the wind flow. A first difference characterizing these methods are the quantities in interest, as one could cite for example: The strong intermittency effects observed in viscous and thermal dissipation rates in Baker and Gibson [1987]; the wind steadiness, or persistance, evaluated in Singer [1967], Nappo et al. [2010], and Mahrt [2011] through variations in the wind direction; the turbulent kinetic energy exploited, e.g., in Nappo et al. [2010], and in Mahrt [2009] together with the different velocity variances; and higher order statistics, such as the kurtosis of different velocity components, in Mahrt [1989] and Mahrt [2009]. Each of these studies also employs different criteria defining intermittent motions, but generally two approaches are identified: Either identifying changes in these quantities with respect to a local multi-resolution basis (Mahrt [2009]), or with respect to the changes in the statistics taken between consecutive segments in a determined scale (Nappo et al. [2010]). There is no universally accepted definition of homogeneity or steadiness criteria. Here, the variability of mean RWS and Turbulence Intensity (TI) are evaluated in the largest scales available with the 1-km/ 3-hrs f-LOS dataset, and the criteria established characterize the rate of change in this variables, between large segments of this dataset, in space and time domains simultaneously.

The definition of intermittent motions being intrinsically scale dependent (c.f. Mahrt [2009]), notably one shall distinguish between small and global scales intermittency that coexist in a turbulent flow (Mahrt [1989]). Avoiding ambiguity it is here addressed the global variability of turbulent statistics. The local variability designating small scales intermittency,

is fully incorporated in the high resolution part of the turbulent spectra discussed in sections II.3.2 and II.3.3. So the large scales variability here accessed designates turbulent motions occurring at scales larger, or comparable, to the low resolution part of the spectral domain defined in section II.2.2. Moreover, the flow is evaluated in two different scales: (i) Large Scales, with distances r_l and periods τ_l comparable to the largest spectral scales considered; (ii) Very large scales, with distances (r_L) and periods (τ_L) larger than the spectral domain extension. Lengths and periods r_l and τ_l split a 10-min series, and so interfere with the space-time averages defined with equation II.1.1; but $\tau_L \geq$10-min, so interfering with the ensemble averages in the same equation.

To evaluate the intermittency level in each scale so defined, the whole dataset ($N_t \times N_x$ instants × gates) is segmented according to figure II.2.3, into: (a) The large scale grid, with ($m_t \times m_x = 9$ [5 × 5]) intervals of $r_l = 1/m_x$ km and $\tau_l = 9 \cdot 10/m_t$ min; and (b) the very large scale grid with ($m_t \times m_x = 9$ [1 × 1]) intervals of $r_L = 1$ km and $\tau_L = 10$ min. A subset is thus composed of $n_t \times n_x$ instants × gates, with $n_t = (N_t/m_t)$ and $n_x = (N_x/m_x)$. The very large distances r_L equal the dataset extension, so preventing the evaluation of the homogeneity level at these scales. In a Cartesian and uniform grid, a subset ab is identified by its middle time-space coordinates (t_a, x_b), and its extension given by (τ_a, r_b).

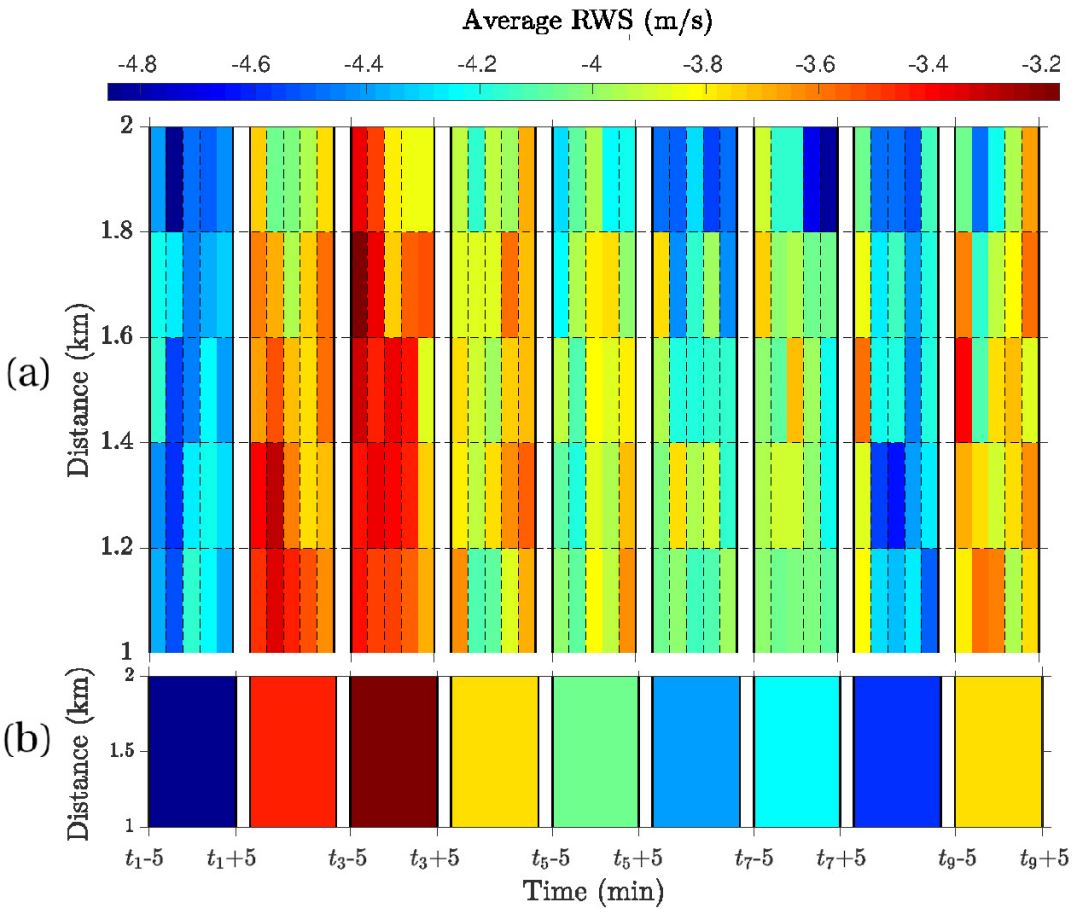

Figure II.2.3: Segmentation of the dataset of Case 01 into different grids (a,b) to address: (a) Large scale steadiness and homogeneity; (b) Very large scale steadiness. The blank spaces between t_i+10 min and t_{i+1} are out of scale, for they correspond to another 10-min intervals where PPI motions are executed.

Figure II.2.3 exemplifies for Case 01, the average procedure as employed for the RWS field, together with the space time limits defining each subset. The space-time average of a generic flow field $\chi(x,t)$, in the segment ab is given by:

$$\overline{\chi}_{ab}(t_a, x_b) = \sum_{\substack{t \in [t_a - \frac{\tau_a}{2}, t_a + \frac{\tau_a}{2}[\\ x \in [x_b - \frac{r_b}{2}, x_b + \frac{r_b}{2}[}} \left[\frac{\overline{\chi}(t,x)}{n_t n_x} \right], \tag{II.2.2}$$

so defining the (very) large scale functions $\overline{u}_{ab}(\overline{u_R}|_{ab})$, and $\mathrm{TI}_{ab}(\overline{u'_R u'_R}|_{ab}, \overline{u_R}|_{ab}) = \sqrt{\left\langle \overline{u'_R u'_R}|_{ab} \div \overline{u_R}|^2_{ab} \right\rangle}$ according to equation II.1.1. Up to this point, no average occurs across different 10-min series, so the ensemble average can be discarded in the evaluation of TI_{ab}.

Let $g_{ab}(t_a, x_b)$ represents a generic large scale function ($\overline{u}_{ab}$, or TI_{ab}), so the intermittency criteria $\mathcal{V}$ are defined in terms of the rate of change in g_{ab} over time (Steadiness, in $\mathcal{V}^{(t)}$), or space (Homogeneity, in $\mathcal{V}^{(x)}$). Two criteria are defined, either as the average ($\mathcal{V}^{(0)}$), or the maximum ($\mathcal{V}^{(1)}$) derivatives, normalized with respect to τ_a, r_b, and $\overline{g}_{ab}$, according to:

$$\begin{aligned}
\mathcal{V}^{(0t)}(g) &= \left(\frac{\tau_a}{\overline{g}_{ab}}\right) \frac{1}{n_t n_x} \sum_{\substack{t_a \in \pm\infty \\ x_b \in \pm\infty}} \left[\frac{\partial g_{ab}}{\partial t_a} \right], \quad \mathcal{V}^{(1t)}(g) = \left(\frac{\tau_a}{\overline{g}_{ab}}\right) \max_{t_a \in \pm\infty} \left\{ \frac{1}{n_x} \sum_{x_b \in \pm\infty} \left[\left| \frac{\partial g_{ab}}{\partial t_a} \right| \right] \right\}, \\
\mathcal{V}^{(0x)}(g) &= \left(\frac{r_b}{\overline{g}_{ab}}\right) \frac{1}{n_t n_x} \sum_{\substack{t_a \in \pm\infty \\ x_b \in \pm\infty}} \left[\frac{\partial g_{ab}}{\partial x_b} \right], \quad \mathcal{V}^{(1x)}(g) = \left(\frac{r_b}{\overline{g}_{ab}}\right) \max_{x_b \in \pm\infty} \left\{ \frac{1}{n_t} \sum_{t_a \in \pm\infty} \left[\left| \frac{\partial g_{ab}}{\partial x_b} \right| \right] \right\},
\end{aligned} \tag{II.2.3}$$

where the derivatives are evaluated in a first order finite difference approach.

II.2.3.1 Large scale non-homogeneity and unsteadiness

The criteria defined in equation II.2.3 are ensemble averaged between the 10-min data-set and depicted in table II.2.1, giving $\mathcal{V}^{(0x,0t)}$, followed by $\mathcal{V}^{(1x,1t)}$ into parenthesis, as the rate of change (%) per $\tau_a = 2$ min or $r_b = 200$ m, for each case and variable considered.

There is no reference classification for these values but, to guide the discussion, in the table they are colored with a 1/3 rule: For each of the 8 criteria ($\mathcal{V}^{(0x,0t,1x,1t)}$ of $\overline{u_R}$ and TI), the values range between $\mathcal{V}_{min}$ and $\mathcal{V}_{max}$ ($\mathcal{V}_{dif} = \mathcal{V}_{max} - \mathcal{V}_{min}$); so green, yellow, and red colors, apply respectively to values in the intervals $\{\mathcal{V}_{min} + [0, \mathcal{V}_{dif}/3]\}$, $\{\mathcal{V}_{min} +]\mathcal{V}_{dif}/3, 2\,\mathcal{V}_{dif}/3[\}$, and $\{\mathcal{V}_{min} + [2\,\mathcal{V}_{dif}/3, \mathcal{V}_{dif}]\}$.

The criteria exposed in table II.2.1 summarize different aspects of the intermittency. The variables in interest are preferably affected by different sources of intermittency, and the changes in TI are significantly more pronounced compared to the changes in the RWS. For instance, changes in the large scale forcing, and/or in the wind direction, would primarily

affect the mean wind velocity, and conserve the turbulence intensity. The turbulence intensity on the other side is particularly influenced by the stratification regime and/or in-land wind sources. At Case 01 in figure II.1.3a, the unsteadiness level is apparently significant in the wind speed and direction, which is confirmed in the values of $\mathcal{V}^{(0t)}(\overline{u}_R) = 0.6$ and $\mathcal{V}^{(1t)}(\overline{u}_R) = 2.5$ shown in the table for the RWS, but not clearly observed for the TI criteria 4.5 (and 19.6). The changes in TI registered at Case 01 are not negligible, but considerably lower than in Case 02b and 02c.

Cases(02a-c) are characterized by winds coming from the land and that introduces significant level of non-homogeneity to the atmosphere, but globally quasi-steady winds are encountered in figure II.1.3b. While Case 01 is critical in terms of the unsteadiness in $\mathcal{V}^{(0t)}(\overline{u}_R)$, it presents significantly lower averaged non-homogeneity criteria $\mathcal{V}^{(0x)}(\overline{u}_R)$. Intermittency in time and space shall invariably affect one another in the scales considered, and even though the averaged criteria $\mathcal{V}^{(0x)}$ is low at Case 01, the maximum criteria $\mathcal{V}^{(1x)}(\overline{u}_R)$ is not.

Because it captures the influence of strong isolated large scale fluctuations, the maximum criteria is important to qualify the quality of the dataset, but it is also very sensitive to different sources of intermittency, and can be rather difficult to interpret. At Case 01 and regarding the non-homogeneity criteria of TI for example, one encounters the lowest average value $\mathcal{V}^{(0x)}(\mathrm{TI}) = 3.2$, but the highest maximum value $\mathcal{V}^{(1x)}(\mathrm{TI}) = 16$. Such discrepancy indicate that there is a comparatively small trend of the TI variation over large distances, but local and intense intermittent motions occurring with $r \sim 200$ m. Indeed turbulence intermittence is favored in stable stratification conditions (c.f. Nappo et al. [2010]), which is the regime characterizing Case 01. Opposite to Case 01, Case 02(a-c) are in the convective turbulent regime, and present higher TI in table II.1.2. In Cases 02(b,c) there is a strong non-homogeneity induced in the TI due to the land effect, the high average criteria indicating a clear tend of TI over large distances, with $\mathcal{V}^{(0x)}(TI) = (5.2, 5.1)$; but the maximum criteria $\mathcal{V}^{(1x)}(TI) = (14.6, 13.3)$ is not as big as in Case 01, probably due to the different stability regimes.

Back to figure II.1.3b, Case 02b presents large variations of the wind speed in comparison to Cases 02(a,c), and indeed Case 02b reveals most of the critical criteria in table II.2.1, with the exception of: Case 01 leading in $\mathcal{V}^{(0t)}(\overline{u}_R)$ and $\mathcal{V}^{(1x)}(TI)$, probably due respectively, to wind direction changes, and stable regime induced intermittence; and $\mathcal{V}^{(1x)}(\overline{u}_R)$ slightly surpassed in Case 02a. The most steady wind occurs at Case 02c, with $\mathcal{V}^{(0t)}(\overline{u}_R) = 0.1$ and $\mathcal{V}^{(0t)}(TI) = 3.6$; the same Case presents one of the highest large scale non-homogeneity tends with $\mathcal{V}^{(0x)}(\overline{u}_R) = 0.7$ and $\mathcal{V}^{(0x)}(TI) = 5.1$, which is due to land-induced intermittence and not very different from the observations in Cases 02(a,b).

Table II.2.1: Steadiness and homogeneity evaluation at the large scale motions of grid (a) in figure II.2.3, through the criteria $\mathcal{V}^{(0x,0t)}$ ($\mathcal{V}^{(1x,1t)}$ in parenthesis) established in equation II.2.3. Rate of change (%) per $\tau = 2$ min (In $\mathcal{V}^{(t)}$), and $r_b = 200$ m (In $\mathcal{V}^{(x)}$).

Case ID	Unsteadiness $\mathcal{V}^{(t)}$ of $\overline{u}_1$	Non-homogeneity $\mathcal{V}^{(x)}$ of $\overline{u}_1$	Unsteadiness $\mathcal{V}^{(t)}$ of TI	Non-homogeneity $\mathcal{V}^{(x)}$ of TI
01	0.6 (2.5)	0.4 (1.5)	4.5 (19.6)	3.2 (16.0)
02a	0.4 (1.9)	0.7 (1.6)	3.7 (13.2)	3.8 (12.2)
02b	0.4 (2.5)	0.9 (1.5)	6.5 (46.4)	5.2 (14.6)
02c	0.1 (1.1)	0.7 (1.2)	3.6 (30.2)	5.1 (13.3)

II.2.3.2 Very large scale unsteadiness

The steadiness criteria $\mathcal{V}^{(0t)}$ ($\mathcal{V}^{(1t)}$) from equation II.2.3 are depicted in table II.2.2, as the rate of change (%) per $\tau_a = 10$ min, for each case and variable considered.

Table II.2.2: Steadiness evaluation at the very large scale motions of grid (b) in figure II.2.3, through the criteria $\mathcal{V}^{(0t)}$ ($\mathcal{V}^{(1t)}$ in parenthesis) established in equation II.2.3. Rate of change (%) per $\tau = 10$ min.

Case ID	Unsteadiness $\mathcal{V}^{(t)}$ of $\overline{u}_1$	Unsteadiness $\mathcal{V}^{(t)}$ of TI
01	0.5 (8.7)	11.2 (39.6)
02a	0.8 (6.6)	6.2 (53.5)
02b	1.4 (6.1)	7.9 (52.7)
02c	1.3 (3.4)	3.2 (53.3)

The unsteadiness criteria shown in table II.2.2 concerning very large motions, are to be compared to the discussion held around table II.2.1 characterizing large scale motions. At first the tables might seem contradictory, but they are in fact complementary. At Case 01, recall from figure II.1.3a that significant unsteadiness is observed in the wind speed and direction, and the same is observed in $\mathcal{V}^{(0t)}$ and $\mathcal{V}^{(1t)}$ at table II.2.1. Now at table II.2.2, Case 01 presents the lowest value of $\mathcal{V}^{(0t)}$. A close look inside Case 01, between the initial and final time-steps depicted as vertical lines in figure II.1.3a, shows that what seemed as a clear trend in the large scale grid, is in fact a very large scale intermittency: In figure II.1.3a the mean wind speed rises, but later decays to wind speeds similar to the initial; in the large scale grid these variations reflect an even larger scale motion, and are captured as a trend in the average criteria $\mathcal{V}^{(0t)}$ at table II.2.1; but in the very large scale grid they appear as intermittence, and reflect only in the maximum criteria at table II.2.2. The turbulence intensity variation criterion is particularly important at the very large scales for Case 01, with the critical value of $\mathcal{V}^{(0t)}(TI) = 11.2$ depicted in table II.2.2, possibly because of the turbulence intermittence induced in the stable ABL. Also in the very large scales, Case 02b is critical by most of the established criteria, significantly surpassed only in $\mathcal{V}^{(1t)}(\overline{u}_R)$ and $\mathcal{V}^{(0t)}(TI)$ by Case 01.

II.3 Field measurements of Wave Induced Disturbances in the WBL

The RWS obtained during the f-LOS measurements above the water surface are analyzed through this section. The wave signature is first sought and observed in the time-space domain, by spatio-temporal maps of the velocity fluctuations in section II.3.1, and by the one-dimension and two-dimension turbulent spectra, in sections II.3.2 and II.3.3, respectively. Section II.3.4 addresses the diminishing of the wave signature with smaller Wave Ages.

II.3.1 Radial Wind Speed fluctuations

Turbulent streaks (Eddies) are usually identified in two-dimensional space mapping of the longitudinal velocities in the ABL, characterized by a coherent pattern of alternated longitudinal velocities, either captured in the $x-y$ or $x-z$ planes. Such pattern can be explained by the coherent vortical structures introduced in section I.3.4, but the definitions are not equivalent. Notably, the velocity field characterizing the stream-wise vortices of figure I.3.7 are almost aligned to the $x-y$ place, and due to their interaction with the mean shear that results in alternated regions of low and high stream-wise velocities, i.e., a turbulent streak [Jiménez, 2018].

Somehow more unusual, here one encounters the two-dimensional space-time mapping of (approximately) longitudinal velocities, in the $x-t$ plane. Figure II.3.1 presents a color plot of the spatio-temporal RWS from two f-LOS 10 min records above the sea surface, for Case 01 (II.3.1a and b) and Case 02a (II.3.1c and d). Also in the spatio-temporal map one encounters alternated low and high speed regions depicting a turbulent streak. Instead of giving two dimensions of the turbulent streak ($x-y$ or $x-z$), a spatio-temporal temporal map identifies its (approximately) longitudinal dimension (span of a streak in the vertical axis at figure II.3.1), and duration (span of a streak in the horizontal axis at the figure).

Approaching the focus of current discussion, a spatio-temporal map also depicts the convection velocity of these turbulent streaks, which is identified by the slopes (length/duration) in figure II.3.1. In a statistical perspective, the expectation for the advection velocities of the turbulent eddies shall follow certain characteristics discussed in this section.

According to the Taylor hypothesis, in a flat bottom scenario the turbulent eddies are advected by the local mean speed, so for its evaluation the mean RWS of the 10 min period is shown as dot-dashed lines in figure II.3.1. Wave induced motions on the other side, are advected by the free-surface and thus follow the dispersion equation that imposes the (peak) wave-phase velocity, computed as $c_p = L_p/T_p$ from Tab II.1.3, and represented in Fig. II.3.1 by two dashed lines separated by T_p.

For each observation in figure II.3.1 the turbulent streaks are strongly correlated to the peak wave-phase velocity c_p, and the time between two streaks qualitatively corresponds to T_p (Distance between two dashed lines in the figure). The close relation between space-time RWS fluctuations and wave characteristics suggests that, at that height, a significant part of the wave motions are transferred to the wind. When looking for the mean RWS (Dot-dashed

lines in the figure) though, the correlation expected from Taylor hypothesis is clearly seen in Case 02a (II.3.1c and d), but not as much for Case 01 (II.3.1a and b). Instead, turbulent streaks in Case 01 appear to be convected by velocities lower than the RWS: The arbitrary value 0.5 RWS appearing as green dot-dashed lines, a reference in figures II.3.1a and b.

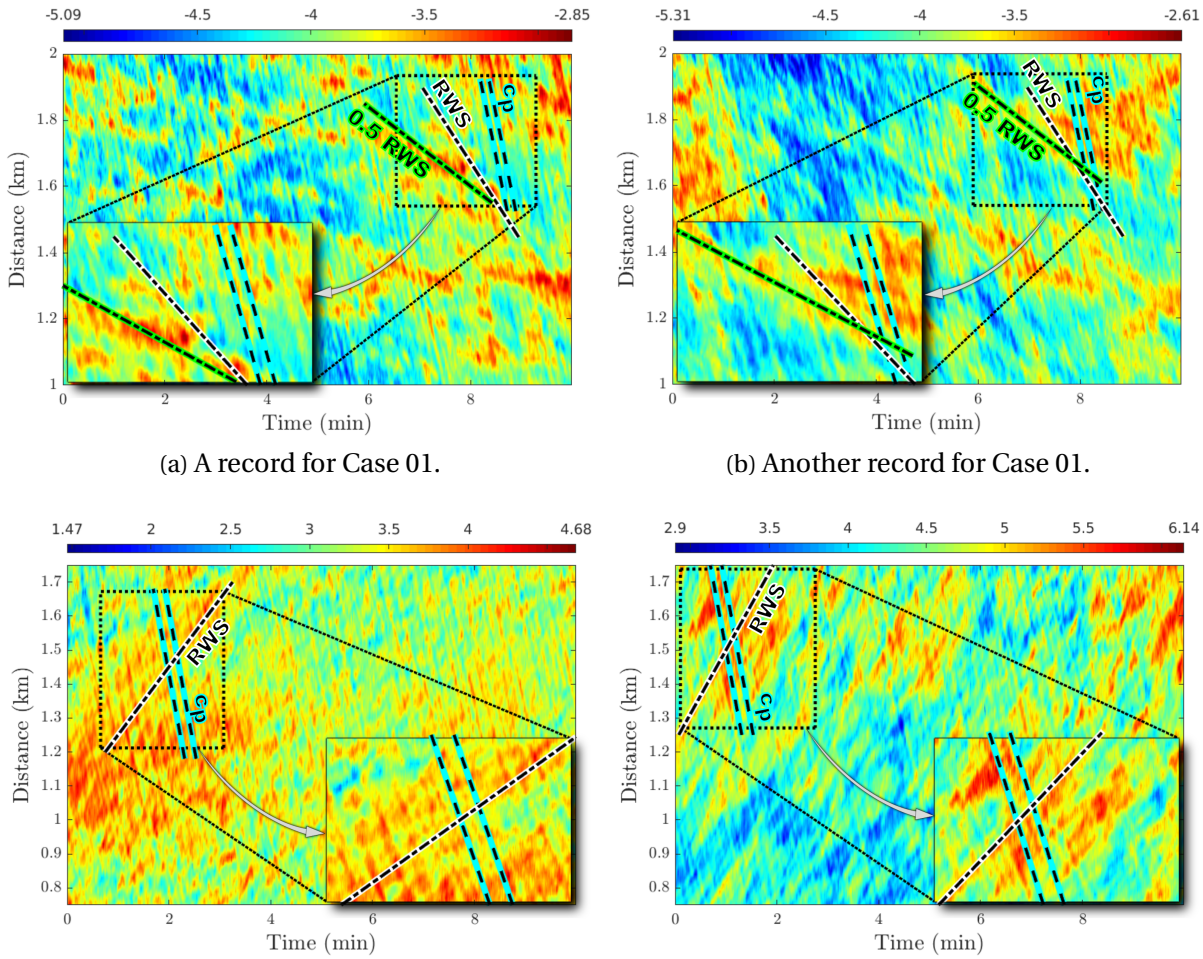

(a) A record for Case 01.

(b) Another record for Case 01.

(c) A record for Case 02a.

(d) Another record for Case 02a.

Figure II.3.1: Staring mode 10-min records of the RWS from Case 01 at (a,b) and Case 02.a at (c,d). Mean RWS (Taylor's hypothesis) and Peak wave phase velocity (Dispersion equation) slopes as dash-dotted and dashed lines, respectively. Wave slope duplicated and spread apart by T_p (tab. II.1.3). At Case 01 the streaks appear to travel with velocities lower than the RWS, the arbitrary value of 0.5 RWS denoted in figures (a,b).

The deviations from the Taylor hypothesis prediction in Case 01 resembles the description in Cheng et al. [2017], where turbulent eddies are distorted and have their life-time reduced. Though the convection velocity is still the RWS, turbulence is not frozen as expected from Taylor's hypothesis, and the alternated dissipation and reestablishment of vortical structures give the impression of lower convection velocities. These observations are recalled in the discussion at section IV.2.3.4.

II.3.2 ONE-DIMENSION TURBULENT SPECTRA

To analyze the spectral transfer from the sea-state to the wind, the RWS fluctuation energy distribution are analyzed in space and time dimensions by one-dimension (1D) wave-number (k) or frequency (f) energy density functions (EDF or turbulent spectra). Figure II.3.2 shows in transparency, for each Case 01 (II.3.2a, b) and Case 02a (II.3.2c, d), k and f spectra for each 10 min record constituting the 3 hours period of each test case. The 3-hour spectral average is depicted by a solid black line.

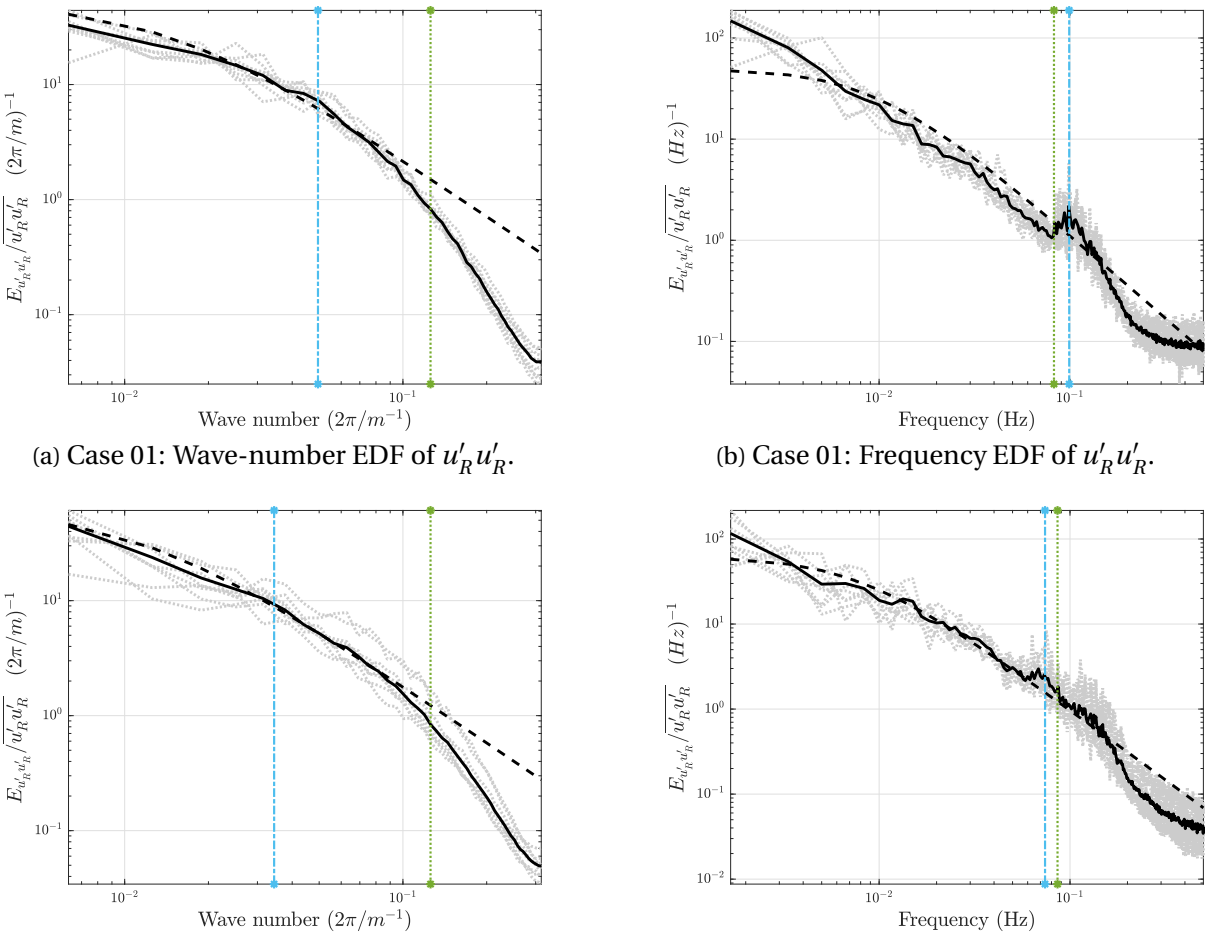

(a) Case 01: Wave-number EDF of $u'_R u'_R$.

(b) Case 01: Frequency EDF of $u'_R u'_R$.

(c) Case 02: Wave-number EDF of $u'_R u'_R$.

(d) Case 02: Frequency EDF of $u'_R u'_R$.

Figure II.3.2: Wave-number (a,c) and frequency (b,d) 1D turbulent spectra for Case 01 (a,b) and Case 02.a (c,d). Observed 10-min spectra in light grey, and the 3-hour average in black full lines. The ESDU reference is given in black dashed lines. Vertical blue lines stand for the wave peak scales k_p and f_p, and green lines show the filter scales $k_{\gamma 0}$ and $f_{\gamma 0}$, for wave-number and frequency spectra, respectively.

The ESDU spectra ESDU 85020 is traced in figure II.3.2 as a dashed black line with parameters $\overline{u_R}$, observed integral length scale ($L_l = \pi E_k(0)/[2R_k(0)]$ obtained from E_k) , altitude 18.33 m, and a boundary layer height estimated to 1 km. The ESDU spectra being defined in the frequency domain, the Taylor's hypothesis is assumed ($k = w/\overline{u_R}$; $E(k) = E(w)\overline{u_R}$) to obtain the reference wave-number spectra depicted in figure II.3.2a,c.

At large scales, the measured spectra are observed in good coherence to the reference through a region of constant slope, i.e. -5/3 through the inertial sub-range, which is reproduced exactly in the reference spectra.

At smaller scales (High k, f), observations deviate from the reference, notably as consequence of the sLiDAR volume filtering (c.f. Bastine et al. [2015]). The spatial filtering characteristic length scale is represented as twice the gate length of the sLiDAR, so $k_{\gamma 0} = 2\pi/(2\ L_\gamma)$, with $2\ L_\gamma = 50$ m, i.e., 5 times the gate spacing. The correspondent filter frequency scale is estimated from Taylor hypothesis with $f_{\gamma 0} = U_R/(2\ L_\gamma)$, where $U_R = 4.12$ and $U_R = 4.29$ for cases 01 and 02a, respectively. Filter scales $k_{\gamma 0}$ and $f_{\gamma 0}$ are reported in figure II.3.2 by vertical green dotted lines.

The peak wave-number of the sea-state $k_p = 2\pi/L_p$ and its corresponding frequency $f_p = 1/T_p$ (Table II.1.3), are depicted as vertical blue dot-dashed lines in the same figure. In figure II.3.2b and d, f_p lies close to $f_{\gamma 0}$, yet, a clear peak is observed in the vicinity of f_p denoting an energy transfer from the waves to the wind. The peak present in Case 02 (II.3.2d) is less pronounced than in Case01a (II.3.2b), but still detectable, and energy does not drop as expected from the spatial filtering. On the contrary, wave-induced motions cannot be detected in the wave-number spectra, and only the spatial filtering effect is appreciated in Figs II.3.2a,c. These remarks are explained in the next section, looking to the two-dimensional wave-number-(angular-)frequency spectra.

II.3.3 Two-dimension turbulent spectra

The sLiDAR in the proposed configuration allows an original 2D spectral analysis rarely possible in the field. Figure II.3.3 presents the 2D spectra of the RWS $E_{u'_R u'_R}(k, w)$, plotted as function of wave length $L = 2\pi/k$ and period $T = 2\pi/w$, for Cases 01 and 02a, respectively in subfigures a and b. To help the analysis, the velocity relations predicted by the Taylor hypothesis and the dispersion equations (3 curves with different depths) are depicted in full and dashed lines, respectively. The sea-state peak scale $[T_p, L_p]$ is marked as a black star. The characteristic filter scales discussed in section II.3.2 still apply, and are reported in the 2D spectra as horizontal and vertical green lines.

As expected from a shear-layer flow (c.f. Wilczek and Narita [2012]), most of the energy is present for long periods/lengths around the mean velocity with significant spreading. Aside from that, and much more interesting here, the 2D spectra clearly show a second, elongated, area of high energy, disconnected from the Taylor hypothesis and precisely following the wave dispersion equation.

The dispersion equation is shown in figure II.3.3 for 3 different water depths roughly representing the uncertainty. Two depths are registered from HOMERE, excluding tidal variations: $d \sim 22m$ at the closest node to the f-LOS last gate, and $d \sim 14m$ closest to the f-LOS first gate. Considering that the WI flow might be generated from waves farther away from the f-LOS, one observes in the figure 3 curves with $d = [14, 22, 30]$ m (22 ± 8 m). Fact is that Case 02a (fig. II.3.3b) agrees well to $d = 22 \pm 8$ m. But as the wind blows from the sea, and the fetch tends to infinite in Case 01 (fig. II.3.3a), wind is mostly affected by waves from higher depths than the LOS, and the signature displaces towards $d \rightarrow 30 \pm 8$ m.

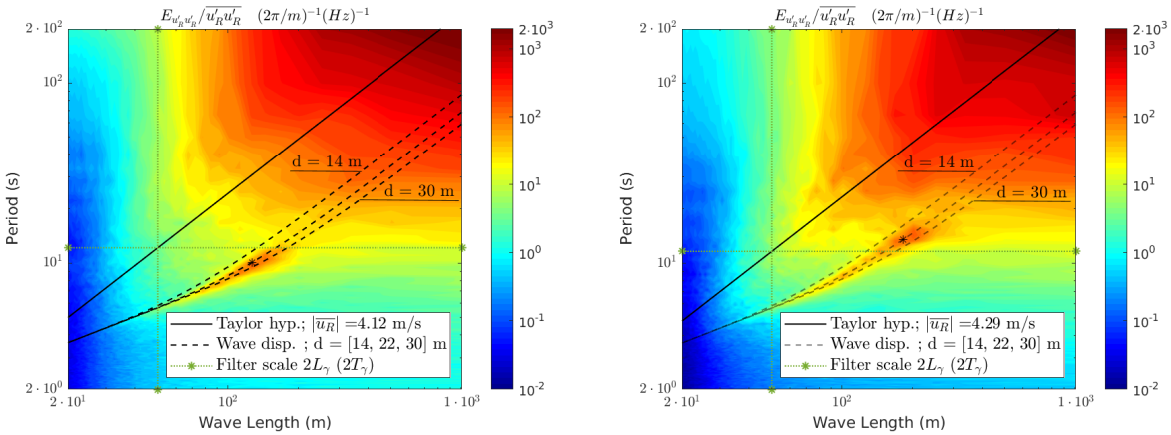

(a) Case 01.

(b) Case 02.a.

Figure II.3.3: Wave-number-angular-frequency 2D turbulent spectra. The mean RWS velocity is depicted in the black full line, and the wave velocity presented in dashed lines for $d = [14, 22, 30]$ m. The wave peak scale (L_p, T_p) is denoted by a star. The sLiDAR filter characteristic period and wave length are given in the green dashed, horizontal and vertical lines, respectively.

In section II.3.2 the wave signature is observable only in the frequency spectra, where actually much of its energy is still hidden beneath the predominant atmospheric turbulence, so one can hardly dissociate one from the other. Contrary to the 1D spectra from section II.3.2, in figure II.3.3, the upward turbulent energy transfer from the waves to the wind is evident and well distinguishable from the atmospheric turbulence. That demonstrates the great added value of this kind of analysis, that allow the detailed assessment the of turbulent energy content in the space-time domain.

Atmospheric (Atm.) and Wave Induced (WI) motions correlate differently in space and/or time domains. The impossibility to see the wave signature in the 1D-spatial spectra (Figures II.3.2a and c) results from their strong coherence to the atmospheric turbulence in space, meaning both systems present considerable energy at similar spatial scales ($\sim L_p$). Due to the different advection velocities between Atm. and WI motions, the wave signature arises in the 1D-temporal spectra (Fig. II.3.2b, d), as the coherence decreases in T_p compared to L_p. At Case02a T_p is higher, the signature moves towards the atmospheric scales in the space-time domain (Fig. II.3.3b), and the coherence increases in 1D-temporal spectra, leading to the less pronounced peak in figure II.3.2d compared to II.3.2b.

The sLiDAR spatial filtering also plays an important role. For instance, the atmospheric turbulence at T_p is largely filtered by the sLiDAR, since following Taylor hypothesis $\overline{u}_R T_p$ approaches (case 02.a) or fall below (case 01) the filter scale $2L_\gamma$. On the other side $L_p \gg 2L_\gamma$, so the wave energy content at T_p is less filtered. One shall consider that the sLiDAR filter effect is distributed in the 2D spectral domain, and a better characterization of the implications that follow is achieved numerically in sections IV.3.3 and IV.3.4

As can be seen, the 1D spectra previously discussed reveal a partial perspective of turbulent fluctuations. The prominence of the wave signature in the 1D spectra is very sensitive to the 1D scale-dependent coherence between WI and Atm. motions, and so might be often

unsuitable for an objective evaluation of the WI flow. In the 2D spectra on the contrary, as long as $\overline{u}_R$ and c_p are sufficiently apart with $c_p > \overline{u}_R$, the 2D scale-dependent coherence between WI and Atm. motions is mitigated, so both systems are well distinguishable from one another in the $k - w$ domain.

II.3.3.1 SPECTRAL GAP DISTURBANCE

In the Space-Time turbulent spectra of figure II.3.3, for both cases but stronger at Case 01 highlighted in figure II.3.4, a valley or gap appears around the convection velocity U. The spectral distribution is still symmetrical to U, but submitted to a bi-modal disturbance, such that the convection velocity is often smaller or bigger than U. This unexpected feature is often observed along the experimental campaign, in other test cases to be presented in future works, and is enhanced when the wind blows from the sea as in Case 01. It is shown in section II.3.4 that the spectral valley vanishes with the wave signature as the WA decreases, and the spectra later presented in figure II.3.8 no longer reveal a significant wave influence, nor the spectral valley: Their shape is coherent with the expected random sweeping [Wilczek and Narita, 2012] behavior, introduced in section I.3.6 (fig. I.3.13), and reviewed in the appendix C.2 (fig. C.2b). Though the observations suggest the disturbance could be wave related, buoyancy forces must be significant and the rough estimations presented in section II.1.3 are insufficient to allow its proper investigation. The spectral gap observed in figure II.3.3 are so believed to be a wave and/or buoyancy induced disturbance in turbulence, to be further investigated in future works.

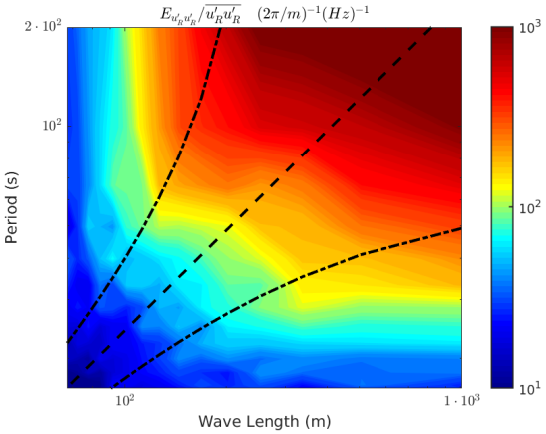

Figure II.3.4: Spectral valley (dashed) and ridges (dot-dashed), observed in the 2D turbulent spectra of Case 01 at figure II.3.3.

II.3.3.2 OPPOSING DIRECTIONS AND THE FOUR QUADRANT SPECTRA

The spectra yet discussed are more precisely defined as the resultant spectra Q_R, because it gives the resultant auto-spectra after the interference of motions propagating in different directions. These resultant spectra are the ones that integrated, lead to the 1D spectra observed in section II.3.2. According to the definitions given in the appendix A.3, more generally the 2D spectra are defined in four quadrants $Q_{\pm\pm}$, normally referred by negative and positives wave-numbers $k_\pm$ or frequencies $w_\pm$. The four quadrant Fourier Transform is conjugate symmetrical, but the EDF of the auto-correlation function is a real number, so $Q_{++} = Q_{--}$ and $Q_{+-} = Q_{-+}$. The different quadrants indicate the components that propagating in different directions interfere to give the resultant spectra $Q_R = 2\,(Q_{++} + Q_{+-})$ previously presented.

The decomposition between signals propagating in opposite directions is particularly

useful at Case 02a, which is demonstrated at figure II.3.5. For clarity and completeness, the four-quadrant spectra of Cases 01 and 02a are given in figure II.3.6, from which figure II.3.5 is extracted for the discussion. Virtually no Wave Induced disturbance is observed for motions traveling from the sLiDAR into the ocean in figure II.3.5a, as they are fully captured traveling in the opposite sense, at figure II.3.5b. From the ocean to the sLiDAR, the atmospheric turbulence is limited to very large scales, so the WI disturbances appear in a well detached region, even more clearly than in the resultant spectra previously depicted at figure II.3.3b.

Note the word virtually: In fact it is possible that WI disturbances are present at motions traveling from the sLiDAR into the ocean, either due to Wind-Wave interactions, or due to the waves reflection at the coast. The reason why they are not seen in the spectra of figure II.3.5a indicate that WI disturbances might be negligible compared to the prevailing Atmospheric contribution, but not necessarily absent. At Case 01, figure II.3.5a for example, one may notice a slight, almost unclear wave signature occurring from the sLiDAR into the ocean, at quadrants Q_{+-} and Q_{-+}. The counter-propagating WI disturbance can be appreciated at Case 01 because this is also the counter-propagating wind direction, where the Atm. turbulence is mostly restricted to very large scales.

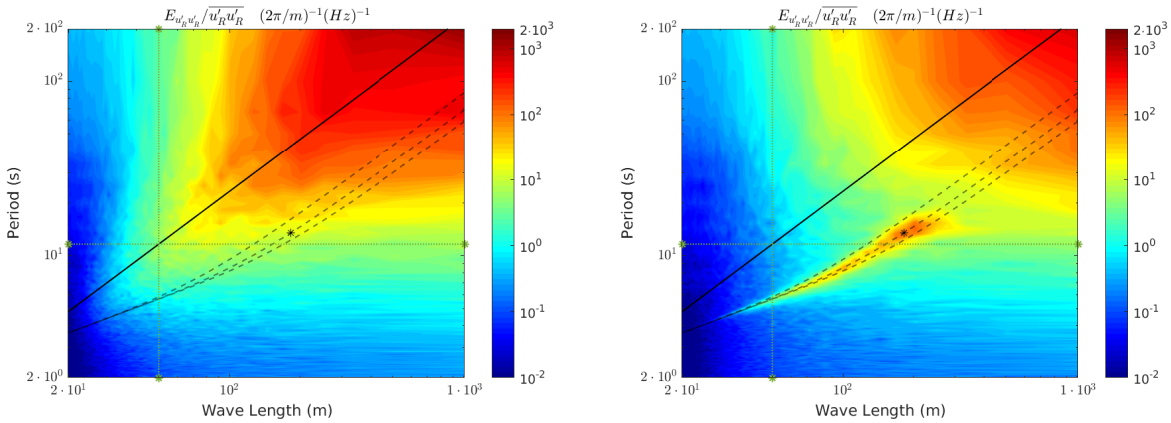

(a) From the sLiDAR to the ocean.

(b) From the ocean to the sLiDAR.

Figure II.3.5: Wave-number-angular-frequency 2D turbulent spectra for Case 02a, decomposed between opposite directions of propagation thanks to the four quadrant 2D spectra. The lines denote the characteristic scales described at figure II.3.3.

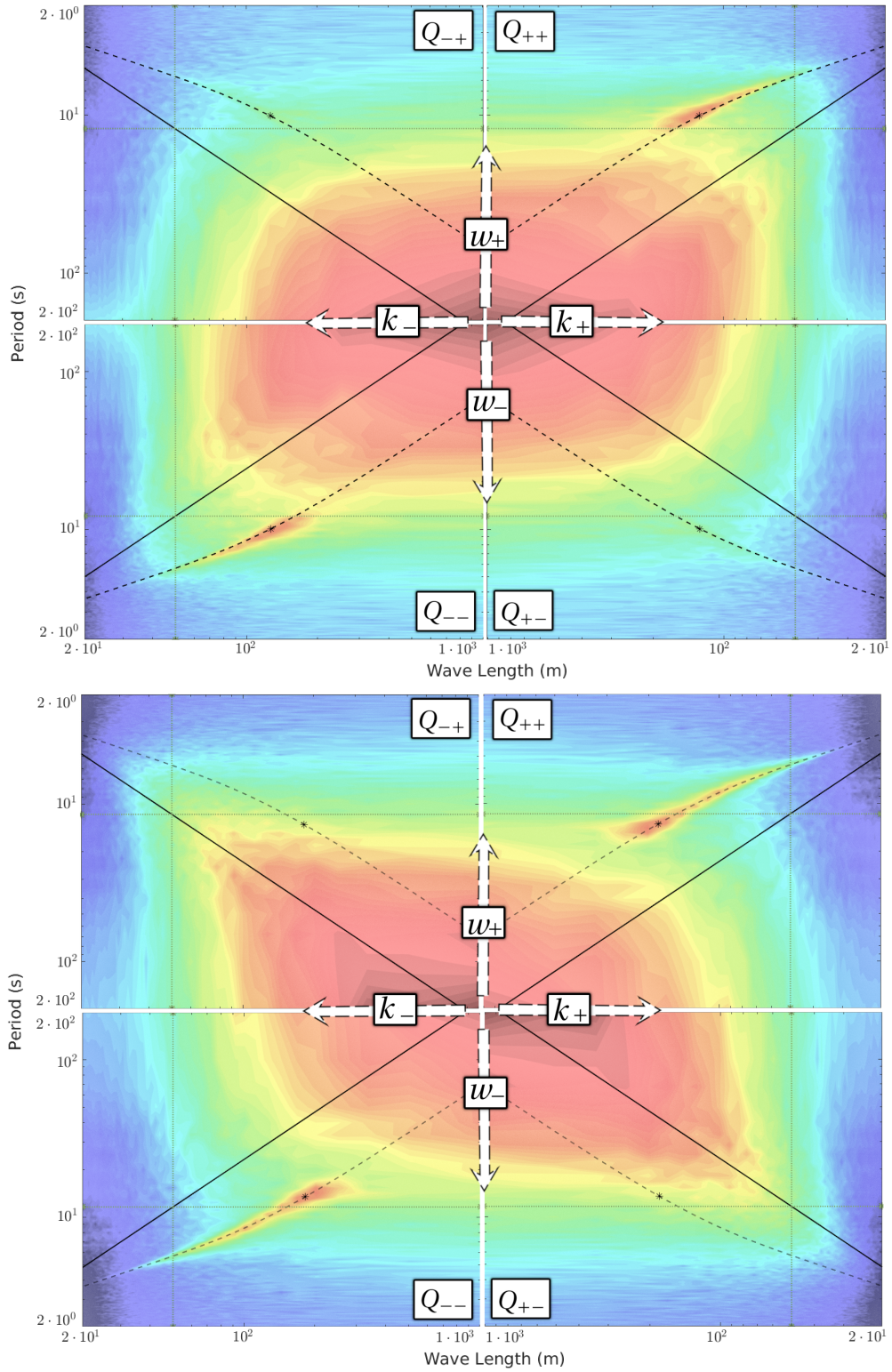

Figure II.3.6: Four quadrants ($Q_{\pm\pm}$, see the appendix A.3) of the EDF of $u'_R u'_R$, referred by negative and positives wave-numbers $k_\pm$ or angular-frequencies $w_\pm$. Considering the EDF of $u'_R u'_R$ is real, $Q_{\pm\pm}$ is fold-symmetric: $Q_{++} = Q_{--}$ and $Q_{+-} = Q_{-+}$. Summing the quadrants one obtains Q_r shown in figure II.3.3. Case 01 is depicted above, with waves and wind aligned in the same sense (Ocean to sLiDAR) at quadrants Q_{++} and Q_{--}. Case 02a is depicted below, with the wind aligned to the opposite sense (sLiDAR to Ocean) at quadrants Q_{+-} and Q_{-+}.

II.3.4 Rising Wind and Diminishing Sea-State

During the next 28 hrs after Case 02.a and as shown in figure II.1.3(b,d), meteocean conditions registered a rising wind with approximately constant off-shore direction, while the swell decayed as the significant height and the peak period diminished. Cases 02.b and 02.c (WA_c=-[2.53, 1.92]) are here presented to evaluate the decay of wave induced motions during this period in comparison to Case 2.a (WA_c=-3.14). The estimated wave peak velocity ($c_p = L_p/T_p$ in table II.1.2) and the mean RWS ($\overline{u}_R$) are used to estimate the wave age $WA_c = c_p/\overline{u}_R$. As the absolute WA_c approaches unity, the wind and waves have the same speed, the Taylor's hypothesis relation matches the Wave dispersion velocity in the so defined critical layer height z_c (Miles [1957]).

The wave boundary layer (WBL) height definition is in debate, but it shall scale with the WA [Hristov, 2018], such that diminishing the absolute WA_c between Cases 02.a-c is somehow equivalent to shrinking the WBL with respect to the ABL, or "moving out of the WBL" when employing a fixed LOS above the sea.

In a first attempt to observe the wave signature, figures II.3.7a and II.3.7b refer to Case02.b and are to be compared with figures II.3.1 and II.3.2 (Case 02.a). The RWS contours reveal streaks that correlate well with the mean RWS value, and the frequency spectra agrees well to the reference, except for the filtering effect in high frequencies. The wave signature on the other side, has vanished from figures II.3.7a and II.3.7b.

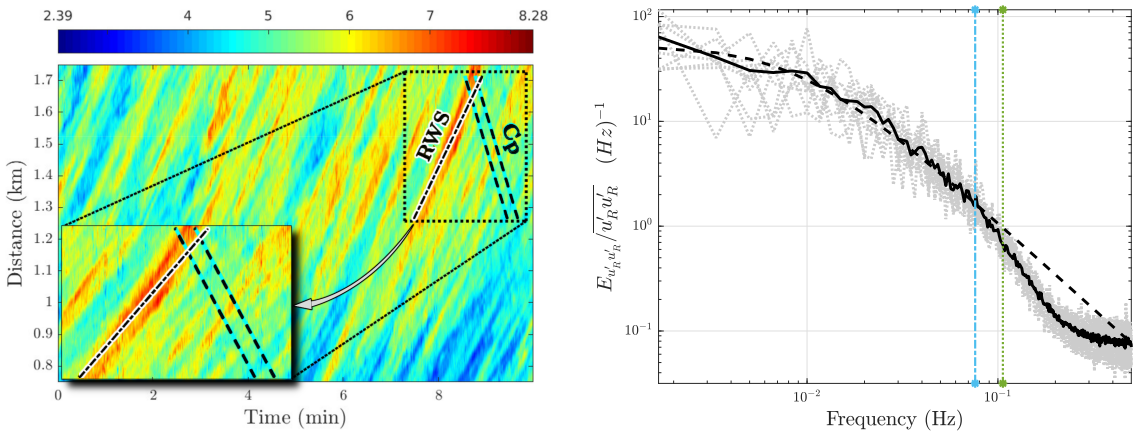

(a) staring mode 10 min records of the RWS. (b) Frequency 1D turbulent spectra.

Figure II.3.7: Case 02b, to be compared to previous figures denoting Case 02a. **(a)** RWS contours as in figure II.3.1(c,d). Mean RWS (Taylor's hypothesis) and Peak wave phase velocity (Dispersion equation) slopes as dash-dotted and dashed lines, respectively. **(b)** 1D frequency spectra as in figure II.3.2d. Observed 10-min spectra in light grey, the 3-hour average in black full lines, and the ESDU reference in black dashed lines.

If one considers instead the $k-w$ spectra from figure II.3.8, to be compared with Case 02a given at figure II.3.3b, the wave signature is noticeable with decreasing importance: Still distinguishable at Case 02.b (WA=-2.53 at II.3.8a), but not anymore at Case02.c (WA=-1.92 at II.3.8b). As the wave signature vanishes, so vanishes the spectral gap described in section II.3.3, which is not detected in figure II.3.8. The 2D spectra shown for Cases 02[b-c] in figure

II.3.8 agree well to the expected random sweeping [Wilczek and Narita, 2012] behavior .

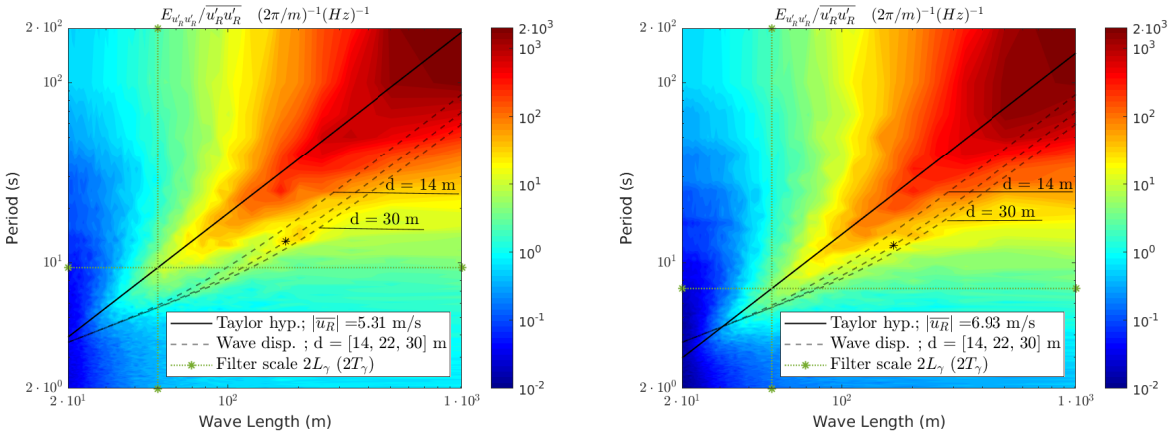

(a) Case 02.b

(b) Case 02.c

Figure II.3.8: Wave-number-angular-frequency 2D turbulent spectra of Cases 02[b-c]. To be compared with the spectrum of Case 02a previously shown at figure II.3.3b. The mean RWS velocity is depicted in the black full line, and the wave velocity presented in dashed lines for $d = [14, 22, 30]$ m. The wave peak scale (L_p, T_p) is denoted by a star. The sLiDAR filter characteristic period and wave length are given in the green dashed, horizontal and vertical lines, respectively.

As in Case 02a, Cases 02b and c also consider wind and waves traveling in opposite directions, and using the four quadrant 2D spectra the resultant spectra might be decomposed as previously exemplified in figure II.3.5. Again the WI flow is observed traveling from the Ocean to the sLiDAR, so that is the component depicted in the 2D spectra of figure II.3.9, for Case 02c. Thanks to the opposing directions, weak as it can be, the WI disturbance is still distinguishable at the lowest Wave Ages characterizing Case 02c.

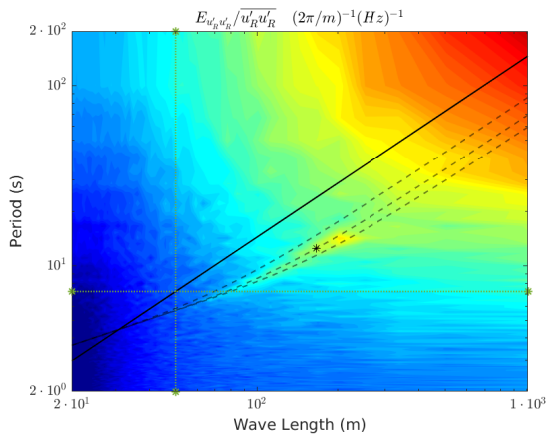

Figure II.3.9: Wave-number-angular-frequency 2D turbulent spectra for Case 02c, decomposed between opposite directions of propagation thanks to the four quadrant 2D spectra. Motions traveling from the Ocean to the sLiDAR are shown. The lines denote the characteristic scales described in figure II.3.8.

As the wave age decreases and the signature diminishes, the principal wave disturbance occurs in scales greater than the wave peak, i.e., $[L_p;\ T_p]$ from tab. II.1.2, indicated by the dots in figures II.3.8 and II.3.9: An indication of the scale-dependent energy transfer occurring between ocean waves and turbulent fluctuations, which favors the propagation of long waves across the WBL.

II.3.5 Overview and discussion

In swell dominated scenarios (Cases 01 and 02.a with higher $|WA_c|$) the Wave Induced (WI) disturbances are qualitatively appreciated in the RWS space-time contours at section II.3.1. The contours slope generally correspond to the Atmospheric (Atm.) and WI characteristic velocities, given respectively by the Taylor Frozen hypothesis and the wave dispersion equation. The exception occurs for Case 01, where the Atm. turbulence appears to propagate at lower velocities than the mean RWS.

In its discussion about the validity of the Taylor hypothesis in the lower part of the Atmospheric Boundary Layer (ABL), Cheng et al. [2017] associate an apparent slow down of turbulent eddies to their distortion and the consequent reduction of their life-time, which can be the case here. As seen in the 2D spectra of figure II.3.3, there is no Doppler shift in the Taylor hypothesis, meaning the overall expected convection velocity for the Atm. turbulence is still the mean RWS. Though, a spectral gap disturbance is particularly evident at Case 01 indicating that the turbulence advection velocity is often slower or faster than the expected. Moreover, the wind-wave interactions are significant in the virtually infinite fetch scenario, and the distortion of Atm. eddies by the WI motions is appreciated in the RWS contours of Case 01 at figures II.3.1a and II.3.1b. As in Cheng et al. [2017], the Taylor's hypothesis fails because turbulence is not frozen, which ultimately gives the impression of the turbulent eddies propagating with lower convection velocities.

The remarks about the RWS contours are consequence of the spectral distribution of the fluctuations, represented by the 1D and 2D turbulent spectra shown in sections II.3.2 and II.3.3, respectively. The 1D spectra analyses reveal the wave signature only in the frequency domain, with the WI spectral contribution becoming prominent in the 1D frequency spectra of figures II.3.2b and d. Contrary to the RWS contours, the frequency spectra allow a partial, but quantitative evaluation of the WI disturbance. The spectral transfer between sea-state and atmospheric motion is thus appreciated, as previously [Tamura et al., 2018] but not that often encountered in the literature [Hristov, 2018].

The Space-Time spectral description of the velocity fluctuations provides an enhanced perspective of the Atm. and WI motions. Contrary to the 1D spectra, the upward turbulent energy transfer from the waves to the wind is evident and well distinguishable from the atmospheric turbulence in the 2D spectra of fig. II.3.3. The 2D spectra reveal that Atm. and WI motions correlate differently (in terms of spectral coherence) in space and/or time domains, explaining the observations previously evaluated in the 1D spectra.

The decomposition between fluctuations traveling in opposite directions is available from the four quadrant 2D spectra as demonstrated in figure II.3.6. Such decomposition is particularly useful when wind and waves propagate in opposite directions, so the wave signature emerges even more clearly in the quadrants representing the 'Ocean to sLiDAR' direction, where the Atm. turbulence in turn is restricted to very large scales.

In decreasing $|WA_c|$ conditions (Section II.3.4), the signature vanishes from the RWS contours and from the 1D frequency spectra, but it's still noticeable in the 2D space-time spectra that are clearly a more sensitive tool to detect WI disturbances. Though observable, the wave signature is very weak in this diminishing WA scenario (Cases 02b,c), that can be taken as a reference to evaluate the WI disturbances previously noted for Case 02a.

The 2D spectra are in fact so sensitive, that it shall be actually hard to find measurements without any WI disturbance during the measurement campaign (October 2020 to January 2021, waves season at Le Croisic, France). The reason of multiple failed attempts (Hristov [2018]) to detect WI disturbances in the frequency 1D turbulent spectra is its partial perspective of modal energy distribution.

The characterization of measured WI motions is further presented in section IV.2.3, following its definition and methodology described in section IV.1. The numerical evaluation of the sLiDAR volume filter effect is evaluated in section IV.3, culminating in the comparison of physical and numerical experiments at section IV.3.5.

Part III

NUMERICAL MODEL DESCRIPTION, DEVELOPMENTS, AND APPLICATIONS

An adaption between: The Great Wave, by Katsushika Hokusai (1831); and The Starry Night, by Vincent van Gogh (1889).

The Marine Atmospheric Boundary Layer (MABL) is investigated with the Large Eddy Simulation (LES) solver developed by Peter Sullivan, from the National Center for Atmospheric Research (NCAR) of the United States of America. As discussed in section I.3.5, the LES is capable of resolving the most energetic scales of turbulence in the MABL, and Sullivan's solver admits the resolution to be achieved above moving waves.

The test cases here presented are built to investigate the WI disturbances above fast moving waves, propagating under comparatively slow wind conditions in a situation commonly described as old seas (see the beginning of section I.3). To focus in the WI disturbances, buoyancy and Coriolis forces are neglected, with the MABL assumed to be in neutral regime (see section I.2.2.2).

Note that the test cases and methodologies here explored follow from the contribution shared in Paskin et al. [2020], which is not plainly repeated hereby. Consulting that reference is not strictly required, because this manuscript shall recover the main elements of discussion, either confirming or complementing previous observations.

The numerical model is described in section III.1, concerning both the problem formulation and the strategy adopted for resolution and post-processing. Section III.2 recalls some of the observations in Paskin et al. [2020] to justify the introduction of a dynamic pressure gradient modeler, capable of achieving a constant average target velocity, at a certain boundary layer height. The dynamic modeler introduced is employed to achieve that goal in the applications that follow. Still in section III.2, one encounters a flat bottom application, and an introductory monochromatic wave application, the latest including a reference test case correspondent to the one presented in Paskin et al. [2020].

Introducing a monochromatic wave to the flat bottom cases presented in section III.2, section III.3 addresses the WI disturbances dependence to the Wave Age parameter. Single and multi-directional irregular sea-states are introduced in section III.4, to identify intrinsic differences between each wave prescription method, while approaching the sea-state and wind conditions observed during the physical experiment, described in section II.1.3 (wind following waves case).

The analyses here presented focus in averaged statistics, presented either as history profiles (function of time), or vertical profiles (function of height). Most of these test cases are revised with spectral analyses during sections IV.1 and IV.2, while also introducing an original characterization of the WI flow, valid for both physical and numerical experiments, and proposed as a major contribution amongst the current developments. The comparison between the numerical experiment of section III.4, and the physical experiment of section II.1.3, is considered at section IV.3.

III.1 Numerical problem formulation and strategy

Some crucial aspects of the numerical formulation employed are recalled in section III.1.1. Next, section III.1.2 presents the general strategies, adopted either in the solver, for the free-surface prescription, or the post-processing phases. The general aspects of the numerical strategy here discussed are common to every test case later presented, so the applications

sections shall only describe the specific aspects concerning each test case.

III.1.1 Problem formulation

A volume domain is defined in the atmosphere with sizes (x_l, y_l, z_l), bounded below at S_{z-} by the free-surface and above by the geostrophic layer at S_{z+}, as exemplified in figure III.1.1. Wind and waves are aligned and propagate in the longitudinal direction x. The coordinate system is specified so z points upwards and the origin is positioned in the inlet, at the mean water level, and such that $y \geq 0$. The domain is defined with dimensions x_l, y_l and z_l. A log-law based wall function mimics the no-slip boundary condition in the free surface S_{z-}, and a free-slip condition is imposed in the upper surface S_{z+} representing the free-stream.

The LES methodology introduced in section I.1.1.6 applies to the atmosphere, with governing equations derived from section I.1.2.2 and here given in section III.1.1.1, to be solved in a moving grid by the pseudo-spectral numerical method described in Sullivan et al. [2008].

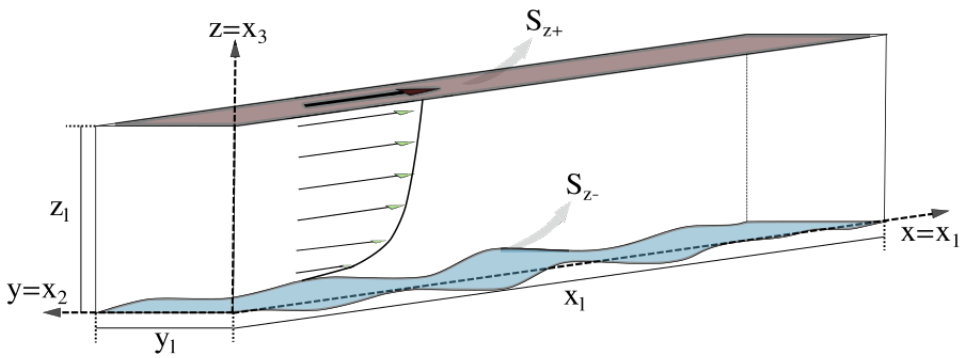

Figure III.1.1: Sketch indicating the Cartesian coordinates, wind and waves aligned to x_1, the volume domain bounded below by an arbitrary single-valued wave, and above by the free-stream velocity.

III.1.1.1 Governing equations and boundary conditions

Recalling the theoretical framework established in section I.1.2.2, an incompressible and fully turbulent flow is considered with the Boussinesq approximation [Spiegel and Veronis, 1960] acting in the buoyancy terms of the momentum and Turbulent Kinetic Energy conservation equations. Coriolis forces are neglected. The balance equations are filtered according to an LES approach. Let $\breve{\boldsymbol{u}}(\boldsymbol{x}, t) = (\breve{u}, \breve{v}, \breve{w})$, $\breve{p}(\boldsymbol{x}, t)$, and $\breve{\theta}$ be the spatially filtered, velocity, pressure, and virtual temperature fields, respectively; $\check{\boldsymbol{u}}$, $\check{p}$, and $\check{\theta}$ are the correspondent residual fields.

The modified pressure is $p'(\boldsymbol{x}, t) = \breve{p} - p_\infty + \overline{\rho} g(z - z_\infty) + (2\check{e}/3)$, accounting for a reference value p_∞; the static pressure $\overline{\rho} g(z - z_\infty)$ dependent on the total average specific mass ρ_∞, the gravitational acceleration g, and height $(z - z_\infty)$; and the residual turbulent kinetic energy $(\check{e} = \check{u}_i \check{u}_i / 2)$ effect. The specific mass is $\rho'(\boldsymbol{x}, t) = -\rho_\infty \beta_\theta (\breve{\theta} - \theta_\infty)$, dependent on the filtered virtual temperature $\breve{\theta}$, the reference values $[p_\infty, \theta_\infty]$, and the coefficient of thermal

expansion β_θ. The filtered strain rate tensor is $\breve{\boldsymbol{S}} = \left[\nabla\breve{\boldsymbol{u}} + (\nabla\breve{\boldsymbol{u}})^T\right]/2$. The sub-grid-scale modeled shear stress tensor $\boldsymbol{\tau}^{SGS} = -2\nu_t\breve{\boldsymbol{S}}$ is defined within the eddy viscosity hypothesis scope and dependent on the turbulent viscosity ν_t.

Mass and momentum balances are written as equations III.1.1 and III.1.2. The residual turbulent kinetic energy is modeled by the Deardorff single equation III.1.3 [Moeng, 1984].

$$\frac{\partial \breve{u}_j}{\partial x_j} = 0, \tag{III.1.1}$$

$$\frac{\partial \breve{u}_i}{\partial t} + \frac{\partial(\breve{u}_j\breve{u}_i)}{\partial x_j} = -\frac{1}{\rho_\infty}\frac{\partial p'}{\partial x_i} - \frac{\partial \tau_{ij}^{SGS}}{\partial x_j} - \frac{\rho'}{\rho_\infty}g\delta_{i3}, \quad \text{and} \tag{III.1.2}$$

$$\frac{\partial \breve{e}}{\partial t} + \frac{\partial(\breve{u}_i\breve{e})}{\partial x_i} = (2\nu_t\breve{S}_{ij})\breve{S}_{ij} - \frac{g}{\theta_\infty}\nu_h\frac{\partial\breve{\theta}}{\partial x_3} + \frac{\partial}{\partial x_j}\left(2\nu_t\frac{\partial\breve{e}}{\partial x_j}\right) - \epsilon. \tag{III.1.3}$$

The turbulent dissipation $\epsilon = c_\epsilon\breve{e}^{3/2}/\Delta_f$ is determined according to the filter length scale $\Delta_f = [(3/2)^2\Delta x_1\Delta x_2\Delta x_3]^{1/3}$. The turbulent kinematic viscosity and diffusivity are respectively $\nu_t = c_k l\breve{e}^{1/2}$ and $\nu_h = (1+2l/\Delta_f)\nu_t$, where l is here equal to Δ_f. The governing equations are transformed from the deformed moving grid into the cartesian numerical space and the full set of equations presented with the constants values, e.g., in Sullivan et al. [2008].

The Geometrical Conservation Law (GCL) introduced by Thomas and Lombard [1979] and described in the appendix A.4.3, reads according to equation A.21, repeated in equation III.1.4:

$$\frac{\partial}{\partial t}\left(\frac{1}{J}\right) = \frac{\partial}{\partial \xi_3}\left(\frac{\partial h}{\partial t}\right), \tag{III.1.4}$$

relating the grid Jacobian J to its vertical position h, for the specific surface following coordinates defined in section III.1.1.2.

Consistent with the spectral discretization adopted, periodic boundary conditions apply to the transversal and longitudinal boundaries, $S_{y\pm}$ and $S_{x\pm}$. The boundary conditions at the upper S_{z+} and lower S_{z-} boundaries are described as follow.

Upper boundary conditions The geostrophic layer is represented by no-penetration and free-slip Boundary Conditions (BCs). These upper BCs in the absence of buoyant forces impose the boundary layer height $\delta \sim z_l$.

- *No-penetration:* The vertical velocities are null (Homogeneous Dirichlet BC for $\breve{u}_3$).
- *Free-slip:* Except for $\breve{u}_3$, all fluxes are null (Homogeneous Neumann BC for $\breve{u}_1$, $\breve{u}_2$, $\breve{\theta}$,$\breve{e}$).

$$\frac{\partial \breve{\theta}}{\partial x_3} = 0, \quad \frac{\partial \breve{e}}{\partial x_3} = 0, \quad \frac{\partial \breve{u}_1}{\partial x_3} = 0, \quad \frac{\partial \breve{u}_2}{\partial x_3} = 0, \quad \text{and} \quad \breve{u}_3 = 0, \quad \text{at} \quad S_{z+}. \tag{III.1.5}$$

Lower boundary condition The free-surface dynamics may be imposed with an arbitrary single-valued function $z = \eta(x, y, t)$, as long as it is consistent with the framework presented in I.1.2.1, and the alternatives exploited are described in section III.1.2.2. As common in fully turbulent atmospheric applications, the lower boundary conditions follow a log-law wall model.

The difference in the tangential and normal velocities ($\Delta \breve{u}_{[\xi_1,\xi_2]}$ and $\Delta \breve{u}_{\xi_3}$, respectively), between the first cell and the surface, are given by a log-law wall-function:

$$\begin{aligned} \Delta \breve{u}_{[\xi_1,\xi_2]} &= \frac{u^*_{[\xi_1,\xi_2]}}{\kappa} \ln\left(\frac{z}{z_0}\right), \qquad \text{and} \\ \Delta \breve{u}_{\xi_3} &= 0, \end{aligned} \tag{III.1.6}$$

with the normalized roughness length $z_0/L_0 = 10^{-6}$ and von Karman constant $\kappa = 0.4$.

The tangential velocities are not imposed directly as a Dirichlet BC from equation III.1.6. Instead $\Delta \breve{u}_{[\xi_1,\xi_2]}$ is computed from the resolved LES field, minus the prescribed surface velocities, and equation III.1.6 is used to obtain the friction velocity $u^*_{[\xi_1,\xi_2]}$. That gives the wall fluxes $\tau^w_{[\xi_1,\xi_2]} = u^{*2}_{[\xi_1,\xi_2]}$, specifying a Robin type of BC for the tangential velocities.

The residual turbulent kinetic energy flux is null (Homogeneous Neumann BC), and the turbulent kinematic viscosity is given by $\nu_t = u^* \kappa x_3$. The temperature θ can be specified either by its surface value or heat flux (Dirichlet or Neumann BC). When the heat flux is non-null, equation III.1.6 is adapted by employing MOST (See I.2.2.3 for MOST, and Sullivan et al. [2014] for more details about the buoyancy-driven BC).

III.1.1.2 Discretization

The Cartesian physical space $(x_1, x_2, x_3) = (x, y, z)$ is mapped into the computational terrain following space, defined from $\xi_1 = x$, $\xi_2 = y$, and $\xi_3 = \xi_3(x, y, z, t)$. The Jacobian of such transformation is given by $J = \partial\xi_3/\partial z$. The fundamental unknowns $(u,\ p,\ e,\ \theta)$ are located at the cell center. The mass equation III.1.1 and the convective term of the momentum equations III.1.2 are written in terms of the 'contra-variant flux' velocities:

$$\hat{U}_i = \frac{u_j}{J} \frac{\partial \xi_i}{\partial x_j}, \tag{III.1.7}$$

to circumvent to saddle point problem of the Navier Stokes equations, as further discussed with the Poisson equation in section III.1.1.3.

The grid is structured. The domain is discretized with (n_x, n_y, n_z) cells sized $(\Delta x, \Delta y, \Delta z)$ respectively. The cells are equally distributed in (x, y), but not in z where it grows according

to an algebraic mapping: The first grid size in z direction is z_{w1}, and it grows with a constant ratio of 1.05. More details are given in section III.1.2.1.

The spectral discretization applies to (ξ_1, ξ_2) directions, in which the unknowns are represented with Fourier transforms and the derivatives evaluated in the spectral wave-number domain $(k_{\xi 1}, k_{\xi 2})$. A second order finite difference applies to ξ_3 direction.

The third-order Runge-Kutta time-stepping scheme described in the appendix A.4.4 admits arbitrarily selected time-steps. An adaptive time step (Δt) procedure is available so that the CFL $= \Delta t \cdot \max(u/\Delta x, v/\Delta y, w/\Delta z)$ is kept constant. Thanks to the explicit time-marching scheme, the first disturbance induced by non-sufficiently small time-steps appears in the maximum divergent of the velocity field $\nabla \cdot \mathbf{u}$, which is required to be below $10^{-21}\ u_0^*/L_0$ for any case here presented. .

III.1.1.3 The role of pressure

Large scale pressure driven flow A uniform pressure gradient $[\partial p/\partial x]_0$ acts in x direction driving the flow, and in flat terrains the stresses' integral balance in the boundaries gives the theoretical friction velocity $u_0^* = [\partial p/\partial x]_0 \cdot z_l$. The uniform pressure gradient is revisited in section III.2 with the introduction of an original dynamically evolving but homogeneous $[\partial p/\partial x]_0$ modeler.

Pressure Poisson equation As usual the mass conservation equation III.1.1 is here enforced by a Poisson equation, such as equation A.18 discussed in the appendix A.4.1. Solved for the pressure field, the Poisson equation is somehow coupled to the momentum equations III.1.2 solved for the velocity field. Now due to the saddle point problem introduced in section I.1.1.1, the exact manner in which the terms are specified and computed in equation A.18, together with the specific discretization and time-marching techniques adopted, determine the behavior of the numerical solution of the Navier Stokes equations.

It is so that the pressure Poisson equation specification and solution, is a crucial aspect determining the specifics of a numerical scheme, and Sullivan et al. [2014] describes the one here employed as the heart of present numerical scheme. One is invited to appreciate the exact form of equation A.18, and a detailed description of its solution method in Sullivan et al. [2014], as the following highlights only a few aspects of that numerical scheme. Notably both pressure and velocity unknowns are positioned in the cell center, but the contra-variant velocities (Equation III.1.7) that determine $\mathscr{R}^{[P]}(\hat{\boldsymbol{U}})$ are considered otherwise to circumvent the saddle point problem: The discretization scheme allows $\hat{U}_1$ and $\hat{U}_2$ to be located at the cell center, while $\hat{U}_3$ is located at the cell upper face. In flat bottom cases equation A.18 assumes a simple form and is directly solved for, but in the terrain following grid it gets considerably more complex, and an iterative method is adopted for the solution of the pressure Poisson equation that considerably increases the overall computational time.

Pressure form drag and momentum flux Recall that in equation I.3.2 the Wave Induced shear stress $\tau_{ij}^{(W)}$ is introduced, and in equation I.3.5 a surface-following coordinate system leads to the appearance of the form drag (or thrust) $\tau_{ij}^{(P0)}$. The total momentum flux $\partial \tau_{ij}/\partial x_j$

also considers viscous $\tau_{ij}^{(v)}$ and turbulent $\tau_{ij}^{(r)}$ contributions, so in the surface equation I.3.5 (repeated below) is exact:

$$u^{*2} = \left[\tau_{ij}^{(v)} - \tau_{ij}^{(r)} - \tau_{ij}^{(W)} + \tau_{ij}^{(P0)}\right], \qquad \text{with} \qquad \tau_{ij}^{(P0)} = \frac{1}{\rho}\overline{p\frac{\partial \eta}{\partial x_i}}. \tag{III.1.8}$$

Above the free-surface, the grid may be arbitrarily defined with vertical position $h = \xi_3(x, y, z, t)$, and so the WI pressure stress is given by:

$$\tau_{ij}^{(P)} = \frac{1}{\rho}\overline{p\frac{\partial \xi_3}{\partial x_i}}. \tag{III.1.9}$$

Equation III.1.9 defines a fictitious (Grid dependent) pressure and wave related momentum flux $\partial\tau_{ij}^{(P)}/\partial\xi_3$ acting between layers of constant ξ_3, that vanishes when the problem is written in Cartesian coordinates such as, e.g. in equation I.3.2. Nevertheless, it reveals a physical mechanism over which the pressure acts into the wave disturbed streamlines, effectively dragging the atmospheric flow as discussed in I.3. In the lower surface the grid matches the free-surface deformation, and so the WI pressure stress given by equation III.1.9 is exact and equal to the form drag in equation III.1.8.

III.1.1.4 Turbulent Kinetic Energy budget

Recall from section I.1.1.4 that the TKE transport equation I.1.9 reveal the production (P), the dissipation (ϵ_e) and fluxes ($T^{(r)}$) terms, defined in equation I.1.10. In the LES formulation the TKE is decomposed in filtered ($\breve{e}$) and residual ($\check{e}$) components, with the residual modeled by the Deardorff single equation III.1.3. The TKE budget decomposes accordingly, and the following equations give the explicit form of resolved and modeled terms, to be exploited in the next sections.

Consistent with a fully turbulent assumption where $Re \to \infty$, the molecular dissipation is neglected in the resolved TKE equation, being exclusively modeled according to $\epsilon = c_\epsilon \check{e}^{3/2}/\Delta_f$ (see section III.1.1.1). In the resolved TKE equations the viscous transport is also neglected, so it remains the triple correlation $\breve{T}^{(u)}$ and pressure terms $\breve{T}^{(p)}$ forming the total TKE resolved transport $\breve{T}^{(r)} = \breve{T}^{(u)} + \breve{T}^{(p)}$. In the residual TKE equation the transport terms are gathered in SGS modeled turbulent transport $\check{T}^{(r)}$. Production contains filtered $\breve{P}$ and sub-grid-scale $\check{P}$ terms. Buoyancy terms are not exploited during the manuscript, and so omitted in the discussion.

The Reynolds average employed in the TKE conservation equation I.1.9 ($\bar{\cdot}$) is here regarded as space averages in the horizontal domain, so giving the vertical dependence of the TKE budget described [Moeng and Sullivan, 1994]. Production and transport terms of the resolved TKE budget are computed as:

$$\breve{P}(z) = -\left[\overline{(\breve{u}_1'\,\breve{u}_3')}\,\frac{\partial\overline{\breve{u}_1}}{\partial x_3} + \overline{(\breve{u}_2'\,\breve{u}_3')}\,\frac{\partial\overline{\breve{u}_2}}{\partial x_3}\right],$$

$$\frac{\partial\breve{T}^{(u)}(z)}{\partial x_3} = \frac{\partial}{\partial x_3}\left[\overline{\breve{u}_3'\breve{e}}\right], \qquad \text{and} \qquad \frac{\partial\breve{T}^{(p)}(z)}{\partial x_3} = \frac{\partial}{\partial x_3}\left[\frac{\overline{\breve{u}_3'\breve{p}'}}{\rho_\infty}\right]. \tag{III.1.10}$$

The sub-grid-scale contributions are:

$$\check{P}(z) = 2\nu_t\left[\frac{\partial\overline{\breve{u}_1}}{\partial x_3}\frac{\partial\overline{\breve{u}_1}}{\partial x_3} + \frac{\partial\overline{\breve{u}_2}}{\partial x_3}\frac{\partial\overline{\breve{u}_2}}{\partial x_3}\right], \qquad \text{and} \qquad \frac{\partial\check{T}^{(r)}(z)}{\partial x_3} = \frac{\partial}{\partial x_3}\overline{\left[2\nu_t\frac{\partial\check{e}}{\partial x_3}\right]}, \tag{III.1.11}$$

with modeled viscous dissipation:

$$\epsilon = c_\epsilon\check{e}^{3/2}/\Delta_f. \tag{III.1.12}$$

III.1.2 General numerical strategy

III.1.2.1 Solver setup

Recall from section III.1.1.2 that the cells (sizes $\Delta x = \Delta z$) are equally distributed in (x, y) but not in z where it grows according to an algebraic mapping $\Delta z_{i+1} = 1.05\cdot\Delta z_i$. The first grid size in z direction is z_{w1}, and its aspect ratio (AR=$z_{w1}/\Delta x$) is set constant and equal to 1/3, as e.g., in Sullivan et al. [2014] and Cathelain [2017].

Given the characteristic length L_0, the presented domain has sizes $(x_l, y_l, z_l) = (4, 2, 5)L_0$. Three different grids are here exploited, with characteristics given in III.1.1. These configurations follow the studies presented in Cathelain [2017], where one encounter systematic studies varying the grid sizes and the domain vertical extension z_l.

Table III.1.1: Description of the structured grids employed. The domain is discretized with $n_{\text{total}} = n_x\, n_y\, n_z$ cells. The aspect ratio at the first grid is kept constant $z_{w1}/\Delta x = 1/3$.

Grid	$\mathbf{n}_{total}$	$\mathbf{n}_x$	$\mathbf{n}_y$	$\mathbf{n}_z$	$\mathbf{z}_{w1}/L_0$
01 (Coarse)	655,360	128	64	66	$1.0416\cdot10^{-2}$
02 (Medium)	3,080,192	256	128	80	$0.5208\cdot10^{-2}$
03 (Fine)	14,155,776	512	256	94	$0.2604\cdot10^{-2}$

For example, assuming the kinematic viscosity of air at 15 °C ($\nu = 1.5 * 10^{-5}$ m^2/s), when employing the grid 02 with WA= 60 in sections III.2 and III.3, if $L_0 = \lambda = 100$ m ($u^* = 0.210$ m/s), then $z^+ = z_{w1}u^*/\nu = 7.3\cdot10^3$. When employing the grid 03 with WA= 85 in section III.4, if $L_0 = 2\,\lambda = 256$ m ($u^* = 0.147$ m/s), then $z^+ = z_{w1}u^*/\nu = 3.3\cdot10^3$.

The cases here presented have been tested in each grid of table III.1.1, and the grids further exploited during very large computations are assumed sufficient to present minimal influence on the second order statistics discussed. An exemplification of grid 02 (table III.1.1) is given at figure III.1.2, fitted to a monochromatic wave prescribed as the lower boundary condition.

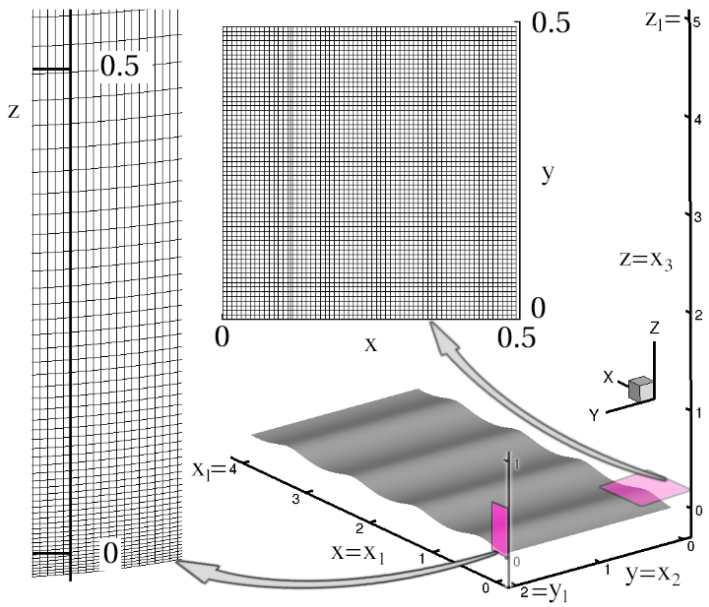

Figure III.1.2: Exemplification of grid 02 (Medium in table III.1.1). From the computation exploited in sections III.2 and III.3 regarding a monochromatic wave prescription.

A uniform pressure gradient $[\partial p/\partial x]_0$ acts in x direction driving the flow, and in flat terrains the stresses' integral balance in the boundaries gives the theoretical friction velocity $u_0^* = [\partial p/\partial x]_0 \cdot z_l$. The uniform pressure gradient is revisited in section III.2 with the introduction of an original dynamically evolving but homogeneous $[\partial p/\partial x]_0$ modeler.

Originally the flow field is constructed from mean theoretical solution for flat plate turbulent boundary layers superposed to artificial, randomly generated turbulent motions. The initialization procedure then considers buoyant effects on the momentum equations to generate resolved turbulence as further initial solution. The results here presented follow from a converged restart after buoyant terms are set back to zero, representing neutral stratification conditions.

III.1.2.2 Water surface prescription

The LES formulation accommodates an arbitrary free-surface (FS) prescription, as long as it is defined by a single-valued function in space. Three methodologies are here explored to generate the wave field prescribed into the LES computation:

i. **Non-linear monochromatic wave**: A monochromatic wave is prescribed from the fifth order Stokes solution given in Fenton [1985], as introduced in section A.1.1.

ii. **Linear Irregular Sea-Sate**: A two dimensional dependent FS spectra $F(k_x, k_y)$ is given. Linear waves components with amplitudes given by the FS spectra (see section I.2.1.1) are initially generated with random phases, afterwards propagating with their phase velocities.

iii. **Arbitrarily non-linear, HOS resolved sea-state**: The free-surface positions and velocities are solved with an arbitrarily level of non-linearity by the HOS formulation (Ducrozet et al. [2016]), and that's coupled to the LES such as described in the appendix B.2.

III.1.2.3 POST-PROCESSING

Mean history and vertical profiles A spatial average, denoted by $(\bar{\cdot}^{[\xi_1,\xi_2]})$, applies to each (ξ_1, ξ_2) horizontal computational plane, and is followed by a moving time average through the period t_{avg}, with the total average operator denoted by $(\bar{\cdot})$.

Fluctuations $(\cdot')$ are obtained deducing spatial averages from the resolved fields, so that a generic quantity decomposes as $\chi = \overline{\chi}^{[\xi_1,\xi_2]} + \chi'$. The fluctuations are then submitted to the moving time average, leading to the total average of turbulent quantities.

Turbulent quantities Unless stated contrary during the text, the turbulent quantities are a sum of resolved and SGS modeled quantities. The turbulent quantities further explored in the numerical applications are:

- Friction velocity $u^*_{[\xi_1,\xi_2]} = \sqrt{\tau^{w}_{[\xi_1,\xi_2]}}$;
- Turbulent Kinetic Energy $\text{TKE} = 0.5\overline{u'_i u'_i} + \overline{\check{e}}$;
- Turbulent Normal stresses, or one-point Auto-correlations $\tau^{(r)}_{ii} = \overline{u'_i u'_i} + 2\overline{\check{e}}/3$;
- Turbulent Shear stresses, or one-point Cross-correlations $\tau^{(r)}_{ij} = (\overline{u'_i u'_j} + \tau^{SGS}_{ij})\,(1 - \delta_{ij})$;
- Turbulence Intensity $\text{TI}_{ii} = \sqrt{\tau^{(r)}_{ii} \div \overline{u_1}^2}$;
- Turbulent kinematic viscosity $\nu_t = -(\tau^{SGS}_{13} + \overline{u'_1 u'_3}) \div (2S_{13})$.
- Wave Induced pressure stress $\tau^{(P)}_{ij} = \overline{(p + 2\check{e}/3) \cdot (\partial\xi_3/\partial x_i)}$.
- Form drag (Or thrust, per m^2 and ρ_∞) $F_p = \overline{(p + 2\overline{e}/3) \cdot (\partial\eta/\partial x_1)} = \tau^{(P0)}_{13}$.
- Total drag (Or thrust, per m^2 and ρ_∞) $F_\tau = F_p + u^{*2}$.

Turbulent spectra The 1D Correlation functions are averaged on each (ξ_1, ξ_2) directions along a horizontal computational plane; while the 2D (Space-Time) correlation functions are averaged in (ξ_1, ξ_2), and time t. The turbulent spectra are then obtained through the FFT of the Correlation functions (see section I.1.1.5), before being (possibly) submitted to a moving time average with period t_{avg}.

Reference Wind Speed profile and turbulent spectra The references are chosen from the ESDU standard ESDU 85020, because it provides accurate empirical models for the mean wind profiles and turbulent spectra descriptions in neutral stratification and flat bottom conditions, as demonstrated e.g. in Paskin et al. [2020], and here at figure III.2.1. The mean wind $\overline{u_1}(z)$ is accurately defined across all the ABL extension, and the turbulent spectra $E(n)$ through a wide range of turbulent frequencies n before the kolmogorov dissipative range. According to the ESDU 85020 parametrization, the boundary layer height δ and the friction velocity u^* relate to the Coriolis parameter f_3 through $f_3 = u^*/[6\delta]$. With the roughness length z_0, that's sufficient to define the Wind Speed:

$$\overline{u_1}(z) = 2.5\ u^* \left[\ln\left(\frac{z}{z_0}\right) + 34.5\ f_3\ \frac{z}{u^*} \right]. \tag{III.1.13}$$

The ESDU norm also gives equations for the one-point auto-correlations of the longitudinal velocity $\sigma^2_{u_1' u_1'} = \overline{u_1' u_1'}$ and the integral length scale l_u, but to avoid combining the errors regarding different estimations, these are directly deduced from the resolved spectra. From the first element of the auto-correlation function of longitudinal velocities one obtains $\sigma^2_{u_1' u_1'} = R_{u_1' u_1'}(0)$. The integral length scale is computed from the wave-number dependent turbulent spectra with $l_u = \pi E_{u_1' u_1'}(k=0)/[2R_{u_1' u_1'}(k=0)]$ (Pope [2000]). The mean velocity $\overline{u_1}$ is also as observed from the space and/or time samples, leading to the wave-number and/or frequency spectra by Taylor hypothesis (see section I.1.1.5). The non-dimensional frequency is defined as $n_u = (l_u n/\overline{u_1})$, and the longitudinal frequency-dependent turbulent spectra (Appendix B in ESDU 85020) are given by:

$$E_{u_1' u_1'}(n) = \frac{\sigma^2_{u_1' u_1'}}{n} \left\{ \beta_1 \frac{2.987\ n_u/\alpha}{\left[1 + (2\,\pi\ n_u/\alpha)^2\right]^{5/6}} + \beta_2\ F_1 \frac{1.294\ n_u/\alpha}{\left[1 + (\pi\ n_u/\alpha)^2\right]^{5/6}} \right\}; \qquad \text{with} \tag{III.1.14}$$

$$\begin{aligned}
F_1 &= 1 + 0.455\ \exp\left[-0.76\ (n_u/\alpha)^{-0.8}\right], \\
\alpha &= 0.535 + 2.76\ (0.138 - A)^{0.68}, \\
\beta_1 &= 2.357\ \alpha - 0.761, \\
\beta_2 &= 1 - \beta_1, \qquad \text{and} \\
A &= 0.115\ (1 + 0.3151\ (1 - z/z_l)^6)^{2/3}.
\end{aligned}$$

Wind profile structure and log-law fit. The resolved wind profiles reveal different regions in the MABL, depicted at figure III.1.3 further obtained and discussed in section III.2.4: In the inner surface layer, turbulence is blocked by the surface, exhibits an isotropic behavior,

and the SGS modeled stresses are significant; in the outer surface region highly anisotropic turbulence dominate the shear flow, the SGS stresses become negligible face to the LES resolved turbulence, and the longitudinal velocity is given by a log-law profile; this so called logarithmic region is observed above a buffer region, and below the outer region; in the outer region the flow adapts to the free-stream condition, turbulence vanishes, and the velocity profiles exhibit an almost linear behavior. The buffer region is here induced by the transition between the wall function model and the full LES resolved turbulence: It does not corresponds to the physical buffer region, characteristic to the flat plate boundary layer solution (appendix A.1.2), and existent between the inner viscous layer and the log-law boundary condition, i.e., below the first cell layer in figure III.1.3.

Introducing the effective friction velocity $C_d u^*$ and roughness length αz_0, the log fit of equation III.1.15 with parameters $[C_d, \alpha]$, is fitted into the wind profile minimizing the RMS difference RMS_{diff} (equation III.1.16) at an arbitrarily region $z_{min} < z < z_{max}$. Depending on the application, one of the parameters between C_d or α might be set constant. The fitting algorithm acts in the log-linear space $\ln(z) \times u_{FIT}$, that leads in fact to a linear optimization problem, solved by a Gauss-Newton algorithm.

$$u_{FIT} = C_d \frac{u^*}{\kappa} \ln\left(\frac{z}{\alpha\, z0}\right) \tag{III.1.15}$$

$$RMS_{diff} = \sqrt{\frac{1}{n}\sum_{n}\left[\frac{(u_{FIT}-u)^2}{u^2}\right]}, \quad \forall \quad \{n \mid z_{min} \le z_n \le z_{max}\} \tag{III.1.16}$$

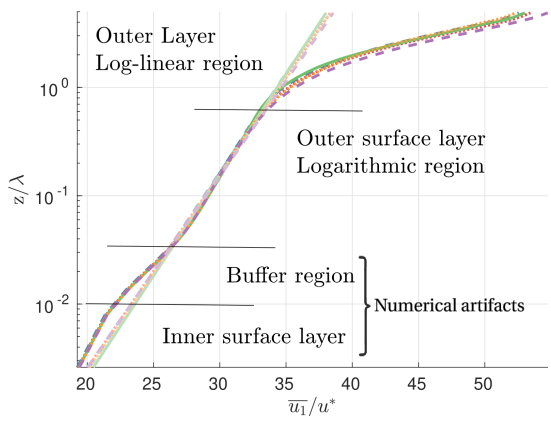

Figure III.1.3: Wind profile obtained and discussed at section III.2.4 (figure III.2.8b) for different flat bottom cases, depicted in linear-log scale revealing different regions inside the ABL. Log-law fitting by equation III.1.15 denoted by straight, transparent lines.

This fitting is embedded in an adaptive procedure determining the log-law region at $z_{min} \le z \le z_{max}$. Starting from a certain height z_s, and given the threshold RMS_c for the maximum allowed RMS_{diff}, the lower (z_{min}) and upper (z_{max}) limits advance while $RMS_{diff} < RMS_c$. The log-law region is so defined as the most extensive portion of the ABL around z_s, in which the log fitting error is below the threshold RMS_c.

III.2 Dynamically evolving pressure-gradients

In the numerical formulation, the flow is driven by the longitudinal large scale pressure gradient $\partial p/\partial x|_0$, that have been considered constant in Sullivan et al. [2014], Cathelain [2017], and Paskin et al. [2020]. The physical interpretation of such driving force is to mimic large scale forcing in the ABL, and in a wider context similar body forces may incorporate Coriolis effects (c.f. Basu et al. [2008]) here neglected. There is no physical reason for $\partial p/\partial x|_0$ to be constant though. Instead, the large-scale pressure gradient varies in scales much larger than the computational domain, and so not resolved by the numerical model.

Although there is no precise information leading to the prescription of $\partial p/\partial x|_0$ in the numerical model, it can be defined such that both $\partial p/\partial x|_0$, and the driven wind behave with certain properties. By the definition here proposed: Inside the numerical domain $\partial p/\partial x|_0$ shall be indeed homogeneous, but in time this homogeneous pressure gradient can well vary in periods much longer than the resolved motions. As consequence, one can achieve an average target velocity at a certain height in the ABL.

A discussion about large scale pressure gradients acting in LES generated ABL is appreciated in Pimont et al. [2020], that notes adaptive pressure-gradient forcing methods can be used to achieve certain wind speeds and directions in LES models. Counting on LiDAR measurements above the ABL, Pedersen et al. [2013] improve its LES simulation accuracy through the prescription of a linear time-varying and homogeneous pressure-gradient. The body forces driving the wind might also be considered height-dependent [Basu et al., 2008], which is not explored hereby. In any case, none of these previous studies consider wavy bottom boundary conditions, nor the resolution of Wind-Wave interactions.

The developments here proposed have been motivated by previous studies discussed in section III.2.1. The fundamental role of the large-scale pressure is examined in section III.2.2. The method developed to control the mean Wind Speed with a dynamic homogeneous but slowly evolving large-scale pressure gradient is presented in section III.2.3, and initially evaluated at section III.2.4 in a flat bottom scenario. In section III.2.5 the method is evaluated for its impact in the wavy bottom case previously presented in Paskin et al. [2020]

III.2.1 Preliminary studies and motivation

Past works (Paskin et al. [2020], exemplified by figure III.2.1) considered old-sea conditions imposing a 5th order stokes solution in the free-surface, and noticed the strong momentum flux to the atmosphere results in the speed-up of longitudinal velocities all along the MABL and up to the upper boundary: An unlikely behavior in the free-stream velocity above the MABL. Figure III.2.1a shows the friction velocity history, for the flat and wavy lower Boundary Conditions (BC) presented in Paskin et al. [2020]. The mean wind profiles probed in the final moments of the history depicted, are shown in figure III.2.1b, superposed to the ESDU standard ESDU 85020 described in section III.1.2.3. The wind profiles are a linear combination of log and linear functions, which match quite accurately the ESDU prediction for the flat bottom case. Otherwise, the wave propagation effectively drags and speeds-up the mean wind across the ABL, and the wind velocity is considerably augmented for the wavy case in figure III.2.1b.

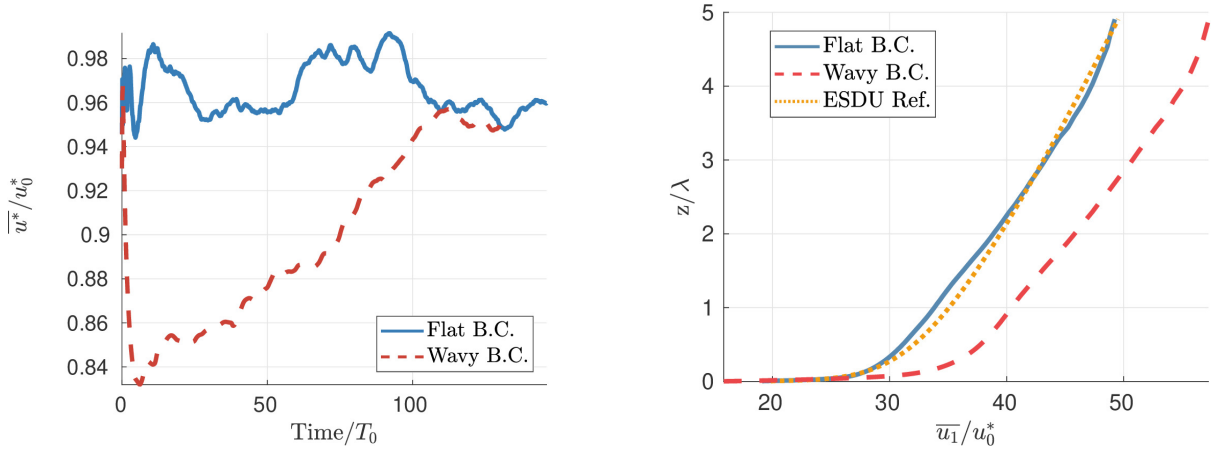

(a) Friction velocity.

(b) Wind speed profile, with the ESDU reference.

Figure III.2.1: From Paskin et al. [2020]. Friction velocity history and velocity profiles for flat and wavy, lower BCs. The reference wind profile is described in III.1.2.3 as given by ESDU 85020.

The free-stream disturbance in the upper boundary is consequence of the numerical problem formulation. The imposed constant pressure gradient shall combine with the case dependent WI momentum stresses, and with free-slip zero-gradient conditions in the upper boundary, so the Wind Speed profile is allowed to vary across the vertical extension of the MABL. The use of no-slip, Dirichlet conditions in the upper boundary is often adopted by URANS methodologies (c.f. O'Sullivan et al. [2011]). The turbulence modeling of URANS is consistent with the dirichlet conditions in the upper boundary, but in the LES resolved turbulence framework, unless the domain vertical extension is sufficiently large, this induces the development of a second non-physical boundary layer in the free-stream. The vertical extension of the domain will be hardly large enough in old-seas conditions, since Wave Induced pressure disturbances are observed to propagate all the way to the upper boundary (Cathelain [2017]) in the LES generated MABL.

Other, preliminary studies examined the effects of no-slip conditions imposed for u_1 in the upper boundary. The results are exemplified for null Dirichlet conditions in figure III.2.2, where the friction velocity and mean velocity profile are shown for three cases: Null Dirichlet upper B.C. (Fix Up) of $\overline{u}$ with flat lower B.C. in blue (full) line; Null Neumann upper B.C. (Free Slip Up) of $\overline{u}$ with wavy lower B.C. in orange (dotted line); Null Dirichlet upper B.C. (Fix Up) of $\overline{u}$ with wavy lower B.C. in gold (dashed line). The numerical strategy and setup are such as given in Paskin et al. [2020], except for: The Dirichlet Upper B.C. in Cases 01 and 03; the reduced mesh $[128 \times 64 \times 80]$; and the higher domain $[4 \times 2 \times 10]L_0$. As in Paskin et al. [2020], one observes the wind speed-up (figure III.2.2b) induced all the way through the ABL in the wave bottom (Wavy) Cases 02 and 03. When the upper velocity is kept constant in Case 02 (Fix Up Wavy), the speed-up still occurs just below, which induces a non-null velocity gradient profile as a second boundary layer develops in the upper boundary. The conclusions are the same when considering null Dirichlet and Newmann conditions combined, except that the upper boundary layer will occur one cell below.

The methodologies here presented instead, keep free-slip (Null Neumann) conditions as in Cathelain [2017] (And Paskin et al. [2020]), but search for a dynamic large-scale pressure

gradient $[\partial p/\partial x]_0$ that targets an average constant longitudinal velocity, e.g., in the upper boundary.

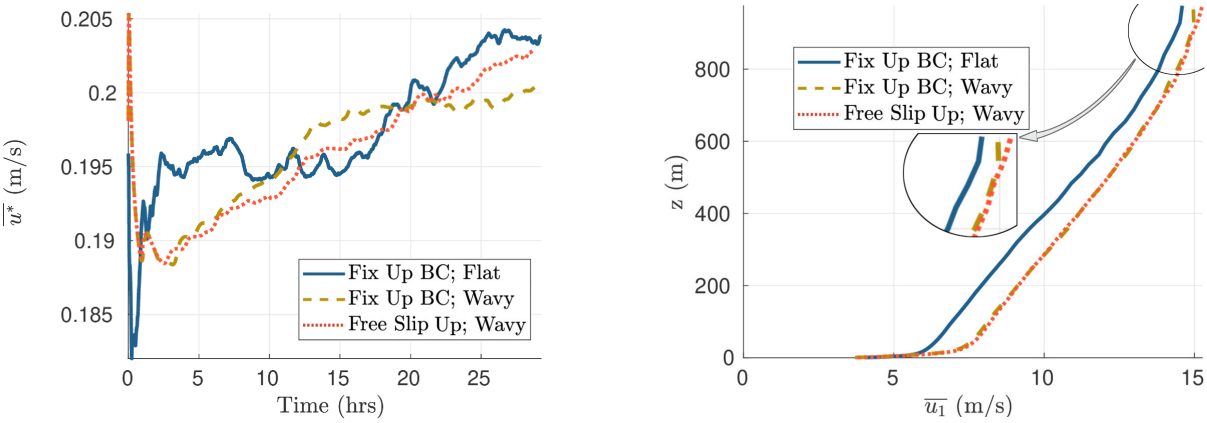

(a) Friction velocity.

(b) Wind Speed profile.

Figure III.2.2: Rejected studies of Dirichlet upper B.C.: Null Dirichlet upper B.C. (Fix Up) of $\overline{u}$ with Flat lower B.C. in blue full line; Null Newmann upper B.C. (Free Slip Up) of $\overline{u}$ with Wavy lower B.C. in orange dotted line; Null Dirichlet upper B.C. (Fix Up) of $\overline{u}$ with Wavy lower B.C. in gold dashed line. The Dirichlet upper condition combined with the Wavy lower surface induce a non-physical velocity gradient in the upper boundary.

III.2.2 THE ROLE OF LARGE-SCALE PRESSURE GRADIENTS

The large-scale $[\partial p/\partial x]_0$ drives the atmospheric flow. Considering the integral balance of longitudinal forces in a statistically steady, flat bottom case: In the upper boundary S_{z+}, free-slip condition imposes null longitudinal forces $\tau_h = 0$; for lateral walls ($S_{y\pm}$), the longitudinal forces vanish in the absence of a transversal pressure gradient $\tau_{lt} = 0$; on the inlet and outlet $S_{x\pm}$, the normal forces give $\tau_{in0} = -[\partial p/\partial x]_0 \cdot (x_l\ y_l\ z_l)$. With the definition of the friction velocity u^*, the tangential forces on the lower boundary integrates into $\tau_w = u^{*2} \cdot (x_l\ y_l)$. The integral balance becomes $\tau_{in0} + \tau_{lt} = 0$, so that $u^{*2} = [\partial p/\partial x]_0 \cdot z_l$.

When a wave suddenly appears, a pressure-related momentum flux occurs between the water surface and the atmosphere, originated from the WI pressure stress τ^P (Or form drag F_p) discussed in sections I.3 and III.1.1.3. First statistical steadiness is lost, while the ABL flow adapts to this changing forcing condition. When statistical steadiness is again reached, the mean velocity u_1 in the bottom is no longer null, but travels with a mean velocity characteristic to the ensemble of the sea-state's wave components, i.e., the stokes drift. The wave-related momentum flux is dominant in the vicinity of the free-surface and vanishes along the ABL, being balanced in the boundaries by a resolved Wave Induced pressure distribution $[\partial p_w(x,z)/\partial x]$ in inlet and outlet. The mean Wave Induced pressure $p_w(x,z)$ vanishes everywhere for its oscillatory nature, but its averaged integration in the inlet, outlet and free surface are non-null because of the moving domain.

III.2.3 A LARGE-SCALE DYNAMICALLY EVOLVING PRESSURE-GRADIENT MODELER.

Isolating the local time derivative in the first component (i=1) of equation III.1.2, and subtracting a constant (negative) longitudinal pressure gradient $-[\partial p/\partial x]_0$ from the right-hand-side $\mathscr{R}^{[P]}$, the large scale wind forcing is achieved in the LES formulation through the momentum balance equation:

$$\frac{\partial u_1}{\partial t} = \mathscr{R}^{[P]} + \left[\frac{\partial p}{\partial x}\right]_0, \tag{III.2.1}$$

which is evaluated at each time-step and Runge-Kutta iteration.

The evaluation of equation III.2.1 leads to a non-zero mean local time derivative on the upper boundary $\partial \overline{u}_{h0}/\partial t$, which could in a first step be corrected according to:

$$\begin{aligned} &\frac{\partial \overline{u}_h}{\partial t} = \frac{\partial \overline{u}_{h0}}{\partial t} + \left[\frac{\partial p}{\partial x}\right]_1, \qquad \text{which is required to be null so,} \\ &\left[\frac{\partial p}{\partial x}\right]_1 = -\frac{\partial \overline{u}_{h0}}{\partial t}, \qquad \text{and} \qquad \overbrace{\left[\frac{\partial p}{\partial x}\right]_0}^{\mathscr{P}} \rightarrow \left[\frac{\partial p}{\partial x}\right]_0 + \overbrace{\left[\frac{\partial p}{\partial x}\right]_1}^{d\mathscr{P}}. \end{aligned} \tag{III.2.2}$$

Through equation III.2.2, $\partial \overline{u}_h/\partial t$ is constant at every instant, and $\left[\partial p/\partial x\right]_0$ incorporates any turbulent disturbances in the upper boundary. This shall be avoided since $\left[\partial p/\partial x\right]_0$ by definition contains only large scale dynamics. Instead it is considered an evolution equation for $\left[\partial p/\partial x\right]_0$, in which it is dynamically filtered responding to the large scale part of equation III.2.2.

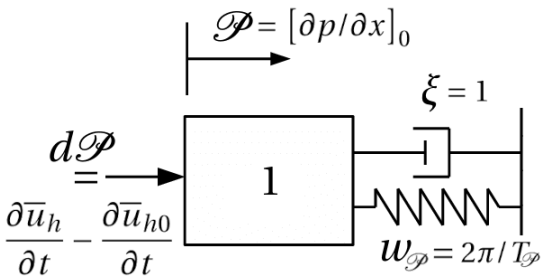

Figure III.2.3: The Mass-Spring-Damper system ruling the evolution of the longitudinal pressure gradient $\mathscr{P} = \left[\partial p/\partial x\right]_0$, according to equation III.2.3.

A Mass-Spring-Damper model, represented in figure III.2.3, determine the evolution of $\mathscr{P} = \left[\partial p/\partial x\right]_0$:

$$\ddot{\mathscr{P}} = -w_{\mathscr{P}}^2 \, d\mathscr{P} - 2\xi \, w_{\mathscr{P}} \, \dot{\mathscr{P}}, \tag{III.2.3}$$

advancing with the same Runge-Kutta scheme applied to other quantities in the LES code as described in the appendix A.4.4. The displacement from the equilibrium state is given by:

$$d\mathscr{P} = \left[\frac{\partial p}{\partial x}\right]_1 = \frac{\partial \overline{u}_h}{\partial t} - \frac{\partial \overline{u}_{h0}}{\partial t}, \qquad \text{and} \qquad \frac{\partial \overline{u}_{h0}}{\partial t} = \frac{\overline{u}_{ref} - \overline{u}_h}{T_{\mathscr{P}}}, \tag{III.2.4}$$

so seeking the equilibrium, $\overline{u}_h$ tends to the target $\overline{u}_{ref}$, over the time $T_{\mathscr{P}} = 2\pi / w_{\mathscr{P}}$. The response shall be limited to occur in large periods $T_{\mathscr{P}}$, and to preserve stability, a critical regime is imposed with the damping ratio ξ:

$$T_{\mathscr{P}} = 10^3 \, \frac{x_l}{\overline{u}_{ref}}; \quad w_{\mathscr{P}} = 2\pi / T_{\mathscr{P}}; \quad \xi = 1, \tag{III.2.5}$$

The pressure gradient is constant is space, but varies instantaneously in time so that the large-scale mean longitudinal velocity in the upper surface tends to the target velocity. That covers the method as applied in sections III.2.4, III.2.5, and III.3, but it can be easily generalized associating the subscript $\cdot_h$ to an arbitrary height instead of the boundary layer height.

III.2.4 Flat bottom application

III.2.4.1 Specific numerical strategy

The wind field initializes from a constant pressure gradient $\partial p / \partial x|_0$ giving nominal friction velocity u_0^*. The characteristic length scaling the domain is L_0. The turbulent characteristic time scale is $T_0 = L_0 / u_0^*$. Results are presented for grid 02 (Medium [256 x 128 x 80] at table III.1.1). A variable time-step Δt is employed ensuring CFL= 0.5.

The initial space averaged free-stream velocity is $\overline{u}_{h0} = 52.11 \; u_0^*$, obtained as the solution of a constant pressure gradient case $\partial p / \partial x|_0 \cdot z_l = \rho u_0^{*2}$. Five cases are presented, varying the the free-stream velocity from its initial value so the dynamical pressure gradient method is employed with varying target velocities: Case [01,02,03,04,05] with $\overline{u}_{ref} = [0.75, 0.90, 1.00, 1.10, 1.25] \; \overline{u}_{h0}$, respectively.

As the continuous solution is self-similar and the characteristic length L_0 is constant for all cases, except for numerical deviations that are assumed negligible, any deviations in turbulent statistics shall scale with the reference velocity $\overline{u}_{ref}$ (And time $\overline{T}_{ref} = L_0 / \overline{u}_{ref}$). The flat bottom cases so introduced generate the initial conditions for the Wave Age variation study in section III.3.

III.2.4.2 Results

The mean wind velocity in the last cell layer $\overline{u}_h$ is shown in figure III.2.4 within the non-dimensional scales employed in the solver. The wind speed slowly tends to the specified values $\overline{u}_{ref}$, depicted by the horizontal lines in the figure. The sliding average period is $t_{avg} = 75\ T_0$ and $t_{avg} = 75 \cdot 10^{-3}\ T_0$, in figures III.2.4a and III.2.4b, respectively. The low level of fluctuations revealed in figure III.2.4b is consistent with the low turbulence level imposed by the upper boundary condition.

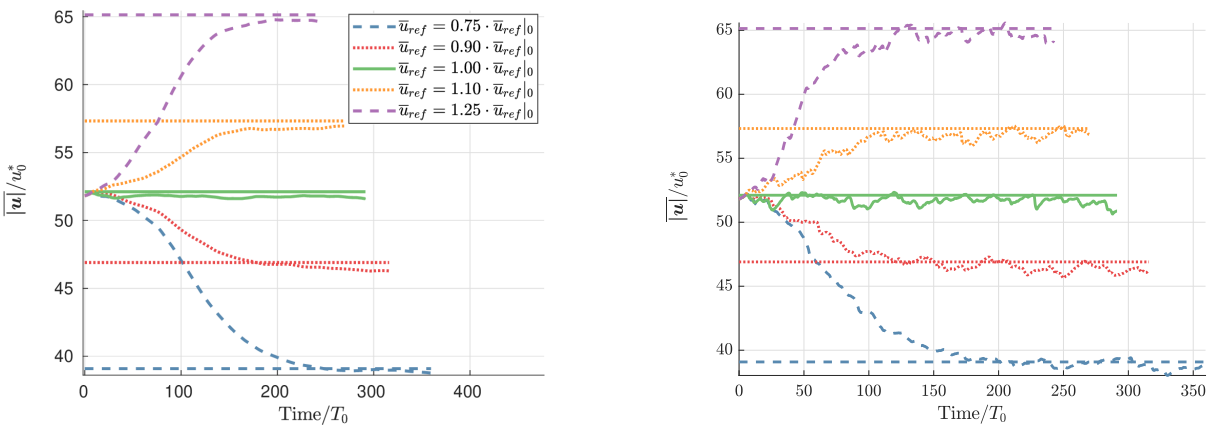

(a) $t_{avg} = 75\ T_0$.

(b) $t_{avg} = 75 \cdot 10^{-3}\ T_0$.

Figure III.2.4: Mean wind velocity in the last cell layer $\overline{u}_h$. Target values $\overline{u}_{ref}$ are remarked by the horizontal lines. The non-dimensional scales are shown as computed in the solver, but the problem is expected to be self-similar with respect to the reference velocity $\overline{u}_{ref}$. Sliding statistics are taken with time averages t_{avg} varying by 10^3.

The vertically integrated non-dimensional homogeneous pressure gradient, imposed in the solver according to the proposed dynamic methodology, is shown in figure III.2.5 ($t_{avg} = 75\ T_0$ and $t_{avg} = 75 \cdot 10^{-3}\ T_0$ in a. and b., respectively). As expected the pressure gradients evolve in much larger scales than the mean velocities of figure III.2.4, with its natural period imposed as $T_{\mathscr{P}} = 10^3\ (x_l/\overline{u}_{ref}) = 77\ T_0$).

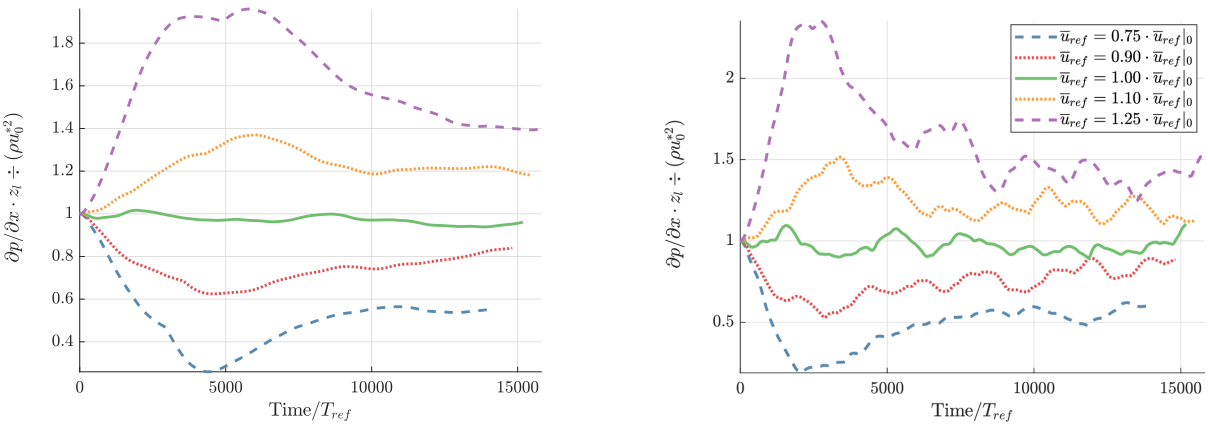

(a) $t_{avg} = 75\ T_0$. (b) $t_{avg} = 75 \cdot 10^{-3}\ T_0$.

Figure III.2.5: Vertically integrated non-dimensional, homogeneous, and large scale pressure gradient. Sliding statistics are taken with time averages t_{avg} varying by 10^3.

The mean target velocity is achieved in the upper boundary and $\partial p/\partial x$ indeed evolves much slower than turbulence. From now turbulent statistics are evaluated to assure the dynamic pressure gradient to not break self-similarity in the LES generated ABL. The friction velocity normalized by the target velocity is shown in figure III.2.6 ($t_{avg} = 75\ T_0$ and $t_{avg} = 75 \cdot 10^{-3}\ T_0$ in a. and b. respectively): As the last cell velocity approaches the target, so the non-dimensional solution converge between the cases. Comparison between figures III.2.6a and III.2.6b show that the friction velocities fluctuate much rapidly than $\overline{u}_h$, and there is no appreciative difference of fluctuation level between the cases.

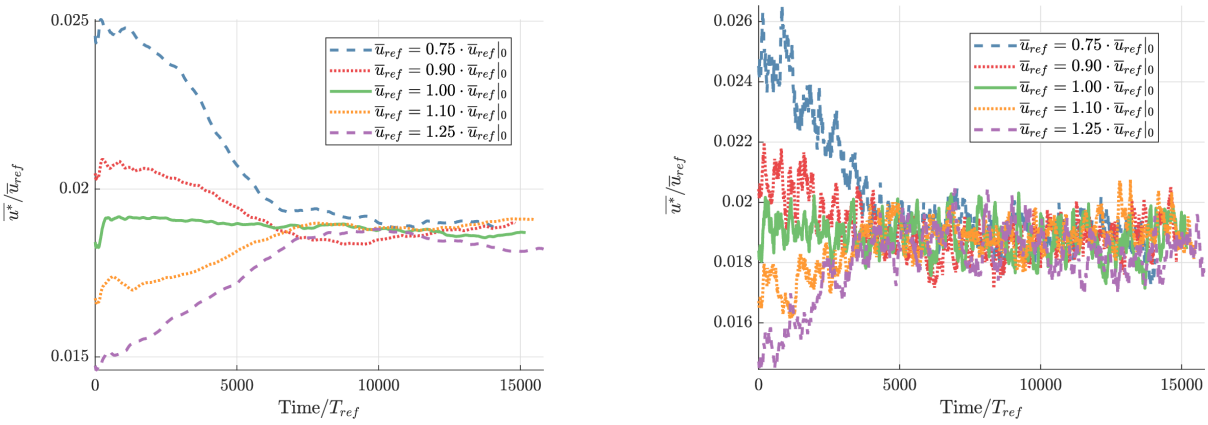

(a) $t_{avg} = 75\ T_0$. (b) $t_{avg} = 75 \cdot 10^{-3}\ T_0$.

Figure III.2.6: Friction velocity normalized by the target velocity. As the upper boundary velocity reaches its target, the solution becomes self-similar and the Cases converge. Sliding statistics are taken with time averages t_{avg} varying by 10^3.

The vertical wind and turbulent profiles are shown in figure III.2.7, and the Cases almost perfectly collapse in the non-dimensional mean longitudinal velocity, turbulent kinetic energy, turbulence intensities, and $u'w'$ cross-correlations shown respectively in figures III.2.7a, b, c, and d. The whole domain extension is shown with $z_l/\lambda = 5$, and to better

appreciate the distributions across the ABL the profiles are shown in vertical log scale at figures III.2.7a,b and c, but not in figure III.2.7d where the cross-correlations exhibit a linear behavior.

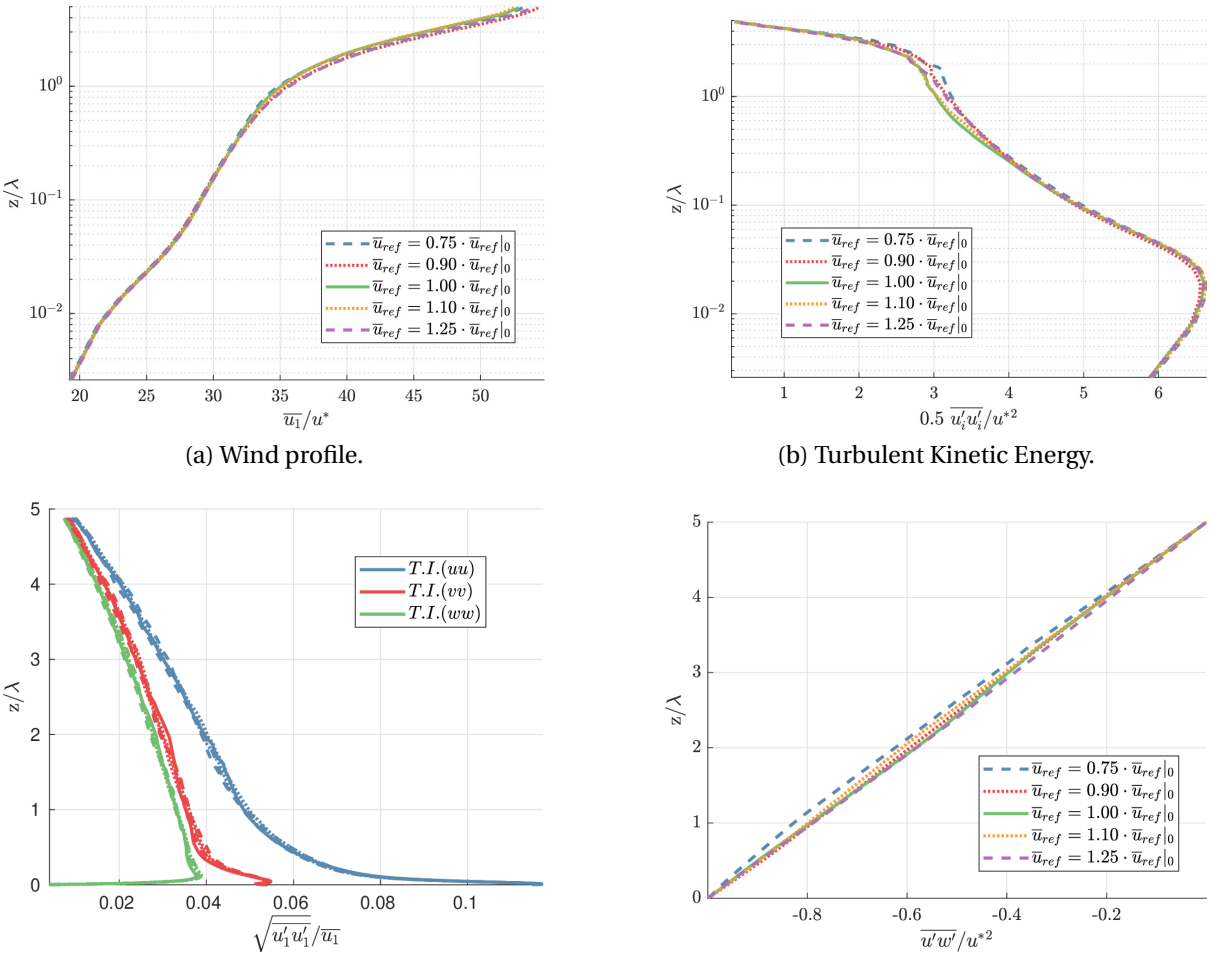

(a) Wind profile.

(b) Turbulent Kinetic Energy.

(c) Turbulence intensities.

(d) $u'w'$ Cross-Correlations.

Figure III.2.7: Vertical mean (in ξ_1, ξ_2 and t) wind and turbulent profiles. The five cases shown with varying free-stream velocity collide with proper normalization. The normalizing friction velocity is obtained from equation III.1.6. Sliding statistics are taken with time averages $t_{avg} = 75\ T_0$.

The fitting described in section III.1.2.3 is applied to the wind profile and depicted in figure III.2.8. To identify the log-law region, the interval $[z_{min}, z_{max}]$ extension is maximized under the constraint $RMS_{diff} < 3 \cdot 10^{-3}$. Two methodologies are compared: In figure III.2.8a the drag coefficient is constant $C_d = 1$, with αz_0 optimized as shown in table III.2.1; in figure III.2.8b both C_d and αz_0 are optimized with values given in table III.2.2. The best fitting behavior is observed in figure III.2.8b that reveals the ABL regions discussed in section III.1.2.3.

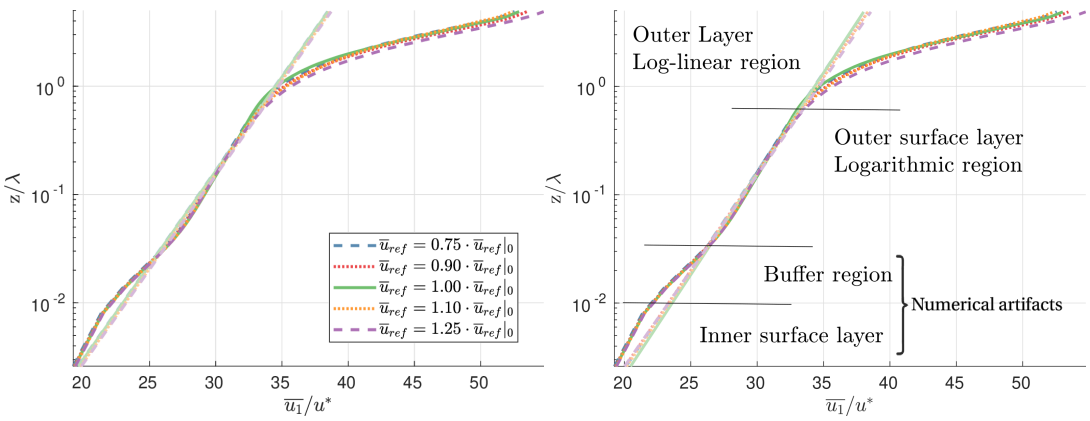

(a) $C_d = 1$; Optimized αz_0.

(b) Optimized C_d and αz_0.

Figure III.2.8: Wind velocity profile and fitting to the outer surface layer according to equation III.1.15. The different regions exposed are discussed in section III.1.2.3, as (b) is replicated at figure III.1.3.

Recall that with $[C_d = 1, \alpha = 1]$, the log-law fitting by equation III.1.15 recovers the lower Boundary Condition (BC) given by equation III.1.6. When $C_d = 1$ is fixed in table III.2.1 and figure III.2.8a, the effective roughness length αz_0 varies up to 8% from the log-law Boundary Condition (BC) where $\alpha = 1$. The fitting is best when C_d is allowed to vary as in table III.2.2 and figure III.2.8b, in which case α decreases up to 60% with respect to the BC. When optimized, C_d is diminished up to 7% in table III.2.2.

The differences observed between the fitting to the log-law region, and the log-law BCs reflect the existence of the numerical induced buffer region depicted in figure III.2.8b, and the differences between the Cases reflect the uncertainties, specially due to the lack of statistical convergence. The latest gives a quantification of the overall procedure uncertainties, to be taken into account when evaluating the wave bottom cases in the next sections. The $[C_d, \alpha]$ combined optimization is said best because it leads to the most extensive log-law region (0.74λ in table III.2.2), and more consistent fitting in view of figure III.2.8.

Table III.2.1: Log-Fit of eq. III.1.15: Optimal $[\alpha]$ for $RMS_{diff} < 3 \cdot 10^{-3}$ in $z_{mid} + \left[-\frac{z_{len}}{2}, +\frac{z_{len}}{2}\right]$.

Case	C_d	α	z_{mid}/λ	z_{len}/λ
1	1.00	1.02	0.39	0.63
2	1.00	0.97	0.39	0.67
3	1.00	1.01	0.38	0.53
4	1.00	0.94	0.39	0.67
5	1.00	0.92	0.39	0.69

Table III.2.2: Log-Fit of eq. III.1.15: Optimal $[C_d/\kappa, \alpha]$ for $RMS_{diff} < 3 \cdot 10^{-3}$ in $z_{mid} + \left[-\frac{z_{len}}{2}, +\frac{z_{len}}{2}\right]$.

iCase	C_d	α	z_{mid}/λ	z_{len}/λ
1	0.95	0.54	0.39	0.74
2	0.97	0.67	0.39	0.74
3	0.93	0.40	0.39	0.74
4	0.97	0.61	0.39	0.74
5	0.99	0.77	0.39	0.74

III.2.5 Wavy bottom application

III.2.5.1 Specific numerical strategy

The wind field initializes from a constant pressure gradient $\partial p/\partial x|_0$ giving nominal friction velocity u_0^*. The characteristic length scaling the domain is L_0. The turbulent characteristic time scale is $T_0 = L_0/u_0^*$. Results are presented for grid 02 (Medium [256 x 128 x 80] at table III.1.1). A variable time-step Δt is employed ensuring CFL= 0.5.

The initial space average free-stream velocity is $\overline{u}_{h0} = 52.11\ u_0^*$. Three cases are presented: Case 01 is the reference, with flat bottom Boundary Condition (BC) and constant $\partial p/\partial x|_0 \cdot z_l = \rho u^{*2}$; Case 02 corresponds to a reproduction of the wavy case exploited in Paskin et al. [2020], with the monochromatic wavy surface introduced in the bottom and still constant $\partial p/\partial x|_0$; Case 03 considers the same wavy prescription as Case 02, but also the dynamic pressure gradient method here discussed with target velocity $u_{ref} = \overline{u}_{h0} = 52.11\ u_0^*$.

The lower free-surface position and velocities are prescribed according to the fifth order Stokes solution given in Fenton [1985]. The wave length $\lambda = 2\pi/k$ equals the characteristic length scale L_0, and the non-dimensional wave height is $ka = 0.2$. The dispersion equation in deep water gives phase velocity $c = \sqrt{g/k}$ (wave period $T_p = \lambda/c$) setting the relation between characteristic length and velocity scales with nominal $\mathrm{WA}_0 = c/u_0^* = 60$. The turbulent characteristic time-scale is $T_0 = \lambda/u_0^* = 60\ T_p$. The wave forcing in the lower BC linearly evolves from null till its 5th order solution during $100T_p = 1.68T_0$. Note that Case 01 and 02 have almost the same setup as in Paskin et al. [2020], except for the wave introduction during $100T_p$ instead of $15T_p$, as an unworthy effort to mitigate the resultant unsteadiness.

III.2.5.2 Results

The mean wind velocity in the last cell layer $\overline{u}_h$ is shown in figure III.2.9a within the non-dimensional scales employed in the solver. At Case 03 (Wavy BC, Dyn $\partial p/\partial x$), the dynamic pressure gradient algorithm is activated, with the target velocity $\overline{u}_{h0} = 52.11\ u_0^*$ shown as the horizontal line in the figure: Due to the dynamic $\partial p/\partial x$ the free-stream velocity deviates only $\sim 1\%$ from the target when $t > 200T_0$. A higher level of unsteadiness is intrinsic even to the flat bottom Case 01, where the free-stream velocity deviates $\sim 2\%$ from its initial value, that equals the target $\overline{u}_{h0}$. Without a dynamic $\partial p/\partial x$ balancing the momentum transfer from the waves to the wind, the free-stream velocity is greatly augmented by the wave introduction in Case 02, reaching values $\sim 14\%$ higher than the reference $\overline{u}_{h0}$.

The friction velocity is normalized by its nominal value in figure III.2.9b. Concerning the Case 02 (Wavy BC, Cte $\partial p/\partial x$), as in Paskin et al. [2020], the wave first leads to a rapid drop in the friction velocity, that later converges towards u_0^* over large periods. Employing the dynamic pressure gradient algorithm in Case 03, the friction velocity does not recover the nominal value, instead being kept at $\sim 0.88\ u_0^*$, so to keep the free-stream velocity close to the target $\overline{u}_{h0}$ during the computation.

Both the free-stream and friction velocities of figures III.2.9a and III.2.9b reveal a great level of unsteadiness for Case 02, that in fact might be only partially converged after the 2M

time-steps and the period of 250 T_0 shown in the figures. The amount of unsteadiness is significantly reduced in Case 03 with the dynamic $\partial p/\partial x$ method, that presents relatively slight velocity variations over the whole computation, reaching a statically steady regime for $t > 200\ T_0$. With the wave introduced in Cases 02 and 03, the ratio between free-stream $\overline{u}_h$ and friction velocity u^* becomes flow dependent, and so the Wave Age behaves differently if defined as function of WA($\overline{u}_h$) in figure III.2.9c, or function of WA(u^*) in figure III.2.9d. The different velocities and Wave Ages might be correlated, but are intrinsically different: For Case 02 the WA($\overline{u}_h$) drops ~ 14%, distancing from the flat bottom (Case 01) reference (~ 1.14) over time, while WA(u^*) actually converges towards the reference (~ 60) over time; On the contrary for Case 03, the WA($\overline{u}_h$) is kept close to the reference, while WA(u^*) is considerably (~ 12%) higher than the reference. Section III.3 shall evaluate the implications of these different WA definitions, and conclude that the WA($\overline{u}_h$) characterizing the free-stream flow is also better suited to characterize the Wind-Wave Interactions. Interestingly for Case 02, the free-stream velocity converges towards the wave phase velocity in figure III.2.9a, as the WA($\overline{u}_h$) converges to unity in figure III.2.9c, which brings Mile's critical height inside the ABL in a physical perspective, or inside the computational domain in a numerical perspective: Such 'coincidence' shall be further explored in future works.

The homogeneous pressure gradient is shown at figure III.2.9e: Constant and equal to $1/z_l$ for Cases 01 and 02; dynamic and slowly evolving at Case 03, that converges towards $\partial p/\partial x|_0 \sim 0.6/z_l$ for $t > 200T_0$. Compared to Case 02, the unsteady $\partial p/\partial x|_0$ in Case 03 is responsible for keeping the quasi-steady wind and friction velocities. The unsteadiness of the wind field reflects into the non-dimensional form drag F_p/F_τ shown in figure III.2.9f. While Case 03 converges towards $F_p/F_\tau \sim -15\%$ for $t > 200T_0$, Case 02 ever increases after its sudden drop and minimum occurring at $t \sim 10T_0$. Moreover in Case 03, $F_p < 0$ and the momentum flux is exclusively upwards, but for Case 02 the form drag will change sign, and becoming positive indicates a downward (Wind to Wave) momentum flux for $t > 100T_0$.

The different Wave Ages between Cases 02 and 03, qualitatively justify the differences in the wind profiles of figure III.2.10b, and in the turbulent profiles of figure III.2.11. In the turbulent profiles, each of the disturbances previously reported in Paskin et al. [2020] for the TKE, the TI, and the $\overline{uw}$ correlations is again observed in figure III.2.11, and augmented at Case 03 where the WA is higher. Nevertheless a steady state regime might not have been reached for Case 02, so that a more quantitative WA comparison shall wait until section III.3.

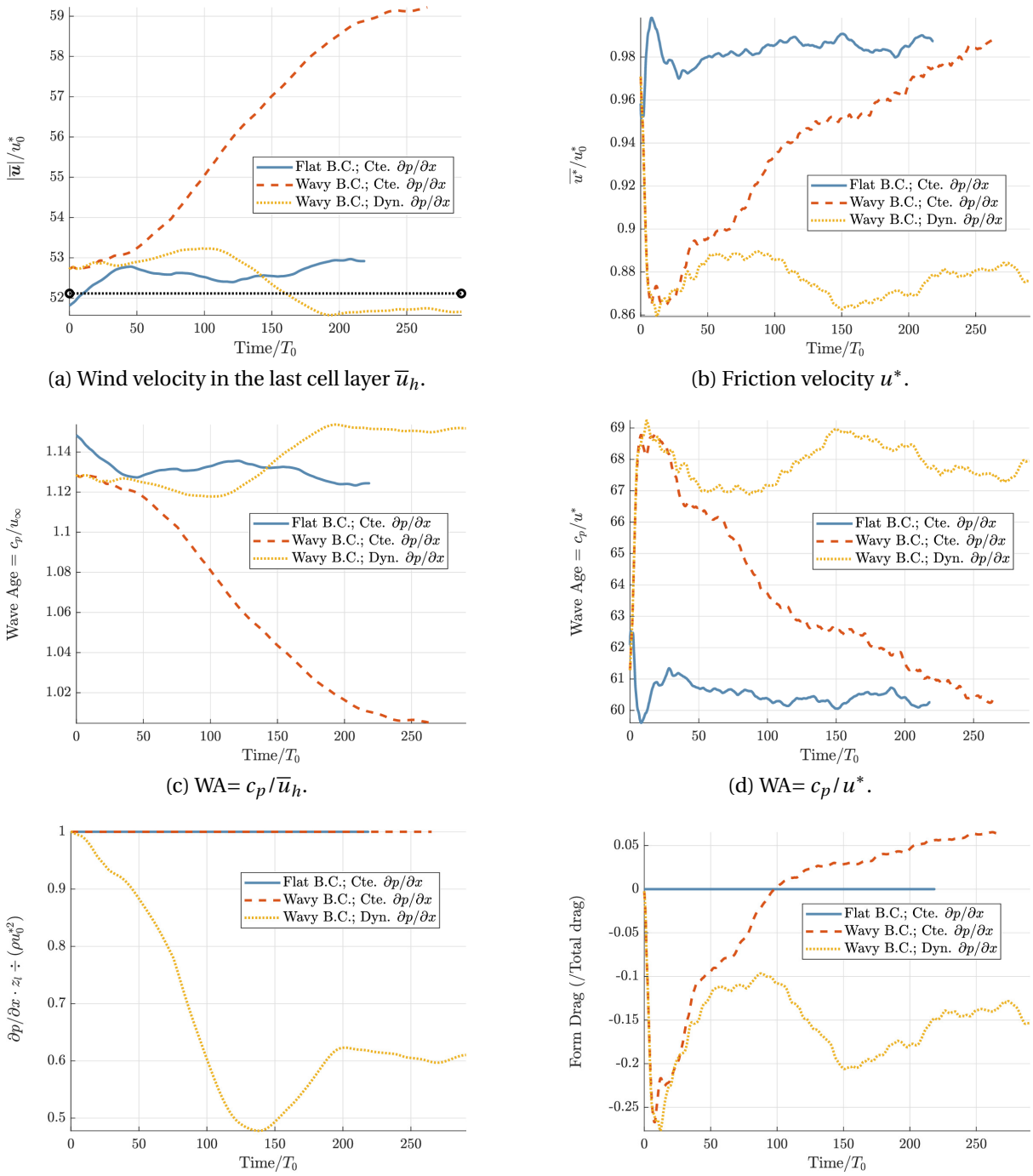

(a) Wind velocity in the last cell layer $\overline{u}_h$.

(b) Friction velocity u^*.

(c) WA= $c_p/\overline{u}_h$.

(d) WA= c_p/u^*.

(e) $\partial p/\partial x|_0$.

(f) Form drag F_p/F_τ.

Figure III.2.9: Different mean (in ξ_1, ξ_2 and t) history profiles for the three cases considered: Flat bottom with constant large scale $\partial p/\partial x|_0$ as the reference; Wavy bottom with constant $\partial p/\partial x|_0$; Wavy bottom with the dynamic $\partial p/\partial x|_0$ modeler here proposed. Sliding statistics are taken with time averages $t_{avg} = 75\ T_0$.

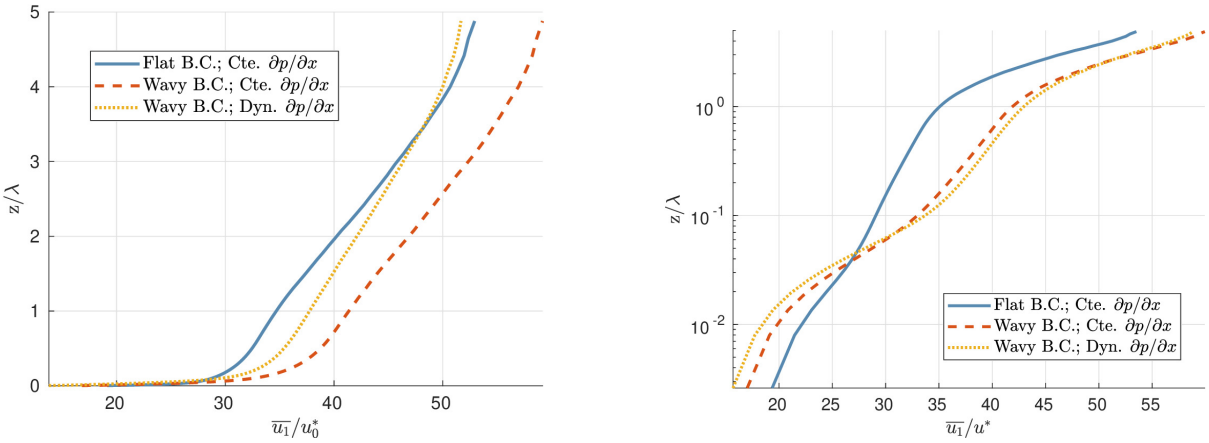

(a) In linear scale normalized by the nominal friction velocity.

(b) In linear-log scale normalized by the resolved friction velocity.

Figure III.2.10: Mean (ξ_1, ξ_2 and t) wind velocity profile for the three cases considered, in different scales and normalized by different friction velocities. Sliding statistics taken with $t_{avg} = 75\ T_0$.

III.2.6 Overview and discussion

With the large scale pressure gradient evolving in much larger times than turbulent fluctuations in the ABL, turbulence statistics are shown invariant to different values of the target velocity $\overline{u}_{ref}$ imposed for the different flat bottom cases presented.

When fast traveling waves are introduced with lengths scales comparable to the ABL height, significant unsteady processes take place in the LES generated ABL. Notably the wave drags the wind, and if the large scale pressure gradient is kept constant, the free-stream velocity speeds-up, eventually dragging back the propagating wave. The flow history is extremely important determining the wind profile speed-up once the steady state regime is reached.

Nevertheless, the transient cycle here observed is artificial and should be avoided, being determined by non-physical aspects of the problem formulation: A wave does not grow linearly over 100 peak periods; the waves shall also be modulated by the evolving form drag; and the large scale pressure gradient might be unknown, but shall certainly not be constant above the ocean. Instead, one shall often desire to achieve statistically steady state regimes, and controllable wind conditions. The dynamic pressure gradient modeler proposed greatly favors the convergence to steady state, and conveniently allows great amount of control over the mean wind profile above propagating waves.

The methodology built for the large scale pressure gradient modeler is physically inspired in the sense that: (i) It is capable of reproducing a quasi-steady state wind regime at the last cell-layer, or a target (measured) velocity at a given height; (ii) It responds exclusively to motions occurring at scales much larger than the considered domain, which can be adjusted in the natural frequency of the mass-spring-damper system. (iii) It is more likely that the large-scale pressure gradient (traveling instantaneously in incompressible flows) adapts to keep a free-stream velocity, rather than the free-stream velocity varying to keep a

constant large-scale pressure gradient condition.

On the other side, the evolution equation built for $\partial p/\partial x|_0$ is artificial in the sense that it does not follow from any conservation law. Then one of the largest appeals of such methodology in the given context appears when it enables the arrival to a steady state regime with the same free-stream velocity imposed as the initial flat bottom condition.

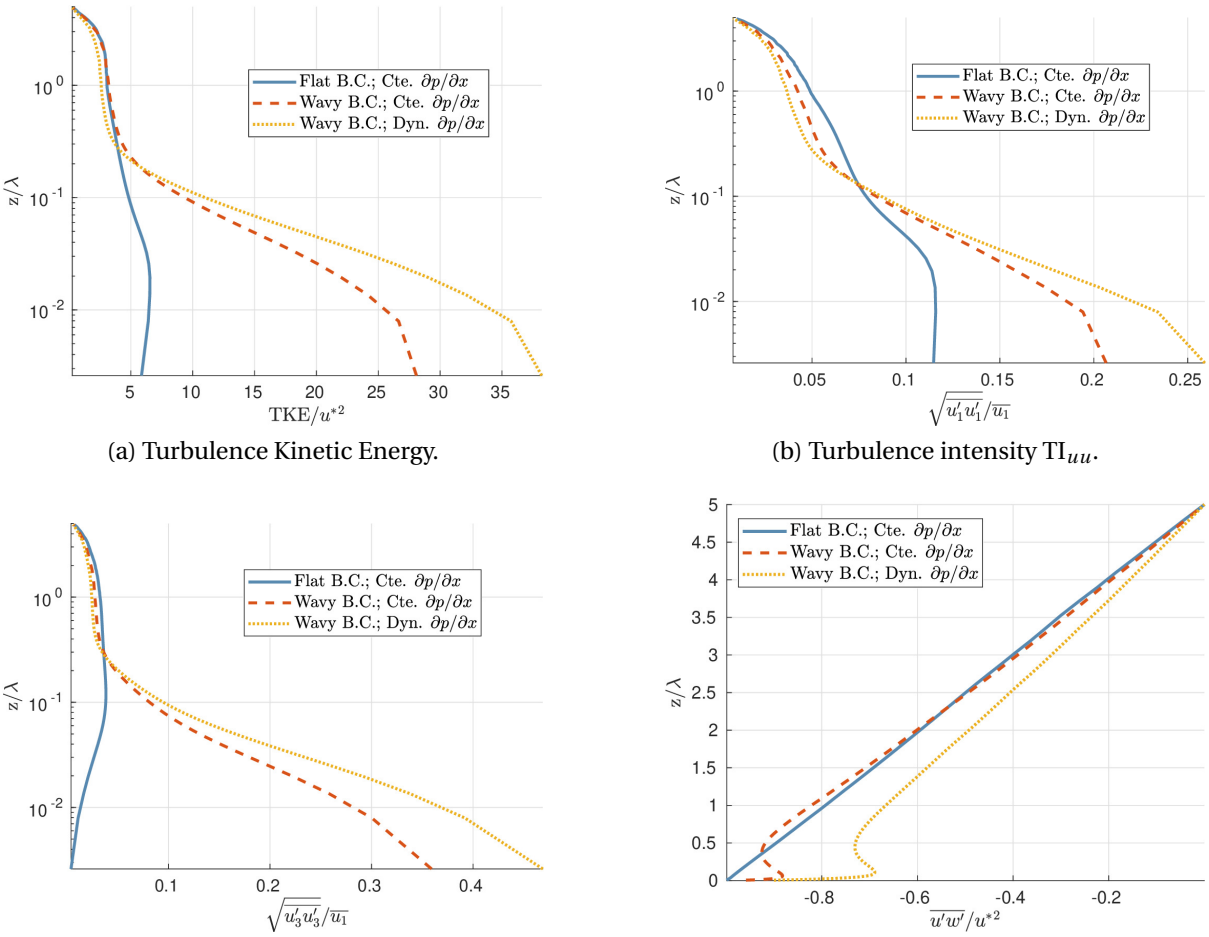

(a) Turbulence Kinetic Energy.

(b) Turbulence intensity TI_{uu}.

(c) Turbulence intensity TI_{ww}.

(d) uw Cross-correlations

Figure III.2.11: Different mean (ξ_1, ξ_2 and t) vertical turbulent profiles for the three cases considered. The normalizing friction velocity is obtained from equation III.1.6. Sliding statistics are taken with time averages $t_{avg} = 75\ T_0$.

III.3 SYSTEMATIC COMPARISONS VARYING THE WAVE AGE

The dimensional analysis of the Navier Stokes equations in section I.1.2.2 reveals the Froude number ***Fr***, quantifying gravitational with respect to inertial forces. Notably, these gravitational effects rule the free-surface dynamics, so that the ***Fr*** number is often the most important non-dimensional parameter in oceanic and wave propagation studies. As seen in section I.1.2.2, stating fully turbulent flow (***Re***$\rightarrow \infty$), neglecting Coriolis forces (***Ro***$\rightarrow 0$), and assuming neutral buoyancy conditions (***Ri***$\rightarrow 0$), the ***Fr*** number is also the only non-dimensional quantity determining the solution of the Navier Stokes momentum equations I.1.29 in an unbounded domain. Prescribing the boundary conditions, other non-dimensional quantities define the solution such as ka, kd, $k\delta$, kL_x, and kL_y; and in the discrete formulation numerical similarity depends in the CFL and Peclet numbers; as discussed in the appendix B.1.1. Through the Wind-Wave Interaction specific literature (Section I.3), it is the Wave Age the most important non-dimensional parameter describing the solution and observations, though its precise definition varies in the literature. Indeed the Wave Age is shown equivalent to the ***Fr*** number in the appendix B.1.1.

With such importance determining the solution of the Navier Stokes equations, it is natural that the literature puts so much effort into determining the parametrization of Wind-Wave interaction phenomena with respect to the Wave Age. The best example of such an effort is probably the parametrization of the drag coefficient through the literature reviewed in section I.3.3, where over six decades of studies since Charnock [1955] evidentiate both the pertinence and the complexity of the drag dependency to the Wave Age condition. Such complexity has just been noted in section III.2.5, where the flow history is crucial for determining the state of the system and so the pressure drag coefficient.

A simple WA parametrization thus depends on a steady state scenario, hardly existent in the offshore environment. Another major simplification is that such parametrization also implies the sea-state spectra similarity with respect to the wave peak period [Donelan et al., 1993]. Besides, previous studies reviewed in section I.3.2, and for example the results in section III.2.5, indicate that WI disturbances can propagate into the ABL up to heights comparable to the wave length λ, which might often approach the ABL height δ in swell dominated conditions; then from the discussion in the appendix B.1.1, it is clear that the non-dimensional ABL height $k\delta$ shall be equally important for determining the solution. The author believes the $k\delta$ dependency has been possibly underrated through the literature, specially for fast waves conditions in stable boundary layers where δ/λ can be in the order of (or even below) unity. With these complexities in mind, Hristov and Ruiz-Plancarte [2014] note a simple and robust parametrization of the surface drag is unlikely to exist.

Present systematic WA variation studies count in the following simplification to accommodate these challenges: A simple monochromatic wave prescription in deep water, so defined by ka and λ; the dynamic pressure gradient modeler presented in III.2, to obtain a quasi-steady state solution in the free-stream velocity; the systematic variation of wind intensity rather than the wave length, so keeping λ and δ constant between the cases. To limit the variations of the Peclet number, the free-stream velocity varies between ±25% from the middle WA case.

III.3.1 SPECIFIC NUMERICAL STRATEGY

The wind field initializes from a constant pressure gradient $\partial p/\partial x|_0$ giving the 0th reference friction velocity $u_0^* = u_{ref0}^*$. The characteristic length scaling the domain is L_0. The nominal turbulent characteristic time scale is $T_0 = L_0/u_0^*$. Results are presented for grid 02 (Medium [256 x 128 x 80] at table III.1.1). A variable time-step Δt is employed ensuring CFL= 0.5.

The initial space-averaged free-stream velocity is $\overline{u}_{h0} = 52.11\ u_{ref0}^*$. Five cases are presented, varying the free-stream velocity from its initial value so the dynamical pressure gradient method is employed with varying target velocities: Case [01,02,03,04,05] with $\overline{u}_{ref} = [0.75, 0.90, 1.00, 1.10, 1.25]\ \overline{u}_{h0}$, respectively. The wavy bottom surface is so introduced to the flat bottom cases previously discussed in section III.2.4.

The free-surface position and velocities are prescribed according to the fifth order Stokes solution given in Fenton [1985]. The wave length $\lambda = 2\pi/k$ equals the characteristic length scale L_0, and the non-dimensional wave height is $ka = 0.2$. The dispersion equation in deep water gives phase velocity $c = \sqrt{g/k}$ (Wave period $T_p = \lambda/c$), setting the relation between characteristic length and velocity scales with nominal $\mathrm{WA}_{ref} = c/u_{ref}^* = [80, 67, 60, 55, 48]$, for cases [01,02,03,04,05], respectively. The turbulent characteristic time-scale relates to the wave period with $T_0 = 60\ T_p$. The wave forcing in the lower BC linearly evolves from null till its 5th order solution in $100T_p = 1.68T_0$. Case 03 is the same as in section III.2.5.

III.3.2 RESULTS

III.3.2.1 MEAN HISTORY PROFILES

The mean wind velocity in the upper cell layer $\overline{u}(z_l)$ is shown in figure III.3.1a within the non-dimensional scales employed in the solver, i.e., normalized by the 0th reference friction velocity u_{ref0}^*. The horizontal lines in the figure depict the target velocities $\overline{u}_h = [0.75,\ 0.90,\ 1.00,\ 1.10,\ 1.25] \cdot \overline{u}_{h0}$, with $\overline{u}_{h0} = 52.11\ u_{ref0}^*$. The highest discrepancy observed between actual and target velocities in the last cell layer is 3.1%, and occurs for Case 01 $\overline{u}_h = 0.75\ \overline{u}_{h0}$ (Highest WA). In the last steps of the evolution profiles, where vertical profiles are to be probed, the discrepancy in Case 01 is still the highest and drops to 1.9%. To keep these free-stream velocities close to the target values, the dynamic pressure gradient evolves as reported in figure III.3.1b: With the WI drag propagating into the atmosphere, $\partial p/\partial x$ drops to meet the criterion, responding to the large scale trend of $\overline{u}(z_l)$.

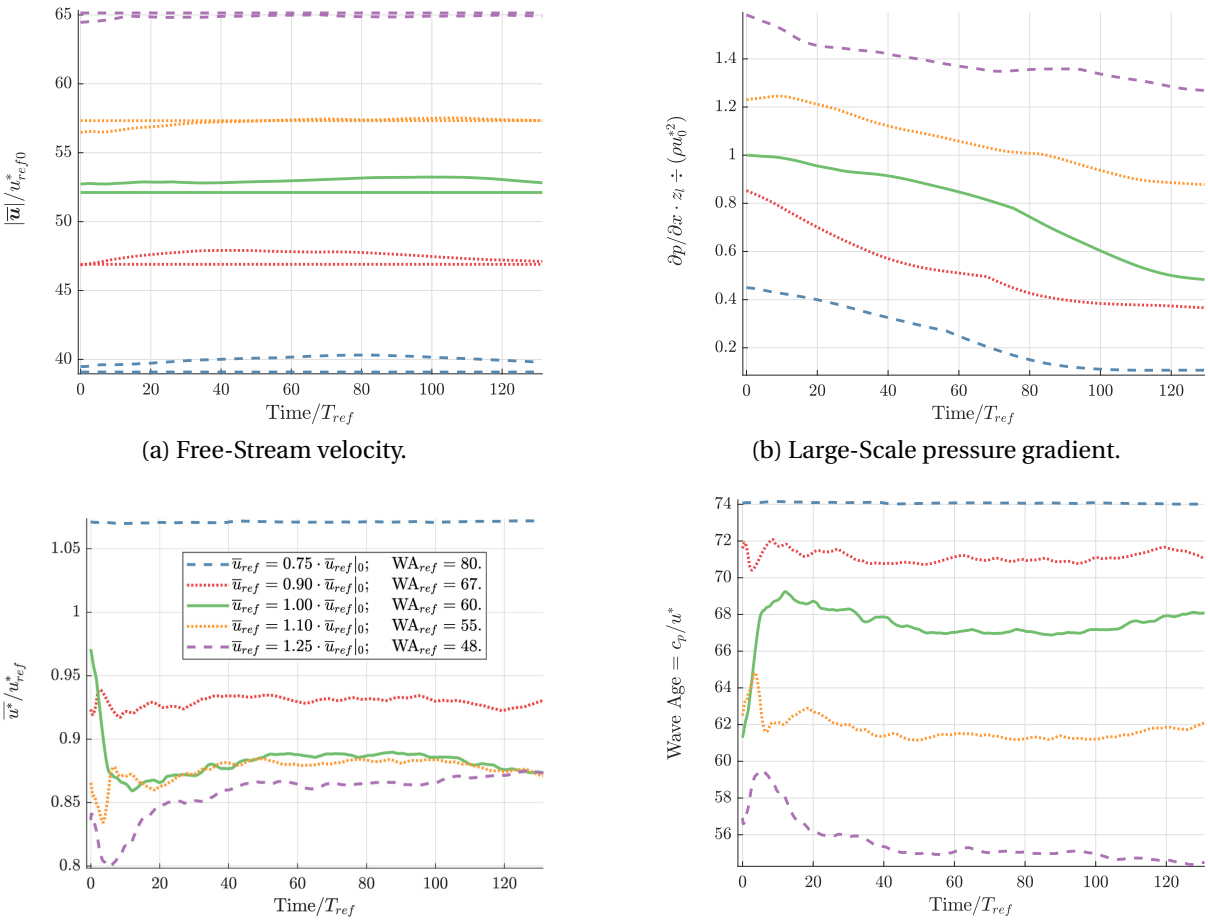

(a) Free-Stream velocity.

(b) Large-Scale pressure gradient.

(c) Friction velocity ratio to undisturbed case.

(d) Resolved Wave Age.

Figure III.3.1: Mean history profiles averaged with $t_{avg} = 75\ T_0$. (a) Wind velocity ($|\boldsymbol{u}|(z_l)$) at last vertical layer, normalized by the middle reference value u^*_{ref0}, as resolved in the computational non-dimensional domain. The horizontal lines stand for the target velocities $u_{ref} = u_h$. (b) Dynamic and slowly evolving pressure gradient controlling $|\boldsymbol{u}|(z_l)$ to match u_h. (c) Ratio between the resolved u^* and reference u^*_{ref} friction velocities, with u^*_{ref}/u^*_{ref0} given in the legend. (d) Resolved Wave Age WA(u^*). The legend shown in (c) applies to (a,b,c,d), relating the line types and colors to each case.

In the flat case scenario of section III.2.4, it is shown the friction velocity scales with $\overline{u}_h$, and the normalized curves of u^*/u_h collapse in figure III.2.6. In the wavy cases here presented the WI drag varies between the cases, and the free-stream velocity kept constant, the friction velocity becomes function of the non-dimensional wave speed, or Wave Age (WA). In the flat case, the nominal friction velocities are $\overline{u}^*_{ref} = [0.75, 0.90, 1.00, 1.10, 1.25] \cdot \overline{u}^*_{ref0}$, and figure III.3.1c shows the ratio between resolved and nominal friction velocities for each wavy case. Except for Case 01 when $\overline{u}_h = 0.75\ \overline{u}_{h0}$ (Highest WA), the friction velocities drop with respect to the reference values, and the discrepancy is larger with larger reference velocities, so largest in Case 05 ($1.25\ \overline{u}_{h0}$, lowest WA) with 13% deviation in the last steps of figure III.3.1c.

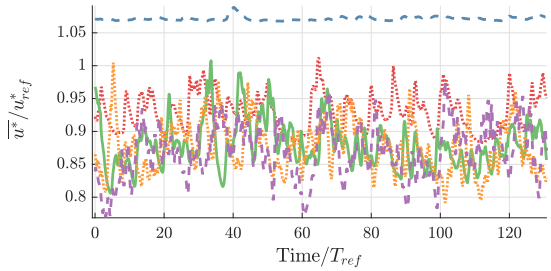

Figure III.3.2: Same as figure III.3.1c, but averaged with $t_{avg} = 75 \cdot 10^{-3}\ T_0$. Ratio between the resolved u^* and reference u^*_{ref} friction velocities, with u^*_{ref}/u^*_{ref0} given in the legend of figure III.3.1c for each line type.

In Case 01, where $\overline{u}^*/\overline{u}^*_{ref}$ actually rises, there is also a significant mitigation of the friction velocities fluctuations. This becomes clear with the lower time averages adopted at figure III.3.2, suggesting there might be a transition to the laminar regime being approached.

The actual friction velocity and so the Wave Age, are consequence of the WI drag combined with the constant free-stream velocity, so the Wave Age shown in figure III.3.1d variates substantially from the nominal values $\mathrm{WA}_{ref} = [80, 67, 60, 55, 48]$. The quantities revealed in figure III.3.1 are probed at the final time-step of the evolution depicted, with values given in table III.3.1, where they can also be compared to the references here discussed.

Table III.3.1: The parameters of figure III.3.1 probed at the final time-step, and the correspondent reference values.

Case ID	$\overline{u}_{h0}/\overline{u}^*_0$	$(\overline{u}_h - \overline{u}_{h0})/\overline{u}_{h0}$	$\partial p/\partial x \cdot z_l$	$\overline{u}^*_{ref}$	$\overline{u}^*$	WA_{ref}	WA
1	39.08	1.85%	0.107	0.157	0.169	79	74
2	46.90	0.18%	0.361	0.189	0.175	66	72
3	52.11	1.24%	0.479	0.210	0.183	60	68
4	57.32	-0.04%	0.876	0.231	0.201	54	62
5	65.14	-0.49%	1.270	0.262	0.228	48	55

It is shown that unlike the flat cases of section III.2.4, to keep a constant free-stream velocity above a propagating wave, the friction velocity must be allowed to vary, and it varies such that here the actual WA differs from its nominal values WA_{ref} up to 15%. On the literature, the WA is computed with different reference velocities, such as the actual or an effective friction velocity, the velocity at an arbitrary (Preferably 10 m) height, or the free-stream velocity. It is here shown that within such detailed resolution of the MABL, the ratio between each of this velocities in not kept constant, rather depending on the WI dynamics and thus on the Froude number, or equivalently on the characteristic WA.

At this point, a question is naturally posed as: Which is the atmospheric characteristic velocity U, that scaling the WA= c_p/U leads to a better characterization of Wind-Wave interaction effects? A first investigation into this issue comes from evaluating the Form drag (F_p), which is normalized in figure III.3.3 by the total drag F_τ. In the literature the normalized form drag, or the growth rate parameter $\beta = 2\ F_p/[u^{*2}(ka)^2]$, are usually assumed function of the WA: Such as denoted by the blue dots in figure III.3.4a, function of the actual WA= c_p/u^*; or in figure III.3.4c, function of the nominal $\text{WA}_{ref} = c_p/\overline{u}^*_{ref}$, with u^*_{ref} scaling linearly to the target velocity $\overline{u}_h$, and $\overline{u}_h$ approximating the actual free-stream velocity $\overline{u}(z_l)$ with better than 3% accuracy.

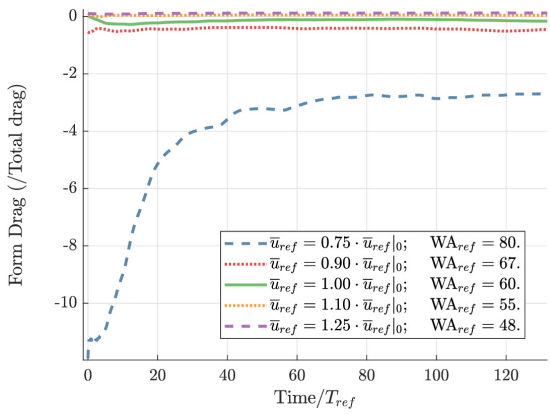

Figure III.3.3: The evolution of F_p/F_τ in time, with $t_{avg} = 75\ T_0$.

Noting that the discrepancy between WA and WA_{ref} monotonically decreases with augmenting u^*_{ref}, three functions are fitted to the data and appear with dotted lines in the figures: The red lines fits to Cases 01-04; the yellow lines to Cases 02-05; and the purple lines to Cases 01-05. The fitting of constants A and B in equation III.3.1 applies to the slopes of the curves, given in the middle of the intervals by a 1st order finite difference, denoted by the blue dots in figures III.3.4b and III.3.4d. The constant part of the approximating function (C in eq. III.3.1) is set so to match exactly the solution in Case 03, where the dotted curves intersect in figures III.3.4a and III.3.4c.

As a function of the actual WA, the fitted curves strongly diverge in figures III.3.4a and III.3.4b. As a function of the nominal WA_{ref} on the contrary, the fitting of the two intervals almost collapse in figures III.3.4c and III.3.4d, indicating that the form drag better scales with the nominal WA_{ref}, which characterizes the non-disturbed flow, and scales with the free-stream velocity (Or u^*_{ref}) in present formulation. Finally, the form drag dependency on the WA is here given by the fitting denoted in purple at figure III.3.4c, obtained with the parameters shown at table III.3.2, and the equation:

$$\frac{F_p}{F_\tau} = -\frac{B\ \exp[A \cdot \text{WA}_{ref}]}{A} + C \tag{III.3.1}$$

Table III.3.2: The form drag dependency on the WA is here represented by equation III.3.1, fitted with parameters given below. The resultant fitting is drawn in purple at figure III.3.4c.

A	B	C
$1.07 \cdot 10^{-1}$	$6.75 \cdot 10^{-6}$	$2.04 \cdot 10^{-1}$

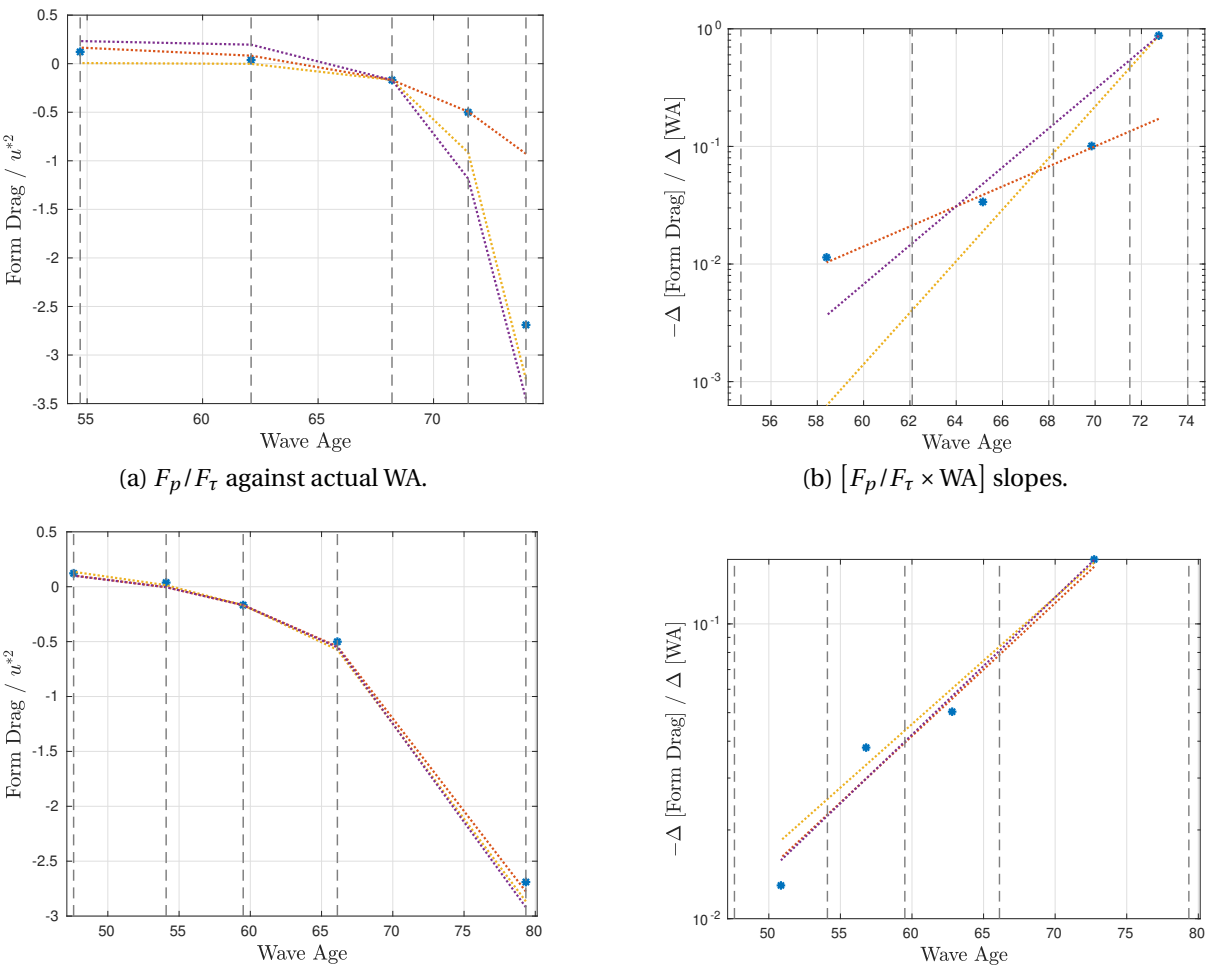

(a) F_p/F_τ against actual WA.

(b) $[F_p/F_\tau \times \mathrm{WA}]$ slopes.

(c) F_p/F_τ against nominal WA_{ref}.

(d) $[F_p/F_\tau \times \mathrm{WA}_{ref}]$ slopes.

Figure III.3.4: Wave Age dependency of the non-dimensional form drag (F_p/F_τ). (a and c) The numerical experiments reveal F_p/F_τ denoted by the blue dots, function of the actual WA in (a), and function of the reference WA_{ref} in (c). (b and d) The negative sign of the slopes between the intervals of figures (a) and (c), respectively denoted by the blue dots in figures (b) and (d). The red dot line fits to the first 4 Cases, the yellow dotted line fits to the last four Cases, and the purple line fits for every Case. The fitted equation is III.3.1, with A and B obtained from figures (b) and (d), and C set as to match exactly the value at Case 03 where $u_{ref} = u_{ref0}$

III.3.2.2 Mean wind velocity profiles

Recall that in section III.2.4 the solutions are shown similar with respect to any characteristic velocity in the MABL, and the 5 flat cases have their wind profiles collapsed as in figure III.3.5a, here repeated to base further discussions. The LES generated MABL may be segmented in the 4 regions exposed in figure III.3.5a: In the outer layer the profiles transit from log into linear behavior adapting to the free stress condition in the upper surface; in the outer surface layer the profiles exhibit a perfect logarithmic behavior above the buffer region; the inner surface layer is modeled below the first grid point by the log-law boundary condition; and so the buffer region is a very limited region above the first grid point upon which the resolved stresses become predominant over the SGS contribution.

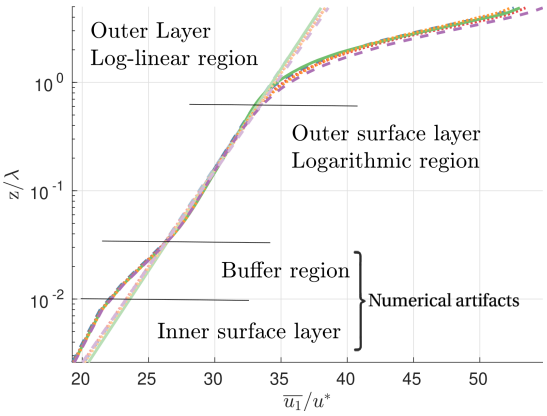

(a) Flat bottom cases; repeated from figure III.2.4 for comparison.

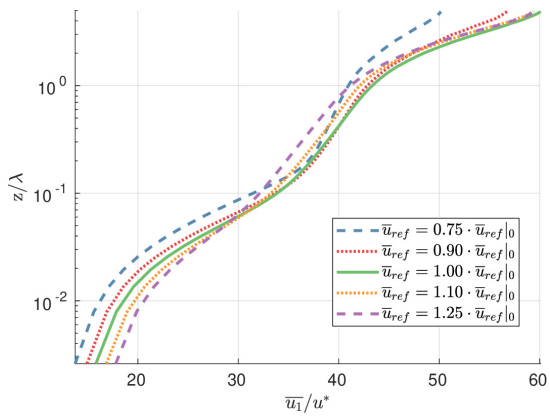

(b) Wavy cases; Normalized by the actual friction velocity u^*.

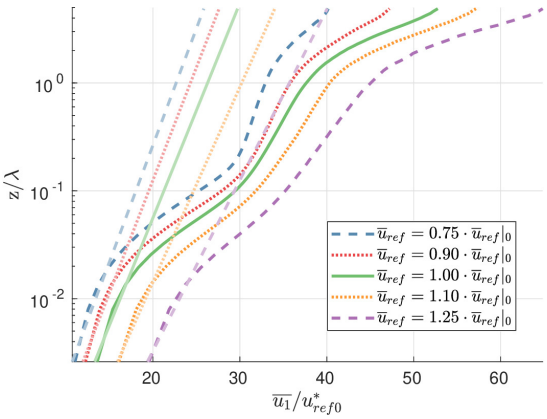

(c) Wavy cases; Normalized by the 0th reference friction velocity $u_0^* = u^*_{ref0}$. Fitting αz_0 in the inner surface layer.

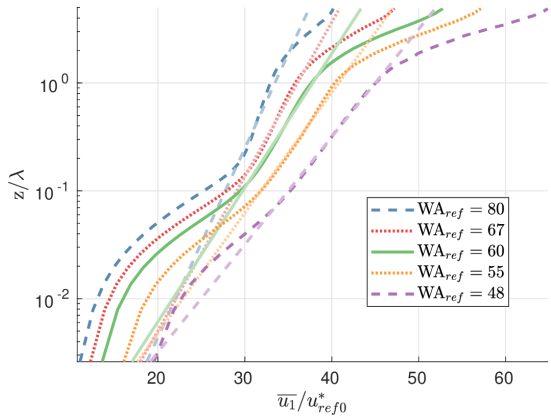

(d) Wavy cases; Normalized by the 0th reference friction velocity $u_0^* = u^*_{ref0}$. Fitting C_d and αz_0 to the outer surface layer.

Figure III.3.5: Mean (in ξ_1, ξ_2 and t) wind velocity profiles and fitting. In (a) the flat bottom cases presented in section III.2.4. In (b-d) the wavy bottom cases here discussed. Log fitted profiles (from equation III.1.15) are shown with transparency in (c,d). (c) Fitting to the inner region. (d) Fitting to the outer region. Sliding statistics are taken with time averages $t_{avg} = 75\ T_0$.

The scenario is significantly more complicated in figure III.3.5b, where the wind profiles vary substantially between the cases, subject to the Wind-Wave interactions in the atmosphere. In the inner surface layer, the roughness length (table III.3.3) is augmented with respect to flat conditions, and increases with the increasing WA between the cases. The buffer region extends higher in the MABL confining the outer surface layer into a smaller logarithmic region if compared to the flat bottom cases. Contrary to the inner surface layer, the roughness length in the outer surface layer (table III.3.4) decreases with augmenting WA. It will be also shown that, differently from the flat case scenario, there is a significant difference between the apparent friction velocity fitted in the logarithmic region and the actual friction velocity that gives the profiles' slope in the inner surface. With so many disturbances in the velocity profiles, the question posed in Cathelain [2017] over the cautiousness of considering log-law profiles in the offshore wind energy is restated: Is a log-law profile representative of the atmospheric wind in neutral conditions above a propagating wave? The short answer

is that it can be representative of the flow in the inner surface layer, or in the outer surface layer, but hardly both at the same time, and its region of validity shrinks with augmenting WBL extension.

For the long answer, log-law functions are fitted to the inner surface layer as in figure III.3.5c, and to the outer surface layer as in figure III.3.5d. The fitting applies to each region according to the procedures described in section III.1.2.3, and that leads to the values reported in tables III.3.3 and III.3.4. Recall that with the fitting defined, the ratio between the effective roughness length αz_0 and the boundary condition $z_0 = 10^{-6}\lambda$ is α. Likewise, C_d gives the ratio between effective friction velocity, and u^* as obtained from equation III.1.6.

The flat cases presented in section III.2.4 appear in the tables with the case average optimization values, and the uncertainties are taken as (±0.5) the maximum variation between the cases: Note that both fittings are comparatively much more similar in flat, rather than wavy bottom cases. In the inner surface layer the fitting applies only to the first two cells, and with $C_d = 1$, the effective roughness length αz_0 is optimized to the values of α given in table III.3.3, to be compared with the flat cases: The effective roughness length (αz_0) is magnified compared to the flat case, increasing up to a factor of ~ 10 in Case 01, and augmenting with rising WA between the cases.

In the outer surface layer, C_d and α are optimized in a variable region between the closed interval $[z_{min}, z_{max}]$, or $z_{mid} \pm 0.5\ z_{len}$, being the bounds $[z_{min}, z_{max}]$ found iteratively so maximizing z_{len} while keeping $\mathrm{RMS}_e < 3 \cdot 10^{-3}$. The optimized parameters C_d, z_0 and $[z_{mid}, z_{len}]$ that describe the wind profiles in the outer surface layer are so given in table III.3.4. Contrary to the inner layer, the roughness length increases with decreasing WA between the cases (as expected from the literature, c.f. section I.3.3), approaching the flat case solution between Cases 01 and 02. Except for Case 01 (highest WA), there are strong C_d disturbances due to the wave incidence, that between Cases 2 and 5 vary from 34% to 53%, compared to only 4% in Case 01, and the uncertainty of ±3%. Finally, the regions over which the log-law applies shrink due to the wave incidence, becoming shorter (46% in Case 01 to 15% in Case 05) in higher Wave ages.

Table III.3.3: Log-Fit of eq. III.1.15 to the inner surface layer (1st two cells): Optimal $[\alpha]$ with $C_d = 1$.

iCase	α
1	12.4
2	7.8
3	5.2
4	3.5
5	2.4
Flat	1.01±0.14

Table III.3.4: Log-Fit of eq. III.1.15 to the outer surface layer: Optimal $[C_d, \alpha]$ for $RMS_{diff} < 3 \cdot 10^{-3}$ in $z_{mid} + \left[-\frac{z_{len}}{2}, +\frac{z_{len}}{2}\right]$.

iCase	$C_d(\kappa = 0.4)$	α	z_{mid}/λ	z_{len}/λ
1	1.04	0.1	0.38	0.40
2	1.34	2.8	0.38	0.46
3	1.54	12.6	0.38	0.53
4	1.52	14.3	0.38	0.55
5	1.53	22.3	0.39	0.63
Flat	0.96± 0.03	0.60±0.19	0.39	0.74

III.3.2.3 MEAN TURBULENT PROFILES

Present section discusses turbulent motions that comprehend both atmospheric turbulence and WI motions in the MABL.

Turbulent Normal stresses The turbulent kinetic energy is presented in figure III.3.6, depicted by the resolved components in solid colors, and the sub-grid-scale component in transparency, or zoomed in the upper-right corner. Close to the surface the modeled contribution is approximately an order of magnitude below the resolved part, and becomes negligible close to the wave amplitude $z = ka$. The resolved part is strongly augmented with increasing Wave Ages, but the SGS contribution on the contrary, diminishes simultaneously. Before discussing the implications of such remarks in the TKE budget analysis, next paragraphs exploit the total (resolved+SGS) TKE behavior, decomposed in longitudinal and vertical variances (transversal omitted).

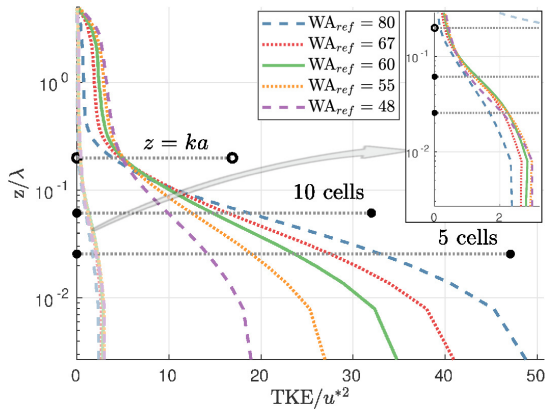

Figure III.3.6: Mean (ξ_1, ξ_2 and t) Turbulent Kinetic Energy (TKE) vertical profiles. Decomposed, with the total TKE appearing in solid and the SGS component with transparency, or zoomed in the upper right corner. The horizontal lines depict: 5th cell layer; 10th cell layer; and non-dimensional wave-height $ka = 0.2$. Sliding statistics are taken with time averages $t_{avg} = 75\ T_0$.

The turbulence intensities for longitudinal and vertical velocities appear respectively in figures III.3.7a and III.3.7b, where the colored lines depict the wavy cases described in the legend, and the light gray lines the reference flat bottom case. As usual the variances are strongly enhanced by the waves introduction close to the surface, but are diminished above, in the outer surface layer. With the WA augmenting, the disturbances are amplified, the variances grow close to the surface and diminish in the outer region.

A striking feature revealed in figure III.3.7, is that for each TI$_{uu}$ and TI$_{ww}$, the point where the cases intersect with each other and the flat solution remains almost constant: $z/\lambda = 0.1$ for TI$_{uu}$ in figure III.3.7a and $z/\lambda = 0.26$ for TI$_{ww}$ in figure III.3.7b. Clearly, the enhancement of TI close to the surface is due to the WI motions, shown in Paskin et al. [2020] (and further in section IV.1.2) to propagate higher in the WBL for the vertical velocities. The TKE budget analysis that follows, suggest that the diminish of TI on the outer region is rather due to an increase of the turbulent transport in the buffer region, bringing turbulent motions from the

outer layer into the WBL where they can be assimilated either by the WI flow (enhanced TKE in the WBL), or by the mean flow (localized negative production, or mitigation of positive production).

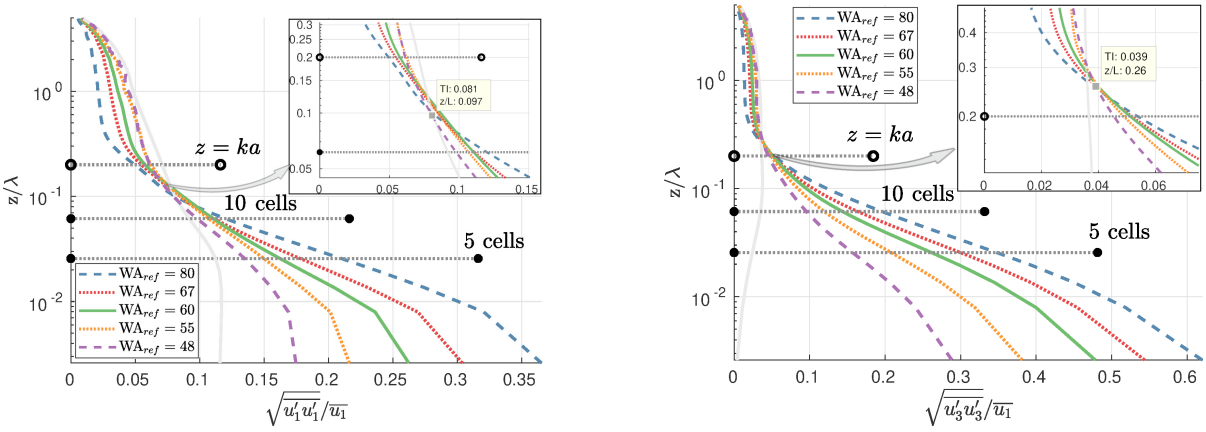

(a) TI_{uu}.

(b) TI_{ww}.

Figure III.3.7: Mean (ξ_1, ξ_2 and t), Turbulence Intensity profiles, for longitudinal (TI_{uu}) and vertical (TI_{ww}) velocity fluctuations. The legends correspond to the wavy cases here presented. The light gray lines represent the flat case solution of figure III.2.7c. The zoomed regions depict the intersections between the curves. Sliding statistics are taken with time averages $t_{avg} = 75\ T_0$.

Turbulent Kinetic energy budget As an introduction to the TKE budget analysis described in section III.1.1.4, production and dissipation terms are first exploited in figure III.3.8. The production is composed of resolved and modeled components. In figure III.3.8a one finds the total TKE production with solid colors, and the resolved components in transparency. Note that the sub-grid-scale production is dominant, at least until the 5 cells mark where the resolved component present a maximum for $WA_{ref} = 48$. As the total production diminishes with increasing Wave Age, so the maximum of the resolved component is displaced upwards, and the sub-grid-scale becomes important even higher on the ABL: For $WA_{ref} = 60$, e.g., the maximum of the resolved production is already close the 10 cells mark. These remarks let clear that the SGS model is significant determining the turbulence behavior in the near surface region, and into the lower part of outer surface layer depicted in figure III.3.5a. Even though one is right to be skeptical about the adequacy of the turbulent model [Hristov, 2018], the proper characterization of turbulent motions occurring in the LES reproduced ABL is given by both resolved and modeled components. So for the sake of brevity, only the total TKE budget terms are discussed forward.

The dissipation acts only in the SGS equations, and is modeled by $\epsilon = c_\epsilon \check{e}^{3/2}/\Delta_f$, i.e., dependent exclusively in a constant c_ϵ, the grid related filter length Δ_f, and the residual TKE $\check{e}$. Then the behavior of the dissipation in figure III.3.8b is determined by the residual TKE previously exposed in figure III.3.6: Close to the surface $\check{e}$ and ϵ diminish consistently with increasing Wave Ages.

Resolved and total variances strongly augment with increasing Wave Ages (figures III.3.6 and III.3.7), so the diminishing production with increasing Wave Ages observed at figure

III.3.8a indicate that a great amount of turbulence is not sustained by the shear production mechanisms of the TKE budget. The following discussion demonstrate that such excess in turbulence is associated to Wave-Induced motions, imposed by the waves orbital velocities in the surface and transported upwards in the ABL.

The production term evaluates the correlation between shear and reynolds stresses. The diminishing production in figure III.3.8a could be explained by either a lack of correlation between those stresses, or locally negative production terms that have already been observed in the literature above propagating waves (c.f. Yousefi and Veron [2020], Yang and Shen [2010]). With the horizontally (not wave phase dependent) averaged TKE budget here presented, it is not possible to distinguish localized regions of diminished or negative TKE production.

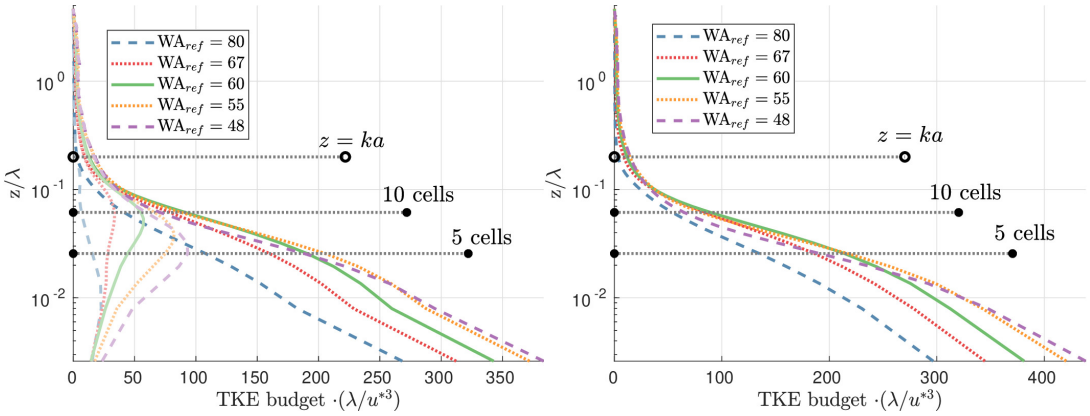

(a) Production term, resolved and total.

(b) Dissipation terms.

Figure III.3.8: Mean (ξ_1, ξ_2 and t) Turbulent kinetic energy budget profiles: Production and dissipation. In (a) the production is decomposed, with the total TKE production appearing in solid, and the resolved component with transparency. In (b) dissipation admits only SGS contributions. Sliding statistics are taken with time averages $t_{avg} = 75\ T_0$.

Figure III.3.9 comprehends all the terms forming the TKE budget in the WBL and described at section III.1.1.4: Production minus dissipation (net production) is shown in figure III.3.9a, turbulent and SGS transport are summed in figure III.3.9b, and the pressure transport shown in figure III.3.9c. In a neutral flat ABL, denoted by the light gray lines in the figures, production and dissipation closely balance each other in the outer layer, and just below the dominance of each term oscillates in a symmetrical pattern, with a minimum in the inner layer followed by a maximum just above in the buffer region. Also in the flat case, the predominance of dissipation and production are balanced respectively by positive and negative TKE transports, that ultimately transfer the turbulence generated near the wall to the outer region. When the WI flow enters the balance in the wavy cases here presented, the situation is drastically changed.

The WI flow does contribute to diminishing both production and dissipation (fig. III.3.8), but clearly it favors diminishing the first over the second, as strong TKE sinks are revealed close to the surface in figure III.3.9a: The wavy cases depart in the surface with considerably more net dissipation (− net production) than the flat case; from Cases 05 to 01 (Lowest to highest WA), the point upon which the dominant production reaches its maximum

is sequentially displaced upwards, and the maximum itself is sequentially diminished until almost vanishing in Cases 01 or 02.

Since dissipation largely dominates in figure III.3.9a, while the dissipation itself diminishes in figure III.3.8b, the resultant sink is instead attributed to an excessive mitigation of the production term, previously observed in figure III.3.8a. It reflects the physical mechanism upon which the WI flow either prevents the mean flow of generating turbulence (lack of correlation between shear and reynolds stresses), or gives energy to the mean flow (localized negative production), in any case contributing to the drag observed in the wind profiles.

The net production is, at least partially, balanced by the turbulent transport terms of figure III.3.9b, and in a pattern almost symmetrical to the flat bottom cases (with opposite signs), it becomes increasingly positive in the near-wall region with increasing Wave Ages. This near-wall region occurs in the buffer and lower part of the outer regions, defined in figure III.3.5a. In the flat bottom case the negative turbulent transport transfer turbulence generated in near-wall region, to be dissipated in the viscous region below, or the outer region above. On the contrary, with increasing wave ages turbulence is brought into the near-region. The amount of turbulence distributed from the outer and inner regions to the near-wall region depends on the WA, as for $\mathrm{WA}_{ref} = 48$ and $\mathrm{WA}_{ref} = 55$, e.g., the turbulent transport in the inner region remains positive or negligible, respectively. Also for $\mathrm{WA}_{ref} = 48$, the WI disturbances are mitigated, and the turbulent transport profiles are more similar to the flat bottom cases, instead of presenting the symmetrical pattern noted for the other cases.

In a flat bottom case, the integration of transport terms in the vertical direction is null [Moeng and Sullivan, 1994], so the only source of turbulence in the TKE budget is the net production: At the wavy cases, actually a strong sink acting through most of the ABL extension as seen in figure III.3.9a. With such turbulent sink induced, the excess of turbulence revealed in figures III.3.6 and III.3.7 is clearly detached from the classical atmospheric turbulence generation mechanisms.

As revealed previously, the excess of TKE is attributed to the so-called WI flow, sustained in the surface by the waves' orbitals (boundary conditions), and notably transported through the atmosphere by the pressure transport term: Strongly disturbed in figure III.3.9c due to the wave incidence. Indeed one notes in the figure, that the pressure transport term is strongly out-of-balance to the remaining TKE budget terms previously discussed, sometimes exceeding the others by an order of magnitude or more. The prevailing TKE Pressure transport justifies the similar overshoot observed in the TKE advection term at figure III.3.9d.

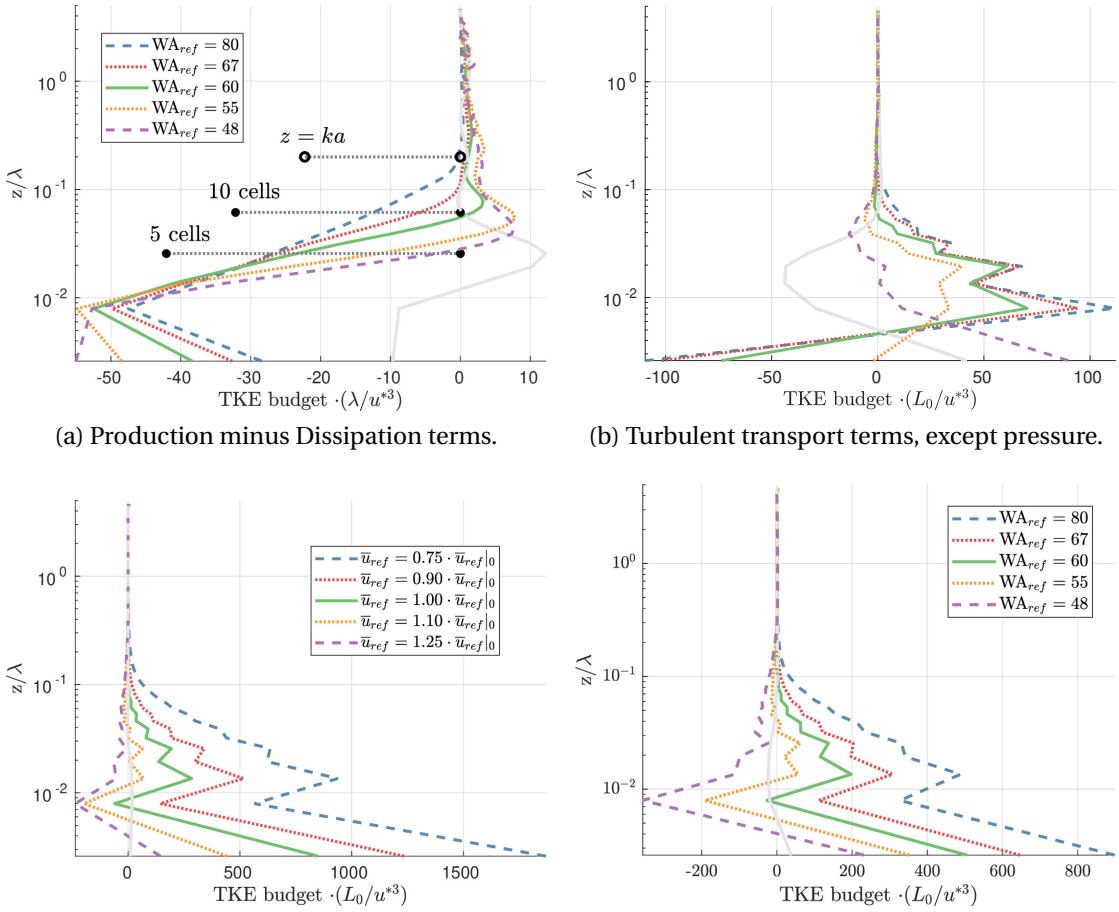

(a) Production minus Dissipation terms.

(b) Turbulent transport terms, except pressure.

(c) Pressure transport term.

(d) TKE Advection term.

Figure III.3.9: Mean (ξ_1, ξ_2 and t) Turbulent kinetic energy budget profiles, comprehending all the terms described at section III.1.1.4. Summing the profiles (a,b,c) one obtains the advection at (d). The legends correspond to the wavy cases here presented, and the light gray lines represent the flat case solution. Sliding statistics are taken with time averages $t_{avg} = 75\ T_0$.

Turbulent Shear stresses The total shear stresses $\tau_{13} = \tau_{13}^{(r)} + \tau_{13}^{(P)}$ are shown in figure III.3.10a, where they exhibit a linear behavior with varying slopes between the cases. A linear fitting applies to each profile and appears with transparency in the figure. The flat bottom solution, appearing in black at the figure, matches quite accurately the solution of Case 4 (WA$_{ref}$ = 55). Due to the waves, the total shear stress profile depart from other values rather than u^{*2} in the bottom, and evolve until vanishing in the upper boundary. The fitted profiles evolve from the values given in table III.3.5 on the surface, and are null when $z = z_l$. In the buffer region zoomed at figure III.3.10a the stresses deviate from the linear behavior.

In figure III.3.10b the total stress is decomposed into: Velocity correlations $\tau_{13}^{(r)} = \overline{u_1' u_3'} + \tau_{ij}^{SGS}$; and WI pressure stress $\tau_{ij}^{(P)} = \overline{(p + 2\check{e}/3) \cdot (\partial \xi_3 / \partial x_i)}$ components. The fictitious decomposition arises from the problem discretization in a moving grid, and is particularly useful because the pressure drag converges exactly to the form drag in the lower surface. The numerical formulation, then reveals a physical mechanism where the turbulent component of the flux responds to the pressure-drag acting in the deformed streamlines above a propagat-

ing wave, and it does so maintaining an almost linear stress profile along the boundary layer, such as observed at the flat bottom case and in the absence of $\tau_{ij}^{(P)}$ at figure III.3.10a. It must be noted though, that the decomposition is inexact above the surface, where the streamlines do not follow the moving grid. The rapid variation of pressure stresses (solid lines in figure III.3.10b) in the near region are sensed by the total stresses, explaining the deviation from the linear flux profile zoomed at figure III.3.10a.

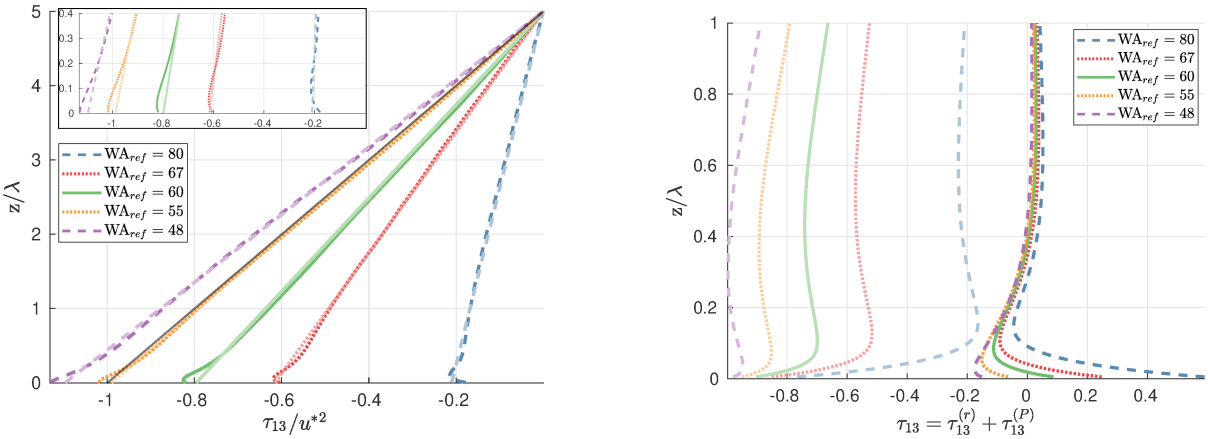

(a) Total shear stress.

(b) $u'w'$ turbulent (Transparent) and WI pressure (Solid) components of the shear stress.

Figure III.3.10: (a) Mean (ξ_1, ξ_2 and t) total shear stress $\tau_{13}(z)$, and (b) its decomposition into: velocity cross-correlation ($\tau_{13}^{(r)}$, transparent in b.), and WI pressure ($\tau_{13}^{(P)}$, solid colors in b.) contributions. In (a) linear fittings appear with transparency, parameterized according to table III.3.5, and the black line represents the flat case solution. The fitting is less accurate in the near-wall region, zoomed at the upper left corner of (a). Sliding statistics are taken with time average $t_{avg} = 75\ T_0$.

Table III.3.5: Linear fitting to the total shear stresses revealed in figure III.3.10a. At the upper boundary $\tau_{13}(z = z_l) = 0$, so the table gives the values of $\tau_{13}(z = 0)$, sufficient to specify the linear approximation.

Case ID	WA_{ref}	Fitted $\tau_{13}(z=0)/u^{2*}$
1	80	-0.21
2	67	-0.62
3	60	-0.80
4	55	-0.98
5	48	-1.10

The wave induced drag $F_p = F_\tau - u^{*2}$ has been previously discussed in figure III.3.4. At Cases 01 and 02, the drag is negative, and the waves are expected to grow, but at Case 02 the value is very close to zero, and not surprisingly the shear stresses closely approach the flat Case ($F_\tau \sim u^{*2}$) in figure III.3.10. The pressure drag is obviously determinant imposing the slope of the profiles in figure III.3.10a. To clarify that relationship, figure III.3.11 compares the dependence of F_τ to WA_{ref}, as obtained from either: $F_\tau = F_p + u^{*2}$, with actual

u^* reported in table III.3.1, and F_p/F_τ discussed in figure III.3.4c; or from the fitted value of $\tau_{13}(z = z_l) = 0$, reported at table III.3.5. One notes a very good agreement between each prediction, for which linear fittings appear as dotted lines in the figures. There is though, a small but persistent bias between these estimations, probably induced by the linear fitting employed to the τ_{13} profile (in figure III.3.10a, leading to table III.3.5).

The coefficients fitting F_τ/u^{*2} and $\tau_{13}(z = 0)/u^{*2}$ (in figure III.3.11) are given at table III.3.6. The offset between each methodology is observed in the 2% discrepancy of the constant coefficient B, which represents either: a 1.84 (3% of 60) offset in the WA_{ref}; or a 0.05 (2% of 2.5) offset in F_τ/u^{*2}; between the curves at figure III.3.11.

Table III.3.6: The total drag F_τ as a function of the WA_{ref}, is approximated in figure III.3.11 by a linear fitting with equation $F_\tau/u^{*2} = A{\cdot}\mathrm{WA}_{ref} + B$; and the coefficients are given hereby.

Case ID	A	B
actual F_τ	$2.84{\cdot}10^{-2}$	-2.54
Fitted from $\tau_{13}(z)$	$2.84{\cdot}10^{-2}$	-2.48

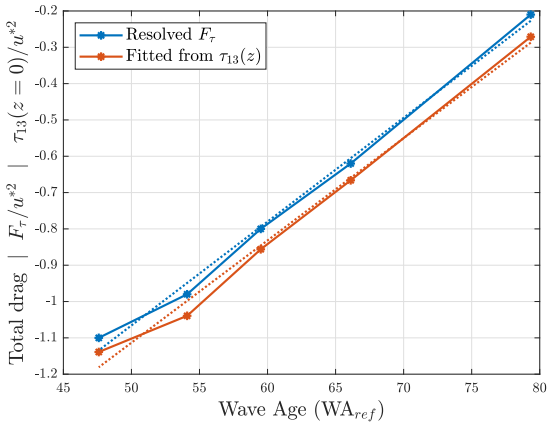

Figure III.3.11: Total drag F_τ as a function of WA_{ref}. Comparison between the actual value, and the one extrapolated from the linear fitting depicted in figure III.3.10a. Here a linear fitting applies to $F_\tau(\mathrm{WA}_{ref})$ and appears with dotted line in the figures; the fitting coefficients are given in table III.3.6.

III.3.3 Discussion

Thanks to the evolving pressure gradient method, the free-stream velocities are kept in a quasi-steady regime, and its averaged evolution converges towards the target value with a discrepancy of less than 3%. The friction velocity on the contrary, strongly deviates from its flat bottom solution, exhibiting a strong dependency to the WA parameter. So if WA is defined as function of the actual friction velocity, one establishes a circular dependency between those two parameters.

Alternatively the WA can be defined, e.g., from the non-disturbed friction velocities, and in the present formulation that will approximately scale with the actual free-stream velocity, here varying less than 3% from its undisturbed values. The two WA definitions are compared in the parametrization of the non-dimensional form drag, and the WA characterizing the non-disturbed or free-stream flow is significantly more consistent to describe the observations. A simple exponential model then accurately fits to the non-dimensional form drag as function of the reference WA. When evaluating the turbulent profiles, this parametriza-

tion also provides a reasonable first order approximation to the approximately linear shear stresses across the boundary layer height.

The waves introduced disturb the wind speed profiles, and notably their behavior through the logarithmic region. Due to waves, the region of validity of the logarithmic wind profile considerably diminishes with increasing wave age, squeezed by the extended inner and buffer regions occurring below. Also the apparent friction velocity that scales the wind profile in the logarithmic region is significantly disturbed by the waves, but such disturbance decreases with increasing wave ages. The effective roughness length fits separately to the inner and log-law regions: In the inner region it increases with increasing WA; but at the outer region the opposite trend is observed, as expected from empirical observations in the offshore environment and available through the literature.

Based on a few relevant observations where resolved and SGS motions are effectively discretized, a choice is made to focus in the total fluctuations, because they better characterize the LES resolved turbulence. Even though one is right to be skeptical about the adequacy of the SGS model [Hristov, 2018], it must be noted that resolved and SGS turbulence are determining each other simultaneously, and their physical meaning can only be properly evaluated together.

The turbulence intensity profiles indicate higher turbulence levels at the lower part of the ABL, due to the existence of the WI fluctuations, but just above that region one observes in fact lower turbulence levels if compared to the flat bottom cases. Such behavior is explained by the TKE budget analyses here presented.

While the total and resolved TKE augment close to the surface, the SGS contribution diminishes simultaneously, so the turbulent dissipation is diminished in the WBL. Regarding production, both the resolved and SGS components diminish in the WBL. The diminish of production is accentuated compared to dissipation, so the waves lead to a strong lack of balance between production and dissipation, ultimately acting as a sink in the total TKE equations. In the horizontally averaged, integral perspective here adopted, the diminished production reflects that less energy is transferred from the mean flow to the turbulent fluctuations. Naturally that suggests local regions of diminished production depending on the wave phase, and possibly local regions of negative production, with fluctuations transferring energy back to the mean flow.

The lack of balance between production and dissipation triggers the disturbance of turbulent transport terms, now bringing turbulent eddies from the outer region to the buffer region, contrary to the flat bottom case. The pressure transport term greatly surpasses the other terms of the TKE budget, and appears as the principal mechanism transferring the waves' orbital velocities to the air-flow. These enormous pressure transport terms imply strong TKE advection in the WBL, which is again consistent to the TKE profiles, presented with strong vertical variations in the analyses.

III.4 Different levels of Sea-State description

A major simplification employed in previous section regards the monochromatic wave prescription. Instead of the canonical regular wave scenario, the sea-state is better described as a continuous spectral distribution of an infinite number of regular waves, as discussed in section I.2.1.1. Approaching realistic offshore conditions estimated during the experimental campaign described in section II.1.3 (Case 01), and reconstructed in section IV.3.1, the sea-state description is considered in three levels of increasing complexity: (i) Regular waves; (ii) Irregular and single directional (1D) Sea-State; (iii) Irregular and multi-directional (2D) Sea-State.

The Sea-States so defined have the same total energy E_t, which for irregular Sea-States gives significant height $H_s = 4\sqrt{E_t} = 1.34$ m. The regular wave with energy E_t has wave height $H = 2\sqrt{2}\sqrt{E_t} = 0.95$ m. The wave peak period is $T_p = 10.10$ s, the peak length $L_p = 126.9$ m and the depth 22 m. The nominal (numerical) peak length is $\lambda = 128$ m, corresponding to the discrete resolved scale closest to L_p. One shall refer to table II.1.3 for other Sea-State quantities, and section IV.3.1 for more details about the Sea-States considered. Note that present section is still framed in a purely numerical perspective, and the comparison between physical and numerical experiments is presented later at section IV.3.4.

Compared to Paskin et al. [2020], and sections III.2, and III.3, the waves here considered have significant less energy. In the regular case here presented the non-dimensional height is $ka = 2\%$, which is quasi-linear, if compared to the previous sections where $ka = 20\%$. The energy scaling with H^2, that represents an 100 times decrease in the sea-state energy density per surface area. The ABL height and the domains' extension ratio to the wave-length here doubles the values presented before. The nominal Wave Age is comparable between those sections, with the value WA_0=85 here contrasting with WA_0=60 adopted in section III.2, or WA_0=80 for Case 01 in section III.3.

The WI disturbances are strongly mitigated compared to previous sections, and for some quantities they are negligible no matter which sea-state here considered. Notable exceptions are the vertical velocities variances or pressure related quantities, and minor disturbances can be evaluated in the wind speed profiles, or the longitudinal velocity variances. Later in section IV.2, the enhanced perspective described in section IV.1 is employed, and in contrast to previous analyses, the WI disturbances become clear at the two-dimensional wave-number-angular-frequency spectra, that also reveal some crucial and intrinsic differences between each sea-state considered.

III.4.1 Specific numerical strategy

The dynamic pressure gradient method developed in section III.2 is used to keep the Wind Speed close to $u_{ref} = u_{ref}|_h$ =4.12 m/s at the sLiDAR measurement height $h = 18.33$ m. Even though the method given in section III.2 can be easily generalized to an arbitrary (measurement) height instead of the boundary layer height δ, in the present case the fluctuations at $h = 18.33$ m greatly exceeds the ones at δ, and that could induce a considerably different behavior of the $\partial p/\partial x|_0$ evolution compared to the previous sections, requiring for example the specification of different natural periods $T_{\mathscr{P}}$. To avoid such differences in the $\partial p/\partial x|_0$

evolution scheme, like-wise in previous sections, here it responds to the free-stream velocity $\overline{u}_1(\delta)$ discrepancy to the target $u_{ref}|_\delta$.

To control the velocity at $h = 18.33$ m close to $u_{ref} = u_{ref}|_h$, the target velocity $u_{ref}|_\delta$ scales dynamically with the mean velocity flow-dependent ratio $\overline{u}_1(\delta)/\overline{u}_1(h)$:

$$u_{ref}|_\delta = u_{ref}|_h \frac{\overline{u}_1(\delta)}{\overline{u_1}(h)}, \tag{III.4.1}$$

evaluated at each period $T_{\mathscr{P}}$, where the spatio-temporal (ξ_1, ξ_2 ,t) averages are computed for $\overline{u}_1(z)$.

The wind field initializes from a constant pressure gradient $\partial p/\partial x|_0$ giving nominal friction velocity $u_0^* = 0.147$ m/s, and then the dynamic $\partial p/\partial x|_0$ algorithm is activated so the actual u^* and $\partial p/\partial x$ values come as consequence. The natural period of the pressure gradient response is $T_{\mathscr{P}} = 10^3\ (L_x/u'_{ref}) = 285\ T_0$, and the dynamic $\partial p/\partial x|_0$ algorithm runs for $400 T_0$ before the moving bottom is introduced.

The characteristic length scaling the domain is $L_0 = 256$ m, which doubles the nominal wave length $\lambda = 128$ m. The boundary layer height ($\delta = L_z$) to wave length ratio is $\delta/\lambda = 10$, and the longitudinal and transversal domain extensions to wave length ratio are respectively $L_x/\lambda = 8$ and $L_y/\lambda = 4$. The turbulent characteristic time scale is $T_0 = \lambda/u_0^* = 14.51$ min, which gives 86 wave peak periods T_p per turbulent time scale. The nominal $\mathrm{WA}_0 = c_p/u_0^*$ is 85.47.

The power density function of the wave elevation spectra is the real-valued input to the LES code. Linear waves components (i, j) with amplitudes given by the power spectra as $a_{ij} = \sqrt{2F(k_{xi}, k_{yj})\Delta k_x \Delta k_y}$, are initially generated with random phases. Afterwards those waves propagate with their phase velocity $c_p(k_{ij})$, given by the linear intermediate water dispersion equation $c_p(k) = \sqrt{(g/k)\tanh(kd)}$. Initializing the wave field from a converged dynamic $\partial p/\partial x|_0$ and flat bottom case, during 100 peak periods the actual wave heights shall linearly evolve from zero to its nominal value a_{ij}.

This numerical strategy is tested in the different grids of table III.1.1, but results are here presented only for grid 03 (Fine [512 x 256 x 94]). The time discretization has also been tested with its results here omitted. The regular wave case is found to require the smallest time steps, and the value CFL= 0.5 is selected that keeps $\nabla \cdot \mathbf{u}$ below $10^{-23}\ u_0^*/L_0$ at any case here presented.

Four cases are here compared: (0) Case 00 is the reference considering a flat terrain; (i) Case 01 introduces the regular monochromatic wave; (ii) Case 02 the 1D Irregular Sea-State; and (iii) Case 03 the 2D Irregular Sea-State. These sea-state conditions correspond to the conditions estimated during the experimental campaign (Section II.3), reconstructed as described in section IV.3.1: (iii) Is the full 2d Spectra $F(n, \phi) \rightarrow F(k_x, k_y)$, reconstructed at the sLiDAR's Line of Sight (LOS); (ii) is $F(n) \rightarrow F(k)$, obtained at the LOS and through the integration of $\int F(n, \phi)\mathrm{d}\phi$, propagating in the wind direction; (i) is the integration of $\int F(n)\mathrm{d}n$ concentrated in the wave peak frequency/ wave-number.

III.4.2 Results

III.4.2.1 Mean History profiles

The moving time average is performed through the period $t_{avg} = 41\ T_0$ (10 hrs) for the quantities presented in this section, but a shorter average $t_{avg} = 0.04\ T_0$ is also employed for the wind speed and the pressure gradient, respectively shown in figures III.4.1 and III.4.2. In figure III.4.1, one observes the resolved velocities at the measurement height ($h = 18.33$ m$= 0.14\lambda$), and the target velocity is denoted by the horizontal black dotted line ($|\overline{\boldsymbol{u}}|_h = 4.12$ m/s$= 28\ u_0^*$). The wind at the measurement height and during the period exposed, deviates less than 4% and 11% from the target, with $t_{avg} = 41\ T_0$ and $t_{avg} = 0.04\ T_0$, respectively. The Wind Speed (And such u^* and WA) is consequence of the dynamic and homogeneous pressure gradient ($\partial p/\partial x|_0$) modeled according to section III.2, and revealed in figure III.4.2. Contrary to the wind speed of figure III.4.1, the different average periods (t_{avg}) have little effect in $\partial p/\partial x|_0$, proving it responds only to very large scale motions.

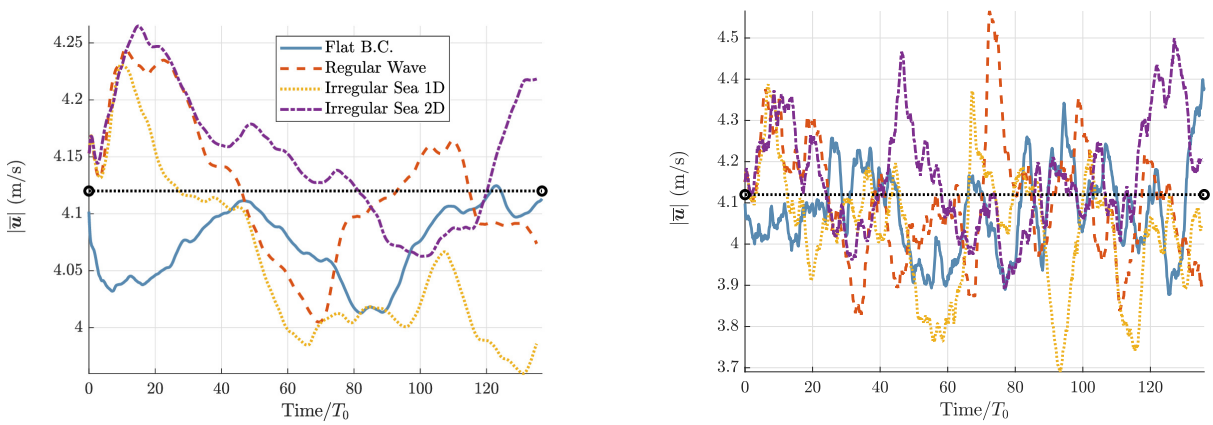

(a) $t_{avg} = 41\ T_0$ (b) $t_{avg} = 0.04\ T_0$

Figure III.4.1: Wind speed at the measurement height. For the flat case, and three different sea-states identified in the legend at (a). The horizontal line depicts the target velocity u_{ref} =4.12 m/s. Sliding statistics are taken with time different averages t_{avg} in (a) and (b).

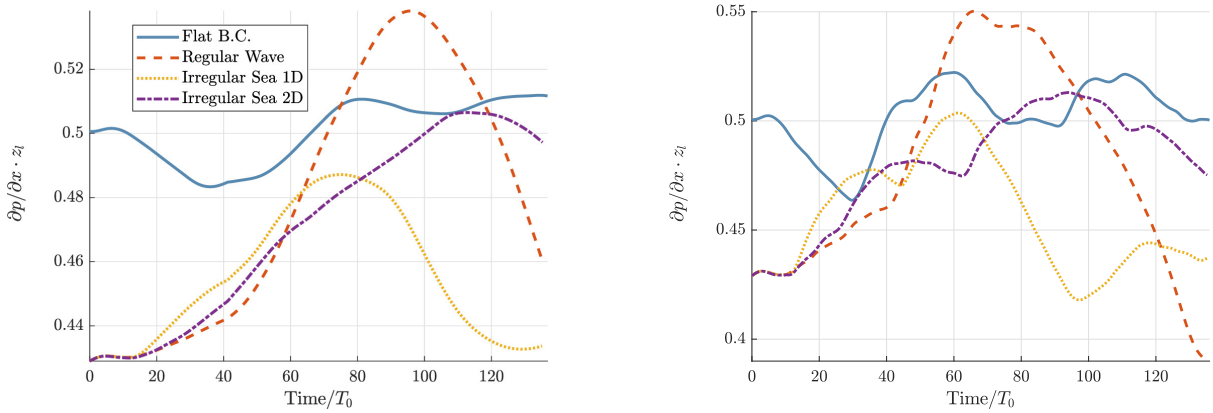

(a) $t_{avg} = 41\ T_0$ (b) $t_{avg} = 0.04\ T_0$

Figure III.4.2: Slowly evolving and homogeneous pressure gradient, modeled according to section III.2 to achieve the target velocity depicted at figure III.4.1. For the flat case, and three different sea-states identified in the legend at (a). Sliding statistics are taken with time different averages t_{avg} in (a) and (b).

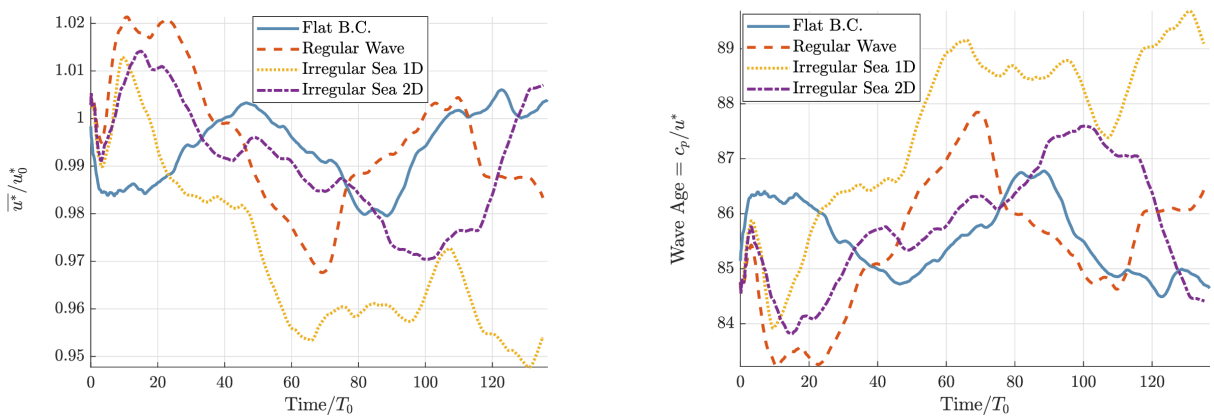

(a) Friction velocity. (b) Resolved Wave Age.

Figure III.4.3: Resolved friction velocity (computed from equation III.1.6), and the correspondent Wave Age. For the flat case, and three different sea-states identified in the legends. Sliding statistics are taken with time average $t_{avg} = 41\ T_0$.

The friction velocity $u^*_{[\xi,\eta]}$ averaged history is presented in figure III.4.3a for each test case. The varying friction velocity represents varying WA, that as shown in figure III.4.3b deviates less than 5.0% from the nominal value WA_0=85.47 in the case of an Irregular 1D spectra, and less than 3.2% otherwise. The Time Step Δt responsible for obtaining a constant CFL = 0.5 is shown in figure III.4.4a. The slighly varying wind induces small changes in Δt, but no direct influence of the Sea-State description is observed: An evidence that the wave orbital velocities do not surpass the maximum velocity obtained in the upper boundary, contrary to the observations in previous sections where $ka = 20\%$.

The non-dimensional form drag F_p/F_τ is shown in figure III.4.4b, revealing the most evident and striking difference between the cases. The Regular Wave is expected to damp, driving the wind with negative form drag, while the irregular waves are actually growing with

positive form drag. The irregular 1D case leads to the highest form drag coefficient. Note that in the irregular cases, waves are being damped or generated at different scales simultaneously, so the positive integrated form drag indicate the predominance of wave generation at lower scales, over the wave damping occurring in larger scales: In these cases the literature often employs the Fourier decomposition of the form drag, defining it as function of the wave-number of frequency scales; such investigation have not yet been employed in current studies, but would certainly allow an interesting perspective of the form drag behavior in the irregular sea-states.

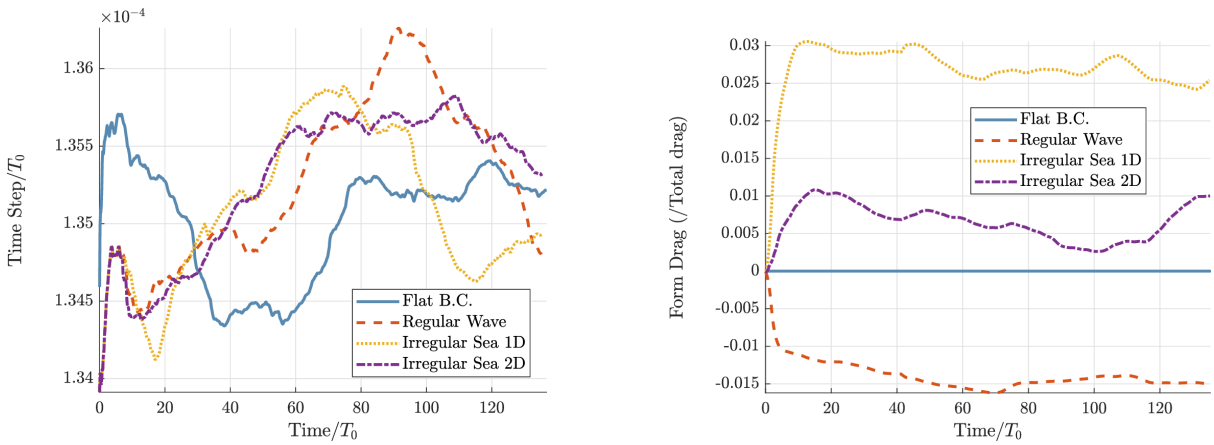

(a) Time-step.

(b) Form drag F_p/F_τ.

Figure III.4.4: Non-dimensional Time step and form drag. For the flat case, and three different sea-states identified in the legends. Sliding statistics are taken with time average $t_{avg} = 41\ T_0$.

The mean vertical profiles are being probed in the last time-step of the mean history profiles, and their values reported in table III.4.1.

Table III.4.1: Mean history quantities, probed at the last time-step of figures III.4.1, III.4.2, and III.4.3. Sliding statistics are taken with time average $t_{avg} = 41\ T_0$.

Case ID	$\lvert\overline{\boldsymbol{u}}\rvert(m/s)$	$\overline{\boldsymbol{u}^*}(m/s)$	WA= c_p/u^*	$\boldsymbol{\partial p/\partial x}\cdot z_l$	$\Delta t/T_0$	$\boldsymbol{F_p/F_\tau}$
1	4.11	0.148	84.9	0.52	$1.35\cdot10^{-4}$	0.0
2	4.07	0.145	86.7	0.46	$1.35\cdot10^{-4}$	-1.5%
3	3.98	0.140	89.7	0.43	$1.35\cdot10^{-4}$	2.5%
4	4.22	0.148	84.9	0.50	$1.35\cdot10^{-4}$	1.0%

III.4.2.2 Mean wind velocity and turbulent profiles

The quantities here exploited are obtained with $t_{avg} = 41\ T_0$, and the measurement height $h = 18.33$ m$= 0.14\ \lambda$ is denoted by the black horizontal dotted lines in the following figures.

The normalized mean wind profiles are shown in figure III.4.5 with the height dependence appearing both in linear (Up to $z = \lambda$) and log (Up to $z = z_l$) scales. The wind profiles

are a combination of logarithmic and linear functions as discussed in section III.2.1, figure III.2.1b. Normalized by the resolved friction velocity in the figures, the wind is intensified across the boundary layer by the waves' introduction, and the speed-up of the wind profile is more significant for the Irregular 1D Sea State, closely followed by the 2D case. The measurement height occurs inside the logarithmic region described in section III.1.2.3.

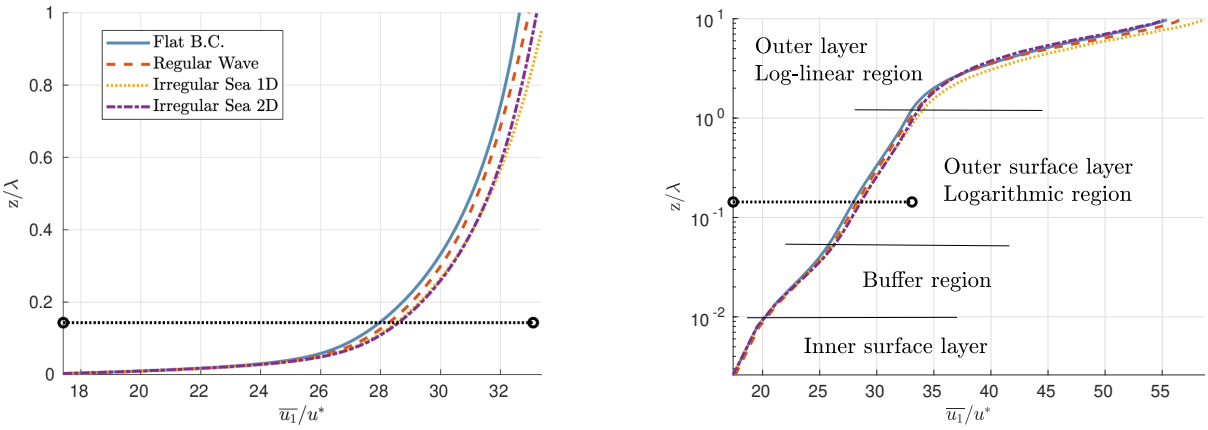

(a) In linear scale.

(b) In log-linear scale.

Figure III.4.5: Longitudinal velocity profile. The horizontal dashed line between circles depicts the measurement height h = 18.33 m= 0.14 λ. The regions discussed in section III.1.2.3 are drawn with the wind profiles at (b). Sliding statistics are taken with time average $t_{avg} = 41\ T_0$.

Table III.4.2: Logarithmic fit of equation III.1.15 to the wind profile in the outer surface layer. Optimal α ($C_d = 1$) for $RMS_{diff} < 3 \cdot 10^{-3}$, in $z_{mid} + \left[-\frac{z_{len}}{2}, +\frac{z_{len}}{2}\right]$.

iCase	α	z_{mid}/L_0	z_{len}/L_0
1	1.00	0.39	0.74
2	0.90	0.39	0.73
3	0.78	0.39	0.76
4	0.79	0.39	0.74

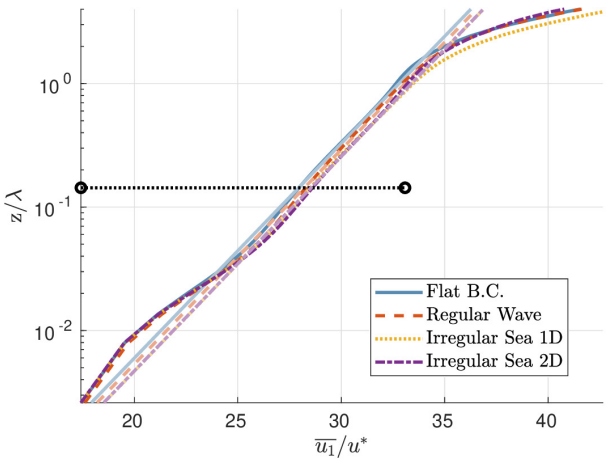

Figure III.4.6: Longitudinal velocity profile and logarithmic fit in the outer surface layer. The horizontal line denotes the measurement height 0.14 λ. $t_{avg} = 41\ T_0$.

As often (but not always) remarked in the literature, the wave induced disturbances in the MABL do not break a log-law behavior in the outer surface layer, which is attested fitting the logarithmic profile of equation III.1.15 with optimal αz_0, to the wind profile at a variable region between the closed interval $[z_{min}, z_{max}]$, or $z_{mid} \pm 0.5\ z_{len}$, being the bounds $[z_{min}, z_{max}]$ found iteratively so maximizing z_{len} while keeping $\mathrm{RMS}_e < 3 \cdot 10^{-3}$. The fitting is

exemplified in figure III.4.6, with the solution given in table III.4.2. Note the boundary condition is imposed with $\alpha = 1$ ($z_0/L_0 = 1 \cdot 10^{-6}$), which is accurately matched in the flat bottom case. The roughness obtained for the wavy cases summarizes the speed up observed in figure III.4.5a: The regular case introduces the slightest (still significant) disturbance with z_0 decreasing of 10%; followed by the irregular 2D sea-state with 21% reduction; and the irregular 1D Sea-State with 22% reduction.

The turbulent kinetic energy (TKE) is shown in figure III.4.7, and is magnified by the wave incidence up to $z/\lambda \approx 0.1$, in the lower part of the logarithmic region. The TKE disturbances become clearer if normalized by the mean velocities through the Turbulence Intensities depicted at figure III.4.8. The turbulence intensity for longitudinal velocities (TI_{uu}) is shown in figure III.4.8a, and as in section III.3, the rise in the turbulent kinetic energy close to the surface is followed by diminishing turbulence intensities above that region ($z/\lambda > 0.1$). The turbulence intensity for vertical velocities (TI_{ww}) is also very sensitive to the wave incidence, significantly increasing up to the measurement height where $z/\lambda \sim 0.14$ as shown in figure III.4.8b. The irregular 1D and 2D cases present similar TI_{ww}, but in the lower part of the logarithmic region the TI_{uu} at the 1D Case naturally exceeds the solution for the 2D Case, since in the former the waves orbital velocities perfect align to the uw plane, while in the second part of the energy is introduced in the transversal direction.

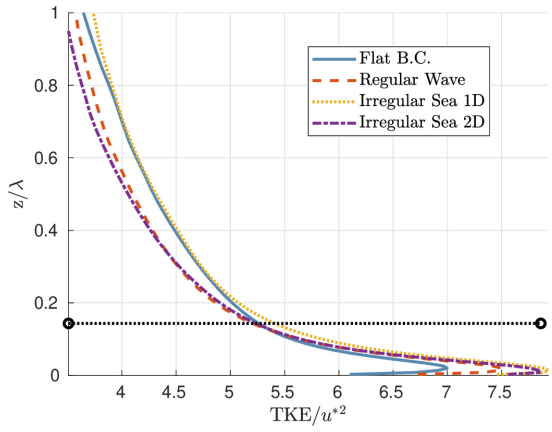

Figure III.4.7: Turbulent kinetic energy profiles. The horizontal lines denote the measurement height 0.14 λ. $t_{avg} = 41\ T_0$.

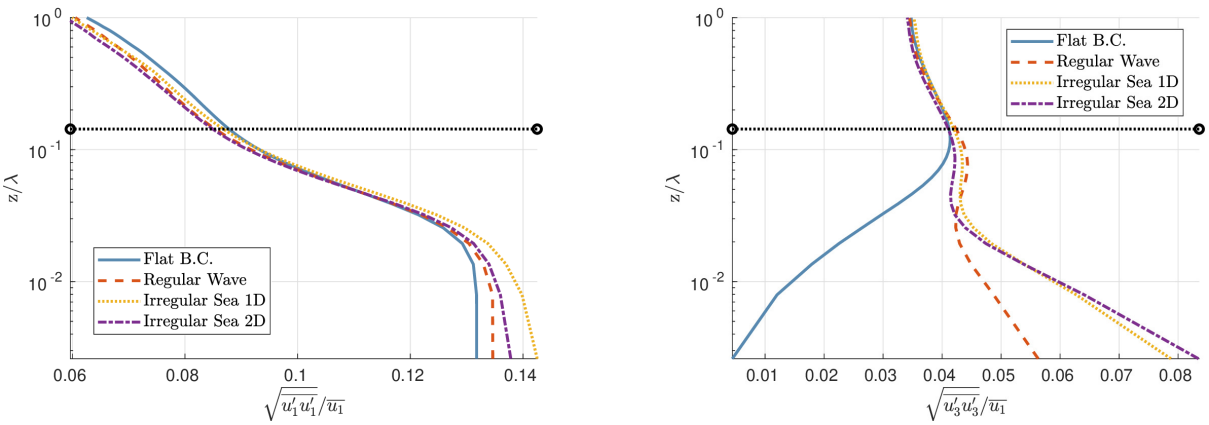

(a) Turbulent Intensity TI_{uu}. At the measurement height, $\mathrm{TI}_{uu} = 8.5\%$.

(b) Turbulent Intensity TI_{ww}.

Figure III.4.8: Turbulent Intensity of longitudinal and vertical velocity variances. The horizontal lines denote the measurement height 0.14 λ. Sliding statistics are taken with time average $t_{avg} = 41\ T_0$.

In the wave bottom cases and according to the numerical formulation, the total flux is given by the contribution of turbulent cross-correlations (Reynolds) stresses, summed with the WI pressure shear stress (c.f., Sullivan et al. [2000] and equation III.1.9), i.e., $\tau_{13}^{(P)}$ shown in figure III.4.9a: It results from the projection of p into the moving grid, and depends on very specific wind-wave interactions that impose the phase difference between pressure fluctuations and the surface elevation. The Regular wave case reveals indeed a very particular regime on the WI pressure stress, with a positive form drag leading to the wave damping, while the Irregular cases with same Wave Age present negative drag such leading to wave growth.

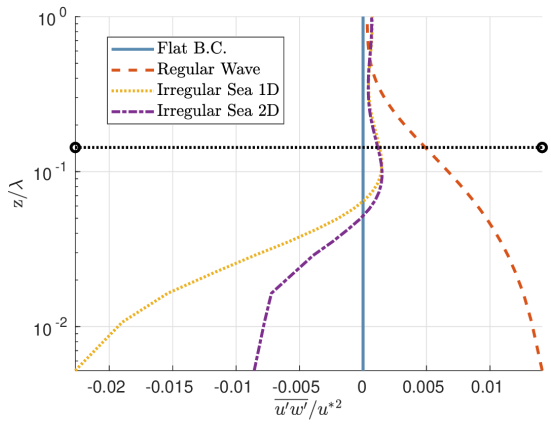

Figure III.4.9: Height dependent fictitious form drag, or WI pressure stress $\tau_{13}^{(P)}$. The horizontal line denotes the measurement height 0.14 λ. $t_{avg} = 41\ T_0$.

The turbulent kinetic energy (TKE) here incorporates Wave Induced motions, and the TKE balance is presented in figure III.4.10: The wavy cases present slight deviations of production, dissipation and transport terms, but the pressure transport is more seriously disturbed.

Production and dissipation are almost symmetric to each other, as shown in figure III.4.10a. They balance each other resulting in the combined, net (source or sink) production, shown in figure III.4.10b and observed to be below 10% of their separated values. Close to the surface and above the inner surface layer, dissipation prevails. Just above, production prevails over dissipation, and above that on the log-law region, production and dissipation balance each other to the order of $\sim 1\%$. The regular wave case hardly disturbs the net production above the inner surface layer, but the irregular waves slightly elevate the height upon which the net production reaches its maxima.

The net production appears with solid lines in figure III.4.10c, to be compared to the turbulent transport given in transparency. The turbulent transport adapts to the lack of balance in production and dissipation, as previously noted in section III.3.9b for the flat bottom reference. Except that here, the wavy cases to not lead to the inversion of the profiles signs.

The most striking difference in the TKE budget appears again the pressure term shown in figure III.4.10d. The pressure transport term is non-null in the flat bottom case, slighly increased in the regular and irregular 1D cases, and greatly increased in the irregular 2D case. The irregular 2D case is the only one for which the wave induced disturbances in the pressure transport are indeed smooth, since the regular and irregular 1D cases present sharp disturbances in the inner surface layer as observed, e.g., in figure III.3.9c.

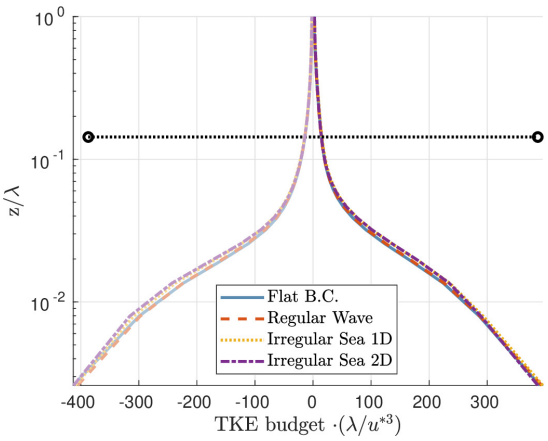

(a) Production (positive) and Dissipation (negative) terms.

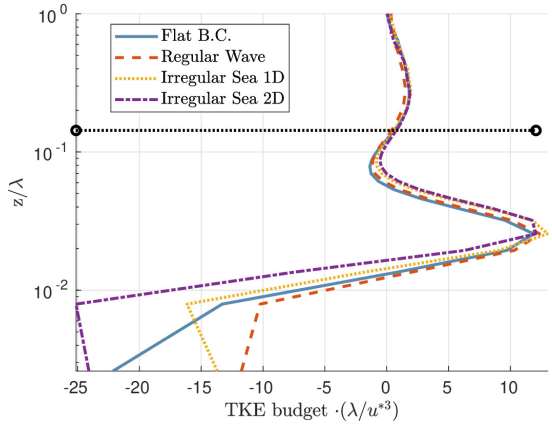

(b) Net production: Production minus Dissipation terms.

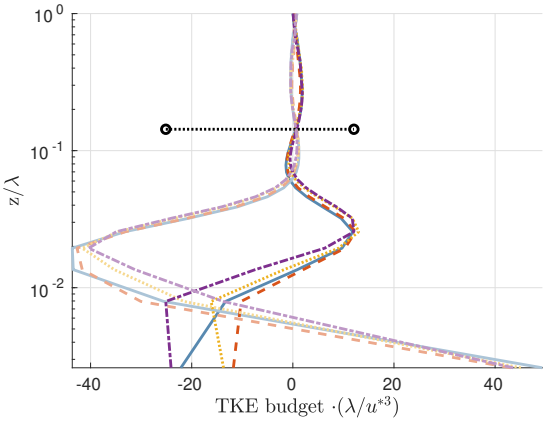

(c) Turbulent transport terms, except pressure, in transparency; Net production term in solid lines.

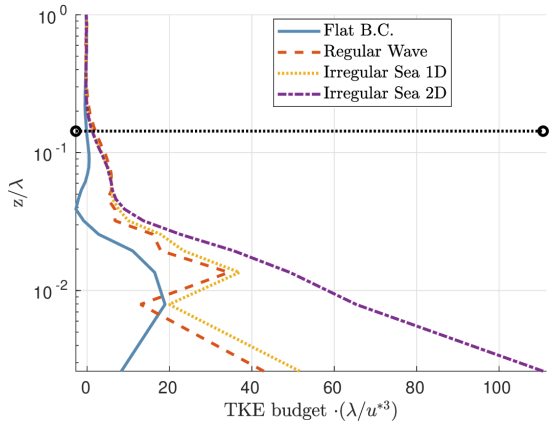

(d) Pressure transport term.

Figure III.4.10: Turbulent kinetic energy budget analysis, considering the terms defined in section III.1.1.4. The horizontal lines denote the measurement height 0.14 λ. Sliding statistics are taken with time average $t_{avg} = 41\ T_0$.

III.4.3 Overview and discussion

Addressing long waves (λ = 128 m) and old seas (WA=85) conditions, with small (quasi-linear) wave amplitudes ($ka \sim 2\%$) if compared to previous sections ($ka = 20\%$), the sea-state description is here considered in three levels of increasing complexity and fidelity to the reproduced experimental conditions observed in section II.3. The dynamic pressure gradient method presented in section III.2.3 is successfully used to keep the mean velocity close to the target u_{ref} =4.12 m/s at the measurement height h = 18 m. The WI disturbances are significantly less pronounced than in previous sections, and a log-law behavior is sustained in the wind profiles, but the turbulent profiles discussed reveal some of the the intrinsic differences between the different sea-state prescriptions, notably remarking the complexity of Wind-Wave interactions.

The sea-state energy here being ~ 100 times smaller, many of the disturbances observed in the previous sections here become negligible, as for example: The logarithmic region is

sustained with undisturbed apparent friction velocity; the $\overline{u'w'}$ cross correlation profiles have not even been discussed, because the disturbances are comparable to the intrinsic level of fluctuation, preventing any meaningful discussion; the turbulence intensities are very weakly disturbed above the measurement height 0.14 λ; and except for the pressure transport term, the TKE budget analyses do not behave drastically different in the wavy compared to the flat bottom cases. Even in this numerical controlled scenario, these disturbances are so hard to catch that the comparison is often contaminated by turbulent uncertainties, and in the offshore environment most of the previous remarks would be undetectable face to the uncertainties of the measurement techniques, unsteadiness, and non-homogeneity effects (Hristov [2018]).

As for the previous test cases, the ones here presented are to be revisited with spectral analyses in section IV.2, after the introduction of an original methodology for identifying the WI motions above arbitrary sea-states, and during physical or numerical experiments. Contrary to the mean history, mean wind and turbulent profiles, and the 1D spectral analyses (later presented), and as argued in section IV.1: The Space-Time (Or $k-w$) perspective of turbulent fluctuations reveals detailed information about the WI flow structure. Thus such approach favors the investigation of consequent WI disturbances and Wind-Wave interactions in the atmospheric flow, revealing intrinsic differences between the test cases discussed. The comparison between physical and numerical experiments is considered at section IV.3.

Part IV

A MECHANISTIC APPROACH TO PHYSICAL AND NUMERICAL EXPERIMENTS

Europa and the Great Red Spot photographed by the Voyager 1 in March, 1979. The Great Red Spot: An enduring large scale anticyclone, larger than earth (Wong et al. [2021]). Europa: One of jupiter's 79 moons; slightly smaller than earth. Colored by the artist Alexis Tranchandon, part of The Bruce Murray Space Image Library collection. Original from Voyager 1 Imaging Science Subsystem (ISS): NASA / JPL-Caltech / Alexis Tranchandon / Solaris.

IV.1 An enhanced perspective of the Wave Induced flow

The Wave Coherent (WC) decomposition, introduced at section I.3.6 and reviewed in section IV.1.1.1, is often adopted in the literature to identify WI motions in the atmosphere. It is here argued that though extremely important, the WC flow evaluates the quality of turbulent motions coherent to the sea-state, rather than giving a precise characterization of the WI flow. The WC flow might cover a large portion of the turbulent spectra, not necessarily capturing any WI disturbance in the airflow, and it does not discriminate different motions occurring at the same scale. In fact, *Atmospheric Turbulence* (Atm.) and *Wave Induced* (WI) motions coexist in the Wave Coherent (WC) flow, that holds all Wind-Wave interaction effects.

Looking forward into the flow description, it is desired to observe what is happening at the WC scales. Notably, Atm. and WI motions occurring at the same scales behave considerably different, e.g., in terms of anisotropy, regeneration cycle and Space-Time correlations. But which are the local processes of Wind-Wave interactions occurring between Atm. and WI motions, and after all, what are these Wave Induced motions? The author believes there is yet place for a more detailed description of the flow topology insight the WBL, and introduces it as follows.

IV.1.1 Theoretical foundation

Two concepts extend the definition of a *Wave Related* flow, from *Wave Coherent* (WC) to *Wave Induced* (WI), leading to WI and WC decompositions that for the first time allow their quantification in the field, without any previous sea-state knowledge required: (i) The existing correlation between *Atmospheric turbulence* (Atm.) and WI motions; and (ii) The Space-Time spectral description of the WI flow. The WI flow is so defined as a specific kind of turbulent fluctuation, that does not behave as expected from atmospheric turbulent flows above fixed terrains, which might be often particularly noticeable in the $k-w$ turbulent spectra that allows the decomposition above arbitrary sea-states.

IV.1.1.1 Wave Coherent and Wave Induced flows

Recall from section I.3.6, equation I.3.1, that the WC filter (superscript $\cdot^C$) is defined by projecting a generic variable χ, into the vector space of all wave (elevation η) coherent signals. Counting in the Hilbert transform discretizing η in the spectral domain, let $\overset{\circ}{\eta}_k(x)$ ($\overset{\circ}{\eta}_w(t)$) be the in-quadrature counterpart of the kth (w^{th}) wave number (angular frequency), one-dimensional free surface elevation $\eta_k(x)$ ($\eta_k(t)$), then repeating equation I.3.1:

$$\tilde{\chi}_k^C(x) = \frac{\overline{\chi(x)\eta_k(x)}^{[x]}}{||\eta_k||^2_{[x]}}\eta_k(x) + \frac{\overline{\chi(x)\overset{\circ}{\eta}_k(x)}^{[x]}}{||\overset{\circ}{\eta}_k||^2_{[x]}}\overset{\circ}{\eta}_k(x)$$

$$\tilde{\chi}^C(x) = \sum_k \tilde{\chi}_k^C(x), \qquad \text{and} \qquad \hat{\chi}^C(x) = \chi(x) - \tilde{\chi}^C(x). \tag{IV.1.1}$$

Consider the numerical case of a monochromatic wave described in section III.2.5, and further explored in section IV.1.2. The wave is highly non-linear $ka = 0.2$, described by a 5th order stokes theory, and considerably fast with WA= $c_p/u^* \sim 60$. The wave-number dependent longitudinal EDF (Turbulent spectra), resolved ~1.1 m above the surface, is depicted in blue full line at figure IV.1.1: The WI flow is observed augmenting the turbulent spectra at five local maxima corresponding to the wave harmonics scales.

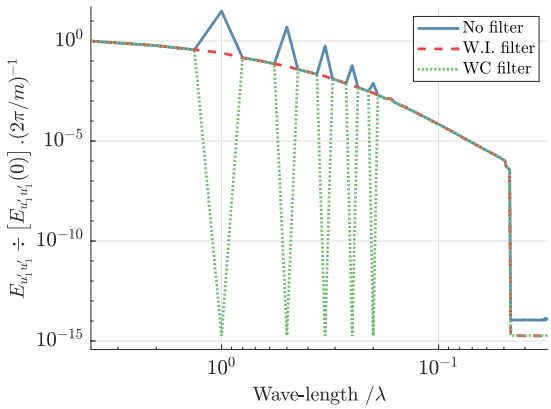

Figure IV.1.1: Numerical experiment of a monochromatic wave described in section IV.1.2. One-dimensional spectral density function $E_{u_1u_1}(l = 2\pi/k)$. Total fluctuation spectra $E_{u_1'u_1'}$ in blue full line; Residual of the Wave Coherent filtered turbulent spectra $E^C_{\hat{u}_1\hat{u}_1}$ in green dotted line; Wave Induced filtered Atmospheric turbulence spectra $E^I_{\hat{u}_1\hat{u}_1}$ in red dashed line.

In this canonical condition, where the sea-state spectrum is infinitely sharp (i.e., a dirac function), applying the Wave Coherent (WC) filter of equation IV.1.1 is straightforward and leads to the green dashed line turbulent spectrum in figure IV.1.1. As expected the WC filter associates all the energy occurring at the waves' scales to the WC flow, leaving nonphysical gaps in the turbulent spectrum, ultimately ensuring the lack of correlations between the decomposed fields $\overline{\tilde{\chi}\hat{\chi}} = 0$. To further evaluate the implications of this assumption, the Wave Induced (WI) filter (red dashed line in fig. IV.1.1) is here proposed as an alternative to the WC filter. Introducing the flow dependent WI fraction $0 \leq \mathscr{F}_\chi(k) \leq 1$, yet defined in the wave-number domain, the WI filter identified by the $\cdot^I$ superscript is defined as a fraction of the Wave Coherent filter:

$$\begin{aligned} \tilde{\chi}_k^I(x,t) &= \mathscr{F}_\chi(k) \cdot \tilde{\chi}_k^C(x,t), \qquad \text{and} \\ \hat{\chi}_k^I(x,t) &= \left[1 - \mathscr{F}_\chi(k)\right] \cdot \tilde{\chi}_k^C(x,t), \end{aligned} \tag{IV.1.2}$$

splitting total fluctuations into *Atmospheric Turbulence* (Atm., $\hat{\chi}$) and *Wave Induced* (WI, $\tilde{\chi}$) fields. Clearly the $\overline{\tilde{\chi}\hat{\chi}} = 0$ property is lost with the WI filter, as Atm. $\hat{\chi}_k^I$ and WI motions $\tilde{\chi}_k^I$ are not perfectly in quadrature, and are allowed to coexist in the same wave-number, unless: $\mathscr{F}_\chi(k) = 0$ that suppresses WI motions in the wave-number k, or $\mathscr{F}_\chi(k) = 1$ that recovers the WC filter in k. Thanks to the linearity of the Fourier Transform operator, $\mathscr{F}$ uniquely defines the auto and cross-correlation EDFs of Atm. and WI motions, in terms of the total auto-correlation spectra $E_{\chi\chi}(k)$:

$$\begin{aligned} E_{\tilde{\chi}\tilde{\chi}}(k) &= \left[\mathscr{F}_\chi(k)\right]^2 E_{\chi\chi}(k) \quad , \\ E_{\hat{\chi}\hat{\chi}}(k) &= \left[1-\mathscr{F}_\chi(k)\right]^2 E_{\chi\chi}(k) \quad , \qquad \text{and} \\ E_{\tilde{\chi}\hat{\chi}}(k) &= \left[\mathscr{F}_\chi(k)\right]\left[1-\mathscr{F}_\chi(k)\right] E_{\chi\chi}(k) \quad , \end{aligned} \tag{IV.1.3}$$

with the total EDF decomposed in $E_{\chi\chi} = E_{\tilde{\chi}\tilde{\chi}} + 2\,E_{\tilde{\chi}\hat{\chi}} + E_{\hat{\chi}\hat{\chi}}$.

If there is a phase shift $\psi(k)$ between $\tilde{\chi}_k^I$ and $\tilde{\chi}_k^C$, then $\mathscr{F}_\chi(k) = |\mathscr{F}| \cdot \exp[i\ \psi]$ shall be a complex valued function. In a statistically steady scenario, it is reasonable to assume that Atm. and WI motions interacting at the same scales will resonate, and one can assume $\psi(k) = 0$. Without any other reason to assume the contrary, the WI flow is here defined perfectly in phase to the WC flow, and $\mathscr{F}_\chi(k) = \mathbb{R}(\mathscr{F})$ is a real-valued function. Note that's a necessary assumption, because the auto-correlation functions do not hold any information about the phase, preventing in principle the deterministic reconstruction of turbulent motions from the turbulent auto-spectra (c.f. Kogan et al. [2016]).

From that assumption and equation IV.1.3, $\mathscr{F}(k)$ can be determined from the magnitude of the turbulent spectra $E_{\chi\chi}(k)$, so that $E_{\hat{\chi}\hat{\chi}}(k) = \left[1-\mathscr{F}_\chi(k)\right]^2 E_{\chi\chi}(k)$ behaves as expected from Atmospheric Turbulence motions. This approach is first tested in figure IV.1.1, where $\mathscr{F}(k)$ is obtained through a linear interpolation of the total turbulent spectra at the waves' harmonic scales, leading to the Atm. turbulence spectrum depicted in red dashed line at the figure, and further explored in section IV.1.2.

With the methodology proposed, $E_{\hat{\chi}\hat{\chi}}(k)$ is by definition extracted from $E_{\chi\chi}(k)$ to follow a certain behavior. The phase $\psi(k)$ would then play its role distributing the energy excess $(E_{\chi\chi} - E_{\hat{\chi}\hat{\chi}})$ between the WI auto and cross spectra $E_{\tilde{\chi}\tilde{\chi}} + 2\,E_{\tilde{\chi}\hat{\chi}}$. The assumption $\psi(k) = 0$ (in-phase signals) maximizes the amount of Atm.-WI correlations in the decomposition, while $\psi(k) \to \pi/2$ (in-quadrature signals), on the contrary, implies a negligible amount of WI-Atm. correlations. Hence, with $\psi(k) = 0$ the WI-Atm. correlations is here approximated by its upper limit, while the exact WI auto-spectra shall range between $E_{\tilde{\chi}\tilde{\chi}}$ and $E_{\tilde{\chi}\tilde{\chi}} + 2\,E_{\tilde{\chi}\hat{\chi}}$.

To be soon overcome by an enhanced perspective of WI motions, such methodology has three major drawbacks: **(i)** As for the WC filter, the WI filter so defined applies easily to a monochromatic WI disturbance, or in a lesser extent to a very sharp sea-state spectrum, but that is a quite different situation from that of a continuous sea-state spectrum observed in the ocean, overlapping with turbulence over multiple scales; **(ii)** Often the case, WI motions that do not introduce significant changes in the 1D turbulent spectra shall not be detected, contrary to the WC filter that on the other side neglects the atmospheric turbulent part independently of any specific WI disturbance; **(iii)** Significant $\overline{\tilde{\chi}\hat{\chi}}$ correlations are frequently observed, which prevent the uncoupling between WI and Atmospheric turbulence govern-

ing equations, defying the notion of a WI flow system (almost) detached from turbulent dynamics.

IV.1.1.2 Joint Space-Time modal perspective

In section II.3, it is argued that compared to the 2D wave-number-angular-frequency ($k-w$) spectra, 1D wave-number (k) or frequency $f = w/2\pi$ turbulent spectra reveal a very limited perspective of the spectral energy distribution. If the mean wind velocity (U) is sufficiently apart from the waves' velocities (c), atmospheric turbulence and WI motions shall be frequently distinguishable in the 2D spectra, whereas they are not in the 1D spectra.

It is also shown in section II.3 that the reason the WI signature emerges preferably in the 2D Spectra, whereas it does not in the 1D Spectra is exactly because the Atm.-WI coherence is diminished in the Space-Time domain, if compared to the 1D Space or Time versions. Within such perspective, the difficulties sooner expressed might be often overcome: **(i)** It will be shown for multiple physical and numerical experiments, and for wind signals measured above arbitrarily sea-states, that the partitioning of the turbulent spectra becomes feasible in the $k-w$ domain, without any sea-state information being known a priori; **(ii)** As long as U and c are sufficiently apart, the WI signature shall be sufficiently separated from the most energetic Atm. turbulence in the 2D Spectra; **(iii)** In the Space-Time ($x-t$) domain the apparent correlations $\overline{\tilde{\chi}\hat{\chi}}$ are much smaller than in the 1D separated Space or Time domains, so without any loss of consistency the URANS equations might be obtained from combined Space-Time averages, and that will frequently lead to a negligible amount of $\overline{\tilde{\chi}\hat{\chi}}$, limiting the Atm.-WI interactions and supporting the relevance of the uncoupled set of equations presented in Hristov and Ruiz-Plancarte [2014].

In the $x-t$ and $k-w$ perspective, the WC and WI filters are defined by the following equations:

$$\tilde{\chi}^{C}_{kw}(x,t) = \frac{\overline{\chi(x,t)\eta_{kw}(x,t)}^{[x,t]}}{||\eta_{kw}||^2_{[x,t]}}\eta_{kw}(x,t) + \frac{\overline{\chi(x,t)\mathring{\eta}_{kw}(x,t)}^{[x,t]}}{||\mathring{\eta}_{kw}||^2_{[x,t]}}\mathring{\eta}_{kw}(x,t)$$

$$\tilde{\chi}^{C}(x,t) = \sum_{w}\sum_{k}\tilde{\chi}^{C}_{kw}(x,t), \qquad \hat{\chi}^{C}(x,t) = \chi(x,t) - \tilde{\chi}^{C}(x,t) \tag{IV.1.4}$$

$$\begin{aligned} \tilde{\chi}^{I}_{kw}(x,t) &= \mathscr{F}_{\chi}(k,w) \cdot\tilde{\chi}^{C}_{kw}(x,t) \\ \hat{\chi}^{I}_{kw}(x,t) &= \left[1-\mathscr{F}_{\chi}(k,w)\right] \cdot\tilde{\chi}^{C}_{kw}(x,t). \end{aligned} \tag{IV.1.5}$$

As before the turbulent spectra scale with the square of $\mathscr{F}$ or its counterpart $1-\mathscr{F}$, such as given in equation IV.1.3 that can be easily generalized for $\mathscr{F}(k,w)$ and $E_{\chi\chi}(k,w)$. Again $\mathscr{F}$ is directly estimated from the turbulent spectra, but the procedure is significantly more complex in the 2D version, so the partition of $E_{\chi\chi}(k,w)$ leading to the real-valued $\mathscr{F}$ is described in section IV.2. The partitioning introduced also allows the estimation of the WC

field, without previous knowledge of the free-surface motions, which is simply recovered when $\mathscr{F} \sim 1$.

IV.1.2 Monochromatic wave application

The Wave Coherent and Wave Induced flow definitions are first exploited in the numerical, canonical case of monochromatic waves described in section III.2.5. Recall that this section presented 3 cases: Case 01 is the flat bottom (flat BC) reference with constant $\partial p/\partial x|_0$; Case 02 considers a wavy bottom (Wavy BC), but still constant $\partial p/\partial x|_0$; and Case 03 considers the Wavy BC introducing the dynamic $\partial p/\partial x|_0$ algorithm. Cases 01 and 02 have been exploited in Paskin et al. [2020] by considering the same analysis followed hereby.

Here, sections IV.1.2.1 and IV.1.2.2 compare the flat and wavy bottom cases, previously presented in section III.2.5 as Case 01 (flat BC and constant $\partial p/\partial x|_0$) and Case 03 (wavy BC and dynamic $\partial p/\partial x|_0$), repeating and confirming the analyses previously presented in Paskin et al. [2020] for Case 02. The wavy case is characterized by $\mathrm{WA}_{ref} = 60$, with non-dimensional wave height $ka = 0.2$, and non-dimensional boundary layer height $\delta/\lambda = 5$. One shall refer to section III.2.5 for other details about the specific numerical setup.

IV.1.2.1 Wave Induced motions

The longitudinal 1D Correlation functions $R(\xi_1)$ are averaged on (ξ_1, ξ_2) directions along each horizontal computational plane. The wave-number dependent turbulent spectra $E(k)$ are then obtained through the FFT of the Correlation functions (see section I.1.1.5), before being submitted to a moving time average with period $t_{avg} = 6.7\ T_0$, so that $E = E(\xi_3, k)$.

These spectra are first evaluated at different heights ξ_3 in figure IV.1.2, for the flat bottom case in (a,b), and the wavy bottom case in (c,d). The turbulent spectra for longitudinal velocities are given in (a,c), and for the vertical velocities in (b,d). In terms of lengths $2\pi/k$, the $E(k)$ spectra ranges between $2\Delta x = \lambda/64$ and $x_l = 4\lambda$, but in the LES a dealising procedure truncates the spectra, damping fluctuations smaller than $3\Delta x$.

The wave signature is evident at the wavy bottom case, figures IV.1.2c and d, leading to peaks occurring in the swell free (k_w) and bounded (nk_w; $n = 2..5$) wave numbers. The spectra are normalized by the one-point auto-correlation, that equals their integral, so the WI localized disturbances introduce large gaps between different heights in undisturbed regions of the spectra depicted. The peaks are gradually damped with increasing height ξ_3, and are more prominent for the vertical velocities.

The WI disturbances are very sharp, mostly detected at single points of the spectra, which is natural because the wave itself is prescribed that way. A monochromatic wave is infinitely sharp in the spectral domain, i.e., a dirac function in the continuous, or a step function (with width $\Delta k = 2\pi/[x_l\ n_x]$) in the discrete formulation.

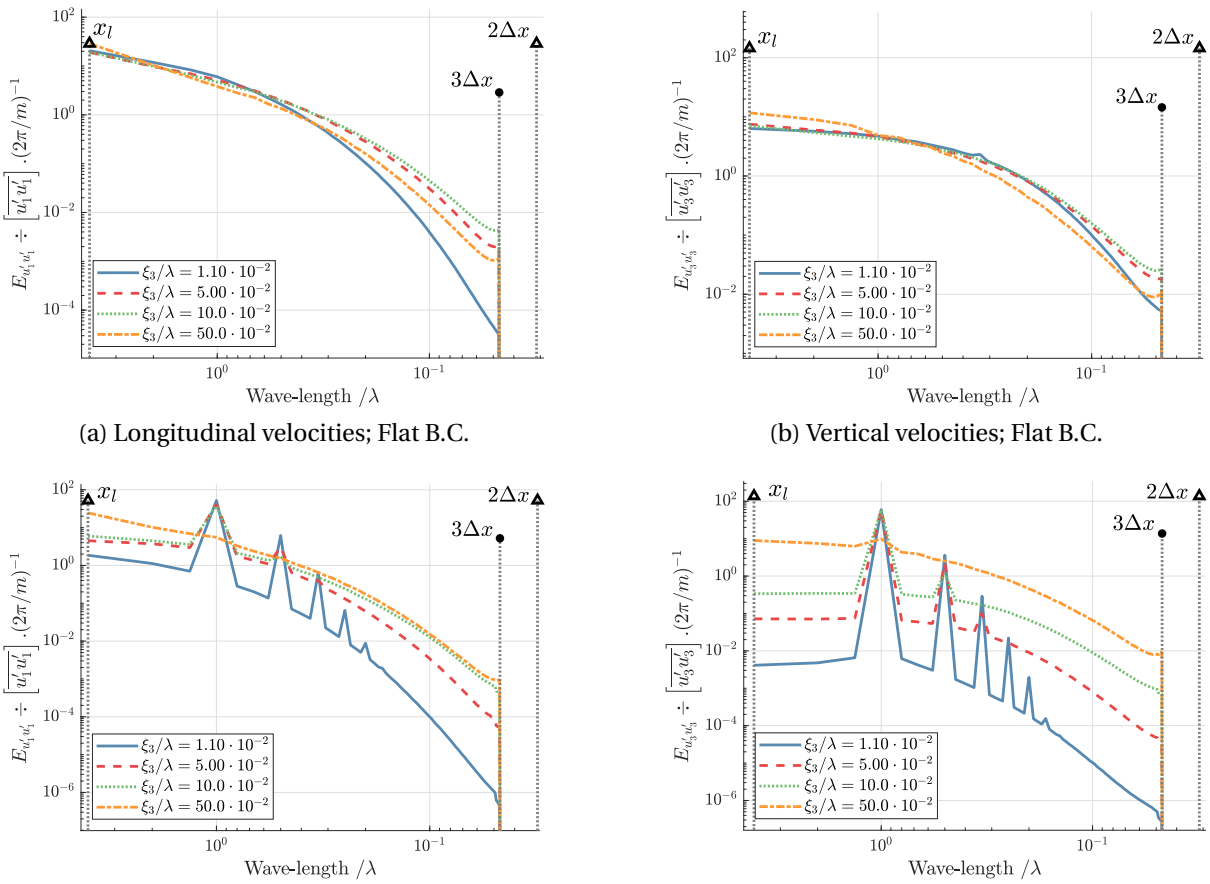

(a) Longitudinal velocities; Flat B.C.

(b) Vertical velocities; Flat B.C.

(c) Longitudinal velocities; Wavy B.C.

(d) Vertical velocities; Wavy B.C.

Figure IV.1.2: One-dimensional wave-number-dependent spectral EDF of longitudinal and vertical velocities. Flat and Wavy bottom cases of section III.2.5. Wave ($WA_{ref} = 60$, $ka = 0.2$) prescribed according to a fifth order solution, leading to WI disturbances at five harmonics. The spectral domain ranges between $2\pi/x_l$ and $\pi/\Delta x$, but in LES it is truncated at $(2/3)\pi/\Delta x$.

The Wave Coherent and Wave Induced flow were introduced in section IV.1, with help of figure IV.1.1, that exemplifies the WC and WI filters employed to the turbulent spectra of figure IV.1.2.

The obtained (squared root of the) wave induced (energy) fraction $\mathscr{F}_k(z)$ is shown in figure IV.1.3 for each of the decomposed velocity fields and wave harmonics lengths. The five different curves in each figure represent each of the five harmonics ($n = 1..5$) with length $\lambda_k = \lambda/n$, and the vertical axes is normalized for each harmonic by λ_k.

Focusing on the principal wave component λ, the decay with height is noted, as $\mathscr{F}$ smoothly decays from $\mathscr{F} \sim 1$ in the bottom, up to $\mathscr{F} \sim 0$ at $z \sim 0.6\lambda$ and $z \sim 0.8\lambda$, respectively for longitudinal and vertical velocities. No Wave Induced flow is observed for transversal velocities, omitted for the sake of brevity.

The decay in $\mathscr{F}_k$ is more rapid for lower wave numbers. It is still unclear how much this is either due to: A weaker BC's wave forcing, because higher wave-number harmonics have smaller non-dimensional amplitudes; or due to the fluctuation behavior at these specific

scales, because e.g., WA and λ_k/δ vary for each harmonic, or because higher than first order harmonics (bounded waves) do not follow the dispersion relation

A natural definition of the WBL height that requires negligible (< 1%) wave induced energy compared to the total energy in the principal wave number occurs when $\mathscr{F} < 0.1$: Leading to a WBL height of $\sim 0.4\lambda$ or $\sim 0.6\lambda$ if longitudinal or vertical motions are respectively considered.

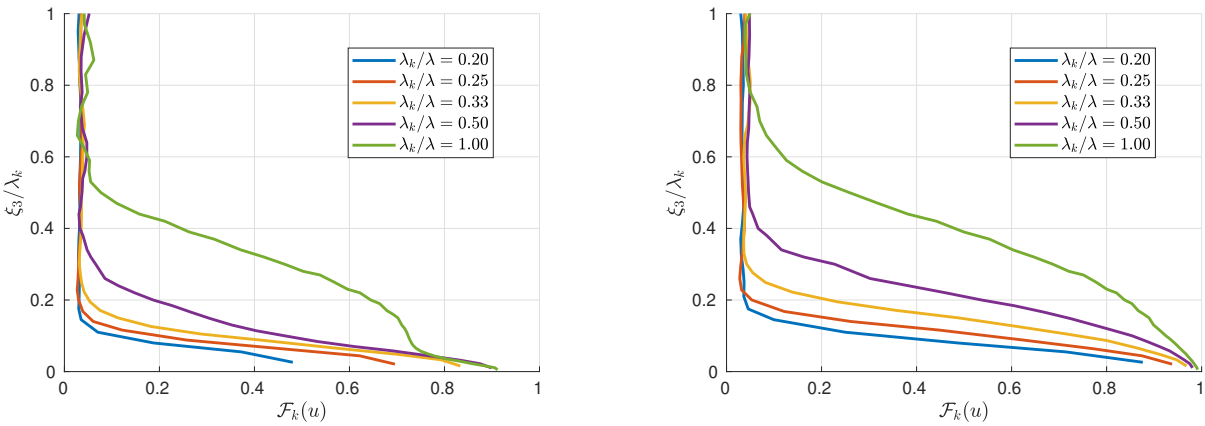

(a) Longitudinal velocity WI fraction $\mathscr{F}_{ku} = f_k$.

(b) Vertical velocity WI fraction $\mathscr{F}_{kw} = f_k$.

Figure IV.1.3: Wave Induced fraction $\mathscr{F}_{\lambda_k}(z)$, corresponding to the squared root of the WI energy fraction according to equations IV.1.2 and IV.1.3. Obtained for longitudinal and vertical velocities. Presented and normalized (in ξ_3) separately for each harmonic ($n = 1..5$) with length $\lambda_k = \lambda/n$.

IV.1.2.2 Atmospheric Turbulence motions

Applying the wave related decompositions allow the comparison of Atm. turbulence in Wavy and Flat bottom cases. So employing the WI filter, the Atm. auto-spectra of both cases are superposed in figure IV.1.4, together with the ESDU reference described in section III.1.2.3. The spectra are presented for the longitudinal velocities at two different heights. There is a slight difference between the cases, but generally both agree well to the ESDU reference on largest scales, then decay faster than the reference at smallest scales due to the SGS modelling. The difference observed between the cases is mostly related to a disturbance on the turbulent integral length scale, demonstrated below.

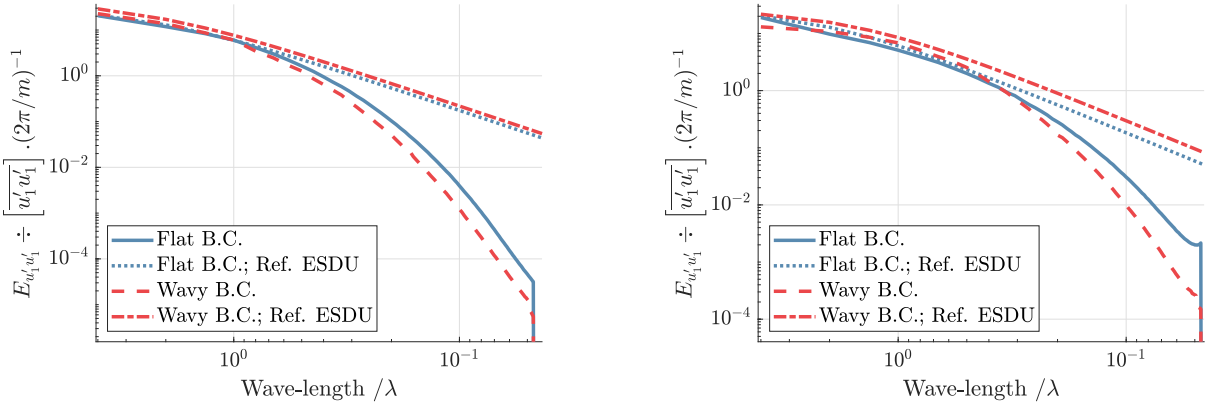

(a) $E_{u'u'}/\sigma_{u'u'}$ at $\xi_3/\lambda = 1.1 \cdot 10^{-2}$ (b) $E_{u'u'}/\sigma_{u'u'}$ at $\xi_3/\lambda = 5.0 \cdot 10^{-2}$

Figure IV.1.4: Atmospheric turbulence spectra of longitudinal velocities presented at two different heights. Wavy and flat bottom cases with the ESDU reference. The WI filter is employed in the wave bottom case. The ESDU reference considers the variances and integral length scales obtained from each spectra, according to section III.1.2.3.

In cases where the auto-correlations are strongly affected by WI motions, the WC and WI filters give meaning to turbulent motions, and thus to the definition of integral length scales $l_L(u'_i)$. For the Wavy BC and the longitudinal velocities, the integral length scale $l_L(u'_1)$ is first presented in figure IV.1.5, as computed from different decompositions. As in figure IV.1.1, blue full lines designate the total fluctuations, red dashed lines the Atm. turbulence given by the WI filter, and green dotted lines the Atm. turbulence given by the WC filter. The integral length scale computed for the total fluctuations are hugely disturbed if compared to what is revealed for the Atm. turbulence by either (WC or WI) methodology. A smaller improvement to the turbulent length scales is further obtained with the WI filter.

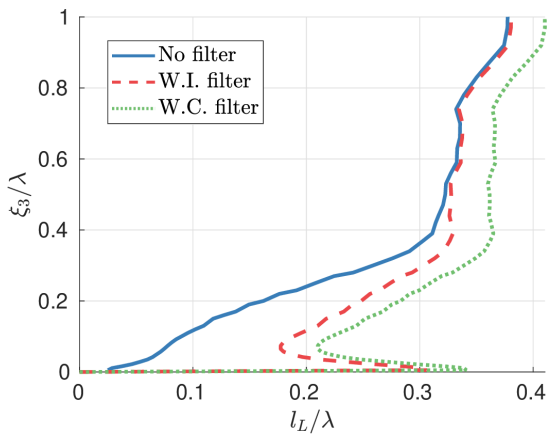

Figure IV.1.5: Integral length scale of longitudinal velocities at the wave bottom case. Extracted from the turbulent spectra revealed by the different spectra in figure IV.1.1. Total fluctuations $l_0(u')$ in blue full line; residual of the Wave Coherent filtered $l_0(\hat{u}^{(C)})$ in green dotted line; WI filtered, Atm. motions $l_0(\hat{u}^{(I)})$ in red dashed line.

So, the integral length scale of the Atm. turbulence revealed by the WI filter is further explored by comparing flat and wavy cases in figures IV.1.6a and IV.1.6b, concerning lon-

gitudinal or vertical velocities, respectively. The diminishing of turbulent integral scales by the wave's introduction is observed in figures IV.1.6a and IV.1.6b, at least up to $\xi_3 > 0.6\lambda$.

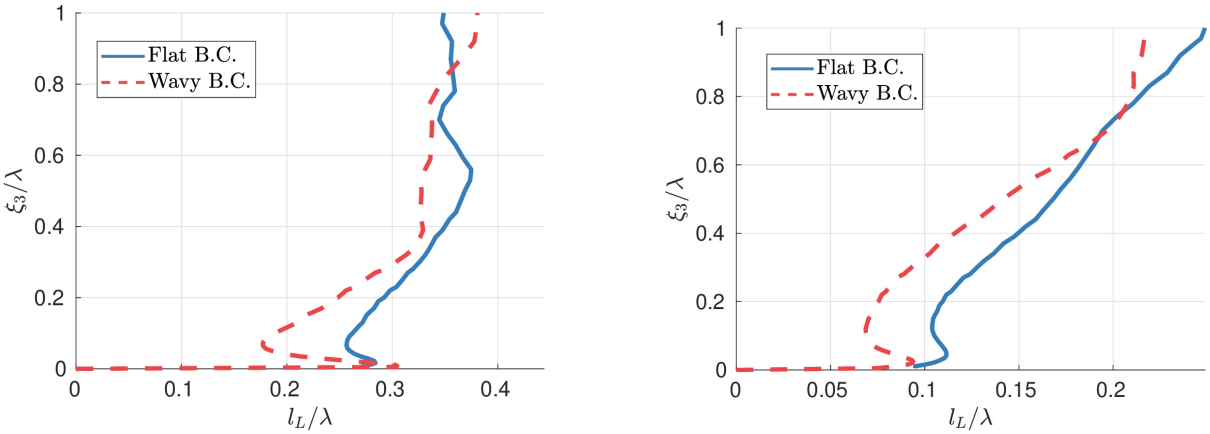

(a) Longitudinal velocities $l_0(\hat{u}^{(I)})$.

(b) Vertical velocities $l_0(\hat{w}^{(I)})$.

Figure IV.1.6: Integral length scale l_0 of longitudinal and vertical velocities, at Flat and Wavy bottom cases. Obtained from the Atm. turbulence auto-spectra employing the WI filter.

Recalling the assumption that Atm. and WI motions occurring at the same scale are in-phase, each field can be reconstructed from the total fluctuations, according to equations IV.1.1 and IV.1.2, and given the real-valued function $\mathscr{F}$ shown in figure IV.1.3. Figure IV.1.7 depicts the reconstructed fields: Atm. turbulence, represented by coherent vortical structures, identified by the Q-criterion, and colored by the $u'w'$ (y-plane) vorticity; and WI motions, represented by a colormap of the longitudinal velocities and the velocity vectors projected in the ($x-z$, normal to y) plane.

The coherent structures identified in figure IV.1.7 are quasi-streamwise aligned, bending downwards at the wave trough as described in Yang and Shen [2010] (reviewed in fig. I.3.7) when considering fast waves conditions. In figure IV.1.7 one observes those coherent structures submitted to the geometrical influence of the wavy bottom, but also to interactions with the Wave Induced flow.

The structure of the WI flow pictured in figure IV.1.7 agrees to the potential theory described at the appendix A.1.1, meaning they qualitatively ressemble the stokes orbitals. But note that means a 180° shift in longitudinal velocities between the sea and air domains, i.e.: At the ocean the longitudinal velocity is positive on the crest and negative on the trough, but at the atmosphere as depicted in the figure, velocities are negative (blue) on the crest, and positive (red) on the trough.

The Atm. turbulence is characterized by a predominance of negative $\overline{u'w'}$ correlations (fig. III.2.7d for example) aligned to the mean shear stresses, and indeed negative vorticity (red) prevails in figure IV.1.7. In two-dimensional flows, it is expected that vortical structures rotating in the same direction break-down into smaller structures, while vortical structures rotating in opposed directions roll-up Jiménez [2004]. That remark could explain the predominance of vortical structures on the crests, and the mitigation of these structures in the trough. Note that at the crest, WI vorticity is positive rotating against the shear stresses, but on the trough the WI vorticity is negative rotating with the shear stresses. These kind of

interactions could also explain, qualitatively at least, the diminishing integral length scales observed at figure IV.1.6.

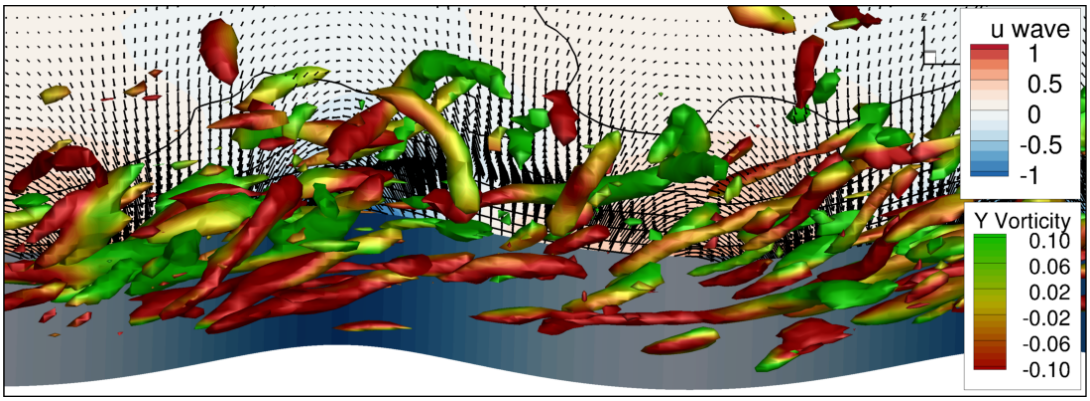

Figure IV.1.7: Assuming in-phase Atm. and WI motions occurring at the same scale, Atm. and WI fields are reconstructed from equations IV.1.1 and IV.1.2. **Atmospheric Turbulence** field: Iso-surfaces of Q-criterion colored by 'y' (x-z plane) vorticity; **Wave Induced** field: Middle 'y' plane, probing velocity vectors, and colored by longitudinal WI velocity.

IV.1.2.3 Joint Space-Time modal distribution

As said, the methodologies here presented for obtaining WC and WI flows can hardly be employed in more complex situations, where the sea-state energy is continuously distributed over a wide range of the 1D spectral domain. It has also been sad that this problem might be overcome by considering the 2D wave-number-frequency spectra $(k-w)$, which is the topic of next section IV.2. So figure IV.1.8 closes this section presenting the 2D spectra $k-w$ spectra that corresponds to the wavy case here discussed.

At figure IV.1.8, the 2D spectra are presented at two different heights, and as a function of the wave length $(2\pi/k)$ period $(1/f)$, so the slopes in the figure indicate velocities. The Taylor hypothesis prediction corresponds to the mean wind velocity, given in full lines. The dispersion relation corresponds to the wave velocity, given in the upper-most dashed lines. There are five dashed lines in figure IV.1.8a resembling the dispersion relation, each one giving the velocity of each of the waves harmonics. The lines corresponding to higher harmonics are omitted in figure IV.1.8b to avoid contaminating the analysis, since WI disturbances start to become unnoticed in some harmonics.

Before properly describing the WI disturbances, one must note a strong anomaly in figure IV.1.8a. The Taylor hypothesis implies that eddies are transported by the mean velocities. In the 2D spectra of figure IV.1.8, that means that the energy shall rise when approaching the full black line in the figure. Note that in figure IV.1.8b, the local maxima of the spectra indeed approach the full black lines. This kind of disturbance characterize a Doppler shift in spectral turbulence with respect to Taylor's prediction, and during the whole manuscript is only observed in figure IV.1.8a. A little bit higher in the ABL for the same test case, in figure IV.1.8b, the anomaly is hardly observed. That's clearly a Wave Induced disturbance in the Atmospheric turbulence, but whether it is a numerical or physical feature remains unanswered. Recall that present sea-state also contains much more energy than the others considered in the manuscript.

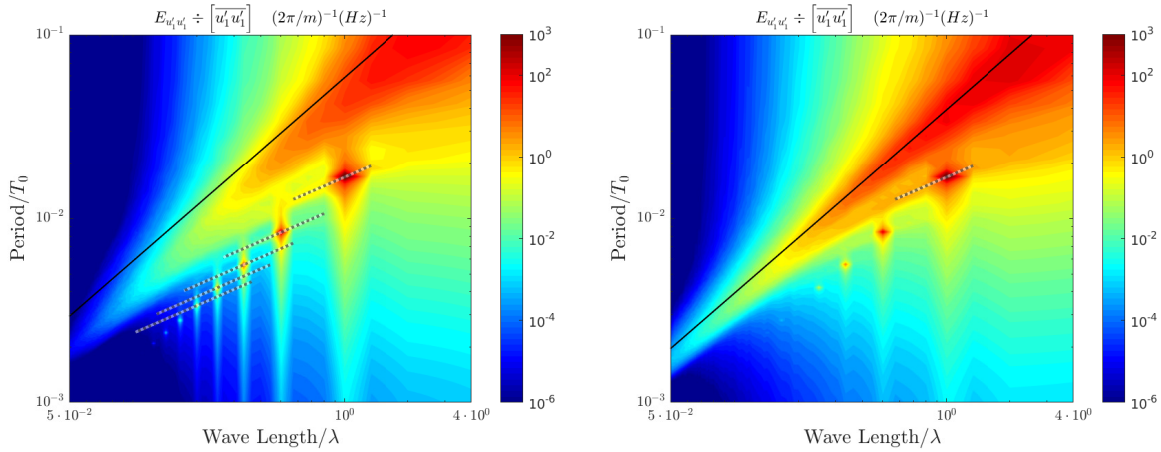

(a) $E_{u'u'}/\sigma_{u'u'}$ at $\xi_3/\lambda = 1.1 \cdot 10^{-2}$

(b) $E_{u'u'}/\sigma_{u'u'}$ at $\xi_3/\lambda = 5.0 \cdot 10^{-2}$

Figure IV.1.8: Wave-number-angular-frequency 2D turbulent spectra for the Wavy bottom case of a monochromatic wave ($WA_{ref} = 60$, $ka = 0.2$). The mean velocity is depicted in the black full line corresponding to Taylor's hypothesis, and the wave velocities presented in dotted lines. In (a) the wave velocities are shown for the first five harmonics. In (b) only the wave velocity is depicted.

Now to the WI flow, the disturbances are clearly noted by the strong peaks occuring in the waves harmonics, and along the dotted lines in figure IV.1.8. Interestingly, there are five harmonics, five dotted lines, but one can observe eight WI disturbances in figure IV.1.8a. That's because the free-surface Boundary Condition (BC) might be prescribed according to a 5th order stokes solution, but in the LES: The vertical velocities of the BC are reconstructed so ensuring the incompressible constraint $\nabla \cdot \boldsymbol{u} = 0$; and the fully non-linear Navier-Stokes equations is solved in the atmosphere. So the WI flow present higher degree of non-linearity if compared to the 5th order wave prescribed. With attention, actually six harmonics can be found in the 1D spectra of figure IV.1.2, but many more can be observed in the 2D spectra hereby. In fact, nine were found by the author by adjusting the color ranges in figure IV.1.8a.

The 2D spectra also reveal that contrary to the sea-state forcing, and to what is suggested from the 1D spectra of figure IV.1.2, actually WI disturbances spread from the wave and its harmonics scales, transferring into a wider part of the 2D spectra. Also section IV.2.2.1 presents a regular wave case, but with ~ 100 times less energy, where this feature is again observed and further characterized with figure IV.2.6b.

IV.1.3 Overview and discussion

An original methodology allows the characterization of the MABL into its Wave Induced and Atm. turbulent motions, considering the correlation between those fields, thus allowing further investigation of the coupled dynamics between them.

The decomposition must rely on turbulent and wave induced characteristics to define the WI fraction $\mathscr{F}$, here obtained to recover turbulent spectral density functions' shapes as expected from classical flat terrain turbulent motions. This particular strategy is suitable for

regular seas but should be adapted otherwise, which is addressed in the next sections.

A canonical test case is presented where a reasonably sized swell ($ka = 0.2$), described by 5th order theoretical solution, meets relatively slow wind conditions (WA = 60) in the neutral MABL resolved by LES. A natural definition of the WBL height that require negligible (< 1%) wave induced energy compared to the total energy in the principal wave number occurs when $\mathscr{F} < 0.1$: Leading to a WBL height of $\sim 0.4\lambda$ or $\sim 0.6\lambda$ if longitudinal or vertical motions are respectively considered in the test case presented.

The Wave Induced filter proposed recover the expected turbulent behavior, though turbulent scales are distorted and particularly the integral scale is diminished. Wave induced motions merge into the turbulent cascade distorting and forcing the turbulent flow above the WBL. Present results indicate statistical models of wind resource could improve their accuracy in offshore environments by considering (i) The distortion of turbulent scales and (ii) The superposition of a Wave Induced field model.

IV.2 Partitioning WI motions in the Turbulent Spectra above arbitrary sea-states

Directly evaluating Wave Induced fluctuations in the atmosphere, the mechanistic approach reviewed in section I.3.6 generally considers the triple decomposition of a flow field $\chi = \overline{\chi} + \hat{\chi} + \tilde{\chi}$ (Such as velocity and pressure) into mean $\overline{\chi}$, turbulent $\hat{\chi}$, and wave related $\tilde{\chi}$ fields, with the total fluctuations given by $\chi' = \hat{\chi} + \tilde{\chi}$. Imposing a filter to retain the Wave Coherent (WC) flow that neglects its correlation with turbulence, Hristov and Ruiz-Plancarte [2014] present dynamic equations (Section I.3.6) for the decomposed fields uncoupled between WC ($\tilde{\chi}^C$) and turbulent ($\hat{\chi}^C$) motions.

Present work proposes at section IV.1 a definition of the Wave Induced (WI, $\tilde{\chi}^I$) flow, and the Atmospheric turbulence (Atm., $\hat{\chi}^I$) counter-part, in an enhanced perspective relying in two crucial aspects: (i) The admissibility of the correlation between WI and Atm. motions as first proposed in Paskin et al. [2020] (Section IV.1.2); and (ii) The Space-Time description of χ, notably counting in the wave-number-angular-frequency ($k-w$, 2D) spectral distribution of the fluctuations. The WI flow is so defined by extending the definition of the WC flow through the introduction of the WI fraction $\mathscr{F}$ in equations IV.1.4 and IV.1.5, here repeated for the sake of completeness:

$$\tilde{\chi}^C_{kw}(x,t) = \frac{\overline{\chi(x,t)\eta_{kw}(x,t)}^{[x,t]}}{||\eta_{kw}||^2_{[x,t]}}\eta_{kw}(x,t) + \frac{\overline{\chi(x,t)\hat{\eta}_{kw}(x,t)}^{[x,t]}}{||\hat{\eta}_{kw}||^2_{[x,t]}}\hat{\eta}_{kw}(x,t)$$

$$\tilde{\chi}^C(x,t) = \sum_w \sum_k \tilde{\chi}^C_{kw}(x,t), \qquad \hat{\chi}^C(x,t) = \chi(x,t) - \tilde{\chi}^C(x,t) \tag{IV.2.1}$$

$$\begin{aligned} \tilde{\chi}^I_{kw}(x,t) &= \mathscr{F}_\chi(k,w) \cdot \tilde{\chi}^C_{kw}(x,t) \\ \hat{\chi}^I_{kw}(x,t) &= \left[1 - \mathscr{F}_\chi(k,w)\right] \cdot \tilde{\chi}^C_{kw}(x,t). \end{aligned} \tag{IV.2.2}$$

Still according to the discussion in section IV.1, WI and Atm. motions occurring at the same scale are assumed in-phase, so a real-valued function $\mathscr{F}$ uniquely describes the auto and cross correlations EDF through equation IV.2.3, rewritten below in the $k-w$ perspective:

$$\begin{aligned} E_{\tilde{\chi}\tilde{\chi}}(k,w) &= \left[\mathscr{F}_\chi(k,w)\right]^2 E_{\chi\chi}(k,w) \\ E_{\hat{\chi}\hat{\chi}}(k,w) &= \left[1-\mathscr{F}_\chi(k,w)\right]^2 E_{\chi\chi}(k,w) \quad , \quad \text{and} \\ E_{\tilde{\chi}\hat{\chi}}(k,w) &= \left[\mathscr{F}_\chi(k,w)\right]\left[1-\mathscr{F}_\chi(k,w)\right] E_{\chi\chi}(k,w) \quad . \end{aligned} \tag{IV.2.3}$$

As discussed and attested in sections IV.2.2 and IV.2.3, respectively in numerical and physical experiments, the $k-w$ EDF of the fluctuations $E_{\chi'\chi'}(k,w) = E_{\hat{\chi}\hat{\chi}} + E_{\tilde{\chi}\tilde{\chi}} + 2\,E_{\hat{\chi}\tilde{\chi}}$ often

contains enough information so that $\mathscr{F}$ can be determined from equation IV.2.3, recovering the Atm. part $E_{\hat{\chi}\hat{\chi}}(k,w)$ that behaves as expected from atmospheric turbulence. These applications rely in the partitioning of the 2D spectra $E_{\chi'\chi'}(k,w)$, here achieved with the method described below, built to operate in generic conditions above arbitrary sea-states, as long as WI disturbances are noticeable in $E_{\chi'\chi'}(k,w)$.

IV.2.1 Contour advancing segmentation of the 2D Turbulent Spectra

A particular contour based segmentation technique is developed to identify Atmospheric (Atm., $\hat{\cdot}$) and Wave Induced (WI, $\tilde{\cdot}$) contributions to the 2D Turbulent spectra $E_{\chi'\chi'}(k,w)$, operating in the image of the logarithmic spectra, given in the wave-length-period (r,τ) domain, i.e., $\log[E_{\chi'\chi'}(r,\tau)]$. In the physical experiment that corresponds to the images of figure II.3.3, for example.

Let $C_i(E_i)$ be the contour of $E_{\chi'\chi'}$ associated with energy E_i, the method advances with decreasing energy ($E_i > E_{i+1}$) classifying sets of C_i into Atm. ($\hat{C}_i$) and/or WI ($\tilde{C}_i$) parts. The procedure is first exemplified in figure IV.2.1; and applies to Cases 01 and 02.a. of section II.3, as exemplified in figure IV.2.2; and to Cases 01, 02 and 03 of section III.4, as in figure IV.2.3. The figures contain a lot of information, that the reader is suggested to unveil during the section. Notably figure IV.2.1 summarizes multiple definitions given hereby, while figures IV.2.2 and IV.2.3 exemplify the overall contour-advancing procedure.

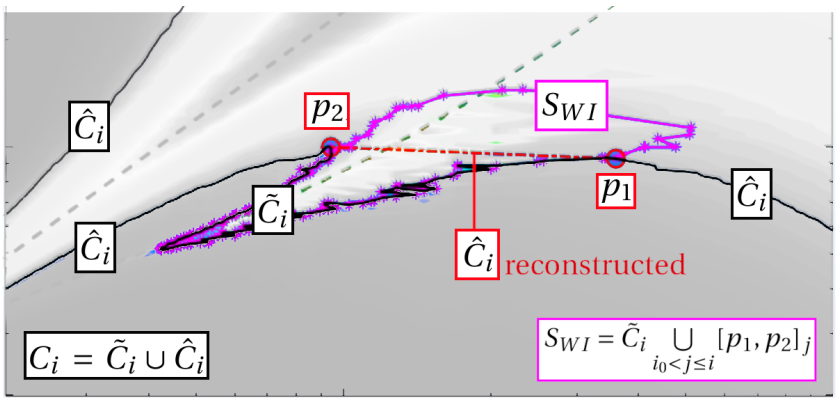

Figure IV.2.1: Schematic of the contour advancing segmentation technique, drawn from figure IV.2.3o at level $i > i_0$. Starting from i_0, the contour is segmented. The current contour C_i is defined in the wave-length-period (r,τ) domain as depicted in full black line at the figure, and is segmented into Atm. ($\hat{C}_i$) and WI ($\tilde{C}_i$) parts by the points $[p_1,p_2]_i$ depicted as red circles. Between $[p_1,p_2]_i$ a red dot-dashed line represents the reconstruction of $\hat{C}_i$. The WI region of influence is bounded by S_{WI} that stands in magenta dots and lines. Below (with smaller energy than) the $[p_1,p_2]_i$ reconstructed line, S_{WI} matches $\tilde{C}_i$. Above (with greater energy than) the $[p_1,p_2]_i$ reconstructed line, S_{WI} is defined by the previous set of points $[p_1,p_2]_j$ for $i0 < j \leq i$.

For each case, figures IV.2.2 and IV.2.3 depict four different levels i, with the black full line standing for the current, total fluctuation contour C_i. As the procedure advances, a

region is identified inside the closed boundary S_{WI} (Magenta lines and dots in the figures), where the WI disturbances in the contours are potentially significant. The Atm. contours $\hat{C}_i$ are linearly reconstructed inside S_{WI} (see fig. IV.2.1). Once the procedure converges, the interpolation of reconstructed $\hat{C}_i$ inside S_{WI} gives a continuous distribution of the Atm. 2D spectra $\hat{E}(k,w) = E_{\hat{\chi}\hat{\chi}}$, from which $\mathscr{F}_\chi = 1 - \sqrt{E_{\hat{\chi}\hat{\chi}}/E_{\chi\chi}}$ is obtained according to equation IV.2.3.

Initially and up to a certain level i_0, registered in figures IV.2.2(a,e) and IV.2.3(a,e,i,m), the classification is trivial because S_{WI} and $\hat{C}_i$ do not overlap: If C_i is open, $C_i \to \hat{C}_i$ is Atm.; if C_i is closed and contains the wave peak scale $[L_p, T_p]$, $C_i \to \tilde{C}_i$ is Wave related; and up to this point $\tilde{C} \to S_{WI}$. After level i_0 though, when C_i contains the saddle point between $\hat{C}_{i0}$ and S_{WI}, the open contours also contain the wave peak scale, and C_i has to be segmented.

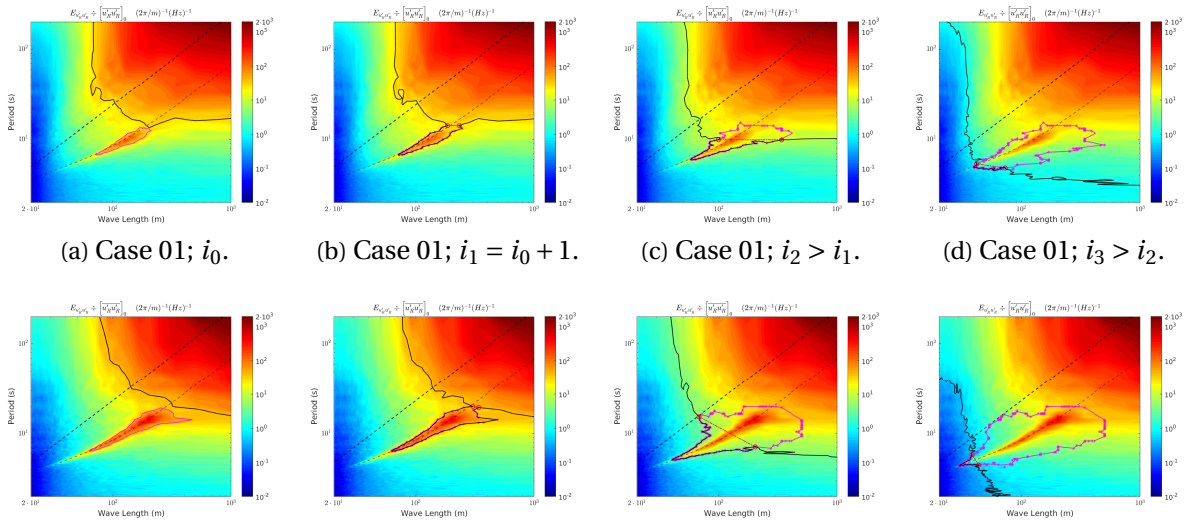

(a) Case 01; i_0. (b) Case 01; $i_1 = i_0 + 1$. (c) Case 01; $i_2 > i_1$. (d) Case 01; $i_3 > i_2$.

(e) Case 02.a; i_0. (f) Case 02.a; $i_1 = i_0 + 1$. (g) Case 02.a; $i_2 > i_1$. (h) Case 02.a; $i_3 > i_2$.

Figure IV.2.2: Turbulent 2D Spectra for Cases 01 and 02.a from section II.3; and the contour based segmentation technique, advancing in i shown at $i_{0..3}$. Lines, dots, and circles are as described in figure IV.2.1.

When $i > i0$ the contour C_i is split in points p_1 and p_2, defining the segments $\tilde{C}_i$ inside, and $\hat{C}_i$ outside of $[p_1, p_2]_i$. The points p_1 and p_2 are found maximizing the coherence between C_i and the previous reference sets, according to the procedure described in section IV.2.1.1. The splitting points p_1 and p_2 are spotted in red circles when $i > i_0$ in figures IV.2.1, IV.2.2, and IV.2.3.

The turbulent contour $\hat{C}_i$ is linearly reconstructed between $[p_1, p_2]_i$, depicted as a red dot-dashed line between the red circles in the figures. Inside (in the augmenting energy sense of) the reconstructed $\hat{C}_i$, S_{WI} is composed of all points $[p_1, p_2]_j$ previously obtained for $i0 < j \leq i$. Outside (in the diminishing energy sense of) $\hat{C}_i$, $S_{WI} = \tilde{C}_i$.

The advancing procedure finishes when the coherence between C_i and the previous reference sets deteriorates (Criterion established in section IV.2.1.1), which happens soon after Figures IV.2.2(d,h), and IV.2.3(d,h,l,p). Outside the region S_{WI}, $E_{\tilde{\chi}\tilde{\chi}}(k,w)$ is null and $E_{\hat{\chi}\hat{\chi}} = E_{\chi'\chi'}$. Inside S_{WI}, $\log[E_{\hat{\chi}\hat{\chi}}]$ is linearly interpolated from the turbulent contours $\hat{C}_i$ reconstructed between $[p_1, p_2]_j$ for $i0 < j \leq i$.

That covers the overall contour-advancing procedure, leading to $E_{\hat{\chi}\hat{\chi}}$, and consequently to $\mathscr{F}_{\chi}$, $E_{\tilde{\chi}\tilde{\chi}}$, and $E_{\tilde{\chi}\hat{\chi}}$ from equation IV.2.3. A single, non-trivial question remains, regarding the actual segmentation procedure, determining points $[p_1, p_2]_j$ according to the next section.

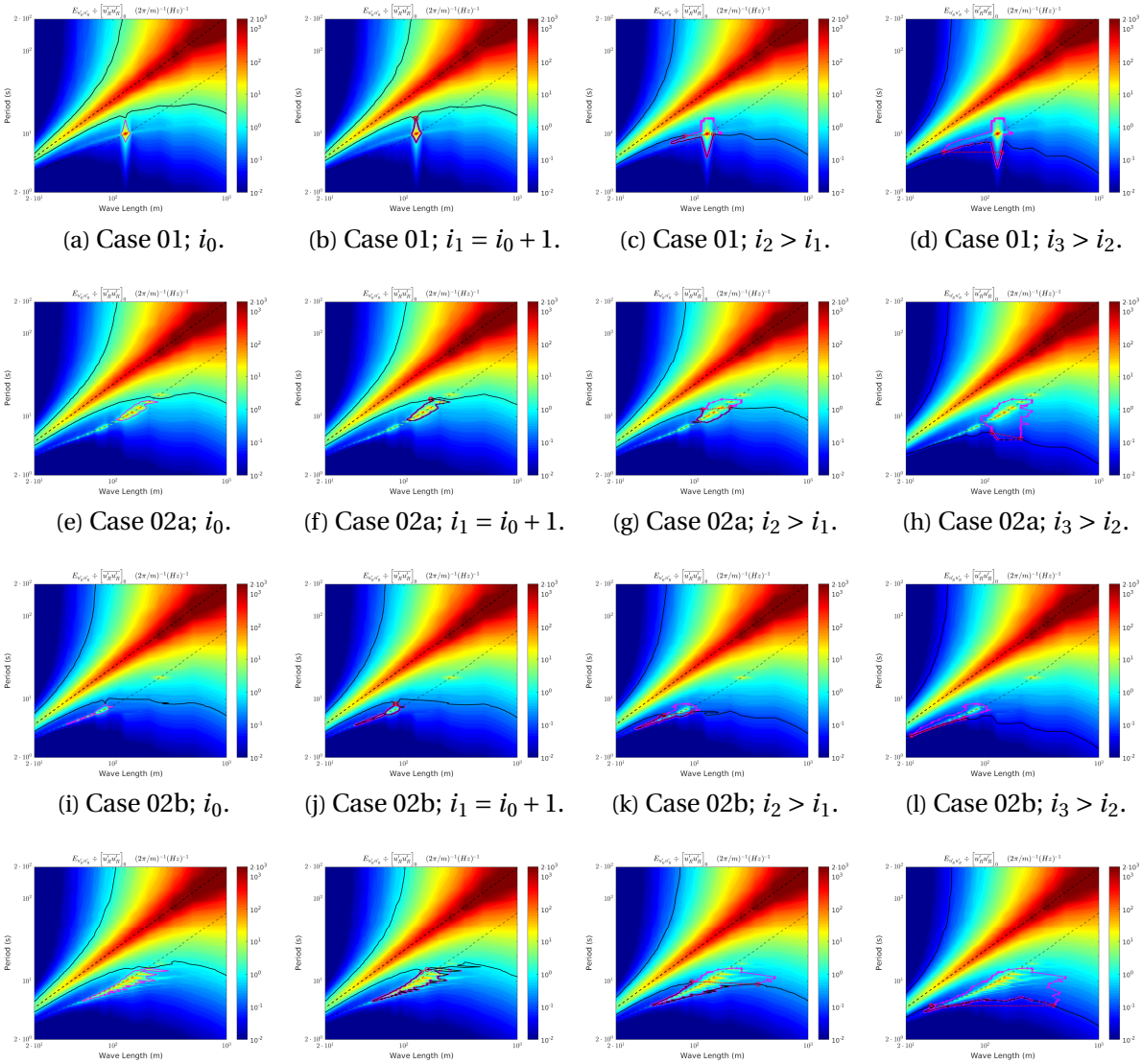

(a) Case 01; i_0. (b) Case 01; $i_1 = i_0 + 1$. (c) Case 01; $i_2 > i_1$. (d) Case 01; $i_3 > i_2$.

(e) Case 02a; i_0. (f) Case 02a; $i_1 = i_0 + 1$. (g) Case 02a; $i_2 > i_1$. (h) Case 02a; $i_3 > i_2$.

(i) Case 02b; i_0. (j) Case 02b; $i_1 = i_0 + 1$. (k) Case 02b; $i_2 > i_1$. (l) Case 02b; $i_3 > i_2$.

(m) Case 03; i_0. (n) Case 03; $i_1 = i_0 + 1$. (o) Case 03; $i_2 > i_1$. (p) Case 03; $i_3 > i_2$.

Figure IV.2.3: Turbulent 2D Spectra for Cases 01 (a-d), 02 (e-l), and 03 (m-p); and the contour based segmentation technique, advancing in i shown at $i_{0..3}$. Case 02 reveal two detached regions of WI disturbances, so the partitioning here is split in Case 02a (e-h) and 02b (i-l). Lines, dots, and circles are as described in figure IV.2.1.

IV.2.1.1 Segmentation procedure

The image defined in (r, τ) is here accessed in non-dimensional coordinates $x = r/\max(r)$ and $y = \tau/\max(\tau)$. To reduce the computational effort and because $c \gg u_1$, the contours are kept only for velocities r/τ above the mean wind speed u_1.

Once the level i_0 has been reached at $i \geq i_0$, the advancing procedure relies in the segmentation of the contour $C_i = \tilde{C}_i \cup \hat{C}_i$, identifying the points $[p_1, p_2]_i$ that define the sets $\tilde{C}_i$ (Between $[p_1, p_2]_i$), and its complement $\hat{C}_i = C_i \setminus \tilde{C}_i$, given the previous level definitions of $S_{WI}|_{i-1}$ and $\hat{C}_{i-1}$ (see fig. IV.2.1, and note that $\tilde{C}_{i-1} \subset S_{WI}|_{i-1}$). An optimization problem is formulated finding $[p_1, p_2]_i$ that maximizes the coherence between previous and current sets, i.e., between $\tilde{C}_i$ and $S_{WI}|_{i-1}$, and between $\hat{C}_i$ and $\hat{C}_{i-1}$.

The contours C_i, $\hat{C}_{i-1}$, and $S_{WI}|_{i-1}$ are respectively defined by the segments c_j, $\hat{c}_j$, and s_j, with $j = 1..n_{\{C,\hat{C},S_{WI}\}}$, and $n_{\{C,\hat{C},S_{WI}\}}$ denoting the number of segments composing contours $\{C, \hat{C}, S_{WI}\}$. The segment c_j for example, is in turn bounded by points p_j and p_{j+1}, and identified by the position vector $\boldsymbol{x}_c$ evaluated at its middle, and the orientation vector $\boldsymbol{o}_c$ in its normal direction, according to:

$$\begin{aligned} \boldsymbol{x}_c = \begin{bmatrix} x_c \\ y_c \end{bmatrix} &= 0.5 \begin{bmatrix} x(p_j) + x(p_{j+1}) \\ y(p_j) + y(p_{j+1}) \end{bmatrix} \\ \boldsymbol{o}_c = \begin{bmatrix} o_c \\ o_c \end{bmatrix} &= \begin{bmatrix} y(p_{j+1}) - y(p_j) \\ x(p_j) - x(p_{j+1}) \end{bmatrix} \end{aligned} \tag{IV.2.4}$$

The coherence $-1 < q < 1$ between two segments c and s (for example) is defined as:

$$\begin{gathered} q(c \cdot s) = q_x(c \cdot s)\ q_o(c \cdot s), \qquad \text{with} \\ q_x(c \cdot s) = \frac{(\boldsymbol{x}_c \cdot \boldsymbol{x}_s)}{\sqrt{(\boldsymbol{x}_c \cdot \boldsymbol{x}_c)(\boldsymbol{x}_s \cdot \boldsymbol{x}_s)}}, \qquad \text{and} \qquad q_o(c \cdot s) = \frac{(\boldsymbol{o}_c \cdot \boldsymbol{o}_s)}{\sqrt{(\boldsymbol{o}_c \cdot \boldsymbol{o}_c)(\boldsymbol{o}_s \cdot \boldsymbol{o}_s)}}. \end{gathered} \tag{IV.2.5}$$

Equation IV.2.5 is evaluated for every segment in C_i, with respect to the segments in $S_{WI}|_{i-1}$ ($n_{C_i}\ n_{S_{WI}|_{i-1}}$ evaluations), and in $\hat{C}_{i-1}$ ($n_{C_i}\ n_{\hat{C}_{i-1}}$ evaluations). The best coherence between c_j, and the segments in $S_{WI}|_{i-1}$, and in $\hat{C}_{i-1}$, are stored respectively in the vectors $\boldsymbol{q}(c_j \cdot s)$ and $\boldsymbol{q}(c_j \cdot \hat{c})$. The best coherence vector is stored together with the corresponding (best) distance vector, i.e., $\boldsymbol{d}(c_j \cdot s)$ and $\boldsymbol{d}(c_j \cdot \hat{c})$, defined by $\boldsymbol{d}(c \cdot s) = \sqrt{(\boldsymbol{x}_c - \boldsymbol{x}_s) \cdot (\boldsymbol{x}_c - \boldsymbol{x}_s)}$.

The following measure is found to increase the method robustness, using the best distance vectors $\boldsymbol{d}$ to impose hard limits in $\boldsymbol{q}$, and constraint the upcoming quality function. Introducing the parameter α_d, tuned to $\alpha_d = 4$ which applies to every case in this manuscript:

- If $d_j(c_j \cdot s) > \alpha_d\ d_j(c_j \cdot \hat{c})$; then $q_j(c_j \cdot s) = -1$.
- If $d_j(c_j \cdot \hat{c}) > \alpha_d\ d_j(c_j \cdot s)$; then $q_j(c_j \cdot \hat{c}) = -1$.

Given the points $[p_1, p_2]_i$ defining the sets $\tilde{C}_i$ and $\hat{C}_i$, the quality function Q to be maximized is:

$$Q_{[p_1,p_2]_i} = Q_s + Q_c, \qquad \text{with}$$
$$Q_s = \sum_{j\subset\tilde{C}_i} \left[q_j(c_j\cdot s)\right], \qquad \text{and} \qquad Q_c = \sum_{j\subset\hat{C}_i} \left[q_j(c_j\cdot \hat{c})\right]. \tag{IV.2.6}$$

The quality function is evaluated for every possible combinations of $[p_1, p_2]_i$, and with the constraint that p_2 comes after p_1, that leads to $n_{C_i}\ (n_{C_i}+1)/2$ evaluations of equation IV.2.6. The solution is rejected if $Q_{[p_1,p_2]_i}/n_{C_i} < 0.1$, in which case C_i is discarded, $\hat{C}_{i-1} \to \hat{C}_i$, and $S_{WI}|_{i-1} \to S_{WI}|_i$. If $Q/n_{C_i} \geq 0.1$ then the procedure succeeds, and $[p_1, p_2]_i$ are used to update $\hat{C}_i$ and $S_{WI}|_i$.

IV.2.1.2 Overview and discussion

The WI flow definition introduced in section IV.1, suggests that if $E_{\chi'\chi'}(k, w)$ can be partitioned between Atm. ($E_{\hat{\chi}\hat{\chi}}$) and WI ($E_{\tilde{\chi}\tilde{\chi}} + 2\ E_{\hat{\chi}\tilde{\chi}}$) parts, then WI motions can be recovered from equations IV.2.1, IV.2.2, and IV.2.3. Present section describes an image processing technique capable of reconstructing $E_{\hat{\chi}\hat{\chi}}$ from $E_{\chi'\chi'}(k, w)$ in almost arbitrary situations, which is attested in the numerical and physical applications considered below.

IV.2.2 NUMERICAL EXPERIMENTS

Present section recall the numerical experiments of section III.4, where the sea-state description is considered at three levels of increasing complexity: (i) Regular waves; (ii) Irregular and single directional (1D) Sea-State; (iii) Irregular and multi-directional (2D) Sea-State. Case 00 is the flat bottom reference. One shall refer to section III.4.1 for the specific numerical strategy.

In the test cases of section III.4, the sea-state energy is ~ 100 times smaller than in the previous sections, so that WI disturbances in the vertical wind and turbulence profiles often become negligible above the measurement height $0.14\,\lambda$, according to the discussion in section III.4.3. Here, the Wave Induced motions are sought through the enhancement perspective introduced in section IV.1, employing the partition of turbulent spectra described in section IV.2, revealing good part of the WI flow structure at the measurement height $0.14\,\lambda$.

IV.2.2.1 ATMOSPHERIC TURBULENCE AND WAVE INDUCED MOTIONS

First, consider the one-dimensional (1D) turbulent spectra of figure IV.2.4, where (a,c,e) correspond to the wave-number, and (b,d,f) to the frequency dependent spectra, with Case 01 (Regular Wave) appearing in (a,b), Case 02 (Irregular 1D sea-state) in (c,d), and Case 03 (Irregular 2D sea-state) in (e,f). The total fluctuation spectra is given as blacked dotted lines, and the partitioning of the 2D spectra described in section IV.2 leads to its decomposition in: Atmospheric turbulence (Atm.) spectrum in blue full lines; Wave Induced (WI) spectrum in red dashed lines; crossed Atm-WI spectrum in magenta dash-dotted lines. The blue vertical line denotes the wave peak period.

For the regular wave at Case 01 (figs. IV.2.4a,b), one observes a sharp disturbance of $E(k)$, in a similar manner to the observations in section IV.1.2, except that here the wave is quasi-linear (~ 100 times less energy), so higher wave harmonics are not detected in the atmosphere. In that case partitioning the 1D spectra through the Wave Coherent (WC) or Wave Induced (WI) filter is feasible as described in section IV.1.2, and the WI alternative leads to results similar to the ones here discussed. At the wave peak scales, the 1D and 2D partitioning methods lead to the same $\mathscr{F}$, but farther away from (L_p, T_p) the 2D alternative capture WI disturbances that introduce negligible changes to the 1D turbulent spectra.

Recall that Cases 02 and 03 (Irregular Sea States) present the same sea-state energy of Case 01, and in section III.4.2 the irregular cases often introduce the most significant disturbances to the turbulent statistics in the ABL. With that in mind, one could be rather disappointed with the 1D fluctuation spectra denoted by black dotted lines in figure IV.2.4(c-f): Virtually no disturbance is seen comparing the total fluctuations (black dotted line) to the atmospheric turbulent part (blue full line) in $E(k)$ at (c,e); and only minor disturbances are appreciated in $E(f)$ at (d,f). In these cases the procedures described in section IV.1.2 are deemed to failure: The WC flow classical definition would attribute large portions of the fluctuations to the wave related field, at scales where the WI flow is in fact negligible compared to the atmospheric turbulence; and the partition of the 1D spectra leading to $\mathscr{F}(k)$ and $\mathscr{F}(f)$ is simply unfeasible face to such smooth disturbances on the turbulent spectra.

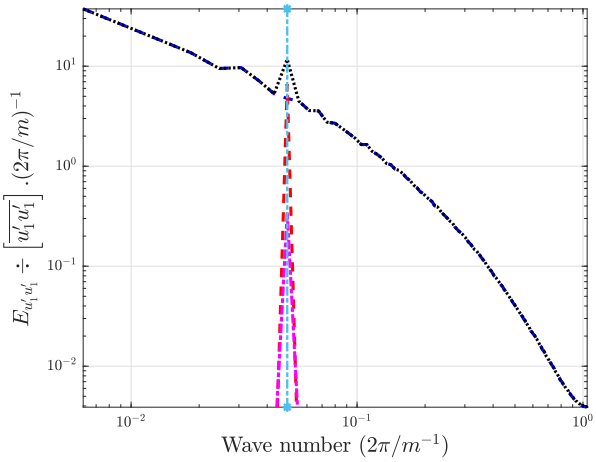

(a) Regular wave; $E(k)$.

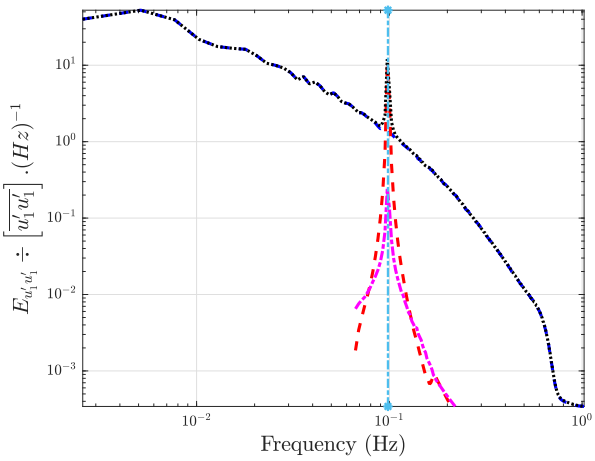

(b) Regular wave; $E(f)$.

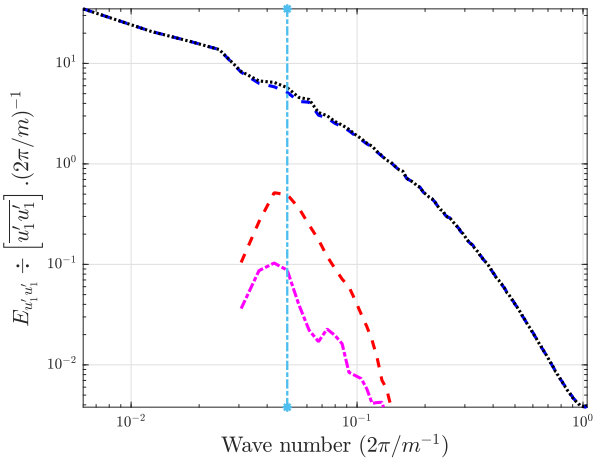

(c) Irregular 1D sea-state; $E(k)$.

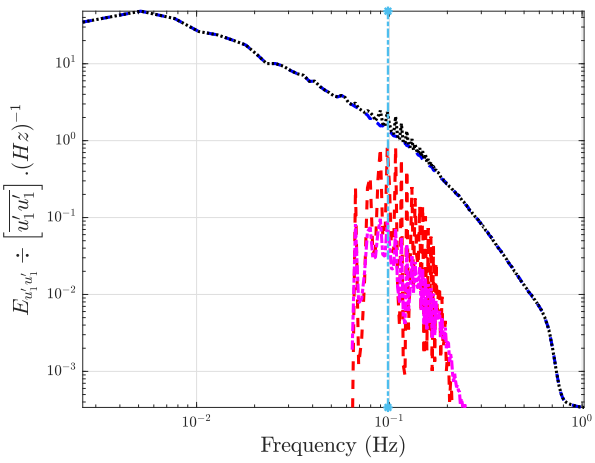

(d) Irregular 1D sea-state; $E(f)$.

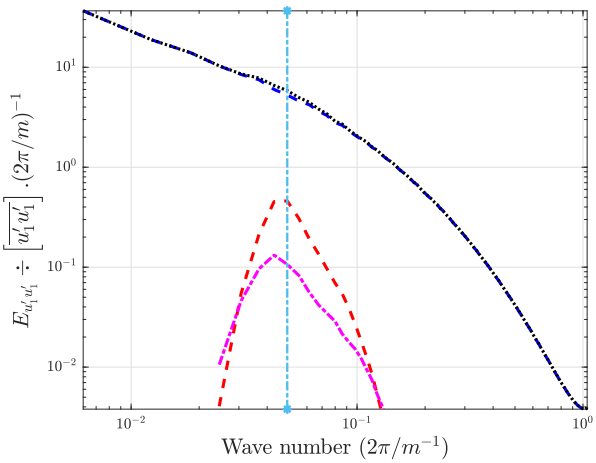

(e) Irregular 2D sea-state; $E(k)$.

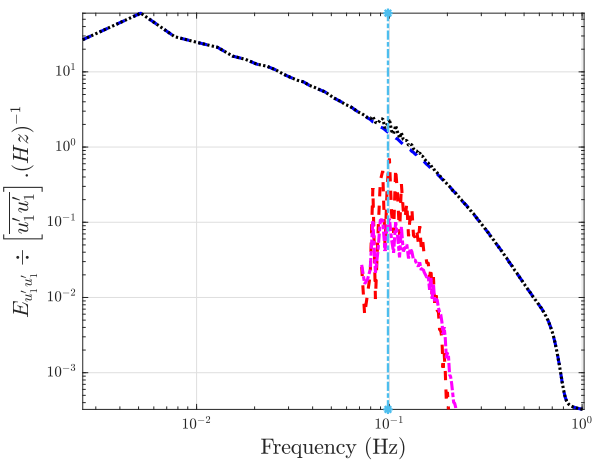

(f) Irregular 2D sea-state; $E(f)$.

Figure IV.2.4: One-dimensional wave-number and angular-frequency EDF of longitudinal velocity fluctuations. Numerical experiments with different types of sea-state prescription. Atmospheric turbulence in blue full line; Total fluctuation spectra in black dotted line; Wave Induced auto-spectra in red dashed line; Wind-Wave cross-spectra in magenta dot-dashed line. The light blue vertical line denotes the wave peak period.

Nevertheless, adopting the 2D Space-Time perspective introduced in section IV.1, and employing the partition of the 2D spectra described in section IV.2, $\mathscr{F}(k,w)$ can be determined for arbitrarily sea-states at heights below the critical height ($c(k) \gg \overline{u}$), and its integration in k or w domains leads to $\mathscr{F}(k)$ and $\mathscr{F}(f)$, and so the partitioned 1D spectra can be shown in figure IV.2.4. That strategy reveals a WI flow that is hidden beneath the atmospheric turbulence 1D spectrum, but is definitely existent at the measuring height, distributed over a broad-band energy auto-spectra depicted by the red-dashed lines in figure IV.2.4.

Naturally to perform the partition of figure IV.2.4, one relies in much more information than what is available from the 1D fluctuation spectra, and that is achieved by the 2D $k-w$ spectra, shown in figure IV.2.5 for Cases 00-03, in (a-d). For the wavy cases in the figures, the lower dashed line represents the dispersion equation corresponding to the WI motions, contrasting to the upper dashed line representing the Taylor hypothesis for the atmospheric turbulent part.

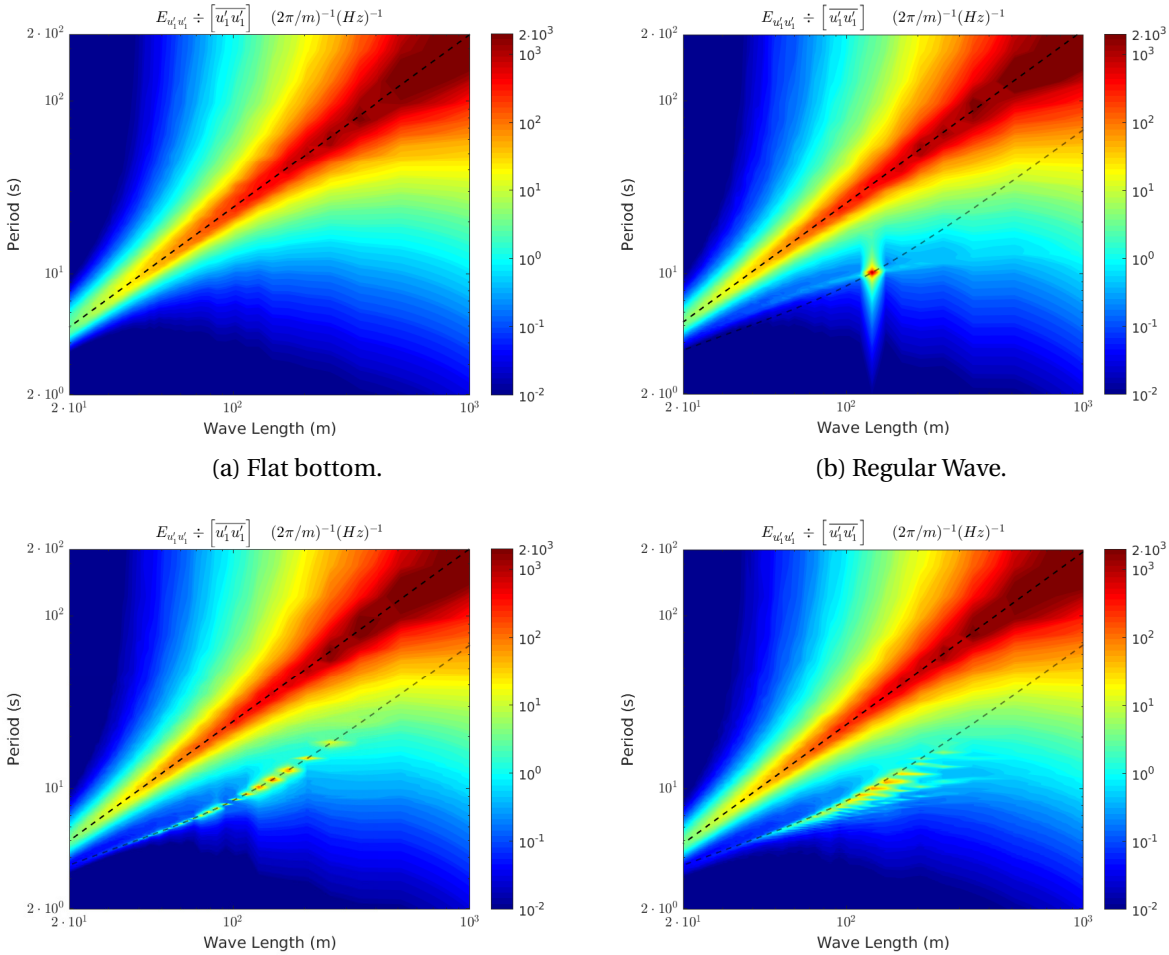

(a) Flat bottom.

(b) Regular Wave.

(c) Irregular 1D sea-state.

(d) Irregular 2D sea-state.

Figure IV.2.5: Wave-number-angular-frequency 2D turbulent spectra. The lower dashed line follow the dispersion equation in the wavy cases (b-d). The upper dashed line follow the mean convection velocity u_1 and represents the Taylor hypothesis for the atmospheric turbulent part.

The 2D spectra lead to the most detailed description of the WI disturbances yet described for these test cases. At the measurement height, where most disturbances in the wind and turbulent profiles and in the 1D spectra appear negligible face to the prevailing atmospheric turbulence behavior, the WI flow is observed directly impacting the 2D spectra at the waves prevailing scales, i.e. across the dispersion equation. The $k-w$ spectra also let clear the intrinsic difference between the wavy cases here considered.

Case 01 (fig. IV.2.5b) is forced by a dirac function perturbation occurring at the wave peak scale, and provides evidence that this monochromatic wave interacts with turbulence in the atmosphere, with the WI disturbances propagating further away from the peak scale along two prevailing $k-w$ paths: One with constant k, and the other following the atmospheric turbulence contours. These paths are highlighted by red dotted lines in figure IV.2.6b, denoting the WI auto-spectra correspondent to the total fluctuations depicted in figure IV.2.5b.

Case 02 (fig. IV.2.5c) considers a continuous wave-number dependent spectra propagating in the wind direction, the WI disturbances are symmetrically distributed around the dispersion relation, but they are not continuous in the $k-w$ domain. Indeed a continuous wave-number-dependent sea-state spectra is not continuous in the $k-w$ domain, because waves are only defined at certain frequencies according to the dispersion relation. The wave directional spreading introduced at Case 03 mitigates, but does not suppress these discontinuities, so that leads to the sharp disturbances of the 1D frequency-dependent WI spectra in figure IV.2.4(d,f), and the multiple detached wave focusing scales of the 2D spectra in figures IV.2.5(c,d).

In Case 03 (fig. IV.2.5d), the wave spreading distributes the WI energy over larger portions of the $k-w$ domain. The WI disturbances in figure IV.2.5d are not symmetrically distributed around the dispersion equation, because the spreading can only diminish the wave period at a given wave length, and both the 1D and 2D spectra are significantly smoother than in the 1D sea-state case.

The 2D spectra partition is depicted in figure IV.2.6, for Cases 01 (a,b), 02 (c,d) and 03 (e,f), with the atmospheric turbulence part shown in (a,c,e) and the WI part in (b,d,f). First note that by definition the Atm. turbulent part is continuous, while the WI part is not. Nevertheless, the WI disturbances are significantly more continuous than the sea-state spectra itself. Reminding that the sea-state spectra is given by: A dirac function in Case 01; a single line (1D dispersion equation) in Case 02; and compared to Case 02, the exclusive diminishing wave periods in Case 03.

In Case 01 (Regular wave) the WI part reveals fluctuations generated far from the dirac forcing and through two preferred paths, highlighted in the lower left corner of figure IV.2.6b: an evidence of the non-linear interactions taking place between Atm. and WI motions. In Cases 02 and 03 (irregular waves) such interactions leads to the smoothness of WI disturbances. Though the 1D WI spectra are continuous in k, they are not in $k-w$, and at Case 02 that reveals to two separate regions of WI motions in figure IV.2.6d.

The Atmospheric turbulence part in figures IV.2.6(a,c,e) closely resemble each other between the wavy cases, also resembling the flat bottom spectra of figure IV.2.5a, which attests the partitioning efficiency in view of the definition given in section IV.1. The main difference between the Atm. spectra reveals the limits of the partitioning. The WI fraction is ill defined when Atm. turbulence largely prevail over WI motions, which will rapidly occur above the

wave peak scale, in the elliptical regions highlighted at figures IV.2.6(a,c,e). In Case 01 that leaves especially the upper part of the non-linear interactions to the Atm. part, and in Cases 02 and 03 that leads to a slight augmentation of the Atm. 2D spectra above the wave peak scale.

IV.2.2.2 Overview and discussion

Contrary to the mean history, mean wind and turbulent profiles, and the 1D spectral analyses; and as argued in section IV.1: The Space-Time (Or $k-w$) perspective of turbulent fluctuations reveals detailed information about the WI flow structure, which favors the investigation of consequent WI disturbances and Wind-Wave interactions in the MABL, demonstrating intrinsic differences between the test cases discussed.

The 1D spectra reveal a partial perspective of the spectral energy distribution. So in more realistic conditions where the sea-state is defined at multiple scales (irregular), it is often unfeasible to employ the WC and WI filters based on the 1D turbulent spectra, such as previously exploited in section IV.1.2 for the regular wave case. Adopting the enhanced perspective of the WI flow proposed in section IV.1, the $k-w$ 2D spectral partition proposed in section IV.2 is shown feasible for each test case, even given the significant differences observed in the correspondent WI 2D spectra, and without any prior information about the Sea-State prescription. When the decomposition based on the 1D spectra is feasible, it leads to accurate approximations of the WI flow at the wave harmonics; but neglect WI disturbances captured in a wider range of scales by the 2D spectral based partitioning.

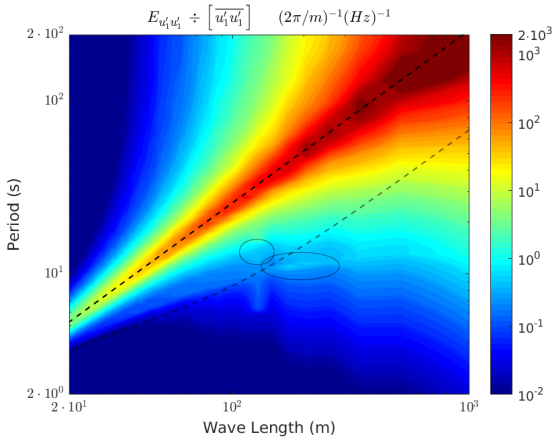

(a) Regular Wave; Atm. turbulence.

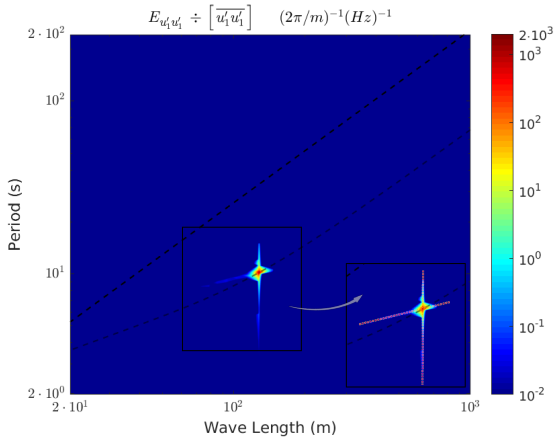

(b) Regular Wave; WI motions.

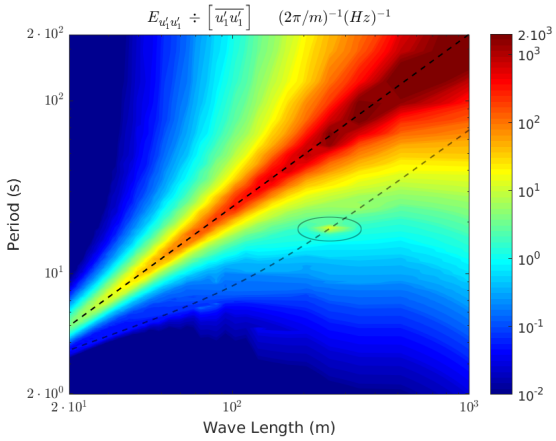

(c) Irregular 1D sea-state; Atm. turbulence.

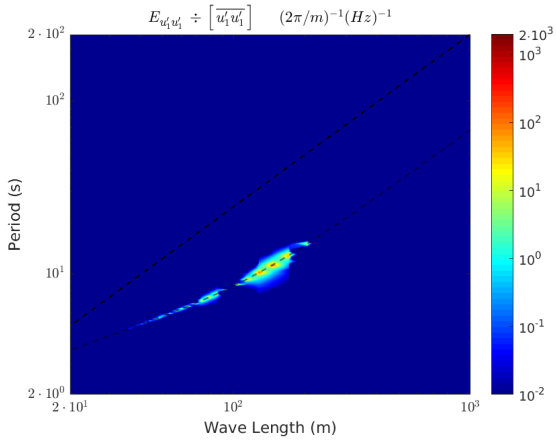

(d) Irregular 1D sea-state; WI motions.

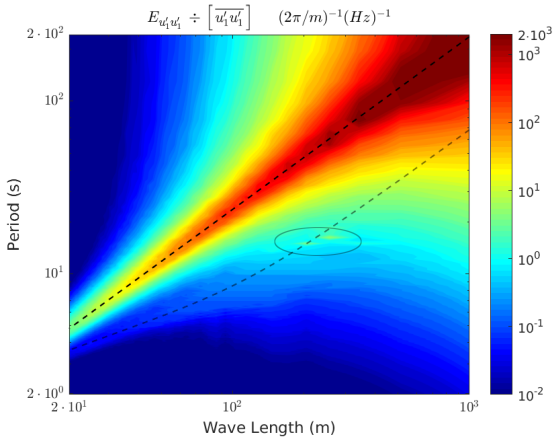

(e) Irregular 2D sea-state; Atm. turbulence.

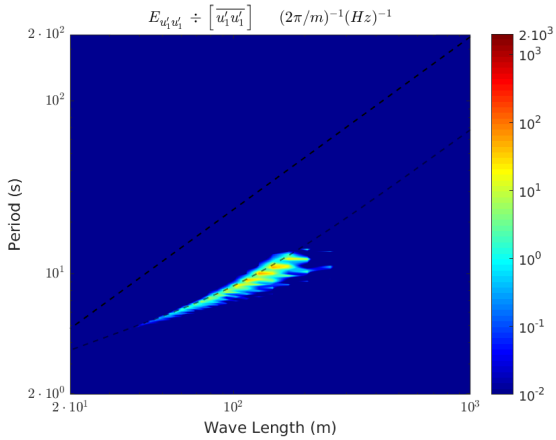

(f) Irregular 2D sea-state; WI motions.

Figure IV.2.6: Wave-number-angular-frequency 2D turbulent spectra partitioning for the wavy Cases 01 (a,b), 02 (c,d) and 03 (e,f). Atmospheric (Atm.) turbulence part in (a,c,e) and Wave Induced (WI) part in (b,d,f). The upper dashed line stands for the Taylor hypothesis and the lower dashed line for the dispersion equation.

IV.2.3 PHYSICAL EXPERIMENTS

Previous results presented in section II.3, concerning the physical experiments described in section II.1, give evidence of wave dynamics, named Wave Induced (WI) motions, propagating through the atmosphere and registered by the sLiDAR in the RWS fluctuations. The original field measurement revealed an enhanced perspective of the velocity fluctuations, in which the WI disturbances emerge distinctively on the 2D spectra, but the WI flow remains to be quantified.

A definition of the WI flow is presented in section IV.1, relying in the introduction of the WI fraction $\mathscr{F}$, and two conceptual expansions of the Wave Coherent (WC) filter presented in Hristov and Ruiz-Plancarte [2014]: (i) The existent coherence between Atmospheric turbulence (Atm.) and WI motions; and (ii) The Space-Time spectral description of turbulent fluctuations. Section IV.2 describes how $\mathscr{F}(k, w)$ can be obtained from partitioning the 2D turbulent spectra, such as the ones discussed along section II.3.3. Partitioning the 2D spectra with the methodology proposed leads to the resultant Atmospheric turbulence spectra shown in figure IV.2.7, to be compared to the total fluctuation spectra previously given in figure II.3.3. The partition is successful, filtering out the WI disturbances and leaving the atmospheric turbulence intact at figure IV.2.7.

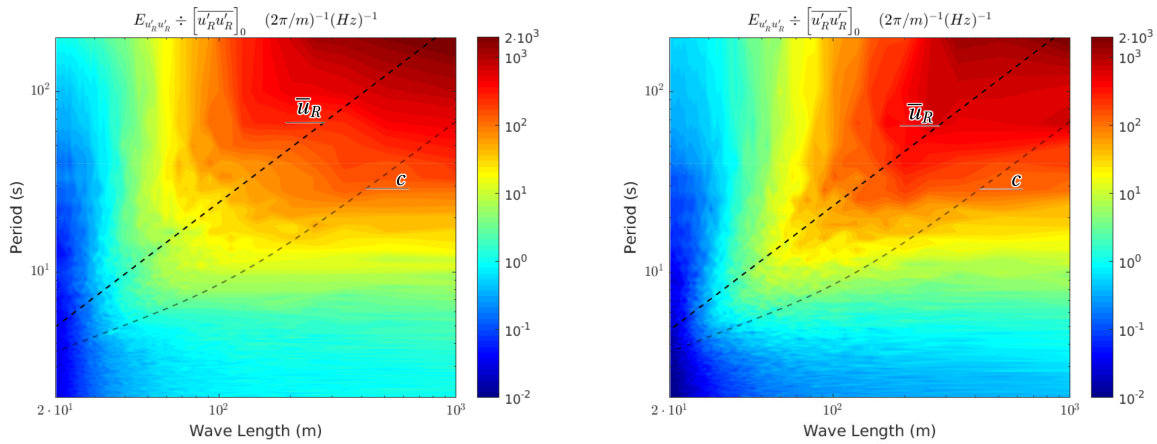

(a) Case 01.

(b) Case 02.a.

Figure IV.2.7: Atmospheric part of the resultant spectra, i.e. the Atm. auto-spectra $E_{\hat{u}_R \hat{u}_R}(k, w)$. Employing the partition described at section IV.2, The WI disturbance has been deduced from the the total fluctuation spectra, previously shown at figure II.3.3. The mean wind velocity $\overline{u}_R$ and the wave velocities c (Dispersion equation with $d = 22$ m), appear in black dashed lines.

In Case 02a, where wind and waves travel in apposite directions, the four quadrant spectrum is used, and the partition is employed exclusively in the Ocean to sLiDAR component, with the total fluctuation spectra previously given in figure II.3.5b, and the decomposed Atmospheric part here given in figure IV.2.8. The resultant atmospheric spectra of figure IV.2.7b is reconstructed from the partitioned four quadrant spectra.

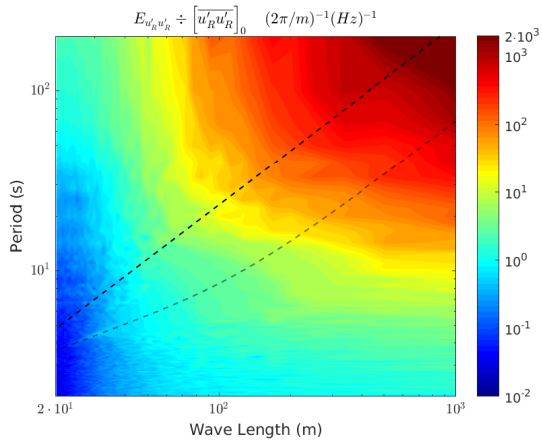

Figure IV.2.8: Decomposed atmospheric part ($E_{\hat{u}_R \hat{u}_R}$) of the 'Ocean to sLiDAR' component, of the four quadrant spectra shown in figure IV.2.7b. The black dashed lines denote wind and wave characteristic scales, as in figure IV.2.7.

IV.2.3.1 Atmospheric and Wave Induced 1D Spectra

The integration of the 2D $k-w$ spectra in k and w domains leads to the wave-number and frequency 1D spectra, decomposed as shown in figure IV.2.9. Case 01 appear above in figures IV.2.9(a,b), and Case 02a below at IV.2.9(c,d). Wave-number dependent spectra are shown in the left at figures IV.2.9(a,c), and frequency dependent spectra in the right at IV.2.9(b,d). The total fluctuation auto-spectra appear in black dotted lines, and the ESDU reference in black dashed lines. The total fluctuation spectra ($E_{u'_R u'_R}$), corresponding to the same 1D spectra previously shown in figure II.3.2, are here decomposed into: The Atm. turbulence auto-spectra ($E_{\hat{u}_R \hat{u}_R}$), given in blue dashed lines; the WI flow auto-spectra ($E_{\tilde{u}_R \tilde{u}_R}$), given in red dashed lines; and the Atm-WI cross-spectra ($2\ E_{\hat{u}_R \tilde{u}_R}$) given in magenta dot-dashed lines. So, $E_{u'_R u'_R} = E_{\hat{u}_R \hat{u}_R} + 2\ E_{\hat{u}_R \tilde{u}_R} + E_{\tilde{u}_R \tilde{u}_R}$.

No WI disturbance is observed in any of the atmospheric parts (blue dashed lines) of figure IV.2.9, that closely resemble the flat bottom ESDU reference (Dashed black lines in the figure), if submitted to the sLiDAR filter as previously discussed in section II.3.2, and further evaluated in the numerical experiments at sections IV.3.3 (flat) and IV.3.4 (wavy). The cross-spectra, and so the cross correlations, are significant between Atm and WI motions, figures IV.2.9(a,b), indicating a strong interaction between coherent Atm and WI motions.

Still in figure IV.2.9, the vertical blue dot-dashed lines correspond to the wave peak scales, and the vertical green dotted lines to the filter scales. Note that the WI auto and cross spectra have their peak close, but slightly larger the the peak scales, as expected from the discussion in section II.3.4, where larger waves travel higher in the ABL.

Recall that in section II.3 the filter characteristic frequency ($f_{\gamma 0}$) assumed that turbulence was advected by the mean wind velocity. However in figure IV.2.9, and in the others to come, the characteristic frequency corresponds to the WI motions and the dispersion equation, rather than the wind velocity and the Taylor's hypothesis. That highlights the filter effect on the WI velocities, as discussed from its numerical evaluation in section IV.3.4. Thus the filter frequency shown further through this section is $f_{\gamma 1} = c/(2\ L_\gamma)$, with $c = \sqrt{(g/k_\gamma)\ \tanh(k_\gamma d)}$,

$k_\gamma = 2\pi/(2\,L_\gamma)$, $L_\gamma = 25$ m, and $d = 22$ m. One notices that the wave disturbances drastically diminish in figure IV.2.9 close to k_γ and $f_{\gamma 1}$, where the sLiDAR filters a significant amount of the WI fluctuations.

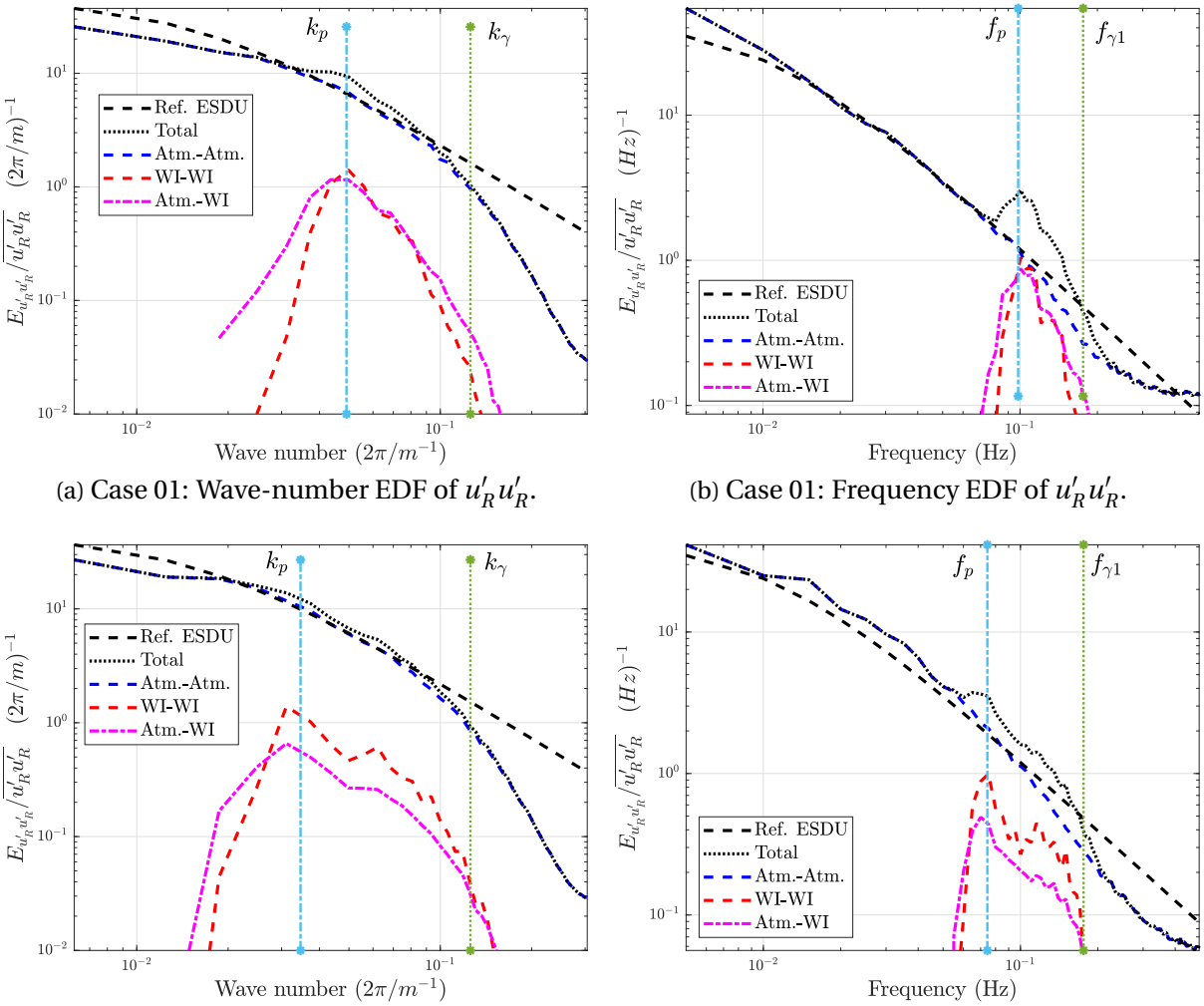

(a) Case 01: Wave-number EDF of $u'_R u'_R$.

(b) Case 01: Frequency EDF of $u'_R u'_R$.

(c) Case 02: Wave-number EDF of $u'_R u'_R$.

(d) Case 02: Frequency EDF of $u'_R u'_R$.

Figure IV.2.9: Resultant wave-number (a,c) and frequency (b,d) 1D decomposed turbulent spectra for Case 01 (a,b) and Case 02.a (c,d). The **legend** associates the five spectra depicted to: The (**Ref. ESDU**) reference; total turbulent fluctuation auto-spectra (**Total**); Atmospheric turbulence auto-spectra (**Atm.-Atm.**); Wave Induced auto-spectra (**WI-WI**); and (**Atm.-WI**) cross spectra. Vertical blue lines stand for the wave peak scales k_p and f_p, and the green lines show filter scales k_γ and $f_{\gamma 1}$.

The partition of the turbulent spectra at Case 02a occurs exclusively at motions traveling from the 'Ocean to sLiDAR' direction, and that can be appreciated from the correspondent quadrant spectra at figure IV.2.10, where the Total, Atm, WI, and Atm-WI spectra, are given as for the resultant spectra in figures IV.2.9(c,d). Note that in both figures (quadrants and resultant spectra) the WI and cross spectra terms (red dashed and magenta dot-dashed lines) are the same. But the atmospheric turbulence and total parts are drastically reduced in the 'Ocean to sLiDAR' direction, so the WI signature emerges distinctively in the directional decomposed spectra of figure IV.2.10. Also in the directional spectra of figure IV.2.10,

the atmospheric turbulence auto-spectra agree considerably well to the ESDU reference.

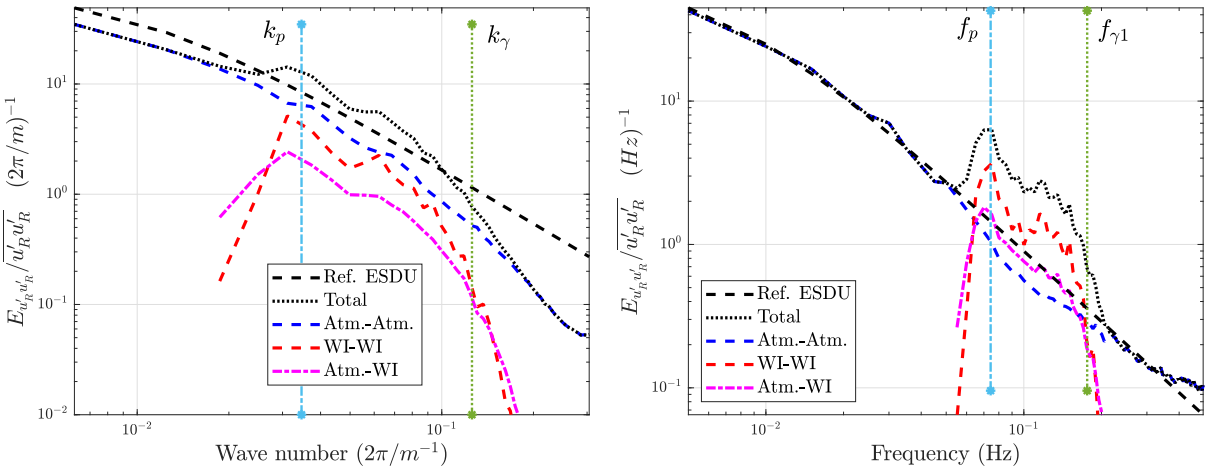

(a) Case 02: Wave-number EDF of $u'_R u'_R$.

(b) Case 02: Frequency EDF of $u'_R u'_R$.

Figure IV.2.10: One-dimensional decomposed spectra ($E_{u'_R u'_R}$, $E_{\hat{u}_R \hat{u}_R}$, $E_{\tilde{u}_R \tilde{u}_R}$, and 2 $E_{\hat{u}_R \tilde{u}_R}$) for fluctuations traveling from the Ocean into the sLiDAR, at Case 02a. The legends apply as for Case 01 in figure IV.2.9, that in turn denote the resultant spectra comprehending motions in both directions, and where the explicit WI auto spectra has been omitted for Case 02a.

IV.2.3.2 Wave Induced fraction

The decomposition presented follows from the determination of the WI fraction $\mathscr{F}(k,w)$ in the 2D $k-w$ domain. Here the WI fraction is reconstructed in the 1D, wave-number or frequency domains, as $\mathscr{F}(k) = \sqrt{E_{\tilde{u}_R \tilde{u}_R}(k)/E_{u'_R u'_R}(k)}$ and $\mathscr{F}(f) = \sqrt{E_{\tilde{u}_R \tilde{u}_R}(f)/E_{u'_R u'_R}(f)}$, as reported in figure IV.2.11 for Cases 01 (Red dashed lines) and 02.a (Black full lines). Recall that $\mathscr{F}$ gives the squared root of the WI energy fraction. For a wide range of scales in figure IV.2.11, $\mathscr{F}(w)$ and $\mathscr{F}(k)$ exceed the threshold of 0.1 (1% of WI energy fraction), suggesting the WI motions are non-negligible and the measurement occurs inside the WBL.

Next to each case spectra in figure IV.2.11, one encounters vertical lines corresponding to the wave peak scales (k_p, f_p), colored according to each case spectra. Note that (k_p, f_p) corresponds to the peak of the sea surface displacement spectrum, but F is the sea surface velocity spectrum, so it is natural that the peak of F occurs at scales smaller than (k_p, f_p). Close to the wave peak scale, both cases (similar |WA|, but different wind directions) present similar values for the WI fraction $\mathscr{F}(k,w)$, that approaches (or even surpasses, for $\mathscr{F}(f)$) the threshold of 0.5, indicating that WI motions are dominant. Towards larger scales (lower k, f), $\mathscr{F}(k,w)$ rapidly diminishes at both cases, but a gradual decay is observed towards smaller scales behaving significantly different at each test case.

As usual the filter scales $(k_\gamma, f_{\gamma 1})$ appear with vertical green lines at figure IV.2.11. The decay in $\mathscr{F}(f)$ is also very rapid at scales smaller than the filter characteristics. It is important to note this is not only due to the physical transfer function between sea-state and atmospheric motions, but also due to the sLiDAR filter effect becoming predominant close to $(k_\gamma, f_{\gamma 1})$. The region of interest is that between (k_p, f_p) and $(k_\gamma, f_{\gamma 1})$, where the WI flow is significant, the sLiDAR effect is mitigated (far enough from $k_\gamma, f_{\gamma 1}$), and the cases behave

considerably differently. Notably, the decay of Case 02a is attenuated, and the WI flow is significant over a wider range of scales at Case 02a, if compared to Case 01.

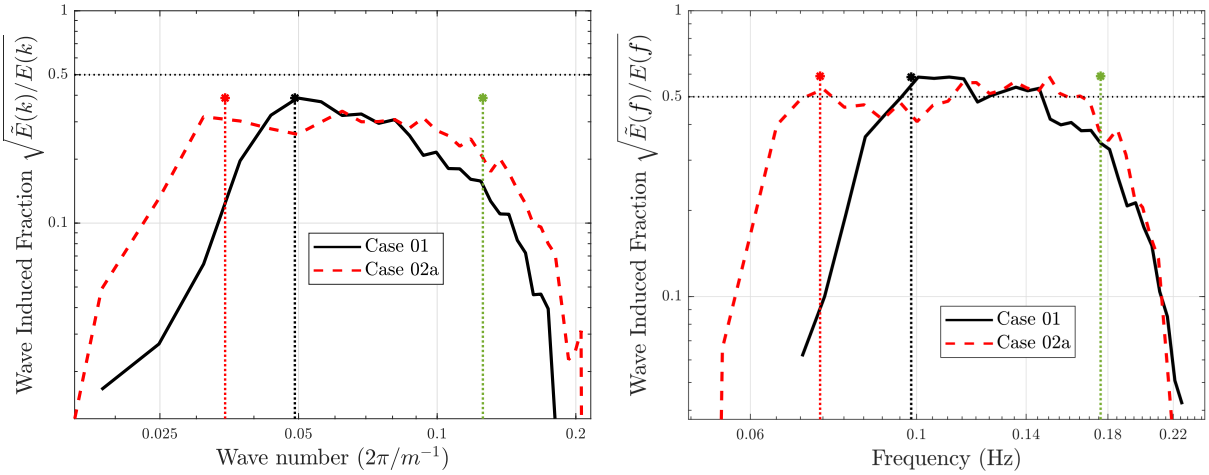

(a) WI fraction $\mathscr{F}(k)$ (b) WI fraction $\mathscr{F}(f)$

Figure IV.2.11: Wave Induced fraction $\mathscr{F}(k)$ (Left) and $\mathscr{F}(w)$ (Right), corresponding to the squared root of the WI energy fraction according to equation IV.1.3. After integrating the 2D decomposed spectra in the 1D spectra of figure IV.2.10, $\mathscr{F}(k)$ and $\mathscr{F}(w)$ are here computed as $\mathscr{F}(k) = \sqrt{E_{\tilde{u}_R\tilde{u}_R}(k)/E_{u'_R u'_R}(k)}$ and $\mathscr{F}(f) = \sqrt{E_{\tilde{u}_R\tilde{u}_R}(f)/E_{u'_R u'_R}(f)}$. Wave peak scales denoted by vertical dotted lines, with black (Case 01) and red (Case 02a) colors corresponding to the curves of $\mathscr{F}$ shown in the legend. The filter characteristic scales (k_γ, $f_{\gamma 1}$) appear in the vertical green dotted line.

IV.2.3.3 Transfer Function of the Sea-State spectra into the atmosphere

The observed WI motions are an extension (transfer) of the wave's orbital at the free-surface, into the atmosphere. Hence, there exists a Transfer Function (TF) linking the Sea-State forcing to the atmospheric response, i.e., to the WI field. The TF is here evaluated as TF= $\sqrt{(E_{\tilde{u}_R\tilde{u}_R})/F}$, where $E_{\tilde{u}_R\tilde{u}_R}$ is the decomposed WI auto-spectra, and F the sea-state auto-spectra of longitudinal orbital velocities, taken from the WaveWatch III oceanic model as described in section II.1.3.

Prior to the transfer function, $E_{\tilde{u}_R\tilde{u}_R}$ and F are superposed in figure IV.2.12: Where the first appear in black full lines for Case 01 and red dashed lines for Case 02a; and the second appear in dotted lines, with colors given by each corresponding case according to the legend. In any case, the peak of $E_{\tilde{u}_R\tilde{u}_R}$ is slightly displaced to lower scales if compared to the peak of F, naturally since long waves disturbances are expected to propagate higher in the MABL. Around the peak scales, both spectra (E and F) are highly coherent, presenting similar slopes. But the slopes highly differ in smaller scales, where both the scale-dependent transfer function and the sLiDAR filter effects are significant. The sea-state spectra present a second, less energetic peak at lower scales, which is captured in $E_{\tilde{u}_R\tilde{u}_R}$ at Case 02a. There is a remarkable similarity between the WI spectra slopes observed for both Cases, at scales smaller than the smallest wave peak (L_p = 126.9 and T_p = 10.10 for Case 01).

The Transfer Functions are finally exposed in figure IV.2.13, for Cases 01 (Black) and 02.a

(Red). The resemblance is clear between the cases, where TF(k) and TF(w) reach a maximum of ~ 0.3, and eventually decay with similar behavior at both cases. The significant difference between the cases is that Case 02a presents a wide range of scales with almost constant TF values, while Case 01 rapidly decays far away from the wave peak scales.

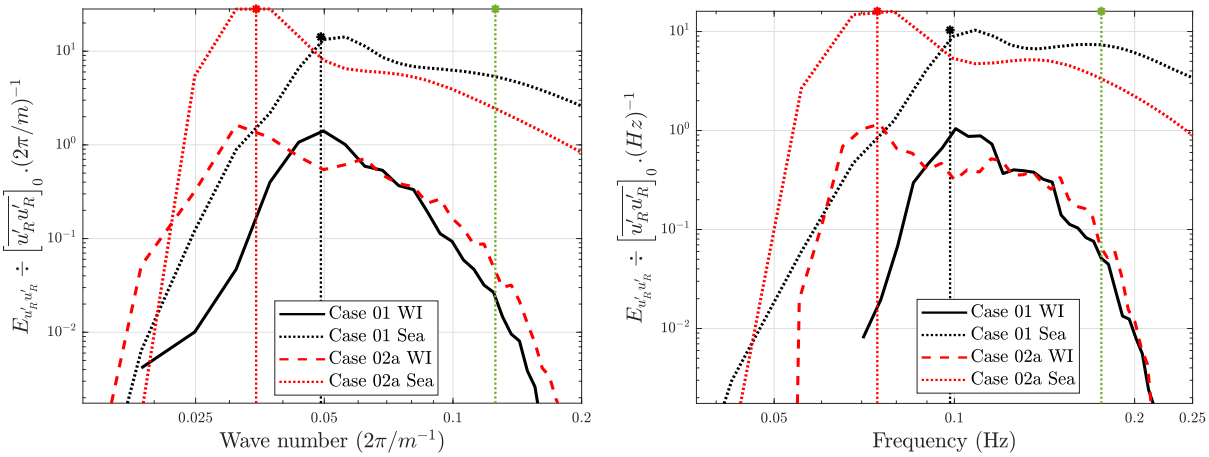

(a) k-dependent spectra. (b) f-dependent spectra.

Figure IV.2.12: Sea-State forcing and the atmospheric response. Sea-State forcing (F): Auto-spectra of the longitudinal orbital velocities on the free-surface (FS). Atmospheric response ($E_{\tilde{u}_R\tilde{u}_R}$): Auto-spectra of the WI flow, as previously shown at figure IV.2.9. Cases 01 and 02a superposed, with line types given in the legend. Together with the sea-state forcing, the corresponding wave peak scales are shown in vertical lines. The peak scales correspond to peaks of the FS displacement spectra, and not to the velocities spectra shown in the figures. The filter characteristic scales (k_γ, $f_{\gamma 1}$) appear in the vertical green dotted line.

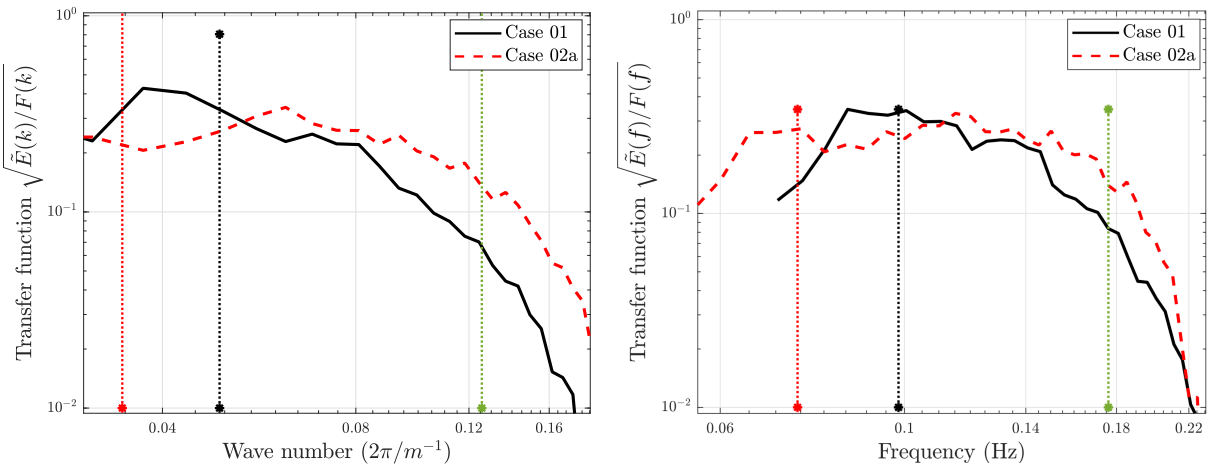

(a) k-dependent TF. (b) f-dependent TF.

Figure IV.2.13: Transfer function between the Sea-State forcing and the atmospheric response shown in figure IV.2.12. Computed as TF= $\sqrt{(E_{\tilde{u}_R\tilde{u}_R})/F}$. Cases 01 and 02a superposed, with line types given in the legend. Together with the TF, the corresponding wave peak scales are given in vertical lines. The filter characteristic scales (k_γ, $f_{\gamma 1}$) appear in the vertical green dotted line.

IV.2.3.4 Overview and discussion

The characterization of measured WI motions is presented in section IV.2.3, following its definition given in section IV.1. With no generalization intent, an image contour-based segmentation method is developed in section IV.2 to obtain $\mathscr{F}(k,w)$ from the 2D Space-Time turbulent spectra. The effectiveness of the employed triple decomposition is established in figures IV.2.7 and IV.2.9 where the WI disturbances have vanished from the Atm. filtered 2D and 1D turbulent spectra, respectively.

Contrary to the decomposed equations of Hristov and Ruiz-Plancarte [2014] and Cifuentes-Lorenzen et al. [2018], the Atm. and WI flows are strongly correlated and coupled in either space and time domains. The idea that Atm. and WI flows are strongly correlated might appear contradictory, for it defies the definition of the WI flow as a particular system detached from atmospheric turbulent motions. In the combined space-time perspective though, the correlation is reduced as long as the wind is sufficiently weak, and the swell is sufficiently fast, so that U and c are sufficiently apart. The correlations shall exist so that WI-Atm. interactions can occur, but the correlations and interactions shall be limited so that WI and Atm. fields can be defined as two different systems. The different propagating velocities of Atm. and WI fluctuations shall limit their interactions in the coupled set of equations governing those fields. Naturally this definition of the WI flow is limited to scenarios where it is detectable, which according to current observations shall occur in the Space-Time spectral distribution $E_{u'_R u'_R}(k,w)$ when $\mathscr{F}(w)$ or $\mathscr{F}(k)$ exceeds 0.1.

From the integration of $\mathscr{F}(w,k)$, figure IV.2.11 presents $\mathscr{F}(f)$ and $\mathscr{F}(k)$. In any case $\mathscr{F}$ exceed the threshold of 0.1 between the wave peak and the filter characteristic scale, suggesting the WI motions are significant and the measurement occurs inside the WBL. For a wide range of scales, and specially at Case 02a, $\mathscr{F}(k)$ and $\mathscr{F}(f)$ approach and surpass the threshold of 0.5, and the WI motions are dominant.

The determination of the transfer function linking the sea-state forcing and the atmospheric response shall precede any parametric description of the WI field in the MABL, but it has not yet been reported in the literature as actual measurements in the offshore environment. That shall occur for the absence of a triple decomposition method capable of measuring the WI field in the ocean environment, characterized by non-regular sea-state situations. Recent developments in sLiDAR measurements technologies and techniques allow the enhanced perspective achieved through the 2D spectra, and together with the triple decomposition proposed, the Transfer Function (TF) is here presented in figure IV.2.13.

IV.3 Towards the numerical reproduction of sLIDAR observations

IV.3.1 Sea State Reconstruction

Estimated quantities that describe the oceanic conditions during the experimental campaign have been described in section II.1.3. These quantities are extracted from HOMERE hind-cast database (Accensi et al. [2017]), hourly and at the closest node to the sLiDAR LOS final gate. Some of the quantities to be exploited at this closest node/probe are the frequency dependent power density function (PDF) of surface elevations $F^*(f)$, the mean direction ϕ_0^*, and the spreading direction β^*. Only at a few nodes of the oceanic grid, the full spectral content of the surface elevations $F(f,\phi)$ is available, being the closest one approximately 9 km south and 2 km east (At 47°12'N,-2°30'E) of the sLiDAR.

It has been discussed in section II.1.3, and observed in figure II.1.4, that significant refraction occurs between the $F(f,\phi)$ probing position and the sLiDAR's. It is further demonstrated how to obtain the description of $F(f,\phi)$ coherent with the global estimations obtained closer to the sLiDAR, and how to generate the initial conditions necessary for its numerical exploitation.

An iterative set of linear transformations applies to $F(f,\phi)$, until it meets the frequency spectra ($F(f) \to F^*(f)$) and the mean and spreading directions ($\phi_0 \to \phi_0^*$ and $\beta \to \beta^*$) registered closer to the sLiDAR, with the definitions:

$$F(f) = \int F(f,\phi)\, d\phi, \qquad \phi_0 = \text{atan}\,[a/b], \qquad \beta = \sqrt{2\,\left(1-\phi_1\right)},$$

$$a = 2\pi \int\int \left[\cos(\phi) F(f,\phi)\right]\, \mathrm{d}\phi\, \mathrm{d}f, \qquad b = 2\pi \int\int \left[\sin(\phi) F(f,\phi)\right]\, \mathrm{d}\phi\, \mathrm{d}f, \tag{IV.3.1}$$

$$\text{and} \qquad \phi_1 = \sqrt{\frac{a^2+b^2}{(\int F(f)\,\mathrm{d}f)^2}}.$$

The correction of $F(f,\phi)$ is sequentially performed with respect to its frequency distribution, mean direction and spreading:

- While β is not converged, i.e., abs $\left[\dfrac{\beta*}{\sqrt{2\,\left(1-\phi_1\right)}} - 1\right] > 10^{-6}$:
  - Correct for F(f), normalizing $F(f,\phi)$ at each frequency:

$$F(f,\phi) \to F(f,\phi)\,\frac{F^*(f)}{F(f)}.$$

– Correct for ϕ_0, shifting the direction domain:

$$\phi \rightarrow \phi - \phi_0 + \phi_0^*.$$

– Correct for β, shrinking or expanding the direction domain around ϕ_0:

$$\phi \rightarrow \phi_0 + (\phi - \phi_0)\,\frac{\beta^*}{\beta}.$$

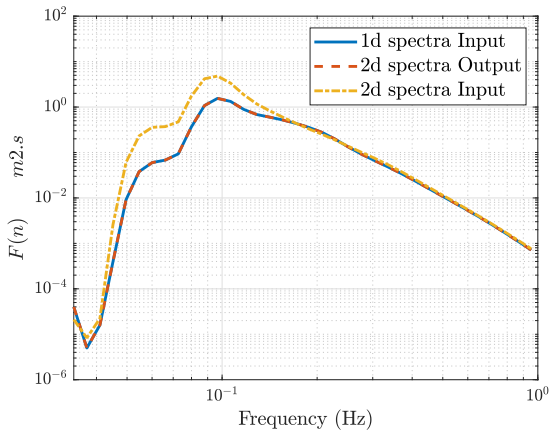

(a) Comparison between $F(f)$: Close to the sLiDAR (1D Input); Far from the sLiDAR (2D Input); Reconstruction (2D Output).

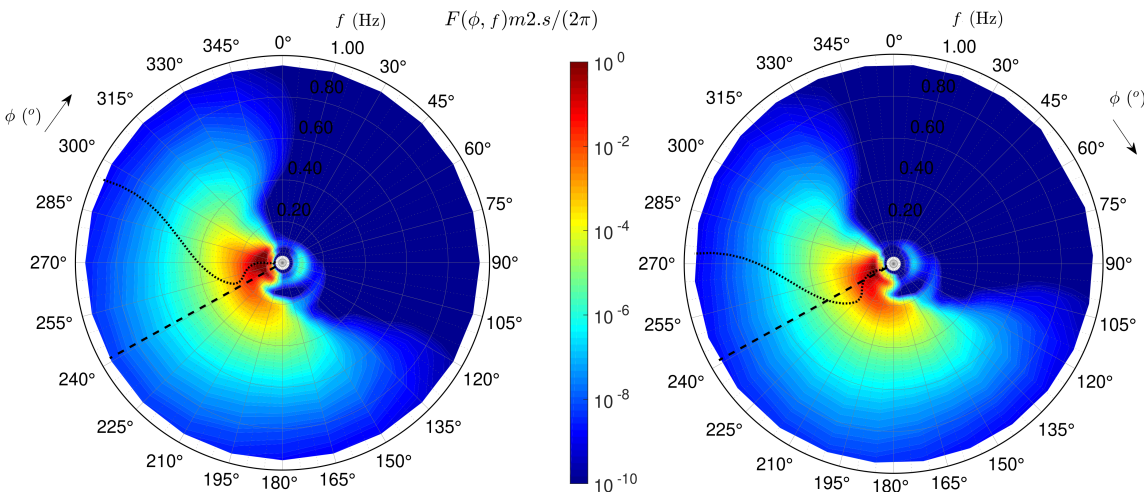

(b) Probed far from the sLiDAR. (c) Reconstructed closer to the sLiDAR.

Figure IV.3.1: The PDF of the surface elevation F. $F(f,\phi)$ is obtained far from the sLiDAR, and reconstructed to match the global parameters obtained closer to the sLiDAR. (a) Integrating $F(f,\phi)$ in ϕ dimension, the reconstruction is evaluated in comparison to the 1D and 2D spectral input, obtained closer and farther to the sLiDAR, respectively. (b) The 2D spectral input $F(f,\phi)$. (c) The 2D spectral output, $F(f,\phi)$ reconstructed to match $F(f)$, ϕ and β closer to the sLiDAR. In (b) and (c) the frequency-dependent mean direction $\beta(f)$ is shown with black dotted lines as obtained from each spectra, and the value of β probed closer to the sLiDAR appears with black dashed lines.

The reconstruction is first shown in figure IV.3.1a, where the initial and final (Input and Output) 2D spectra $F(f,\phi)$ integrated in ϕ dimension, lead to the 1D frequency spectra shown in yellow dot-dashed and red dashed lines, respectively. The $F(f)$ 1D spectra (Input) is shown in blue full line at the same figure. Transforming the input to output 2D spectra, $F(f)$ is strongly diminished at lower frequencies, accurately matching the input 1D spectra as consequence.

The input directional Sea-State spectra from figure II.1.4 is repeated in figure IV.3.1b to be compared with the output $F(f,\phi)$ spectra given in figure IV.3.1c. One can readily note a significant change in the mean direction ϕ_0, by shifting the frequency-dependent mean direction $\phi(f)$ denoted by black dotted lines in the figures. The target, total average mean direction ϕ_0^* is denoted by the dashed line, and is accurately matched by the output spectrum at figure IV.3.1c. The sea-state spreading β is slightly diminished, shrinking the direction domain closer to $\phi_0 = 241°$: Note the large spacing between angles 45° and 75° at figure IV.3.1c.

The reconstructed spectrum $F(f,\phi)$ is then interpolated into the LES numerical grid. In the frequency domain the interpolation is log-linear (Linear in logarithmic scale such as in figure IV.3.1a), and in the direction domain (Between $\phi_0 - 0.5\,\pi$ and $\phi_0 + 0.5\,\pi$) the interpolation is FFT-based. Only a π sector is considered around the mean direction ϕ_0. In the domain of $F(f,\phi)$, a scatter plot of the LES surface nodes ([512x256] grid and [5x4]L_0 domain with L_0 = 256 m) is shown in figure IV.3.2a, colored by the interpolated values of $F(f,\phi)$ in the nodes. Note that integrated in the LES domain the mean direction is slightly different from ϕ_0, and the domain is adjusted from black to red bounds in figure IV.3.2a, in order to have the waves mean direction (almost) perfectly aligned to the ABL longitudinal direction.

Finally with the group velocity definition $c_g = \partial w/\partial k$, F is scaled to the $[k_x, k_y]$ space:

$$F(k_x,k_y) = F(f,\phi)\,\frac{c_g}{(k_x^2+k_y^2)^{0.5}}, \tag{IV.3.2}$$

with result shown in figure IV.3.2b, ready to be read by the LES code.

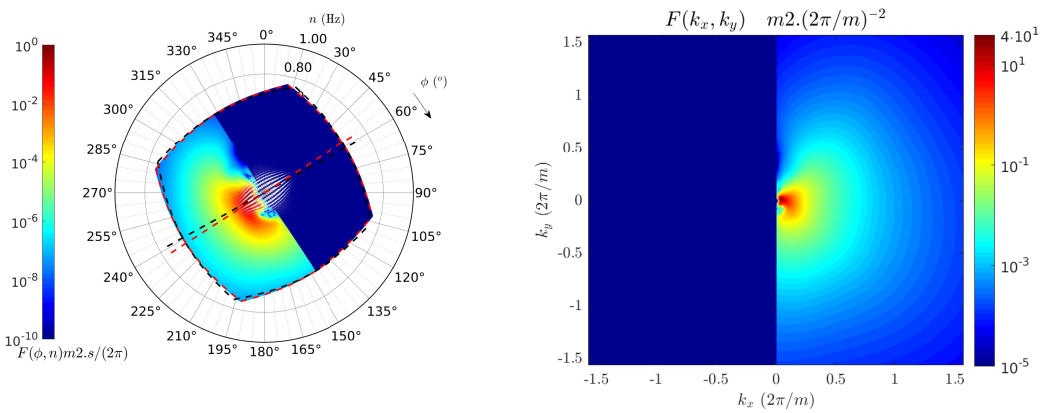

(a) A scatter plot of $F(f,\phi)$ in the LES interpolated grid $(k_x,k_y)_{ij}$.

(b) $F(k_x,k_y)$, input to the LES code.

Figure IV.3.2: The interpolation of $F(f,\phi)$ into $F(k_x,k_y)$.

IV.3.2 A NUMERICAL SLIDAR MODELLING THE FILTER EFFECT

Section II.3 presents original analyses based on measurements with a sLiDAR staring into the WBL above the Ocean. As discussed in section II.1.2.1, the sLiDAR imposes a filter to the measured Radial Wind Speed (RWS). The impact of such filter in the frequency or wave-number 1D spectra is often documented in the literature (c.f. Bastine et al. [2015]) with the aid of another instrument such as a Sonic Anemometer. Besides not disposing of an anemometer, the author does not know any instrument other than the sLiDAR capable of evaluating the wave-number-frequency 2D Spectra at similar scales. So due to the sLiDAR filter, a BIAS is expected in current experimental observations, which behavior in the wave-number-frequency spectra is not reported in the literature.

As explained in section II.1.2.1 the filter is physically imposed through the light-speed traveling ray beam emitted by the sLiDAR. To control the filter and mitigate the BIAS, the sLiDAR system employs a weight function convolution to the received signal. This weight function is system dependent and generally protected by the manufacturer. Instead, the sLiDAR user controls the Gate Length L_f, that in present application corresponds to the Full Width at Half Maximum (FWHM) of the filter ensemble, i.e., considering the convolution of the physical filter and the weight function. So consistent with the manufacturer suggestion, given the gate length L_f (FWHM) the filter is here modeled by a gaussian function with standard deviation $\sigma_f = L_f/(2\sqrt{2\ln 2})$, and the filtered RWS is:

$$\tilde{u}_R(x,t) = \int_0^\infty \frac{u_R(x_0,t)}{\sqrt{2\pi}\sigma_f} \exp\left[-\frac{(x_0-x)^2}{2\sigma_f^2}\right] \mathrm{d}x_0, \tag{IV.3.3}$$

In the LES, $u_R(x,t) = u_1(x, y = y_l/2, z = h, t)$ is the longitudinal velocity field, probed at a half of the domain width ($y = y_l/2$) and at the sLiDAR's height ($h = 18.33$ m). Note that contrary to the real world sLiDAR, the LES resolved velocities already embody the SGS filter effect, and are discretized within a grid, so not defined in the continuum.

To properly evaluate the sLiDAR filter uncoupled to the LES filter, the grid size shall be sufficiently small if compared to L_f. The filter is imposed in the experimental campaign with $L_f = 25$ m, and requires our finest mesh (Grid 03 at table III.1.1) for the analysis, so that $\Delta x = L_f/10$. The gate spacing $\Delta x_0 = 10$ m is such that a numerical gate is placed at each four LES nodes, and the ensemble (101 gates or 401 nodes over 1 km) almost covers the whole numerical domain's extension (512 nodes over 1.28 km). Equation IV.3.3 is evaluated at every gates, and integrated along the 401 LES nodes at the probing line $[y = y_l/2, z = h]$.

IV.3.3 NUMERICAL EXPERIMENT IN THE FLAT BOTTOM ABL

Present section introduces the effect of sLiDAR induced filtering in the flat bottom, LES generated ABL, to be later discussed in section IV.3.4 for the LES generated WBL above an irregular 2D sea-state.

IV.3.3.1 SPECIFIC NUMERICAL STRATEGY

The numerical Case here exploited has previously been presented, as Case 00 (Flat bottom) in section III.4.1, that one shall consult for the detailed description about the numerical strategy. The dynamic pressure gradient method developed in section III.2 is used to keep the Wind Speed close to u_{ref} =4.12 m/s at the sLiDAR measurement height $h = 18.33$ m. The nominal friction velocity is $u_0^* = 0.147$ m/s, and the natural period of the pressure gradient response is $T_{\mathscr{P}} = 285\ T_0$.

The characteristic length scaling the domain is $L_0 = 256$ m, which is twice the wave length λ employed in the wavy cases, previously at section III.4.1 and further at section IV.3.4. The turbulent characteristic time scale is $T_0 = 0.5\ L_0/u_0^* = 14.51$ min, so that is equivalent to $T_0 = \lambda/u_0^*$ employed for the wavy cases. The boundary layer height ($\delta = L_z$) is $\delta = 5\ L_0$, and the longitudinal and transversal domain extensions are respectively $L_x = 4\ L_0$ and $L_y = 2\ L_0$.

Results are presented for grid 03 (Fine [512 x 256 x 94] from table III.1.1). The next remarks are specific to current application, so contrasting to section III.4.1 that provides in Case 00 (Flat bottom) the initial conditions to current computations.

A fixed time-step $\Delta t = 0.244$ s is employed ensuring CFL< 0.5 and approximating a fourth of the sLiDAR acquisition period 1 s (f-LOS 01 at table II.1.1). The average of $\tilde{u}_R(x,t)$ over the acquisition period have also been studied but revealed no impact on the observed quantities, probably because the SGS filter becomes important at periods below 1 s, making further time refinement irrelevant below that period.

Three cases are presented: (0) No filter; (1) sLiDAR's filter imposed with $L_f = 25$ m; (2) sLiDAR's filter imposed with $L_f = 50$ m. Case 00 is the reference, probing u_R at every time and in the numerical grid (512 Nodes over 1.28 km) along the line $[y = y_l/2, z = h]$; Case 01 considers the filter adopted in the experimental campaign; and Case 02 doubles the filter width of Case 01. For Case 01 and Case 02 $\tilde{u}_R(x,t)$ is probed at the measurement line (101 Gates over 1 km), and averaged over 4 time steps $4\Delta t = 0.98$ s.

IV.3.3.2 THE SLIDAR FILTERING EFFECT IN THE ATMOSPHERIC TURBULENCE

The 1D wave-number and frequency dependent energy density functions (Turbulent spectra) are shown in figure IV.3.3, superposing Cases 00 in blue full line, Case 01 in red dashed line, and Case 02 in green dash-dotted line. The spatial filtering characteristic scale $k_{\gamma 0} = 2\pi/(2\ L_\gamma)$ and its frequency equivalent $f_{\gamma 0} = U/(2\ L_\gamma)$ are denoted by the vertical lines in the same figure, with line types and colors equal to the correspondent (Case 01 or Case 02) spectra. The ESDU 85020 reference spectra described in section III.1.2.3 appears as black dotted lines in figure IV.3.3, with the ESDU parameters obtained for Case 00. All spectra are normalized by the space-time averaged auto-correlations obtained for the reference Case 00: $\left[u_R' u_R'\right]_0$. To help the comparison to the filtered spectra, the wave-number domain is truncated for Case 00 at figure IV.3.3a, showing only the scales obtained with the sLiDAR's gate space resolution $k < \pi/\Delta x_0$ and numerical frequency acquisition $n < 1/(8\Delta t)$.

The wave-number spectra for Case 00 and the ESDU reference collide almost perfectly

in figure IV.3.3a, suggesting the adequacy of the adopted space resolution, since the SGS filtering effect is not observed at wave-numbers lower than $\pi/\Delta x_0$. In the frequency spectra of figure IV.3.3b though, Case 00 slightly deviates from the reference in higher frequencies, suggesting the SGS filter effects are not negligible in periods comparable to $8\Delta t$. Indeed the sLidar acquisition period (1 s) captures much smaller turbulent structures than the available from its gate space resolution (10 m). The sLiDAR filtering is significant in Cases 01 and 02, mostly above but also below the filter scales $k_{\gamma 0}$ and $f_{\gamma 0}$.

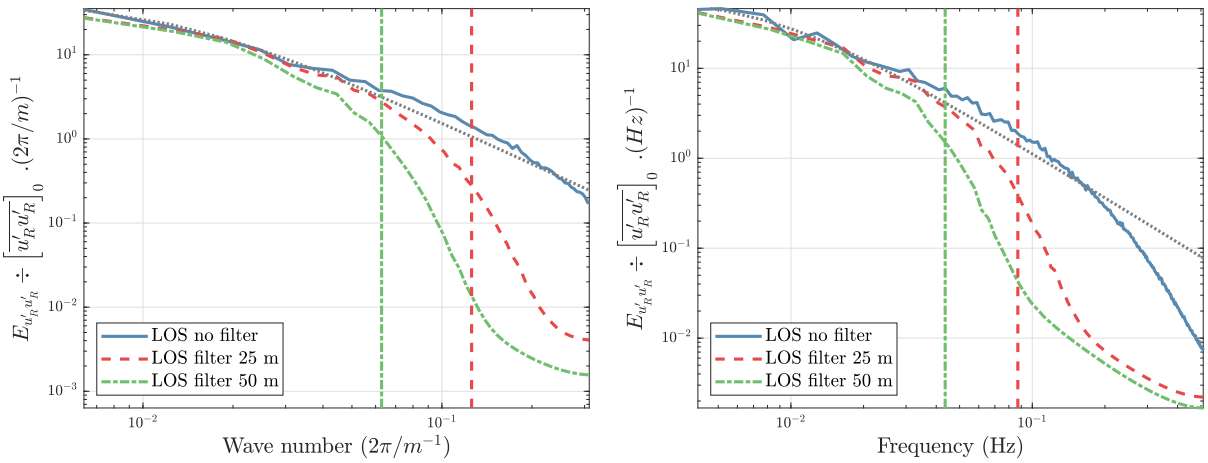

(a) Wave-number EDF of $u'_R u'_R$.

(b) Frequency EDF of $u'_R u'_R$.

Figure IV.3.3: Flat bottom numerical experiment evaluating the sLiDAR filter effect. Wave-number (a) and frequency (b) 1D turbulent spectra. Cases 00 (No filter) in blue full line, Case 01 ($L_\gamma = 25$ m) in red dashed line, and Case 02 ($L_\gamma = 50$ m) in green dashed-dotted line. The filter scales $k_{\gamma 0}$ and $f_{\gamma 0}$ appear in the vertical lines associated to Case 01 and Case 02. The reference ESDU 85020 spectra is traced in black dotted lines, with parameters obtained for Case 00. The auto-correlations $\left[u'_R u'_R\right]_0$ normalizing the spectra are also obtained for Case 00.

The fraction of energy filtered in Cases 01 and 02 in comparison to Case 00 is shown in table IV.3.1. According to the table giving energy losses of [30,32]% and [49,50]%, Case 01 presents ~70%, and Case 02 ~50% of the total energy observed in Case 00. The energy loss is critical above the filter k_γ and f_γ scales, with Cases 01 and 02 presenting less than 10% of the energy (>90% loss) observed in Case 00; and that is mitigated below these same scales where the energy loss is ~21% and ~27%, at Cases 01 and 02, respectively.

Table IV.3.1: Fraction of energy lost below or above the filter characteristic scales; Ratio between the integrated EDF for Cases 01 and 02, and the integrated EDF of Case 00.

Fraction of energy lost (%) in range →	$\boldsymbol{k < k_\gamma}$ or $\boldsymbol{n < n_\gamma}$	$\boldsymbol{k > k_\gamma}$ or $\boldsymbol{n > n_\gamma}$	**Total**
Case 01 in E_k	20	93	30
Case 01 in E_w	21	93	32
Case 02 in E_k	26	94	49
Case 02 in E_w	27	93	50

The Taylor hypothesis $f_\gamma = k_\gamma U/(2\pi)$ leads to consistent definitions of the filter frequency f_γ scale, with the E_k and E_f spectra leading to similar conclusions in table IV.3.1. The filter scale definition $k_\gamma = 2\pi/(2\ L_\gamma)$ seems appropriate in the sense that the fraction

of energy loss above that scale is relatively predominant (>90%), and slightly varies (<1%) between Cases 01 and 02 in the table. Nevertheless the energy loss below k_γ and f_γ is not negligible, and varies ~6% between the cases.

The 2D wave-number-frequency dependent turbulent spectra is shown in figure IV.3.4. The Taylor hypothesis stands in dashed black line together with the 2D turbulent spectra. For Cases 01 and 02, one notices the filter scales $L_{\gamma 0} = 2\pi / k_\gamma$ and $T_{\gamma 0} = 1/f_\gamma$ in green dotted lines. The filtering is effective below $L_{\gamma 0}$ and $T_{\gamma 0}$, and close to the Taylor hypothesis, or more generally at whatever scales the turbulent energy is significant below $L_{\gamma 0}$.

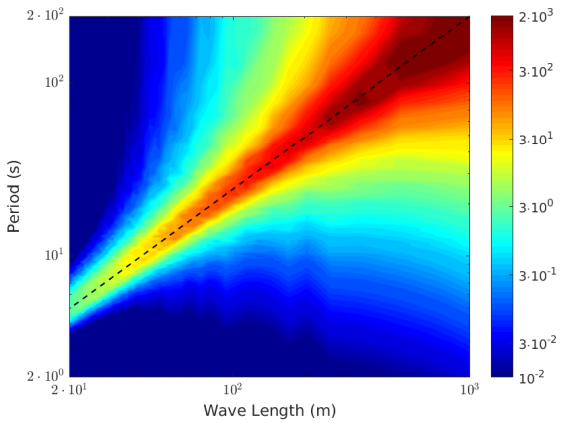

(a) Case 00: No filter

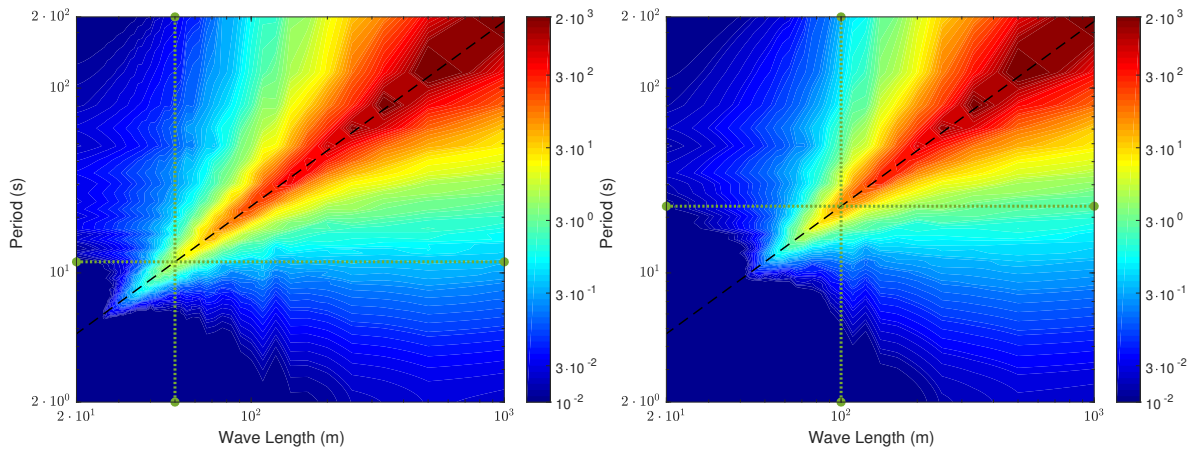

(b) Case 01: $L_\gamma = 25$ m (c) Case 02: $L_\gamma = 50$ m

Figure IV.3.4: Wave-number-angular-frequency 2D turbulent spectra, for the flat bottom numerical experiment evaluating the sLiDAR filter effect. The mean wind velocity corresponding to the Taylor hypothesis appears in black dashed line. In Cases 01 and 02 the green dotted lines denote the characteristic filter scales L_γ and $T_{\gamma 0}$.

IV.3.3.3 Overview and discussion

A numerical model of the sLiDAR filter is established to evaluate it's impact on the original analyses presented in section II.3, and particularly the filter behavior in the joint Space-Time distribution of turbulent correlations. Even though the sLiDAR's filter is originally presented

in space, the flow dependency is such that the turbulent fluctuations are like-wise filtered in time and space domains. In this flat Case scenario the Taylor's hypothesis is observed to hold, and correctly describes the filter scaling in k and w domains with respect to the mean RWS velocity u_1.

IV.3.4 Numerical experiment in the wavy bottom ABL

IV.3.4.1 Specific numerical strategy

The numerical case here exploited has already been introduced as Case 03 (Irregular 2D Sea-State) in section III.4.1, that one shall consult for the detailed description about the numerical strategy. The dynamic pressure gradient method developed in section III.2 is used to keep the Wind Speed close to u_{ref} =4.12 m/s at the sLiDAR measurement height $h = 18.33$ m. The nominal friction velocity is $u_0^* = 0.147$ m/s, and the natural period of the pressure gradient response is $T_{\mathscr{P}} = 285\ T_0$.

The characteristic length scaling the domain is $L_0 = 256$ m, which doubles the nominal wave length $\lambda = 128$ m. The boundary layer height ($\delta = L_z$) to wave length ratio is $\delta/\lambda = 10$, and the longitudinal and transversal domain extensions to wave length ratio are respectively $L_x/\lambda = 8$ and $L_y/\lambda = 4$. The turbulent characteristic time scale is $T_0 = \lambda/u_0^* = 14.51$ min, which gives 86 peak periods T_p per turbulent time scale. The nominal $\mathrm{WA}_0 = c_p/u_0^*$ is 85.47.

Results are presented for grid 03 (Fine [512 x 256 x 94] from table III.1.1). The next remarks are specific to current application, so contrasting to section III.4.1 that provides in Case 03 (Irregular 2D Sea-State) the initial conditions to current computations.

To exploit the turbulent spectra, short computations are performed with fixed time-step $\Delta t = 0.122$ s ensuring CFL< 0.5, with Δt approximating 1/8 of the sLiDAR acquisition period 1 s (f-LOS 01 at table II.1.1).

A single computation (Irregular 2D Sea-State) is presented in three cases to evaluate the sLiDAR filter effect, as for the flat bottom experiment previously presented in section IV.3.3: (0) Case 00 is the reference, probing u_R at every time-step and in the numerical grid (512 Nodes over 1.28 km) along the line $[y = y_l/2, z = h]$; (1) Case 01 considers the filter adopted in the experimental campaign with $L_f = 25$ m; and (2) Case 02 doubles the filter width of Case 01 with $L_f = 50$ m. For Case 01 and Case 02, $\tilde{u}_R(x,t)$ is probed at the measurement line (101 Gates over 1 km) and averaged over 8 time steps ($8\Delta t = 0.98$ s). The spectra of Case 00 are truncated to be presented in the same k, f, and $k-w$ domains as Case 01 and Case 02.

IV.3.4.2 The sLiDAR filtering effect in the WBL

The 1D wave-number and frequency dependent energy density functions (EDF or Turbulent spectra) are shown in figure IV.3.5, superposing Cases 00 in blue full line, Case 01 in red dashed line, and Case 02 in green dash-dotted line. The spatial filtering characteristic wave-number $k_\gamma = 2\pi/(2\ L_\gamma)$ and its frequency equivalent $f_{\gamma 0} = U/(2\ L_\gamma)$ are denoted by the vertical lines in the same figure, with line types and colors equal to the correspondent (Case 01

or Case 02) spectra. The ESDU 85020 reference spectra described in section III.1.2.3 appear in black dashed lines in figure IV.3.5, with its parameters obtained for Case 00. All spectra are normalized by the (Space or Time averaged) auto-correlations obtained for the reference Case 00: $\left[\overline{u'_R u'_R}\right]_0$.

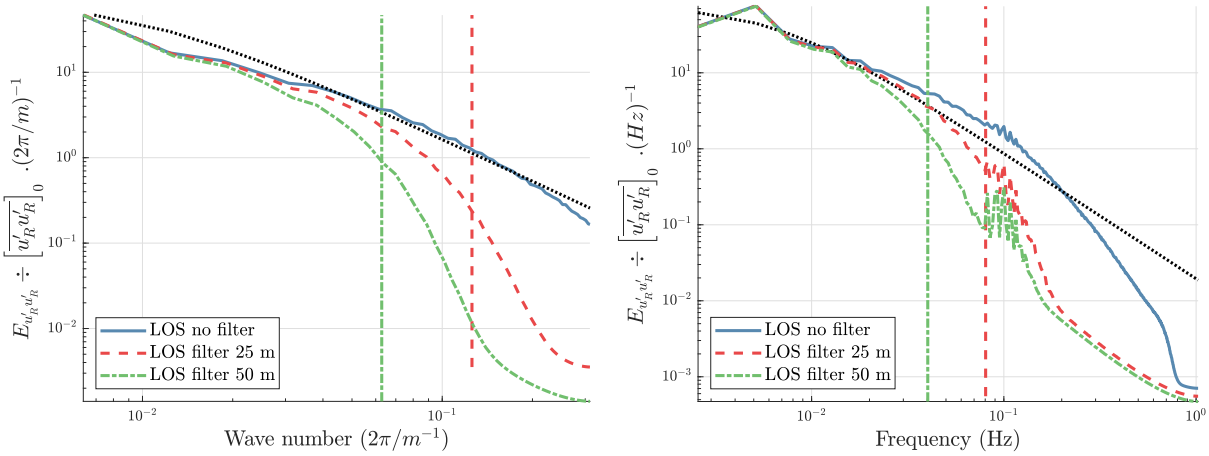

(a) Wave-Number 1D spectra.

(b) Frequency 1D spectra.

Figure IV.3.5: Wavy bottom numerical experiment evaluating the sLiDAR filter effect. One dimensional turbulent spectra as: Case 00 (No filter) in blue full lines; Case 01 (L_γ = 25 m) in red dashed lines; Case 02 (L_γ = 50 m) in green dot-dashed lines. The filter characteristic scales k_γ and $f_{\gamma 0}$ appear in the vertical lines, with types and colors corresponding to their Case spectra. Everything normalizes by the auto-correlation $\overline{u'_R u'_R}|_0$ obtained for Case 00. The ESDU reference appears in black dashed lines with its parameters obtained for Case 00.

As for the physical experiment presented in section II.3, the wave disturbances are only detectable in the frequency dependent 1D spectra (Fig. IV.3.5a), and not in the wave-number-dependent spectra (Fig. IV.3.5b) that closely resemble those presented in flat bottom scenarios and discussed in figure IV.3.3a. The filter effect is significant in smaller scales including the ones containing Wave Induced motions. Even if the filter diminishes both Wave Induced motions and Atmospheric turbulence indistinctly, as it becomes more effective the Wave signature becomes prominent in Case 02 compared to 01, and Case 01 compared to 00. In the cases addressed, the waves are faster than the wind. So at a given period (say $1/f_{\gamma 0}$), WI motions have lengths larger than the atmospheric turbulence (L_γ), and are thus less affected by the filter (at L_γ).

The 2D wave-number-frequency dependent turbulent spectra are shown in figure IV.3.6. The mean RWS (Taylor hypothesis) stands in full green lines and the waves' velocity (Dispersion relation) in red dashed lines together with the 2D turbulent spectra. For Cases 01 and 02 one observes the filter scales in dotted lines: Twice the filter length 2 L_γ in yellow; the filter period correspondent to Atmospheric turbulence and Wave Induced motions ($T_{\gamma 0}$ and $T_{\gamma 1}$), respectively in green and red.

Analogous to section IV.2.3.1, the filter frequency $1/T_{\gamma 1}$ corresponding to WI motions is defined as $f_{\gamma 1} = c/(2\ L_\gamma)$, but here one observes the k dependency of $f_{\gamma 1}(k)$, since $c(k) = \sqrt{(g/k)\tanh(kd)}$. A discussion on the significance of such definition of a wave-number

dependent characteristic frequency might be appreciated in the Appendix C.1, and its determination exemplified in figure C.1.

The filter acts in the atmospheric turbulence as described in section IV.3.3, and is particularly effective below 2 $L_{\gamma 0}$ and 2 $T_{\gamma 0}$. The flow dependency of the filter effect becomes clear in figures IV.3.6b and IV.3.6c, where the period $T_{\gamma 1}$ below which it becomes effective in the WI motions is considerably lower than $T_{\gamma 0}$. Contrary to the atmospheric turbulence, Wave Induced motions are hidden from the filter effect between $T_{\gamma 1}$ and $T_{\gamma 0}$, and thus comparatively magnified in the frequency spectra of numerical and physical experiments, given respectively in figures IV.3.5b and II.3.2b.

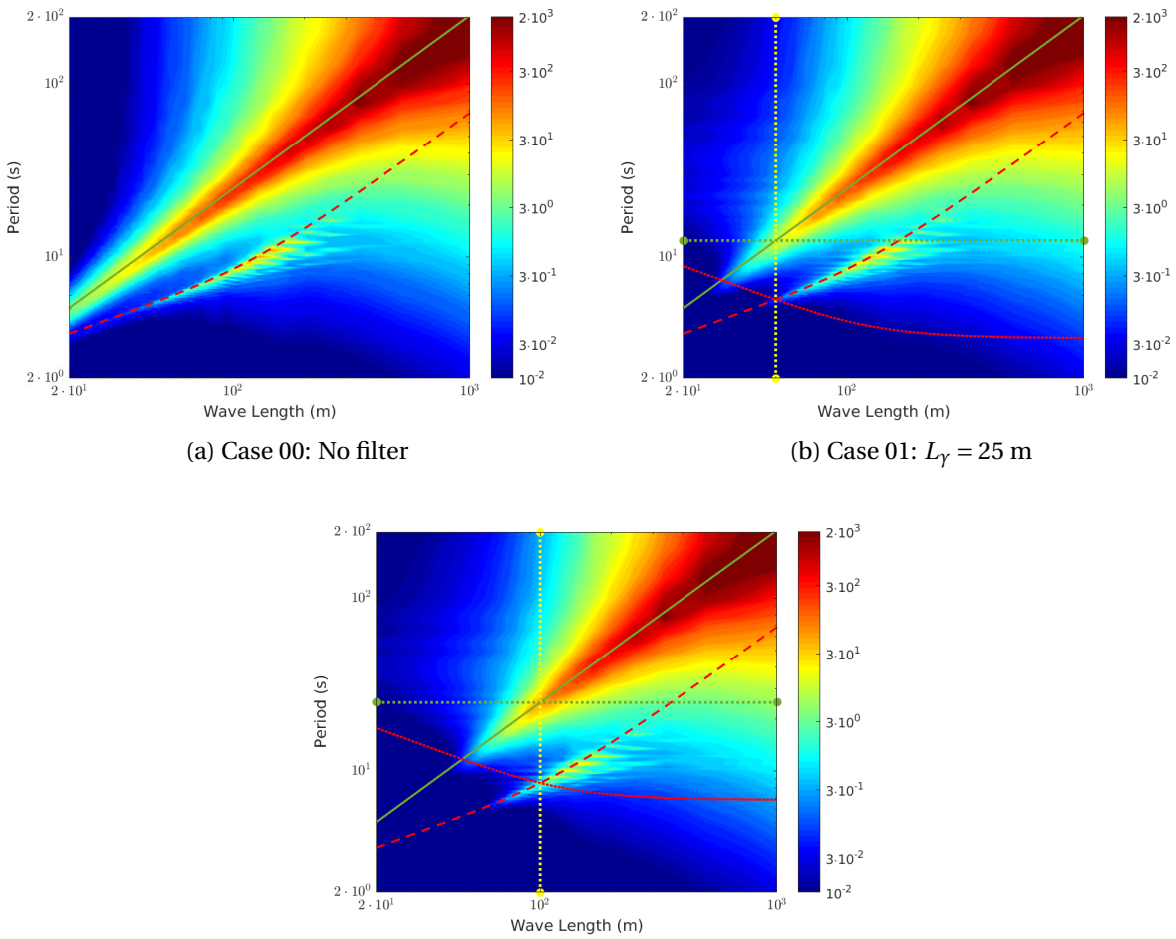

(a) Case 00: No filter

(b) Case 01: $L_\gamma = 25$ m

(c) Case 02: $L_\gamma = 50$ m

Figure IV.3.6: Wave-number-angular-frequency 2D turbulent spectra, for the wavy bottom numerical experiment evaluating the sLiDAR filter effect. The mean wind velocity corresponding to the Taylor hypothesis appears in green full lines, and the waves velocities given by the intermediate water dispersion equation appears in red dashed lines. In Cases 01 and 02 the dotted lines denote the characteristic filter scales: L_γ in yellow, $T_{\gamma 0}$ corresponding to Taylor hypothesis in green, $T_{\gamma 1}$ corresponding to the dispersion equation in red.

The decomposition technique developed in section IV.2 is employed to the 2D spectra of figure IV.3.6, leading to the Atmospheric turbulence (Atm.) and Wave Induced (WI) parts, shown respectively at figures IV.3.7 and IV.3.8. Again, the filter scales 2 L_γ, 2 $T_{\gamma 0}$ and 2 $T_{\gamma 1}$ are depicted respectively as yellow, green and red dotted lines in the figures. The Atm. part closely resembles the flat case spectra previously shown in figure IV.3.4, which attests the faithful reproduction of the Atmospheric turbulence, meaning the filter effect in atmospheric turbulence still applies as evaluated in section IV.3.3.

Present section evaluates the filter effect in the WI part revealed in figure IV.3.8. At Case 01 employing $L_\gamma = 25\ m$ such as in the physical experiment, it seems most of the WI motion is protected from the filter effect at scales larger than the filter period 2 $T_{\gamma 1}$. At Case 02 employing $L_\gamma = 50\ m$, the filter period 2 $T_{\gamma 1}$ gets comparable to the waves predominant periods, and the filter becomes more significant in the WI flow.

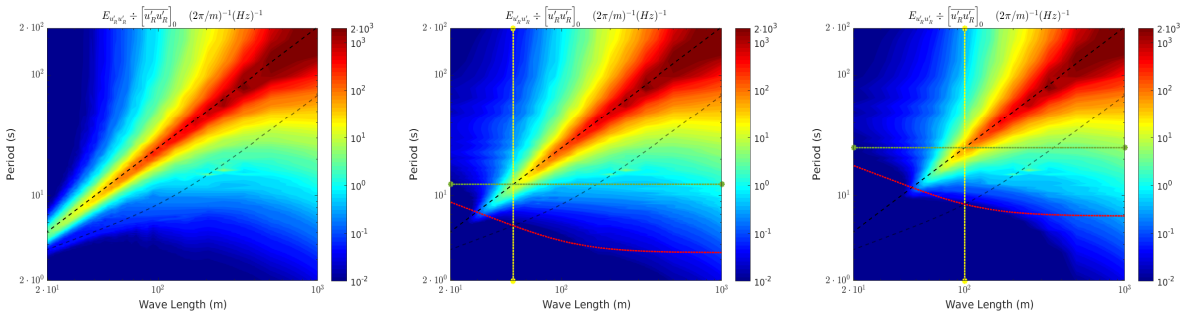

(a) Case 00: No filter (b) Case 01: $L_\gamma = 25$ m (c) Case 02: $L_\gamma = 50$ m

Figure IV.3.7: Wave-number-frequency 2D turbulent spectra for the decomposed Atmospheric Turbulence part. Wavy bottom numerical experiment evaluating the sLiDAR filter effect. The mean wind and the waves velocities appear in black dashed lines. Again, the dotted lines denote the characteristic filter scales: L_γ in yellow, $T_{\gamma 0}$ in green, $T_{\gamma 1}$ in red.

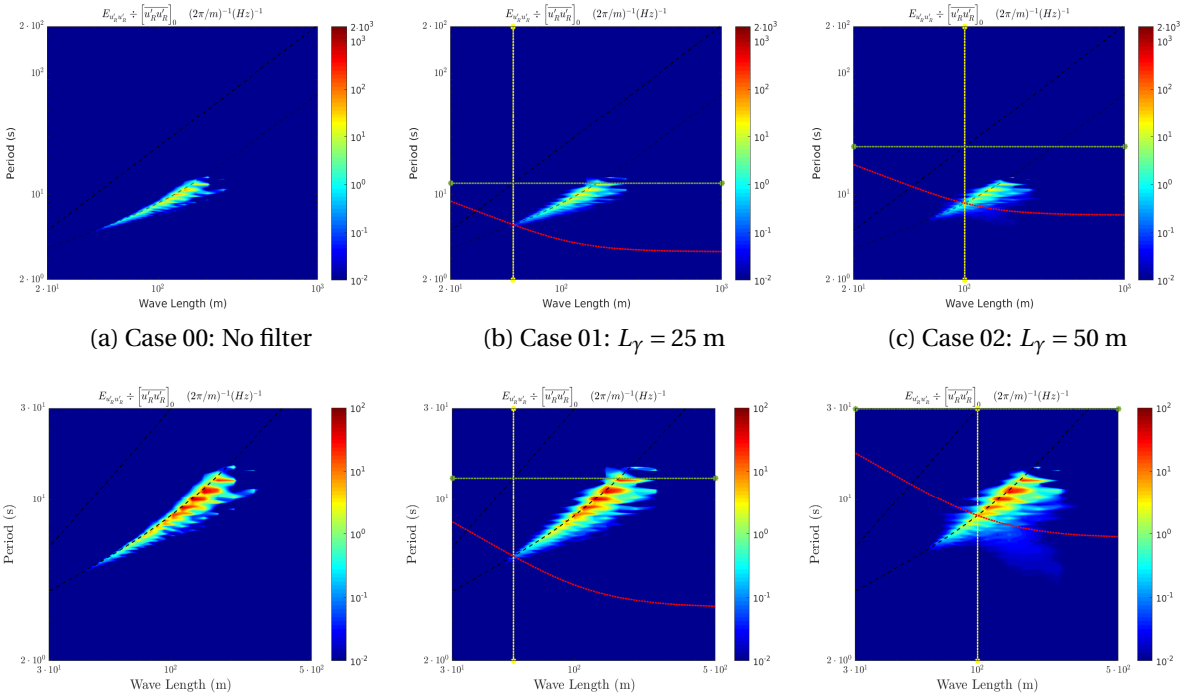

(a) Case 00: No filter (b) Case 01: $L_\gamma = 25$ m (c) Case 02: $L_\gamma = 50$ m

(d) Case 00: No filter; Zoomed. (e) Case 01: $L_\gamma = 25$ m; Zoomed. (f) Case 02: $L_\gamma = 50$ m; Zoomed.

Figure IV.3.8: Wave-number-frequency 2D turbulent spectra for the decomposed Wave Induced part. Wavy bottom numerical experiment evaluating the sLiDAR filter effect. Same scales as usual in (a,b,c); Scales adjusted to highlight the comparison in (d,e,f). The mean wind and the waves velocities appear in black dashed lines. Again, the dotted lines denote the characteristic filter scales: L_γ in yellow, $T_{\gamma 0}$ in green, $T_{\gamma 1}$ in red.

As discussed in section IV.2.2.1 (Fig. IV.2.6), the WI decomposition is sensitive to small values of the WI fraction $\mathscr{F}(k, w)$, i.e., the squared root of the ratio between the WI motions and the total fluctuations energy at a given (k, w) scale. It will be soon shown that, filtering preferably the Atm. rather than WI motions, the WI fraction is artificially magnified by the sLiDAR filtering, so that it acts somehow favorably to the proposed decomposition. As consequence, the WI flow definition extends wider in the spectral domain, meaning the region over which it is defined enlarges perpendicularly to the dispersion relation at figure IV.3.8: In Case 02 compared to 01, and Case 01 compared to Case 00.

The integration of the decomposed 2D spectra leads to the 1D wave-number and frequency spectra, respectively shown in figures IV.3.9 and IV.3.10, where the total energy appears in dotted black line, the Atm. part in blue dashed line, and the WI part in red dashed line. The ESDU reference appears in the figures as dashed black lines.

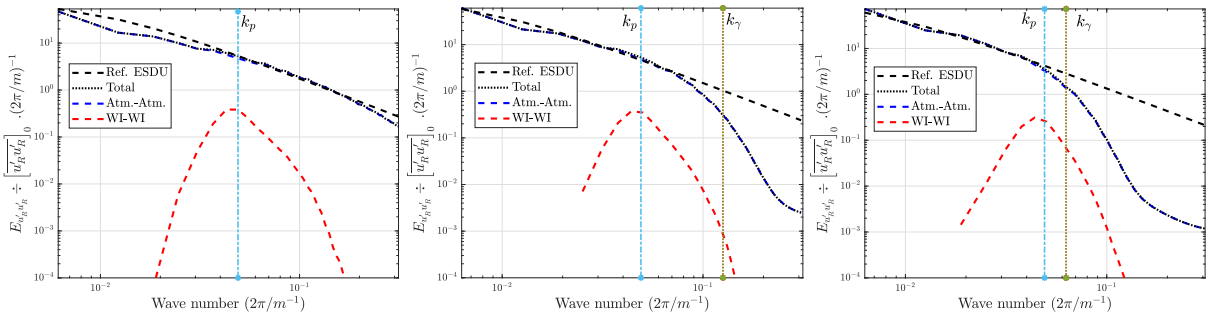

(a) Case 00: No filter (b) Case 01: $L_\gamma = 25$ m (c) Case 02: $L_\gamma = 50$ m

Figure IV.3.9: Wave-number dependent 1D spectra, decomposed into Atm. turbulence and WI flow. To be compared to the ESDU reference. Wavy bottom numerical experiment evaluating the sLiDAR filter effect. The vertical dotted light blue lines stand for the wave peak wave-number, and the green for the wave-number filter scale k_γ. The ESDU reference appears in the dashed black lines.

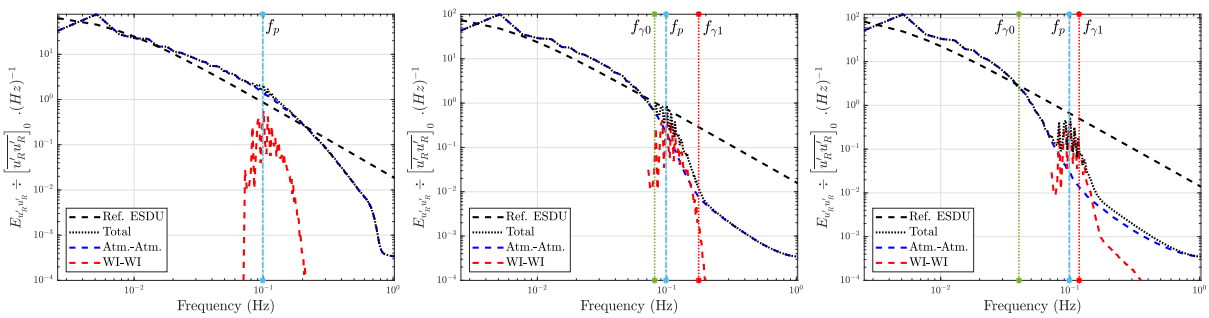

(a) Case 00: No filter (b) Case 01: $L_\gamma = 25$ m (c) Case 02: $L_\gamma = 50$ m

Figure IV.3.10: Frequency dependent 1D spectra, decomposed into Atm. turbulence and WI flow. To be compared to the ESDU reference. Wavy bottom numerical experiment evaluating the sLiDAR filter effect. The vertical dotted light blue lines stand for the wave peak frequency. The vertical green and red lines stand for the filter frequencies $f_{\gamma 0}$ and $f_{\gamma 1}$, respectively.

As discussed in section IV.3.3, the filter strongly affects the Atm. part, but its effect is mitigated in the Wave Induced 1D spectra. In the wave-number spectra of figure IV.3.9, independently of the filter length, the WI contribution remains hidden beneath the prevailing Atm. part. In the frequency spectra of figure IV.3.10 though, the different filtering appreciated by WI and Atm. motions becomes clear, with the WI part mostly preserved, thus emerging from beneath the Atm. part that is strongly mitigated by the filtering effect.

Note that in the non-filtered signal at figures IV.3.9a and IV.3.10a, the WI part does not follow the slope of the total or Atm. parts, but once the filter becomes significant at figures IV.3.9(b-c) and IV.3.10(b-c) they do present similar slopes: Probably a mere but striking coincidence that the filter imposed slope is very close to the WI spectra slope.

Table IV.3.2 summarizes the energy distribution per decomposed parts (Total, Atm., WI, and Atm-WI correlated) and test cases. In the table, the cross-correlation energy $2E_{\tilde{u}_1\hat{u}_1}$

(the Atm-WI correlated part) is also evaluated, though it is often neglected in the other discussions through this section. Case 00 is the reference, characterized by $\overline{u}_h$ = 4.0 m/s and TI=6.7%, for which the table shows: 1.09% of the total fluctuation energy is held by WI motions, and 0.36% by the correlations between Atm. and WI parts; so the cross-correlations contain 33% of the energy contained by the WI flow alone, and are apparently not negligible.

Then taking 1 minus the ratio from Case 01 and Case 02 to Case 00, table IV.3.2 shows the amount of energy filtered from each of the total or decomposed parts: With L_γ = 25 m, 24% and 34% of the energy from Atm. and WI parts is respectively lost; and with L_γ = 50 m the amount rises to 37% and 60%, respectively. It was previously noted that if compared to Atm. turbulence occurring in the same wave lengths or periods, the filter effect is mitigated at the WI flow, and that ultimately leads to the pronounced enhancement of WI motions in the 1D frequency spectra. This is true, but it is here demonstrated that WI motions are also significantly filtered by the sLiDAR.

Table IV.3.2: Energy distribution and filtering deficit per Case. In Case 00 the total energy (Giving TI = 6.7% with U = 4.0 m/s) is distributed into Atm. turbulence ($E_{\hat{u}_1\hat{u}_1}$), WI motions ($E_{\tilde{u}_1\tilde{u}_1}$), and Atm-WI cross-correlations ($2E_{\tilde{u}_1\hat{u}_1}$). For Cases 01 and 02 it is shown the energy deficit with respect to Case 00, for each spectral contribution.

	Total	Atmospheric Turbulence	Wave Induced	Atm.-WI Correlated
Case 00÷$\overline{u_i'u_i'}\|_0$	100.00%	98.47%	1.09%	0.36%
1-[Case 01÷Case 00 Energy ratio]	24%	24%	34%	20%
1-[Case 02÷Case 00 Energy ratio]	38%	37%	60%	62%

The WI part of the 1D spectra is highlighted in figure IV.3.11, where Case 00 (No filter) appears in blue full line, Case 01 (L_γ = 25 m) in red dashed line and Case 02 (L_γ = 50 m) in green dashed-dot line. The forcing sea-state spectra $F(k)$ and $F(f)$ are drawn at the figure with black dotted lines and circles. The wave peak wave-number or frequency is depicted with the vertical black line, and the filter scales k_γ, $f_{\gamma 1}$ by the vertical dotted lines with colors corresponding to their Case.

Like for the Atm. turbulence, the filter invariably induces the mitigation of WI motions across the whole range of scales, but it is strongly magnified for $k > k_\gamma$ and $f > f_{\gamma 1}$. Unlike the Atm. turbulence, the WI part is smoothly filtered: There is a very small change of slopes between the WI wave-number spectra shown in figure IV.3.11a, and an even smaller one between the frequency spectra of figure IV.3.11b, which is another indication that the sLiDAR filter imposes a slope to the spectra that coincidentally approaches the slope of the WI spectra.

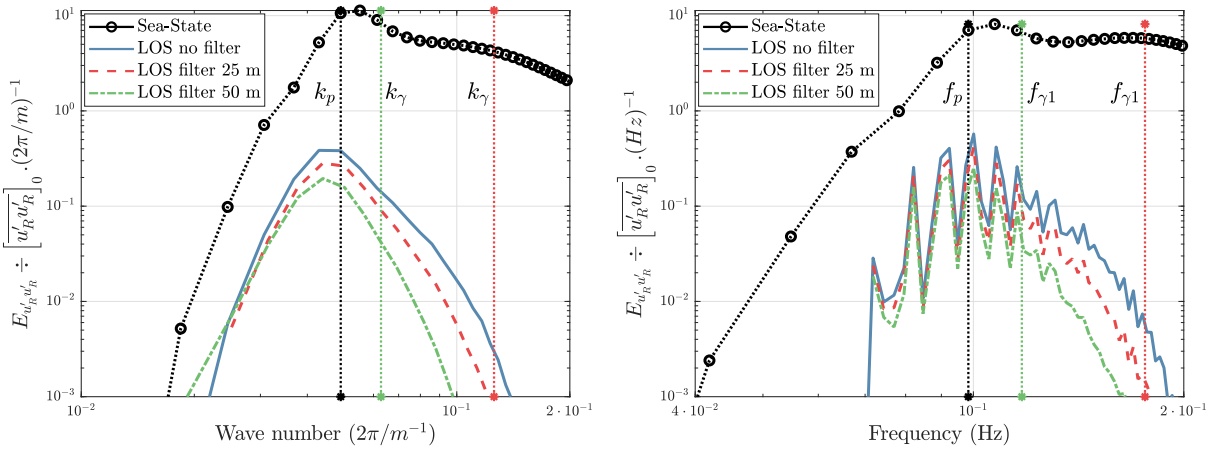

(a) Wave-Number 1D spectra

(b) Frequency 1D spectra

Figure IV.3.11: Sea-State forcing and the atmospheric response, for the wavy bottom numerical experiments evaluating the sLiDAR filter effect. Sea-State forcing (F) in black dotted lines and circles: Auto-spectra of the longitudinal orbital velocities on the free-surface (FS). Atmospheric response ($E_{\tilde{u}_R\tilde{u}_R}$): Auto-spectra of the WI flow, as previously shown at figures IV.3.9 and IV.3.10. The vertical lines colored accordingly to each spectra denote the filter characteristic scales k_γ, $f_{\gamma 1}$. The vertical black line denote the wave peak scales k_p and f_p.

The ratio between the WI and total fluctuation spectra of figures IV.3.9 and IV.3.10, gives the squared of the wave-number and frequency dependent WI fractions, i.e., $\mathscr{F}(k)$ and $\mathscr{F}(f)$, respectively shown in figures IV.3.12a and IV.3.12b. The flow dependency of the sLiDAR effect is evident, leading to the artificial enhancement of the WI fraction as the filter acts more significantly in the Atm. turbulence. In the wave-number spectra of figure IV.3.12a, the different filtering of Atm. and WI motions appears significant only in Case 02 ($L_\gamma = 50$ m), for which the WI fraction is artificially augmented at $k > k_\gamma$. In the frequency spectra of figure IV.3.12b, the disturbance appears as soon as in Case 01 where $L_\gamma = 25$ m, and the WI fraction is so magnified by a factor of ~2, thus becoming the predominant contribution to the 1D spectra of figure IV.3.5b when $\mathscr{F}(f) > 0.5$.

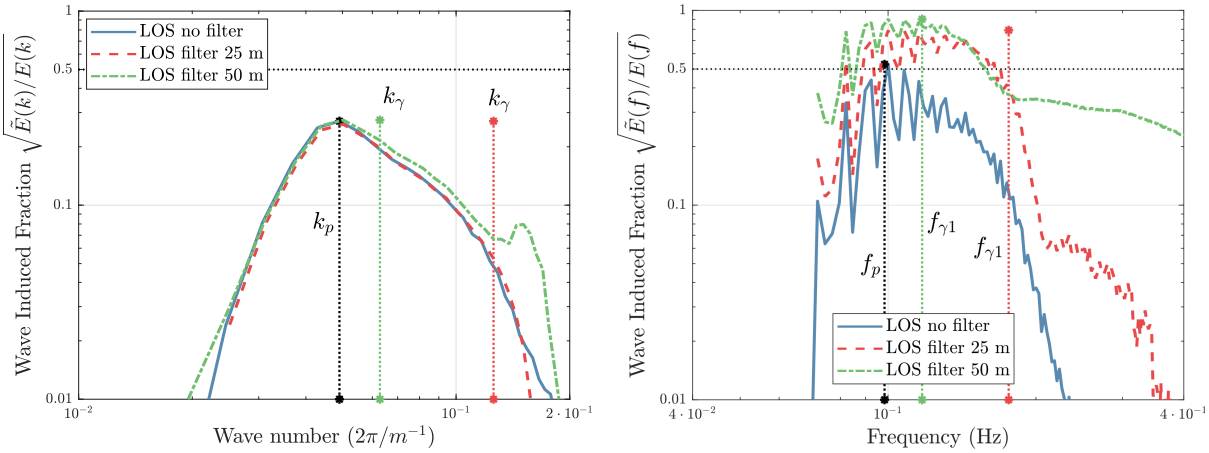

(a) Wave-Number dependent $\mathscr{F}(k)$ (b) Frequency dependent $\mathscr{F}(f)$

Figure IV.3.12: Wave Induced fraction $\mathscr{F}(k)$ and $\mathscr{F}(f)$, for the wavy bottom numerical experiments evaluating the sLiDAR filter effect. The vertical lines colored accordingly to each spectra denote the filter characteristic scales k_γ, $f_{\gamma 1}$. The vertical black line denote the wave peak scales k_p and f_p.

IV.3.4.4 Overview and discussion

In the absence of other instruments capable of evaluating the sLiDAR filtering effect in the results of section II.3, and without any previous measurements of the 2D spectra reported in the literature at similar scales and at the offshore environment, present section gathers multiple developments presented during this thesis to numerically evaluate the sLiDAR filtering effect in the results obtained during the experimental campaign. For instance: The numerical setup is established in section III.4; the reconstruction of the sea-state spectra observed during the experimental campaign is described in section IV.3.1; and a numerical sLiDAR model is introduced to the numerical framework according to section IV.3.3, that also describes the filtering effect in the flat bottom cases.

The decomposition proposed in section IV.2 enables the separated evaluation of the sLiDAR filter acting in Atm. and WI motions. The decomposition recovers the Atm. turbulent part as observed in flat bottom cases, for which the discussion in section IV.3.3 still applies. Present section instead, focuses on the sLiDAR filter effects to the WI part.

Contrary to section IV.3.3, where the filtering effect scales simply with the mean wind velocity, the WI disturbances in 1D and 2D turbulent spectra reveal the strong flow dependency of the sLiDAR filtering effect. The filter length scale is constant, but the corresponding filter period scales differently for Atm. and WI motions, according to the Taylor hypothesis for the former and the wave dispersion relation for the second.

As in the experimental campaign, at any case the WI disturbances remain hidden in the 1D wave-number dependent turbulent spectra, and appear only in the 1D frequency dependent, and specially in the 2D $k-w$ dependent turbulent spectra. The filter effect is notable in the 1D frequency spectra, and at a given frequency the filter acts preferably in Atm. rather than WI motions. So as the filter becomes more important, the WI flow is relatively magnified in the 1D frequency spectra.

IV.3.5 Comparison between physical and numerical experiments

The presented test cases and methodologies allow a very detailed comparison between physical and numerical experiments rarely observed in the literature. The numerical Cases 00.Num (No filter) and 01.Num (L_γ = 25 m) just discussed in section IV.3.4.3 are here compared to the physical experiment Case 01.Phys, previously presented in section II.3 and exploited in section IV.2.3. The triple decomposition developed in section IV.2 has already been applied to each case, but for the sake of completeness, Atm. and WI parts of the 2D spectra are repeated respectively in figures IV.3.13 and IV.3.14. At these figures, Cases 01.Num (L_γ = 25 m) and 00.Phys appear respectively in subfigures (a) and (b).

As noted before in section II.3, the Atm. turbulence appears in the physical experiment of Case 01.Phys (figure IV.3.13b) with an unexpected shape that contradicts the one expected on a simple shear flow, i.e., the one observed in the numerical experiment of figure IV.3.13a, and in the experimental campaign at other instants such as Case 02.c (Figure II.3.8b). The atypical shape of the 2D spectra in the physical experiment is believed to be due to buoyancy forces. These forces are neglected in the numerical model, and so the Atm. turbulence cannot be properly evaluated by the current numerical setup.

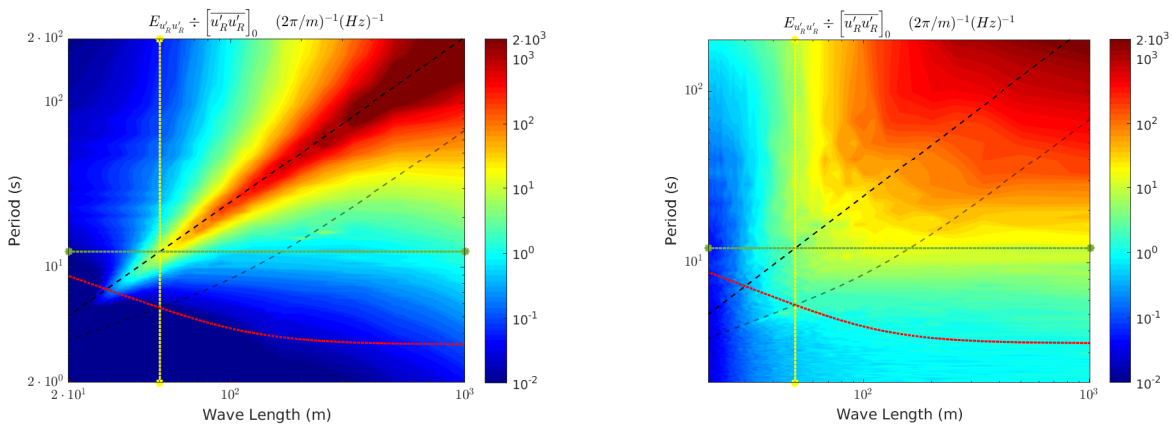

(a) Numerical Case 01.Num

(b) Numerical Case 01.Phys

Figure IV.3.13: Wave-number-frequency 2D turbulent spectra for the decomposed Atmospheric Turbulence part. Comparison between physical and numerical experiments. The mean wind and the waves velocities appear in black dashed lines. The dotted lines denote the characteristic filter scales: L_γ in yellow, $T_{\gamma 0}$ in green, $T_{\gamma 1}$ in red.

There is also considerable uncertainty regarding the sea-state modelling in WaveWatch III, and introduced by sea-state reconstruction at section IV.3.1. Even though the uncertainties regarding the sea-state and the error assumed in the background turbulence are significant, it is yet worth to compare the WI motions revealed in figures IV.3.14a and IV.3.14b, for the numerical Case 01.Num and experimental Case 01.Phys, respectively.

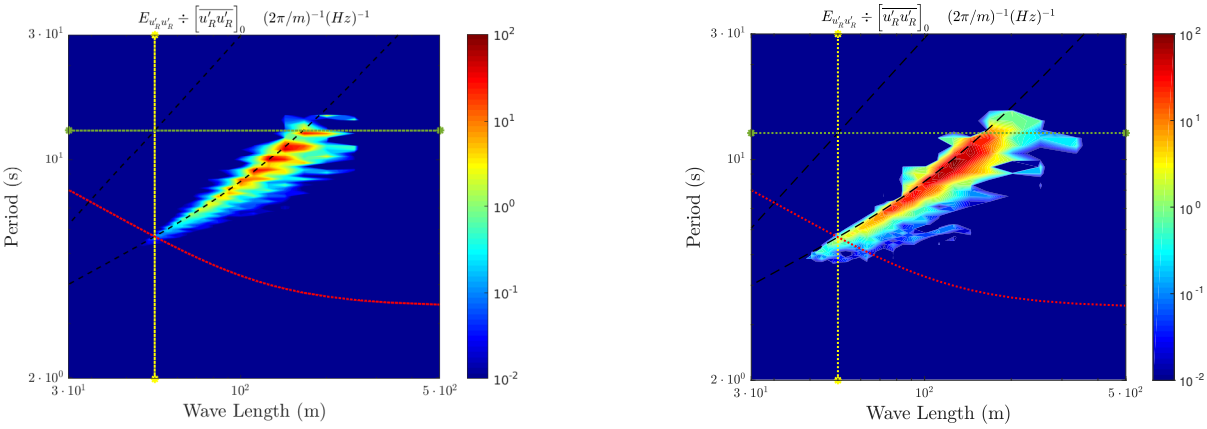

(a) Numerical Case 01.Num

(b) Numerical Case 01.Phys

Figure IV.3.14: Wave-number-frequency 2D turbulent spectra for the decomposed Wave Induced part. Comparison between physical and numerical experiments. The mean wind and the waves velocities appear in black dashed lines. The dotted lines denote the characteristic filter scales: L_γ in yellow, $T_{\gamma 0}$ in green, $T_{\gamma 1}$ in red.

As usual, the integration of the WI 2D spectra leads to the k and f 1D spectra of figure IV.3.15, where: Case 00.Num given in blue full lines; Case 01.Num in red dashed lines; and Case01.Phys in golden dot-dashed lines; are to be compared to the free-surface EDF of longitudinal velocities, given in dotted black lines and circles.

The spectra are normalized in figures IV.3.15a and IV.3.15b by the integral corresponding to the total fluctuation energy of Case00.Num. Note that the forcing spectra is exact for the numerical cases, but just an estimation for the experimental case. Besides, the forcing $F(k_x, k_y)$ is discretized in the numerical wave-number domain, for which there is a one-to-one correspondence to the frequency domain that does not necessarily covers the whole range of frequencies resolved: As a consequence, the numerical WI frequency spectra present strong oscillations at larger scales, being magnified in the frequencies where $F(k_x, k_y)$ is defined, and mitigated in between.

The WI spectra are also considerably lower in the numerical reproduction, but when one evaluates the spectral shape with the spectra normalized by their own energy, such as remarked in figures IV.3.15c and IV.3.15d, there is an astonishing similarity between the numerical and physical experiments. The slopes drawn in the figures are just an approximation to the observations, closely followed by each test case below the wave peak scales k_p and f_p, and above the filter scales k_γ and $f_{\gamma 0}$.

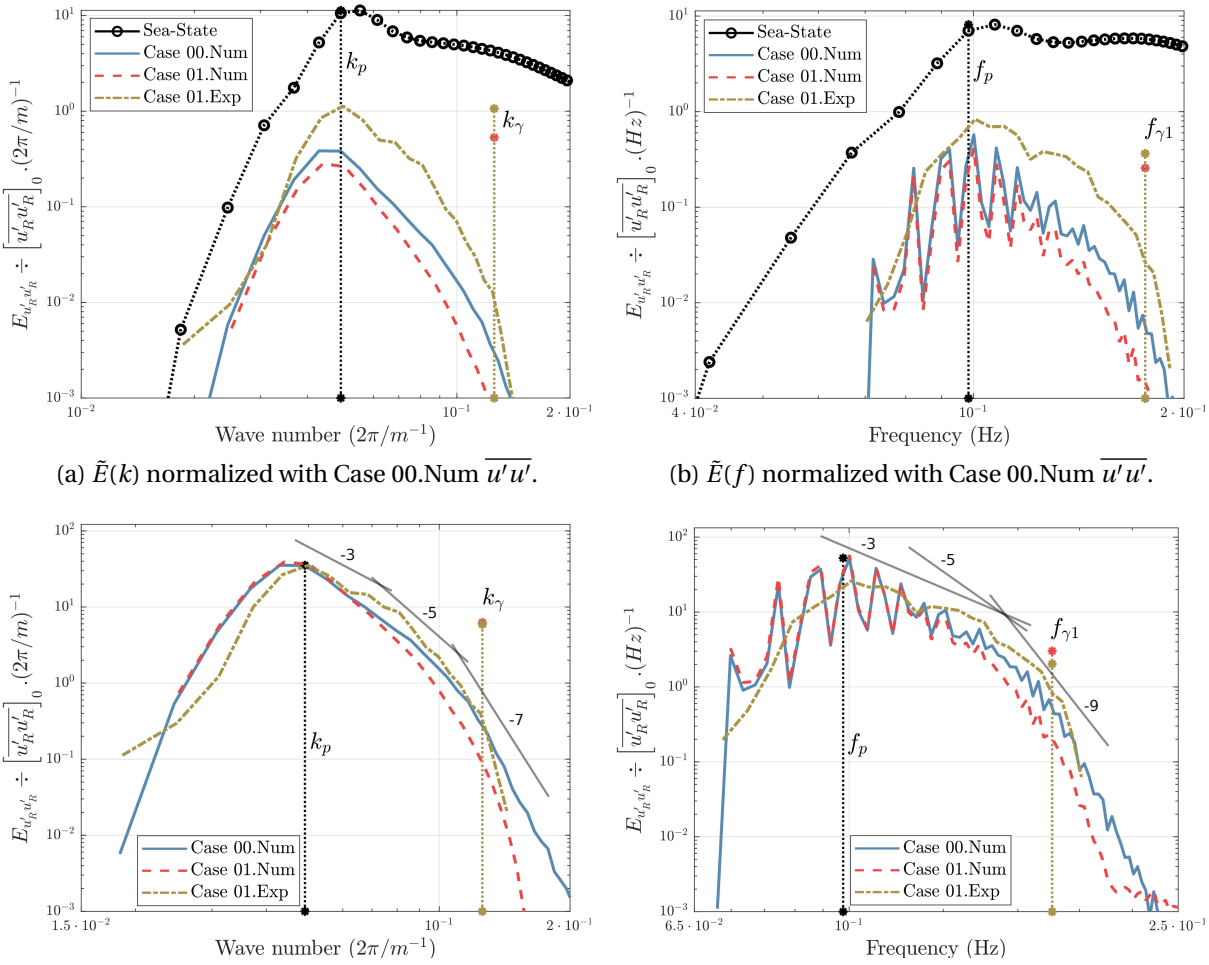

(a) $\tilde{E}(k)$ normalized with Case 00.Num $\overline{u'u'}$.

(b) $\tilde{E}(f)$ normalized with Case 00.Num $\overline{u'u'}$.

(c) $\tilde{E}(k)$ normalized with each case $\overline{\tilde{u}\tilde{u}}$.

(d) $\tilde{E}(f)$ normalized with each case $\overline{\tilde{u}\tilde{u}}$.

Figure IV.3.15: Wave Induced 1D spectra. Comparison between physical and numerical experiments: Case 00.Num in blue full lines; Case 01.Num in red dashed lines; Case 01.Phys in golden dot-dashed lines. The dotted vertical black lines stand for the wave peak scales k_p and f_p, and the other vertical lines for the filter characteristic scales k_γ and $f_{\gamma 1}$. The black dotted lines and circles denote the sea-state longitudinal velocity EDF $F(k)$ or $F(f)$. Above (a,b), the spectra are normalized by the total auto-correlation obtained in Case 00, and below (c,d) the normalization occurs with respect to the WI auto-correlation obtained for each case.

The WI fraction is obtained from the ratio between WI and total 1D spectral distributions, observed at each case as shown in figure IV.3.16. Considering the predominance of Atm. turbulence and its improper numerical evaluation demonstrated in figure IV.3.13, it was not expected a faithful reproduction of the WI fraction. Nevertheless, when the filter becomes important in the frequency spectra revealed by Case 01.Num and Case01.Phys, the WI fractions match quite accurately in figure IV.3.16b, suggesting that the filter effect is properly taken into account by the numerical model.

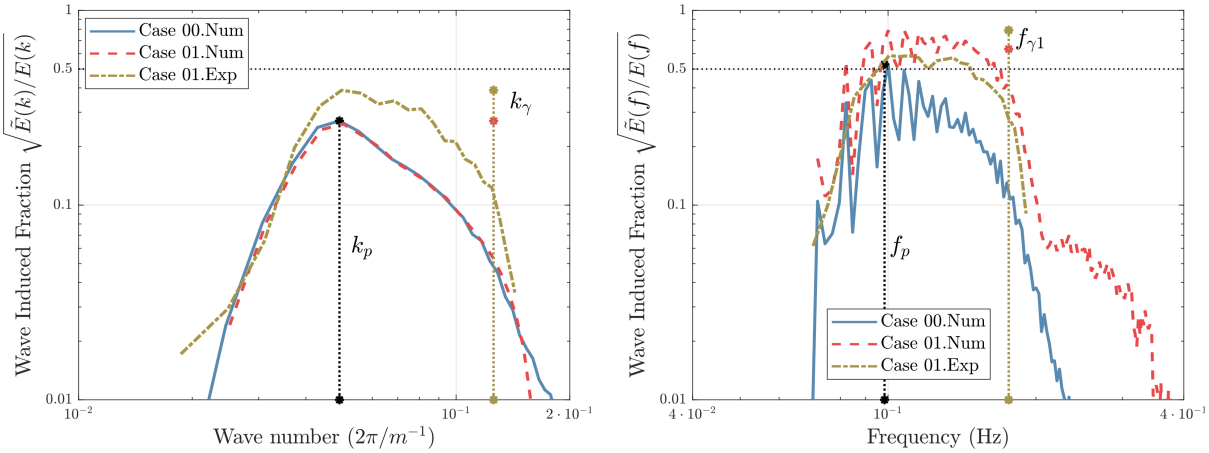

(a) Wave-Number dependent $\mathscr{F}(k)$ (b) Frequency dependent $\mathscr{F}(f)$

Figure IV.3.16: Wave Induced fraction, giving the relative intensity of WI in Total fluctuations. Comparison between physical and numerical experiments: Case 00.Num in blue full lines; Case 01.Num in red dashed lines; Case 01.Phys in golden dot-dashed lines. The vertical black lines correspond to the wave peak scales k_p and f_p, and the others to the filter characteristic scales k_γ and $f_{\gamma 1}$.

While the WI fraction inherit a numerical bias, assumed to be due to the neglected buoyancy effects in the numerical experiment, the transfer functions presented in figure IV.3.17 incorporate a bias regarding the sea-state spectra estimated at the experimental campaign, which is of course exact in the numerical cases. The transfer functions are presented in figures IV.3.17a and IV.3.17b, where the WI 1D spectra are normalized by the sea-state forcing spectra.

As for the WI spectra itself, the transfer functions have similar shapes but different magnitudes in the numerical and physical experiments. So in figures IV.3.17c and IV.3.17d the transfer functions appear normalized by its value in the peak wave-number/ frequency, and the similarities between the experiments is remarkable.

In figure IV.3.17c, the transfer functions in numerical and physical experiments reveal an inflection point occurring in the vicinity of the peak scale, separating two regions of approximately constant slopes that apparently converge between the cases. The inflection is stronger in the experimental case, so the two constant slope regions become further apart, and a local maximum appears below the peak scale, which is not observed in the numerical experiments. Again, the approximated slopes observed between the wave peak and sLiDAR filter scales is drawn in the figures to help the comparison.

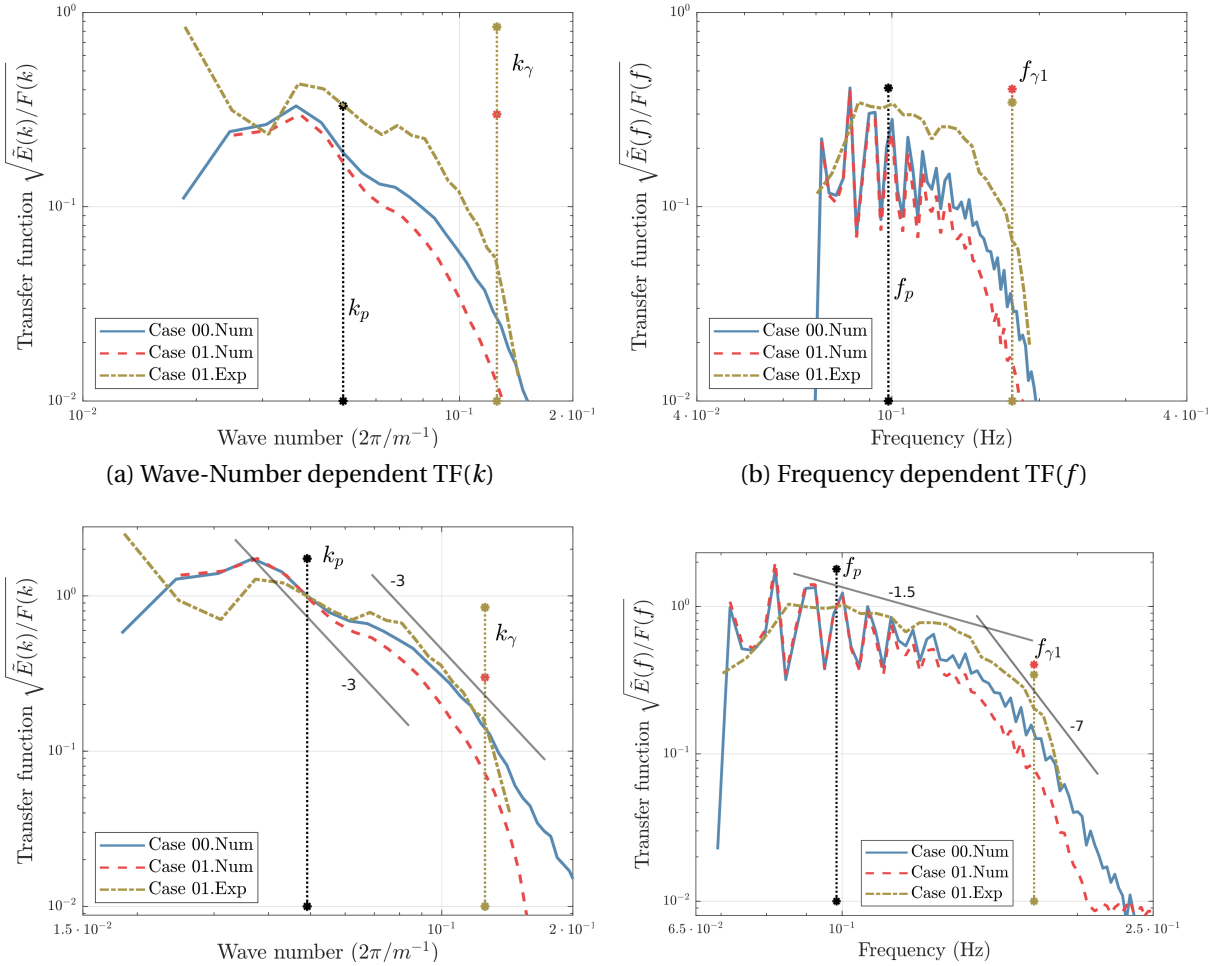

(a) Wave-Number dependent TF(k)

(b) Frequency dependent TF(f)

(c) Wave-Number dependent TF(k), normalized by the wave peak value

(d) Frequency dependent TF(f), normalized by the wave peak value

Figure IV.3.17: Transfer function, giving the ratio between the WI atmospheric response to the sea-state longitudinal velocity spectra. Comparison between physical and numerical experiments: Case 00.Num in blue full lines; Case 01.Num in red dashed lines; Case 01.Phys in golden dot-dashed lines. The vertical black lines correspond to the wave peak scales k_p and f_p, and the others to the filter characteristic scales k_γ and $f_{\gamma 1}$.

IV.3.5.1 Overview and discussion

Ultimately, the proposed framework allows the direct comparison between the physical and numerical experiments, in a level of detail rarely observed in the literature. The artificial enhancement of WI motions due to the sLiDAR filter is seemingly well described in the numerical case, as its employment leads to much accurate magnitude and shape of the 1D frequency-dependent WI fraction.

The uncertainties leading to such comparison are still significant, as for example: The boundary layer height is unknown in the physical experiment, so chosen arbitrary in its numerical reproduction; and the sea-state spectra has not been measured, but estimated during the experimental campaign. Besides and more critical, buoyancy forces are neglected in the numerical model, but are probably significant during the physical experiment, esti-

mated to be in a stable stratification regime. These buoyancy forces lead to very peculiar behaviors of the 2D spectral distribution of Atm. motions, so the physical and numerical experiments are characterized by drastically different Atm. turbulence spectral distributions.

The WI disturbances are significantly stronger in the physical experiment, probably due to the sea-state uncertainty between the cases, or the buoyancy effects neglected in the numerical model. Nevertheless, the comparison reveals remarkable similarities between the Wave Induced flow, observed in physical and numerical experiments.

Notably, each of the features revealed in the WI spectral distribution of the physical experiment as discussed in section IV.2.3, are reproduced in the numerical model. The WI spectra almost collapse between the cases when normalized by the case-specific total WI energy. Considering the same sea-state forcing at each test case, the same remarks apply to the transfer function: It is amplified in the physical experiment, but if normalized to the same value at the wave peak scales, their curves agree well in numerical and physical applications.

CONCLUSION

As proposed in the introduction, this Thesis reviews and extends the current knowledge regarding Wind-Wave interactions in the lower part of the Marine ABL (MABL), where they are indeed observed to be significant in the characterization of the wind resource. Thanks to the use of complementary physical and numerical experiments, new insights on the wind-wave interaction processes are obtained, revealing good part of the role of Wave Induced (WI) motions transferred from the sea into the atmosphere.

Overview and Main Findings

An overview of the most relevant aspects of discussion is presented below. Some of the findings are fully original, which is properly remarked during the text. Many of the findings support the results presented in the literature review of section I.3, but all consider a certain level of originality in the analyses.

Physical Experiment

The field experiment conducted during the Thesis' experimental campaign has been presented at part II. A scanning Light Detection and Ranging (LiDAR) system is deployed to observe the propagation of Wave Induced (WI) motions into the lower part of the Marine Atmospheric Boundary Layer (MABL), approximately 18 m above the ocean.

As remarked through the literature, WI disturbances are captured in the one-dimensional (1D) frequency dependent turbulent spectra, but not in the wave-number dependent spectra. It is only in the two-dimensional (2D) combined wave-number-angular-frequency ($k-w$) perspective, that the characterization of WI motions can be fully appreciated. This is a first to demonstrate the applicability of sLiDAR systems to measure $k-w$ dependent turbulent spectra in the Offshore Environment, and though the difficulties might still be significant, the LiDAR is currently the only measurement device capable to perform the task in the micro-scales of the WBL above the ocean.

The Space-Time spectral description of the velocity fluctuations provides an enhanced perspective of the Atmospheric (Atm.) and WI motions. Contrary to the 1D spectra, the upward turbulent energy transfer from the waves to the wind is evident and well distinguishable from the atmospheric turbulence in the 2D turbulent spectra. The 2D spectra reveal that Atm. and WI motions correlate differently (in terms of spectral coherence) in space and/or time domains, explaining the observations previously evaluated in the 1D spectra.

The 2D spectra are in fact so sensitive, that it shall be actually hard to find measurements without any WI disturbance during the measurement campaign (October 2020 to January 2021, waves season at Le Croisic, France). The reason of multiple failed attempts [Hristov,

2018] to detect WI disturbances in the frequency 1D turbulent spectra is its partial perspective of modal energy distribution.

Numerical Experiment

The numerical model exploited during the Thesis is presented at part III. The MABL is investigated employing the Large Eddy Simulation (LES) solver described in section III.1. The test cases presented are built to investigate the WI disturbances above fast traveling waves, propagating under comparatively slow wind conditions in a situation commonly described as *old seas*. Contrary to the physical experiment, where measurements are restricted to a certain height and to the Radial Wind Speed measurements, the numerical approach gives the detailed information of the overall flow behavior across the ABL and in highly controlled, simplified, neutral stratification conditions.

When fast traveling waves are introduced with lengths scales comparable to the ABL height, significant unsteady processes take place in the LES generated ABL. Notably the wave drags the wind, and if the large scale pressure gradient is kept constant, the free-stream velocity speeds-up, eventually dragging back the propagating wave. The flow history is extremely important determining the wind profile speed-up once the steady state regime is reached.

An original large scale pressure gradient modeler is proposed in section III.2, shown capable of achieving a target, averaged constant longitudinal velocity at a certain height in the ABL. With the large scale pressure gradient evolving in much larger times than turbulent fluctuations in the ABL, turbulence statistics are shown invariant to different values of the target velocity $\overline{u}_{ref}$ imposed in different flat bottom cases. The pressure gradient evolution scale can be adjusted in the natural frequency of the mass-spring-damper system modeler. One of the largest appeals of such methodology in the given context appears when it enables the arrival to a steady state regime with the same free-stream velocity imposed as the initial flat bottom condition.

The WI disturbances are investigated as function of varying Wave Age conditions in section III.3. The wind speed profile is observed to be dependent on the incident wave, so before considering the parametrization of WI disturbances, it is first discussed the definition of the WA parameter with respect to the friction or free-stream velocities. Thanks to the evolving pressure gradient method, the free-stream velocities are kept in a statistically steady regime. The friction velocity on the contrary, strongly deviates from its flat bottom solution. The WA characterizing the non-disturbed or free-stream flow is significantly more consistent to describe the observations. A simple exponential model then accurately fits to the non-dimensional form drag as function of the reference WA. When evaluating the turbulent profiles, this parametrization also provides a reasonable first order approximation to the approximately linear shear stresses observed across the boundary layer height.

The waves introduced disturb the wind speed profiles, and notably their behavior through the logarithmic region. Due to waves, the region of validity of the logarithmic wind profile considerably diminishes with increasing wave age, squeezed by the extended inner and buffer regions occurring below. Also the apparent friction velocity and roughness lengths that scales the wind profile in the logarithmic region are significantly disturbed by the waves.

The turbulence intensity profiles indicate higher turbulence levels at the lower part of the ABL, due to the existence of the WI fluctuations, but just above that region one observes in fact lower turbulence levels if compared to the flat bottom cases. Such behavior is explained by the TKE budget analyses. In increasing WA, turbulent production and dissipation diminish in the WBL. The reduction of production is accentuated compared to dissipation, so the waves lead to a strong lack of balance between production and dissipation, ultimately acting as a sink in the total TKE equations. The lack of balance between production and dissipation triggers the disturbance of turbulent transport terms, now bringing turbulent eddies from the outer region to the buffer region, contrary to the flat bottom case. The pressure transport term greatly surpasses the other terms of the TKE budget, and appears as the principal mechanism transferring the waves' orbital velocities to the air-flow.

Non-monochromatic waves are presented in section III.4, with the comparison between regular, 1D irregular, and 2D irregular sea-states. In the comparison of section III.4, the two-dimensional irregular sea-state corresponds to the conditions estimated during the experimental campaign, and the mean velocity at the measurement height also matches the one observed during the campaign. The sea-state energy being ~ 100 times smaller, many of the disturbances observed in the previous sections become negligible. Even in this numerical controlled scenario, these disturbances are so hard to catch that the comparison is often contaminated by turbulent uncertainties, and in the offshore environment most of the previous remarks would be undetectable face to the uncertainties of the measurement techniques, unsteadiness, and non-homogeneity effects [Hristov, 2018].

These test cases of section III.4 are revisited with spectral analyses in section IV.2. Contrary to the mean history, mean wind and turbulent profiles, and the 1D spectral analyses; and as argued in section IV.1: The Space-Time (Or $k-w$) perspective of turbulent fluctuations reveals detailed information about the WI flow structure, which favors the investigation of consequent WI disturbances and Wind-Wave interactions in the MABL, demonstrating intrinsic differences between the test cases discussed.

A MECHANISTIC APPROACH TO PHYSICAL AND NUMERICAL EXPERIMENTS

According to the discussion in the literature review, the recent developments in measuring and modelling techniques open the path to what Hristov and Ruiz-Plancarte [2014] describe as the mechanistic approach for obtaining wind-wave interaction observational insight: It consists in the direct estimation of WI velocities and pressure in the atmosphere, rather than the inference of WI disturbances in vertical wind profiles, total momentum fluxes, or TKE budget. That path is widely pursued through this Thesis, in physical and numerical experiments as discussed along part IV.

An original methodology is proposed in section IV.1 to characterize WI motions from the measurements in instantaneous velocities. Two concepts extend the definition of a *Wave Related* flow, from *Wave Coherent* (WC) to *Wave Induced* (WI), leading to WI and WC decompositions that for the first time allow their quantification in the field, without any previous sea-state knowledge required: (i) The existing correlation between *Atmospheric turbulence* (Atm.) and WI motions; and (ii) The Space-Time spectral description of turbulent fluctuations.

The WI flow is so defined as a specific kind of turbulent fluctuation, that does not behave as expected from atmospheric turbulent flows above fixed terrains. The different behavior of both fields shall be often particularly noticeable in the $k-w$ turbulent spectra, that allows the decomposition above arbitrary sea-states. The WI flow is obtained as a fraction of the WC flow, so introduced as the WI fraction $\mathscr{F}$. The squared of the WI fraction gives the fraction of WI energy in total fluctuations, so leading to precise (not unique) definitions of the WBL height when the WI energy is negligible (~1% if $\mathscr{F} = 0.1$). This definition of the WI flow is limited to scenarios where it is detectable.

That methodology is first exploited in section IV.1.2, where the simplistic monochromatic wave scenario still allows the WC decomposition, to be compared with the WI decomposition yet based on the 1D wave-number or frequency dependent spectra. Contrary to the WC alternative, the WI filter recovers the expected turbulent behavior at the WC scales. Though, due to Wind-Wave interactions, turbulent scales are distorted and particularly the integral scale is diminished in the WBL. Wave induced motions merge into the turbulent cascade distorting and forcing the turbulent flow in the WBL.

In more realistic conditions where the sea-state is defined at multiple scales (irregular), it is often unfeasible to employ the WC and WI filters based on the 1D turbulent spectra, such as otherwise exploited for the regular wave case. Adopting the enhanced perspective of the WI flow proposed in section IV.1, the 2D $k-w$ spectral partition proposed in section IV.2 is shown feasible for every test case here presented, even given the significant differences observed in the correspondent WI 2D spectra, and without any prior information about the Sea-State prescription. The effectiveness of the employed triple decomposition is established with the WI disturbances vanishing from the Atm. filtered 1D and 2D turbulent spectra.

The comparison of physical and numerical experiments closes part IV in section IV.3. A numerical model of the sLiDAR filter is established to evaluate it's impact on the original analyses presented in section II.3, and particularly the filter behavior in the joint Space-Time distribution of turbulent correlations. Even though the sLiDAR's filter is originally presented in space, the flow dependency is such that the turbulent fluctuations are like-wise filtered in space and time domains.

The decomposition proposed enables the separated evaluation of the sLiDAR filter acting in Atm. and WI motions. Contrary to the Atm. turbulence, where the filtering effect scales simply with the mean wind velocity, the WI disturbances in 1D and 2D turbulent spectra reveal the strong flow dependency of the sLiDAR filtering effect. The filter length scale is constant, but the corresponding filter period scales differently for Atm. and WI motions, according to the Taylor hypothesis for the former, and the wave dispersion relation for the second.

Ultimately, the proposed framework allows the direct comparison between physical and numerical experiments, in a level of detail rarely observed in such complex Fluid Mechanic's studies. The artificial enhancement of WI motions due to the sLiDAR filter is seemingly well described in the numerical case, as its employment leads to much accurate intensity and shape of the 1D frequency-dependent WI fraction. The WI disturbances are significantly stronger in the physical experiment, probably due to the sea-state uncertainty between the cases, or the buoyancy effects neglected in the numerical model. Nevertheless, the compar-

ison reveals remarkable similarities between the Wave Induced flow observed in physical and numerical experiments.

Notably, each of the features revealed in the WI spectral distribution of the physical experiment are qualitatively reproduced in the numerical model. The WI spectra almost collapse between the cases when normalized by the case-specific total WI energy. The same applies to the transfer function: It is amplified in the physical experiment, but if normalized to the same value at the wave peak scales, their curves agree well in numerical and physical applications.

SCIENTIFIC DISCUSSION

The introduction stated some fundamental ***scientific questions*** regarding **wind-wave interactions**. Each of them is briefly reconsidered hereby, explicitly stating the corresponding ***answer***, and indicating the interests in future studies.

WAVE BOUNDARY LAYER

The observations presented support the literature review, where the Wave Induced disturbances extend into limited regions above the free surface. A more precise definition of the WBL remains elusive though, as the WI disturbances significance strongly depends on the variable of interest, which is discussed in Hristov [2018] and sustained by current observations.

The physical experiment presented gives access to space-time velocity measurements at a single height that, depending on the variable of interest, might be considered below or above the WBL height. At the 1D turbulent spectra of section II.3.2, for example, the wave-number-dependent spectra do not present any WI disturbances, yet they are significant in the 1D frequency-dependent spectra at the same section.

The numerical experiments reveal the vertical evolution of mean wind velocity and turbulent quantities. Indeed the WI disturbances vanish sufficiently far from the surface, but the height below which they are significant depends on vertical profile considered. Notably in the Turbulent Intensity (TI) profiles of section III.3.2, there is a relatively precise height below which the TI is augmented, and above which it is diminished. Though, that height is different if considering longitudinal or vertical velocity variances.

A precise definition of the WBL may be taken from imposing a criteria for the WI fraction ($\mathscr{F}$) introduced at section IV.1, that corresponds to the squared root of the WI energy fraction in the total energy density function. Such definition is also not unique, as different conclusions are obtained if $\mathscr{F}$ is wave-number and/or angular-frequency dependent, or if $\mathscr{F}$ corresponds to a particular velocity component. Vertical velocities are shown to propagate higher in the ABL, and the sLiDAR filter will artificially augment $\mathscr{F}(w)$, rather than $\mathscr{F}(k)$.

It is thus, unreasonable to expect a single definition to the WBL height, as it is strongly

dependent in the variable of interest.

Wave Induced Stress

The **WI Stress** has drawn considerable attention of the scientific community over the last decades, and is often recognized as playing a most important role in wind-wave interactions. Notably, if the waves travel sufficiently fast with respect to the mean wind speed, the momentum transfer occurs upwards, and the wind speeds up due to the waves' incidence.

The radial velocity component and single height measurement of the physical experiment do not give access to shear stresses in the ABL. The numerical experiment on the contrary, gives the detailed evolution of Total, SGS, resolved, turbulent and WI stresses along the ABL. Besides, the numerical experiment present simplified and controlled conditions, allowing to study the influence of single varying parameters in the results. As drawback, the LES formulation introduces numerical modelling and discretization errors, that have not been the focus of present studies.

Section III.2 revealed that the WI pressure drag is very sensitive to the flow history. In section III.3, the WI pressure drag is shown to impose the disturbance of the shear stresses profile in the ABL. In the controlled scenario presented, characterized by the LES generated MABL in neutral conditions with almost constant free-stream velocity, the WI pressure drag and the total shear stresses are consistently parameterized as functions of the WA.

The WI stress and the wind speed-up become significant in sufficiently old seas regimes, characterized by high Wave Ages. Though, the precise relation here presented are limited to very simplistic environmental conditions, and valid for a specific set of numerical parameters.

Further works could evaluate the sensitivity of the analyses with respect to the numerical setup, and the importance of physical phenomena neglected in the numerical model, e.g., buoyancy forces, and the two-way coupling between ocean waves and atmospheric winds. But one shall note that a perfectly steady state condition can hardly ever be found in the offshore environment. With these and others complexities in mind, Hristov and Ruiz-Plancarte [2014] note that a simple and robust parametrization of the surface drag is unlikely to exist, which is supported in current discussions.

Wave Induced Flow

The **WI flow** is generally defined in the literature review of section I.3.2, as wave related dynamics (Velocities and Pressure) that advect through the atmosphere, yet maintaining some of its original aspects. Through the experimental literature, one often observes the consequence of WI motions distorting turbulent statistics in the WBL, but one rarely encounters a direct characterization of the WI field.

An original methodology is here proposed in section IV.1 to characterize WI motions from measurements in instantaneous velocities, that for the first time allows its quantification in the field, without any previous sea-state knowledge required. The WI flow is so

defined as a specific kind of turbulent fluctuation, that does not behave as expected from atmospheric turbulent flows above fixed terrains.

Effectively extracting the WI flow above arbitrary sea-states requires considering correlated WI motions and Atm. turbulence, and the wave-number-angular-frequency perspective of modal energy distribution. As the methodology relies in the partitioning of the turbulent auto-correlation spectra, the inference of deterministic and decomposed WI motions encounters the phase retrieval problem [Kogan et al., 2016], here circumvented assuming that coherent WI motions and Atm. turbulence are in-phase.

Employing the proposed methodology, the WI flow is extracted from the instantaneous wind speed measurements, observed for each of the experimental and numerical cases presented.

The assumption of in-phase Wave coherent signals determine the amount of WI-Atm. cross correlations, according to the discussion in section IV.1. The assumption seems reasonable, because in a statistically steady scenario the coherent signals shall resonate with each other. Though, there is yet no observational support to that assumption, which shall be explored in further works. The interest in determining the exact amount of WI-Atm. cross-correlations is because that term shall hold all the wind-wave interactions effects in the decomposed WI and Atm. momentum equations.

Transfer Function

The determination of the transfer function linking the sea-state forcing and the atmospheric response shall precede any parametric description of the WI field in the MABL, but it has not yet been reported in the literature as actual measurements in the offshore environment. That shall occur for the absence of a triple decomposition method capable of measuring the WI field in the ocean environment, characterized by non-regular sea-state situations.

Recent developments in sLiDAR measurements technologies and techniques allow the enhanced perspective achieved through the 2D spectra, and together with the triple decomposition proposed, the Transfer Function (TF) is here presented for the physical experiments at section IV.2.3. The critical issue in the Tranfer Function obtained in the physical experiment, is that the Sea-State spectra has not been measured, rather being estimated from a well established WaveWatch III hind-cast database.

For a parametric description valid in low-fidelity applications, it is also desired to reproduce the Transfer Function in high fidelity numerical tools. To evaluate the numerical model capabilities, the transfer function is also obtained for the numerical experiments, and the comparison is presented in section IV.3.5. It is then observed a high similarity between the Transfer Function shape obtained in physical and numerical experiments, though it is considerably augmented in the physical experiment test case. Another critical issue with the comparison, is that buoyancy forces are neglected in the numerical experiment, and the Atm. turbulence contribution behaves considerably different in each case.

The Transfer Function establishes a link between multi-scale waves and wave induced motions in the atmosphere, and is here reported for the first time as actual measurements in

the offshore environment. In order to obtain more precise estimates of the Transfer Function, it is desirable to measure the sea-state spectra as part of future experimental campaigns, and to consider buoyancy forces in future numerical experiments.

STATE-OF-THE-ART WIND MODELS

It has been discussed in the literature review of section I.2.2.4, that prediction tools for design and operational purposes rely in state-of-the-art wind models considering a mean wind log-law profile based on the Monin-Obukhov Similarity Theory (MOST), superposed to randomly generated turbulent components with statistics given, e.g, by the Mann spectra. It is observed though, that the mean wind profiles and its turbulent statistics considerably deviate from MOST and Mann's predictions on the vicinity of ocean waves.

The main key-point to the current discussion is the artificial turbulence modal distribution assumed in these models. The modal distribution is critical in the wind turbine structure perspective, as the turbine is characterized by its natural lengths and frequencies that shall be set sufficiently apart from the principal loading scales. Recall that wind and waves velocity fluctuations cover a wide range of length scales, including the rotor's blade length. The design criteria of offshore wind turbines, then require that the rotor frequencies are sufficiently higher than wind and waves frequencies [Nikitas et al., 2016]. In old seas situations where waves' travel faster than the wind, the waves become the critical loading imposing the turbine's frequency. The main issue here is that the exact amount of gap required between the wave peak frequency and the turbine frequency is subject to significant uncertainty, depending in very complex wind-wave-structure interactions.

In the design phase of wind turbines, waves loadings are usually considered as acting in the water domain, but the state-of-the-art wind models do not consider any kind of WI motions in the wind source. As noted, in old seas WI motions approach the natural frequency of wind turbines, and along the current Thesis they are often observed significant, sometimes predominant, determining the modal distribution of velocity fluctuations in the WBL at Wave Coherent scales.

Present developments suggest that the total fluctuations can be decomposed in WI motions and Atm. turbulence in the WBL. The Atm. turbulence obtained with such a decomposition behaves similarly to the one obtained in flat bottom cases, and thus agree well, e.g., to Mann's prediction. Though, when considering the monochromatic wave in section IV.1.2, it is shown that due to Wind-Wave interactions, turbulent scales are distorted, and particularly the integral scale is diminished in the Atm. turbulence spectra.

Moreover, present observations reveal an even more fundamental limitation of the artificial turbulence considered in current state-of-the-art wind models. Indeed, the one dimensional wave-number or frequency spectra employed in these models reveal a very limited perspective of turbulence modal distribution, even in canonical, flat bottom numerical experiments. The artificial turbulence considered in these models is defined with the Taylor's hypothesis relation.

Recall that in the wave-number-angular-frequency spectra, the Taylor hypothesis corresponds to a straight line, strongly contrasting to the continuous observations here pre-

sented, as further discussed in the appendix C.2. The appendix also discusses existing and original wave-number-angular-frequency spectra models, neither of which has been actually tested in a wind turbine structure to access the implications. Notably, if turbulence strictly follows the Taylor hypothesis, it is trivial to obtain non-coherent turbulence and wind turbine motions in the ABL. But the 2D perspective reveals the modal spreading phenomena, so that turbulence is actually existent through a wide range of space-time scales in the ABL.

State-of-the-art wind models could improve their accuracy in offshore environment by considering: (i) The superposition of a Wave Induced field model to the existing Atm. turbulence models; and (ii) The distortion of turbulent scales in the Atm. turbulence, due to wind-wave interactions. Additionally, it is suggested that they can also improve their accuracy in generic conditions by considering a wave-number-angular-frequency turbulent spectra description, rather than strictly adopting the Taylor's hypothesis.

Looking forward to future works, it seems important to evaluate the implications of such improvements to the structural and productive performance of wind turbines.

BIBLIOGRAPHY

Mickael Accensi, Christophe Maisondieu, Jean-Francois Le Roux, and Edwige Boudière. Manuel de l'utilisateur de la base de données homere. mise à jour 2017 du jeu de données de hindcast. https://archimer.ifremer.fr/doc/00415/52606/, 2017.

Ronald Adrian. Hairpin vortex organization in wall turbulence. *Physics of Fluids*, 19, 04 2007. doi: 10.1063/1.2717527.

Ronald Adrian, Carl Meinhart, and Chris Tomkins. Vortex organization in the outer region of the turbulent boundary layer. *Journal of Fluid Mechanics*, 422:1–54, 11 2000. doi: 10.1017/S0022112000001580.

John D. Anderson. Ludwig prandtl's boundary layer. *Physics Today*, 58(12):42–48, 2005. doi: 10.1063/1.2169443. URL https://doi.org/10.1063/1.2169443.

Fabrice Ardhuin. Prévisions de vagues (ww3) pour la façade golfe de gascogne / nord atlantique (grille régulière) (ww3-norgas-2min). https://sextant.ifremer.fr/record/fde1f80f-b0a7-45ba-bad6-2343bb4e9a9f/, 2012.

Alex Ayet. *Air-sea momentum fluxes in the vicinity of the sea surface : a theoretical study of the coupling between turbulence and wind-waves*. Theses, Université de Bretagne occidentale - Brest, September 2020. URL https://tel.archives-ouvertes.fr/tel-03043743.

Taha Aziz, A. Fatima, C. M. Khalique, and F. M. Mahomed. Prandtl's boundary layer equation for two-dimensional flow: Exact solutions via the simplest equation method. *Mathematical Problems in Engineering*, 2013:724385, Apr 2013. ISSN 1024-123X. doi: 10.1155/2013/724385. URL https://doi.org/10.1155/2013/724385.

Mark A. Baker and Carl H. Gibson. Sampling turbulence in the stratified ocean: Statistical consequences of strong intermittency. *Journal of Physical Oceanography*, 17(10):1817 – 1836, 1987. doi: 10.1175/1520-0485(1987)017<1817:STITSO>2.0.CO;2. URL https://journals.ametsoc.org/view/journals/phoc/17/10/1520-0485_1987_017_1817_stitso_2_0_co_2.xml.

D Bastine, M Wächter, J Peinke, D Trabucchi, and M Kühn. Characterizing wake turbulence with staring lidar measurements. *Journal of Physics: Conference Series*, 625:012006, jun 2015. doi: 10.1088/1742-6596/625/1/012006. URL https://doi.org/10.1088/1742-6596/625/1/012006.

S. Basu, J. Vinuesa, and A. Swift. Dynamic les modeling of a diurnal cycle,. *Journal of Applied Meteorology and Climatology*, 47(4):1156–1174, 2008.

G. K. Batchelor. *An Introduction to Fluid Dynamics*. Cambridge University Press, 2000.

J. A. Battjes, T. J. Zitman, and L. H. Holthuusen. A reanalysis of the spectra observed in jonswap. *Journal of Physical Oceanography*, 17(8):1288 – 1295, 1987. doi: 10.1175/1520-0485(1987)017<1288:AROTSO>2.0.CO;2. URL https://journals.ametsoc.org/view/journals/phoc/17/8/1520-0485_1987_017_1288_arotso_2_0_co_2.xml.

Hauke Beck and Martin Kühn. Dynamic data filtering of long-range doppler lidar wind speed measurements. *Remote Sensing*, 9(6), 2017. ISSN 2072-4292. doi: 10.3390/rs9060561. URL https://www.mdpi.com/2072-4292/9/6/561.

S. E. Belcher and J. C. R. Hunt. Turbulent shear flow over slowly moving waves. *Journal of Fluid Mechanics*, 251:109–148, 1993.

B. Blocken. 50 years of computational wind engineering : past, present and future. *Journal of Wind Engineering and Industrial Aerodynamics*, 129:69–102, 2014. ISSN 0167-6105. doi: 10.1016/j.jweia.2014.03.008.

BME. Establishment of an atmospheric flow laboratory at the budapest university of technology and economics (bme). https://bmeafl.com/jav_hatarreteg_en/. Accessed: 2021-10-16.

D. Bourras, H. Branger, G. Reverdin, L. Mari?, R. Cambra, L. Baggio, C. Caudoux, G. Caudal, S. Morisset, N. Geyskens, A. Weill, and D. Hauser. A new platform for the determination of air?sea fluxes (ocarina): Overview and first results. *Journal of Atmospheric and Oceanic Technology*, 31(5):1043 – 1062, 2014. doi: 10.1175/JTECH-D-13-00055.1. URL https://journals.ametsoc.org/view/journals/atot/31/5/jtech-d-13-00055_1.xml.

M. P. Buckley, F. Veron, and K. Yousefi. Surface viscous stress over wind-driven waves with intermittent airflow separation. *Journal of Fluid Mechanics*, 905:A31, 2020. doi: 10.1017/jfm.2020.760.

J. A. Businger. *A Note on the Businger-Dyer Profiles*, pages 145–151. Springer Netherlands, Dordrecht, 1988. ISBN 978-94-009-2935-7. doi: 10.1007/978-94-009-2935-7_11. URL https://doi.org/10.1007/978-94-009-2935-7_11.

J. A. Businger, J. C. Wyngaard, Y. Izumi, and E. F. Bradley. Flux-profile relationships in the atmospheric surface layer. *Journal of Atmospheric Sciences*, 28(2):181 – 189, 1971. doi: 10.1175/1520-0469(1971)028<0181:FPRITA>2.0.CO;2. URL https://journals.ametsoc.org/view/journals/atsc/28/2/1520-0469_1971_028_0181_fprita_2_0_co_2.xml.

Marie Cathelain. *Development of a deterministic numerical model for the study of the coupling between an atmospheric flow and a sea state*. PhD thesis, Ecole Centrale de Nantes (ECN), 2017.

Met Office's National Climate Information Centre. National meteorological library and archive fact sheet 6 - the beaufort scale., 2010. URL https://web.archive.org/web/20121002134429/http://www.metoffice.gov.uk/media/pdf/4/4/Fact_Sheet_No._6_-_Beaufort_Scale.pdf. Accessed: 2021-10-19.

H. Charnock. Wind stress on a water surface. *Quarterly Journal of the Royal Meteorological Society*, 81(350):639–640, 10 1955. ISSN 1477-870X. doi: 10.1002/qj.49708135027. URL https://doi.org/10.1002/qj.49708135027.

Yu Cheng, Chadi Sayde, Qi Li, Jeffrey Basara, John Selker, Evan Tanner, and Pierre Gentine. Failure of taylor's hypothesis in the atmospheric surface layer and its correction for eddy-covariance measurements. *Geophysical Research Letters*, 44(9):4287–4295, 2017. doi: https://doi.org/10.1002/2017GL073499.

Alejandro Cifuentes-Lorenzen, James B. Edson, and Christopher J. Zappa. Air–sea interaction in the southern ocean: Exploring the height of the wave boundary layer at the air–sea interface. *Boundary-Layer Meteorology*, 169:461–482, 2018.

A. Cimarelli, A. Leonforte, E. De Angelis, A. Crivellini, and D. Angeli. On negative turbulence production phenomena in the shear layer of separating and reattaching flows. *Physics Letters A*, 383(10):1019–1026, 2019. ISSN 0375-9601. doi: https://doi.org/10.1016/j.physleta.2018.12.026. URL https://www.sciencedirect.com/science/article/pii/S0375960118312477.

J. E. Cohen and S. E. Belcher. Turbulent shear flow over fast-moving waves. *Journal of Fluid Mechanics*, 386:345–371, 1999. doi: 10.1017/S0022112099004383.

J. Counihan. Adiabatic atmospheric boundary layer: A review and analysis of data from the period 1880-1972. *Atmospheric Environment*, 1975.

Peter D. Craig and Michael L. Banner. Modeling wave-enhanced turbulence in the ocean surface layer. *Journal of Physical Oceanography*, 24:2546–2559, 1994.

Alex D.D. Craik. The origins of water wave theory. *Annual Review of Fluid Mechanics*, 36(1): 1–28, 2004. doi: 10.1146/annurev.fluid.36.050802.122118. URL https://doi.org/10.1146/annurev.fluid.36.050802.122118.

Isaac Van der Hoven. Power spectrum of horizontal wind speed in the frequency range from 0.0007 to 900 cycles per hour. *Journal of Atmospheric Sciences*, 14(2):160 – 164, 1957. doi: 10.1175/1520-0469(1957)014<0160:PSOHWS>2.0.CO;2. URL https://journals.ametsoc.org/view/journals/atsc/14/2/1520-0469_1957_014_0160_psohws_2_0_co_2.xml.

M. A. Donelan, W. M. Drennan, and A. K. Magnusson. Nonstationary analysis of the directional properties of propagating waves. *Journal of Physical Oceanography*, 26(9):1901 – 1914, 1996. doi: 10.1175/1520-0485(1996)026<1901:NAOTDP>2.0.CO;2. URL https://journals.ametsoc.org/view/journals/phoc/26/9/1520-0485_1996_026_1901_naotdp_2_0_co_2.xml.

Mark A. Donelan, Fred W. Dobson, Stuart D. Smith, and Robert J. Anderson. On the dependence of sea surface roughness on wave development. *Journal of Physical Oceanography*, 23(9):2143–2149, 1993. doi: 10.1175/1520-0485(1993)023<2143:OTDOSS>2.0.CO;2.

David A. Drazen, W. Kendall Melville, and Luc Lenain. Inertial scaling of dissipation in unsteady breaking waves. *Journal of Fluid Mechanics*, 611:307–332, 2008. doi: 10.1017/S0022112008002826.

Guillaume Ducrozet, Félicien Bonnefoy, David Le Touzé, and Pierre Ferrant. Hos-ocean: Open-source solver for nonlinear waves in open ocean based on high-order spectral method. *Computer Physics Communications*, 203:245–254, 2016.

Guillaume Ducrozet, Félicien Bonnefoy, and Yves Perignon. Applicability and limitations of highly non-linear potential flow solvers in the context of water waves. *Ocean Engineering*, 142:233–244, 2017. ISSN 0029-8018. doi: https://doi.org/10.1016/j.oceaneng.2017.07.003. URL https://www.sciencedirect.com/science/article/pii/S0029801817303748.

Thibault Désert, Graham Knapp, and Sandrine Aubrun. Quantification and correction of wave-induced turbulence intensity bias for a floating lidar system. *Remote Sensing*, 13(15), 2021. ISSN 2072-4292. doi: 10.3390/rs13152973. URL https://www.mdpi.com/2072-4292/13/15/2973.

Michael Eckert. Turbulence research in the 1920s and 1930s between mathematics, physics, and engineering. *Science in Context*, 31(3):381–404, 2018. doi: 10.1017/S026988971800025X.

J. B. Edson and C. W. Fairall. Similarity relationships in the marine atmospheric surface layer for terms in the tke and scalar variance budgets. *Journal of the Atmospheric Sciences*, 55(13):2311 – 2328, 1998. doi: 10.1175/1520-0469(1998)055<2311:SRITMA>2.0.CO;2. URL https://journals.ametsoc.org/view/journals/atsc/55/13/1520-0469_1998_055_2311_sritma_2.0.co_2.xml.

James Edson, Timothy Crawford, Jerry Crescenti, Tom Farrar, Nelson Frew, Greg Gerbi, Costas Helmis, Tihomir Hristov, Djamal Khelif, Andrew Jessup, Haf Jonsson, Ming Li, Larry Mahrt, Wade McGillis, Albert Plueddemann, Lian Shen, Eric Skyllingstad, Tim Stanton, Peter Sullivan, Jielun Sun, John Trowbridge, Dean Vickers, Shouping Wang, Qing Wang, Robert Weller, John Wilkin, Albert J. Williams, D. K. P. Yue, and Chris Zappa. The coupled boundary layers and air?sea transfer experiment in low winds. *Bulletin of the American Meteorological Society*, 88(3):341 – 356, 2007. doi: 10.1175/BAMS-88-3-341. URL https://journals.ametsoc.org/view/journals/bams/88/3/bams-88-3-341.xml.

James B. Edson, Venkata Jampana, Robert A. Weller, Sebastien P. Bigorre, Albert J. Plueddemann, Christopher W. Fairall, Scott D. Miller, Larry Mahrt, Dean Vickers, and Hans Hersbach. On the exchange of momentum over the open ocean. *Journal of Physical Oceanography*, 43(8):1589–1610, 2013. doi: 10.1175/JPO-D-12-0173.1.

Fc C. Emejeamara, As S. Tomlin, and Joel Millward-Hopkins. Urban wind: Characterisation of useful gust and energy capture. 2015.

M.A. Escalante Soberanis and W. Mérida. Regarding the influence of the van der hoven spectrum on wind energy applications in the meteorological mesoscale and microscale. *Renewable Energy*, 81:286–292, 2015. ISSN 0960-1481. doi: https://doi.org/10.1016/j.renene.2015.03.048. URL https://www.sciencedirect.com/science/article/pii/S096014811500230X.

ESDU 85020. Characteristics of atmospheric turbulence near the ground. Part 2: Single point data for strong winds (neutral atmosphere). Technical report, Eng. Sci. Data Unit 85020, October 1985.

John D Fenton. A fifth-order stokes theory for steady waves. *Journal of waterway, port, coastal, and ocean engineering*, 111(2):216–234, 1985.

Thomas Foken. 50 years of the monin–obukhov similarity theory. *Boundary-Layer Meteorology*, 119(3):431–447, 2006a.

Thomas Foken. 50 years of the monin-obukhov similarity theory. *Boundary-Layer Metereology*, 2006b.

Bishakdatta Gayen and Sutanu Sarkar. Negative turbulent production during flow reversal in a stratified oscillating boundary layer on a sloping bottom. *Physics of Fluids*, 23, 10 2011. doi: 10.1063/1.3651359.

Alan L. M. Grant and Stephen E. Belcher. Characteristics of langmuir turbulence in the ocean mixed layer. *Journal of Physical Oceanography*, 39(8):1871 – 1887, 2009. doi: 10.1175/2009JPO4119.1. URL https://journals.ametsoc.org/view/journals/phoc/39/8/2009jpo4119.1.xml.

Laurent Grare, Luc Lenain, and W. Kendall Melville. Wave-coherent airflow and critical layers over ocean waves. *Journal of Physical Oceanography*, 43(10):2156 – 2172, 2013a. doi: 10.1175/JPO-D-13-056.1. URL https://journals.ametsoc.org/view/journals/phoc/43/10/jpo-d-13-056.1.xml.

Laurent Grare, William L. Peirson, Hubert Branger, J. Walker, Jean-Paul Giovanangeli, and Vladimir K. Makin. Growth and dissipation of wind forced, deep water waves. *Journal of Fluid Mechanics*, 722:5–50, 2013b. doi: 10.1017/jfm.2013.88. URL https://hal.archives-ouvertes.fr/hal-00850963.

Sven-Erik Gryning and Rogier Floors. Carrier-to-noise-threshold filtering on off-shore wind lidar measurements. *Sensors*, 19(3), 2019. ISSN 1424-8220. doi: 10.3390/s19030592. URL https://www.mdpi.com/1424-8220/19/3/592.

Sven-Erik Gryning, Rogier Floors, Alfredo Peña, Ekaterina Batchvarova, and Burghard Brümmer. Weibull wind-speed distribution parameters derived from a combination of wind-lidar and tall-mast measurements over land, coastal and marine sites. *Boundary-Layer Meteorology*, 159:329–348, 2016. ISSN 1573-1472. doi: 10.1007/s10546-015-0113-x. URL https://doi.org/10.1007/s10546-015-0113-x.

Hervé Guillard and Charbel Farhat. On the significance of the geometric conservation law for flow computations on moving meshes. *Computer Methods in Applied Mechanics and Engineering*, 190(11):1467 – 1482, 2000. ISSN 0045-7825. doi: https://doi.org/10.1016/S0045-7825(00)00173-0. URL http://www.sciencedirect.com/science/article/pii/S0045782500001730.

Kirsty E. Hanley and Stephen E. Belcher. Wave-driven wind jets in the marine atmospheric boundary layer. *Journal of the Atmospheric Sciences*, 65(8):2646 – 2660, 2008. doi: 10.1175/2007JAS2562.1. URL https://journals.ametsoc.org/view/journals/atsc/65/8/2007jas2562.1.xml.

Xuanting Hao and Lian Shen. Wind–wave coupling study using les of wind and phase-resolved simulation of nonlinear waves. *Journal of Fluid Mechanics*, 874:391–425, 2019. doi: 10.1017/jfm.2019.444.

Tetsu Hara and Stephen E. Belcher. Wind forcing in the equilibrium range of wind-wave spectra. *Journal of Fluid Mechanics*, 470:223–245, 2002. doi: 10.1017/S0022112002001945.

D. Lee Harris. The wave-driven wind. *Journal of the Atmospheric Sciences*, 23(6):688–693, 1966.

K. Hasselmann. On the mass and momentum transfer between short gravity waves and larger-scale motions. *Journal of Fluid Mechanics*, 50(1):189–205, 1971. doi: 10.1017/S0022112071002520.

K. Hasselmann, T. P. Barnett, E. Bouws, H. Carlson, D. E. Cartwright, K. Enke, J. A. Ewing, H. Gienapp, D. E. Hasselmann, P. Kruseman, A. Meerburg, P. Muller, D. J. Olbers, K. Richter, W. Sell, and H. Walden. Measurement of wind-wave growth and swell decay during the joint north sea wave project (jonswap). 1973.

Guo-Wei He and Jin-Bai Zhang. Elliptic model for space-time correlations in turbulent shear flows. *Phys. Rev. E*, 73:055303, May 2006. doi: 10.1103/PhysRevE.73.055303. URL https://link.aps.org/doi/10.1103/PhysRevE.73.055303.

T. S. Hristov, S. D. Miller, and C. A. Friehe. Dynamical coupling of wind and ocean waves through wave-induced air flow. *Nature*, 422(6927):55–58, Mar 2003. ISSN 1476-4687. doi: 10.1038/nature01382. URL https://doi.org/10.1038/nature01382.

Tihomir Hristov. Mechanistic, empirical and numerical perspectives on wind-waves interaction. *Procedia IUTAM*, 26:102–111, 2018.

Tihomir Hristov and Jesus Ruiz-Plancarte. Dynamic balances in a wavy boundary layer. *Journal of Physical Oceanography*, 44(12):3185–3194, 2014. doi: 10.1175/JPO-D-13-0209.1.

Tihomir Hristov, Carl Friehe, and Scott Miller. Wave-coherent fields in air flow over ocean waves: Identification of cooperative behavior buried in turbulence. *Phys. Rev. Lett.*, 81:5245–5248, Dec 1998. doi: 10.1103/PhysRevLett.81.5245. URL https://link.aps.org/doi/10.1103/PhysRevLett.81.5245.

S. J. Jacobs. An asymptotic theory for the turbulent flow over a progressive water wave. *Journal of Fluid Mechanics*, 174:69–80, 1987. doi: 10.1017/S0022112087000041.

Peter A. E. M. Janssen. *The interaction of ocean waves and wind*. Cambridge University Press, 2004.

Peter A. E. M. Janssen. Ocean wave effects on the daily cycle in sst. *Journal of Geophysical Research: Oceans*, 117(C11), 2012. doi: https://doi.org/10.1029/2012JC007943. URL https://agupubs.onlinelibrary.wiley.com/doi/abs/10.1029/2012JC007943.

Peter A. E. M. Janssen, Ø. Breivik, Kristian Mogensen, Frédéric Vitart, Magdalena Alonso-Balmaseda, Jean-Raymond Bidlot, Sarah Keeley, Martin Leutbecher, L. Magnusson, and Franco Molteni. Air-sea interaction and surface waves. *ECMWF Technical Memorandum*, 2013.

Harold Jeffreys. On the formation of water waves by wind. In The Royal Society, editor, *Procceedings of the Royal Society of London*, volume 107, pages 189–206, 1925.

Javier Jiménez. Turbulence and vortex dynamics, 2004. URL https://torroja.dmt.upm.es/area_alumnos/Introduccion_a_la_turbulencia/apuntes.pdf.

Javier Jiménez. Coherent structures in wall-bounded turbulence. *Journal of Fluid Mechanics*, 842:P1, 2018. doi: 10.1017/jfm.2018.144.

J.M.J. Journée and W.W.Massie. Offshore hydromechanics, 2001. URL https://ocw.tudelft.nl/wp-content/uploads/OffshoreHydromechanics_Journee_Massie.pdf.

Kimmo K. Kahma and Charles J. Calkoen. Reconciling discrepancies in the observed growth of wind-generated waves. *Journal of Physical Oceanography*, 22(12):1389 – 1405, 1992. doi: 10.1175/1520-0485(1992)022<1389:RDITOG>2.0.CO;2. URL https://journals.ametsoc.org/view/journals/phoc/22/12/1520-0485_1992_022_1389_rditog_2_0_co_2.xml.

J. C. Kaimal and J. J. Finnigan. *Atmospheric Boundary Layer Flows: Their Structure and Measurement*. Oxford University Press, 1994.

N. Kalthoff, F. Lohou, B. Brooks, G. Jegede, B. Adler, K. Babić, C. Dione, A. Ajao, L. K. Amekudzi, J. N. A. Aryee, M. Ayoola, G. Bessardon, S. K. Danuor, J. Handwerker, M. Kohler, M. Lothon, X. Pedruzo-Bagazgoitia, V. Smith, L. Sunmonu, A. Wieser, A. H. Fink, and P. Knippertz. An overview of the diurnal cycle of the atmospheric boundary layer during the west african monsoon season: results from the 2016 observational campaign. *Atmospheric Chemistry and Physics*, 18(4):2913–2928, 2018. doi: 10.5194/acp-18-2913-2018. URL https://acp.copernicus.org/articles/18/2913/2018/.

Siri Kalvig, Ove Tobias Gudmestad, and Nina Winther. Exploring the gap between 'best knowledge' and 'best practice' in boundary layer meteorology for offshore wind energy. *Wind Energy*, 17(1):161–171, 2014. doi: https://doi.org/10.1002/we.1572. URL https://onlinelibrary.wiley.com/doi/abs/10.1002/we.1572.

Gabriel G. Katul, Alexandra G. Konings, and Amilcare Porporato. Mean velocity profile in a sheared and thermally stratified atmospheric boundary layer. *Phys. Rev. Lett.*, 107:268502, Dec 2011. doi: 10.1103/PhysRevLett.107.268502. URL https://link.aps.org/doi/10.1103/PhysRevLett.107.268502.

Elizabeth C. Kent and Peter K. Taylor. Choice of a beaufort equivalent scale. *Journal of Atmospheric and Oceanic Technology*, 14(2):228 – 242, 1997. doi: 10.1175/1520-0426(1997)014<0228:COABES>2.0.CO;2. URL https://journals.ametsoc.org/view/journals/atot/14/2/1520-0426_1997_014_0228_coabes_2_0_co_2.xml.

S. A. Kitaigorodskii. On the theory of the equilibrium range in the spectrum of wind-generated gravity waves. *Journal of Physical Oceanography*, 13(5):816 – 827, 1983. doi: 10.1175/1520-0485(1983)013<0816:OTTOTE>2.0.CO;2. URL https://journals.ametsoc.org/view/journals/phoc/13/5/1520-0485_1983_013_0816_ottote_2_0_co_2.xml.

Dani Kogan, Yonina C. Eldar, and Dan Oron. On the 2d phase retrieval problem. *CoRR*, abs/1605.08487, 2016. URL http://arxiv.org/abs/1605.08487.

A. N. Kolmogorov. The local structure of turbulence in incompressible viscous fluid for very large reynolds numbers. *Proceedings: Mathematical and Physical Sciences*, 434(1890):9–13, 1991. ISSN 09628444. URL http://www.jstor.org/stable/51980.

Robert H. Kraichnan. Kolmogorov's hypotheses and eulerian turbulence theory. *The Physics of Fluids*, 7(11):1723–1734, 1964. doi: 10.1063/1.2746572.

Søren Ejling Larsen, N. E. Busch, and D. W. Thomson. Data analysis of atmospheric measurements. In *Proceedings of the Dynamic Flow Conference 1978 on Dynamic Measurements in Unsteady Flows*, pages 887–908. DISA, 1979. Dynamic Flow Conference 1978 on

Dynamic Measurements in Unsteady Flows ; Conference date: 11-09-1979 Through 14-09-1979.

Pascal Lazure and Franck Dumas. An external–internal mode coupling for a 3d hydrodynamical model for applications at regional scale (mars). *Advances in Water Resources*, 31 (2):233–250, 2008. ISSN 0309-1708. doi: https://doi.org/10.1016/j.advwatres.2007.06.010. URL https://www.sciencedirect.com/science/article/pii/S0309170807001121.

Patrick Le Quéré, Bérengere Podvin, S Xin, and P Le Quéré. Méthodes numériques pour les écoulements incompressibles. 2010.

Xuhui Lee. *Balance of Forces in the Atmospheric Boundary Layer*, pages 101–120. Springer International Publishing, Cham, 2018. ISBN 978-3-319-60853-2. doi: 10.1007/978-3-319-60853-2_6. URL https://doi.org/10.1007/978-3-319-60853-2_6.

M. J. Lighthill. Physical interpretation of the mathematical theory of wave generation by wind. *Journal of Fluid Mechanics*, 14:385–398, 1962.

M. S. Longuet-Higgins. The directional spectrum of ocean waves, and processes of wave generation. *Proceedings of the Royal Society of London. Series A, Mathematical and Physical Sciences*, 265(1322):286–315, 1962. ISSN 00804630. URL http://www.jstor.org/stable/2414167.

L. Mahrt. Intermittency of atmospheric turbulence. *Journal of Atmospheric Sciences*, 46(1):79 – 95, 1989. doi: 10.1175/1520-0469(1989)046<0079:IOAT>2.0.CO;2. URL https://journals.ametsoc.org/view/journals/atsc/46/1/1520-0469_1989_046_0079_ioat_2_0_co_2.xml.

Larry Mahrt. Characteristics of submeso winds in the stable boundary layer. *Boundary-Layer Meteorology*, 130(1):1–14, Jan 2009. ISSN 1573-1472. doi: 10.1007/s10546-008-9336-4. URL https://doi.org/10.1007/s10546-008-9336-4.

Larry Mahrt. Surface wind direction variability. *Journal of Applied Meteorology and Climatology*, 50(1):144 – 152, 2011. doi: 10.1175/2010JAMC2560.1. URL https://journals.ametsoc.org/view/journals/apme/50/1/2010jamc2560.1.xml.

Jakob Mann. The spatial structure of neutral atmospheric surface-layer turbulence. *Journal of Fluid Mechanics*, 273:141–168, 1994. doi: 10.1017/S0022112094001886.

Jakob Mann. Wind field simulation. *Probabilistic Engineering Mechanics*, 13(4):269 – 282, 1998. ISSN 0266-8920. doi: https://doi.org/10.1016/S0266-8920(97)00036-2. URL http://www.sciencedirect.com/science/article/pii/S0266892097000362.

C. Mastenbroek. *Wind–wave interaction*. PhD thesis, 01 1996.

D. Mehta, A.H. van Zuijlen, B. Koren, J.G. Holierhoek, and H. Bijl. Large eddy simulation of wind farm aerodynamics: A review. *Journal of Wind Engineering and Industrial Aerodynamics*, 133:1–17, 2014. ISSN 0167-6105. doi: https://doi.org/10.1016/j.jweia.2014.07.002. URL https://www.sciencedirect.com/science/article/pii/S0167610514001391.

John W. Miles. On the generation of surface waves by shear flows, parti. *Journal of Fluid Mechanics*, 3:185–204, 1957.

John W. Miles. On the generation of surface waves by shear flows, partii. *Journal of Fluid Mechanics*, 6:568–582, 1959.

C. Moeng, Margaret A. LeMone, Marat F. Khairoutdinov, Steve K. Krueger, and Peter A. Bogenschutz. The tropical marine boundary layer under a deep convection system: a large-eddy simulation study. *Journal of advaces in modelling earth systems*, 2009.

Chin-Hoh Moeng. A large-eddy-simulation model for the study of planetary boundary-layer turbulence. *Journal of Atmospheric Sciences*, 41(13):2052 – 2062, 1984. doi: 10.1175/1520-0469(1984)041<2052:ALESMF>2.0.CO;2. URL https://journals.ametsoc.org/view/journals/atsc/41/13/1520-0469_1984_041_2052_alesmf_2_0_co_2.xml.

Chin-Hoh Moeng and Peter P. Sullivan. A comparison of shear- and buoyancy-driven planetary boundary layer flows. *Journal of Atmospheric Sciences*, 51(7):999 – 1022, 1994. doi: 10.1175/1520-0469(1994)051<0999:ACOSAB>2.0.CO;2. URL https://journals.ametsoc.org/view/journals/atsc/51/7/1520-0469_1994_051_0999_acosab_2_0_co_2.xml.

A. Monin and Alexander Mikhailovich Obukhov. Basic laws of turbulent mixing in the surface layer of the atmosphere. 2009.

P. Montalvo, J. Dorignac, M.A. Manna, C. Kharif, and H. Branger. Growth of surface wind-waves in water of finite depth. a theoretical approach. *Coastal Engineering*, 77:49–56, 2013. ISSN 0378-3839.

Carmen J. Nappo, April L. Hiscox, and David R. Miller. A note on turbulence stationarity and wind persistence within the stable planetary boundary layer. *Boundary-Layer Meteorology*, 136(1):165–174, Jul 2010. ISSN 1573-1472. doi: 10.1007/s10546-010-9483-2. URL https://doi.org/10.1007/s10546-010-9483-2.

Y. Narita. Spectral moments for the analysis of frequency shift, broadening, and wavevector anisotropy in a turbulent flow. *Earth, Planets and Space*, 69:73–83, May 2017. doi: 10.1186/s40623-017-0658-7. URL https://doi.org/10.1186/s40623-017-0658-7.

H. Nfaoui. 2.04 - wind energy potential. In Ali Sayigh, editor, *Comprehensive Renewable Energy*, pages 73–92. Elsevier, Oxford, 2012. ISBN 978-0-08-087873-7. doi: https://doi.org/10.1016/B978-0-08-087872-0.00204-3. URL https://www.sciencedirect.com/science/article/pii/B9780080878720002043.

George Nikitas, Nathan Vimalan, and Subhamoy Bhattacharya. An innovative cyclic loading device to study long term performance of offshore wind turbines. *Soil Dynamics and Earthquake Engineering*, 82:154–160, 03 2016. doi: 10.1016/j.soildyn.2015.12.008.

A. M. Obukhov. Turbulence in an atmosphere with a non-uniform temperature. *Boundary-Layer Meteorology*, 2(1):7–29, Mar 1971. ISSN 1573-1472. doi: 10.1007/BF00718085. URL https://doi.org/10.1007/BF00718085.

Michael Optis, Adam Monahan, and Fred C. Bosveld. Moving beyond monin–obukhov similarity theory in modelling wind-speed profiles in the lower atmospheric boundary layer under stable stratification. *Boundary-Layer Meteorology*, 153(3):497–514, Dec 2014. ISSN 1573-1472. doi: 10.1007/s10546-014-9953-z. URL https://doi.org/10.1007/s10546-014-9953-z.

J.P. O'Sullivan, R.A. Archer, and R.G.J. Flay. Consistent boundary conditions for flows within the atmospheric boundary layer. *Journal of Wind Engineering and Industrial Aerodynamics*, 99(1):65 – 77, 2011.

Liad Paskin, Yves Perignon, Boris Conan, and Sandrine Aubrun. Numerical study on the wave boundary layer, its interaction with turbulence and consequences on the wind energy resource in the offshore environment. *Journal of Physics: Conference Series*, 1618: 062046, sep 2020. doi: 10.1088/1742-6596/1618/6/062046. URL https://doi.org/10.1088/1742-6596/1618/6/062046.

Edward G. Patton, Peter P. Sullivan, Branko Kosović, Jimy Dudhia, Larry Mahrt, Mark Žagar, and Tomislav Marić. On the influence of swell propagation angle on surface drag. *Journal of Applied Meteorology and Climatology*, 58(5):1039–1059, 2019.

Jesper Grønnegaard Pedersen, Mark Kelly, Sven-Erik Gryning, and Burghard Brümmer. The effect of unsteady and baroclinic forcing on predicted wind profiles in large eddy simulations: Two case studies of the daytime atmospheric boundary layer. *Meteorologische Zeitschrift*, 22(6):661–674, 12 2013. doi: 10.1127/0941-2948/2013/0477. URL http://dx.doi.org/10.1127/0941-2948/2013/0477.

Yves Perignon, Félicien Bonnefoy, Guillaume Ducrozet, and P. Ferrant. Wind forcing and dissipation in three-dimensional high order spectra deterministic sea state modeling. 05 2010.

Yves Perignon, Fabrice Ardhuin, Marie Cathelain, and M Robert. Swell dissipation by induced atmospheric shear stress. *Journal of Geophysical Research*, 12 2014.

Alfredo Peña and Jakob Mann. Turbulence measurements with dual-doppler scanning lidars. *Remote Sensing*, 11(20), 2019. ISSN 2072-4292. URL https://www.mdpi.com/2072-4292/11/20/2444.

O. M. Phillips. On the generation of waves by turbulent wind. *Journal of Fluid Mechanics*, 2: 417–445, 1957.

O. M. Phillips. The equilibrium range in the spectrum of wind-generated waves. *Journal of Fluid Mechanics*, 4(4):426–434, 1958. doi: 10.1017/S0022112058000550.

W. J. Pierson and W. Marks. The power spectrum analysis of ocean-wave records. *Eos, Transactions American Geophysical Union*, 33(6):834–844, 1952. doi: https://doi.org/10.1029/TR033i006p00834. URL https://agupubs.onlinelibrary.wiley.com/doi/abs/10.1029/TR033i006p00834.

W.J. Pierson, G. Neuman, and R.W. James. Practical methods for observing and forecasting ocean waves by means of wave spectra and statistics. 1955. doi: http://dx.doi.org/10.25607/OBP-985.

Willard J. Pierson Jr. and Lionel Moskowitz. A proposed spectral form for fully developed wind seas based on the similarity theory of s. a. kitaigorodskii. *Journal of Geophysical Research (1896-1977)*, 69(24):5181–5190, 1964. doi: https://doi.org/10.1029/JZ069i024p05181. URL https://agupubs.onlinelibrary.wiley.com/doi/abs/10.1029/JZ069i024p05181.

François Pimont, Jean-Luc Dupuy, Rodman R. Linn, Jeremy A. Sauer, and Domingo Muñoz-Esparza. Pressure-gradient forcing methods for large-eddy simulations of flows in the lower atmospheric boundary layer. *Atmosphere*, 11(12), 2020. ISSN 2073-4433. doi: 10.3390/atmos11121343. URL https://www.mdpi.com/2073-4433/11/12/1343.

Stephen B. Pope. *Turbulent Flows*. Cambridge University Press, 2000.

S. Porchetta, O. Temel, D. Muñoz Esparza, J. Reuder, J. Monbaliu, J. van Beeck, and N. van Lipzig. A new roughness length parameterization accounting for wind–wave (mis)alignment. *Atmospheric Chemistry and Physics*, 19(10):6681–6700, 2019. doi: 10.5194/acp-19-6681-2019. URL https://www.atmos-chem-phys.net/19/6681/2019/.

Nicolas Reul, Hubert Branger, and Jean-Paul Giovanangeli. Air-Flow separation above unsteady breaking waves. *Physics of Fluids*, 11(7):1959–1961, 1999. URL https://hal.archives-ouvertes.fr/hal-00192471.

Nicolas Reul, Hubert Branger, and Jean-Paul Giovanangeli. Air flow structure over short-gravity breaking water waves. *Boundary-Layer Meteorology*, 126:477–505, 04 2008. doi: 10.1007/s10546-007-9240-3.

Abdolrahim Rezaeiha, Ricardo Pereira, and Marios Kotsonis. Fluctuations of angle of attack and lift coefficient and the resultant fatigue loads for a large Horizontal Axis Wind turbine. *Renewable Energy*, 114(PB):904–916, 2017.

Lewis Fry Richardson and William Napier Shaw. The supply of energy from and to atmospheric eddies. *Proceedings of the Royal Society of London. Series A, Containing Papers of a Mathematical and Physical Character*, 97(686):354–373, 1920. doi: 10.1098/rspa.1920.0039. URL https://royalsocietypublishing.org/doi/abs/10.1098/rspa.1920.0039.

Philip L. Richardson. Leonardo da vinci's discovery of the dynamic soaring by birds in wind shear. *Notes and Records: the Royal Society Journal of the History of Science*, 73(3):285–301, 2019. doi: 10.1098/rsnr.2018.0024. URL https://royalsocietypublishing.org/doi/abs/10.1098/rsnr.2018.0024.

Benbouzid Mohamed Le Boulluec Marc Salic Tom, Charpentier Jean Frédéric. Control strategies for floating offshore wind turbine: Challenges and trends, 2019. URL https://archimer.ifremer.fr/doc/00588/69991/.

Betsy R. Seiffert and Guillaume Ducrozet. Simulation of breaking waves using the high-order spectral method with laboratory experiments: wave-breaking energy dissipation. *Ocean Dynamics*, 68(1):65–89, Jan 2018. ISSN 1616-7228. doi: 10.1007/s10236-017-1119-3. URL https://doi.org/10.1007/s10236-017-1119-3.

Betsy R. Seiffert, Guillaume Ducrozet, and Félicien Bonnefoy. Simulation of breaking waves using the high-order spectral method with laboratory experiments: Wave-breaking onset. *Ocean Modelling*, 119:94–104, 2017. ISSN 1463-5003. doi: https://doi.org/10.1016/j.ocemod.2017.09.006. URL https://www.sciencedirect.com/science/article/pii/S1463500317301427.

A. Semedo, Ø. Saetra, A. Rutgersson, K. K. Kahma, and H. Pettersson. Wave-induced wind in the marine boundary layer. *Journal of the Atmospheric Sciences*, 66(8):2256–2271, 2009.

Susumu Shimada, Jay Prakash Goit, Teruo Ohsawa, Tetsuya Kogaki, and Satoshi Nakamura. Coastal wind measurements using a single scanning lidar. *Remote Sensing*, 12(8):1347, 2020.

J. H. Simpson. Observations of the Directional Characteristics of Sea Waves. *Geophysical Journal International*, 17(1):93–120, 01 1969. ISSN 0956-540X. doi: 10.1111/j.1365-246X.1969.tb06380.x. URL https://doi.org/10.1111/j.1365-246X.1969.tb06380.x.

Irving A. Singer. Steadiness of the wind. *Journal of Applied Meteorology and Climatology*, 6(6):1033 – 1038, 1967. doi: 10.1175/1520-0450(1967)006<1033:SOTW>2.0.CO;2. URL https://journals.ametsoc.org/view/journals/apme/6/6/1520-0450_1967_006_1033_sotw_2_0_co_2.xml.

Anna Sjöblom and Ann-Sofi Smedman. The turbulent kinetic energy budget in the marine atmospheric surface layer. *Journal of Geophysical Research: Oceans*, 107(C10):6–1–6–18, 2002. doi: https://doi.org/10.1029/2001JC001016. URL https://agupubs.onlinelibrary.wiley.com/doi/abs/10.1029/2001JC001016.

D. Smith, Stuart, J. Anderson, Robert, A. Oost, Wiebe, C. Kraan, Nico Maat, Janice DeCosmo, B. Katsaros, Kristina, L. Davidson, Kenneth, Karl Bumke, Lutz Hasse, and M. Chadwick, Helen. Sea surface wind stress and drag coefficients: The hexos results, 1991. URL https://calhoun.nps.edu/handle/10945/40122.

R. L. Snyder, F. W. Dobson, J. A. Elliott, and R. B. Long. Array measurements of atmospheric pressure fluctuations above surface gravity waves. *Journal of Fluid Mechanics*, 102:1–59, 1981. doi: 10.1017/S0022112081002528.

Philippe R Spalart, Robert D Moser, and Michael M Rogers. Spectral methods for the navier-stokes equations with one infinite and two periodic directions. *Journal of Computational Physics*, 96(2):297 – 324, 1991. ISSN 0021-9991. doi: https://doi.org/10.1016/0021-9991(91)90238-G. URL http://www.sciencedirect.com/science/article/pii/002199919190238G.

E. A. Spiegel and G. Veronis. On the boussinesq approximation for a compressible fluid. *Astrophysical Journal, vol. 131, p.442*, 1960.

Erik Stenberg. On numerical simulations of turbulent flows subjected to system rotation, 2016.

G.G. Stokes. On the theory of oscillatory waves. *Mathematical and Physical Papers, Volume I*, page 197–229, 1880.

Peter P. Sullivan, James C. McWilliams, and Chin-Hoh Moeng. Simulation of turbulent flow over idealized water waves. *Journal of Fluid Mechanics*, 404:47–85, 2000. doi: 10.1017/S0022112099006965.

Peter P. Sullivan, James B. Edson, Tihomir Hristov, and James C. McWilliams. Large-eddy simulations and observations of atmospheric marine boundary layers above nonequilibrium surface waves. *Journal of the Atmospheric Sciences*, 65(4):1225–1245, 2008. doi: 10.1175/2007JAS2427.1.

Peter P. Sullivan, James C. McWilliams, and Edward G. Patton. Large-eddy simulation of marine atmospheric boundary layers above a spectrum of moving waves. *Journal of the Atmospheric Sciences*, 71(11):4001–4027, 2014.

Irene Suomi, Sven-Erik Gryning, Ewan J. O'Connor, and Timo Vihma. Methodology for obtaining wind gusts using doppler lidar. *Quarterly Journal of the Royal Meteorological Society*, 143(706):2061–2072, 2017. doi: https://doi.org/10.1002/qj.3059. URL https://rmets.onlinelibrary.wiley.com/doi/abs/10.1002/qj.3059.

H.U. Sverdrup. *The Eddy Conductivity of the Air Over a Smooth Snow Field: Results of the Norwegian-Swedish Spitsbergen Expedition in 1934*. Geofysiske publikasjoner. I kommisjon hos Cammermeyers boghandel, 1936. URL https://books.google.fr/books?id=ASFCOQAACAAJ.

Hitoshi Tamura, William M. Drennan, Clarence O. Collins, and Hans C. Graber. Turbulent airflow and wave-induced stress over the ocean. *Boundary-Layer Meteorology*, 2018.

G. I. Taylor. The spectrum of turbulence. *Proceedings of the Royal Society of London. Series A - Mathematical and Physical Sciences*, 164(919):476–490, 1938. doi: 10.1098/rspa.1938.0032. URL https://royalsocietypublishing.org/doi/abs/10.1098/rspa.1938.0032.

P. D. Thomas and C. K. Lombard. Geometric conservation law and its application to flow computations on moving grids. *AIAA Journal*, 17(10):1030–1037, 1979. doi: 10.2514/3.61273. URL https://doi.org/10.2514/3.61273.

William Thomson. Hydrokinetic solutions and observations. *Philosophical Magazine*, 42: 326–378, 1871.

Yoshiaki Toba. Local balance in the air-sea boundary processes. *Journal of the Oceanographical Society of Japan*, 29(5):209–220, Sep 1973. ISSN 1573-868X. doi: 10.1007/BF02108528. URL https://doi.org/10.1007/BF02108528.

Chenning Tong and Mengjie Ding. Velocity-defect laws, log law and logarithmic friction law in the convective atmospheric boundary layer. *Journal of Fluid Mechanics*, 883, 01 2020. doi: 10.1017/jfm.2019.898.

Ib Troen and Erik Lundtang Petersen. *European Wind Atlas*. Risø National Laboratory, 1989. ISBN 87-550-1482-8.

Cornelis A. Van Duin and Peter A. E. M. Janssen. An analytic model of the generation of surface gravity waves by turbulent air flow. *Journal of Fluid Mechanics*, 236:197–215, 1992. doi: 10.1017/S0022112092001393.

F. Veron, G. Saxena, and S. K. Misra. Measurements of the viscous tangential stress in the airflow above wind waves. *Geophysical Research Letters*, 34(19), 2007. doi: https://doi.org/10.1029/2007GL031242. URL https://agupubs.onlinelibrary.wiley.com/doi/abs/10.1029/2007GL031242.

T. von Kármán. Progress in the statistical theory of turbulence. *Proceedings of the National Academy of Sciences of the United States of America*, 34(11):530–539, Nov 1948. ISSN 0027-8424. doi: 10.1073/pnas.34.11.530. URL https://pubmed.ncbi.nlm.nih.gov/16588830. 16588830[pmid].

Li-Hao Wang, Wu-Yang Zhang, Xuanting Hao, Wei-Xi Huang, Lian Shen, Chun-Xiao Xu, and Zhaoshun Zhang. Surface wave effects on energy transfer in overlying turbulent flow. *Journal of Fluid Mechanics*, 893:A21, 2020. doi: 10.1017/jfm.2020.246.

M. Wilczek and Y. Narita. Wave-number–frequency spectrum for turbulence from a random sweeping hypothesis with mean flow. *Phys. Rev. E*, 86:066308, Dec 2012. doi: 10.1103/PhysRevE.86.066308. URL https://link.aps.org/doi/10.1103/PhysRevE.86.066308.

Andreas Will, Naveed Akhtar, Jennifer Brauch, Marcus Breil, Edouard Davin, Ha Ho-Hagemann, Eric Maisonnave, Markus Thürkow, and Stefan Weiher. The cosmo-clm 4.8 regional climate model coupled to regional ocean, land surface and global earth system models using oasis3-mct: Description and performance. *Geoscientific Model Development*, 10:1549–1586, 04 2017. doi: 10.5194/gmd-10-1549-2017.

Michael H. Wong, Philip S. Marcus, Amy A. Simon, Imke de Pater, Joshua W. Tollefson, and Xylar Asay-Davis. Evolution of the horizontal winds in jupiter's great red spot from one jovian year of hst/wfc3 maps. *Geophysical Research Letters*, 48(18):e2021GL093982, 2021. doi: https://doi.org/10.1029/2021GL093982. URL https://agupubs.onlinelibrary.wiley.com/doi/abs/10.1029/2021GL093982. e2021GL093982 2021GL093982.

Di Yang and Lian Shen. Characteristics of coherent vortical structures in turbulent flows over progressive surface waves. *Physics of Fluids*, 21(12):125106, 2009. doi: 10.1063/1.3275851. URL https://doi.org/10.1063/1.3275851.

Di Yang and Lian Shen. Direct-simulation-based study of turbulent flow over various waving boundaries. *Journal of Fluid Mechanics*, 650:131–180, 2010. doi: 10.1017/S0022112009993557.

Di Yang and Lian Shen. Simulation of viscous flows with undulatory boundaries: Part ii. coupling with other solvers for two-fluid computations. *Journal of Computational Physics*, 230(14):5510–5531, 2011. ISSN 0021-9991. doi: https://doi.org/10.1016/j.jcp.2011.02.035. URL https://www.sciencedirect.com/science/article/pii/S0021999111001240.

Di Yang, Charles Meneveau, and Lian Shen. Effect of downwind swells on offshore wind energy harvesting – a large-eddy simulation study. *Renewable Energy*, 2014.

Zixuan Yang, Bing-Qing Deng, and Lian Shen. Direct numerical simulation of wind turbulence over breaking waves. *Journal of Fluid Mechanics*, 2018.

Kianoosh Yousefi and Fabrice Veron. Boundary layer formulations in orthogonal curvilinear coordinates for flow over wind-generated surface waves. *Journal of Fluid Mechanics*, 888: A11, 2020. doi: 10.1017/jfm.2020.32.

V. E. Zakharov and N. N. Filonenko. Weak turbulence of capillary waves. *Journal of Applied Mechanics and Technical Physics*, 8(5):37–40, Sep 1967. ISSN 1573-8620. doi: 10.1007/BF00915178. URL https://doi.org/10.1007/BF00915178.

Yunyan Zhang and Stephen A. Klein. Mechanisms affecting the transition from shallow to deep convection over land: Inferences from observations of the diurnal cycle collected at the arm southern great plains site. *Journal of the Atmospheric Sciences*, 67(9):2943 – 2959, 2010. doi: 10.1175/2010JAS3366.1. URL https://journals.ametsoc.org/view/journals/atsc/67/9/2010jas3366.1.xml.

APPENDIX

A THEORETICAL, EMPIRICAL AND NUMERICAL FRAMEWORKS

A.1 CANONICAL ANALYTICAL SOLUTIONS

A.1.1 STOKES WAVE THEORY

The analytical solution for a monochromatic wave propagating within the framework established in section I.1.2.1 is available from the development of a perturbation series by Sir George Stokes (1847, reprinted in Stokes [1880]). The solution is presented up to 5th order accuracy e.g., in Fenton [1985] also considering the Doppler effect due to currents. The equations below are restricted to the first other solution, also know as Airy wave theory first published at the Encyclopaedia Metropolitana in 1841 [Craik, 2004].

Monochromatic waves are described by the free parameters: period T, height $H = 2a$ and water depth d. Other wave properties are the angular frequency $w = 2\pi/T$, frequency $f = 1/T$, wave length λ and wave number $k = 2\pi/\lambda$. Linearization relies in non-shallow water (dispersion parameter $kd \geq O(1)$) and low steepness $ka << O(1)$ assumptions. The wave propagates into x direction through the time t. z vertical axis is directed upwards and has origin in the still water position. $g = 9.81$ m/s^2 stands for gravity constant. The specific mass is $\rho \sim 10^3$ kg/m^3, but the quantities here presented are given per specific mass.

The linear dispersion equation relates the wave angular frequency, and period, to its length on a given depth:

$$\omega^2 = gk\tanh(kd) \tag{A.1}$$

The analytical solution of the linear model presents the free surface elevation $\eta(x,t)$ and the velocity potential $\phi_{\boldsymbol{u}}(x,z,t)$, such as:

$$\begin{aligned} \eta &= a\cos(kx - \omega t) \\ \phi_{\boldsymbol{u}} &= \frac{ag}{\omega}\frac{\cosh[k(z+d)]}{\cosh[kd]}\sin(kx - \omega t) \end{aligned} \tag{A.2}$$

The velocity field (v_x, v_z) is by definition:

$$\begin{aligned} v_x &= \frac{\partial \phi_{\boldsymbol{u}}}{\partial x} = \frac{agk}{\omega}\frac{\cosh[k(z+d)]}{\cosh[kd]}\cos(kx-\omega t) \\ v_z &= \frac{\partial \phi_{\boldsymbol{u}}}{\partial z} = \frac{agk}{\omega}\frac{\sinh[k(z+d)]}{\cosh[kd]}\sin(kx-\omega t) \end{aligned} \tag{A.3}$$

Group velocity c_g is the velocity at which energy is propagated with the waves. Is it so that a regular wave front travels with velocity c_g. No wave can be observed beneath its front. The free surface elevation appears to travel with phase velocity $c = \lambda/T$, which is always greater than c_g. Just before the wave front, the free surface perturbation disappears limiting the energy propagation velocity to c_g. The velocities c_g and c are defined in equation A.4, and related by equation A.5.

$$c_g \equiv \frac{\partial w}{\partial k} \qquad c \equiv \frac{w}{k} \tag{A.4}$$

$$\begin{aligned} c_g &= c \cdot n \\ n &= 0.5\left[1 + \frac{2kd}{\sinh(2kd)}\right] \end{aligned} \tag{A.5}$$

Higher order phenomena Higher n_{th} order effects occurs in the n_{th} multiplied frequency/ wave-number of the wave frequency/ wave-number, and do not follow the dispersion relation, being so called Bounded Waves (Opposed to 1st order Free Waves). They are generally secondary to lower order effects, but may become important when kd gets sufficiently low, or ka gets sufficiently high. The free surface profile resultant from higher order approaches is not symmetric with respect to the mean surface $z = 0$, as the crests are amplified and the troughs are flattened. The orbitals do not form a closed curve as predicted in first order theory, but rather advance constantly on the wave propagation direction, with the appearance of the Stokes Drift as an effective mass transportation mechanism (comparable to ocean currents) due to Ocean Waves.

Variable bathymetry The depth is considered constant through current employed numerical framework, and no solid boundaries are placed in the domain. But in a variable bathymetry scenario, the wave length and group velocity change, and so do the wave height as consequence, to conserve power in a phenomena called shoaling. In a multi-directional and changing depth scenario, refraction also occurs with the local deformation of the wave front line. The generation of waves induced by moving boundaries such as an offshore platform is called radiation.

A.1.2 Boundary Layer theory

The boundary layer theory is first attributed to Ludwig Prandtl in his revolutionary presentation at the Third International Mathematics Congress, at 1904 (See, e.g., Anderson [2005]).

With major assumptions introduced to the theoretical framework established, this canonical case is crucial for the development of more complex situations characterizing the Atmospheric Boundary Layer described in section I.2.2. The theory here presented goes well beyond the initial development of Prandtl, and one shall notably remark the contributions of Theodore von Kármán in 1930 (c.f. Tong and Ding [2020] and Eckert [2018]).

Coriolis and buoyancy forces are neglected. The mean flow occurs in two dimensions, and being statistically steady is described by the steady Reynolds Averaged Navier Stokes Equations I.1.7 (With $\partial\overline{u_i}/\partial t = 0$). The free-stream undisturbed velocity is U_∞, the longitudinal length is L_0, and the boundary layer thickness $\delta(x_1)$ is defined as the distance to the wall (x_3) on which the velocity is $0.99U_\infty$. That defines the non dimensional length $x_1^* = x_1/L_0$ and wall distance $x_3^* = x_3/\delta$ scales. The non dimensional velocity vector $\boldsymbol{u}^* = u_1 U^{-1}\hat{\boldsymbol{j}}_{\mathbf{1}} + u_3 V^{-1}\hat{\boldsymbol{j}}_{\mathbf{3}}$ is also defined, so that the mass conservation equation I.1.1 reveals that the vertical velocity scales according to $V \sim U\delta/L_0$.

Characteristic convection and diffusion time scales are respectively $t^{(cnv)} = L_0/U$ and $t^{(dif)} = \delta^2/\nu$. In laminar flows one can assume $t^{(cnv)} \sim t^{(dif)}$ revealing a non dimensional viscosity $\nu^* = \nu \cdot U\delta^2/L_0$. In turbulent flows the velocity fluctuations $\boldsymbol{u}'$ can be estimated as, e.g., $\boldsymbol{u}' \sim 0.1\overline{\boldsymbol{u}}$, so considering that δ/L_0 is typically about 1%, its non dimensional form is defined as $\boldsymbol{u}'^* = \boldsymbol{u}'/(U\sqrt{\delta/L_0})$. Thus, the time scale for turbulent diffusion is $t^{(tur)} = \delta/\boldsymbol{u}' \sim (\delta/L_0)^{0.5} t^{(cnv)}$, and the characteristic turbulent viscosity $\nu^{(tur)} = \delta^2/t^{(tur)}$. Finally it is assumed that δ is very small compared to L_0.

Neglecting terms on the order of $\delta/L_0 << 1$, the momentum RANS equations I.1.26 are significantly simplified:

$$\overline{u}_1 \frac{\partial \overline{u}_1}{\partial x_3} + \overline{u}_3 \frac{\partial \overline{u}_1}{\partial x_3} = \frac{\partial}{\partial x_3}\left[\nu \frac{\partial \overline{u}_1}{\partial x_3} - \overline{u_1' u_3'}\right] - \frac{1}{\rho_0}\frac{\partial \overline{p}}{\partial x_1}, \tag{A.6}$$

$$\frac{\partial\left(u_3' u_3'\right)}{\partial x_3} - \frac{1}{\rho_0}\frac{\partial p'}{\partial x_3} = 0. \tag{A.7}$$

The integration of equation A.7 from $x_3 = (0..x_3)$ gives the algebraic relation $\overline{p}(x_1, x_3, t) = \overline{p}_w(x_1, t) - \rho_0\left(u_3' u_3'\right)$.

Representative of the overall momentum flux, the wall stress $\tau_w = \mu\partial\overline{u}_1/\partial x_3$ characterizes the friction velocity $u^* = \sqrt{\tau_w/\rho}$ and the non dimensional wall distance $z^+ = zu^*/\nu$. The flow is fully determined by ρ, μ, δ and $\partial p_w/\partial x$, or equivalently, e.g., ρ, μ, δ and u^*. Two independent non dimensional variables can be formed to characterize the velocity profiles $\overline{u}_1/(u^*) = f_u(x_3/\delta, \delta u^2\rho/\mu)$ or its derivatives $\partial\overline{u}_1/\partial x_3 = (u^*/x_3) f_{du}(z^+, x_3/\delta)$.

If the flow is considered either close or distant enough from the wall, further simplifications take place. The inner region occurs when $x_3/\delta << 1$ (< 0.1), in which case according to Prandtl's (1925) postulate and its observation through physical and numerical experiments (c.f. [Pope, 2000], pg. 272 and section 7.3.3), the velocity profile is invariant to δ, so $\partial\overline{u}_1/\partial x_3 = (u^*/x_3) f_{du}(z^+)$. On the outer region for which $x_3 >> z^+ (> 50)$, the flow

is invariant to viscosity such that the velocity defect may be evaluated by $\partial(\overline{u}_1 - \overline{u}_\infty)/\partial x_3 = -u^* g_{du}(z/\delta)$. The viscous sublayer is a most confined region ($z^+ < 5$) where turbulence is negligible such that integration of the friction velocity definition on $0 < z^+ < 1$ leads to $u_1 = u^* z^+$.

Being the global Reynolds large enough, the inner and outer regions are expected to superpose within $z_3/\delta < 0.3$ and $z^+ > 30$. (c.f. [Pope, 2000], pg. 275). Consequently in this region the flow is invariant to thickness δ and viscosity ν, so that the function $f_{du}(z^+, x_3/\delta)$ evaluates into a constant, i.e., the von Karman constant κ^{-1}. Hence the name log-law region, where $\partial\overline{u}_1/\partial x_3 = (u^*/x_3)\kappa^{-1}$ integrates from 0 to x_3 according to a friction log-law velocity profile:

$$\overline{u}_1 = \frac{u^*}{\kappa} \ln\left(z^+\right) + B, \tag{A.8}$$

where the integration constant B may be arbitrarily defined to incorporate a physically inspired roughness length z_o:

$$\overline{u}_1 = \frac{u^*}{\kappa} \ln\left(\frac{z^+}{z_o^+}\right). \tag{A.9}$$

According to [Pope, 2000] (pg. 274) values for the introduced constants are usually observed within 5% discrepancy from $\kappa = 0.41$ and $B = 5.2$. Alternatively, one may use the velocity defect law $\partial(\overline{u}_1 - \overline{u}_\infty)/\partial x_3 = -u^* g_{du}(z/\delta)$, where $g_{du}(z/\delta) = f_{du}(z^+, x_3/\delta) = \kappa^{-1}$, which integrates from x_3 to δ into the defect log-law:

$$\overline{u}_1 - \overline{u}_\infty = \frac{u^*}{\kappa} \ln\left(\frac{z}{\delta}\right) + B_\delta, \tag{A.10}$$

being B_δ a flow dependent constant.

Considering the eddy viscosity hypothesis where the Reynolds Shear Stresses (Or fluxes) are given by $\tau_{12}^{(r)} = \overline{u_1' u_3'} = \nu_t\, \partial\overline{u}_1/\partial x_3$ in the outer region where $\tau = \tau^{(r)}$, the only possible choice for ν_t consistent with the constant flux ($\tau = \tau_w$) and the log-law regions is $\nu_t = u^* \kappa x_3$.

A.2 Wind-Wave interaction mechanisms

A.2.1 Flow description

The effort to describe metocean conditions in a causal approach leads to fundamental questions such as: How are Ocean waves generated; and what drives the wind close to the Ocean surface? These two questions are intrinsically related to each other, and result from complex

wind-wave interactions taking place in the lower layers of the ABL above the ocean. As discussed in section I.3.1 the wind is responsible for the waves generation and damping, and the waves disturb the wind as introduced in section I.3.2.

Related as they can be these two fundamental problems, i.e., of wave growth and wave induced disturbances in the wind, are rarely evaluated together in Wind-Wave interaction studies. It happens that these physics evolve in very different time scales: Waves will develop much slower than the wind, and particularly in deep waters, swells may travel during a few days and over hundreds or thousands of kilometers, before being submitted to significant changes; the wind dynamics on the other side might significantly change in a few minutes and over short distances due to atmospheric changes in pressure distribution or stratification regime. A consequence is that, though Wave and Wind dynamics shall tend to an equilibrium, this situation is rarely observed in the field.

Away from the idealized equilibrium condition, one distinguish the young and old sea regimes. Young sea conditions occur when rapid winds force the free-surface, transferring its momentum to comparatively slow traveling waves. Old seas occur when fast traveling waves (Notably a swell) encounter comparatively slow wind conditions in the lower part of the MABL. The non-dimensional quantity usually employed in the literature to characterize the wind-wave interaction regime is the Wave Age WA= c/U, defined as the ratio between the wave phase velocity c, and a characteristic velocity scale in the atmosphere U. The wave induced disturbances into the wind are more significant in Old sea conditions, e.g., a swell encountering light winds, which happens quite often in coastal areas.

As an introduction to the described scenario, the asymptotic cases where the wind is static (Old seas), and where the wave lengths are on the order of the ABL roughness length (Young seas), are respectively shown in figures A.1 and A.2. Note that neither of the cases are expected to hold, and will slowly tend to equilibrium: The swell effectively drives the wind which will not hold still, and the fast traveling waves are damped accordingly as their energy transfers upwards into the atmosphere; The short ripples that initially allow the ABL to be considered a rough but flat terrain will grow in energy and length, soon becoming significant and eventually focusing in large scale motions, i.e., a swell.

In the absence of wind and assuming an irrotational framework, the Stokes solutions described in the appendix A.1.1 are extended to the atmosphere such as shown in figure A.1: A discontinuity then appears between the opposed longitudinal velocities at crests and troughs, of air and water domains. In the viscous (rotational) flow the discontinuity is balanced by the viscous boundary layer developed in the interface and highlighted in the figure. The vertical motions are perfectly in phase between air and water, and the air pressure distribution (fictitious resultant force F_p in the figure) is perfectly out of phase with the wave slope, resulting in the wave damping. The stokes drift also applies to the atmosphere, which will induce a wave-driven jet in the lower part of the ABL.

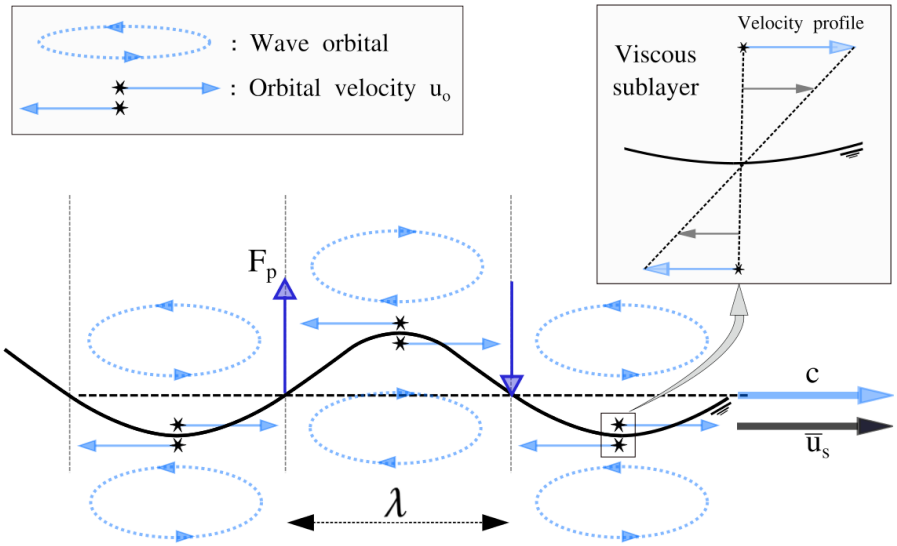

Figure A.1: Asymptotic Old-Sea: Monochromatic wave (Swell) of length λ and phase velocity c propagating under static wind and neutral atmospheric condition. The Stokes orbitals (represented by the spirals) and drift are extended to the atmosphere. In crests and troughs the longitudinal velocities (horizontal arrows with opposite senses) are discontinuous. The discontinuity reveals a viscous boundary layer across the free-surface. The wave is damped by the pressure distribution perfectly out of phase with the wave slope, represented by the fictitious resultant force F_p.

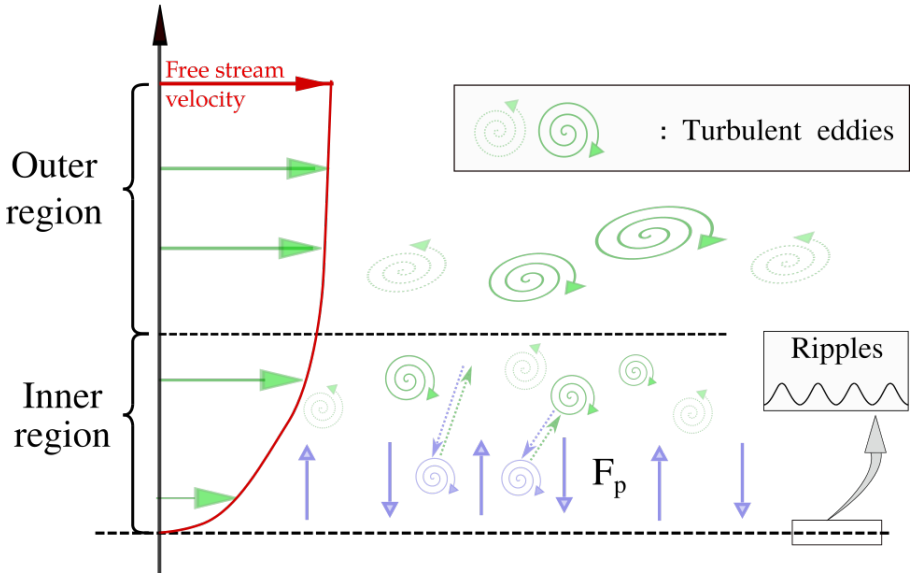

Figure A.2: Asymptotic Young-Sea: Waves with lengths on the order of the ABL roughness length may occur in the free-surface. Turbulence generates and feeds energy to the ripples by means of fluctuating pressure forces F_p [Phillips, 1957]. In the inner region, turbulence is mostly isotropic and blocked by the free-surface. In the outer region turbulence is highly anisotropic and dependent on the other boundary conditions. The shear is positive, and the $u'w'$ correlations predominantly negative (Clock-wise turning eddies).

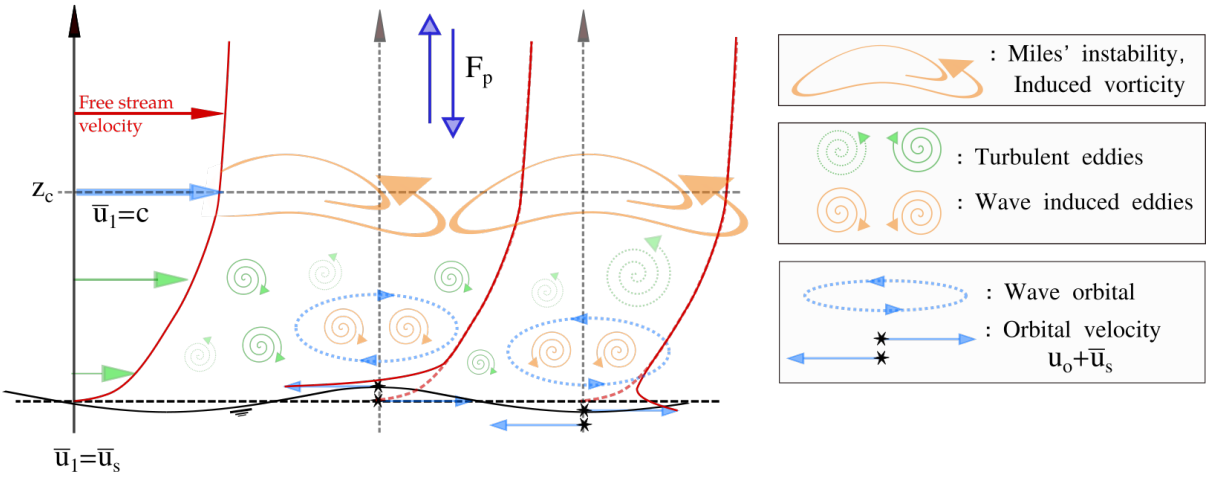

Figure A.3: A monochromatic wave with phase velocity c drags an initially undisturbed ABL flow. The problem is usually described in the wave following frame of reference, and a reversed flow appears below z_c where $\overline{u}_1(z_c) = c$, inducing the vorticity distribution attributed to the solution of Miles' BVP, in Miles [1957].

Now in the asymptotic case of young (new-born) seas pictured in figure A.2, the ABL is described such as in section I.2.2, with a modified roughness length accounting for the free-surface ripples. The fully turbulent flow, which is above the viscous inner layer, is characterized in two regions: The inner region, where turbulence is blocked by the free-surface and exhibits an isotropic, quasi-equilibrium behavior; The outer region where large scale anisotropic turbulence is strongly dependent on the other boundary conditions. The positive shear generates predominantly negative $u'w'$ correlations, depicted by the predominant clock-wise turning eddies in figure A.2. Very close to the surface a resonance mechanism [Phillips, 1957] between turbulent pressure fluctuations and the free-surface dynamics induces the (F_p) appearance and growing of small waves (Or ripples) in the initially calm water, changing the roughness length that in turn controls turbulence statistics across the ABL extension.

A more general case is depicted in figure A.3 when the arbitrary wave of fig. A.1 with phase velocity c encounters the initially undisturbed ABL flow of fig. A.2. The velocity profile equals the mean surface velocity $\overline{u_s}$ at the mean surface height, which might account for ocean currents and the stokes drift acting in the surface. The stokes orbital propagate into the atmosphere, so the mean profiles are periodically disturbed: Above the crests the mean velocity is $\overline{u_s} - \overline{u_o}$; and above the thoughts $\overline{u_s} + \overline{u_o}$. The waves orbitals, irrotational by definition from the potential theory framework, are now submitted to shear turbulent dynamics, and will periodically feed turbulent eddies of opposite rotations into the atmosphere through processes of vortex roll-up and break-down. Unless the free-stream velocity is lower than c, then far enough from the surface there exists a critical height (z_c) where the mean flow velocity is $\overline{u}_1 = c$.

In a moving frame traveling with velocity c, one observes the reversed flow below z_c, and the instability mechanism of Miles [1957] induce a continuous vorticity distribution at z_c, which is depicted in detail at figure A.4. The geometrical effects of the moving bottom induce periodic disturbances of the flow streamlines such as depicted in figure A.5. In this last figure one observes other wave growing mechanisms, such as the separated sheltering

of Jeffreys [1925], and the non-separated sheltering and outer flow perturbations introduced in Belcher and Hunt [1993].

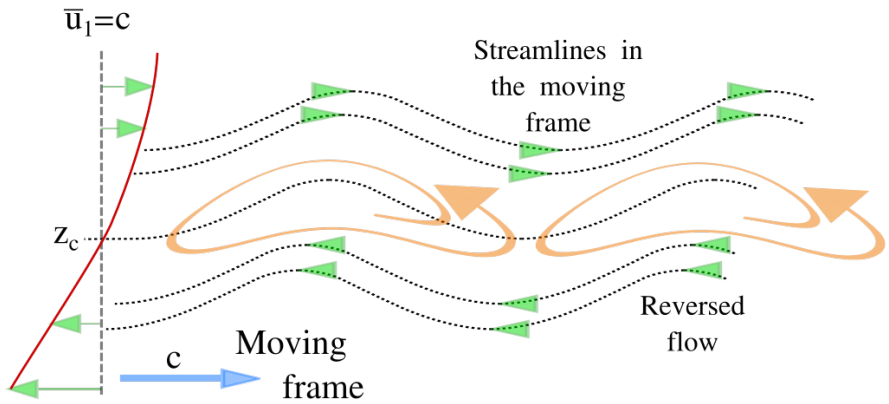

Figure A.4: Miles mechanism of wave growth/ damping, relying in the existence of a critical height z_c where the mean wind $\overline{u}_1$ equals the phase velocity of the wave. A discontinuity in the BVP posed by Miles [1957] appears through a continuous vorticity distribution (Orange spirals) in the critical height, which is responsible for the wave growth/ damping (F_p).

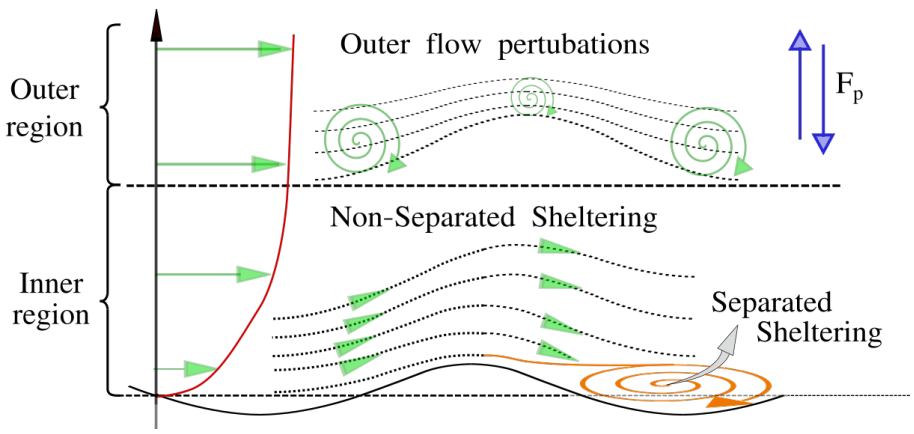

Figure A.5: Sheltering related mechanisms of wave grow or damping (F_p). The (separated) sheltering theory of Jeffreys [1925] relies in the flow detachment denoted by the orange spiral. The detachment can only occur in large wave slopes, but a non-separated sheltering effect invariably occurs as described in Belcher and Hunt [1993]. In the inner region there is an asymmetric disturbance of the streamlines and stresses. In the outer region the disturbance is mostly symmetric, but displaced by the non-separated sheltering of the inner region. The (partially) out-of-phase pressure distributions leads to the resultant pressure forces F_p.

A.3 Fourier Transforms

Definitions - Complex The two-dimensional (2D) Fourier Transform (FT) of the field variable $\chi(x,t)$, in this example function of the longitudinal position x and time t, gives the approximation of χ in the wave-number-angular-frequency ($k = 2\pi/x$ and $w = 2\pi/t$) do-

main. So if the k and w domains are discretized respectively in $2M+1$ and $2N+1$ intervals, then the discrete FT is defined in complex notation as:

$$\chi(x,t) = \sum_{m=-M}^{M} \sum_{n=-N}^{N} \left[c_{mn}\, e^{i(mx+nt)} \right], \tag{A.11}$$

being the complex-valued Fourier coefficients $c_{mn}(k,w)$ (physically meaning the EDF, or energy spectra) determined by a Fast Fourier Transform (FFT) algorithm. If the EDF is computed from an auto-correlation function $\chi(x,t) \rightarrow R(r,\tau)$, then $c_{mn}(k,w)$ is real.

That can be alternatively written in terms of the four quadrant spectra $Q_{\pm\pm}$:

$$\begin{aligned} \chi(x,t) = b0 + \sum_{m=1}^{M} \sum_{n=1}^{N} \Bigg[& \overbrace{c1_{mn}}^{Q_{--}(k,w)}\; e^{i(-kx-wt)} + \overbrace{c2_{mn}}^{Q_{-+}(k,w)}\; e^{i(-kx+wt)} \\ & + \underbrace{c3_{mn}}_{Q_{+-}(k,w)}\; e^{i(+kx-wt)} + \underbrace{c4_{mn}}_{Q_{++}(k,w)}\; e^{i(+kx+wt)} \Bigg]. \end{aligned} \tag{A.12}$$

The 2D FT is separable, so that a 2D FFT can be obtained from multiple one-dimensional FFTs, acting sequentially in k and w directions, or vice-versa. It is also conjugate fold-symmetric, meaning $c1 = c4^*$ ($|c1| = |c4|$) and $c2 = c3^*$ ($|c2| = |c3|$).

According to Parseval's theorem, $\sum\sum |\chi(x,t)|^2 \mathrm{d}x\mathrm{d}t = \sum\sum |c_{mn}(k,w)|^2 \mathrm{d}k\mathrm{d}w$, with $|c_{mn}(k,w)|^2$ commonly referred as the power spectrum Q_R^2. So taking the square of the spectral content (inside the summation) in equation A.12, yields:

$$\sum_{m=1}^{M} \sum_{n=1}^{N} \left[\overbrace{(c1_{mn} + c2_{mn} + c3_{mn} + c4_{mn})}^{Q_R}{}^2\; e^{-2i(kx+wt)} \right], \tag{A.13}$$

defined in terms of the resultant one-sided energy spectrum Q_R.

Definitions - Trigonometric In the numerical application the FT is rather defined in the real valued formulation:

$$\begin{aligned} \chi(x,t) = b0 + \sum_{m=1}^{M} \sum_{n=1}^{N} \Big[& d1_{mn}\, \sin(kx)\sin(wt) - d2_{mn}\, \sin(kx)\cos(wt) \\ & - d3_{mn}\, \cos(kx)\sin(wt) + d4_{mn}\, \cos(kx)\cos(wt) \Big]. \end{aligned} \tag{A.14}$$

Taking the square of the spectral content (inside the summation) in equation A.14 yields to the power spectrum Q_R^2:

$$\sum_{m=1}^{M}\sum_{n=1}^{N}\left[\overbrace{(d1_{mn}+d2_{mn}+d3_{mn}+d4_{mn})}^{Q_R}{}^2\ [\sin(kx)\sin(wt)]^2\right]. \tag{A.15}$$

Trigonometric and Complex FT conversion Using the identity $e^{\pm ix} = \cos(x) \pm i\sin(x)$ in equation A.12, and comparing it to equation A.14, one establish the relation between trigonometric and complex Fourier coefficients:

$$\begin{bmatrix} c1 \\ c2 \\ c3 \\ c4 \end{bmatrix} = \begin{bmatrix} -1 & +i & +i & +1 \\ +1 & +i & -i & +1 \\ +1 & -i & +i & +1 \\ -1 & -i & -i & +1 \end{bmatrix} \begin{bmatrix} d1 \\ d2 \\ d3 \\ d4 \end{bmatrix}, \tag{A.16}$$

or conversely:

$$\begin{bmatrix} d1 \\ d2 \\ d3 \\ d4 \end{bmatrix} = \frac{1}{4} \begin{bmatrix} -1 & +1 & +1 & -1 \\ -i & -i & +i & +i \\ -i & +i & -i & +i \\ +1 & +1 & +1 & +1 \end{bmatrix} \begin{bmatrix} c1 \\ c2 \\ c3 \\ c4 \end{bmatrix} \tag{A.17}$$

A.4 Numerical modelling aspects

A.4.1 Pressure Poisson equation

As discussed in section I.1.1.1 the incompressibility constraint (eq. I.1.1) has several implications on the flow behavior, ultimately introducing the saddle point problem to the Navier Stokes (NS) equations (Le Quéré et al. [2010]). As the NS equations are to be solved for $(\boldsymbol{u}, p)$ from equations I.1.1 and I.1.2, numerical approaches often rely in a Poisson equation enforcing the incompressibility constraint through the determination of the pressure field. Generally the Poisson equation is built taking the divergence of the momentum equation I.1.2, that leads to an equation on the form:

$$\nabla^2 p = \mathscr{R}^{[P]}, \tag{A.18}$$

where $\mathscr{R}^{[P]}$ stands for a generic right hand side, resulting from the combination of the of the mass conservation equation with the specific discretization scheme adopted. In a continuous medium:

$$\mathscr{R}^{[P]} = -\rho \frac{\partial u_i}{\partial x_j}\frac{\partial u_j}{\partial x_i}, \tag{A.19}$$

and equation A.18 is necessary and sufficient to enforce the incompressibility constraint in mean and fluctuation pressure fields (Pope [2000], pg. 18-19). Nevertheless due to the saddle point problem the situation is more complicated in a discrete formulation, and the topic revised in section III.1.1.3.

A.4.2 Turbulent-Viscosity models

The turbulent/eddy viscosity hypothesis is hardly locally verified on complex flows but constitutes a powerful simplification that turned possible most of the nowadays engineering scale applications of CFD. Its success comes to the fact that it is built to capture some of the basic phenomena in interest on turbulent flows s.a. boundary and mixing layers, homogeneous decay and isotropic turbulence. In LES formulations (Section I.1.1.6) the hypothesis gains additional credibility as the Sub-Grid modeled turbulence is indeed supposed to be isotropic and homogeneous.

The eddy viscosity hypothesis is stated so the Reynolds stress tensor $\tau^{(r)}$ is modeled by introducing the turbulent kinematic viscosity ν_t:

$$\tau^{(r)}_{ij} = \frac{2}{3}\, e\, \delta_{ij} - 2\nu_t\, \overline{S}_{ij}, \qquad \text{where} \tag{A.20}$$

$$\tau^{(r)}_{ij} = \overline{u'_i u'_j}, \qquad \overline{S}_{ij} = \frac{1}{2}\left(\frac{\partial \overline{u_i}}{\partial x_j} + \frac{\partial \overline{u_j}}{\partial x_i}\right), \qquad \text{and} \qquad e = \frac{\overline{u'_k u'_k}}{2}.$$

Equation A.20 comes from analogy with the Newtonian fluid constitutive equation I.1.3, and implies that the anisotropy of the Reynolds Stress Tensor $\tau^{(r)}$ depends linearly on the symmetric part of the velocity gradient $\overline{S}$ through the scalar ν_t.

The assumption that $\tau^{(r)}$ anisotropy depends only on $\overline{S}$ means that turbulence straining history is lost with $\overline{S}$ being a local quantity. The viscous law of equation I.1.3 is generally valid because the molecular processes timescales is much smaller then the shear processes timescales, so that both phenomena are uncoupled, anisotropy history is rapidly lost and the shear stresses determined by local quantities. Being the turbulent processes timescales comparable to the mean shear timescale, the anisotropy history becomes important so that equation A.20 has no general validity.

On simple shear flows, where the velocity gradients change slowly and the turbulent production and dissipation terms are comparable in the turbulent stresses transport equations (omitted), the local gradients $\overline{S}$ characterize the strain history to which the turbulence has been subjected, so the hypothesis becomes more accurate.

Moreover it is observed that the turbulent diffusion $\tau^{(r)}$ anisotropy is usually not aligned with the molecular diffusion anisotropy $\overline{S}$ as suggested by the eddy-viscosity hypothesis on equation A.20. Being the relationship between $\tau^{(r)}$ anisotropy and $\overline{S}$ limited to a scalar, the

eddy-viscosity assumption states that both tensors have aligned principal axes, a condition hardly satisfied on many of the simplest flows. Anisotropic models can be build considering relationships with other tensors, such as the mean rate of rotation, and a greater number of scalars other then ν_t.

Keeping the hypothesis limitations in mind, its success into engineering applications is quite amazing. Having specified ν_t and e, the relationship of eq. A.20 states a most convenient form of closure where the equations I.1.7 behave in the same way, and can be similarly treated, as the Navier Stokes equations with a modified viscosity.

A.4.3 Geometric conservation law

From the mass conservation equation, one arrives in the Geometrical Conservation Law (GCL) introduced by Thomas and Lombard [1979]. A transport equation is built for the Jacobian J including only geometrical parameters of the grid. For the specific surface following coordinates defined in section III.1.1.2, J depends on the grid vertical position h:

$$\frac{\partial}{\partial t}\left(\frac{1}{J}\right) = \frac{\partial}{\partial \xi_3}\left(\frac{\partial h}{\partial t}\right). \tag{A.21}$$

Solving the equation A.21 with the same time-marching scheme as the conservation equations on a moving grid, ensures conservation in constant flows, and according to Guillard and Farhat [2000] is a sufficient condition for the whole scheme to be at least first-order time-accurate on moving meshes. Taking $\mathscr{R}^{[G]}$ as the right-hand-side of equation A.21 and applying the RK3 method, a general sub-step evolution equation is on the form:

$$J_m = J_{m-1} + \Delta t \alpha_m \mathscr{R}^{[G]}_{m-1} + \Delta t \beta_m \mathscr{R}^{[G]}_{m-2}, \tag{A.22}$$

which is solved for $\mathscr{R}^{[G]}_{m-1}$ to obtain the current grid velocity $\dot{h} = \partial h/\partial t$ that satisfies the GCL. A first order finite difference scheme is used to integrate the grid velocity, known in the first cell layer where $k = 1$, so that $\dot{h}_{k+1} = \dot{h}_k + \Delta\xi_3 \mathscr{R}^{[G]}_{m-1}$.

A key-point to this scheme is that to obtain the grid velocity in $m-1$, used to march the conservation equations to m, the grid should be known not only in the past (Grid velocity in $m-2$), but also in the current (unknown) step (Jacobian at $m-1$), and in the future (Jacobian at m). In coupled schemes where the grid depends on the LES solution, requiring for example the pressure feedback into HOS, this non-linearity requires proper considerations, further discussed in section B.2.

A.4.4 Time-marching scheme

The 3rd order Runge-Kutta (RK3) employed in the LES is the one refered as '*Method B*' in Spalart et al. [1991]: No implicit treatment is considered in viscous terms, being the method fully explicit. Consider each transport equation solved by the LES for the unknown χ, on the form:

$$\frac{\partial \chi}{\partial t} = \mathscr{R}^{[R]}(\chi), \tag{A.23}$$

so that the evolution occurs in 3 stages:

- 1: $\chi^{'} = \chi_n + \Delta t \gamma_1 \mathscr{R}_n^{[R]}$;
- 2: $\chi^{''} = \chi_n^{'} + \Delta t \left[\gamma_2 \mathscr{R}^{[R]'} + \zeta_1 \mathscr{R}_n^{[R]}\right]$;
- 3: $\chi_{n+1} = \chi_n^{''} + \Delta t \left[\gamma_3 \mathscr{R}^{[R]''} + \zeta_2 \mathscr{R}^{[R]'}\right]$;

with $\gamma_1 = 8/15$, $\gamma_2 = 5/12$, $\gamma_3 = 3/4$, $\zeta_1 = -17/60$ and $\zeta_2 = -5/12$. The sub-time steps sizes are thus: [8/15,2/15,5/15] Δt.

This method have been adapted by Sullivan et al. [2008], considering the implicit treatment of the pressure term to enforce the incompressibility constraint with the Poisson equation.

B Numerical model description, developments, and applications

B.1 Physical scaling in the LES generated neutral MABL

B.1.1 Geometrical and dynamical similarities

Recall from section I.1.2.2, that stating fully turbulent and neutral flow is respectively equivalent to consider $\boldsymbol{Re} \to \infty$ and $\boldsymbol{Ri} \to 0$ in equation I.1.29. In flat bottom cases, where gravitational forces are linear, $\boldsymbol{Fr}^{-1}\delta_{3,i}$ might be fully incorporated as a static pressure in p', and the problem's dependency in the Froude number $\boldsymbol{Fr}$ is dropped: In this canonical case the solution of I.1.29 is self-similar, scaling independently with the characteristic scales $[L_0, U_0]$. Nevertheless, the Froude Fr number is essential to describe the non-linear gravitational forces characteristic to wave-induced perturbations: Once a wave system exists, dynamical similarity is only granted for constant Fr numbers, as the solution of equation I.1.29 becomes Fr dependent.

Froude number and Wave Age Equality in Froude number is equivalent to equality in the wave-age (WA= c/u^*), which can be shown as follow. Consider the comparison of two geometrically similar (Non-dimensional ABL height $k\delta$; water depth kd and wave slope ka constant; wave lengths $\lambda_1/\lambda_2 = L_1/L_2$ with $k = 2\pi/\lambda$) models with characteristic scales $[L_1, U_1]$ and $[L_2, U_2]$. If their wave age is constant so $u_1^*/u_2^* = c_1/c_2$, and if they are dynamically similar $u_1^*/u_2^* = U_1/U_2$. The dispersion equation of those waves will give $c_1/c_2 = \sqrt{\lambda_1/\lambda_2}$ so that:

$$Fr = \frac{U_1^2}{gL_1} = \frac{U_2^2}{gL_2} \tag{B.1}$$

Numerical similarity Up to here the similarities discussed apply to a continuous medium with infinite extension in the horizontal directions, but due to the limited domains extension and discretization, numerical similarities can also determine the solution. Unless convergence is strictly achieved for space and time discretizations and domains' extension, turbulence non-linearities are such that the instantaneous disturbances due to the lack of numerical similarity is likely to be significant, and the convergence has to be seek in a statistical perspective. Space resolution-independent solutions are unfeasible in LES formulations, where the SGS model is grid dependent. The domains' extension convergence is also hardly achieved. For limited resources that obliges to focus in certain scales of interest.

Regarding the discretization, numerical dynamical similarity is achieved matching the CFL= $U\Delta t/\Delta x$ and the Peclet number $U\Delta x/\nu^{(tur)}$ (With $\nu^{(tur)} = \delta^2/t^{(tur)}$ as in section A.1.2), with time and space discretizations Δt and Δx. Matching the CFL is trivial in present time-adaptive scheme, but matching the Peclet number with the introduction of a wave propagation would require an adaptive grid re-meshing procedure currently unavailable for that task.

In the absence of buoyancy forces, the domain's vertical extension z_l is the numerical approximation of the ABL physical height δ, assuming that above δ the flow remains undisturbed and so independent from the free-surface condition. To mimic an unbounded domain in the horizontal directions one imposes periodic conditions in x_l that (as for δ) relate geometrical and dynamic similarities.

B.1.2 Systematic comparisons varying the wave age

According to section B.1.1 the dynamic similarity is trivial in flat bottom cases, but ***Fr*** dependent otherwise. So a wave bottom model, with solution given for example in non-dimensional units, might be arbitrarily scaled with length and velocity $[L_0, U_0]$, as long as the Fr number (Or alternatively the WA) is kept constant through the scaling.

The wave age changes through systematic variations in waves (Length λ) or wind (Forcing parameter $[\partial p \partial x]_0 \cdot\ z_l \sim u_0^{*2}$, see section III.2.2) conditions. Once two different wave cases are in comparison, if geometrical similarity is imposed $L_0 = \lambda$ and only one between length and velocity spaces can be set to similar magnitudes through the procedures below:

- Varying WA from changing wave lengths:
  - ◇ The wave-length ($\lambda_1 \neq \lambda_2$) is shifted; the non-dimensional wave amplitude ka, and depth kd are constant; the domain's dimensions scale with the respective λ ($L_0 = \lambda$) so $k\delta$ is constant. The Boundary layer height vary between the cases. If the ABL height is very large ($\delta >> \lambda$), or adapting $[\partial p \partial x]_0$ (c.f. section III.2), the Wind speed is possibly constant between the cases.
- Varying WA from changing wind intensity:

- ◇ One varies the imposed ($[\partial p \partial x]_0 \cdot z_l$), and keep L_0 (And λ; δ; d) constant in the solver. The Wind Speed vary between the cases.

Varying λ keeps u_0^* constant, while varying $[\partial p \partial x]_0 \cdot z_l$ keeps the heights and lengths constants. Neglecting numerical similarity discrepancies (Hardly acceptable from the discussion in B.1.1), both solutions would be similar and convertible into one another in post-processing phase as long as $\lambda \neq 0$ and WA=cte.

- Post-processing scaling to match dimensional quantities:
  - ◇ The Boundary Layer height: Setting L_0 (And λ) to match a certain δ, scaling U_0 accordingly so Fr =cte. The wave-length and the Wind speed are consequential.
  - ◇ The Wind Speed: Setting U_0 to match a certain velocity scale (e.g. u^*, u_{10} or u_∞), scaling L_0 (And λ) accordingly so Fr =cte. The wave-length and the ABL height are consequential.

The geometrical similarity constraint is problematic imposing δ/λ =cte., for once one compares or superposes two waves where $\lambda_1/\lambda_2 = 10$, it is often of no use to consider atmospheric boundary layer heights that differ by a factor of 10. Besides if $\delta \sim \lambda$, the problem is ill defined in the asymptotic young wave scenario, with the ABL vanishing when $\lambda \to 0$. The point is that, just as for the water depth in ocean waves, δ/λ might be just as important as the WA to define the problem. When different waves propagate in the ocean or in the atmosphere, the depth and the ABL height do not scale accordingly.

B.2 Review and improvement of the coupling between LES and HOS codes

The two-way coupling occurs between the Atmospheric LES, and the Oceanic HOS codes: The pressure field resolved in LES forces the HOS evolution; the free-surface position and velocities solved in HOS, act as boundary conditions and impose the grid configuration in the LES resolution. The LES evolves with an arbitrarily set (Often CFL-adaptive) time-step, and a 3rd order Runge-Kutta (RK3) time-marching scheme. The HOS considers a fully adaptive (Residual reduction) time-step, and a 4th order Runge-Kutta (RK4) time-marching scheme.

As the atmospheric perturbations evolve in smaller time-scales compared to the Ocean response, the coupling is stronger from HOS to LES: For a whole LES time-step, the HOS considers a single pressure solution and evolves during as many inner time-steps as required to converge its equations. The free-surface input from HOS on the other side, is updated in LES at each sub-step of the RK3 scheme. This is achieved by using the sub-steps sizes from the LES, as output periods in HOS-Ocean. The non-synchronous exchange between the LES and HOS solutions qualifies this strategy as a weakly coupling procedure.

The RK3 scheme advances so that in the sub-step m, the solution is known in $m-1$ and solved for m. The boundary conditions and the grid speed are so constantly required at $m-1$ with the fully explicit scheme given in section A.4.4. Nevertheless, to obtain the

grid speed according to the GCL as in section A.4.3, one also require the grid metrics to be known in the current and future steps at m and $m+1$. The grid is imposed by the HOS, and in a strongly coupled scenario is dependent on the pressure resolution at multiple HOS time-steps, between (and including) m and $m+1$.

The weakly coupling procedure relies in two aspects: (i) The pressure is sent to HOS at each global time-step, and is regarded as constant in between, where the HOS advances multiple (> 3) inner time-steps; (ii) When the pressure evolves in the future at m, a simple predictor-corrector scheme addresses the coupling non-linearity, i.e., the HOS predicts the surface at $m+1$ with the pressure at $m-1$, so that the LES may solve the pressure at m, and finally the HOS corrects its solution at $m+1$ with the updated pressure.

The aspects discussed so far are common to past and current developments, summarized in figures B.1 and B.2, respectively. But they are easier to grasp in view of the scheme in figure B.2, which strictly represents the current algorithm described in section B.2.2.

In figure B.2 (or B.1), one shall note the definitions to: the LES time-steps (it); the LES sub-steps (i_{stage}); and the HOS outer time-steps (it_{out}). In LES, the free-surface information is required twice per sub-step, in the routines responsible for marching either the grid speed, or the other unknowns,respectively depicted by the red circles or blue squares in the figures. One may also note the weak coupling concept, with LES sending the information to HOS once at each time-step. Other aspects of the algorithms depicted in the figures are revealed in the next sections.

Though it represents a conceptual simplification that better exemplifies the concepts introduced so far, current developments are just an improvement to the previous algorithm developed in Cathelain [2017], and first presented in section B.2.1.

B.2.1 Previous Coupling procedure

At each global time step, HOS freezes its solution at $i_{stage} = 0$, and advances as needed by the LES discarding intermediate solutions. The LES will ask for the HOS solution twice per sub-step: At $m+1$ for the GCL, and $m-1$ for the explicit quantities in the RK3 scheme. After performing 2 outer steps per LES sub-step, the HOS performs a 7th computation to advance its solution to the next global time-step. Each HOS computation advances from the solution in $i_{stage} = 0$ (Or $it_{out} = 1$) to the current time received from LES. Referring to figure B.1, when $it_{out} = 1$ no computation is done ($\Delta t_{out} = 0$) and HOS send the results obtained at $it_{out} = 7$. At $it_{out} = 7$ no message is sent to LES so that $it_{out} = 1$ and $it_{out} = 7$ are in fact an algorithmical split of a single outer step in HOS. Twice per sub-step the LES will ask for HOS results and wait for the solution before advancing its own computations: This may potentially block hundreds of LES processors waiting for the communication.

At each global time step Δt, the HOS performs a minimum of 6 inner steps (One per outer step, $it_{out} = 1$ and $it_{out} = 7$ degenerated), with the actual number of inner steps depending on Δt and the problem's non-linearity. Given the sub-steps sizes of the RK3 ([8/15,2/15,5/15] Δt), the HOS computes a total of 5.4 Δt per Δt in LES: 3.6 times the computation required with the algorithm presented in section B.2. A numerical imprecision is that the HOS solution at $m+1$ do not necessarily passes through m, but the introduced error shall be negligi-

ble as long as the HOS adaptive step tolerance is set sufficiently small. Both codes operate in different dimensions, and every physical quantity exchanged between them have to be scaled accordingly.

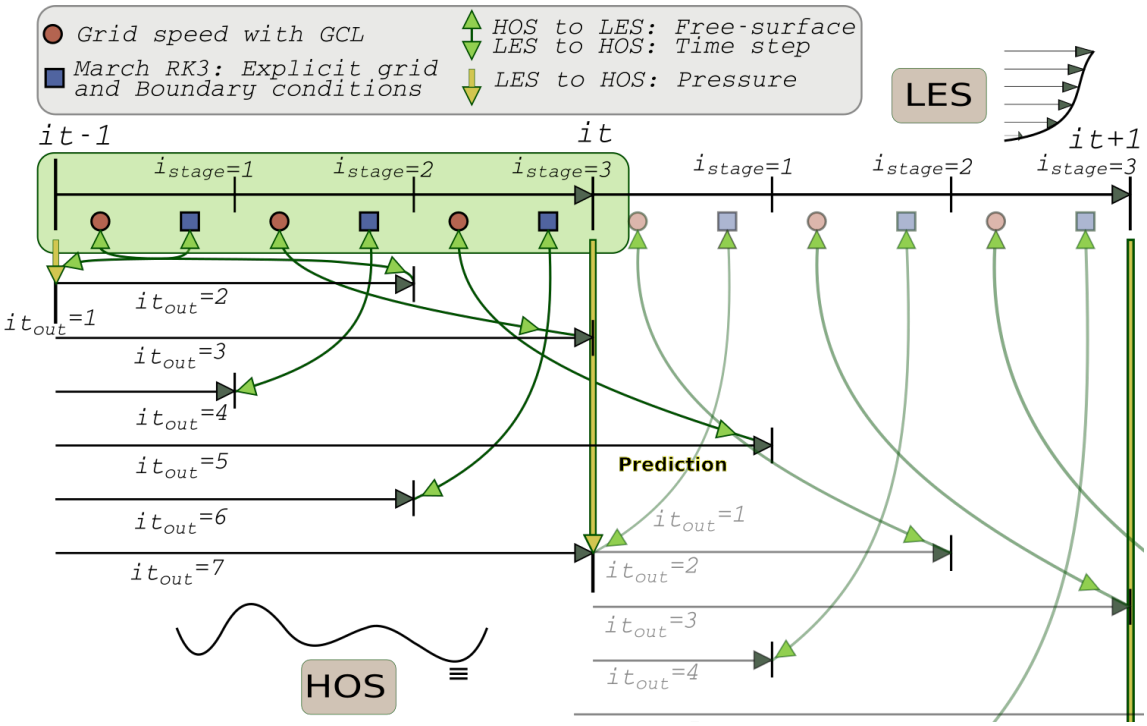

Figure B.1: Previous coupling procedure developed in Cathelain [2017].

- Loop in global time steps:
  - Loop in LES sub-steps:
    - As needed, the LES send the time-steps and wait for the HOS solution.
    - The HOS computations advances from $i_{stage} = 0$ (Or $it_{out} = 1$) to the current time received from LES.
    - Communication (And HOS outer steps computations) are done twice:
      1: Before the GCL, for $m+1$.
      2: With the boundary conditions, for $m-1$.
  - LES sends the resolved pressure to HOS.
  - The HOS advances a full time step and updates its solution.

B.2.2 Current Coupling procedure

The HOS receives the sub-step sizes and the pressure from LES once at each global time-step. Four outer steps are performed by the HOS each global time-step, being the last one a prediction (with a predicted time step). The HOS outer-steps are performed and their solution successively sent to LES: Those are non-blocking operations, independent from the LES processors availability to receive the data. The LES receives the HOS solution before

computing the grid speed: twice at the first sub-step, once at the next two. The HOS solution is stored in $m-1$, m and $m+1$, to be accessed implicitly at the GCL and explicitly otherwise. The prediction is discarded in the end of the global time step, so that correction takes it place.

At each global time step Δt, the HOS performs a minimum of 4 inner steps (One per outer step), with the actual number of inner steps depending on Δt and the non-linearity level. Given the actual sub-steps sizes of the RK3 ([8/15,2/15,5/15] Δt), the HOS will compute a total of ~ 1.5 Δt per Δt in LES. Both codes operate in same non-dimensional spaces, and no scaling is required for the exchange.

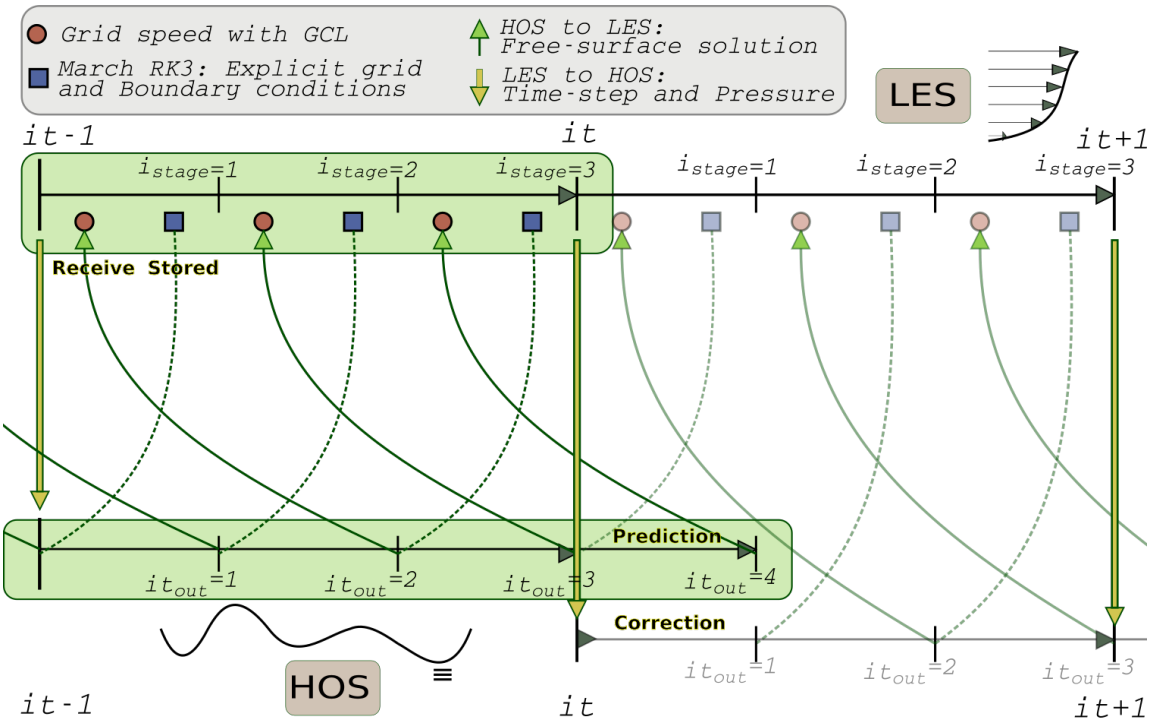

Figure B.2: Current coupling procedure, here developed.

- Loop in global time steps:
  - LES send the time step and its sub-steps to HOS.
  - HOS performs 4 'outer steps', being the last one a prediction.
  - Each HOS solution is sent sequentialy to the LES (Non-blocking operation).
  - LES Loop in sub-steps:
    - The HOS solution is received before computing the grid speed.
    - Two HOS solutions are received in the first sub-step, one otherwise.
    - The solution is stored in $m-1$, m and $m+1$ so it can be accessed implicitly in the GCL and explicitly otherwise.
  - LES sends the resolved pressure to HOS.
  - The HOS latest solution (Prediction) is discarded in both codes, giving place to correction in the next step.

B.2.3 Overview and discussion

Current development introduces significant improvements to the coupling methodology, besides the conceptual simplification and a more rigorous numerical precision. The computational gain in HOS computations is between 33% (4/6 HOS outer step) and 72% (1.5/5.4 Δt), depending whether the non-linearities and/or Δt are sufficiently small (33%), or significantly large (72%).

The MPI communication gain is computation-dependent, but potentially huge as the previous algorithm more easily admits the situation where multiple LES tasks hang-on waiting for the HOS response. The total number of MPI communications is reduced, and the number of operations per steps is also reduced with both codes operating in the same non-dimensional space.

C A mechanistic approach to Physical and Numerical experiments

C.1 An equivalent time scale for a space dependent filter

During the experimental campaign presented in part II, special attention is given to the sLiDAR volume filter effect that mitigates small scale motions in the RWS fluctuations. The sLiDAR spatial filter is approximately Gaussian, as further described and evaluated in the flat bottom experiments along section IV.3.3. One shall then note that the filter strictly applies to the space domain, and is so characterized by a single characteristic scale L_γ (and $k_\gamma = 2\pi/L_\gamma$). Though, it is observed during these sections that the filter translates into the mitigation of motions in the 1D frequency (f) dependent turbulent spectra, and moreover its effect distributes jointly in the 2D $k-w$ dependent spectra.

Considering the flat bottom atmospheric boundary layer, it is common to assume Taylor hypothesis associating a characteristic time to its equivalent length scale. So given the mean wind speed U, the filter characteristic time scale becomes $T_\gamma = L_\gamma/U$. The filter time scale defined that way indeed appears to be significant in view of the one dimensional frequency dependent spectra exploited in section IV.3.3.

The wave is introduced in the numerical experiment at section IV.3.4, where it is discussed the filter characteristic time scale associated to Wave Induced motions. Assuming these motions are following the dispersion equation, they travel with velocity $c(k) = \sqrt{(g/k)\tanh(kd)}$, and so the filter characteristic time scale becomes $T_\gamma(k) = L_\gamma/c(k)$.

Further developments outline the mathematical reasoning supporting the association of a filter characteristic time scale to its characteristic space scale, noting the dependency of this relation to the wave velocity c.

Counting on a Fourier Decomposition of a given space-time dependent signal, and considering an arbitrary wave component on the $k-w$ spectral domain that propagates with velocity $c = w/k$: To its convolution with any linear filter employed in space, corresponds

an equivalent time-dependent filter...

C.1.1 Mathematics

Consider the space time function $h(x,t)$ as the convolution of a wave component $f(x,t)$ and the filter function $g(x-x_0)$:

$$\begin{aligned} h(x,t) &= (f * g)(x,t) \\ &= \int_{-\infty}^{\infty} f(x_0,t) \cdot g(x-x_0) \mathrm{d}x_0. \end{aligned} \tag{C.1}$$

The filter function acts in space, and might be possibly Gaussian, but surely linear and symmetric:

$$\begin{aligned} f(x_0,t) &= A_1 \cos(x_0 - ct + \phi_1), \quad \text{and} \\ g(x-x_0) &= \frac{1}{\sigma\sqrt{2\pi}} \exp\left[\frac{-(x-x_0)^2}{2\sigma^2}\right] \end{aligned} \tag{C.2}$$

A propriety of such **linear** convolution h is that it integrates into the same vector space as the wave component f:

$$h(x,t) = A_2 \cos(x - ct + \phi_2), \tag{C.3}$$

*OBS: and because g is **symmetric** $\phi_1 = \phi_2$.*

So h inherits the property:

$$h(x,t) = h(x_0 + c(t-t_0), t) \tag{C.4}$$

And we may apply the variable transformation, with Jacobian:

$$\mathrm{d}x = c\,\mathrm{d}t \tag{C.5}$$

So from equation C.1:

$$\begin{aligned} h(x,t) &= (f * g)(x_0 + c(t-t_0), t) \\ &= \int_{-\infty}^{\infty} f(x,t_0)\; g[c(t-t_0)] c \mathrm{d}t_0 \end{aligned} \tag{C.6}$$

Showing the equivalency between the filter in space and time, with:

$$g[c(t-t_0)] = \frac{1}{\sigma\sqrt{2\pi}} \exp\left[\frac{-c^2\,(t-t_0)^2}{2\sigma^2}\right] \tag{C.7}$$

C.1.2 Consequence

The sLiDAR filter is physically employed in space, with standard deviation σ given as function of the gate length L_f, so $\sigma = \sigma_L = L_f/(2\sqrt{2\ln 2})$. The given reasoning supports that the equivalent time filter is such that the (time-dependent) standard deviation becomes $\sigma_T = \sigma/c$. So meaning that for a gate length L_f and the wave speed c, the characteristic filter period is $T_f = L_f/c$.

Such reasoning gives the mapping of T_f, in the $k-w$ two-dimensional spectral domain depicted in figure C.1, which is to be associated to the turbulent spectra depicted along section IV.3.4. The figure exemplifies the determination of T_f for atmospheric and WI motions, by probing T_f along the Taylor hypothesis and the dispersion relation, respectively.

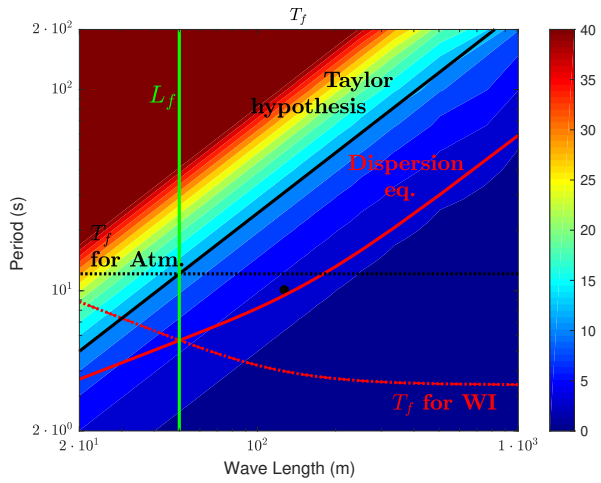

Figure C.1: Two-dimensional spectral mapping of T_f. The mean wind velocity corresponding to the Taylor hypothesis appears in black full line, and the waves velocities given by the dispersion equation appears in red full line. The filter characteristic length is L_f denoted by the green vertical line. Probing T_f along the Taylor hypothesis gives the characteristic $T_f = L_f/U$ for atmospheric motions, denoted by a black dotted line. Probing T_f along the dispersion relation gives the characteristic $T_f = L_f/c(k)$ for WI motions, denoted by a red dash-dotted line.

C.2 On the reconstruction of velocity wave-number-frequency spectra

The joint space-time distribution of turbulent correlations introduced in section IV.1, has been shown to reveal crucial aspects of the MABL, and notably some of the main differences between Atmospheric turbulence (Atm.) and Wave Induced (WI) motions inside the Wave Boundary Layer. In section IV.1.2 (Paskin et al. [2020]), it is argued that statistical models of wind resource reconstruction could improve their accuracy in the offshore environments by considering the superposition of a WI flow model, to the background Atmospheric turbulence, possibly occurring with distorted scales due to non-linear Wind-Wave interactions. It is so desired to parameterize Atm and WI motions in the MABL but first, one is required to characterize each contribution from the observations in total measured fluctuations.

In sections II.3 (For the physical experiment) and III.4 (For the numerical experiment), the 1D wave-number (k) and frequency ($f = w/2\pi$) dependent turbulent spectra reveal a partial perspective of the turbulent fluctuations, shown insufficient to allow the decomposition for arbitrary Sea-States. On the contrary, the 2D $k-w$ dependent turbulent spectra shown at the same sections reveal enough information about the Atm. and WI fluctuations, so enabling the decomposition through the partitioning algorithm described in section IV.2. Employing such decomposition, one might hope to establish simple models representing each contribution to the 2D turbulent spectra, which enables the parametrization of the total fluctuations with respect to the atmospheric and sea-state parameters. Once established, such models would also provide the segregated reconstruction of Atm. and WI components to the 2D spectra, so giving an alternative procedure for the 2D spectra partitioning previously described in section IV.2.

Nevertheless, even in flat bottom conditions, the study of the 2D $k-w$ turbulent spectra has not been addressed in the literature as much as the wave-number 1D spectra, for which the Kolmogorov hypothesis (Kolmogorov [1991], from the original of 1941) was developed as described in section I.1.1.5. There is no universally accepted model for the $k-w$ turbulent spectra in simple shear flows, and as far as the author knows, none of the existing models are sufficiently accurate to allow the proposed decomposition of the spectra as an alternative to section IV.2. So the description of the $k-w$ spectra in flat bottom conditions is the first (and only, due to the Thesis time constraint) topic revisited in present section.

The first and most explored model for the $k-w$ turbulent spectra has been proposed by Taylor [1938], stating Taylor's frozen hypothesis where turbulence evolves so slowly compared to the mean velocity U_0, that neglecting its evolution, it is advected by the mean flow as:

$$E(k,w) = E_k(k)\delta\left(k - \frac{w}{U_0}\right) = E_w(w)\delta(w - U_0 k); \tag{C.8}$$

where δ is the dirac function, and E_k and E_w the one-dimensional wave-number and frequency turbulent spectra. In the $k-w$ domain, the Taylor's hypothesis corresponds to a straight line, contrasting to the continuous distributions observed in reality, as the EDF spreads in the vicinity of this linear prediction as shown in figure C.2. The concept of spreading is exploited by Kraichnan [1964] to develop a universal model for isotropic turbulent

spectra, based on the random sweeping hypothesis, and observed to lack accuracy in the case of turbulent shear flows.

The elliptic model for space-time correlation functions of He and Zhang [2006] extends the random sweeping hypothesis (of Kraichnan [1964]) with a more general second order approximation to determine elliptical iso-contours of these correlations. Departing from the elliptical model of space-time correlations, Wilczek and Narita [2012] derive an improved second-order model for the $k-w$ turbulent spectra. A state-of-the-art review of the $k-w$ spectra models is presented in Narita [2017], and its effectiveness is exemplified for Gaussian and power-law second-order approximations, with the reconstruction based on measured first and second order spectral moments of the 2D turbulent spectra. Inspection of figure C.2b confirms the elliptical spectral shape expected from these models, to be further discussed along this section.

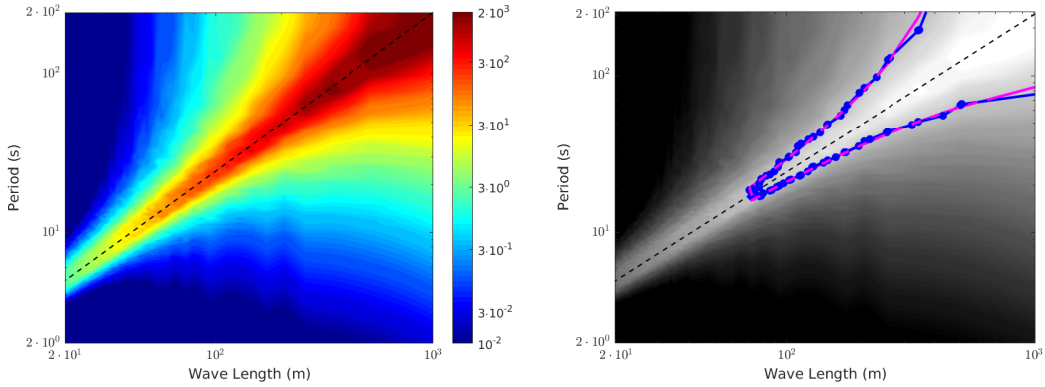

(a) 2D turbulent spectra.

(b) Fitting of an elliptical contour.

Figure C.2: Wave-number-frequency 2D turbulent spectra for Case 00 (No filter) exploited in section IV.3.3. The dashed line corresponds to the characteristic convective velocity given by the Taylor hypothesis. In (b) an elliptical model denoted by the magenta dashed line, fits to the contour given in blue full line and dots.

A methodology is build and presented below, to find an approximation functional $g(k, w, a_i)$ that can accurately reproduce the Atm. and WI parts of the observed $k-w$ spectra, in terms of an optimized set of parameters a_i. The base-line function developed and presented in section C.2.2, leads to the consistent parametrization of the spectral decay far from the Taylor hypothesis, introducing additional degrees of freedom and versatility, and thus improving the accuracy of the power law functional employed in Narita [2017]. The methodology so introduced is first exploited in section C.2.4 considering the flat bottom case of figure C.2.

C.2.1 One-dimensional base-line function

The base-line function of the proposed model is inspired from the power law (Narita [2017]) model, but we start from the rational function $A/[(w-B1)(w-B2)]$. The rational function goes to infinity approaching the roots $[B1, B2]$, requiring a penalization that limits the curve behavior in that region. The rational is then multiplied by $(1-\exp^{-\lambda\,(w-B1)(w-B2)})$, where the exponential term goes to zero more rapidly than $1/[(w-B1)(w-B2)]$ goes to infinity on the roots. Further introducing the exponents α and β as additional degrees of freedom to control the functions' decay far from the roots, the complex-valued base-line function is:

$$h(w) = A\frac{1-\exp^{-\lambda\,(w-B1)^{\alpha}(w-B2)^{\beta}}}{(w-B1)^{\alpha}(w-B2)^{\beta}}. \tag{C.9}$$

The parameter λ has to be big enough for the penalization to vanish far away from the roots, but not so big that it introduces numerical issues. Most important, it will determine the function's behavior close to the roots. If:

$$\begin{aligned} &B1 = w_0 - 0.5\,w_1, \qquad \text{and} \qquad B1 = w_0 + 0.5\,w_2, \qquad \text{so} \\ &\lim_{w\to w_0} h(w) = A_p, \qquad \text{is true if} \end{aligned} \tag{C.10}$$

$$\begin{aligned} &\lambda = -\epsilon\,c_\epsilon\,(-w_1)^{-\alpha}\,(w_2)^{-\beta} \qquad \text{with} \\ &\epsilon = \log\left[\frac{A\,c_\epsilon}{A\,c_\epsilon - A_p\,(-w_1)^{\alpha}\,(w_2)^{\beta}}\right], \qquad \text{and} \qquad c_\epsilon = 2^{\alpha+\beta}. \end{aligned} \tag{C.11}$$

The magnitude of the base-line function is exemplified in figure C.3 for multiple combinations of the parameters $[A,\ w_0,\ w_1,\ w_2,\ A_p,\ \alpha,\ \beta]$. A local maximum occurs in the vicinity of w_0 at $0.5(B1+B2)$. The maximum value is constrained by A_p as seen in figure C.3a.

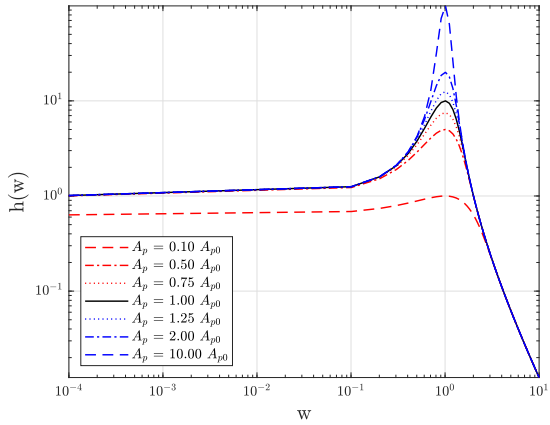

(a) Varying A_p.

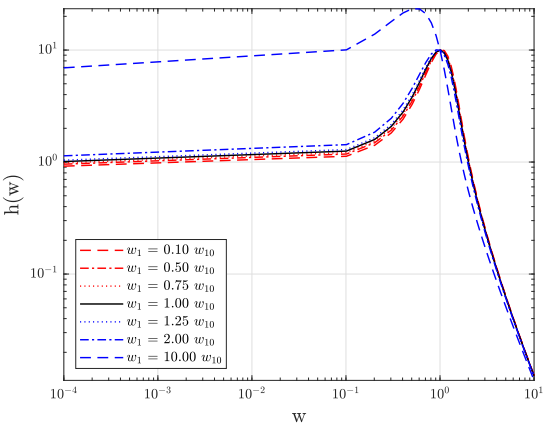

(b) Varying w_1.

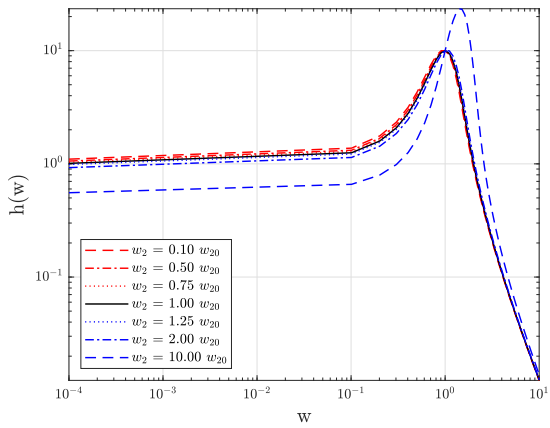

(c) Varying w_2.

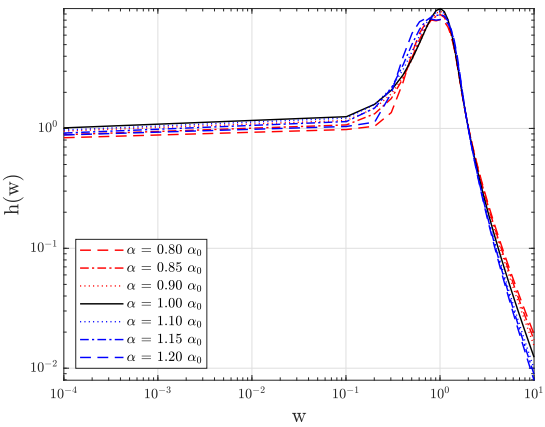

(d) Varying α.

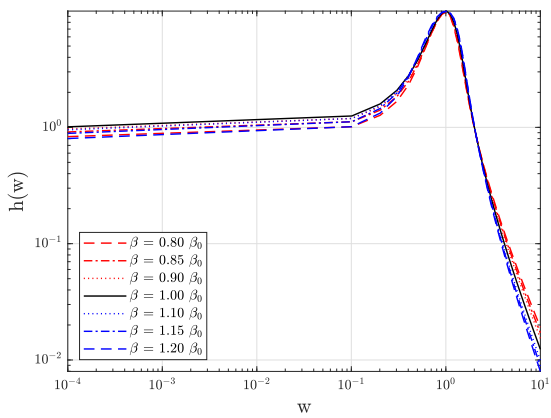

(e) Varying β.

Figure C.3: The base-line function of the proposed model, defined in equation C.9; Multiple deviations from $[A,\ w_0,\ w_1,\ w_2, \lambda,\ \alpha,\ \beta] \leftrightarrow [A = 1,\ w_0 = 1,\ w_{10} = 0.2,\ w_{20} = 0.2,\ A_p = 10,\ \alpha_0 = 1,\ \beta_0 = 1]$.

A first comparison between the proposed base-line function and the functionals exploited by Narita [2017] in the context of an elliptical model is shown in figure C.4. The Gaussian $A\ \exp[-0.5\ (w - w_0)^2/k^2]$ and Power law functions $A\ [(w - w_0)^2]^{-k}$ are fitted to $h(w)$ given by three sets of parameters: $[A_0 = 1,\ w_0 = 1,\ w_{10} = 0.2,\ w_{20} = 0.2,\ \alpha_0 = 1,\ \beta_0 = 1]$, with A_p either equals to 10, 10^2 or 10^5. While the Gaussian function is highly compromised

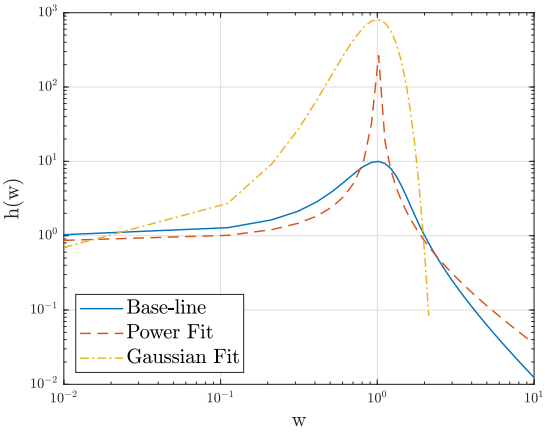

(a) $A_p = 10$

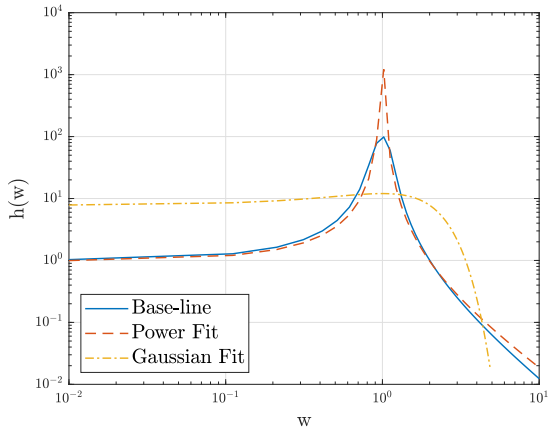

(b) $A_p = 10^2$

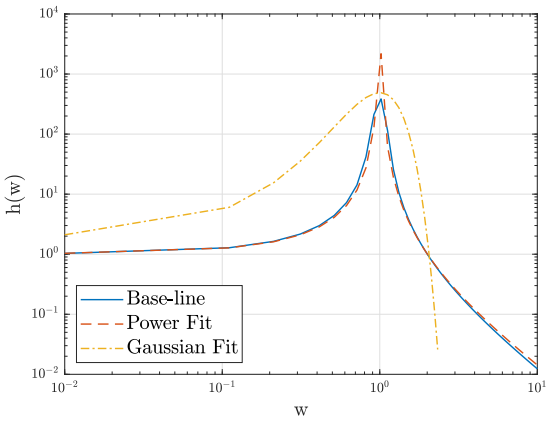

(c) $A_p = 10^5$

Figure C.4: The base-line function of the proposed model. Defined in equation C.9 with $[A_0 = 1,\ w_0 = 1,\ w_{10} = 0.2,\ w_{20} = 0.2,\ \alpha_0 = 1,\ \beta_0 = 1]$, and varied A_p. Fitted Gaussian $A\ \exp[-0.5\ (x - x0)^2/k^2]$ and Power law $A\ [(x - x0)^2]^{-k}$ for comparison with Narita [2017].

through a very bad behavior with increasing w, the power law has a limited deviation in the vicinity of w_0. Indeed, the base-line function degenerates to this power law function when $\alpha = \beta$ and $B2 = B1 \rightarrow w_0$, in which case:

$$h_{pow}(w) \rightarrow A \frac{1 - \exp^{-\lambda\ [(w - w_0)^2]^{\alpha/2}}}{[(w - w_0)^2]^{\alpha/2}}. \tag{C.12}$$

The power law $h_{pow}(w)$ will be further exploited imposing $\alpha = \beta$ and $w_1 = w_2 = 10^{-6}$ in equation C.11, to obtain the value of λ that closes equation C.12.

C.2.2 Two-dimensional approximation function

The 2D approximation function $g(k, w, a_i)$ is defined in terms of the base-line function $h(w)$, with the parameters $[A,\ w_1,\ w_2, \alpha,\ \beta]$ depending in the optimized set of parameters

a_i, and k. The presented cases consider a maximum of 11 parameters $a_{i=1..11}$, with the variables in $h(w)$ polynomial defined as:

$$\begin{aligned} A &= E_k(k)\, L_w \quad (a_1 + a_2\, k + a_3\, k^2), \\ w_1 &= L_k \quad (a_4 + a_5\, k), \\ w_2 &= L_k \quad (a_6 + a_7\, k), \\ \alpha &= (a_8 + a_9\, k + a_{12}\, k^2), \quad \text{and} \\ \beta &= (a_{10} + a_{11}\, k), \end{aligned} \tag{C.13}$$

where $E_k(k)$ is the wave-number dependent spectra, and $L_w = 3.212\ \pi/Hz$ the normalizing scale used so that $a_{i=1..11}$ are non-dimensional. The polynomial terms in C.12 might be independently suppressed reducing the total degree of freedom of the model. When a_6 and a_7 are suppressed, $w_2 = w_1$; and when $[a_{10}, a_{11}]$ are suppressed, $\beta = \alpha$. The methodology admits an arbitrary number of degrees of freedom, but 11 are here exploited.

The $E_k(k)$, $A_p(k)$ and $w_0(k)$ are necessary to close the model, and are directly obtained from the spectra to guide the optimization. These are case-dependent and shall be described for each application.

C.2.3 Optimization Algorithm

An evolutionary algorithm is developed to perform the global search procedure. A population of n_p, initially identical individuals, is characterized by their n_t coefficients (a_{ij}, i = $1..n_p$, j = $1..n_t$). Each coefficient a_{ij} is linked to a random, Gaussian distributed with standard deviation 0.1, mutation factor ($-0.5 < m_{ij} < 0.5$). An auxiliary array o_{ij}, initially set to unity, indicates whether a mutation is active ($o_{ij} = 1$) or dormant ($o_{ij} = 0$). Depending on the quality of the first solution and population size, multiple randomly selected mutation factors are set to zero ($m_{ij} = 0.0$; $o_{ij} = 0$) before evolution takes place. The factor γ_g control the step size and is usually set to one.

Evolution occurs, looping successively in n_g generations:

- If $o_{ij} = 1$: Update $a_{ij} = a_{ij}\ (1 + \gamma_g\ m_{ij})$.
- Fitness: the log-RMS$_e$ (Defined in section C.2.3) is stored for each individual.
- Selection: The individuals are ordered in ascendance of their log-RMS$_e$.
- Reproduction: Mating occurs between each consecutive pair of parents. Each pair of parents generate $n_o = 2$ pair of offsprings. Only the first n_p/n_o individuals will thus reproduce. One pair of children is submitted to crossover and another to mutation. The crossover and mutation processes occur on the parameter $j = r$, where $1 \le r \le n_t$ is a uniformly distributed random integer:
    - o Crossover: Generate a random integer r; Exchange m_{ir} and o_{ir} between the parents, resulting in a pair of offsprings.

- o Mutation: For each parent generate a random integer r; Generate a new random (Gaussian distributed) number for $-0.5 < m_{ir} < 0.5$ and set $o_{ir} = 1$ as the parents become offsprings.

The error function The Round-Mean-Squared error (RMS_e) is usually considered as the optimizing value function, but as one usually prefers to graphically examine $E(k, w)$ in log space, also the numerical procedure is found to be better behaved in terms of the so defined log-RMS_e (χ):

$$\chi = \sqrt{\int\int \phi(k,w)\ \left\{\log[E(k,w)] - \log[g(k,w,a_i)]\right\}^2 d\log(k)\ d\log(w)}, \tag{C.14}$$

where $\phi(k, w)$ is a generic weighting function.

C.2.4 The reconstruction of Atm. Turbulent flow in Neutral Flat ABLs

The approximation function $g(k, w, a_i)$ is fitted to the $E(k, w)$ spectra in 4 different forms, considered in this section as different specifications of equation C.12, with optimized parameters given in table C.1. The fitting error log-RMS_e for each test case is also presented in the table. The power law is referred as Case01.Exp-n6 and defined with 6 degrees of freedom (dof); The base-line model is further explored as Case01.Bas-(n3,n5,n7), considering (3,5,7) dof. The dormant parameters appear in red and the active ones in blue, in table C.1.

Table C.1: Optimized values for the parameters determining the approximated functions with four different sets (Cases) of different degrees of freedom. Fitting error log-RMS_e for each test case given in the last row.

	Case01.Exp.n6	**Case01.Bas.n3**	**Case01.Bas.n5**	**Case01.Bas.n7**
a_1	3.263e-04	3.554e-04	2.396e-04	2.624e-04
a_2	6.085e-06	0	0	0
a_3	3.982e-05	0	0	0
a_4	1.000e-06	0	7.463e-02	6.186e-02
a_5	0	9.386e-02	1.116e-01	9.438e-02
a_6	a_4	0	a_4	6.939e-02
a_7	0	a_5	a_5	1.273e-01
a_8	1.187e+00	1.259e+00	7.730e-01	7.978e-01
a_9	5.739e-02	0	0	0
a_{10}	a_8	a_8	2.563e+00	2.521e+00
a_{11}	a_9	0	0	0
a_{12}	-1.339e-02	0	0	0
log-RMS_e	1.46	0.90	0.46	0.31

The wave-number dependent spectra is obtained from the integration of $E(k, w)$; the peak line $w_0(k) = U\ k$ is taken from Taylor's hypothesis; and the $A_p(k)$ vector interpolated from the spectra so $A_p(k) = E(k, w_0(k))$. The vectors $E(k, w)$ and $A_p(k)$ are shown in figure C.5, and $w_0(k)$ is traced as a dotted line in the 2D spectra that follow next. The target spectra $E(k, w)$ is shown in figure C.6a, and the approximation functions $g(k, w, a_i)$ (Parameters given in table C.1) shown between figures C.6b and C.6e. The power law function behaves reasonably well, but even with only 3 dof the non-deprecated base-line model perform better, with the log-RMS$_e$ diminishing of 39% between Cases Exp-n6 and Bas-n3. With additional 2 dof, the gain in log-RMS$_e$ between Bas-n3 and Bas-n5 is 49% (69% with respect to Exp-n6). The fitted spectra behave particularly well in figures C.6d and C.6e, where the log-RMS$_e$ gain between Bas-n5 and Bas-n7 is of 33%.

The error distribution (log[$g(k, w)$]-log[$E(k, w)$]) is shown in figure C.7. The non-symmetrical error distribution occurs when symmetrical functionals of g are prescribed in Cases Exp-n6 and Bas-n3. Once g becomes assymmetrical the error tends to get symmetrical in figures C.7c and C.7d.

The main advantages of the baseline-function with respect to its degenerated power law version are: The spectra broadening close to the peak line; the asymmetrical form of the approximation function; the high versatility to raise the total number of dof considerably improving the solution. The power law introduced through the degeneration of the base-line function benefits from the penalization of equation C.11, that induces g to approximately match E instead of going to infinity in w_0.

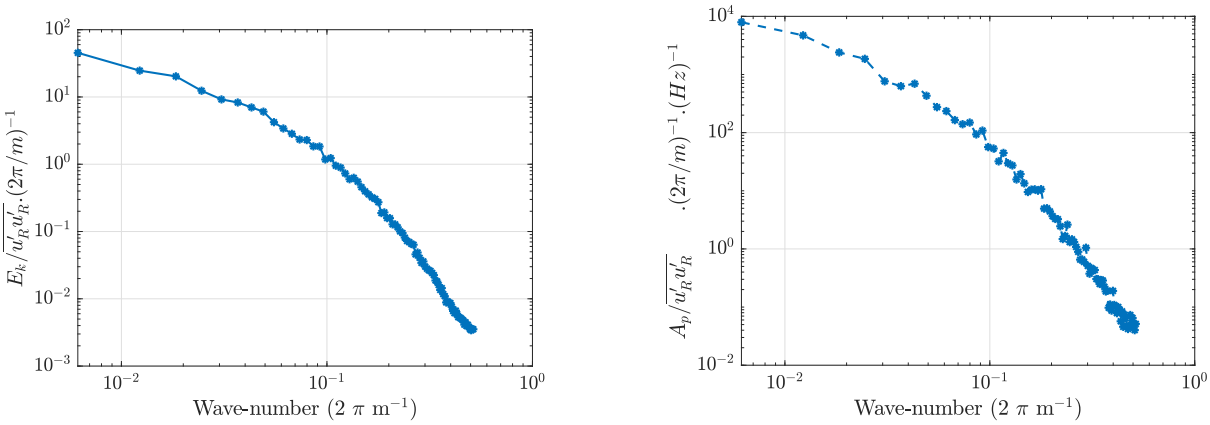

(a) $E_k(k)$.

(b) $A_p(k)$.

Figure C.5: Wave-number spectrum E_k and the peak value $A_p = E(k, w_0(k))$.

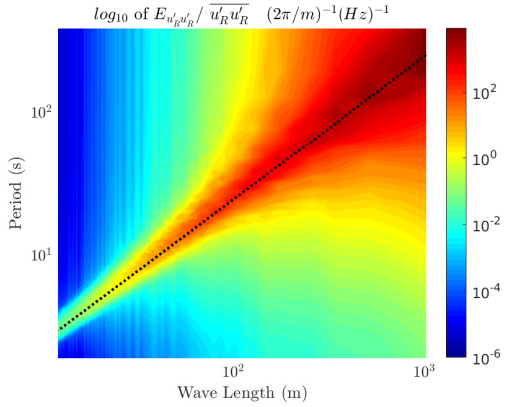

(a) Target spectra $E(k, w)$.

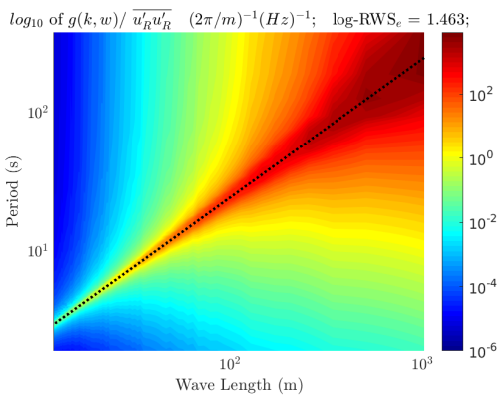

(b) $g(k, w)$ for Case Exp-n6.

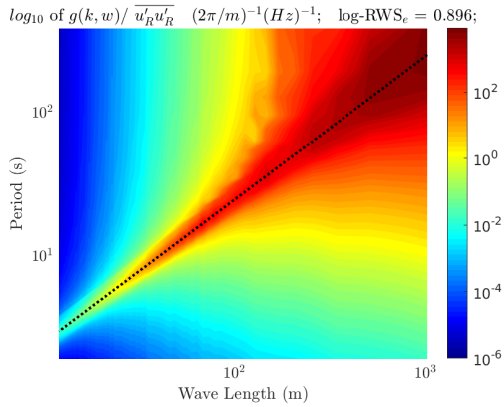

(c) $g(k, w)$ for Case Bas-n3.

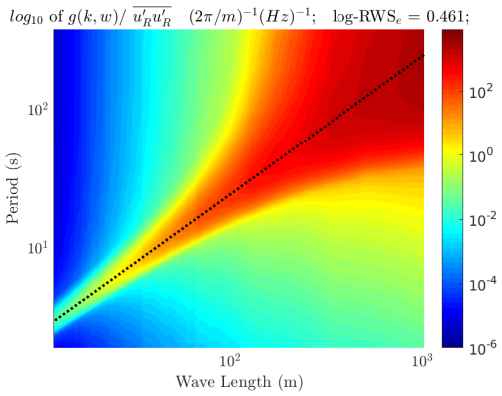

(d) $g(k, w)$ for Case Bas-n5.

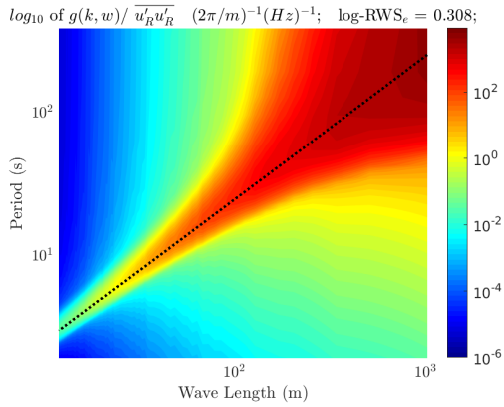

(e) $g(k, w)$ for Case Bas-n7.

Figure C.6: 2d spectra $E(k, w)$ and four fitting functions $g(k, w)$ defined in table C.1.

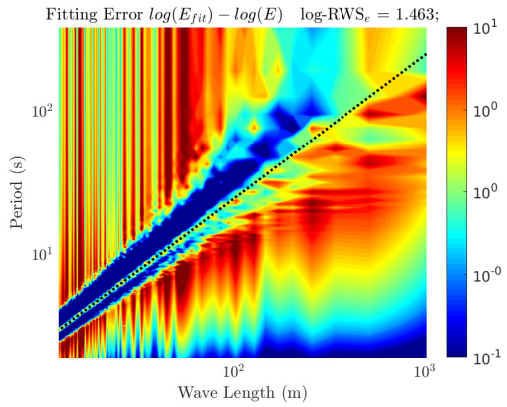

(a) Fit error for Case Exp-n6.

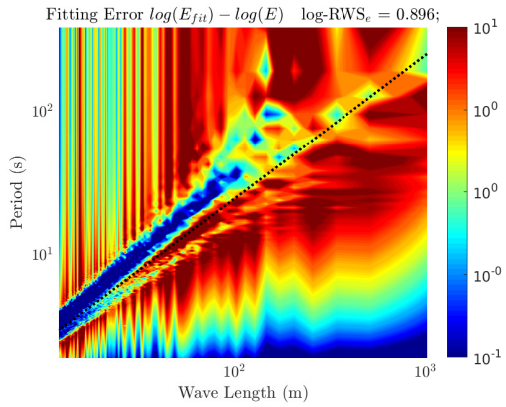

(b) Fit error for Case Bas-n3.

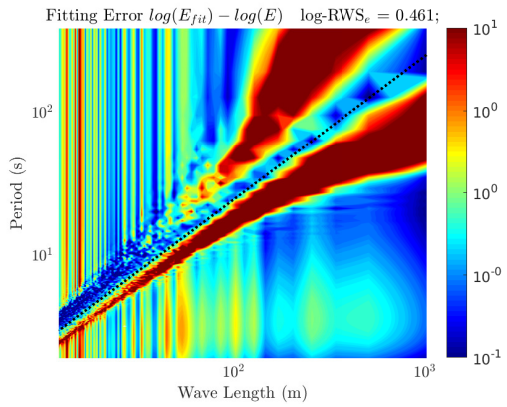

(c) Fit error for Case Bas-n5.

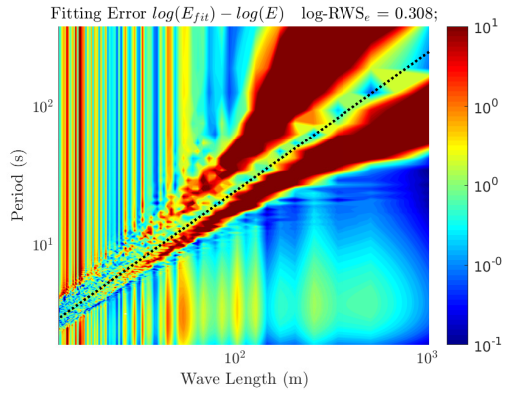

(d) Fit error for Case Bas-n7.

Figure C.7: Fitting error distribution (log[$g(k,w)$]-log[$E(k,w)$]) for the functions $g(k,w)$ defined in table C.1.

C.2.5 Overview and discussion

Unfortunately the PhD time and scope constraints impose the end of current section at this point. The WI contributions to the turbulent spectra discussed in section IV.3, require specific approximation functions to be built for each test case (Regular wave, 1D, and 2D Irregular Sea-states), which are not sufficiently matured to be shared yet. Also the 2D spectra measured during the experimental campaign is still under study. Considering that the elliptic pattern of the spectral contours is broken, probably due to the buoyancy forces not considered in the numerical case, according to the discussion in section IV.3.5. So, present section is finally limited to the numerical flat bottom case scenario, and provides a consistent basis to further developments.

The state-of-the-art $k-w$ turbulent spectra models are revisited, and the most satisfactory reconstruction is obtained employing a power law approximation function. A generic procedure is developed around the base-line function $h(w)$, that provides consistent approximations of the w profiles at a given wave-number. The base-line function degenerates into a power law approximation function, submitted to a penalization procedure that imposes $g(k,w) \sim E(k,w)$, instead of $g(k,w) \to \infty$ at the roots $w = w_0(k)$. Besides and contrary to the power law, the base-line function defined from a quadratic rational equation

also admits non-symmetrical approximations to the 2D spectra, through the specification of additional and important degrees of freedom, that effectively enhance the versatility of $h(w)$.

The whole procedure admits an arbitrary number of degrees of freedom. Contrary to local derivative-based optimization methods, the genetic algorithm here presented can be easily adapted to other functionals, rather then the ones presented hereby: It has been used, for example, to fit the elliptical contour in figure C.2, modifying the method exclusively regarding the computation of the approximation function values. The global optimization procedure also admits an arbitrary level of non-linearity in the approximation, and arbitrary ill defined initial conditions as long as the optimization parameters are set accordingly.

Four approximation functions are compared, with different levels of degrees of freedom (dof): 3; 5; 6; 7. The reference case refers to the degenerated power law function with 6 dof. Even with only 3 dof the non-degenerated base-line function performs better than the power law, and the fitting quality is considerably increased with 5 or 7 dof.

Titre : Sur l'interaction entre la houle et la couche limite atmosphérique : Une approche phénoménologique combinant des mesures de terrain et des simulations de haute fidélité.

Mot clés : environnement offshore, couche limite atmosphérique, turbulence, interactions vent-vagues, Simulation des grandes échelles, Lidar météorologique

Résumé : Dans les zones côtières, l'industrie de l'énergie éolienne migre vers l'environnement marin, où de vastes espaces sont encore disponibles avec des conditions de vent plus fort et mieux contrôlé. L'environnement marin impose de nouveaux défis à une industrie éolienne pourtant bien établie. Il est impératif de prédire et de décrire avec précision la ressource éolienne en mer afin de concevoir des solutions techniques rentables. L'écoulement concerné est caractérisé par une couche limite atmosphérique (CLA), turbulente, où la dynamique de l'océan modifie considérablement l'écoulement atmosphérique par une capacité thermique plus élevée, et par des interactions vent-vagues complexes, importantes dans des situations assez courantes.

Cette thèse passe en revue et étend les connaissances actuelles concernant les interactions vent-vagues dans la partie inférieure de la CLA Marine (CLAM), où elles peuvent être importantes pour la caractérisation de la ressource éolienne. La CLAM est étudiée par des expériences physiques et numériques, afin de révéler le rôle des mouvements Induits par les Vagues (IV) transférés de la mer vers l'atmosphère. Grâce à l'utilisation d'expériences physiques et numériques complémentaires, de nouvelles perspectives sur les processus d'interaction vent-vague sont obtenues. (...)

Title: On the interaction of fast traveling Ocean Waves and the Atmospheric Boundary Layer: A Mechanistic Approach combining Field Measurements and High-fidelity Simulations

Keywords: offshore environment, atmospheric boundary layer, turbulence, wind-wave interactions, large eddy simulation, remote sensing

Abstract: In coastal areas, the wind energy industry migrates to the offshore environment, where huge spaces are still available in stronger and better behaved wind conditions. The offshore environment imposes new challenges to a well established wind energy industry. It is imperative to accurately predict and describe the offshore wind resource in order to design cost efficient solutions. The concerned flow is characterized by a turbulent Atmospheric Boundary Layer (ABL) where the ocean's dynamics significantly alter the atmospheric flow through higher heat capacity and complex wind-wave interactions important in fairly common situations.

So this Thesis reviews and extends the current knowledge regarding Wind-Wave interactions in the lower part of the Marine ABL (MABL), where they are possibly significant in the characterization of the wind resource. The MABL is investigated through physical and numerical experiments, to reveal the role of Wave Induced (WI) motions transferred from the sea into the atmosphere. Thanks to the use of complementary physical and numerical experiments, new insights on the wind-wave interaction processes are obtained. (...)